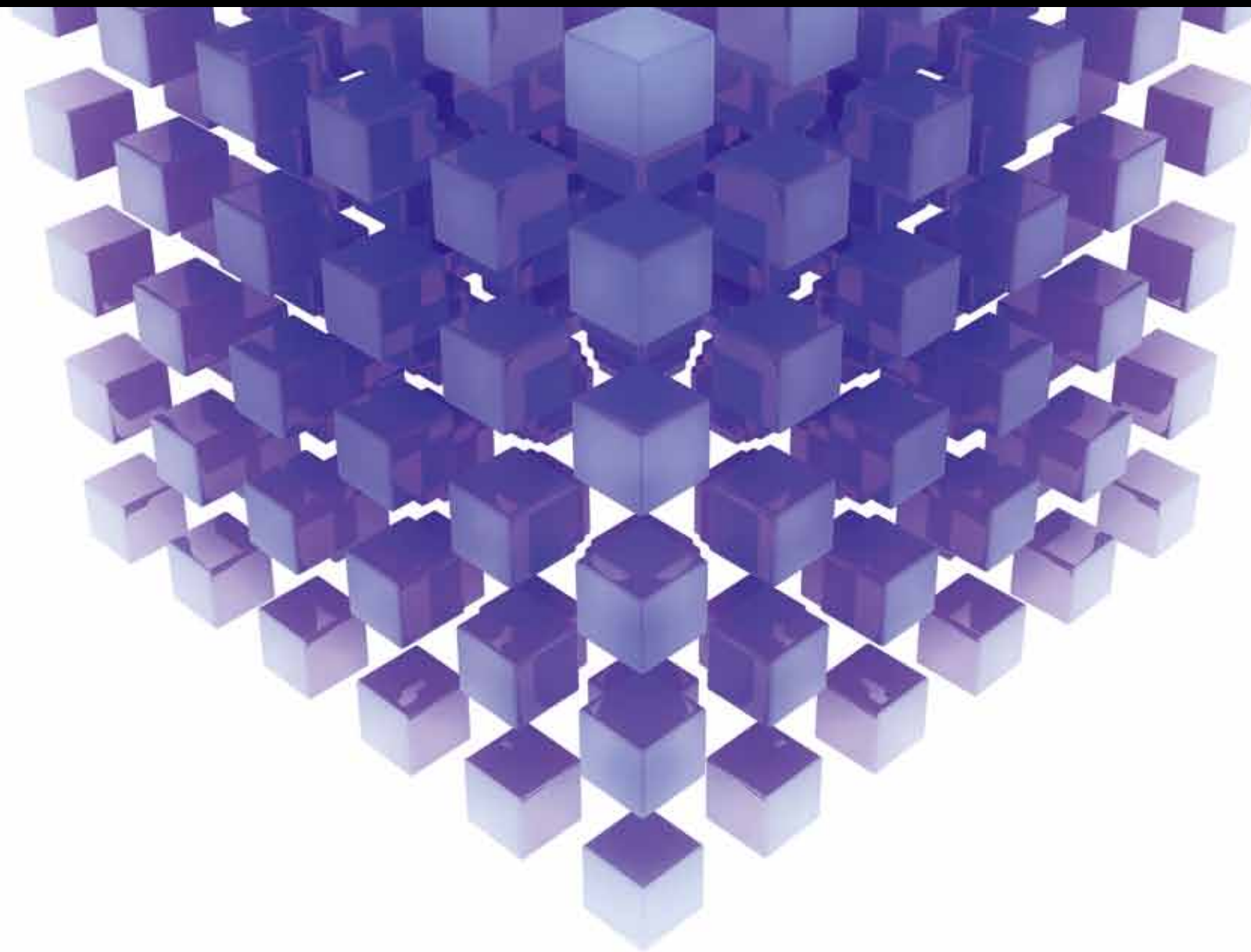


MATHEMATICAL PROBLEMS IN ENGINEERING

# MATHEMATICAL MODELING of HEAT AND MASS TRANSFER in ENERGY SCIENCE AND ENGINEERING

GUEST EDITORS: ZHIJUN ZHANG, HUA-SHU DOU, IRENEUSZ ZBICINSKI, ZHONGHUA WU,  
AND JUN LIU





---

# **Mathematical Modeling of Heat and Mass Transfer in Energy Science and Engineering**



Mathematical Problems in Engineering

---

# **Mathematical Modeling of Heat and Mass Transfer in Energy Science and Engineering**

Guest Editors: Zhijun Zhang, Hua-Shu Dou,  
Ireneusz Zbicinski, Zhonghua Wu, and JunLiu



---

Copyright © 2013 Hindawi Publishing Corporation. All rights reserved.

This is a special issue published in “Mathematical Problems in Engineering.” All articles are open access articles distributed under the Creative Commons Attribution License, which permits unrestricted use, distribution, and reproduction in any medium, provided the original work is properly cited.

## Editorial Board

Mohamed Abd El Aziz, Egypt  
E. M. Abdel-Rahman, Canada  
Rashid K. Abu Al-Rub, USA  
Sarp Adali, South Africa  
Salvatore Alfonzetti, Italy  
Igor Andrianov, Germany  
Sebastian Anita, Romania  
W. Assawinchaichote, Thailand  
Erwei Bai, USA  
Ezzat G. Bakhoun, USA  
José Manoel Balthazar, Brazil  
Rasajit Kumar Bera, India  
Jonathan N. Blakely, USA  
Stefano Boccaletti, Spain  
Stephane P.A. Bordas, USA  
Daniela Boso, Italy  
M. Boutayeb, France  
Michael J. Brennan, UK  
Salvatore Caddemi, Italy  
Piermarco Cannarsa, Italy  
Jose E. Capilla, Spain  
Carlo Cattani, Italy  
Marcelo M. Cavalcanti, Brazil  
Diego J. Celentano, Chile  
Mohammed Chadli, France  
Arindam Chakraborty, USA  
Yong-Kui Chang, China  
Michael J. Chappell, UK  
Kui Fu Chen, China  
Xinkai Chen, Japan  
Kue-Hong Chen, Taiwan  
Jyh-Horng Chou, Taiwan  
Slim Choura, Tunisia  
Cesar Cruz-Hernandez, Mexico  
Swagatam Das, India  
Filippo de Monte, Italy  
Antonio Desimone, Italy  
Yannis Dimakopoulos, Greece  
Baocang Ding, China  
Joao B. R. Do Val, Brazil  
Daoyi Dong, Australia  
B. Dubey, India  
Horst Ecker, Austria  
M. Onder Efe, Turkey  
Elmetwally Elabbasy, Egypt

A. Elías-Zúñiga, Mexico  
Anders Eriksson, Sweden  
Vedat S. Erturk, Turkey  
Moez Feki, Tunisia  
Ricardo Femat, Mexico  
R. A. Fontes Valente, Portugal  
C. R. Fuerte-Esquivel, Mexico  
Zoran Gajic, USA  
Ugo Galvanetto, Italy  
Furong Gao, Hong Kong  
Xin-Lin Gao, USA  
Behrouz Gatmiri, Iran  
Oleg V. Gendelman, Israel  
Didier Georges, France  
Paulo B. Gonçalves, Brazil  
Oded Gottlieb, Israel  
Fabrizio Greco, Italy  
Quang Phuc Ha, Australia  
M. R. Hajj, USA  
Tony Sheu Wen Hann, Taiwan  
Thomas Hanne, Switzerland  
K. (Stevanovic) Hedrih, Serbia  
M.I. Herreros, Spain  
Wei-Chiang Hong, Taiwan  
Jaromir Horacek, Czech Republic  
Huabing Huang, China  
Chuangxia Huang, China  
Gordon Huang, Canada  
Yi Feng Hung, Taiwan  
Hai-Feng Huo, China  
Asier Ibeas, Spain  
Anuar Ishak, Malaysia  
Reza Jazar, Australia  
Zhijian Ji, China  
Jun Jiang, China  
J. J. Judice, Portugal  
Tadeusz Kaczorek, Poland  
Tamas Kalmar-Nagy, USA  
Tomasz Kapitaniak, Poland  
Hamid Reza Karimi, Norway  
Metin O. Kaya, Turkey  
Nikolaos Kazantzis, USA  
Farzad Khani, Iran  
K. Krabbenhoft, Australia  
Ren-Jieh Kuo, Taiwan

Jurgen Kurths, Germany  
Claude Lamarque, France  
Usik Lee, Korea  
Marek Lefik, Poland  
Stefano Lenci, Italy  
R. Lewandowski, Poland  
Shanling Li, Canada  
Ming Li, China  
Jian Li, China  
Shihua Li, China  
Teh-Lu Liao, Taiwan  
Panos Liatsis, UK  
Shueei M. Lin, Taiwan  
Yi-Kuei Lin, Taiwan  
Jui-Sheng Lin, Taiwan  
Yuji Liu, China  
Wanquan Liu, Australia  
Bin Liu, Australia  
Paolo Lonetti, Italy  
V. Loukopoulos, Greece  
Junguo Lu, China  
Chien-Yu Lu, Taiwan  
Alexei Mailybaev, Brazil  
Manoranjan K. Maiti, India  
Oluwole Makinde, South Africa  
Rafael Martinez-Guerra, Mexico  
Driss Mehdi, France  
Roderick Melnik, Canada  
Xinzhu Meng, China  
Yuri V. Mikhlin, Ukraine  
Gradimir Milovanovic, Serbia  
E. Momoniat, South Africa  
Trung Nguyen Thoi, Vietnam  
Hung Nguyen-Xuan, Vietnam  
Ben T. Nohara, Japan  
Sotiris K. Ntouyas, Greece  
Gerard Olivar, Colombia  
Claudio Padra, Argentina  
Bijaya Ketan Panigrahi, India  
Francesco Pellicano, Italy  
Matjaz Perc, Slovenia  
Vu Ngoc Phat, Vietnam  
Maria do Rosário Pinho, Portugal  
A. Pogromsky, The Netherlands  
Seppo Pohjolainen, Finland

Stanislav Potapenko, Canada  
Sergio Preidikman, USA  
Carsten Proppe, Germany  
Hector Puebla, Mexico  
Justo Puerto, Spain  
Dane Quinn, USA  
Kumbakonam R. Rajagopal, USA  
Gianluca Ranzi, Australia  
Sivaguru Ravindran, USA  
G. Rega, Italy  
Pedro Ribeiro, Portugal  
J. Rodellar, Spain  
Rosana Rodriguez-Lopez, Spain  
Alejandro J. Rodriguez-Luis, Spain  
Hamid Ronagh, Australia  
Carla Roque, Portugal  
Rubén Ruiz García, Spain  
Manouchehr Salehi, Iran  
Miguel A. F. Sanjuán, Spain  
Ilmar Ferreira Santos, Denmark  
Nickolas S. Sapidis, Greece  
Evangelos J. Sapountzakis, Greece  
Bozidar Sarler, Slovenia  
Andrey V. Savkin, Australia  
Massimo Scalia, Italy  
Mohamed A. Seddeek, Egypt  
Alexander P. Seyranian, Russia  
Leonid Shaikhet, Ukraine  
Cheng Shao, China

Bo Shen, Germany  
Jian-Jun Shu, Singapore  
Zhan Shu, UK  
Dan Simon, USA  
Luciano Simoni, Italy  
Grigori M. Sisoiev, UK  
Christos H. Skiadas, Greece  
Davide Spinello, Canada  
Sri Sridharan, USA  
Rolf Stenberg, Finland  
Changyin Sun, China  
Jitao Sun, China  
Xi-Ming Sun, China  
Andrzej Swierniak, Poland  
Yang Tang, Germany  
Allen Tannenbaum, USA  
Cristian Toma, Romania  
Irina N. Trendafilova, UK  
Alberto Trevisani, Italy  
Jung-Fa Tsai, Taiwan  
Kuppalapalle Vajravelu, USA  
Victoria Vampa, Argentina  
Josep Vehi, Spain  
Stefano Vidoli, Italy  
Xiaojun Wang, China  
Dan Wang, China  
Youqing Wang, China  
Yongqi Wang, Germany  
Cheng C. Wang, Taiwan

Moran Wang, China  
Yijing Wang, China  
Gerhard-Wilhelm Weber, Turkey  
J. A. S. Witteveen, The Netherlands  
Kwok-Wo Wong, Hong Kong  
Ligang Wu, China  
Zhengguang Wu, China  
Gongnan Xie, China  
Wang Xing-yuan, China  
Xi Frank Xu, China  
Xuping Xu, USA  
Jun-Juh Yan, Taiwan  
Xing-Gang Yan, UK  
Suh-Yuh Yang, Taiwan  
Mahmoud T. Yassen, Egypt  
Mohammad I. Younis, USA  
Bo Yu, China  
Huang Yuan, Germany  
S.P. Yung, Hong Kong  
Ion Zaballa, Spain  
A. M. Zenkour, Saudi Arabia  
Jianming Zhan, China  
Xu Zhang, China  
Yingwei Zhang, China  
Lu Zhen, China  
Liancun Zheng, China  
Jian Guo Zhou, UK  
Zexuan Zhu, China  
Mustapha Zidi, France

**Mathematical Modeling of Heat and Mass Transfer in Energy Science and Engineering**, Zhijun Zhang, Hua-Shu Dou, Ireneusz Zbicinski, Zhonghua Wu, and Jun Liu  
Volume 2013, Article ID 241646, 3 pages

**A Linear Stability Analysis of Thermal Convection in a Fluid Layer with Simultaneous Rotation and Magnetic Field Acting in Different Directions**, Ruben Avila and Ares Cabello  
Volume 2013, Article ID 236901, 15 pages

**Estimation of Wellbore and Formation Temperatures during the Drilling Process under Lost Circulation Conditions**, Mou Yang, Yingfeng Meng, Gao Li, Yongjie Li, Ying Chen, Xiangyang Zhao, and Hongtao Li  
Volume 2013, Article ID 579091, 11 pages

**The Instability of an Electrohydrodynamic Viscous Liquid Micro-Cylinder Buried in a Porous Medium: Effect of Thermosolutal Marangoni Convection**, Galal M. Moatimid and Mohamed A. Hassan  
Volume 2013, Article ID 416562, 14 pages

**3D Model-Based Simulation Analysis of Energy Consumption in Hot Air Drying of Corn Kernels**, Shiwei Zhang, Ninghua Kong, Yufang Zhu, Zhijun Zhang, and Chenghai Xu  
Volume 2013, Article ID 579452, 12 pages

**Numerical Simulation of Air Inlet Conditions Influence on the Establishment of MILD Combustion in Stagnation Point Reverse Flow Combustor**, Xiao Liu and Hongtao Zheng  
Volume 2013, Article ID 593601, 9 pages

**Research on Three-Dimensional Unsteady Turbulent Flow in Multistage Centrifugal Pump and Performance Prediction Based on CFD**, Zhi-jian Wang, Jian-she Zheng, Lu-lu Li, and Shuai Luo  
Volume 2013, Article ID 589161, 7 pages

**Heat and Mass Transfer with Free Convection MHD Flow Past a Vertical Plate Embedded in a Porous Medium**, Farhad Ali, Ilyas Khan, Sharidan Shafie, and Norzieha Musthapa  
Volume 2013, Article ID 346281, 13 pages

**Analytical Solutions for Steady Heat Transfer in Longitudinal Fins with Temperature-Dependent Properties**, Partner L. Ndlovu and Raseelo J. Moitsheki  
Volume 2013, Article ID 273052, 14 pages

**Cortex Effect on Vacuum Drying Process of Porous Medium**, Zhijun Zhang, Shiwei Zhang, Tianyi Su, and Shuangshuang Zhao  
Volume 2013, Article ID 120736, 8 pages

**A Numerical Study on Premixed Bluff Body Flame of Different Bluff Apex Angle**, Gelan Yang, Huixia Jin, and Na Bai  
Volume 2013, Article ID 272567, 9 pages

**Mathematical Modeling of Double-Skin Facade in Northern Area of China**, Zou Huifen, Fei Yingchao, Yang Fuhua, Tang Hao, Zhang Ying, and Ye Sheng  
Volume 2013, Article ID 712878, 10 pages

## Contents

---

**Numerical Simulation and Stability Study of Natural Convection in an Inclined Rectangular Cavity,**  
Hua-Shu Dou, Gang Jiang, and Chengwang Lei  
Volume 2013, Article ID 198695, 12 pages

**A Numerical Study on the Supersonic Steam Ejector Use in Steam Turbine System,** Lin Cai and Miao He  
Volume 2013, Article ID 651483, 9 pages

**Research on Performance of  $H_2$  Rich Blowout Limit in Bluff-Body Burner,** Hongtao Zheng,  
Yajun Li, and Lin Cai  
Volume 2012, Article ID 298685, 28 pages

## Editorial

# Mathematical Modeling of Heat and Mass Transfer in Energy Science and Engineering

**Zhijun Zhang,<sup>1</sup> Hua-Shu Dou,<sup>2</sup> Ireneusz Zbicinski,<sup>3</sup> Zhonghua Wu,<sup>4</sup> and Jun Liu<sup>5</sup>**

<sup>1</sup> School of Mechanical Engineering and Automation, Northeastern University, Shenyang 110004, China

<sup>2</sup> Faculty of Mechanical Engineering and Automation, Zhejiang Sci-Tech University, Hangzhou, Zhejiang Province 310018, China

<sup>3</sup> Faculty of Process and Environmental Engineering, Technical University of Lodz, 90-924 Lodz, Poland

<sup>4</sup> Institute of Drying and Dewatering, College of Mechanical Engineering, Tianjin University of Science and Technology, 1038 Daguan Road, Hexi District, Tianjin 300222, China

<sup>5</sup> Institute of Biology and Chemistry, Shenyang University, Shenyang 110044, China

Correspondence should be addressed to Zhijun Zhang; zhjzhang@mail.neu.edu.cn

Received 18 August 2013; Accepted 18 August 2013

Copyright © 2013 Zhijun Zhang et al. This is an open access article distributed under the Creative Commons Attribution License, which permits unrestricted use, distribution, and reproduction in any medium, provided the original work is properly cited.

Technologically advanced societies have become increasingly dependent on external energy sources for transportation, the production of many manufactured goods, and the delivery of energy services. This energy allows people who can afford the cost to live under otherwise unfavorable climatic conditions through the use of heating, ventilation, and/or air conditioning. Level of use of external energy sources differs across societies, as do the climate, convenience, levels of traffic congestion, pollution, and availability of domestic energy sources.

The idea of this special issue of is to consider the study and applications of mathematical modeling method on energy science and technology. For example, the Polymer Electrolyte Membrane Fuel Cells (PEMFC) modeling has become standard module of some commercial software; the US Green Building Council's Leadership in Energy and Environmental Design Rating System (LEED) requires energy modeling to assess the energy use of a building and to quantify the savings attributable to the proposed design; Advanced Modeling and Simulation program was used to improve the reliability, sustain the safety, and extend the life of current reactors.

The modeling and simulation in Energy Science and Engineering is a significant topic. This special issue contains 14 papers, the contents of which are summarized as follows.

In "Research on performance of  $H_2$  rich blowout limit in bluff-body burner" by H. Zheng et al., a CFD software FLUENT was used to simulate  $H_2$  burning flow field in bluff-body burner, and the software CHEMKIN was adopted to

analyze the sensitivity of each elementary reaction. Composition Probability Density Function (C-PDF) model was adopted to simulate  $H_2$  combustion field in turbulence flame.

In "A numerical study on the supersonic steam ejector use in steam turbine system" by L. Cai and M. He, the Computational Fluids Dynamics (CFD) method was employed to simulate a supersonic steam ejector, and SST  $k-\omega$  turbulence model was adopted, and both real gas model and ideal gas model for fluid property were considered and compared. The mixing chamber angle, throat length, and nozzle exit position (NXP) primary pressure and temperature effects on entrainment ratio were investigated.

In "Numerical simulation and stability study of natural convection in an inclined rectangular cavity" by H. S. Dou et al., the process of instability of natural convection in an inclined cavity based on numerical simulations is examined. The energy gradient method is employed to analyze the physics of the flow instability in natural convection. It is found that the maximum value of the energy gradient function in the flow field correlates well with the location where flow instability occurs. Meanwhile, the effects of the flow time, the plate length, and the inclination angle on the instability have also been discussed.

In "Mathematical modeling of double-skin facade in northern area of China" by Z. Huifen et al., this paper focuses on the operation principles of the double-skin facade (DSF) in winter of severe cold area. The paper discussed the main



influence factors of building energy consumption, including the heat storage cavity spacing, the air circulation mode, the building envelope, and the building orientation.

In “*A numerical study on premixed bluff body flame of different bluff apex angle*” by G. Yang et al., in order to investigate effects of apex angle ( $\alpha$ ) on chemically reacting turbulent flow and thermal fields in a channel with a bluff body V-gutter flame holder, a numerical study has been carried out in this paper. With a basic geometry used in a previous experimental study, the apex angle varied from  $45^\circ$  to  $150^\circ$ . Eddy dissipation concept (EDC) combustion model was used for air and propane premixed flame. LES-Smagorinsky model was selected for turbulence. The grid-dependent learning and numerical model verification were done. Both nonreactive and reactive conditions were analyzed and compared.

In “*Cortex effect on vacuum drying process of porous medium*” by Z. Zhang et al., based on the theory of heat and mass transfer, a coupled model for the porous medium vacuum drying process with cortex effect is constructed. The model is implemented and solved using COMSOL software. The water evaporation rate is determined using a nonequilibrium method with the rate constant parameter  $K_r$  that has been studied. The effects of different vapor pressures, initial moisture contents, drying temperatures, and intrinsic permeability for cortex part on vacuum drying process were studied.

In “*Analytical solutions for steady heat transfer in longitudinal fins with temperature-dependent properties*” by P. L. Ndlovu and R. J. Moitsheki, explicit analytical expressions for the temperature profile, fin efficiency, and heat flux in a longitudinal fin are derived. Here, thermal conductivity and heat transfer coefficient depend on the temperature. The differential transform method (DTM) is employed to construct the analytical (series) solutions. Thermal conductivity is considered to be given by the power law in one case and by the linear function of temperature in the other, whereas heat transfer coefficient is only given by the power law.

In “*Heat and mass transfer with free convection MHD flow past a vertical plate embedded in a porous medium*” by F. Ali et al., an analysis to investigate the combined effects of heat and mass transfer on free convection unsteady magnetohydrodynamic (MHD) flow of viscous fluid embedded in a porous medium is presented. The flow in the fluid is induced due to uniform motion of the plate. The dimensionless coupled linear partial differential equations are solved by using Laplace transform method. The solutions that have been obtained are expressed in simple forms in terms of elementary function and complementary error function.

In “*Research on three-dimensional unsteady turbulent flow in multistage centrifugal pump and performance prediction based on CFD*” by Z. J. Wang et al., the three-dimensional flow physical model of any stage of the 20BZ4 multistage centrifugal pump is built which includes inlet region, impeller flow region, guide-vane flow region, and exit region. The three-dimensional unsteady turbulent flow numerical model is created based on Navier-Stokes solver and standard  $k$ - $\epsilon$  turbulent equations. The method of multireference frame (MRF) and SIMPLE algorithm are used to simulate the flow in multistage centrifugal pump based on FLUENT software. The distributions of relative velocity, absolute velocity, static

pressure, and total pressure in guide vanes and impellers under design condition are analyzed.

In “*Numerical simulation of air inlet conditions influence on the establishment of MILD combustion in stagnation point reverse flow combustor*” by X. Liu and H. Zheng, this paper presents a numerical study of the nonpremixed stagnation point reverse flow (SPRF) combustor, especially focusing on the influence of air inlet conditions. Modified eddy dissipation concept (EDC) with a reduced mechanism was used to calculate the characteristic of MILD combustion.

In “*3D model-based simulation analysis of energy consumption in hot air drying of corn kernels*” by S. Zhang et al., to determine the mechanism of energy consumption in hot air drying, it simulates the interior heat and mass transfer processes that occur during the hot air drying for a single corn grain. The simulations are based on a 3D solid model. The 3D real body model is obtained by scanning the corn kernels with a high-precision medical CT machine. The Fourier heat conduction equation, the Fick diffusion equation, the heat transfer coefficient, and the mass diffusion coefficient are chosen as the governing equations of the theoretical dry model. The calculation software, COMSOL Multiphysics, is used to complete the simulation calculation. The influence of air temperature and velocity on the heat and mass transfer processes is discussed.

In “*The instability of an electrohydrodynamic viscous liquid micro-cylinder buried in a porous medium: effect of thermosolutal marangoni convection*” by G. M. Moatimid, and M. Hassan, the electrohydrodynamic (EHD) thermosolutal Marangoni convection of viscous liquid, in the presence of an axial electric field through a micro cylindrical porous flow, is considered. It is assumed that the surface tension varies linearly with both temperature and concentration. The instability of the interface is investigated for the free surface of the fluid. The expression of the free surface function is derived taking into account the independence of the surface tension on the heat and mass transfer. The transcendental dispersion relation is obtained considering the dependence of the surface tension on the heat and mass transfer. Numerical estimations for the roots of the transcendental dispersion relation are obtained indicating the relation between the disturbance growth rate and the variation of the wave number.

In “*A linear stability analysis of thermal convection in a fluid layer with simultaneous rotation and magnetic field acting in different directions*” by R. Avila and A. Cabello, it uses the Tau Chebyshev spectral method to calculate the value of the critical parameters (wave number and Rayleigh number at the onset of convection) as a function of (i) different kinds of boundaries, (ii) angle between the three vectors, and (iii) different values of the Taylor number  $T$  (rate of rotation) and magnetic parameter  $Q$  (strength of the magnetic force). For the classical problems previously reported in the literature, it compares our calculations with Chandrasekhar's variational method results and shows that the present method is applicable.

In “*Estimation of wellbore and formation temperatures during the drilling process under lost circulation conditions*” by M. Yang et al., based on energy exchange mechanisms of wellbore and formation systems during circulation and shut-in

stages under lost circulation conditions, a set of partial differential equations were developed to account for the transient heat exchange process between wellbore and formation. A finite difference method was used to solve the transient heat transfer models, which enables the wellbore and formation temperature profiles to be accurately predicted. Moreover, heat exchange generated by heat convection due to circulation losses to the rock surrounding a well was also considered in the mathematical model.

## **Acknowledgments**

The authors are grateful to the authors of the special issue for their contributions. They thank the reviewers for their valuable comments on the submissions. They highly appreciate the support from the editorial members of Mathematical Problems in Engineering. Dr. Zhijun Zhang acknowledges the support from the National Natural Science Foundation of China (Grant nos. 31000665 and 51176027).

*Zhijun Zhang  
Hua-Shu Dou  
Ireneusz Zbicinski  
Zhonghua Wu  
Jun Liu*

## Research Article

# A Linear Stability Analysis of Thermal Convection in a Fluid Layer with Simultaneous Rotation and Magnetic Field Acting in Different Directions

Ruben Avila and Ares Cabello

*Departamento de Termodinámicos, Facultad de Ingeniería, Universidad Nacional Autónoma de México, 04510 México, DF, Mexico*

Correspondence should be addressed to Ruben Avila; [ravila@unam.mx](mailto:ravila@unam.mx)

Received 11 February 2013; Accepted 22 May 2013

Academic Editor: Zhijun Zhang

Copyright © 2013 R. Avila and A. Cabello. This is an open access article distributed under the Creative Commons Attribution License, which permits unrestricted use, distribution, and reproduction in any medium, provided the original work is properly cited.

The onset of thermal convection of a Boussinesq fluid located in an unbounded layer heated from below and subject simultaneously to rotation and magnetic field, whose vectors act in different directions, is presented. To the knowledge of the authors, the convective thermal instability analysis for this complex problem has not been previously reported. In this paper, we use the Tau Chebyshev spectral method to calculate the value of the critical parameters (wave number and Rayleigh number at the onset of convection) as a function of (i) different kinds of boundaries, (ii) angle between the three vectors, and (iii) different values of the Taylor number  $T$  (rate of rotation) and magnetic parameter  $Q$  (strength of the magnetic force). For the classical problems previously reported in the literature, we compare our calculations with Chandrasekhar's variational method results and show that the present method is applicable.

## 1. Introduction

The thermal instability of a horizontal layer of fluid heated from below (Rayleigh-Bénard problem) is an important and classical fluid dynamics problem in science and engineering. The linear stability analysis of this problem, in terms of normal modes, has been carried out and reported in several investigations.

The rotating Rayleigh-Bénard problem has also been widely studied and it has been found that the effect of the Coriolis force due to rotation of the infinite layer of fluid, when the rotation vector  $\Omega$  acts about the vertical direction, that is, parallel to the gravity force vector  $\mathbf{g}$ , inhibits the onset of convection and thus induces a stabilizing effect [1–3]. The amount of the stabilizing effect depends on the rate of rotation (the Taylor number  $T$ ). Results for the problem in which the vectors  $\Omega$  and  $\mathbf{g}$  act in different directions, with an angle  $\vartheta_R$  between them, were not explicitly reported by [1, 4]; instead an analogy with the closely related problem of thermal convection subject to the action of a magnetic field was presented by [1].

Moreover, it has also been reported that, in the magnetic Rayleigh-Bénard problem, a stabilizing effect is obtained when the layer of an electrically conducting fluid is immersed in a uniform magnetic field vector  $\mathbf{H}$  that is parallel to the gravity force vector  $\mathbf{g}$  [5]. The extent of the inhibition depends on the value of the nondimensional magnetic parameter  $Q$ . It has been found that when  $\mathbf{H}$  and  $\mathbf{g}$  are parallel, convection at marginal stability is characterized by a cellular pattern; hence, longitudinal and transverse rolls appear simultaneously. Results for the problem in which the vectors  $\mathbf{g}$  and  $\mathbf{H}$  act in different directions, with an angle  $\vartheta_H$  between them, and when instability sets in as stationary convection have been previously obtained by considering two cases: (i) solution of the perturbation equations which are independent of  $x_1$  and (ii) solutions of the perturbation equations that conduct to a more general patterns of motion. In the former case, the onset of instability is characterized by rolls in the  $x_1$  direction, whereas in the latter case, by using a variational procedure, [1] shows that as the parameter  $C_H$ , defined as  $C_H = a_x \tan \vartheta_H$  (where  $a_x$  is the wave number in the  $x_1$  direction), increases, keeping the Chandrasekhar number  $Q$

TABLE 1: Linear problems under study.  $\vartheta_R$  is the angle between the rotation vector  $\Omega$  and the gravity vector  $\mathbf{g}$ . If  $\vartheta_R \neq 0$ ,  $\Omega$  lies in the  $x_1x_3$ -plane.  $\vartheta_H$  is the angle between the magnetic field vector  $\mathbf{H}$  and the gravity vector  $\mathbf{g}$ . If  $\vartheta_H \neq 0$ ,  $\mathbf{H}$  lies in the  $x_1x_3$ -plane.  $\mathbf{g}$  acts along the  $x_3$  direction; see Figure 1.

Problem	Gravity, $\mathbf{g}$	Rotation, $\Omega$	Magnetic field, $\mathbf{H}$	$\vartheta_R$	$\vartheta_H$
1 (Section 5.1)	Yes	Yes	No	$=0$	—
2 (Section 5.2)	Yes	Yes	No	$\neq 0$	—
3 (Section 5.3)	Yes	No	Yes	—	$=0$
4 (Section 5.4)	Yes	No	Yes	—	$\neq 0$
5 (Section 5.5)	Yes	Yes	Yes	$=0$	$=0$
6 (Section 5.6)	Yes	Yes	Yes	$\neq 0$	$\neq 0$

(defined by  $Q = \mu^2(H \cos \vartheta_H)^2 \widehat{D}^2 \widehat{\sigma} / \rho_0 \nu$ , where  $\mu$ ,  $H$ ,  $\widehat{D}$ ,  $\widehat{\sigma}$ ,  $\rho_0$ , and  $\nu$  are the magnetic permeability, the magnitude of the magnetic field, the distance between the two plates, the coefficient of electrical conductivity, the density of reference, and the kinematic viscosity, resp.) as a constant value, both the critical Rayleigh number  $R$  and the wave number  $a = \sqrt{a_x^2 + a_y^2}$  (where  $a_y$  is the wave number in the  $x_2$  direction) at the onset of stationary convection shift to higher values. It has been shown that when  $\mathbf{H}$  is very slightly inclined to the direction of gravity, the extent to which transverse rolls are suppressed at marginal stability is also very slight. According to [1], when longitudinal rolls and transverse rolls appear simultaneously, a cellular pattern of convection emerges. Therefore if  $\mathbf{H}$  and  $\mathbf{g}$  (as well as  $\Omega$  and  $\mathbf{g}$ ) are not parallel, convection at marginal stability occurs as longitudinal rolls. On the other hand, when  $\mathbf{H}$  is impressed with an inclination angle  $\vartheta_H = \pi/2$  to the direction of the vertical and  $\mathbf{H}$  lies in the  $x_1x_3$ -plane, the vertical component of the magnetic field ( $H \cos \vartheta_H$ ) is equal to zero. The authors in [6] found that a magnetic field, impressed in a horizontal direction ( $\vartheta_H = \pi/2$ ), did not inhibit convection, even though the magnetic field was five times stronger than that one needed to suppress convection when acting in the vertical direction ( $\vartheta_H = 0$ ); hence, it was experimentally confirmed that the vertical component of the magnetic field ( $H \cos \vartheta_H$ ) is the critical parameter to inhibit the onset of convection as it is included in the Chandrasekhar number  $Q$ . According to the experimental and theoretical evidence, it is well known that rotation and magnetic field have a stabilizing effect on the Rayleigh-Bénard problem when they act separately [2, 4, 5, 7].

When rotation and magnetic field act simultaneously and when both of them are parallel to the gravity vector, the stabilizing effects have conflicting tendencies; that is, the results reveal some very unexpected features showing the complex behaviour of the flow; thus, it has been found that the total effect is not always stabilizing with respect to both fields [1, 4, 8, 9]. The conflictual behaviour depends on the values of the parameters of the system: rotation rate (Taylor number  $T$ ) and magnetic parameter (Chandrasekhar number  $Q$ ). Reference [4] only shows explicit results on the dependence of the critical Rayleigh number  $R$  on  $Q$  and  $T$ , for the problem in which the conducting liquid is located between two free boundaries, and when the medium adjoining the fluid is nonconducting, because in this situation the system of equations can be solved explicitly.

To the knowledge of the authors, the solution of the problem, in which the three implicated vectors ( $\mathbf{g}$ ,  $\mathbf{H}$ , and  $\Omega$ ) are

not parallel, has not been previously reported. In this paper we show, for the rotating-magnetic Rayleigh-Bénard problem with rigid and free surfaces and nonconducting boundaries, the influence on the critical Rayleigh number  $R$  of the cooperative work (or competition), between the strength of the magnetic field and the Coriolis force, when they act simultaneously, but in different directions relatively with the gravity vector. In the literature, very few investigations have been carried out aimed to study the cooperative work of perturbations in the flow to inhibit the thermal convection of an infinite layer of fluid; for example, [7, 10, 11] have found that when the layer of fluid is simultaneously subject to rotation and to a salt concentration field, the stabilizing effects are cumulative; that is, rotation and salt concentration (salted from below) show a cooperative behaviour.

By using the Tau Chebyshev method, we find that depending on the value of the parameters  $C_R = a_x \tan \vartheta_R$  and  $C_H = a_x \tan \vartheta_H$ , a critical situation may appear, at which the competition between  $\mathbf{H}$  and  $\Omega$  conduct to an unstable system; however as the values of  $C_R$  or  $C_H$  are modified, a cooperative work between  $\mathbf{H}$  and  $\Omega$  may appear which leads to a system in which the thermal convection of the layer of fluid is inhibited.

The paper is organized as follows. In Section 2 we briefly describe the physical model of the problem under study. In Section 3 we formulate the general perturbation equations, from which we get the solution of the problems 1 to 6 described in Table 1. Note that the classical linear problems 1 to 5 of this table have been previously solved by [1], while the linear problem 6 of Table 1 is the subject of the present paper that is, thermal instability analysis of a fluid layer subject to gravity  $\mathbf{g}$ , rotation  $\Omega$ , and magnetic field  $\mathbf{H}$  vectors, with angles  $\vartheta_R$  and  $\vartheta_H$  different from zero. In Section 4 we describe the Tau Chebyshev spectral method that is used to solve the set of perturbation equations. Section 5 shows the solution of the six formulated linear problems by using the Tau Chebyshev method, together with a comparison of our calculations with the solution of the classical problems previously published in the literature; see problems 1 to 5 of Table 1. Finally, in Section 6 we present our concluding remarks.

## 2. Physical Situation

Figure 1 shows a schematic representation of the geometry under study. A layer of fluid of constant thickness  $\widehat{D} = 2\widehat{d}$  parallel to the  $x_1x_2$ -plane with no lateral boundaries is considered. The upper and lower boundaries are located at

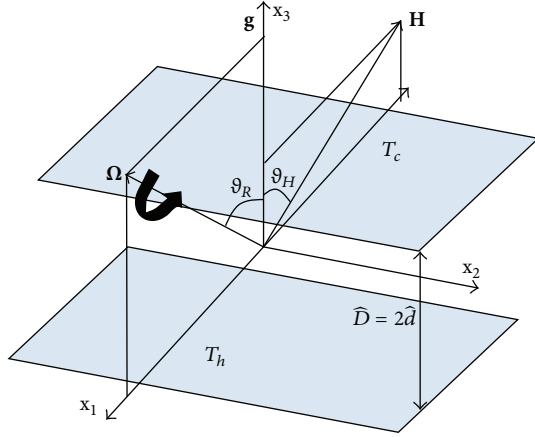


FIGURE 1: Thermal instability analysis in the presence of a rotation vector  $\Omega$  and a magnetic field  $\mathbf{H}$ . The gravity vector  $\mathbf{g}$  acts in the negative  $x_3$ -direction. The temperatures  $T_h$  and  $T_c$  (where  $T_h > T_c$ ) are applied at the lower and upper boundaries, respectively. The distance between the two surfaces is  $\widehat{D} = 2\widehat{d}$ . The angle between  $\mathbf{g}$  and  $\Omega$  is  $\vartheta_R$ , while the angle between  $\mathbf{g}$  and  $\mathbf{H}$  is  $\vartheta_H$ . Note that the vectors  $\Omega$  and  $\mathbf{H}$  lay in the  $x_1x_3$ -plane. The surfaces are electrically nonconducting; thus, no currents can cross the boundary.

$x_3 = \pm \widehat{d}$ . The temperatures  $T_h$  and  $T_c$  (where  $T_h > T_c$ ) are applied at the lower and upper boundaries, respectively. The whole layer can rotate with an angular velocity vector  $\Omega$ , which can be inclined at an angle  $\vartheta_R$  to the direction of the vertical  $x_3$ -axis, in such a way that  $\Omega$  lies in the  $x_1x_3$ -plane. Gravity acts in the negative  $x_3$ -direction  $\mathbf{g} = -g\mathbf{i}_3$ . The fluid layer is assumed to be located in a magnetic field represented by the vector  $\mathbf{H}$ , which can also be inclined at an angle  $\vartheta_H$  to the direction of the vertical  $x_3$ -axis, in such a way that  $\mathbf{H}$  also lies in the  $x_1x_3$ -plane. The surfaces are electrically nonconducting; thus, no currents can cross the boundary, and hence we must require  $J_3 = 0$ , where  $J_3$  is the third component of the current density vector  $\mathbf{J}$ .

### 3. Thermal Instability Analysis in the Presence of a Rotation Vector and a Magnetic Field

In this section we analyse the linear thermal instability of a rotating infinite layer of an incompressible, electrically conducting fluid upon which a uniform magnetic field is impressed. The gravity vector  $\mathbf{g}$ , the rotation vector  $\Omega$ , and the magnetic field vector  $\mathbf{H}$  may act in different directions.

**3.1. Governing Equations.** Let us consider an infinite fluid layer of an electrically conducting fluid upon which a uniform magnetic field  $\mathbf{H}$  is impressed. The fluid is also subjected to rotation about a fixed axis. For an incompressible conducting fluid, the linear convective thermal stability of a fluid layer (initially at rest and with a steady adverse temperature gradient) is analyzed by solving the following perturbation

equations in the Boussinesq approximation and in a rotating frame of [1, page 199]:

$$\frac{\partial u_i}{\partial t} = -\frac{\partial}{\partial x_i}(\delta\omega) + \beta\theta g\lambda_i + \nu\nabla^2 u_i + 2\epsilon_{ijk}u_j\Omega_k \quad (1)$$

$$+ \frac{\mu}{4\pi\rho_o}H_j\frac{\partial h_i}{\partial x_j},$$

$$\frac{\partial\theta}{\partial t} = \beta\lambda_j u_j + \alpha\nabla^2\theta, \quad (2)$$

$$\frac{\partial u_i}{\partial x_i} = 0, \quad (3)$$

$$\frac{\partial h_i}{\partial t} = H_j\frac{\partial u_i}{\partial x_j} + \eta\nabla^2 h_i, \quad (4)$$

$$\frac{\partial h_i}{\partial x_i} = 0, \quad (5)$$

where  $t$  is the time,  $u_i$  are the components of the velocity vector,  $\nu$  denotes the kinematic viscosity,  $\Omega_k$  are the components of the rotation vector,  $\beta$  is the coefficient of volume expansion,  $\alpha$  is the thermal diffusivity,  $\theta$  is the perturbation in the temperature,  $g$  is the acceleration of gravity,  $\mu$  is the magnetic permeability,  $\eta$  denotes the resistivity,  $\mathbf{H}$  is the impressed magnetic field,  $\mathbf{h}$  is the perturbation of the magnetic field,  $\lambda = (0, 0, 1)$  is the unit vector in the direction of the vertical, and  $\beta$  is the imposed adverse temperature gradient defined as

$$\beta = \frac{T_h - T_c}{\Delta x_3}, \quad (6)$$

where  $T_h$  and  $T_c$  are the temperature of the lower hot surface and the temperature of the upper cold surface, respectively. The last two terms on the right hand side of (1) are the Coriolis force and the Lorentz force, respectively, and the term  $\delta\omega$  is defined as

$$\delta\omega = \frac{\delta p}{\rho_o} - \frac{1}{2}|\Omega \times \mathbf{r}|^2 + \mu \frac{\mathbf{H} \cdot \mathbf{h}}{4\pi\rho_o}, \quad (7)$$

where

$$\frac{1}{2}|\Omega \times \mathbf{r}|^2 \quad (8)$$

is the centrifugal force,  $\delta p$  is the perturbation in the pressure, and  $\rho_o$  is the density at a mean temperature  $T_o$ .

Taking the curl of (1) we may write

$$\frac{\partial \omega_i}{\partial t} = g\beta\epsilon_{ijk}\frac{\partial\theta}{\partial x_j}\lambda_k + \nu\nabla^2\omega_i + 2\Omega_j\frac{\partial u_i}{\partial x_j} + \frac{\mu}{4\pi\rho_o}H_j\frac{\partial v_i}{\partial x_j}, \quad (9)$$

where  $\omega_i$  are the components of the vorticity vector and the vector  $\mathbf{v} = v_i\mathbf{i}_i = \nabla \times \mathbf{h}$  is the current density induced by the perturbation. Taking the curl of (9) once again, we obtain

$$\frac{\partial \nabla^2 u_i}{\partial t} = g\beta\left(\lambda_i\nabla^2\theta - \lambda_j\frac{\partial^2\theta}{\partial x_j\partial x_i}\right) + \nu\nabla^4 u_i - 2\Omega_j\frac{\partial \omega_i}{\partial x_j} \quad (10)$$

$$+ \frac{\mu}{4\pi\rho_o}H_j\frac{\partial}{\partial x_j}\nabla^2 h_i.$$



Taking the curl of (4) we have

$$\frac{\partial v_i}{\partial t} = H_j \frac{\partial \omega_i}{\partial x_j} + \eta \nabla^2 v_i, \quad (11)$$

Multiplying (2), (4), (9), (10), and (11) by the components  $\lambda_i$  we get

$$\frac{\partial \theta}{\partial t} = \hat{\beta} u_3 + \alpha \nabla^2 \theta, \quad (12)$$

$$\frac{\partial h_3}{\partial t} = H_j \frac{\partial u_3}{\partial x_j} + \eta \nabla^2 h_3, \quad (13)$$

$$\frac{\partial v_3}{\partial t} = H_j \frac{\partial \omega_3}{\partial x_j} + \eta \nabla^2 v_3, \quad (14)$$

$$\frac{\partial \omega_3}{\partial t} = \nu \nabla^2 \omega_3 + 2\Omega_j \frac{\partial u_3}{\partial x_j} + \frac{\mu}{4\pi\rho_0} H_j \frac{\partial v_3}{\partial x_j}, \quad (15)$$

$$\begin{aligned} \frac{\partial \nabla^2 u_3}{\partial t} &= g\beta \left( \frac{\partial^2 \theta}{\partial x_1^2} + \frac{\partial^2 \theta}{\partial x_2^2} \right) + \nu \nabla^4 u_3 - 2\Omega_j \frac{\partial \omega_3}{\partial x_j} \\ &+ \frac{\mu}{4\pi\rho_0} H_j \frac{\partial}{\partial x_j} \nabla^2 h_3, \end{aligned} \quad (16)$$

where  $h_3$ ,  $v_3$ ,  $\omega_3$ , and  $u_3$  are the  $x_3$  components of the perturbation of the magnetic field, the current density, the vorticity, and the velocity, respectively. In this investigation the set of equations to be solved are (12)–(16). Let the rotation vector  $\mathbf{\Omega}$  be inclined at an angle  $\vartheta_R$  to the direction of the vertical  $x_3$ -axis. Additionally let the magnetic field vector  $\mathbf{H}$  be also inclined at an angle  $\vartheta_H$  to the direction of the vertical  $x_3$ -axis. The  $x_1$ -axis of the Cartesian coordinate system is defined such as the vectors  $\mathbf{\Omega}$  and  $\mathbf{H}$  lie in the  $x_1x_3$ -plane; see Figure 1. Thus the unit vector in the direction of the vertical, the rotation vector, and the magnetic field vector are written as

$$\begin{aligned} \lambda &= (0, 0, 1), \quad \mathbf{\Omega} = \Omega (\sin \vartheta_R, 0, \cos \vartheta_R), \\ \mathbf{H} &= H (\sin \vartheta_H, 0, \cos \vartheta_H), \end{aligned} \quad (17)$$

where  $\Omega$  and  $H$  are the magnitude of the rotation vector  $\mathbf{\Omega}$  and the magnitude of the magnetic field vector  $\mathbf{H}$ , respectively. Using (17) into (13)–(16) we obtain

$$\frac{\partial h_3}{\partial t} = H \left( \cos \vartheta_H \frac{\partial}{\partial x_3} + \sin \vartheta_H \frac{\partial}{\partial x_1} \right) u_3 + \eta \nabla^2 h_3,$$

$$\frac{\partial v_3}{\partial t} = H \left( \cos \vartheta_H \frac{\partial}{\partial x_3} + \sin \vartheta_H \frac{\partial}{\partial x_1} \right) \omega_3 + \eta \nabla^2 v_3,$$

$$\begin{aligned} \frac{\partial \omega_3}{\partial t} &= \nu \nabla^2 \omega_3 + \frac{\mu}{4\pi\rho_0} H \left( \cos \vartheta_H \frac{\partial}{\partial x_3} + \sin \vartheta_H \frac{\partial}{\partial x_1} \right) v_3 \\ &+ 2\Omega \left( \cos \vartheta_R \frac{\partial}{\partial x_3} + \sin \vartheta_R \frac{\partial}{\partial x_1} \right) u_3, \\ \frac{\partial \nabla^2 u_3}{\partial t} &= g\beta \left( \frac{\partial^2 \theta}{\partial x_1^2} + \frac{\partial^2 \theta}{\partial x_2^2} \right) + \nu \nabla^4 u_3 \\ &+ \frac{\mu}{4\pi\rho_0} H \left( \cos \vartheta_H \frac{\partial}{\partial x_3} + \sin \vartheta_H \frac{\partial}{\partial x_1} \right) \nabla^2 h_3 \\ &- 2\Omega \left( \cos \vartheta_R \frac{\partial}{\partial x_3} + \sin \vartheta_R \frac{\partial}{\partial x_1} \right) \omega_3. \end{aligned} \quad (18)$$

**3.1.1. The Analysis into Normal Modes.** We analyse the perturbations  $\theta$ ,  $h_3$ ,  $v_3$ ,  $\omega_3$ , and  $u_3$  into two dimensional periodic waves characterized by a particular wave number  $k$ . We assume the forms of the perturbations as

$$\begin{aligned} \theta &= \Theta(x_3) \exp \left[ i(k_x x_1 + k_y x_2) + pt \right], \\ h_3 &= K(x_3) \exp \left[ i(k_x x_1 + k_y x_2) + pt \right], \\ v_3 &= X(x_3) \exp \left[ i(k_x x_1 + k_y x_2) + pt \right], \\ \omega_3 &= Z(x_3) \exp \left[ i(k_x x_1 + k_y x_2) + pt \right], \\ u_3 &= W(x_3) \exp \left[ i(k_x x_1 + k_y x_2) + pt \right]. \end{aligned} \quad (19)$$

If we define the wave number of the disturbance  $k$  as  $k = (k_x^2 + k_y^2)^{1/2}$  and  $p$  as a constant, (12) and (18) can be written as

$$\begin{aligned} \Theta p &= \hat{\beta} W + \alpha \left[ \frac{d^2}{dx_3^2} - k^2 \right] \Theta, \\ Kp &= H \cos \vartheta_H \frac{dW}{dx_3} + H \sin \vartheta_H W k_x i + \eta \left[ \frac{d^2}{dx_3^2} - k^2 \right] K, \\ Xp &= H \cos \vartheta_H \frac{dZ}{dx_3} + H \sin \vartheta_H Z k_x i + \eta \left[ \frac{d^2}{dx_3^2} - k^2 \right] X, \\ Zp &= \nu \left[ \frac{d^2}{dx_3^2} - k^2 \right] Z + \frac{\mu}{4\pi\rho_0} H \cos \vartheta_H \frac{dX}{dx_3} \\ &+ \frac{\mu}{4\pi\rho_0} H \sin \vartheta_H X k_x i + 2\Omega \cos \vartheta_R \frac{dW}{dx_3} \\ &+ 2\Omega \sin \vartheta_R W k_x i, \end{aligned}$$

$$\begin{aligned}
\left[ \frac{d^2}{dx_3^2} - k^2 \right] W &= -g\beta k^2 \Theta + \nu \left[ \frac{d^2}{dx_3^2} - k^2 \right]^2 W \\
&+ \frac{\mu}{4\pi\rho_o} H \cos \vartheta_H \frac{d}{dx_3} \left[ \frac{d^2}{dx_3^2} - k^2 \right] K \\
&+ \frac{\mu}{4\pi\rho_o} H \sin \vartheta_H \left[ \frac{d^2}{dx_3^2} - k^2 \right] K k_x i \\
&- 2\Omega \cos \vartheta_R \frac{dZ}{dx_3} - 2\Omega \sin \vartheta_R Z k_x i.
\end{aligned} \quad (20)$$

As it is shown in Figure 1, the origin of the coordinate system is located at the middle between the two surfaces; hence, the distance between the two surfaces is  $\widehat{D} = 2\widehat{d}$ . If we define the following nondimensional variables

$$\begin{aligned}
a &= k\widehat{D}, \quad \sigma = \frac{p\widehat{D}^2}{\nu}, \quad x_3^* = \frac{2x_3}{\widehat{D}}, \\
\text{Pr} &= \frac{\nu}{\alpha}, \quad \text{Pr}_2 = \frac{\nu}{\eta},
\end{aligned} \quad (21)$$

(20) is written as

$$\left[ 4D^2 - a^2 - \sigma \text{Pr} \right] \Theta = - \left( \frac{\widehat{D}^2 \widehat{\beta}}{\alpha} \right) W, \quad (22)$$

$$\begin{aligned}
\left[ 4D^2 - a^2 - \sigma \text{Pr}_2 \right] K &= - \frac{2\widehat{D}}{\eta} H \cos \vartheta_H DW \\
&- \frac{\widehat{D}}{\eta} H \sin \vartheta_H a_x i W,
\end{aligned} \quad (23)$$

$$\begin{aligned}
\left[ 4D^2 - a^2 - \sigma \text{Pr}_2 \right] X &= - \frac{2\widehat{D}}{\eta} H \cos \vartheta_H DZ \\
&- \frac{\widehat{D}}{\eta} H \sin \vartheta_H a_x i Z,
\end{aligned} \quad (24)$$

$$\begin{aligned}
\left[ 4D^2 - a^2 - \sigma \right] Z &= - \frac{4\widehat{D}}{\nu} \Omega \cos \vartheta_R DW - \frac{2\widehat{D}}{\nu} \Omega \sin \vartheta_R a_x i W \\
&- \frac{\mu\widehat{D}}{2\pi\rho_o\nu} H \cos \vartheta_H DX \\
&- \frac{\mu\widehat{D}}{4\pi\rho_o\nu} H \sin \vartheta_H a_x i X,
\end{aligned} \quad (25)$$

$$\begin{aligned}
&\left[ 4D^2 - a^2 \right] \left[ 4D^2 - a^2 - \sigma \right] W \\
&+ \frac{\mu\widehat{D}}{2\pi\rho_o\nu} H \cos \vartheta_H D \left[ 4D^2 - a^2 \right] K \\
&+ \frac{\mu\widehat{D}}{4\pi\rho_o\nu} H \sin \vartheta_H \left[ 4D^2 - a^2 \right] a_x i K \\
&- \frac{4\widehat{D}^3}{\nu} \Omega \cos \vartheta_R DZ - \frac{2\widehat{D}^3}{\nu} \Omega \sin \vartheta_R a_x i Z \\
&= \frac{\widehat{D}^2}{\nu} g\beta a^2 \Theta,
\end{aligned} \quad (26)$$

where  $a_x = \widehat{D}k_x$ . If instability sets in as stationary convection,  $\sigma = 0$ , we can operate (25) by  $[4D^2 - a^2]$  and in the resulting equation we use (24) to get (let us assume that  $\widehat{D} = 2$ )

$$\begin{aligned}
&\left[ (4D^2 - a^2)^2 - \widehat{Q}D^2 - \widehat{Q}C_H i D + \frac{1}{4}\widehat{Q}C_H^2 \right] Z \\
&= -T^{1/2} D \left[ 4D^2 - a^2 \right] W - \frac{T^{1/2}}{2} C_R i \left[ 4D^2 - a^2 \right] W,
\end{aligned} \quad (27)$$

where

$$T = \frac{4\Omega^2 \widehat{D}^4 \cos^2 \vartheta_R}{\nu^2} \quad (28)$$

is the Taylor number,

$$C_H = a_x \tan \vartheta_H, \quad C_R = a_x \tan \vartheta_R, \quad (29)$$

$$\frac{4\widehat{D}}{\nu} \Omega \cos \vartheta_R = \frac{2}{\widehat{D}} T^{1/2}, \quad \frac{2\widehat{D}}{\nu} \Omega \cos \vartheta_R = \frac{T^{1/2}}{\widehat{D}}, \quad (30)$$

$$\widehat{Q} = \frac{\mu\widehat{D}^2 (H \cos \vartheta_H)^2}{\pi\rho_o \eta}. \quad (31)$$

If we define the resistivity  $\eta$  as

$$\eta = \frac{1}{4\pi\mu\widehat{\sigma}}, \quad (32)$$

it is possible to write (31) as

$$\widehat{Q} = 4 \left( \frac{\mu^2 (H \cos \vartheta_H)^2 \widehat{D}^2 \widehat{\sigma}}{\rho_o \nu} \right) = 4Q, \quad (33)$$

where the variable  $Q$  defined by Chandrasekhar [1] is written as

$$Q = \frac{\mu^2 (H \cos \vartheta_H)^2 \widehat{D}^2 \widehat{\sigma}}{\rho_o \nu}. \quad (34)$$

We can eliminate  $K$  from (26) by using (23), then we obtain

$$\begin{aligned}
&\left[ (4D^2 - a^2)^2 - \widehat{Q}D^2 - \widehat{Q}C_H i D + \frac{1}{4}\widehat{Q}C_H^2 \right] W \\
&- \frac{4\widehat{D}^3}{\nu} \Omega \cos \vartheta_R DZ - \frac{2\widehat{D}^3}{\nu} \Omega \cos \vartheta_R C_R i Z \\
&= \left( \frac{\widehat{D}^2 g\beta}{\nu} \right) a^2 \Theta.
\end{aligned} \quad (35)$$



We operate (35) by  $(4D^2 - a^2)$ , and in the resulting equation we use (22); hence, we obtain

$$\begin{aligned} (4D^2 - a^2) \left\{ \left[ (4D^2 - a^2)^2 - \widehat{Q}D^2 - \widehat{Q}C_H iD + \frac{1}{4}\widehat{Q}C_H^2 \right] W \right. \\ \left. - \frac{4\widehat{D}^3}{\nu} \Omega \cos \vartheta_R DZ - \frac{2\widehat{D}^3}{\nu} \Omega \cos \vartheta_R C_R iZ \right\} \\ = -Ra^2 W, \end{aligned} \quad (36)$$

where the Rayleigh number  $R$  is defined as

$$R = \frac{\widehat{D}^4 g \beta \widehat{\beta}}{\nu \alpha}. \quad (37)$$

From (36) we can define the variable  $F$  as

$$\begin{aligned} F = \left[ (4D^2 - a^2)^2 - \widehat{Q}D^2 - \widehat{Q}C_H iD + \frac{1}{4}\widehat{Q}C_H^2 \right] W \\ - \frac{4\widehat{D}^3}{\nu} \Omega \cos \vartheta_R DZ - \frac{2\widehat{D}^3}{\nu} \Omega \cos \vartheta_R C_R iZ; \end{aligned} \quad (38)$$

hence, (36) is written as

$$(4D^2 - a^2) F = -Ra^2 W. \quad (39)$$

By using the following relationships

$$\begin{aligned} \frac{4\widehat{D}^3}{\nu} \Omega \cos \vartheta_R &= 2\widehat{D}T^{1/2}, \\ \frac{2\widehat{D}^3}{\nu} \Omega \cos \vartheta_R &= \widehat{D}T^{1/2}, \end{aligned} \quad (40)$$

into (38) we can formulate the relevant equations to be solved as

$$\begin{aligned} 16D^4 W - (8a^2 + 4Q) D^2 W - 4QC_H iDW + (a^4 + QC_H^2) W \\ - 4T^{1/2} DZ - 2T^{1/2} C_R iZ - F = 0, \end{aligned} \quad (41)$$

$$4D^2 F - a^2 F = -Ra^2 W, \quad (42)$$

$$\begin{aligned} 16D^4 Z - (8a^2 + 4Q) D^2 Z - 4QC_H iDZ + (a^4 + QC_H^2) Z \\ + 4T^{1/2} D^3 W - T^{1/2} a^2 DW + 2T^{1/2} C_R iD^2 W \\ - \frac{1}{2} T^{1/2} C_R i a^2 W = 0. \end{aligned} \quad (43)$$

Notice that when the magnetic field is negligible  $\mathbf{H} = 0$ , that is, pure rotation, and the relevant equations to be solved are the following:

$$16D^4 W - 8a^2 D^2 W + a^4 W - 4T^{1/2} DZ - 2T^{1/2} C_R iZ - F = 0, \quad (44)$$

$$4D^2 F - a^2 F = -Ra^2 W, \quad (45)$$

$$\begin{aligned} 16D^4 Z - 8a^2 D^2 Z + a^4 Z + 4T^{1/2} D^3 W - T^{1/2} a^2 DW \\ + 2T^{1/2} C_R iD^2 W - \frac{1}{2} T^{1/2} C_R i a^2 W = 0 \end{aligned} \quad (46)$$

together with the following boundary conditions.

(a) For rigid surfaces at  $x_3^* = -1$  and at  $x_3^* = 1$ :

$$\begin{aligned} F = 0, \quad Z = 0, \quad W = 0, \quad DW = 0, \\ \text{at } x_3^* = -1, \text{ at } x_3^* = 1. \end{aligned} \quad (47)$$

(b) For free surfaces at  $x_3^* = -1$  and at  $x_3^* = 1$ :

$$\begin{aligned} F = 0, \quad DZ = 0, \quad W = 0, \quad D^2 W = 0, \\ \text{at } x_3^* = -1, \text{ at } x_3^* = 1. \end{aligned} \quad (48)$$

(It must be pointed out that due to the process we follow to derive the general relevant equations, the vorticity equation (46) has both different form and higher order than the one we obtained by following Chandrasekhar's procedure; see Chandrasekhar [1], Chapter III, page 90. The equation for the vorticity that we obtained by considering only rotation without magnetic field is  $4D^2 Z - a^2 Z + T^{1/2} DW + (1/2)T^{1/2} C_R iW = 0$ , which is the same as the one obtained by Chandrasekhar [1].)

On the other hand when the rotation vector  $\Omega$  is equal to zero, the relevant equations are

$$\begin{aligned} 16D^4 W - (8a^2 + 4Q) D^2 W - 4QC_H iDW + (a^4 + QC_H^2) W \\ - F = 0, \end{aligned}$$

$$4D^2 F - a^2 F = -Ra^2 W, \quad (49)$$

together with the following boundary conditions.

(a) For rigid surfaces at  $x_3^* = -1$  and at  $x_3^* = 1$ :

$$F = 0, \quad W = 0, \quad DW = 0, \quad \text{at } x_3^* = -1, \text{ at } x_3^* = 1. \quad (50)$$

(b) For free surfaces at  $x_3^* = -1$  and at  $x_3^* = 1$ :

$$F = 0, \quad W = 0, \quad D^2 W = 0, \quad \text{at } x_3^* = -1, \text{ at } x_3^* = 1. \quad (51)$$

(For this particular case in which  $\Omega = 0$ , the  $x_3$  component of vorticity  $Z$  vanishes, see Chandrasekhar [1], Chapter IV, page 166; hence the general equation (43) is not taken into account in the analysis.)

Therefore the boundary conditions needed to solve the general equations (41)–(43) are defined by (47) and (48).

TABLE 2: Critical Rayleigh numbers and wave numbers at marginal stability for the onset of stationary convection when both bounding surfaces are rigid. Gravity vector  $\mathbf{g}$  parallel to the rotation vector  $\mathbf{\Omega}$ .  $T$  is the Taylor number.  $R$  is the Rayleigh number obtained by the Tau Chebyshev method.  $R_{\text{Ch}}$  is the Rayleigh number obtained by Chandrasekhar [1].

$T$	$a$	$R$	$R_{\text{Ch}}$
10	3.1	1.7127E3	1.713E3
$10^2$	3.15	1.756E3	1.7566E3
$10^3$	3.50	2.1514E3	2.1517E3
$10^5$	7.20	1.6720E4	1.6721E4
$10^{10}$	55.5	4.476E7	3.4574E7

#### 4. The Tau Chebyshev Numerical Method

In order to find an approximate solution to the set of perturbations equations formulated in the previous section, together with the boundary conditions, we use expansions in Chebyshev polynomials. Therefore we expand the variables  $W(x_3^*)$ ,  $F(x_3^*)$ , and  $Z(x_3^*)$  as well as their derivatives  $D = d/dx_3^*$ ,  $D^2 = d^2/dx_3^{*2}$ ,  $D^3 = d^3/dx_3^{*3}$ , and  $D^4 = d^4/dx_3^{*4}$ , in the interval  $-1 \leq x_3^* \leq 1$  as follows:

$$W(x_3^*) = \sum_{n=0}^N a_{Wn} T_n(x_3^*), \quad (52)$$

$$F(x_3^*) = \sum_{n=0}^N a_{Fn} T_n(x_3^*), \quad (53)$$

$$Z(x_3^*) = \sum_{n=0}^N a_{Zn} T_n(x_3^*), \quad (54)$$

$$\frac{d^q W}{dx_3^{*q}} = \sum_{n=0}^N a_{Wn} \frac{d^q T_n(x_3^*)}{dx_3^{*q}} = \sum_{n=0}^N b_{Wn} T_n(x_3^*), \quad (55)$$

$$\frac{d^q F}{dx_3^{*q}} = \sum_{n=0}^N a_{Fn} \frac{d^q T_n(x_3^*)}{dx_3^{*q}} = \sum_{n=0}^N b_{Fn} T_n(x_3^*), \quad (56)$$

$$\frac{d^q Z}{dx_3^{*q}} = \sum_{n=0}^N a_{Zn} \frac{d^q T_n(x_3^*)}{dx_3^{*q}} = \sum_{n=0}^N b_{Zn} T_n(x_3^*), \quad (57)$$

where  $q$  is an integer number defining the order of the derivative of the functions  $W$ ,  $F$ , and  $Z$ , and  $T_n(x_3^*)$  are the  $n$ th-degree Chebyshev polynomials of the first kind (with  $N$  as the maximum degree used for the polynomials). The Chebyshev polynomials satisfy the orthogonality relation [12–14]:

$$\int_{-1}^1 T_n(x_3^*) T_m(x_3^*) (1 - x_3^{*2})^{-1/2} dx_3^* = \frac{\pi}{2} c_n \delta_{nm}, \quad (58)$$

where  $c_0 = 2$ ,  $c_n = 1$  for  $n > 0$ . Equations for the expansion coefficients  $a_{Wn}$ ,  $a_{Fn}$ ,  $a_{Zn}$ ,  $b_{Wn}$  (in terms of  $a_{Wn}$ ),  $b_{Fn}$  (in terms of  $a_{Fn}$ ), and  $b_{Zn}$  (in terms of  $a_{Zn}$ ) are generated by substituting (52)–(57) into the set of perturbation equations shown in the previous section and applying the orthogonality property

(58). In the literature it is possible to find explicit formulae for the expansion coefficients  $b_{Wn}$  in terms of  $a_{Wn}$ ,  $b_{Fn}$  in terms of  $a_{Fn}$ , and  $b_{Zn}$  in terms of  $a_{Zn}$  [12, 15].

The method that we have selected to obtain the equations for the coefficients  $a_{Wn}$ ,  $a_{Fn}$ , and  $a_{Zn}$  is the Tau Chebyshev method. The Tau Chebyshev method is an efficient numerical procedure for finding eigenvalues and eigenfunctions of systems in fluid and solid mechanics theories. One advantage of the algorithm is that it is able to calculate as many eigenvalues as required, not just the dominant one [13, 14]. Using this numerical methodology we generate, by substituting (52), (53), (55), and (56) into the couple of the general perturbation equations for the case when  $\Omega = 0$ ; see (49), one equation for each  $n = 0, 1, 2, \dots, 2N + 2 - 6$ . The remaining six equations, those for  $2N + 2 - 6 + 1 \leq n \leq 2N + 2$ , are generated by using the six boundary conditions. Hence for rigid surfaces, the set of boundary conditions are written as

$$\begin{aligned} W(1) = \sum_{n=0}^N a_{Wn} &= 0, \quad \frac{dW(1)}{dx_3^*} = \sum_{n=0}^N a_{Wn} n^2 = 0, \\ W(-1) = \sum_{n=0}^N a_{Wn} (-1)^n &= 0, \end{aligned} \quad (59)$$

$$\frac{dW(-1)}{dx_3^*} = \sum_{n=0}^N a_{Wn} (-1)^{n-1} n^2 = 0,$$

$$F(1) = \sum_{n=0}^N a_{Fn} = 0, \quad F(-1) = \sum_{n=0}^N a_{Fn} (-1)^n = 0,$$

whereas for free surfaces the set of boundary conditions are written as

$$W(1) = \sum_{n=0}^N a_{Wn} = 0,$$

$$\frac{d^2 W(1)}{dx_3^{*2}} = \sum_{n=0}^N a_{Wn} n^2 \left( \frac{n^2 - 1}{3} \right) = 0,$$

$$W(-1) = \sum_{n=0}^N a_{Wn} (-1)^n = 0, \quad (60)$$

$$\frac{d^2 W(-1)}{dx_3^{*2}} = \sum_{n=0}^N a_{Wn} (-1)^{n+2} n^2 \left( \frac{n^2 - 1}{3} \right) = 0,$$

$$F(1) = \sum_{n=0}^N a_{Fn} = 0, \quad F(-1) = \sum_{n=0}^N a_{Fn} (-1)^n = 0.$$

Using the Tau Chebyshev method in the cases with rotation ( $\Omega \neq 0$ ) we generate, by substituting (52)–(57) into the three perturbation equations, one equation for each  $n = 0, 1, 2, \dots, 3N + 3 - 8$ . The remaining eight equations, those for  $3N + 3 - 8 + 1 \leq n \leq 3N + 3$ , are generated by using

TABLE 3: Critical Rayleigh numbers and wave numbers at marginal stability for the onset of stationary convection when both bounding surfaces are free. Gravity vector  $\mathbf{g}$  parallel to the rotation vector  $\mathbf{\Omega}$ .  $T$  is the Taylor number.  $R$  is the Rayleigh number obtained by the Tau Chebyshev method.  $R_{\text{Ch}}$  is the Rayleigh number obtained by Chandrasekhar [1].

$T$	$a$	$R$	$R_{\text{Ch}}$	$T$	$a$	$R$	$R_{\text{Ch}}$
$10^2$	2.594	8.262E2	8.263E2	$10^6$	12.86	9.222E4	9.222E4
$10^3$	3.710	1.676E3	1.676E3	$10^8$	28.02	1.897E6	1.897E6
$10^4$	5.698	5.377E3	5.377E3	$10^{11}$	88.87	1.875E8	1.876E8
$10^5$	8.626	2.130E4	2.131E4	$10^{13}$	191.51	4.037E9	4.037E9

TABLE 4: Thermal instability analysis in the presence of a rotation vector when both bounding surfaces are rigid: gravity vector and rotation vector acting in different directions. Rayleigh numbers  $R$  for the Taylor number  $T = 100$  and for various values of  $a$  and  $C_R$ .

$C_R$	$a$	$R$	$C_R$	$a$	$R$
0.0	3.15	1756.37	—	—	—
	3.0	1765.91		3.0	1806.85
0.5	3.15	1758.85	2.0	3.15	1796.01
	3.35	1767.31		3.35	1800.20
	3.0	1774.10		3.0	1937.84
1.0	3.15	1766.28	4.0	3.35	1905.43
	3.35	1773.89		3.45	1908.84

TABLE 5: Thermal instability analysis in the presence of a rotation vector when both bounding surfaces are free: Gravity vector and rotation vector acting in different directions. Rayleigh numbers  $R$  for the Taylor number  $T = 100$  and for various values of  $a$  and  $C_R$ .

$C_R$	$a$	$R$	$C_R$	$a$	$R$
0.0	2.594	826.28	—	—	—
	2.5	836.54		2.62	943.16
0.5	2.6	833.77	2.0	2.74	932.00
	2.64	833.84		3.00	933.42
	2.5	861.92		2.76	1228.56
1.0	2.66	855.00	4.0	3.2	1145.92
	2.72	855.35		3.4	1151.32

TABLE 6: Critical Rayleigh numbers and wave numbers at marginal stability for the onset of stationary convection when both bounding surfaces are rigid. Gravity vector  $\mathbf{g}$  parallel to the magnetic field vector  $\mathbf{H}$ .  $Q$  is the dimensionless magnetic parameter.  $R$  is the Rayleigh number obtained by the Tau Chebyshev method.  $R_{\text{Ch}}$  is the Rayleigh number obtained by Chandrasekhar [1].

$Q$	$a$	$R$	$R_{\text{Ch}}$
10	3.25	1945.8	1945.8
100	4.00	3757.27	3757.3
1000	5.80	17102.94	17103
4000	7.40	54696.93	54700
10000	8.66	124508.47	124509

the eight boundary conditions. Hence for rigid surfaces, the set of boundary conditions are written as

$$\begin{aligned}
 W(1) &= \sum_{n=0}^N a_{Wn} = 0, \quad \frac{dW(1)}{dx_3^*} = \sum_{n=0}^N a_{Wn} n^2 = 0, \\
 W(-1) &= \sum_{n=0}^N a_{Wn} (-1)^n = 0, \\
 \frac{dW(-1)}{dx_3^*} &= \sum_{n=0}^N a_{Wn} (-1)^{n-1} n^2 = 0, \\
 F(1) &= \sum_{n=0}^N a_{Fn} = 0, \quad F(-1) = \sum_{n=0}^N a_{Fn} (-1)^n = 0, \\
 Z(1) &= \sum_{n=0}^N a_{Zn} = 0, \quad Z(-1) = \sum_{n=0}^N a_{Zn} (-1)^n = 0,
 \end{aligned} \tag{61}$$

whereas for free surfaces the set of boundary conditions are written as

$$\begin{aligned}
 W(1) &= \sum_{n=0}^N a_{Wn} = 0, \\
 \frac{d^2 W(1)}{dx_3^{*2}} &= \sum_{n=0}^N a_{Wn} n^2 \left( \frac{n^2 - 1}{3} \right) = 0, \\
 W(-1) &= \sum_{n=0}^N a_{Wn} (-1)^n = 0, \\
 \frac{d^2 W(-1)}{dx_3^{*2}} &= \sum_{n=0}^N a_{Wn} (-1)^{n+2} n^2 \left( \frac{n^2 - 1}{3} \right) = 0, \\
 F(1) &= \sum_{n=0}^N a_{Fn} = 0, \\
 F(-1) &= \sum_{n=0}^N a_{Fn} (-1)^n = 0, \\
 \frac{dZ(1)}{dx_3^*} &= \sum_{n=0}^N a_{Zn} n^2 = 0, \\
 \frac{dZ(-1)}{dx_3^*} &= \sum_{n=0}^N a_{Zn} (-1)^{n-1} n^2 = 0.
 \end{aligned} \tag{62}$$

TABLE 7: Critical Rayleigh numbers and wave numbers at marginal stability for the onset of stationary convection when both bounding surfaces are free. Gravity vector  $\mathbf{g}$  parallel to the magnetic field vector  $\mathbf{H}$ .  $Q$  is the dimensionless magnetic parameter.  $R$  is the Rayleigh number obtained by the Tau Chebyshev method.  $R_{\text{Ch}}$  is the Rayleigh number obtained by Chandrasekhar [1].

$Q$	$a$	$R$	$R_{\text{Ch}}$	$Q$	$a$	$R$	$R_{\text{Ch}}$
10	2.590	923.069	923.070	7500	8.159	91705.75	91705.7
100	3.702	2653.708	2653.71	9000	8.429	108622.9	108623
1000	5.684	15207.01	15207.0	15000	9.227	175279.33	175279
2000	6.453	27699.95	27699.9	17000	9.433	197248.97	197249
5000	7.585	63135.98	63135.9	35000	10.70	392013.13	392013

TABLE 8: Thermal instability analysis in the presence of a magnetic field when both bounding surfaces are rigid: gravity vector and magnetic field vector acting in different directions. Rayleigh numbers for the dimensionless parameter  $Q = 100$  and for various values of  $a$  and  $C_H$ .  $R$  is the Rayleigh number obtained by the Tau Chebyshev method.  $R_{\text{Ch}}$  is the Rayleigh number obtained by Chandrasekhar [1].

$C_H$	$a$	$R$	$R_{\text{Ch}}$	$C_H$	$a$	$R$	$R_{\text{Ch}}$
0.0	4.0	3757.27	3757.3	—	—	—	—
	3.9	3785.12	3797.0		3.9	4146.18	4190.0
0.5	4.0	3780.70	3793.0	2.0	4.0	4136.55	4181.0
	4.1	3782.82	3795.0		4.1	4133.94	4178.0
	3.9	3856.64	3875.0		3.9	5356.98	5523.0
1.0	4.0	3851.20	3878.0	4.0	4.0	5328.39	5494.0
	4.1	3852.41	3871.0		4.1	5308.46	5474.0

TABLE 9: Thermal instability analysis in the presence of a magnetic field when both bounding surfaces are free: gravity vector and magnetic field vector acting in different directions. Rayleigh numbers for the dimensionless parameter  $Q = 100$ , and for various values of  $a$  and  $C_H$ .  $R$  is the Rayleigh number obtained by the Tau Chebyshev method.  $R_{\text{Ch}}$  is the Rayleigh number obtained by Chandrasekhar [1].

$C_H$	$a$	$R$	$C_H$	$a$	$R$
0.0	3.702	2653.70	—	—	—
	3.6	2679.49		3.6	3028.72
0.5	3.7	2676.17	2.0	3.8	3017.01
	3.8	2678.55		3.9	3020.24
	3.6	2748.31		3.6	4226.99
1.0	3.7	2743.9	4.0	4.1	4151.21
	3.8	2745.3		4.2	4157.48

Notice that the high frequency behaviour (i.e., high  $n$ ) of the solution is not governed by the perturbation equations but by the boundary conditions [12]. The Tau equations can be written as a generalized eigenvalue problem  $(\mathbf{A}\mathbf{x}) = R(\mathbf{B}\mathbf{x})$ , where the vector  $\mathbf{x}$  includes the coefficients  $a_{Wn}$ ,  $a_{Fn}$  (and  $a_{Zn}$ ),  $R$  is the Rayleigh number, and  $\mathbf{A}$  and  $\mathbf{B}$  are  $(2N + 2) \times (2N + 2)$  matrices (or  $(3N + 3) \times (3N + 3)$  matrices) whose first  $2N + 2 - 6$  (or  $3N + 3 - 8$ ) rows are defined by the two (or three) perturbation equations. The last six (or eight) rows of  $\mathbf{A}$  are given by the boundary conditions, and the last six (or eight) rows of  $\mathbf{B}$  vanish [16]. The system of equations has been solved numerically by using the routine F02GJF from the NAG library. The routine F02GJF calculates all the eigenvalues of the eigenproblem  $\mathbf{A}\mathbf{x} = \lambda\mathbf{B}\mathbf{x}$ , by using the QZ algorithm (see <http://www.nag.co.uk/numeric/F1/manual/xhtml/F02/f02gjf.xml>).

## 5. Results

**5.1. Thermal Instability Analysis in the Presence of a Rotation Vector,**  $\vartheta_R = 0$ ,  $\mathbf{H} = 0$ . Tables 2 and 3 show the critical Rayleigh number  $R$  and wave number  $a$  of the unstable modes at marginal stability for the onset of stationary convection when both bounding surfaces are rigid and when both bounding surfaces are free, respectively. It is possible to observe that the results obtained by the Tau Chebyshev method are in full agreement with the variational formulation; see [1]. It is also observed the inhibition effect of the Coriolis force as the Taylor number  $T$  increases. As  $T$  becomes greater, the value of the critical wave number also increases.

**5.2. Thermal Instability Analysis in the Presence of a Rotation Vector,**  $\vartheta_R \neq 0$ ,  $\mathbf{H} = 0$ . Tables 4 and 5 show the results obtained by the Tau Chebyshev method when both bounding surfaces are rigid and when both bounding surfaces are free, respectively. It is observed that when the Taylor number is  $T = 100$ , as the value of the  $C_R$  parameter increases, the critical parameters (Rayleigh number  $R_c$  and wave number  $a_c$ ) become greater. Note in Table 4 that when  $C_R = 1$ ,  $a_c = 3.15$  and  $R_c = 1766.28$ ; however, when  $C_R = 4$ ,  $a_c = 3.35$  and  $R_c = 1905.43$ . Also note in Table 5 that when  $C_R = 1$ ,  $a_c = 2.66$  and  $R_c = 855.0$ ; however, when  $C_R = 4$ ,  $a_c = 3.2$  and  $R_c = 1145.92$ . Hence for a fixed Taylor number, the net effect of increasing  $C_R$  is to stabilize the system.

**5.3. Thermal Instability Analysis in the Presence of a Magnetic Field,**  $\vartheta_H = 0$ ,  $\mathbf{\Omega} = 0$ . Tables 6 and 7 show the critical Rayleigh number  $R$  and wave number  $a$  of the unstable modes at marginal stability for the onset of stationary convection

TABLE 10: Thermal instability analysis in the presence of a rotation and a magnetic field when both bounding surfaces are free: gravity vector  $\mathbf{g}$  parallel to both rotation vector  $\mathbf{\Omega}$  and magnetic field vector  $\mathbf{H}$ . Critical Rayleigh numbers and wave numbers at marginal stability for the onset of stationary convection. Taylor number  $T_1 = T/\pi^4 = 10^5$  for various values of the dimensionless magnetic parameter  $Q_1 = Q/\pi^2$ .  $R$  and  $a$  are the Rayleigh number and the wave number, respectively, obtained by the Tau Chebyshev method.  $R_{\text{Ch}}$  and  $a_{\text{Ch}}$  are the Rayleigh number and the wave number, respectively, obtained by Chandrasekhar [1]. The superscripts 1 and 2 mean the two minima of the Rayleigh number.

$Q_1$	$a^1$	$R^1$	$a_{\text{Ch}}^1$	$R_{\text{Ch}}^1$	$a^2$	$R^2$	$a_{\text{Ch}}^2$	$R_{\text{Ch}}^2$
10	18.87	4.066E5	18.9	4.067E5	—	—	—	—
50	18.58	4.028E5	18.6	4.028E5	3.49	7.261E5	3.48	7.261E5
100	18.2	3.976E5	18.2	3.977E5	3.365	3.932E5	3.37	3.933E5
1000	—	—	—	—	5.675	1.828E5	5.67	1.829E5
10000	—	—	—	—	12.29	1.081E6	12.3	1.082E6
100000	—	—	—	—	18.9	1.015E7	18.9	1.015E7

when both bounding surfaces are rigid and when both bounding surfaces are free, respectively. It is possible to observe that the results obtained by the Tau Chebyshev method are in full agreement with the variational formulation; see [1]. It is also observed the inhibition effect of the magnetic field, as the magnetic number  $Q$  increases. As  $Q$  becomes greater, the value of the critical wave number also increases.

**5.4. Thermal Instability Analysis in the Presence of a Magnetic Field,  $\vartheta_H \neq 0$ ,  $\mathbf{\Omega} = 0$ .** Tables 8 and 9 show the results obtained by the Tau Chebyshev method when both bounding surfaces are rigid and when both bounding surfaces are free, respectively. It is observed that when the Chandrasekhar number  $Q$  is fixed to  $Q = 100$ , as the value of the  $C_H$  parameter increases, the critical Rayleigh number becomes greater. In Table 8 we present a comparison between the results obtained by [1] and the results of the Tau Chebyshev method. We observe that if the data obtained by Chandrasekhar are the exact values, the maximum percentage error (% error), when  $C_H \neq 0$ , of the critical  $R$  number calculated by the Tau Chebyshev method occurs when  $C_H = 4.0$  and  $a = 4.1$ , with an error of 3%, while the minimum percentage error occurs when  $C_H = 0.5$  and  $a = 3.9$ , with an error of 0.3%. Thus we may conclude that our calculations are in good agreement with Chandrasekhar's results. Note in Table 8 that when  $C_H = 1$ , the critical wave number  $a = 4$ ; however, when  $C_H = 4$ , the critical wave number  $a = 4.1$ . Also note in Table 9 that when  $C_H = 1$ , the critical wave number  $a = 3.7$ ; however, when  $C_H = 4$ , the critical wave number  $a = 4.1$ . Hence for a fixed Chandrasekhar number  $Q$ , the net effect of increasing  $C_H$  is to stabilize the system.

**5.5. Thermal Instability Analysis in the Presence of a Rotation Vector and a Magnetic Field,  $\vartheta_R = 0$ ,  $\vartheta_H = 0$ .** Table 10 shows a comparison between the results obtained by the Tau Chebyshev method and those of Chandrasekhar's variational formulation when both bounding surfaces are free. The results have been obtained for several values of the modified magnetic number  $Q_1 = Q/\pi^2$  and for a fixed value of the modified Taylor number  $T_1 = T/\pi^4 = 10^5$ . Notice that the agreement is encouraging. Also note that the two minima of the Rayleigh number are successfully reproduced by the Tau

Chebyshev method. It is interesting to mention that by using the Tau Chebyshev method we found two additional critical Rayleigh numbers that were not reported by Chandrasekhar (see [1], Table XVIII, page 205, for  $T_1 = 10^5$ ). We found (not shown in Table 10) that when  $Q_1 = 30$ ,  $a = 3.93$  and  $R = 1.125 \times 10^6$ , and when  $Q_1 = 200$ ,  $a = 17.1$  and  $R = 3.855 \times 10^5$ . Figure 2 shows that if  $T_1 = 10^5$ , when both bounding surfaces are free (see row (a)), and the magnetic parameter  $Q_1$  is either  $Q_1 = 40$  (curve labelled a),  $Q_1 = 100$  (curve labelled b), or  $Q_1 = 200$  (curve labelled c), see left panel, the two minima of the Rayleigh number curves reported by Chandrasekhar are recovered (see [1], Figure 49, page 208). Row (b), left panel of Figure 2, shows that when the bounding surfaces are rigid, the two minima only slightly appear when  $Q_1 = 100$  (curve labelled b) and  $Q_1 = 200$  (curve labelled c); however, when  $Q_1 = 40$  (curve labelled a), only one minimum value is present. Figure 2 shows on the left panel of both rows the case with pure rotation  $T_1 = 10^5$ , that is, without magnetic field (see the curves with circles). It is pointed out that when the surfaces are free (row (a), left panel), the effect of the magnetic field is to destabilize the system, particularly when  $Q_1 = 200$  (curve labelled c). This effect is clearly observed for low values of the modified wave number  $x = a^2/\pi^2$ . It is also observed that the system with  $Q_1 = 200$  is more unstable than the pure rotation case. However when the surfaces are rigid (see row (b), left panel), it is possible to observe that as the magnetic field becomes greater, it firstly induces a stabilizing effect, with respect to the pure rotation case (see curve labelled a for  $Q_1 = 40$  and the curve with circles), but for  $Q_1 = 100$  and 200, it initiates a destabilizing effect; however, the pure rotation case (see the curve with circles) is more unstable. On the other hand Figure 2 shows, on the right panel of both rows, the influence of greater magnetic numbers ( $Q_1 = 400$  (see continuous lines),  $Q_1 = 1500$  (see dashed lines),  $Q_1 = 2000$  (see dotted lines), and  $Q_1 = 4000$  (see dash-dotted lines)). Also shown on the right panel of both rows is the case with pure magnetic field  $Q_1 = 4000$ , that is, without rotation (see the curves with asterisks). It is pointed out that when the surfaces are free or rigid, when  $Q_1 = 400$  (see the continuous lines), the system reaches its critical situation; that is, the minimum value of the Reynolds number is attained. However as  $Q_1$  increases even more, the system becomes more stable. Now when the surfaces are free (row (a)), and when the curve with asterisks



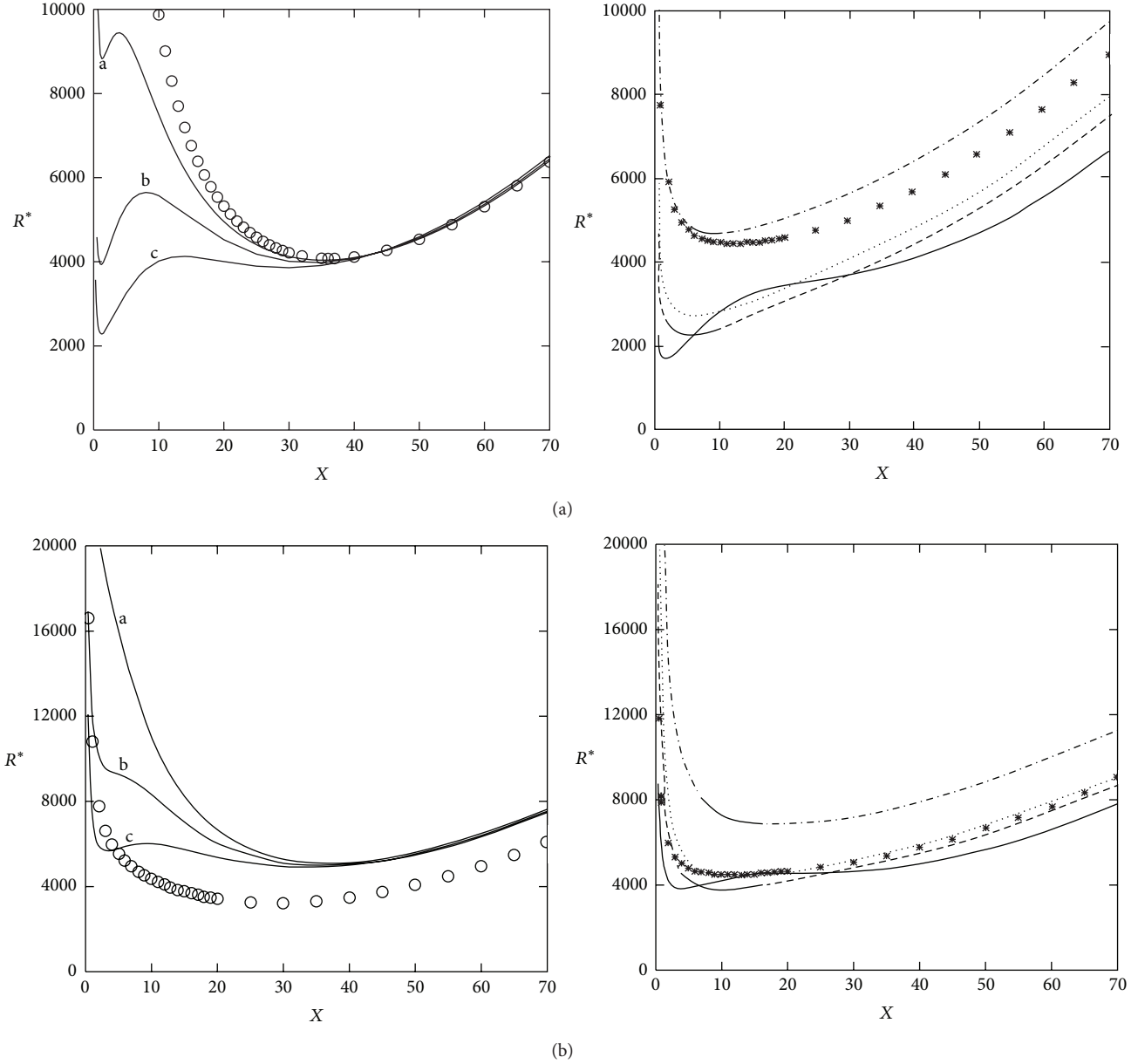


FIGURE 2: Thermal instability analysis in the presence of a rotation and a magnetic field. Gravity vector parallel to both rotation vector and magnetic field vector. The dependence of the Rayleigh number  $R$  ( $R^* = R/100$ ) on the wave number  $a$  ( $x = a^2/\pi^2$ ) when  $T_1 = 10^5$ . Left panels:  $Q_1 = 40$  (curves labelled a),  $Q_1 = 100$  (curves labelled b),  $Q_1 = 200$  (curves labelled c), circles: pure rotation  $T_1 = 10^5$  without magnetic field. Right panels:  $Q_1 = 400$  (continuous lines),  $Q_1 = 1500$  (dashed lines),  $Q_1 = 2000$  (dotted lines),  $Q_1 = 4000$  (dash-dotted lines), asterisks: pure magnetic field  $Q_1 = 2000$ , without rotation. Row (a): free boundaries. Row (b): rigid boundaries.

( $Q_1 = 4000$ , without rotation) is compared with the dash-dotted line ( $Q_1 = 4000$ ,  $T_1 = 10^5$ ), it is possible to observe that the Coriolis force induces a marginal stabilizing effect. However when the surfaces are rigid (row (b)) and when the curve with asterisks ( $Q_1 = 4000$ , without rotation) is compared with the dash-dotted line ( $Q_1 = 4000$ ,  $T_1 = 10^5$ ), we observe that rotation has a significant stabilizing effect. According to the previous discussion we confirm the fact that when  $\mathbf{H}$  and  $\mathbf{\Omega}$  act simultaneously and when both are parallel to the gravity vector, the stabilizing effects have conflicting tendencies. Figure 3 shows the influence of the Coriolis force

when the magnetic number is fixed to  $Q_1 = 2000$  and when the surfaces are free (left panel) and rigid (right panel). Notice that when the surfaces are free, the Coriolis force when  $T_1 = 1000$  (curve labelled a) does not produce any effect on the system as compared to that when there is no rotation (see the asterisks curve for  $T_1 = 0$ ). However when the surfaces are rigid (right panel), the Coriolis force when  $T_1 = 1000$  induces a stabilizing effect as compared with the case without rotation (see the asterisks curve for  $T_1 = 0$ ). It is clearly observed that as the modified Taylor number  $T_1$  acquires the values  $5 \times 10^5$  and  $10^6$ , the system becomes more stable.

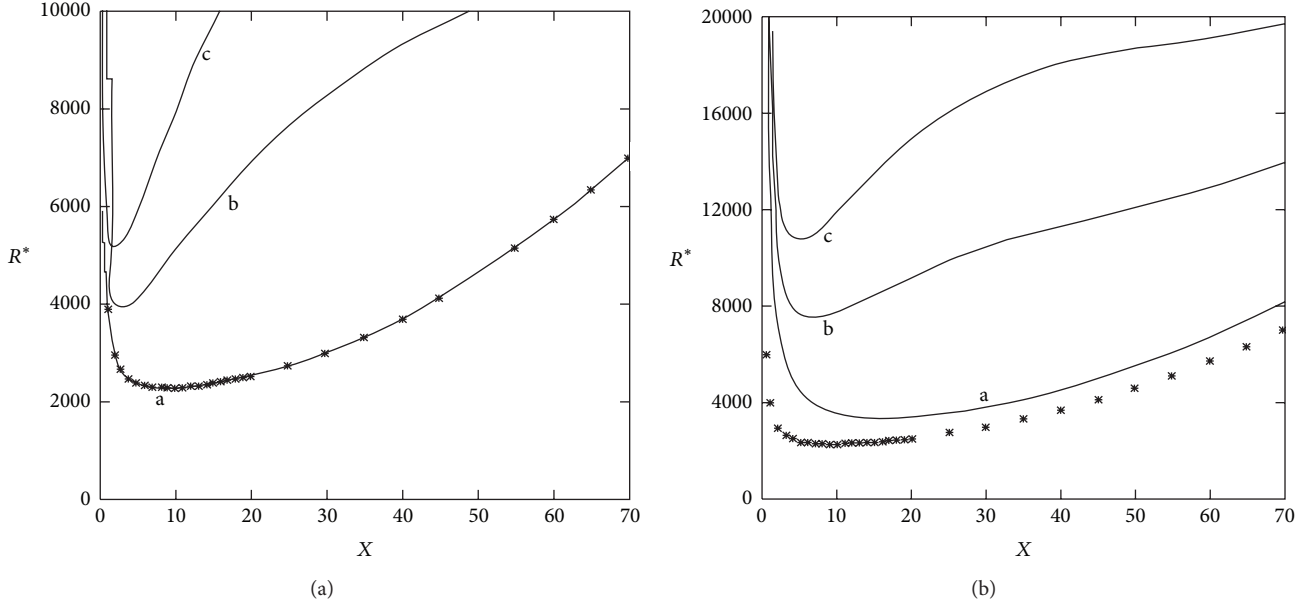


FIGURE 3: Thermal instability analysis in the presence of a rotation and a magnetic field. Gravity vector parallel to both rotation vector and magnetic field vector. The dependence of the Rayleigh number  $R$  ( $R^* = R/100$ ) on the wave number  $a$  ( $x = a^2/\pi^2$ ) when  $Q_1 = 2000$ . The effect of the Coriolis force:  $T_1 = 0$  (without rotation, asterisks curves),  $T_1 = 1000$  (curves labelled a),  $T_1 = 5 \times 10^5$  (curves labelled b), and  $T_1 = 10^6$  (curves labelled c). Left panel: free boundaries. Right panel: rigid boundaries.

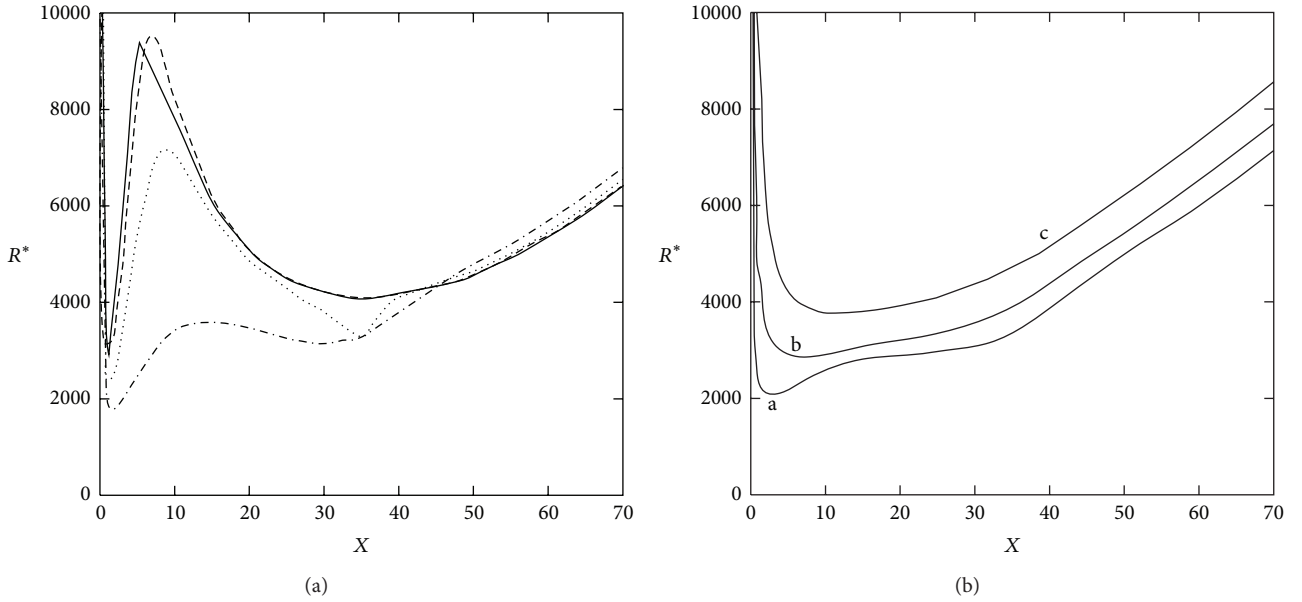


FIGURE 4: Thermal instability analysis in the presence of a rotation and a magnetic field. Gravity vector parallel to the magnetic field vector ( $C_H = 0$ ). Rotation vector at different values of  $C_R \neq 0$ . The dependence of the Rayleigh number  $R$  ( $R^* = R/100$ ) for the onset of instability on the wave number  $a$  ( $x = a^2/\pi^2$ ) when  $T_1 = 10^5$  and  $Q_1 = 40$  (for free surfaces).  $Q_1 = Q/\pi^2$  and  $T_1 = T/\pi^4$ . Left panel:  $C_R = 0.5$  (continuous line),  $C_R = 1$  (dashed line),  $C_R = 2$  (dotted line), and  $C_R = 4$  (dotted-dashed line). Right panel:  $C_R = 6$  (curve labelled a),  $C_R = 8$  (curve labelled b), and  $C_R = 10$  (curve labelled c).

**5.6. Thermal Instability Analysis in the Presence of a Rotation Vector and a Magnetic Field,  $\vartheta_R \neq 0$ ,  $\vartheta_H \neq 0$ .** Figure 4 shows, for free surfaces, the dependence of the critical Rayleigh number  $R^* = R/100$  and the critical wave number  $x = a^2/\pi^2$ , on the parameter  $C_R$ , when the Taylor number

$T_1 = T/\pi^4 = 10^5$ , the magnetic parameter  $Q_1 = Q/\pi^2 = 40$ , and the gravity vector  $\mathbf{g}$  is parallel to the magnetic field vector  $\mathbf{H}$  ( $C_H = 0$ ). On the left panel the competition between the stabilizing effect of the Coriolis force and the strong destabilizing properties of the  $C_R$  parameter when it is in



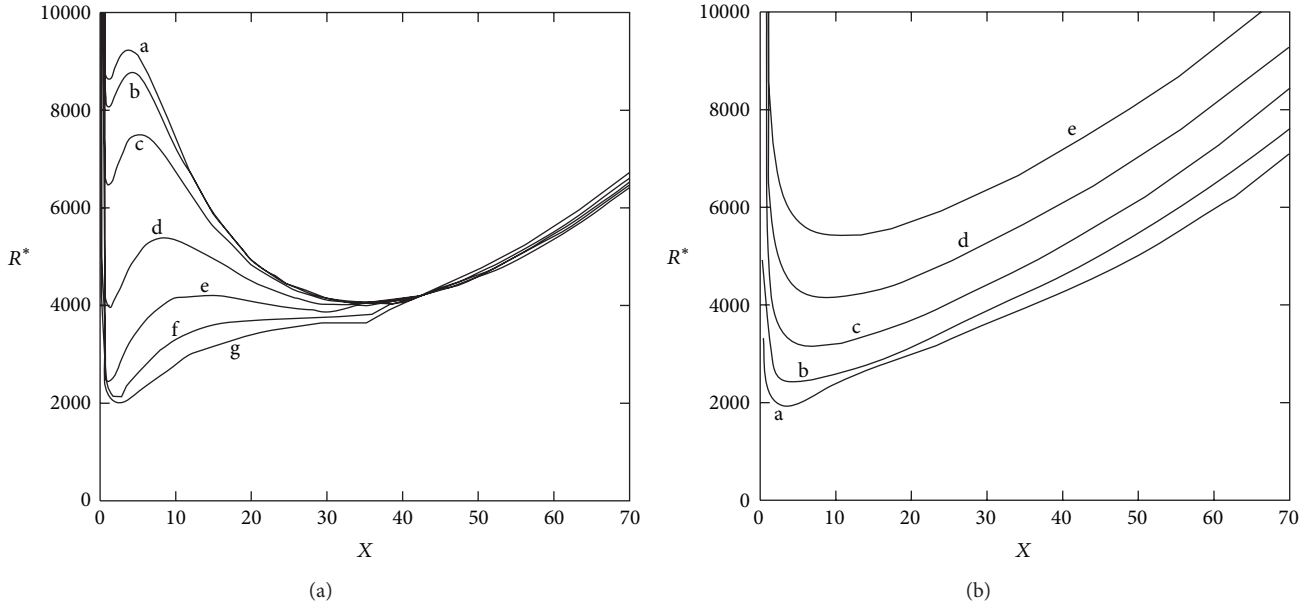


FIGURE 5: Thermal instability analysis in the presence of a rotation and a magnetic field. Gravity vector parallel to the rotation vector ( $C_R = 0$ ). Magnetic field vector at different values of  $C_H \neq 0$ . The dependence of the Rayleigh number  $R^*$  for the onset of instability on the wave number  $x$  when  $T_1 = 10^5$  and  $Q_1 = 40$  (for free surfaces). Left panel:  $C_H = 0.5$  (curve labelled a),  $C_H = 1$  (curve labelled b),  $C_H = 2$  (curve labelled c),  $C_H = 4$  (curve labelled d),  $C_H = 6$  (curve labelled e),  $C_H = 8$  (curve labelled f), and  $C_H = 10$  (curve labelled g). Right panel:  $C_H = 15$  (curve labelled a),  $C_H = 20$  (curve labelled b),  $C_H = 25$  (curve labelled c),  $C_H = 30$  (curve labelled d), and  $C_H = 35$  (curve labelled e).

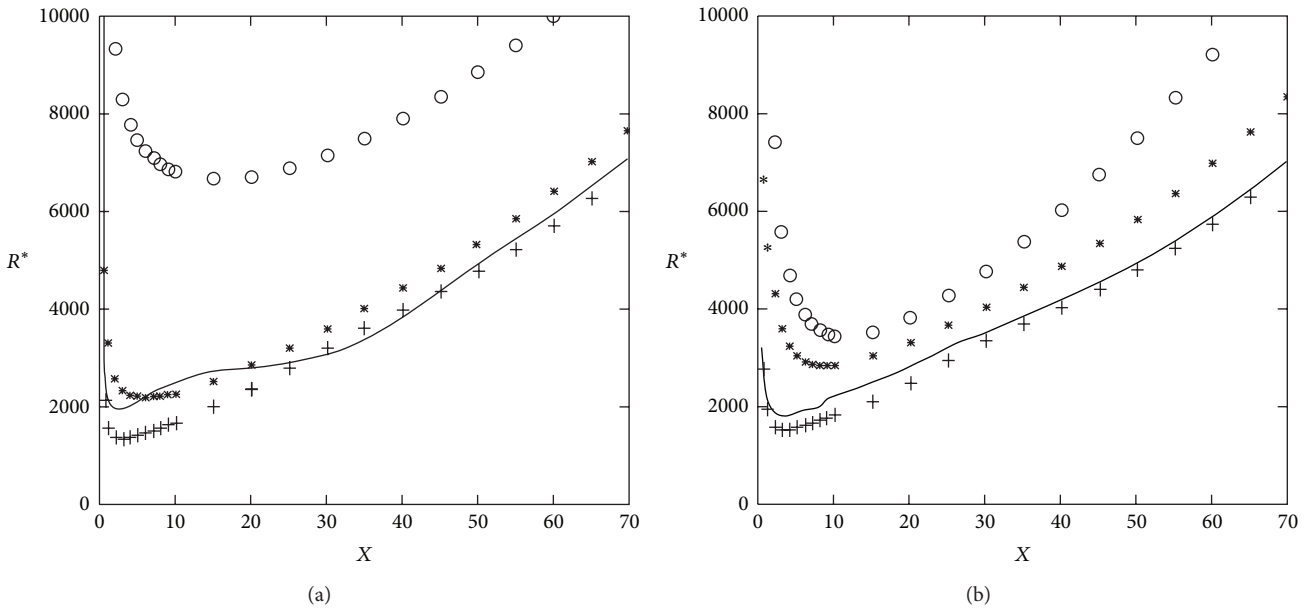


FIGURE 6: Thermal instability analysis in the presence of a rotation and a magnetic field. The dependence of the Rayleigh number  $R^*$  for the onset of instability on the wave number  $x$  when  $T_1 = 10^5$  and  $Q_1 = 40$  (for free surfaces). Left panel: rotation vector at  $C_R = 6$ , for different values of  $C_H$ ,  $C_H = 2$  (continuous line),  $C_H = 10$  (+ curve),  $C_H = 20$  (\* curve), and  $C_H = 40$  (o curve). Right panel: magnetic field vector at  $C_H = 15$ , for different values of  $C_R$ ,  $C_R = 0.5$  (continuous line),  $C_R = 2$  (+ curve),  $C_R = 10$  (\* curve), and  $C_R = 15$  (o curve).

the range  $0.5 \leq C_R \leq 4$  is observed. When  $C_R = 0$  and  $C_H = 0$ , the critical Rayleigh number is  $R^* = 8829.8$ ; see left panel of Figure 2, while left panel of Figure 4 shows that when  $C_R = 0.5$ , the critical Rayleigh number has been lowered to  $R^* = 3009.2$ . Note, on the left panel, the presence of the two

minima in the curves of the Rayleigh number  $R^*$ . On the right panel of Figure 4 it is shown that when the  $C_R$  parameter is in the range  $6 \leq C_R \leq 10$ , the fluid layer becomes more stable as  $C_R$  increases. Therefore, we have found that there is a critical value of the  $C_R$  parameter at which the destabilizing

behaviour is changed to a stabilizing performance, and the critical value occurs around  $C_R = 6$  (see right panel). It is also possible to observe that the curves corresponding to  $C_R = 8$  (curve labelled b) and  $C_R = 10$  (curve labelled c) only show one minimum value. In general it is observed that as the  $C_R$  parameter increases, the wave number  $x = a^2/\pi^2$  also increases and a tendency to get only one minimum is apparent.

Figure 5 shows, for free surfaces, the dependence of the critical Rayleigh number  $R^*$  and the critical wave number  $x$  on the parameter  $C_H$ , when the Taylor number  $T_1 = 10^5$ , the magnetic parameter  $Q_1 = 40$ , and the gravity vector  $\mathbf{g}$  is parallel to the rotation vector  $\mathbf{\Omega}$  ( $C_R = 0$ ). On the left panel it is shown that the influence of the parameter  $C_H$ , when its value is 0.5 (curve labelled a), is almost negligible; hence, curve for  $C_H = 0.5$  resembles curve labelled a, of Figure 2 left panel, when  $C_R = 0$  and  $C_H = 0$ . On the left panel of Figure 5, it is possible to observe the competition between the stabilizing effect of the Coriolis force and the destabilizing influence of the  $C_H$  parameter when its values are in the range  $0.5 \leq C_H \leq 10$ ; that is, as the  $C_H$  parameter increases, the fluid layer gets more unstable. Right panel of Figure 5 shows the cooperative behaviour between the Coriolis force and the  $C_H$  parameter; that is, as the  $C_H$  parameter increases even more in the range  $15 \leq C_H \leq 35$ , the fluid layer becomes more stable. Hence we have found again that a critical value of the  $C_H$  parameter exists at which the destabilizing performance of  $C_H$  is transformed to a stabilizing behaviour. The critical  $C_H$  is around  $C_H = 15$ . We can also conclude that as the  $C_H$  parameter increases, the wave number  $x = a^2/\pi^2$  also increases and the tendency to get only one minimum is clear.

Finally left panel of Figure 6 shows for free surfaces, the dependence of the Rayleigh number  $R^* = R/100$  on the wave number  $x = a^2/\pi^2$  when  $C_R$  is a fixed value equal to  $C_R = 6$  and  $C_H$  has the values  $C_H = 2, 10, 20$ , and 40. Right panel of Figure 6 also shows for free surfaces the dependence of the Rayleigh number  $R^*$  on the wave number  $x$  when  $C_H$  is a fixed value equal to  $C_H = 15$  and  $C_R$  has the values  $C_R = 0.5, 2, 10$ , and 15. In both panels of Figure 6, the modified Taylor and magnetic numbers are  $T_1 = 10^5$  and  $Q_1 = 40$ , respectively. When  $C_R$  is fixed to  $C_R = 6$  (see left panel), we observe that the curve  $C_H = 2$  (continuous line) resembles the curve  $a$  (for  $C_H = 0$ ) shown in right panel of Figure 4. However the case  $C_H = 2$  is a bit more unstable than the case  $C_H = 0$ . When  $C_H$  increases to  $C_H = 10$  (+ curve), the system becomes even more unstable; however, it is clearly observed that there exists a critical value of  $C_H$  (around 10), at which the system shifts its unstable behaviour to a more stable performance, see the curves for  $C_H = 20$  (\* curve) and  $C_H = 40$  (o curve). When  $C_H$  is fixed to  $C_H = 15$  (see right panel), we observe that the curve  $C_R = 0.5$  (continuous line) is very similar to the curve  $a$  (for  $C_R = 0$ ) shown in Figure 5 right panel. When  $C_R$  increases to  $C_R = 2$  (+ curve), the system becomes more unstable, however it is clearly observed that there also exists a critical value of  $C_R$  (around 2), at which the system shifts its unstable behaviour to a more stable performance; see the curves for  $C_R = 10$  (\* curve) and  $C_R = 15$  (o curve). In both panels of Figure 6 it is observed

that before the critical situation there exists a competition between  $C_H$  and  $C_R$  parameters, and the result is that the fluid layer is transformed into a more unstable system. However after the critical situation, there is a cooperative work of  $C_H$  and  $C_R$  to inhibit the thermal convection of the infinite layer of fluid.

## 6. Conclusions

The Tau Chebyshev method has been used to solve the classical problem of thermal convection on an infinite fluid layer with rotation and an impressed magnetic field. Our methodology has been verified with results previously published in the literature, through the solution of the first five cases shown in Table 1. By using the Tau Chebyshev method, we find that, for the sixth case shown in Table 1, a critical value of the  $C_R$  and  $C_H$  parameters exists at which the competition between  $\mathbf{H}$  and  $\mathbf{\Omega}$ , which leads to an unstable system, can be transformed to a cooperative work that promotes a system in which the thermal convection of the layer of fluid is inhibited.

## Acknowledgments

Financial support for this investigation was provided by the Center for Aerospace Research & Education, University of California, Irvine, CA, USA. R. Avila thanks Professor. Dr. Satya Atluri for his encouragement.

## References

- [1] S. Chandrasekhar, *Hydrodynamic and Hydromagnetic Stability*, Clarendon Press, Oxford, UK, 1961.
- [2] S. Chandrasekhar, "The instability of a layer of fluid heated below and subject to Coriolis forces," *Proceedings of the Royal Society. London A*, vol. 217, pp. 306–327, 1953.
- [3] S. Chandrasekhar and D. D. Elbert, "The instability of a layer of fluid heated below and subject to Coriolis forces. II," *Proceedings of the Royal Society. London A*, vol. 231, pp. 198–210, 1955.
- [4] S. Chandrasekhar, "The instability of a layer of fluid heated below and subject to the simultaneous action of a magnetic field and rotation," *Proceedings of the Royal Society. London A*, vol. 225, pp. 173–184, 1954.
- [5] S. Chandrasekhar, "On the inhibition of convection by a magnetic field," *The Philosophical Magazine*, vol. 43, pp. 501–532, 1952.
- [6] B. Lehnert and N. C. Little, "Experiments on the effect of inhomogeneity and obliquity of a magnetic field in inhibiting convection," *Tellus*, vol. 9, pp. 97–103, 1957.
- [7] P. Falsaperla and S. Lombardo, "Competition and cooperation of stabilizing effects in the Bénard problem with Robin type boundary conditions," in *Proceedings of the 15th Conference on Waves and Stability in Continuous Media (WASCOM '09)*, pp. 140–145, World Scientific, 2010.
- [8] S. Chandrasekhar, "The instability of a layer of fluid heated below and subject to the simultaneous action of a magnetic field and rotation. II," *Proceedings of the Royal Society. London A*, vol. 237, pp. 476–484, 1956.
- [9] P. Falsaperla, *Stability in convection problems for fluids and flows in porous media with general boundary conditions [Ph.D. thesis]*, Università degli Studi di Catania, 2010.

- [10] S. Lombardo, "Stability in the Bénard problems with competing effects via the reduction method," in *Proceedings of the 14th Conference on Waves and Stability in Continuous Media (WASCOM '08)*, pp. 372–377, World Scientific, 2008.
- [11] P. Falsaperla and G. Mulone, "Stability in the rotating Bénard problem with Newton-Robin and fixed heat flux boundary conditions," *Mechanics Research Communications*, vol. 37, no. 1, pp. 122–128, 2010.
- [12] A. S. Orszag, "Accurate solution of the Orr-Sommerfeld stability equation," *Journal of Fluid Mechanics*, vol. 50, pp. 689–703, 1971.
- [13] J. J. Dongarra, B. Straughan, and D. W. Walker, "Chebyshev tau-QZ algorithm methods for calculating spectra of hydrodynamic stability problems," *Applied Numerical Mathematics*, vol. 22, no. 4, pp. 399–434, 1996.
- [14] D. Bourne, "Hydrodynamic stability, the Chebyshev tau method and spurious eigenvalues," *Continuum Mechanics and Thermodynamics*, vol. 15, no. 6, pp. 571–579, 2003.
- [15] D. Gottlieb and S. A. Orszag, "Numerical analysis of spectral methods: theory and applications," in *CBMS-NSF Regional Conference Series in Applied Mathematics*, vol. 26, SIAM, Philadelphia, Pa, USA, 1977.
- [16] G. B. McFadden, B. T. Murray, and R. F. Boisvert, "Elimination of spurious eigenvalues in the Chebyshev tau spectral method," *Journal of Computational Physics*, vol. 91, no. 1, pp. 228–239, 1990.

## Research Article

# Estimation of Wellbore and Formation Temperatures during the Drilling Process under Lost Circulation Conditions

Mou Yang,<sup>1</sup> Yingfeng Meng,<sup>1</sup> Gao Li,<sup>1</sup> Yongjie Li,<sup>1</sup> Ying Chen,<sup>1</sup>  
Xiangyang Zhao,<sup>2</sup> and Hongtao Li<sup>1</sup>

<sup>1</sup> State Key Laboratory of Oil and Gas Reservoir Geology and Exploitation, Southwest Petroleum University, Chengdu 610500, China

<sup>2</sup> Research Institute of Petroleum Engineering, SINOPEC, Beijing 100101, China

Correspondence should be addressed to Yingfeng Meng; [cwctmyf@vip.sina.com](mailto:cwctmyf@vip.sina.com) and Gao Li; 546652841@qq.com

Received 4 February 2013; Revised 22 June 2013; Accepted 24 June 2013

Academic Editor: Zhijun Zhang

Copyright © 2013 Mou Yang et al. This is an open access article distributed under the Creative Commons Attribution License, which permits unrestricted use, distribution, and reproduction in any medium, provided the original work is properly cited.

Significant change of wellbore and surrounding formation temperatures during the whole drilling process for oil and gas resources often leads by annulus fluid fluxes into formation and may pose a threat to operational security of drilling and completion process. Based on energy exchange mechanisms of wellbore and formation systems during circulation and shut-in stages under lost circulation conditions, a set of partial differential equations were developed to account for the transient heat exchange process between wellbore and formation. A finite difference method was used to solve the transient heat transfer models, which enables the wellbore and formation temperature profiles to be accurately predicted. Moreover, heat exchange generated by heat convection due to circulation losses to the rock surrounding a well was also considered in the mathematical model. The results indicated that the lost circulation zone and the casing programme had significant effects on the temperature distributions of wellbore and formation. The disturbance distance of formation temperature was influenced by circulation and shut-in stages. A comparative perfection theoretical basis for temperature distribution of wellbore-formation system in a deep well drilling was developed in presence of lost circulation.

## 1. Introduction

Annulus fluid fluxed into formation usually in presence of lost circulation problem occurs in oil-gas and geothermal wells during the drilling stage with increasing well depth, thus resulting in continuous variation of the temperature of wellbore (inside drilling string fluid, drilling pipe, and annulus) and surrounding formation (casing, cement sheath, static drilling fluid, and rock). Moreover, the determination of transient temperature distributions in and around oil-gas well under circulation and shut-in conditions is a complex task because of the occurrence of lost circulation due to the change of drilling fluid flow state and formation property [1–3]. Therefore, it is important to obtain the accurate temperature distributions of wellbore and formation under lost circulation conditions, which can develop the adequate drilling style and design the excellent property of drilling fluids and cement slurries [4, 5].

A reliable and accurate estimation of such temperature distribution requires a complete dynamic thermal study related to the drilling fluid flow in and around the wellbore, which includes a set of numerical models as well as boundary and initial conditions. At present, the estimation temperature method in and around oil-gas well is mainly classified into two classes. One deals with using classical analytical methods based on conductive heat flow in cylindrical coordinate [6–11], exclusive of conductive-convective heat flow method [12] and the spherical and radial heat flow method [13]. These models have been considered as excellent methods in many applications due to their simplicity, whereas the formation temperature obtained by these methods is normally lower than the initial temperature [14]. The other class attempts to describe the transient heat transfer processes using numerical models based on the energy balance principle in each region of a well during circulation and shut-in stages [15–19].

The previous estimation methods are mainly focused on studying the wellbore and formation temperatures under no lost circulation condition. That is to say, these methods cannot accurately estimate the wellbore and formation temperatures in presence of lost circulation. Recently, with regard to this, only a few studies involved several aspects for estimating the temperatures of fluid and formation when lost circulation is being [20–22]. However, those studies have little attention on studying the heat exchanged mechanism and law between wellbore and formation under lost circulation conditions by the numerical model.

Therefore, in this work, the development of transient heat transfer model for estimation of wellbore and formation temperatures in oil-gas wells during circulation and shut-in stages under lost circulation condition are presented. Here, the well-formation interface is considered as a porous medium through which fluid lost by circulation [23]. Moreover, to deeply analyze lost circulation process for radial heat transfer equation, the model also takes the radial fluid motion and the radial heat flow from annulus to formation into consideration. Thereby, under lost circulation, the comprehensive model is applied to estimate each heat transfer region in a well according to the actual data of well drilling.

## 2. Physical Model

The physical model of lost circulation during circulation stage is shown in Figure 1. The process of circulation is considered as three distinct phases: (1) fluid enters the drill pipe with a specified temperature ( $T_{in}$ ) at the surface and passes down with flow velocity  $v_{z1}$  in the  $z$  direction; (2) fluid exits the drill pipe through the bit and enters the annulus at the bottom; (3) fluid passes up the annulus with flow velocity  $v_{z3}$  and exits the annulus with a specified temperature ( $T_{out}$ ) at the surface [15, 18]. If lost circulation is being in a certain formation, drilling fluid would be flown into surrounding formation so that it becomes hard to precisely define the temperature profile of a well. Therefore, to simulate thermal behavior of fluid during the circulation process, it is necessary to develop a set of partial differential equations under the actual casing program and drill string assembly conditions, which is illustrated in Figure 1. Mass and energy conservation is considered as incompressible flow in the axial ( $z$ ) and radial ( $r$ ) directions. Meanwhile, the effect factors of boundary conditions among each control unite are taken into account in the solving model.

During the circulation stage, the fluid passes down the pipe in the  $z$  direction, and its temperature distribution is determined by the rate of heat convection down the drilling pipe and heat exchange with the metallic pipe wall. At the bottom, the fluid temperature at the outlet of the drill pipe is the same as the fluid temperature at the entrance of the annulus, and then the fluid keeps on flowing up in the annulus. Similarly, the annulus fluid temperature is determined by the rate of heat convection up the annulus, the rate of heat exchange between the annulus and drill pipe wall, and the rate of heat exchange between the wall of the well and annulus fluid [23]. Meanwhile, well depth and flow rate

of lost circulation have great effects on annulus temperature. In addition, fluid friction, rotational energy, and drill bit energy also have significant influence on the overall energy balance of the wellbore [24]. During shut-in stage, above the lost depth, all wellbore fluid will flow into formation. Therefore, the temperatures in the wellbore which are decided by fluid flow state depend upon a number of different thermal processes involving conductive and convective mechanisms in different sections of well. When wellbore fluid is in flowing state, the fluid temperatures of inside drill string and annulus are strong dependent upon the rate of lost circulation in heat convection way; if all of wellbore fluid above the loss depth flow into formation, the heat exchange between wellbore and formation is only in a conduction way.

## 3. Mathematical Model

**3.1. Assumption Conditions.** The mathematical model consisted of a set of partial differential equations used to describe the temperatures of wellbore and formation. The fundamental assumptions of numerical model include the following.

- (i) Each control unit of wellbore and formation system is cylindrical geometry.
- (ii) The physical properties of the formation, cement, and metal pipe are constant with the change of depths [5]. The parameters include thermal conductivity, density, heat capacity, and viscosity.
- (iii) The radial temperature gradient within the fluid may be neglected.
- (iv) The heat conduction equation through surrounding wellbore is solved by using a two-dimensional transient axial-symmetric temperature distribution.
- (v) Viscous dissipation and thermal expansion effects are neglected.

Under these conditions, the governing equations and initial and boundary conditions for each region are as follows.

### 3.2. Mathematical Formulation

#### 3.2.1. Transient Heat Transfer during Circulation Stage

**(1) Inside the Drilling String.** The numerical model which can calculate the temperature distribution of inside drilling string is complemented by the following three considerations: (1) the inlet fluid temperature is the boundary condition of the model; (2) the flow velocity of fluid in the  $z$  direction is also defined by mass flow rate; and (3) heat generated by fluid friction. Therefore, based on energy conservation principle, the model is expressed as follows:

$$\frac{Q_m}{\pi r_1^2} - \frac{\partial(\rho_1 c_1 T_1 q)}{\pi r_1^2 \partial z} - \frac{2h_1(T_1 - T_2)}{r_1} = \frac{\partial(\rho_1 c_1 T_1)}{\partial t}. \quad (1)$$



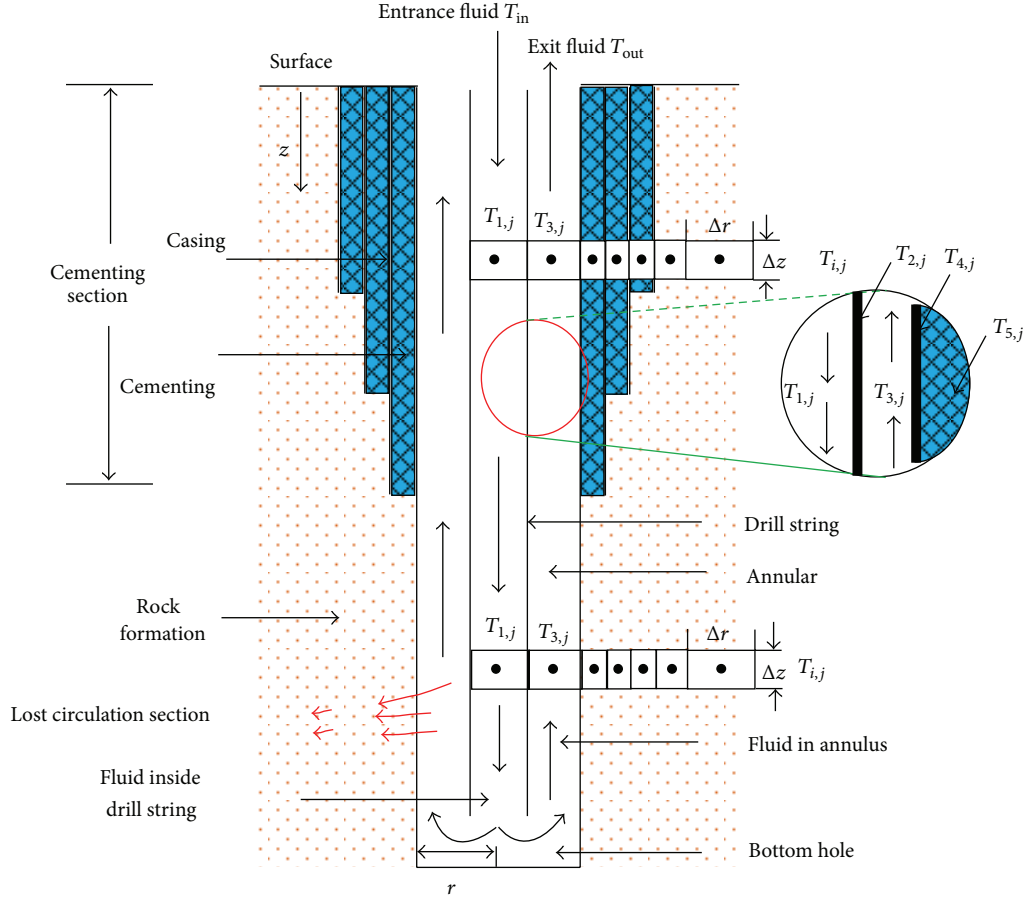


FIGURE 1: Physical model of drilling fluid circulation under lost circulation condition.

The boundary condition between fluid and inner wall of drill string is written as follows:

$$-\lambda_2 \left( \frac{\partial T_2}{\partial r} \right)_{r=r_1} = h_1 (T_2 - T_1), \quad (2)$$

where  $T_1$ ,  $T_2$  are the temperatures of inside drilling string fluid and drilling string wall, respectively;  $Q_m$  is the energy source term of unit length inside the drilling string;  $\rho_1$  is the density of drilling fluid;  $q$  is the flow rate of inside drill string;  $c_1$  is the specific heat capacity of drilling fluid;  $r_1$  is the radius of inside drill string;  $\lambda_2$  is the thermal conductivity of drill string; and  $h_1$  is the convection coefficient of inside drilling string wall.

(2) *Drill String Wall.* The formulation calculates the temperature distribution of drill string wall, and the conditions here are defined by the three sections: (1) the mass flow rate of fluid in the inside drill string and annulus; (2) the vertical conduction of heat in the drill pipe; and (3) the radial exchange of heat between the drill pipe and the fluid inside

and outside the string. The numerical model of the drill string wall is given as follows:

$$\begin{aligned} \frac{\partial}{\partial z} \left( \lambda_2 \frac{\partial T_2}{\partial z} \right) + \frac{2r_1 h_1}{(r_2^2 - r_1^2)} (T_1 - T_2) \\ - \frac{2r_2 h_2}{(r_2^2 - r_1^2)} (T_2 - T_3) = \frac{\partial (\rho_2 c_2 T_2)}{\partial t}. \end{aligned} \quad (3)$$

The boundary condition influenced the temperature distribution of drill string wall includes two parts: one is the heat exchange between fluid of inside drill string and drill string, which is expressed by (2), and the other is heat exchange between annulus and the drill string which is written as

$$-\lambda_2 \left( \frac{\partial T_2}{\partial r} \right)_{r=r_2} = h_2 (T_2 - T_3), \quad (4)$$

where  $T_3$  is the temperature of annulus fluid;  $\rho_2$  is the density of drill string wall;  $c_2$  is the specific heat capacity of drill string;  $r_2$  is the outer radius of drill string;  $\lambda_2$  is the thermal conductivity of drill string; and  $h_2$  is the convection coefficient of outer drilling string wall.

(3) *In the Annulus.* The factors that influenced the annulus temperature are consisted of three sections: (1) the mass flow

rate of fluid; (2) the temperature distributions of drill string and wellbore walls; and (3) heat generated by fluid friction and drilling string rotation. The transient heat transfer model in the annulus is expressed as follows:

$$\frac{\partial(\rho_3 c_3 q' T_3)}{\pi(r_3^2 - r_2^2) \partial z} + \frac{2r_2 h_2 (T_2 - T_3)}{r_3^2 - r_2^2} - \frac{2r_3 h_{ef} (T_3 - T_4)}{r_3^2 - r_2^2} + \frac{Q_a}{\pi(r_3^2 - r_2^2)} = \frac{\partial(\rho_3 c_3 T_3)}{\partial t}. \quad (5)$$

The interface between annulus and wellbore wall is important since it mathematically couples the surrounding formation with the flow in the annulus. Therefore, to guarantee continuity of heat flux during circulation and shut-in condition, the boundary conditions are

$$-\lambda_3 \left( \frac{\partial T_3}{\partial r} \right)_{r=r_3} + h_{ef} (T_4 - T_3) = \lambda_{ef} \left( \frac{\partial T_4}{\partial r} \right)_{r=r_3}, \quad (6)$$

where  $T_4$  is the interface temperature between annulus fluid and borehole wall;  $Q_a$  is the energy source term of unit length inside annulus;  $q'$  is the flow rate of annulus;  $r_3$  is the radius of borehole wall;  $\lambda_3$  is the thermal conductivity of annulus fluid; effective thermal conductivity  $\lambda_{ef}$  considers the effect of porosity;  $h_3$  is the convection coefficient of borehole wall;  $h_{ef}$  is the effective heat transfer coefficient which considers the effect porosity.

(4) *Each Heat Transfer Region in Surrounding Wellbore.* The effect of factor on heat exchange for the surrounding wellbore includes four sections: (1) the vertical conduction of heat in the medium; (2) the rate of heat exchange among volume elements; and (3) the rate of heat exchange for formation fluid which can flow in the porous medium. The energy balance in each heat transfer medium is

$$\begin{aligned} \frac{\partial}{\partial z} \left( \lambda_{ef} \frac{\partial T_i}{\partial z} \right) + \frac{1}{r_i} \frac{\partial}{\partial r} \left( \lambda_{ef} r_i \frac{\partial T_i}{\partial r} \right) \\ = (\rho c_p)_{ef} \left( \frac{\partial T_i}{\partial t} + v_r \frac{\partial T_i}{\partial r} \right), \end{aligned} \quad (7)$$

where

$$\begin{aligned} (\rho c_p)_{ef} &= \phi (\rho c_p)_s + (1 - \phi) (\rho c_p)_l \\ v_r &= f(\phi, m, m_{fu}, \rho_{in}, A_l). \end{aligned} \quad (8)$$

The mathematical formulation for the hydrodynamic model of rock formation is based on one-dimensional volume-averaging equations that govern the hydrodynamic phenomena of an incompressible fluid across an isotropic porous medium [22], which are represented as follows:

$$\begin{aligned} v_r &= -\frac{K}{\mu} \frac{\partial p}{\partial r}, \\ \frac{K_l}{\mu} \left( \frac{\partial^2 p}{\partial r^2} + \frac{1}{r} \frac{\partial p}{\partial r} \right) + \frac{\tilde{q}}{\rho_{in}} &= 0, \end{aligned} \quad (9)$$

where  $T_i$  is different unit temperature of porous medium in the formation;  $r_i$  is the radius of porous medium in the formation; the magnitude of  $i$  is decided by casing program ( $i \geq 4$ );  $\phi$  is an effective porosity of formation;  $s$  and  $l$  represent rock and pore fluid, respectively;  $v_r$  is the radial flow velocity;  $m_{fu}$  is formation fluid mass flow to annulus;  $m$  is the drilling fluid of mass flow;  $A_l$  is the lateral flow area;  $\mu$  is the dynamic viscosity;  $p$  is the intrinsic average pressure;  $K$  is the absolute permeability of the isotropic porous medium;  $\tilde{q}$  is the mass source term; and  $K_l$  is the relative permeability.

3.2.2. *Transient Heat Transfer during Shut-In Stage.* During stop circulation stage, the heat exchange method can be classified into two ways, which is dependent on the interface between gas and liquid. Therefore, combined with the study of heat exchange mechanism between wellbore and formation during fluid circulation stage and energy and mass conservation principles, the description of heat exchange types during shut-in stage is presented by a set of partial difference equations.

#### (1) In the Drill String

- (1) The transient heat transfer model of above interface between gas and liquid and below lost formation is expressed as

$$\begin{aligned} \frac{2\lambda'_1 \lambda'_2 (T'_2 - T'_1)}{\lambda'_2 r_1^2 \ln[(r_1 + r_2)/2r_1] + \lambda'_1 r_1^2 \ln[2r_2/(r_1 + r_2)]} \\ = \frac{\partial(\rho'_1 c'_1 T'_1)}{\partial t}. \end{aligned} \quad (10)$$

- (2) The transient heat transfer model of below interface between gas and liquid and above lost formation is described as

$$\frac{Q'_m}{\pi r_1^2} - \frac{\partial(\rho'_1 c'_1 q' T'_1)}{\pi r_1^2 \partial z} - \frac{2h'_1 (T'_1 - T'_2)}{r_1} = \frac{\partial(\rho'_1 c'_1 T'_1)}{\partial t}. \quad (11)$$

#### (2) Drill String Wall

- (1) The transient heat transfer model of above interface between gas and liquid and below lost formation is expressed as

$$\begin{aligned} \frac{2\lambda'_3 \lambda'_2 (T'_3 - T'_2)}{(\lambda'_3 \ln((r_1 + r_2)/2r_1) + \lambda'_2 \ln(2r_2/(r_1 + r_2))) (r_1^2 - r_0^2)} \\ + \lambda'_2 \frac{\partial^2 T'_2}{\partial z^2} \\ - \frac{2\lambda'_1 \lambda'_2 (T'_2 - T'_1)}{(\lambda'_2 \ln((r_0 + r_1)/2r_0) + \lambda'_1 \ln(2r_1/(r_0 + r_1))) (r_1^2 - r_0^2)} \\ = \frac{\partial(\rho'_2 c'_2 T'_2)}{\partial t}. \end{aligned} \quad (12)$$



- (2) The transient heat transfer model of below interface between gas and liquid and above lost formation is expressed as

$$\begin{aligned} \frac{\partial}{\partial z} \left( \lambda'_2 \frac{\partial T'_2}{\partial z} \right) + \frac{2r_1 h'_1}{(r_2^2 - r_1^2)} (T'_1 - T'_2) \\ - \frac{2r_2 h'_2}{(r_2^2 - r_1^2)} (T'_2 - T'_3) = \frac{\partial (\rho'_2 c'_2 T'_2)}{\partial t}. \end{aligned} \quad (13)$$

(3) In the Annulus

- (1) The transient heat transfer model of above interface between gas and liquid and below lost formation is expressed as

$$\begin{aligned} \frac{2\lambda'_3 \lambda'_{ef} (T'_4 - T'_3)}{(\lambda'_{ef} \ln((r_2 + r_3)/2r_2) + \lambda'_3 \ln(2r_3/(r_2 + r_3))) (r_2^2 - r_1^2)} \\ - \frac{2\lambda'_3 \lambda'_2 (T'_3 - T'_2)}{(\lambda'_3 \ln((r_1 + r_2)/2r_1) + \lambda'_2 \ln(2r_2/(r_1 + r_2))) (r_2^2 - r_1^2)} \\ = \frac{\partial (\rho'_3 c'_3 T'_3)}{\partial t}. \end{aligned} \quad (14)$$

- (2) The transient heat transfer model of below interface between gas and liquid and above lost formation is described as

$$\begin{aligned} \frac{\partial (\rho'_3 c'_3 q'' T'_3)}{\pi (r_3^2 - r_2^2) \partial z} + \frac{2r_2 h'_2 (T'_2 - T'_3)}{r_3^2 - r_2^2} - \frac{2r_3 h'_{ef} (T'_3 - T'_4)}{r_3^2 - r_2^2} \\ + \frac{Q'_a}{\pi (r_3^2 - r_2^2)} = \frac{\partial (\rho'_3 c'_3 T'_3)}{\partial t}, \end{aligned} \quad (15)$$

where the meaning parameters of the shut-in stage defined from (10) to (15) are the same as that of circulation stage.

The form of transient numerical model for each heat transfer region surrounding wellbore during shut-in stage is also the same as (7).

#### 4. Numerical Solutions

To obtain the temperature distribution on the term of time, the solution of these equations is complicated. Developed models incorporate solution methods which are based on finite difference techniques. The wellbore and the adjacent formation are represented by a two-dimensional, mesh grid including a number of radial elements due to casing program and a variable number of vertical elements depending on the well depth. Each of radial elements corresponds to different portion of the wellbore cross-section from inside drill string into the formation [21]. Therefore, a set of partial differential equations can be presented as finite difference form using finite differences technique for each element of grid so as to describe the transient heat exchange in each element for an

implicit form [25]. A set of nonlinear algebraic equations are then solved using an iterative method until the error range can be accepted. The case of finite difference can be defined as follows. The spatial derivatives and the time derivatives are the first-order as exhibited in (16):

$$\frac{\partial T}{\partial z} \approx \frac{T_{i,j}^{n+1} - T_{i,j-1}^{n+1}}{\Delta z_j}. \quad (16)$$

The second-order spatial derivatives are represented by three-point central difference approximations [26, 27]:

$$\frac{\partial^2 T}{\partial z^2} \approx \frac{1}{\Delta z_j} \left( \frac{T_{i,j+1}^{n+1} - T_{i,j}^{n+1}}{\Delta z_{j+0.5}} - \frac{T_{i,j}^{n+1} - T_{i,j-1}^{n+1}}{\Delta z_{j-0.5}} \right). \quad (17)$$

The time discretization at node is expressed in

$$\frac{\partial T}{\partial t} \approx \frac{T_{i,j}^{n+1} - T_{i,j}^n}{\Delta t}. \quad (18)$$

Application of earlier definitions enables the equation for each node to be written in single generalized vector form:

$$\alpha_{ij} T_{i-1,j}^{n+1} + \beta_{ij} T_{i,j}^{n+1} + \gamma_{ij} T_{i+1,j}^{n+1} + \delta_{ij} T_{i,j-1}^{n+1} + \lambda_{ij} T_{i,j+1}^{n+1} = C_{ij}. \quad (19)$$

The matrix form of finite difference for each node is given:

$$a \vec{T}^{n+1} = \vec{C}. \quad (20)$$

The finite difference equations are solved by fast successive overrelaxation (SOR) iteration method; the following general form for each node is expressed as follows:

$$\begin{aligned} T_{i,j}^{v+1} = \frac{\omega}{B_{i,j}} \left[ F_{i,j} T_{i,j}^N + A_{i,j} T_{i-1,j}^{v+1} \right. \\ \left. + C_{i,j} T_{i+1,j}^v + D_{i,j} T_{i,j-1}^{v+1} + E_{i,j} T_{i,j+1}^v \right] \\ + (1 - \omega) T_{i,j}^{N+1}. \end{aligned} \quad (21)$$

Using implicit form of finite difference method, (1) and (2) are, respectively, shown as follows:

$$-\frac{\rho_1 q c_1}{\pi r_1^2 \Delta z_j} \cdot T_{1,j-1}^{n+1} + \left( \frac{\rho_1 c_1}{\Delta t} + \frac{\rho_1 q c_1}{\pi r_1^2 \Delta z_j} + \frac{2h_1}{r_1} \right) \cdot T_{1,j}^{n+1} \quad (22)$$

$$-\frac{2h_1}{r_1} \cdot T_{2,j}^{n+1} = \frac{Q_1}{\pi r_1^2} + \frac{\rho_1 c_1}{\Delta t} \cdot T_{1,j}^n$$

$$\begin{aligned} \frac{2r_1 h_1}{(r_2^2 - r_1^2)} \cdot T_{1,j}^{n+1} + \frac{\lambda_2}{\Delta z_j \Delta z_{j-0.5}} \cdot T_{2,j-1}^{n+1} \\ + \frac{\lambda_2}{\Delta z_j \Delta z_{j+0.5}} \cdot T_{2,j+1}^{n+1} + \frac{2r_2 h_2}{(r_2^2 - r_1^2)} \cdot T_{3,j}^{n+1} \\ - \left( \frac{\lambda_2}{\Delta z_j \Delta z_{j-0.5}} + \frac{\lambda_2}{\Delta z_j \Delta z_{j+0.5}} + \frac{2r_1 h_1}{(r_2^2 - r_1^2)} \right. \\ \left. + \frac{2r_2 h_2}{(r_2^2 - r_1^2)} + \frac{\rho_2 c_2}{\Delta t} \right) \cdot T_{2,j}^{n+1} = -\frac{\rho_2 c_2}{\Delta t} \cdot T_{2,j}^n, \end{aligned} \quad (23)$$

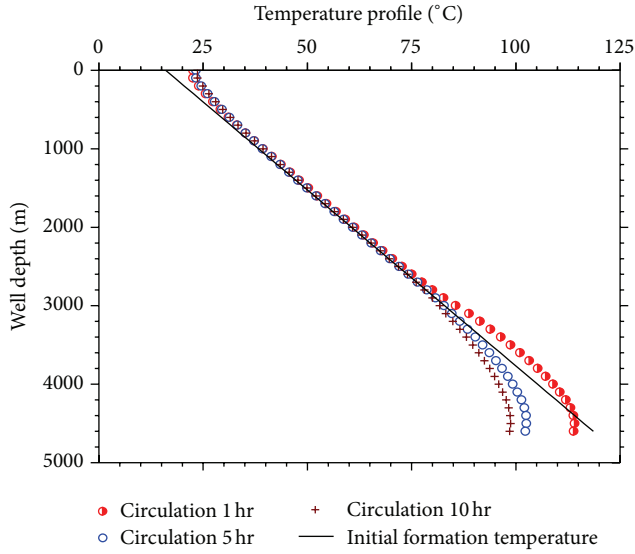


FIGURE 2: Annulus temperature profiles at different circulation time under no lost circulation conditions.

where  $T$  is the variable temperature;  $\Delta z$  is the step increment in the space coordinate;  $n$  is the time node;  $i$  indicates the node number in the  $r$  direction;  $j$  is the node number in the  $z$  direction;  $a_{ij}$ ,  $\beta_{ij}$ ,  $\gamma_{ij}$ ,  $\delta_{ij}$ , and  $\lambda_{ij}$  are the matrices of coefficients; SOR is the Gauss-Seidel iterative method if  $\omega$  is equal to 1 in (21); the SOR is overrelaxation method if  $\omega$  is more than 1; SOR is under relaxation method if  $\omega$  is less than 1.

The calculation accuracy depends on the meshing elements and the size of the interval values. In general, it is observed that the vertical element size is less than 3% of the total well depth to ensure that the annulus temperature profile remains independent of the vertical element size [6].

## 5. Model Solution Procedure

**5.1. Basic Data.** The basic data of calculation in this study are the referenced literatures reports [6], which are shown in Tables 1, 2, and 3. The flow rate and depth of lost circulation are assumed as 4.0 l/s and 3500 m, respectively.

### 5.2. Numerical Model Application

**5.2.1. Example Analysis in Circulation Operation Condition.** As shown in Figure 2, the annulus temperature distributions as a function of depth at different circulation time under no lost circulation conditions are presented. As intermediate casing depth is 3000 m (Table 1), the annulus temperatures of cementing section vary under different circulation time, whereas the annulus temperature of open-hole section gradually decreases with the increase of the circulation time. That is because casing thermal conductivity coefficient is 19.4 times than that of formation, resulting in more amount of heat exchange between annulus energy of cementing section and formation compared with that of open hole. Meanwhile, the

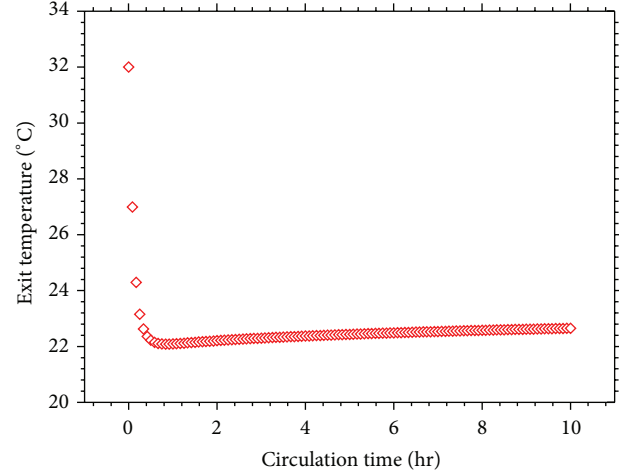


FIGURE 3: Outlet temperature distribution as a function of circulation time under lost circulation condition.

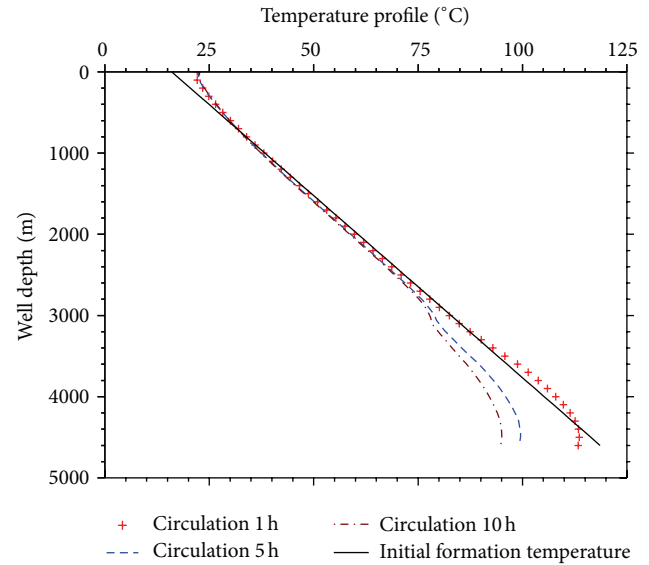


FIGURE 4: Annulus temperature profiles as a function of circulation time under lost circulation conditions.

annulus heat quantity is gradually carried to surface with the increase of the circulation time and thus results in the decrease of annulus temperature of open-hole section [18].

The relationship between outlet temperature and circulation time under lost circulation condition is also investigated. As shown in Figure 3, the outlet temperature rapidly decreases within the initial circulation (0.5 h) and then gradually increases during the latter circulation. One plausible explanation is that more heat quantity is carried to well mouth at initial circulation compared to that at latter circulation and thus leads to the wellbore wall of well mouth heat.

Under lost circulation conditions, the effect of alterations in circulation time on the annulus temperature distribution is shown in Figure 4. It is found that the annulus temperature of open-hole section continuously decreases as the increase of

TABLE 1: Basic data of drill string assembly and casing program.

	Drill pipe	Drill collar	First casing	Second casing	Third casing
Inner diameter (mm)	151	70	486	318	224
Outer diameter (mm)	168	171	508	340	244
Depth (m)	4000	—	600	1500	3000
Depth to cement (m)	—	—	0	300	1400

TABLE 2: Basic data of thermal physical parameters.

	Drill pipe/casing	Drill string	Drill fluid	Cement	Formation	Formation fluid
Density ( $\text{kg}/\text{cm}^3$ )	8000	8900	1200	2140	2640	1050
Heat capacity ( $\text{J}/\text{kg}\cdot^\circ\text{C}$ )	400	400	1600	2000	800	4200
Thermal conductivity ( $\text{W}/\text{m}\cdot^\circ\text{C}$ )	43.75	43.75	1.75	0.70	2.25	0.50

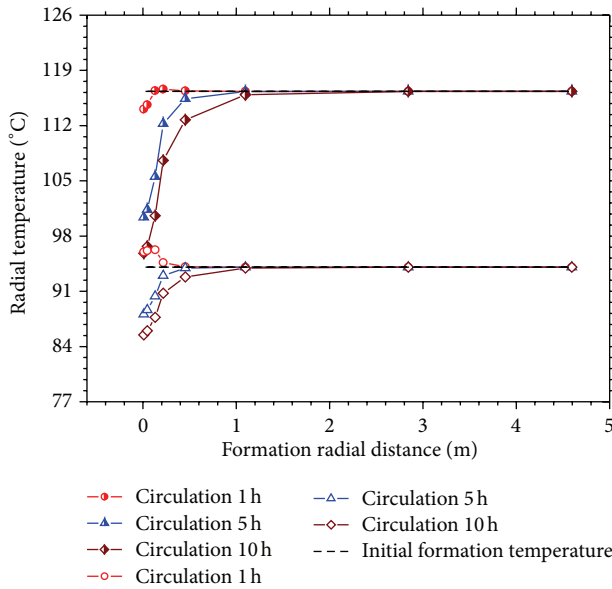


FIGURE 5: Formation radial temperature distributions of lost depth and bottom hole.

the circulation time. Additionally, the closer the bottom hole is, the less decrease the temperature will be, which is in accordance with the result of Figure 2. Meanwhile, the annulus temperature profiles of circulation 5 h and 10 h are both lower than the formation temperature below 1500 m. Compared to Figure 2, Figure 4 indicates that the annulus temperature of cement section decreases under lost circulation conditions. The reason is that the annulus fluid temperature at 3500 m is higher than that of annulus fluid at any depth of cement section. Herein, heat quantity of annulus fluid at 3500 m flows into the formation increased, which can result in the decrease of the annulus temperature.

Similarly, Figure 5 also reflects the formation radial temperature distributions of lost depth and bottom hole under different circulation time. Noticeably, the formation radial temperature decreases with the increase of the circulation time, whereas the decrease of the surrounding formation temperature at lost depth is less than that of at bottom hole

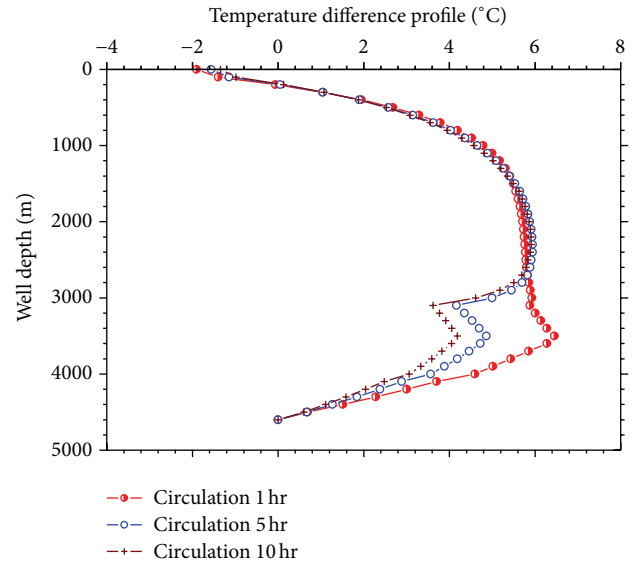


FIGURE 6: Temperature difference profiles between annulus and inside pipe fluid during different circulation time.

during the latter circulation. The surrounding formation is continuously heated by annulus fluid at lost depth during initial circulation stage and then leads to its temperature rise beyond its initial formation temperature as shown in Figure 5 (circulation 1 h). Meanwhile, the annulus temperature is lower than formation temperature after long circulation time and thus leads to formation temperature decrease. However, the formation is continuously cooled by circulation fluid at bottom hole and then leads to the temperature of the surrounding formation decrease below the initial formation temperature.

To get a deep insight of the heat transfer mechanism for wellbore during the circulation stage, the temperature difference distribution between annulus and inside pipe fluid under different circulation time is studied. As shown in Figure 6, the temperature difference remarkably decreases from bottom-hole to casing shoe with increasing the circulation time. Meanwhile, the temperature difference changes

TABLE 3: Other basic data of bottom hole.

Depth (m)	Total well diameter (mm)	Open hole diameter (mm)	Flow rate (l/s)	Surface temperature (°C)	Geothermal gradient (°C/100 m)
4600	660	213	13.2	16	2.23
Inlet temperature (°C)	Outlet temperature (°C)	Plastic viscosity (mPa·s)	Yield value (mPa)	Consistency coefficient (mPa·s <sup>n</sup> )	Fluidity point
24	32	34	10	0.34	0.65

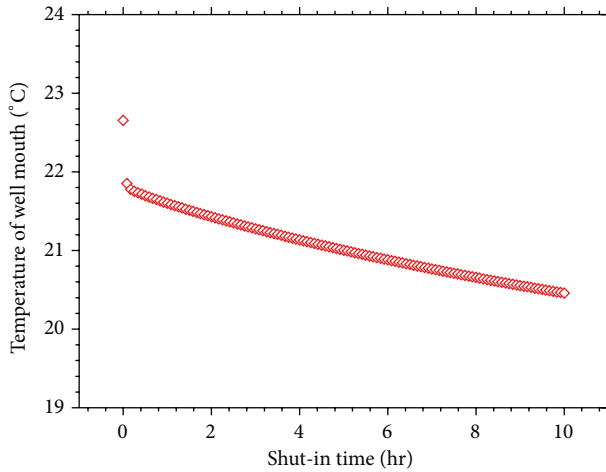


FIGURE 7: Temperature of well mouth during shut-in stage under lost circulation condition.

at the lost circulation point. Additionally, the annulus temperature is higher than the inside pipe fluid temperature in the wellbore except for well mouth section during the whole circulation stage.

**5.2.2. Example Analysis in Shut Condition.** As shown in Figure 7, the temperature of well mouth continuously decreases during the whole shut-in stage. The result of Figure 3 shows that the outlet temperature increases during the latter circulation, resulting in surrounding formation continuously heated. However, during shut-in stage, as gas is instead of fluid at well mouth, heat exchange between wellbore and formation is less due to heat conductivity of gas. Therefore, the temperature of well mouth gradually decreases with shut-in time increased.

As it is seen from Figure 8, the annulus temperature continuously increases with the increase of shut-in time when the well depth is beyond casing shoe, whereas the annulus temperature hardly varies when the well depth is above the casing shoe point. It spends about 8.5 h on all fluids of inside pipe and annulus above lost depth flows into formation. Therefore, the heat exchange between the wellbore and formation by heat conduction is more than that of heat convection during 8.5 h of shut-in. After that, the formation energy fluxes into annulus in the heat conduction way as wellbore fluid is in the static state beyond 8.5 h, thus resulting in the improvement of temperature. Furthermore, the temperature eventually increases to be equal to the formation

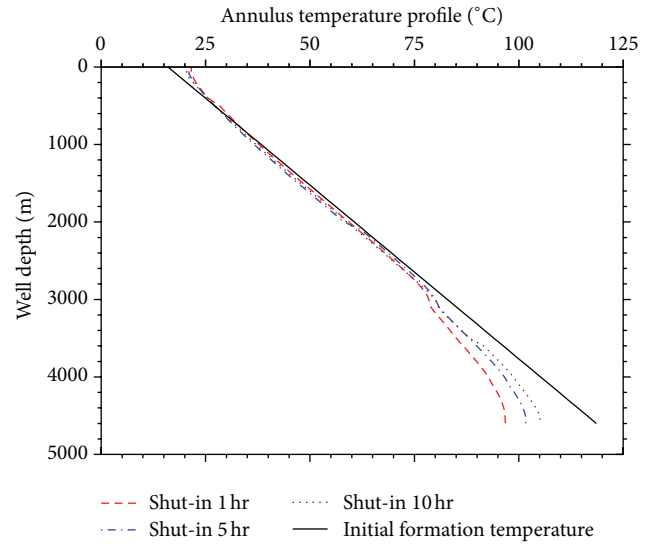


FIGURE 8: Annulus fluid temperature profiles during different shut-in time.

temperature. However, when the temperature is above the lost depth, annulus energy which arose from formation is nearly equal to that of the annulus gas transferring to the surrounding formation and the inside pipe drilling fluid by the heat convective way, which leads to the temperature hard change.

Figure 9 indicates that the radial formation temperature decreases with increasing the shut-in time at lost circulation depth and bottom hole, and both of them are lower than that of initial temperature. However, the radial formation temperature at lost depth slowly decreases with the increase of the shut-in time, and temperature change at the bottom hole is larger than that of at lost depth. The reasonable explanation is that the temperature difference between annulus and formation at bottom hole is larger than that of at lost circulation point during circulation stage. Compared to Figure 5, it is surprising that Figure 9 implies that the formation temperature disturbance distance in shut-in stage is larger than that of circulation stage. It is derived from that the starting point of disturbance distance for radial formation temperature is at well wall during the circulation stage, but the starting point of disturbance distance is at inside formation during the shut-in stage which is the destination point of disturbance distance for circulation stage.

As shown in Figure 10, the annulus temperature from top hole (500 m) to bottom hole is higher than the inside

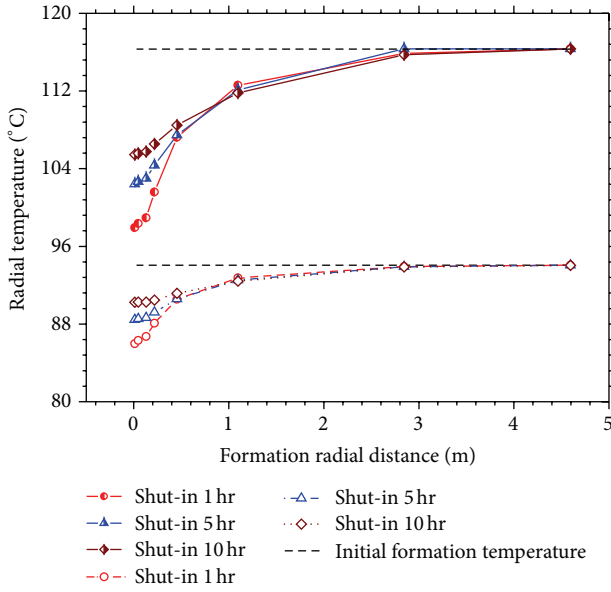


FIGURE 9: Formation radial temperature distributions of lost circulation point and bottom hole during shut-in stage.

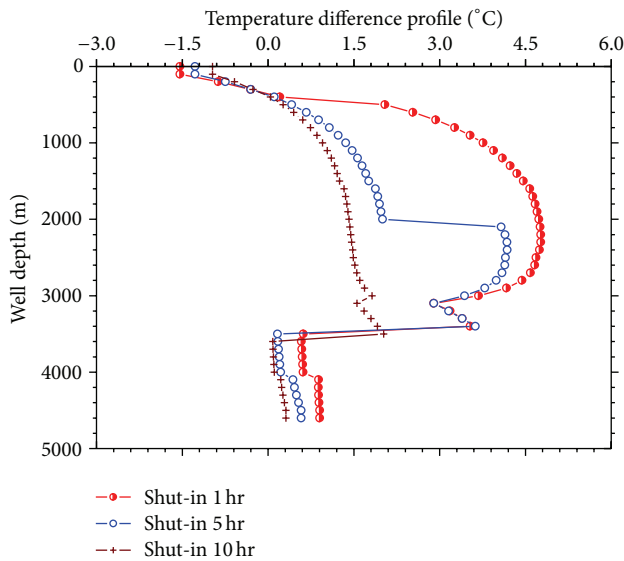


FIGURE 10: Temperature difference profiles between annulus and inside pipe during shut-in stage.

pipe temperature during the whole shut-in stage, and only the temperature difference between annulus and inside pipe from well mouth to the depth of 500 m is negative value. Furthermore, the temperature difference between annulus and inside pipe gradually decreases with increasing shut-in time and then trends to thermodynamic equilibrium state. From Figure 10, it is observed that the temperature difference between annulus and inside pipe is greatly influenced by the lost depth, make up of string, and casing program.

As shown in Figures 11 and 12, annulus temperature changes of lost depth and bottom hole are related to the

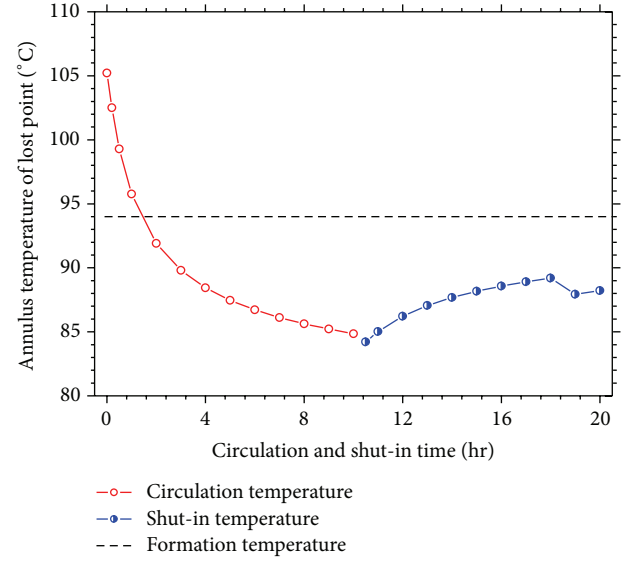


FIGURE 11: Annulus temperature distributions of lost circulation depth during circulation and shut-in stages.

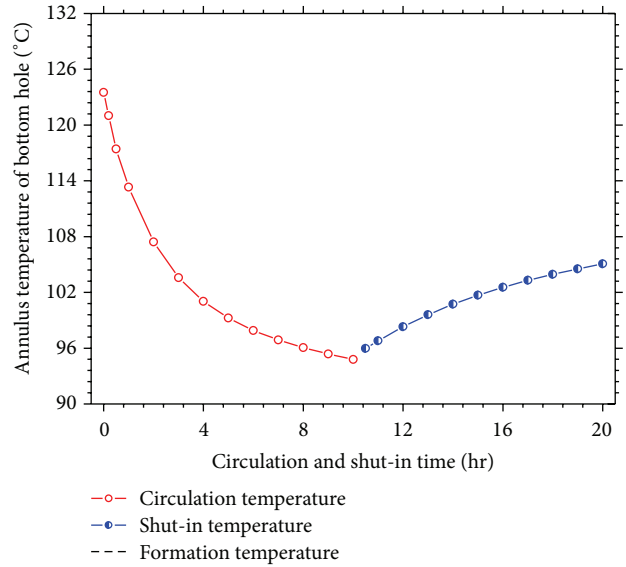


FIGURE 12: Annulus temperature distributions of bottom hole during circulation and shut-in stages.

circulation and the shut-in stages. It can be seen that the annulus temperature rapidly decreases during the initial circulation stage and slowly varies in the latter circulation and shut-in stage, followed by the change of annulus temperature showing the same tendency under the two conditions earlier. Meanwhile, the annulus temperatures at initial circulation stage are both higher than that of the initial formation temperature at lost depth and bottom hole, and then both of them are lower than initial formation temperature during latter circulation and shut-in stages. However, before wellbore fluid above the lost depth flows into formation (8.5 h), it is interestingly noted that the annulus temperature gradually

increases with the increase of shut-in time at lost depth by heat convection, followed by quickly decreasing, and then slowly increases at bottom hole by heat conduction. Figures 11 and 12 also show that if the annulus temperature after circulation recovers to the initial formation temperature, shut-in time can be longer than that of circulation time [28]. The phenomenon accounts for the reason why long time for shut-in is needed to obtain initial formation temperature.

## 6. Discussion

To demonstrate the applicability of the methodology developed in this work, the OM-16C geothermal well was considered. This well is in Kenya, which was drilled with borehole diameters of 26, 17.5, 12.25, and 8.5 in. The casing has 20, 13.375, 9.625, and 7 in diameters at 60, 300, 750, and 2680 m depths, respectively. Temperatures in and around the OM-16C geothermal well during circulation and shut-in stages were estimated by the transient heat transfer models. The Horner (Dowdle and Cobb, 1975) and Hasan and Kabir (1994) methods were used to compare our numerical results [6, 12].

The input data to simulate the geothermal well are drilling fluid flow rate of 125.3 m<sup>3</sup>/h, surface temperature of 21.6 °C, and drilling fluid properties which include the thermal conductivity of 0.85 W/m·°C, the density of 1100 kg/m<sup>3</sup>, the viscosity of 0.052 Pa.s, and specific heat of 1200 J/kg·°C. Circulation time was 16 h.

A compilation of main results obtained in these thermal studies was presented in Figure 13. We reckoned that the logged temperature of shut-in 27 days was approximately equal to the static formation temperature (SFT) due to thermal recovery conditions during the long time shut-in. As shown in Figure 13, it can be observed that the measured temperature was satisfactorily matched with the simulated temperature (continuous line). Figure 13 also showed the SFT calculated by means of Horner (Dowdle and Cobb, 1975) and Hasan and Kabir (1994) methods [6, 12]. Obviously, as shown in Figure 13, the Hasan-Kabir method is closer to the SFT compared to the Horner method. Differences between the computed data (or simulated 27 days) and measured values were estimated and expressed as a percentage deviation based on the result of Figure 13, and the percentage deviation between the simulated SFT and analytical methods as also computed from Figure 13. It can be observed the maximum deviation between measured and simulated data is 3.1% and minimum deviation is 2.24%, which corresponded to the control error in engineering. The best approximation to the simulated SFT values corresponded to the Hasan-Kabir, which presented minimum differences of 3.50%, 4.12%, and 4.08%. Therefore, the simulated SFT method in this work is better than that of the analytical methods (Horner and Hasan and Kabir).

## 7. Conclusions

In this study, a set of numerical models have been developed to study the transient heat transfer processes which occurs

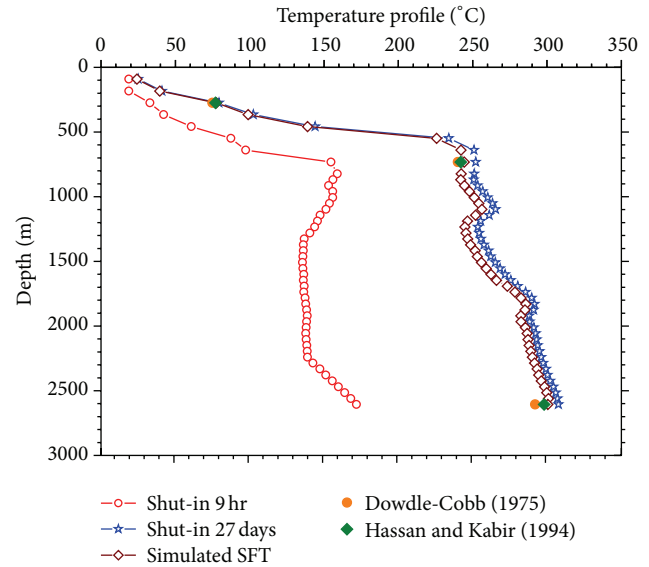


FIGURE 13: Simulated and logged temperature profiles in OM-16C geothermal well during shut-in stages. Also shown the SFTs estimated with the Horner (Dowdle and Cobb, 1975) and Hasan and Kabir (1994) methods and with this work [6, 12].

in oil-gas or geothermal well during circulation and shut-in stages under lost circulation conditions. The equations properly account for the energy conservation in each region of a well, and mass balances are performed at any numerical node where annulus fluid fluxes into formation. Heat transfer coefficients and thermophysical properties (gas instead of fluid) in the annulus and the surrounding formation change due to lost circulation. Simulation results show that the temperature distributing characters of the wellbore and surrounding formation are remarkably influenced by the lost depth and casing program during the whole circulation and shut-in stage. Additionally, the disturbance distance of formation temperature at shut-in stage is larger than that of at circulation stage at the same time. Moreover, it is necessary to prolong shut-in time than circulation time in order to obtain accurate initial formation temperature. The present work can provide a new way to improve the present methodology.

## Acknowledgments

The authors appreciate the financial support by China National Natural Science Foundation (no. 51134004; 51104124; 51204142; 51204140), Major State Science and Technology Special Project of China (no. 2011ZX05021-003), Ph.D. Programs Foundation of Ministry of Education of China (no. 20125121110001), and Southwest Petroleum University of Young Scientific Research Innovation Team Foundation (no. 2012XJZT003). The authors would also like to appreciate their laboratory members for the generous help.

## References

- [1] S. Fomin, V. Chugunov, and T. Hashida, "Analytical modelling of the formation temperature stabilization during the borehole



- shut-in period," *Geophysical Journal International*, vol. 155, no. 2, pp. 469–478, 2003.
- [2] S. Fomin, T. Hashida, V. Chugunov, and A. V. Kuznetsov, "A borehole temperature during drilling in a fractured rock formation," *International Journal of Heat and Mass Transfer*, vol. 48, no. 2, pp. 385–394, 2005.
  - [3] A. Bassam, E. Santoyo, J. Andaverde, J. A. Hernández, and O. M. Espinoza-Ojeda, "Estimation of static formation temperatures in geothermal wells by using an artificial neural network approach," *Computers and Geosciences*, vol. 36, no. 9, pp. 1191–1199, 2010.
  - [4] A. Garcia, I. Hernandez, G. Espinosa, and E. Santoyo, "TEMLOPI: a thermal simulator for estimation of drilling mud and formation temperatures during drilling of geothermal wells," *Computers and Geosciences*, vol. 24, no. 5, pp. 465–477, 1998.
  - [5] G. Espinosa-Paredes, A. Garcia, E. Santoyo, and I. Hernandez, "TEMLOPI/V.2: a computer program for estimation of fully transient temperatures in geothermal wells during circulation and shut-in," *Computers and Geosciences*, vol. 27, no. 3, pp. 327–344, 2001.
  - [6] W. L. Dowdle and W. M. Cobb, "Static formation temperature from well logs—an empirical method," *Journal of Petroleum Technology*, vol. 27, no. 11, pp. 1326–1330, 1975.
  - [7] J. L. G. Santander, P. Castañeda Porras, J. M. Isidro, and P. Fernández de Córdoba, "Calculation of some integrals arising in heat transfer in geothermics," *Mathematical Problems in Engineering*, vol. 2010, Article ID 784794, 13 pages, 2010.
  - [8] I. M. Kutasov, "Dimensionless temperature, cumulative heat flow and heat flow rate for a well with a constant bore-face temperature," *Geothermics*, vol. 16, no. 5-6, pp. 467–472, 1987.
  - [9] I. M. Kutasov and L. V. Eppelbaum, "Prediction of formation temperatures in permafrost regions from temperature logs in deep wells-field cases," *Permafrost and Periglacial Processes*, vol. 14, no. 3, pp. 247–258, 2003.
  - [10] I. M. Kutasov and L. V. Eppelbaum, "Determination of formation temperature from bottom-hole temperature logs—a generalized Horner method," *Journal of Geophysics and Engineering*, vol. 2, no. 2, pp. 90–96, 2005.
  - [11] X. C. Song and Z. C. Guan, "Coupled modeling circulating temperature and pressure of gas–liquid two phase flow in deep water wells," *Journal of Petroleum Science and Engineering*, vol. 92-93, pp. 124–131, 2012.
  - [12] A. R. Hasan and C. S. Kabir, "Static reservoir temperature determination from transient data after mud circulation," *SPE Drilling and Completion*, vol. 9, no. 1, pp. 17–24, 1994.
  - [13] F. Ascencio, A. García, J. Rivera, and V. Arellano, "Estimation of undisturbed formation temperatures under spherical-radial heat flow conditions," *Geothermics*, vol. 23, no. 4, pp. 317–326, 1994.
  - [14] E. Santoyo, *Transient numerical simulation of heat transfer processes during drilling of geothermal wells [Ph.D. thesis]*, University of Salford, Salford, UK, 1998.
  - [15] L. R. Raymond, "Temperature distribution in a circulating drilling fluid," *Journal of Petroleum Technology*, vol. 21, no. 3, pp. 333–341, 1969.
  - [16] G. R. Wooley, "Computing dowhole temperatures in circulation, injection and production wells," *Journal of Petroleum Technology*, vol. 32, no. 9, pp. 1509–1522, 1980.
  - [17] R. M. Beirute, "A circulating and shut-in well-temperature-profile simulator," *Journal of Petroleum Technology*, vol. 43, no. 9, pp. 1140–1146, 1991.
  - [18] G. Espinosa-Paredes and A. Garcia-Gutierrez, "Thermal behaviour of geothermal wells using mud and air—water mixtures as drilling fluids," *Energy Conversion and Management*, vol. 45, no. 9-10, pp. 1513–1527, 2004.
  - [19] O. García-Valladares, P. Sánchez-Upton, and E. Santoyo, "Numerical modeling of flow processes inside geothermal wells: an approach for predicting production characteristics with uncertainties," *Energy Conversion and Management*, vol. 47, no. 11-12, pp. 1621–1643, 2006.
  - [20] M. N. Luheshi, "Estimation of formation temperature from borehole measurements," *Geophysical Journal of the Royal Astronomical Society*, vol. 74, no. 3, pp. 747–776, 1983.
  - [21] A. García, E. Santoyo, G. Espinosa, I. Hernández, and H. Gutiérrez, "Estimation of temperatures in geothermal wells during circulation and shut-in in the presence of lost circulation," *Transport in Porous Media*, vol. 33, no. 1-2, pp. 103–127, 1998.
  - [22] G. Espinosa-Paredes, A. Morales-Díaz, U. Olea-González, and J. J. Ambriz-Garcia, "Application of a proportional-integral control for the estimation of static formation temperatures in oil wells," *Marine and Petroleum Geology*, vol. 26, no. 2, pp. 259–268, 2009.
  - [23] G. Espinosa-Paredes and E. G. Espinosa-Martínez, "A feedback-based inverse heat transfer method to estimate unperturbed temperatures in wellbores," *Energy Conversion and Management*, vol. 50, no. 1, pp. 140–148, 2009.
  - [24] H. H. Keller, E. J. Couch, and P. M. Berry, "Temperature distribution in circulating mud columns," *Journal of the Society of Petroleum Engineering*, vol. 13, no. 1, pp. 23–30, 1973.
  - [25] M. C. Zhong and R. J. Novotny, "Accurate prediction wellbore transient temperature profile under multiple temperature gradients: finite difference approach and case history," in *Proceedings of the SPE Annual Technical Conference and Exhibition*, pp. 5389–5401, Denver, Colo, USA, October 2003.
  - [26] K.-L. Hsiao, "Viscoelastic fluid over a stretching sheet with electromagnetic effects and nonuniform heat source/sink," *Mathematical Problems in Engineering*, vol. 2010, Article ID 740943, 14 pages, 2010.
  - [27] D. W. Marshall and R. G. Bentsen, "A computer model to determine the temperature distributions in a wellbore," *Journal of Canadian Petroleum Technology*, vol. 21, no. 1, pp. 63–75, 1982.
  - [28] L. V. Eppelbaum and I. M. Kutasov, "Determination of the formation temperature from shut-in logs: estimation of the radius of thermal influence," *Journal of Applied Geophysics*, vol. 73, no. 3, pp. 278–282, 2011.



## Research Article

# The Instability of an Electrohydrodynamic Viscous Liquid Micro-Cylinder Buried in a Porous Medium: Effect of Thermosolutal Marangoni Convection

**Galal M. Moatimid and Mohamed A. Hassan**

*Department of Mathematics, Faculty of Education, Ain Shams University, Roxy, Cairo 11511, Egypt*

Correspondence should be addressed to Mohamed A. Hassan; [m\\_a\\_hassan\\_gk@hotmail.com](mailto:m_a_hassan_gk@hotmail.com)

Received 9 November 2012; Revised 4 June 2013; Accepted 5 June 2013

Academic Editor: Zhijun Zhang

Copyright © 2013 G. M. Moatimid and M. A. Hassan. This is an open access article distributed under the Creative Commons Attribution License, which permits unrestricted use, distribution, and reproduction in any medium, provided the original work is properly cited.

The electrohydrodynamic (EHD) thermosolutal Marangoni convection of viscous liquid, in the presence of an axial electric field through a micro cylindrical porous flow, is considered. It is assumed that the surface tension varies linearly with both temperature and concentration. The instability of the interface is investigated for the free surface of the fluid. The expression of the free surface function is derived taking into account the independence of the surface tension of the heat and mass transfer. The transcendental dispersion relation is obtained considering the dependence of the surface tension on the heat and mass transfer. Numerical estimations for the roots of the transcendental dispersion relation are obtained indicating the relation between the disturbance growth rate and the variation of the wave number. It is found that increasing both the temperature and concentration at the axial microcylinder has a destabilizing effect on the interface, according to the reduction of the surface tension. The existence of the porous structure restricts the flow and hence has a stabilizing effect. Also, the axial electric field has a stabilizing effect. Some of previous analytical and experimental results are recovered upon appropriate data choices.

## 1. Introduction

The fluid flow in microjet has various applications in medical, biomedical, computer chips and chemical separations. Advent of microelectrical mechanical systems is one of the major advances in industrial technologies. Also, microjets are fundamental to connecting different devices, utilized in biochemical reaction chamber, in physical particle separation, in inkjet print heads, in infrared detectors, in diode lasers, in miniature gas chromatographs, and in heat exchanger for cooling computer chips. Understanding the flow characteristics through a microjet is very important in determining the free surface instability of the fluid flow. The augmentation of heat transfer from a solid cylinder wrapped with a porous layer was considered by Bhattacharyya and Singh [1]. An experimental analysis of unsteady heat and moisture transfer around a heated cylinder buried into a porous medium was performed by Moya et al. [2]. Furlani [3] studied the temporal instability of an infinite Newtonian cylindrical microjet (as

a cylindrical fluid surface) that is subjected to a sinusoidal variation of surface tension along its length. Furlani and Hanchak [4] developed the same problem to study numerically the nonlinear analysis of the deformation and breakup of viscous microjets. The instability of non-Newtonian liquid jets (viscoelastic and power law) was investigated by Gao [5] and Gao and Ng [6]. The dispersion relation between the growth rate and the wave number for a non-Newtonian cylindrical liquid jets was derived and the instability behavior of viscoelastic jets was investigated.

The interaction of electric fields with moving fluids makes EHD a very complicated phenomenon. The process of EHD is dependent on many parameters and properties of the liquid and environment of the flow. On the other hand, EHD can be considered as the branch of fluid mechanics concerned with the electrical force effects or as the part that is involved in the influence of moving media on electric fields. It is thus concerned with the interaction between electrical fields and free or polarized charges in fluids. In the EHD stability, the

electric field plays an important role in many practical problems of chemical engineering, biophysics and many other fields. Mohamed and Nayyar [7] have investigated the stability of a cylindrical jet of incompressible inviscid liquid in the presence of an axial electric field. They showed that the uniform axial electric field has a strong stabilizing influence on the cylindrical interface for short and long wavelengths in all symmetric and asymmetric modes of perturbation.

Marangoni boundary layers are dissipative layers which may occur along liquid-liquid or liquid-gas interfaces. When a free liquid surface is present, the surface tension variation is resulting from the temperature gradients along the surface. It can also induce a motion within the fluid which is called thermocapillary flow (thermal Marangoni convection) [8]. The surface tension gradients that are responsible for Marangoni convection depend on both temperature and/or concentration gradients. Earliest work in this field was first investigated by Napolitano [9, 10]. Surfactants or surface contaminants are used to control the stability of the free surface by lowering surface tension. Variations in surface tension that are introduced by surfactant can substantially alter interfacial evolution and flow. The effect of surfactants on liquid has been studied by many authors [11–15]. McGough and Basaran [16] studied the breakup mechanisms of the fluid threads containing surfactant by solving the Navier-Stokes equations. The effect of the Prandtl number on Marangoni convection over a flat plate was studied by Christopher and Wang [17]. Physically, the heat and mass transfer across the interface play an essential role in determining the flow field in some cases. For instance, when the fluid is boiling, whether it is a film or bubble, the motion of the film and bubbles is mainly dependent on the effect of mass and heat transfer. In chemical industry, the interfacial stability problems are important in the presence of mass and heat transfer. The mechanism of heat and mass transfer across an interface is of a great importance in numerous industrial and environmental problem processes. These include the design of many types of contacting equipment, for example, boilers, condensers, evaporators, gas absorbers, pipelines, chemical reactors, and nuclear reactors. The effect of heat and mass transfer in the absence of gravity on the surface tension was studied by Straub [18].

The flow through porous media is usually described by the Darcy's law that relates the movement of the fluid to the pressure gradient acting on a parcel of the fluid. Meanwhile, the Darcy's equations are not the fundamental equations for the flow through porous media. It is an approximation for the balance of linear momentum for the fluid flow through a porous solid within the context of mixtures. For example, the interactive force between the fluid and the porous medium, the frictional effects due to viscosity, and the inertial nonlinearities are not included in the Darcy's model [19]. These effects can be included in more generality model like Brinkman-Darcy's model. The basic assumptions that lead to the Brinkman-Darcy equation were illustrated by Rajagopal [19]. Elcoot and Moatimid [20] studied the instability of finitely conducting cylindrical flows through porous media, under the influence of an axial electrostatic field. They found that, under certain conditions, the field may have a stabilizing or destabilizing effect. An experimental study of

the steam injection into a porous media and the stability of the interface between the steam and the water was carried out by Catton and Chung [21].

The aim of this work is to discuss the effect of axial electric field with the existence of the porous structure on the stability of the microcylindrical flow of a viscous liquid past a microsolid cylindrical surface. Also, the effect of the Marangoni thermosolutal convection (according to the dependence of the surface tension on the heat and mass transfer) is discussed. The main construction of the problem is as follows. Firstly, we studied the problem according to spatial surface tension. So, the expression of the free surface function is obtained. Secondly, the problem is studied in the presence of the heat and mass transfer rates with thermosolutal surface tension. The dispersion relation, in the latter case, is obtained as a transcendental function of the growth rate and the wave number. Finally, we studied the effect of the porous medium and the axial electric field on the stability of viscous liquid interface and tabulated results are obtained.

To clarify the problem, in Section 2, the physical description of the problem including the basic equations that govern the motion is presented. Section 3 is devoted to introducing the interfacial conditions for both the fluid and the electric field together with the boundary conditions. The method of solution according to the normal modes technique is presented in Section 4. In Section 5, the instability analysis in the absence of the heat and mass transfer is studied and the expression of the free surface function is derived. The transcendental dispersion relation in the presence of the heat and mass transfer is obtained in Section 6. Throughout Section 7, we introduced numerical estimations and gave a discussion for the stability picture according to the relation between the growth rate and the wave number. Finally, in Section 8, we give concluding remarks for this study based on the obtained results of the stability analysis.

## 2. Formulation of the Problem

Consider a microcylindrical layer of viscous fluid with density  $\rho$ , viscosity  $\mu$ , and radius  $r_0$  flowing past an axial solid cylinder of infinitely small radius. The flow is surrounded by a vacuum (which has zero density and zero viscosity) with hypothetical sufficiently large radius  $R_2$ . The axial microsolid cylinder is elongated along the  $z$ -axis. It is earthed and has a radius  $R_1$  (where  $R_1 \ll R_2$ ). The axial microcylindrical solid rod, which induces temperature and concentration gradients, is considered to be at a constant temperature  $T_1$  and constant concentration  $C_1$ . The subscripts (1) and (2) refer to the liquid and the surrounding vacuum, respectively. The fluid and the vacuum are influenced by an external uniform electric field of intensity  $E_0$  which acts along the positive  $z$ -axis. The dielectric constants for the liquid and the vacuum are  $\epsilon_1$  and  $\epsilon_2$ , respectively. The interface between the fluid and the surrounding vacuum is considered to be free of charges. The flow jet is considered as a microcylindrical porous structure with Darcy's coefficient  $\nu$ , while its porosity is assumed to be unity (this will be explained physically later). Also, we neglect the effects of gravity. Considering the previous hypotheses, the model may be illustrated graphically as in Figure 1.

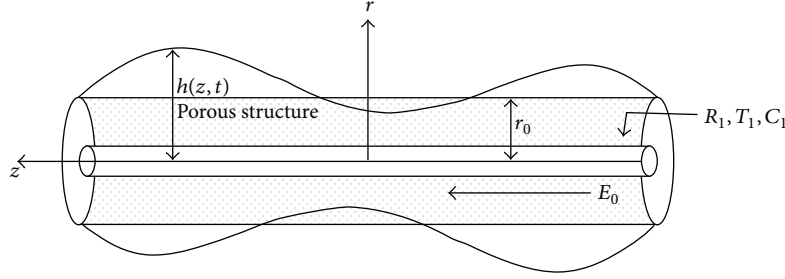


FIGURE 1: Physical model and flow cylindrical geometry.

After making a small disturbance, the interface function becomes

$$F(r, z, t) = r - h(z, t), \quad (1)$$

and the unit outward normal vector  $\hat{n}$  and the unit tangential one  $\hat{t}$  are given by

$$\begin{aligned} \hat{n} &= \frac{1}{\sqrt{1+h_z^2}} \hat{r} - \frac{h_z}{\sqrt{1+h_z^2}} \hat{z}, \\ \hat{t} &= \frac{h_z}{\sqrt{1+h_z^2}} \hat{r} + \frac{1}{\sqrt{1+h_z^2}} \hat{z}, \end{aligned} \quad (2)$$

where  $\hat{r}$  and  $\hat{z}$  are the unit vectors along the radial and axial cylindrical coordinate directions and  $h_z = \partial h / \partial z$ .

According to the assumption of the viscosity of the fluid, considering the existence of the porous structure and the heat and mass transfer, the basic equations of the problem may take the following form [3, 19].

The continuity equation (incompressibility condition) requires

$$\nabla \cdot \underline{v} = 0. \quad (3)$$

The balance of linear momentum (Navier-Stokes) gives

$$\rho \left[ \frac{1}{\zeta} \frac{\partial \underline{v}}{\partial t} + \frac{1}{\zeta^2} (\underline{v} \cdot \nabla) \underline{v} \right] = -\nabla P + \mu_{\text{eff}} \nabla^2 \underline{v} - \nu \underline{v}. \quad (4)$$

The balance of energy is

$$\frac{DT}{Dt} = \alpha \nabla^2 T. \quad (5)$$

And finally the concentration equation becomes

$$\frac{DC}{Dt} = \beta \nabla^2 C. \quad (6)$$

In the previous equations (3)–(6),  $\zeta$  is the porosity of the porous medium,  $\mu_{\text{eff}}$  is the effective viscosity of the fluid ( $\mu_{\text{eff}} = \mu/\zeta$  and if  $\zeta = 1$  then  $\mu_{\text{eff}} = \mu$  as we mention in the next paragraph), and  $(D/Dt) = (\partial/\partial t) + (\underline{v} \cdot \nabla)$ . Also,  $\alpha$  is the thermal diffusivity,  $\beta$  is the mass diffusivity,  $T$  is the temperature,  $C$  is the concentration,  $P$  is the pressure,  $\underline{v}$  is the velocity vector,  $\nu$  is the Darcy's coefficient, and  $\rho$  is the density.

The basic assumptions that lead to the Brinkman-Darcy equation and the form of the basic assumptions that lead to the Brinkman-Darcy equation were illustrated by Rajagopal [19], and can be summarized in the following points.

- (1) The porous medium is solid and thus the balance of linear momentum of the porous medium can be ignored.
- (2) The interactive force between the fluid and the porous medium is due to the frictional forces only and this force is proportional to the flow velocity which is represented by the term  $\nu \underline{v}$ , where  $\nu = \mu/\lambda$ ,  $\mu$  is the fluid viscosity and  $\lambda$  is the permeability of the porous medium.
- (3) The frictional effects due to viscosity were taken into account by the term  $\mu_{\text{eff}} \nabla^2 \underline{v}$ , where  $\mu_{\text{eff}} = \mu/\zeta$ .
- (4) The flow is unsteady and sufficiently fast, so that the inertial nonlinearities cannot be ignored; thus the term  $(1/\zeta^2)(\underline{v} \cdot \nabla) \underline{v}$  needs to be retained.

According to the previous assumptions, the balance of linear momentum can be written as in (4). Also, we want to confirm the following points.

- (1) The velocity of the flow through the porous medium is the average of the fluid velocity. This quantity has been given various names by different authors, such as seepage velocity, filtration velocity, superficial velocity, or Darcy velocity [22]. The seepage velocity  $\underline{v}$  is related by the velocity of the fluid  $\underline{V}$  (where  $\underline{V}$  is the flow velocity in the absence of the porous medium) by  $\underline{v} = \zeta \underline{V}$ .
- (2) The porosity  $\zeta$  for natural media does not normally exceed 0.6. For beds of solid spheres of uniform diameter  $\zeta$  can vary between the limits 0.2595 (rhombohedral packing) and 0.4764 (cubic packing). Nonuniformity of grain size tends to lead to smaller porosities than those for uniform grains, because smaller grains fill the pores formed by larger grains. For man-made materials such as metallic foams  $\zeta$  can approach the value 1 (see the tabulated values for the porosity and permeability in [22, page 5]).
- (3) The term  $(1/\zeta^2)(\underline{v} \cdot \nabla) \underline{v}$  is inappropriate if the flow is sufficiently slow. Then the inertial nonlinearities can be neglected [19]. However, this term needs to

be retained in the case of highly porous media where the flow is sufficiently fast and at least the irrotational part of this term needs to be retained [22] and for incompressible fluids this term reduces to  $\zeta^{-1} \nabla[\zeta^{-1} \underline{v} \cdot \underline{v}]$ , and for highly porous media we can assume  $\zeta = 1$  (as we assume in the present problem).

- (4) Brinkman sets the viscosity  $\mu$  and the effective viscosity  $\mu_{\text{eff}}$  equal to each other but in general that is not true [22]. The difference between  $\mu$  and  $\mu_{\text{eff}}$  is due to the momentum dispersion and  $\mu_{\text{eff}}$  is dependent on the type of the porous medium as well as the strength of flow, and it is common practice to take  $\mu_{\text{eff}}$  equal to  $\mu$  for high porosity media [23].
- (5) Experimental checks of Brinkman's theory have been indirect and few in number. The Brinkman's equation reduces to Darcy's equation when the spatial length scale is much greater than  $(\mu_{\text{eff}} \lambda / \mu)^{1/2}$ . Therefore the term  $\nabla^2 \underline{v}$  is negligible in comparison with the term proportional to  $\underline{v}$  [22]. But, the Brinkman's model holds only for particles whose size is of order  $\vartheta^3$ , where  $\vartheta \ll 1$  is the distance between neighboring particles, and for large particles the fluid filtration is governed by Darcy's law [22].

Because of the quasi-static approximation and in poorly conducting fluid [24, 25], the induced magnetic field is negligible. Also, we deal with very small electric conductivity and there is no applied magnetic field. So, the electric field is conservative. Since, the electric field is curl free vector the Maxwell's equations are  $\nabla \times \underline{E} = 0$  and  $\nabla \cdot \underline{\varepsilon E} = 0$ . So, the electric field has an electric scalar potential  $\phi$  such that  $\underline{E} = E_0 \hat{z} - \nabla \phi$ . Therefore the electric potential  $\phi_j$  satisfies the Laplace's equation

$$\nabla^2 \phi_j = 0 \quad (j = 1, 2). \quad (7)$$

The boundary and interfacial conditions for the problem may be displayed in the following section.

### 3. Boundary Conditions

The boundary conditions adopted here must be classified into three categories. The first relates the hydrodynamic part at the boundaries. The second is concerned with the electric part at the boundaries. Meanwhile, the third relates the combination condition of the electric and hydrodynamic balance of the stress tensor components at the interface between the liquid and the surrounding vacuum.

(1) For the hydrodynamic part, because  $F$  (in (1)) is a scalar function that is always equal to zero at any point on the fluid interface, its time derivative following any material point on the interface is obviously equal to zero, which means that there is no phase transformation occurring [26, Chapter 2, page 75]. So, the continuity of the normal velocity at the interface requires

$$\frac{D}{Dt} [r - h(z, t)] = 0, \quad \text{at } r = h, \quad (8)$$

where  $r$  is the radial distance and  $h$  is the radius for the disturbed fluid surface.

According to the microscale of the cylindrical fluid radius, the standard no-slip boundary condition in the classical fluid mechanics does not apply, so that the shear stress at the boundary vanishes (i.e., there is no considerable surface fraction between the fluid and the axial bar) and hence  $\partial v_z / \partial r = 0$  at the axial bar. Meanwhile, the normal velocity must be vanishing at the axial bar. So the boundary conditions for the velocity at the surface of the microcylindrical axis may be written as follows:

$$v_r = 0, \quad r = R_1, \quad \frac{\partial v_z}{\partial r} = 0, \quad r = R_1, \quad (9)$$

where  $R_1$  is the microradius of the axial microcylindrical bar such that  $R_1$  is sufficiently small ( $R_1 \ll 1$ ) and  $v_r, v_z$  are the radial and axial velocity components, respectively.

(2) For the electric part, because there is no surface charges accumulated at the interface, the normal electric displacement must be continuous across the interface. So that  $\underline{n} \cdot \|\underline{\varepsilon E}\| = 0$  and the interfacial condition for the normal electric field displacement, in the linear form, yields

$$E_0 h_z \|\underline{\varepsilon}_j\| + \left\| \underline{\varepsilon}_j \frac{\partial \phi_j}{\partial r} \right\| = 0, \quad \text{at } r = h, \quad (10)$$

where the notation  $\|\cdot\|$  denotes the subtract at the fluid and surrounding vacuum. In other words  $\|f\| = f_1 - f_2$ . The subscript  $j$ , in the electric potential  $\phi_j$  and the dielectric constant  $\varepsilon_j$ , takes the values  $j = 1, 2$  at the fluid and the surrounding vacuum, respectively.

The continuity of the tangential electric field components at the interface requires  $\underline{n} \times \|\underline{E}\| = 0$  and in the linear form (where the linear terms only are retained and the nonlinear terms are omitted) becomes

$$\left\| \frac{\partial \phi_j}{\partial z} \right\| = 0, \quad \text{at } r = h. \quad (11)$$

Since the axial microsolid bar and the vacuum at infinity have no electric field, the electric potential at the boundaries satisfies

$$\nabla \phi_1 = 0, \quad r = R_1, \quad \nabla \phi_2 = 0, \quad r = R_2. \quad (12)$$

(3) The balance of the stress components at the interface may be presented as follows.

At the interface between the liquid and vacuum, the fluid and the electrical stresses must be balanced. The components of these stresses consist of the electric hydrodynamic stresses together with the surface tension force [27]. The combination of the electric stress  $\tau_{ij}^{\text{electro}}$  and hydrodynamic stress  $\tau_{ij}^{\text{hydro}}$  parts may be presented in the total stress as

$$\tau_{ij} = \tau_{ij}^{\text{hydro}} + \tau_{ij}^{\text{electro}}. \quad (13)$$

The electric force density  $\underline{F}_e$  can be written in terms of the electric field as  $\underline{F}_e = (\nabla \cdot \underline{\varepsilon E}) \underline{E}$ . Since  $\nabla \times \underline{E} = 0$ , the electric force can be written as  $\underline{F}_e = (\nabla \cdot \underline{\varepsilon E}) \underline{E} + (\nabla \times \underline{E}) \times \underline{\varepsilon E}$  and the Maxwell stress tensor  $\tau_{ij}^{\text{electro}}$ , in the index notation, may be written as [28]

$$\tau_{ij}^{\text{electro}} = \varepsilon E_i E_j - \frac{1}{2} \varepsilon E^2 \Delta_{ij}, \quad (14)$$

meanwhile, the hydrodynamic stress tensor may be described by the constitutive relation

$$\tau_{ij}^{\text{hydro}} = -P\Delta_{ij} + \mu \left( \frac{\partial v_i}{\partial x_j} + \frac{\partial v_j}{\partial x_i} \right), \quad (15)$$

where  $\Delta_{ij}$  is the usual kronecker delta and  $v_i, v_j, x_i, x_j$  are a general notations for the velocity components and the coordinates, respectively.

According to the simple interface description, which involves only interfacial tension, the forces acting on any segment of an interface are of two kinds. First, there are the bulk pressure and stresses that act on the faces of the interface element and produce a net effect that is proportional to the surface area; second, there is a tensile force that is due to surface or interfacial tension that acts in the plane of the interface at the edges of the surface element and is specified by means of the magnitude of the surface or interfacial tension as a force per unit length [26, Chapter 2, page 76]. So, the stress balance can be written as [3]

$$\hat{n} \cdot \tau = -2H\sigma(z)\hat{n} + \nabla_s \sigma(z), \quad (16)$$

where  $H$  is the curvature of the interface,  $\nabla_s$  is the surface gradient at the interface, and  $\sigma(z)$  is the surface tension.

The previous condition can be decomposed into the normal and tangential stress tensor components as follows.

(i) The normal stress component requires

$$(\hat{n} \cdot \tau) \cdot \hat{n} = -2H\sigma(z). \quad (17)$$

(ii) The tangential stress components yield

$$(\tau \cdot \hat{n}) \cdot \hat{t} = \hat{t} \cdot \nabla_s \sigma(z), \quad (18)$$

where the surface curvature and the gradient at the interface may be given as follows:

$$H = \frac{1}{2} \nabla \cdot \hat{n} = \frac{1}{2} \left( \frac{1}{h \sqrt{1+h_z^2}} - \frac{h_{zz}}{(1+h_z^2)^{3/2}} \right), \quad (19)$$

$$\nabla_s \equiv \frac{1}{2} (\nabla - \hat{n}(\hat{n} \cdot \nabla)) = \hat{r} \frac{h_z}{1+h_z^2} \frac{\partial}{\partial z} + \hat{z} \frac{1}{1+h_z^2} \frac{\partial}{\partial z}.$$

Finally, the normal and tangential stress tensor conditions as given in (17) and (18) (at  $r = h$ ) may be written as follows:

$$\begin{aligned} & -P + \frac{2\mu}{1+h_z^2} \left[ \frac{\partial v_r}{\partial r} + h_z^2 \frac{\partial v_z}{\partial z} - h_z \left( \frac{\partial v_r}{\partial z} + \frac{\partial v_z}{\partial r} \right) \right] \\ & + \frac{1}{2(1+h_z^2)} \left\| \varepsilon_j \left[ (1-h_z^2) \left( \frac{\partial \phi_j}{\partial r} \right)^2 \right. \right. \end{aligned}$$

$$\begin{aligned} & \left. - (1-h_z^2) \left( E_0 - \frac{\partial \phi_j}{\partial z} \right)^2 + 4h_z \frac{\partial \phi_j}{\partial r} \left( E_0 - \frac{\partial \phi_j}{\partial z} \right) \right\| \\ & = -2\sigma(z)H, \\ & \frac{\mu}{1+h_z^2} \left[ 2h_z \left( \frac{\partial v_r}{\partial r} - \frac{\partial v_z}{\partial z} \right) + (1-h_z^2) \left( \frac{\partial v_r}{\partial z} + \frac{\partial v_z}{\partial r} \right) \right] \\ & + \frac{1}{(1+h_z^2)} \left\| \varepsilon_j \left[ h_z \left( \frac{\partial \phi_j}{\partial r} \right)^2 - h_z \left( E_0 - \frac{\partial \phi_j}{\partial z} \right)^2 \right. \right. \\ & \left. \left. - (1-h_z^2) \frac{\partial \phi_j}{\partial r} \left( E_0 - \frac{\partial \phi_j}{\partial z} \right) \right] \right\| \\ & = \hat{t} \cdot \nabla_s \sigma(z). \end{aligned} \quad (20)$$

(21)

We study the solution of the equations of motion (4) according to the boundary and interfacial conditions in two cases. The first case is obtained in the absence of the heat and mass transfer where the spatial surface tension is independent of the rate of heat and mass transfer. In this case, we follow the same analysis of Furlani [3] to gain the function of the free surface of the microcylindrical fluid flow. In the second one, taking into account the dependence of the surface tension on the heat and mass transfer, the surface tension becomes a function of the time and the axial distance. So, in this case, the dispersion relation may be obtained as a transcendental function and its roots can be computed numerically hence the stability picture may be obtained graphically. Before studying the previous cases, we obtain the solution of the electric field according to the boundary and interfacial conditions.

#### 4. Solution of the Eclectic Field

Our analysis will be based on the normal modes technique. Therefore, the electric potential may take the following form:

$$\phi_j(r, z, t) = \varphi_j(r) e^{\omega t + ikz}, \quad (22)$$

where  $\omega$  is the frequency of the surface wave and  $k$  is its wave number which is assumed to be real and positive. Using (7) with the boundary conditions (10)–(12), we may obtain the solution for the electric potential functions as follows:

$$\begin{aligned} \phi_1(r, z, t) &= \frac{ir_0 E_0 (\varepsilon_2 - \varepsilon_1) g_2(k)}{\varepsilon_2 g_1(k) G_2(k) - \varepsilon_1 g_2(k) G_1(k)} \\ &\times [K_0(kr) I_0'(kR_1) - K_0'(kR_1) I_0(kr)] e^{\omega t + ikz}, \end{aligned}$$



$$\begin{aligned} \phi_2(r, z, t) &= \frac{ir_0 E_0 (\varepsilon_2 - \varepsilon_1) g_1(k)}{\varepsilon_2 g_1(k) G_2(k) - \varepsilon_1 g_2(k) G_1(k)} \\ &\times [K_0(kr) I_0'(kR_2) - K_0'(kR_2) I_0(kr)] e^{\omega t + ikz}, \end{aligned} \quad (23)$$

where  $I_0$  and  $K_0$  are the modified Bessel's functions of first and second kinds of order zero, respectively. The dashes denote the differentiation with respect to  $r$  and  $i = \sqrt{-1}$ . Also, the functions  $g_1(k)$ ,  $g_2(k)$ ,  $G_1(k)$ , and  $G_2(k)$  are given in the appendix.

### 5. Instability in the Absence of Heat and Mass Transfer

This section is devoted to solving the equations of motion and the continuity equation (see (3) and (4)) according to the interfacial and boundary conditions (see (8) and (9)) with employing the normal and tangential stress tensor interfacial conditions. We follow the same procedure given by Furlani [3] to get the function that describes the free surface. So, we expand the velocity components and the pressure as a power of  $r$  (depending on the microradius of the flow jet), as follows:

$$\begin{aligned} v_z(r, z, t) &= v_0(z, t) + v_2(z, t) r^2 + \dots, \\ P(r, z, t) &= P_0(z, t) + P_2(z, t) r^2 + \dots. \end{aligned} \quad (24)$$

From the continuity equation (3), one gets

$$v_r(r, z, t) = -\frac{\partial v_0(z, t)}{\partial z} \frac{r}{2} - \frac{\partial v_2(z, t)}{\partial z} \frac{r^3}{4} + \dots, \quad (25)$$

where  $v_0(z, t)$ ,  $v_2(z, t)$  are perturbed velocity functions and  $P_0(z, t)$ ,  $P_2(z, t)$  are the perturbed pressure functions. It is important to notice here that the expansions in (24)-(25) are compatible with the boundary conditions in (9) and with the continuity equation (3). Where  $R_1$  and  $r$  are a microradii of the axial microcylinder and the microporous cylinder that contains the fluid, respectively. So, all terms containing  $O(r)$  and  $O(R_1)$  or higher orders can be neglected according to their tendency to zero.

According to the previous expansions, the equation of motion (4) for  $v_r$  can be neglected because it is identical to the lowest order of  $r$ . Therefore the equation of motion for  $v_z$  can be written as

$$\begin{aligned} \rho \left( \frac{\partial v_0}{\partial t} + v_0 \frac{\partial v_0}{\partial z} \right) &= -\frac{\partial P_0}{\partial z} + \mu \left( 4v_2 + \frac{\partial^2 v_0}{\partial z^2} \right) - \nu v_0. \end{aligned} \quad (26)$$

The second order term of the velocity  $v_2$  can be determined from the tangential stress condition as given in (21); on

neglecting the terms of  $O(r)$  and all higher orders, it can be written as follows:

$$\begin{aligned} v_2 &= \frac{1}{2\mu h} \frac{\partial \sigma}{\partial z} + \frac{3h_z}{2h} \frac{\partial v_0}{\partial z} + \frac{1}{4} \frac{\partial^2 v_0}{\partial z^2} \\ &+ \left\| \frac{\varepsilon_j E_0}{2\mu h} \frac{\partial \phi_j}{\partial r} - \frac{\varepsilon_j E_0 h_z}{\mu h} \frac{\partial \phi_j}{\partial z} \right\|. \end{aligned} \quad (27)$$

The zero order term of the pressure  $P_0$  can be determined from the normal stress condition, as given in (20), in the form

$$P_0 = -\mu \frac{\partial v_0}{\partial z} + 2\sigma H + \left\| \varepsilon_j E_0 \frac{\partial \phi_j}{\partial z} \right\|. \quad (28)$$

Now, substituting from (27) and (28) into (26), we obtain

$$\begin{aligned} \rho \left( \frac{\partial v_0}{\partial t} + v_0 \frac{\partial v_0}{\partial z} \right) &= -\frac{\partial}{\partial z} (2\sigma H) \\ &+ \left\| \frac{2\varepsilon_j E_0}{h} \frac{\partial \phi_j}{\partial r} - \frac{4\varepsilon_j E_0 h_z}{h} \frac{\partial \phi_j}{\partial z} - \varepsilon_j E_0 \frac{\partial^2 \phi_j}{\partial z^2} \right\| \\ &+ \frac{3\mu}{h^2} \frac{\partial}{\partial z} \left( h^2 \frac{\partial v_0}{\partial z} \right) + \frac{2}{h} \frac{\partial \sigma}{\partial z} - \nu v_0. \end{aligned} \quad (29)$$

The kinematic condition equation (8) gives

$$\frac{\partial h}{\partial t} = -v_0 \frac{\partial h}{\partial z} - \frac{h}{2} \frac{\partial v_0}{\partial z}. \quad (30)$$

Also, the axial velocity  $v_0(z, t)$ , the radial position  $h(z, t)$ , and the surface tension  $\sigma(z)$  can be represented in a perturbed and unperturbed parts as follows:

$$v_0(z, t) = u_0 + u(z, t), \quad (31)$$

$$h(z, t) = r_0 (1 + \delta(z, t)), \quad (32)$$

$$\sigma(z) = \sigma_0 + \sigma_1(z), \quad (33)$$

where  $u_0$ ,  $r_0$ , and  $\sigma_0$  are the constant unperturbed axial streaming velocity, radius, and surface tension, respectively. The analysis may be simplified by using the transformation

$$\eta = z - u_0 t. \quad (34)$$

By using (31)–(34) into (29) and (30), after linearizing the resulting equations, we can obtain

$$\begin{aligned} \rho \left( \frac{\partial u}{\partial t} \right) &= \frac{1}{r_0} \frac{\partial \sigma_1}{\partial \eta} + \left\| \frac{2\varepsilon_j E_0}{r_0} \frac{\partial \phi_j}{\partial r} - \varepsilon_j E_0 \frac{\partial^2 \phi_j}{\partial \eta^2} \right\| \\ &+ 3\mu \frac{\partial^2 u}{\partial \eta^2} + \frac{\sigma_0}{r_0} \frac{\partial \delta}{\partial \eta} + \sigma_0 r_0 \frac{\partial^3 \delta}{\partial \eta^3} - \nu u, \\ \frac{\partial^2 u}{\partial \eta^2} &= -2 \frac{\partial^2 \delta}{\partial \eta \partial t}. \end{aligned} \quad (35)$$



Equations (35) can be combined into one equation that determines the free surface function  $\delta(\eta, z)$  as follows:

$$\begin{aligned} & \frac{\partial^2 \delta}{\partial t^2} + \frac{\partial}{\partial t} \left( \frac{\nu}{\rho} \delta - \frac{3\mu}{\rho} \frac{\partial^2 \delta}{\partial \eta^2} \right) \\ & + \frac{\sigma_0}{2\rho r_0} \left( \frac{\partial^2 \delta}{\partial \eta^2} + r_0^2 \frac{\partial^4 \delta}{\partial \eta^4} \right) \\ & + \left\| \frac{\varepsilon_j E_0}{2\rho r_0} \left( 2 \frac{\partial^2 \phi_j}{\partial r \partial \eta} - r_0 \frac{\partial^3 \phi_j}{\partial \eta^3} \right) \right\| \\ & = -\frac{1}{2\rho r_0} \frac{\partial^2 \sigma_1}{\partial \eta^2}. \end{aligned} \quad (36)$$

Initially, the disturbed fluid radius  $\delta(\eta, t)$  is independent of the time (also its partial derivative with respect to the time). So, the disturbed fluid radius  $\delta(\eta, t)$  has the following initial conditions:

$$\delta(\eta, 0) = 0, \quad \frac{\partial}{\partial t} \delta(\eta, 0) = 0. \quad (37)$$

Assuming that the surface tension  $\sigma_1(\eta)$  has a spatially periodic form, which is independent of the heat and mass transfer. Then, the surface tension function may be written in the following form:

$$\sigma_1(\eta) = -\frac{\Delta\sigma}{2} (1 + e^{ik\eta}), \quad (38)$$

where  $\Delta\sigma$  is a constant variation of the surface tension.

The initial value problem given by (36) and the initial conditions equation (37) can be solved by decomposing the solution into a homogenous and particular parts,  $\delta_h(\eta, t)$  and  $\delta_p(\eta, t)$ , respectively. Based on the form of the surface tension  $\sigma_1(\eta)$ , which is given in (38), the homogenous solution of the wave function  $\delta_h(\eta, t)$  may be written in the form

$$\delta_h(\eta, t) = e^{\omega t + ik\eta}. \quad (39)$$

The final form of the general solution of the free surface function,  $\delta(\eta, t) = \delta_h(\eta, t) + \delta_p(\eta, t)$ , can be written as follows:

$$\delta(\eta, t) = -\frac{\Delta\sigma k^2}{4\rho r_0 b_0} \left[ \frac{\omega_-}{\omega_+ - \omega_-} e^{\omega_+ t} - \frac{\omega_+}{\omega_+ - \omega_-} e^{\omega_- t} + 1 \right] e^{ik\eta}, \quad (40)$$

where, the roots  $\omega_{\pm}$  and  $b_0$  are defined in the appendix.

It is worthwhile to mention here that the final solution in (40) reduces to the same solution obtained earlier by Furlani [3] for the flow of cylindrical microjet surface in the absence of the electric field ( $E_0 = 0$ ). It is worthwhile to mention here that the final solution in (40) reduces to the same solution that was obtained earlier by Furlani [3] for the flow of cylindrical microjet surface in the absence of the electric field ( $E_0 = 0$ ) with neglecting the porous structure ( $\nu = 0$ ) and with taking the real part only of the free surface function.

## 6. Instability of Thermosolutal Marangoni Convection

If the two-fluid system is a multicomponent system, it is often the case that there may be a preferential concentration of one or more of the components at the interface (e.g., if we consider a system of pure  $A$  and pure  $B$ , which are immiscible, with a third solute component  $S$  that is soluble in  $A$  and/or  $B$  but that is preferentially attracted to the interface), and then the interfacial tension will also be a function of the (surface-excess) concentration of these solute components. Both the temperature and the concentrations of adsorbed species can be functions of position on the interface, thus leading to spatial gradients of the surface tension [26]. So, to study the effect of the heat and mass transfer on the interfacial instability of the microcylindrical surface, the surface tension is assumed to be a function of the temperature and the solute concentration and the surface tension will depend on temperature and concentration linearly [29], as follows:

$$\begin{aligned} \sigma(\eta, t) &= \sigma_0 + \sigma_1(\eta, t) \\ &= \sigma_0 [1 - \gamma_T (T - T_0) - \gamma_C (C - C_0)], \end{aligned} \quad (41)$$

where  $\gamma_T$  and  $\gamma_C$  denote the temperature and concentration coefficients of the surface tension. Also,  $T_0$  and  $C_0$  are the reference temperature and concentration, respectively. Note that (41) is the same as (33) with  $\sigma_1(z)$  being  $\sigma_1(\eta, t)$  that depends on the heat and mass transfer as in (41).  $\sigma_0$  is the unperturbed constant value of the surface tension.

To determine the form of the surface tension, we need firstly to obtain the solution of the heat and concentration equations. Again, the analysis will be based on the normal modes technique as given by

$$\begin{aligned} T(r, \eta, t) &= T_s(r) e^{\omega t + ik\eta}, \\ C(r, \eta, t) &= C_s(r) e^{\omega t + ik\eta}. \end{aligned} \quad (42)$$

With the help of the coordinate transformation in (34), the energy and concentration equations (see (5) and (6)) may be written in the following forms:

$$\frac{d^2 T_s}{dr^2} + \frac{1}{r} \frac{dT_s}{dr} - m^2 T_s = 0, \quad (43)$$

$$\frac{d^2 C_s}{dr^2} + \frac{1}{r} \frac{dC_s}{dr} - n^2 C_s = 0, \quad (44)$$

where  $m^2 = k^2 + (\omega/\alpha)$  and  $n^2 = k^2 + (\omega/\beta)$ .

If we consider the diffusion of the thermal energy and the concentration in an infinite isolated column of stationary flow of radius  $r_0$  then there are no temperature and concentration gradients at  $r = r_0$ . So, the temperature and concentration boundary conditions are as follows [3]:

$$\begin{aligned} T_s &= T_1, \quad C_s = C_1, \quad \text{at } r = R_1, \\ \frac{\partial T_s}{\partial r} &= 0, \quad \frac{\partial C_s}{\partial r} = 0, \quad \text{at } r = r_0. \end{aligned} \quad (45)$$

Equations (43) and (44) represent the standard Bessel's differential equation. Therefore, the general solution of the temperature and concentration function may be written as follows:

$$\begin{aligned}
 T(r, \eta, t) &= \frac{T_1 [K'_0(mr_0) I_0(mr) - I'_0(mr_0) K_0(mr)]}{K'_0(mr_0) I_0(mR_1) - K_0(mR_1) I'_0(mr_0)} e^{\omega t + ik\eta}, \\
 C(r, \eta, t) &= \frac{C_1 [K'_0(nr_0) I_0(nr) - I'_0(nr_0) K_0(nr)]}{K'_0(nr_0) I_0(nR_1) - K_0(nR_1) I'_0(nr_0)} e^{\omega t + ik\eta}.
 \end{aligned} \quad (46)$$

On combining the following equations:

- (1) the general solution of the heat and mass transfer (see (46)),
- (2) the surface tension expression (see (41)),
- (3) the expression of the free surface function, which may be given based on the normal modes technique as  $\delta(\eta, t) = e^{\omega t + ik\eta}$ , into the free surface deferential equation given by (36).

We finally get the transcendental dispersion relation of the instability of the interfacial free surface as

$$f(\omega, k) = \omega^2 + a_1(k)\omega + b_1(\omega, k) = 0, \quad (47)$$

where the functions  $a_1(k)$  and  $b_1(\omega, k)$  are defined in the appendix.

It is convenient to write the stability criterion in an appropriate dimensionless form. This can be done in a number of ways depending primarily on the choice of the characteristic length, time, temperature, and mass. Consider the following dimensionless forms depending on the characteristic length  $= r_0$ , the characteristic time  $= 1/\hat{\omega}$ , the characteristic temperature  $= T_1$ , and the characteristic mass  $= \sigma_0/\hat{\omega}^2$ , where  $\hat{\omega}$  is a characteristic value of  $\omega$ . The other dimensionless quantities are given by

$$\begin{aligned}
 k &= \frac{k^*}{r_0}, & \rho &= \rho^* \frac{\sigma_0}{r_0^3 \hat{\omega}^2}, & E_0^2 &= E_0^{*2} \frac{\sigma_0}{r_0}, \\
 \mu &= \mu^* \frac{\sigma_0}{\hat{\omega} r_0}, & T &= T_1 T^*, & \gamma_T &= \frac{\gamma_T^*}{T_1}, \\
 \nu &= \nu^* \frac{\sigma_0}{r_0 \hat{\omega}}, & r &= r^* r_0, & \omega &= \hat{\omega} \omega^*, \\
 \alpha &= \alpha^* r_0^2 \hat{\omega}, & \beta &= \beta^* r_0^2 \hat{\omega}.
 \end{aligned} \quad (48)$$

The superscript asterisks refer to the dimensionless quantities. From now on, these will be omitted for simplicity. The dispersion relation in (47) and its coefficients  $a_1(k)$  and  $b_1(\omega, k)$  may be written as follows:

$$f(\omega, k) = \omega^2 + a(k)\omega + b(\omega, k) = 0, \quad (49)$$

where the functions  $a(k)$  and  $b(\omega, k)$  are defined in the appendix.

The dimensionless transcendental dispersion relation in (49) describes the instability of the interfacial free surface of the microfluid jet. We will discuss the instability criteria numerically and graphically in the next section.

## 7. Numerical Estimations

In the case of the thermosolutal Marangoni convection, the surface tension depends on the heat and mass transfer and the dispersion relation is the transcendental equation (49). The stability criteria of the system may be discussed by getting the values of the growth rate  $\omega$  from the roots of the transcendental equation (49). The positive values of  $\omega$  indicate a disturbance that grows with time (instability) and the negative values indicate decays with time (stability). So, to study the instability of the microcylindrical surface, we indicate the relation between the growth rate  $\omega$  and the wave number  $k$  graphically. In all coming curves, the positive values region of  $\omega$  indicates the instability region, denoted by letter  $U$ . Meanwhile, the negative values region of  $\omega$  indicates the stability region, denoted by letter  $S$ .

It is well known that increasing the wave number enhances the stability of the system. As seen in Figure 2, the stability occurs at  $k \cong 0.7$ , when the intensity of the electric field  $E_0 = 1000$ . Meanwhile, at  $E_0 = 1$  the stability occurs at  $k \cong 1$ . This means that the stability occurs at less value of  $k$  and at the higher value of  $E_0$ , which means that the system is more stable at highly electric field intensity and the electric field has a stabilizing effect. This is an early result obtained by many researchers [7, 20, 24, 25]. Also, we can notice that the maximum instability in all figures, except Figure 2, according to the peak of the curve occurs at  $k \cong 0.6$ . But at high values of the electric field, the peak of the curve approaches the stability region and the maximum instability occurs at  $k \cong 0.4$ . This implies that existence of the electric field causes a high stability of the interface.

Figure 3 illustrates the electric field and the growth rate relation. It is clear from this figure that the maximum value of the electric field  $E_0$  is congruent to the zero value of the growth rate  $\omega$ . The zero value the growth rate  $\omega$  corresponds to the steady state of the interface. This result confirms the same result of Figure 2; that is, the electric field has a stabilizing effect. Figure 4 illustrates the effect of the dielectric constants difference  $\hat{\epsilon} = \epsilon_1 - \epsilon_2$  on the stability picture. The dielectric difference  $\hat{\epsilon}$  has a stabilizing effect, where the higher value of  $\hat{\epsilon}$  is identical to the minimum peak value of the curve.

Figures 5–7 illustrate the effect of Darcy's coefficient, the viscosity, and the density of fluid on the stability behavior. The of Darcy's coefficient, the viscosity, and the density of fluid have stabilizing effect for  $k \leq 1$  according to reducing the peak of the curve and decreasing the number of the points in the instability region. Figure 5 illustrates the effect of the existence of the porous structure, according to the different values of the Darcy's coefficient, on the stability picture. It is clear that the microcylindrical surface is more stable, in case of the flow through a porous medium for majority values of the wave number, due to an increase in the values of the

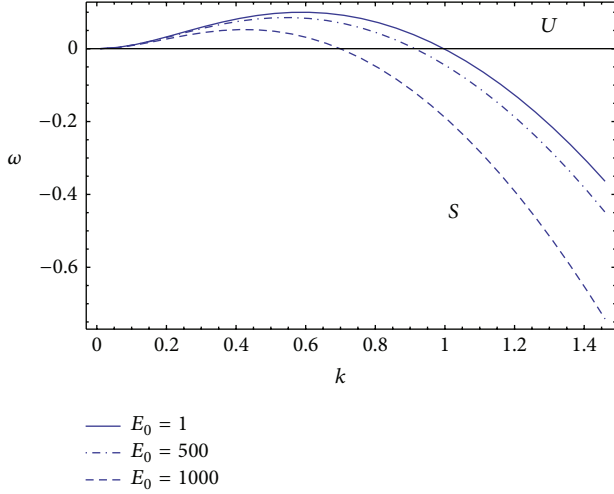


FIGURE 2: Stability diagram for a system having the particulars  $\rho = 1$ ,  $\mu = 0.5$ ,  $R_1 = 10^{-5}$ ,  $R_2 = 10$ ,  $\nu = 0.5$ ,  $\varepsilon_1 = 5 \times 10^{-5}$ ,  $\varepsilon_2 = 10^{-4}$ ,  $r_0 = 5 \times 10^{-3}$ ,  $\gamma_T = 0.01$ ,  $\gamma_C = 0.2$ ,  $\alpha = 0.01$ ,  $T_1 = 0.05$ ,  $C_1 = 0.03$ , and  $\beta = 0.2$ .

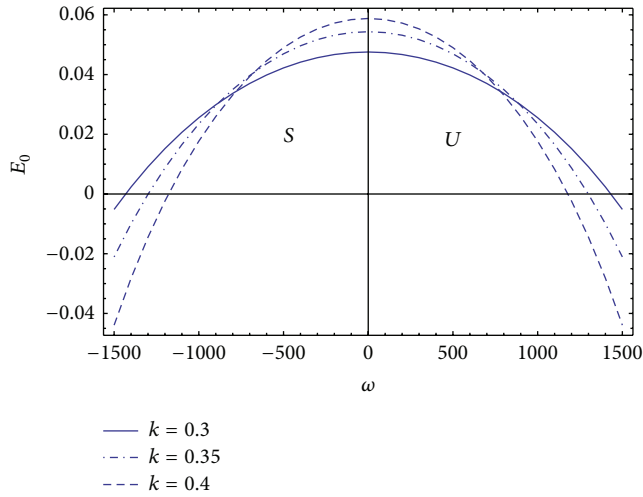


FIGURE 3: The electric field plotted versus the growth rate at  $\rho = 1$ ,  $\mu = 0.5$ ,  $R_1 = 10^{-5}$ ,  $R_2 = 10$ ,  $E_0 = 10$ ,  $\gamma_T = 0.01$ ,  $\gamma_C = 0.03$ ,  $r_0 = 5 \times 10^{-3}$ ,  $\alpha = 0.01$ ,  $C_1 = 10$ ,  $T_1 = 10$ ,  $\beta = 0.2$ ,  $\varepsilon_1 = 5 \times 10^{-5}$ , and  $\varepsilon_2 = 10^{-4}$ .

Darcy's coefficients in comparison with the case of the pure flow ( $\nu = 0$ ). This is due to the fact that the greatest peak value of the curve in the instability region is at  $\nu = 0$ . Hence the Darcy's coefficient  $\nu$  is equal to  $\mu/\lambda$ , where  $\lambda$  is the permeability of the porous medium, so an increase in the values of the Darcy's coefficients corresponds to a decrease in the permeability of the porous medium. This in turn restricts the streaming velocity of the fluid flow. It is known that when the streaming velocity decreases, the stability of the system increases. In other words, when the permeability of the medium increases ( $\lambda$  increases and  $\nu$  decreases) the holes of the porous medium are very large and the resistance of the medium may be neglected so that the streaming velocity

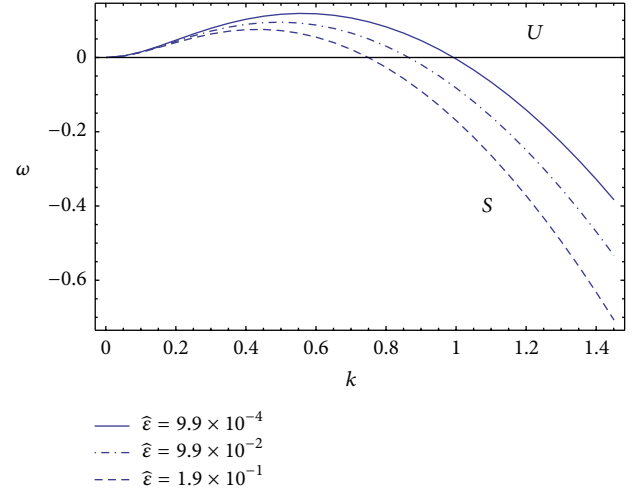


FIGURE 4: Stability diagram for a system having the particulars  $\rho = 1$ ,  $\mu = 0.5$ ,  $R_1 = 10^{-5}$ ,  $R_2 = 10$ ,  $E_0 = 10$ ,  $\gamma_T = 0.01$ ,  $\gamma_C = 0.03$ ,  $r_0 = 5 \times 10^{-3}$ ,  $\alpha = 0.01$ ,  $C_1 = 0.04$ ,  $T_1 = 1$ , and  $\beta = 0.2$ .

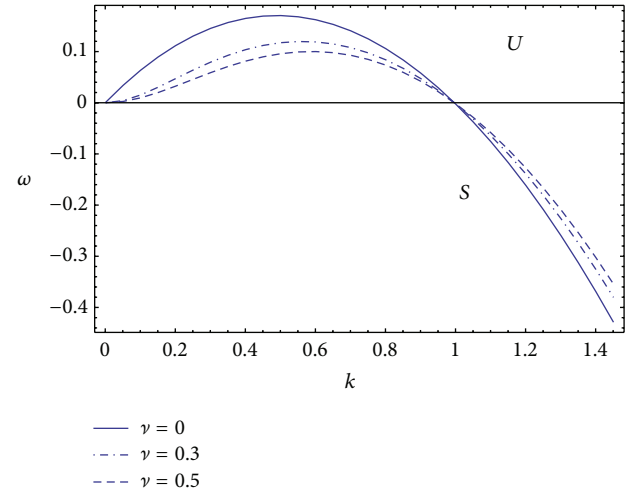


FIGURE 5: Stability diagram for a system having the particulars  $\rho = 1$ ,  $\mu = 0.5$ ,  $R_1 = 10^{-5}$ ,  $R_2 = 10$ ,  $E_0 = 10$ ,  $\varepsilon_1 = 5 \times 10^{-5}$ ,  $\varepsilon_2 = 10^{-4}$ ,  $r_0 = 5 \times 10^{-3}$ ,  $\gamma_T = 0.01$ ,  $\gamma_C = 0.2$ ,  $\alpha = 0.01$ ,  $T_1 = 0.05$ ,  $C_1 = 0.03$ , and  $\beta = 0.2$ .

increases and causes instability of the system. The same result was illustrated experimentally by Catton and Chung [21], where the authors studied the interfacial stability between the water and the steam. Two porous media were studied experimentally: a bead of glass with diameter 0.6, 2, and 6 and with permeability 0.14, 1.57, and 18.0 ( $\times 10^{-9} \text{ m}^2$ ), respectively, and a bead of steel with diameter 4 and with permeability 9.02 ( $\times 10^{-9} \text{ m}^2$ ). It was found that in the more permeable cylinder the steam bubble is chaotic just after it has been formed. This means that the interface becomes unstable and the chaotic turbulence becomes more and more profound as the water flow rate increases (according to increasing the permeability of the porous medium).

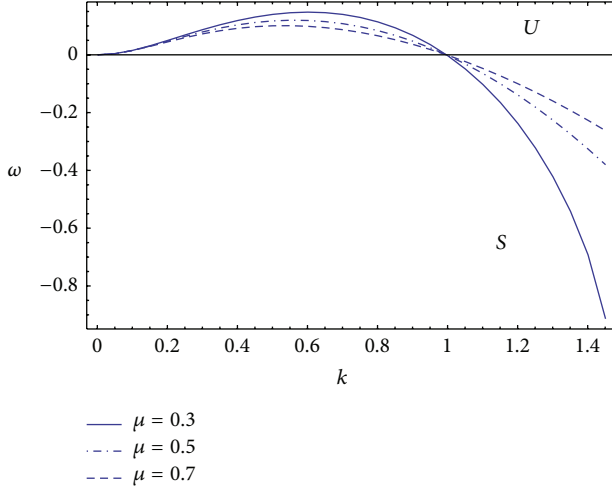


FIGURE 6: Stability diagram for a system having the particulars  $\rho = 1$ ,  $\nu = 0.3$ ,  $R_1 = 10^{-5}$ ,  $R_2 = 10$ ,  $E_0 = 10$ ,  $\varepsilon_1 = 5 \times 10^{-5}$ ,  $\varepsilon_2 = 10^{-4}$ ,  $r_0 = 5 \times 10^{-3}$ ,  $\gamma_T = 0.01$ ,  $\gamma_C = 0.2$ ,  $\alpha = 0.01$ ,  $T_1 = 0.05$ ,  $C_1 = 0.03$ , and  $\beta = 0.2$ .

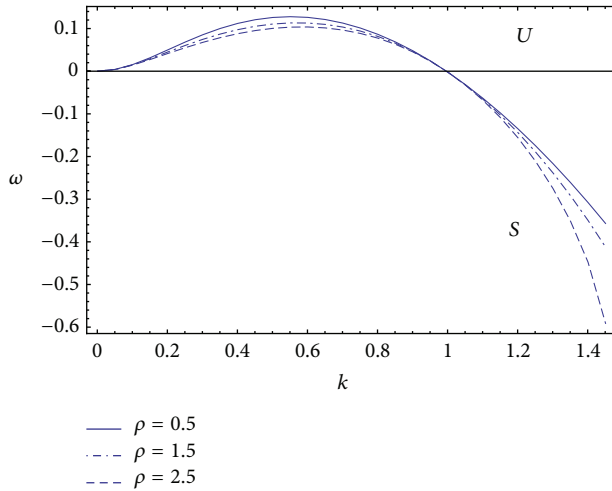


FIGURE 7: Stability diagram for a system having the particulars  $\nu = 0.3$ ,  $\mu = 0.5$ ,  $R_1 = 10^{-5}$ ,  $R_2 = 10$ ,  $E_0 = 10$ ,  $\varepsilon_1 = 5 \times 10^{-5}$ ,  $\varepsilon_2 = 10^{-4}$ ,  $r_0 = 5 \times 10^{-3}$ ,  $\gamma_T = 0.01$ ,  $\gamma_C = 0.2$ ,  $\alpha = 0.01$ ,  $T_1 = 0.05$ ,  $C_1 = 0.03$ , and  $\beta = 0.2$ .

The viscosity  $\mu$  and the density  $\rho$  have a stabilizing effect, for larger values of the wave number, as shown in Figures 6 and 7. This influence occurs due to an increase in the viscosity damping and in the inertia. So, the interface of the micro-cylindrical surface becomes stable with an increase in the viscosity and the density.

The effect of heat transfer on the free surface is illustrated in Figure 8. To study the instability influence, according to the heat transfer, we notice that the temperature coefficient is  $\gamma_T = \pm(1/\sigma_0)(d\sigma/dT)$  [30], where  $\gamma_T$  has a positive or negative sign according to the increasing or decreasing of the surface tension. When  $T < T_1$ , the axial microsolid cylinder, which induces the heat and mass gradients, is heated and then

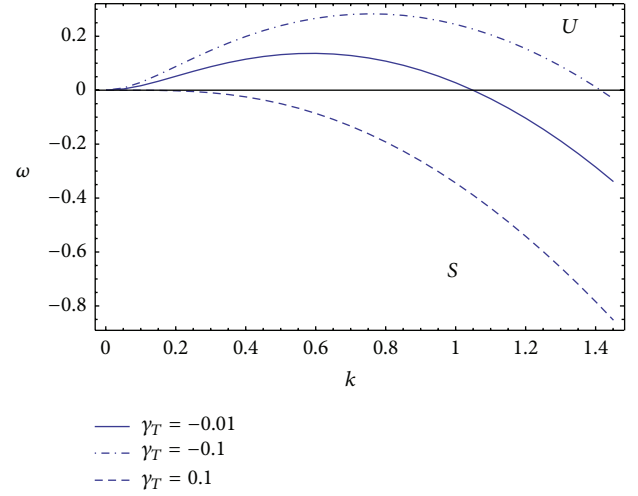


FIGURE 8: Stability diagram for a system having the particulars  $\rho = 1$ ,  $\mu = 0.5$ ,  $R_1 = 10^{-5}$ ,  $R_2 = 10$ ,  $E_0 = 10$ ,  $\varepsilon_1 = 5 \times 10^{-5}$ ,  $\varepsilon_2 = 10^{-4}$ ,  $r_0 = 5 \times 10^{-3}$ ,  $\gamma_C = -0.03$ ,  $\alpha = 0.01$ ,  $\nu = 0.3$ ,  $C_1 = 0.03$ ,  $\beta = 0.2$ , and  $T_1 = 10$ .

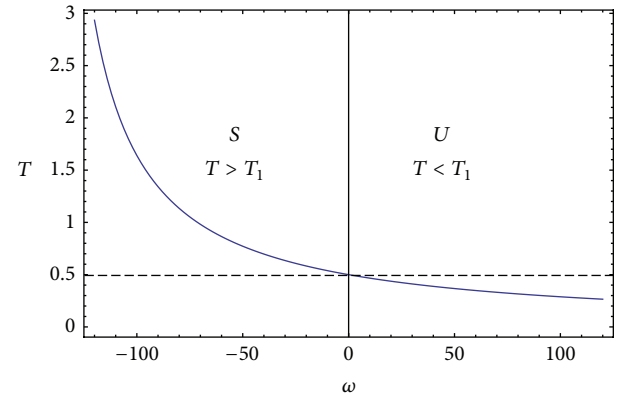


FIGURE 9: The temperature plotted versus the growth rate at  $\rho = 1$ ,  $\mu = 0.5$ ,  $R_1 = 10^{-5}$ ,  $R_2 = 10$ ,  $E_0 = 10$ ,  $\gamma_T = 0.01$ ,  $\gamma_C = 0.03$ ,  $r_0 = 5 \times 10^{-3}$ ,  $\alpha = 0.01$ ,  $C_1 = 10$ ,  $T_1 = 0.5$ ,  $\beta = 0.2$ ,  $\varepsilon_1 = 5 \times 10^{-5}$ , and  $\varepsilon_2 = 10^{-4}$ .

the temperate transfers from it to the free surface by convection currents. This in turn tends to evaporate the fluid easily and provokes higher instabilities at the interface. So, in this case,  $\gamma_T$  has a negative value according to the decreasing of the surface tension. Conversely,  $\gamma_T$  has a positive value when  $T > T_1$ . In this case the free surface loses its temperature that is transferred to the core region of the flow jet and hence the free surface becomes stable. This phenomenon was illustrated in Figure 8 where the temperature coefficient  $\gamma_T$  has a stabilizing effect when it is positive and the inverse occurs at  $\gamma_T < 0$ . In other words, heating the axial microsolid surface  $T_1$  has destabilizing effect at the interface and conversely for cooling. Figure 9 confirms this result. We notice from this figure that the unstable state, for the positive values of the growth rate  $\omega$ , occurs at the temperature values corresponding to  $T < T_1$ . Meanwhile, the temperature  $T > T_1$  is for the negative

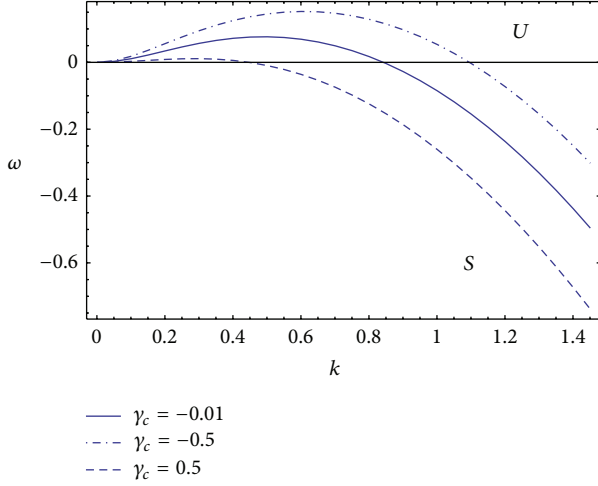


FIGURE 10: Stability diagram for a system having the particulars  $\rho = 1$ ,  $\mu = 0.5$ ,  $R_1 = 10^{-5}$ ,  $R_2 = 10$ ,  $E_0 = 10$ ,  $\varepsilon_1 = 5 \times 10^{-5}$ ,  $\varepsilon_2 = 10^{-4}$ ,  $r_0 = 5 \times 10^{-3}$ ,  $\gamma_T = -0.01$ ,  $\alpha = 0.01$ ,  $\nu = 0.3$ ,  $T_1 = 1$ ,  $\beta = 0.2$ , and  $C_1 = 10$ .

growth rate in the stability region. This result was obtained experimentally by D'Aubeterre et al. [31]. The authors stated that the temperature has a destabilizing effect due to the fact that a substance is more volatile for increasing the temperature; this means that when a temperature gradient occurs, the substance tends to evaporate easily and provokes higher instabilities at the interface. Also, depending on the alcohol studied [31], turbulence begins at the interface at different temperature gradients. Instabilities begin near the interface, showing a sinuous movement. At higher temperatures and temperature gradients, instabilities increase and movements become continuous. The most evident effect occurs when temperature gradients are  $15\text{--}17^\circ\text{C}$ ; at these values a sinuous wave was observed [31].

Similar behavior can be noticed for the concentration as seen in Figure 10. In this figure we use  $\gamma_C = \pm(1/\sigma_0)(d\sigma/dC)$  [30]. The concentration coefficients of the surface tension  $\gamma_C$  become negative if  $C < C_1$ . This implies that the concentration at the interface is less than the concentration at the core region. Because the surface tension is proportional with the concentration, the surface tension at the free surface accordingly reduces. So, the free surface loses its interfacial rigidity and its ability to movement increases. Therefore the instability of the free surface occurs. On the other hand, when the concentration of the interface is higher than that of the core region, the stability in the interface occurs. This means an increase of the interfacial rigidity, which in turn restricts any surface movements or Marangoni convection. Therefore, the surface becomes stable when  $\gamma_C > 0$  and the instability occurs for  $\gamma_C < 0$ , as shown in Figure 10. Figure 11 confirms this result, where the concentration is plotted versus the growth rate. The region of the positive values of the growth rate  $\omega$ , that is, the unstable region, occurs at  $C < C_1$ . Meanwhile, the stable region, that is, the negative growth rate values, occurs at  $C > C_1$ . Similar results were obtained by Agble and Mendes [32] and compared with experimental results.

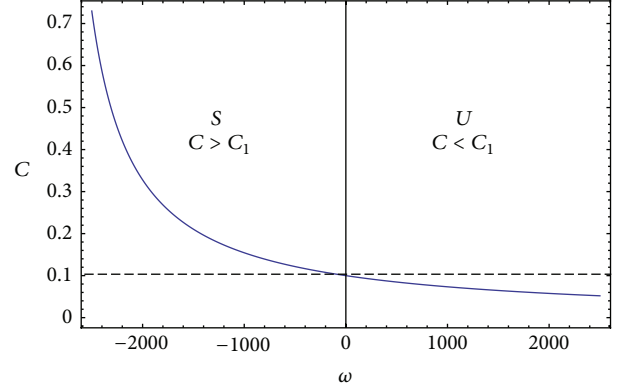


FIGURE 11: The concentration plotted versus the growth rate at  $\rho = 1$ ,  $\mu = 0.5$ ,  $R_1 = 10^{-5}$ ,  $R_2 = 10$ ,  $E_0 = 10$ ,  $\gamma_T = 0.01$ ,  $\gamma_C = 0.03$ ,  $r_0 = 5 \times 10^{-3}$ ,  $\alpha = 0.01$ ,  $C_1 = 0.1$ ,  $T_1 = 0.5$ ,  $\beta = 0.2$ ,  $\varepsilon_1 = 5 \times 10^{-5}$ , and  $\varepsilon_2 = 10^{-4}$ .

TABLE 1: The root of the growth rate  $\omega$  for different values of the micro radius  $r_0$  at  $\rho = 1$ ,  $\mu = 0.5$ ,  $\varepsilon_1 = 10^{-5}$ ,  $\varepsilon_2 = 10^{-3}$ ,  $R_1 = 10^{-5}$ ,  $E_0 = 10$ ,  $R_2 = 10$ ,  $\gamma_T = 0.5$ ,  $\gamma_C = 0.03$ ,  $\alpha = 0.01$ ,  $\beta = 0.2$ ,  $T_1 = 1$ ,  $C_1 = 0.04$ , and  $\nu = 0.3$ .

$r_0$	$k$	$\omega$
$5 \times 10^{-3}$	$10^{-3}$	$1.63164 \times 10^{-6}$
	$10^{-1}$	0.0148314
	$10^1$	-48.76930
	$10^2$	-4998.710
$5 \times 10^{-1}$	$10^{-3}$	$1.02608 \times 10^{-8}$
	$10^{-1}$	0.0146367
	$10^1$	-48.82320
	$10^2$	-4998.800

Finally, the instability criterion of the system can be discussed by studying the roots of the dispersion relation (49) to get the values of the growth rate  $\omega$ , as shown in Table 1. The negative values of the roots of  $\omega$  indicate stability of the microcylindrical surface and the inverse occurs of the positive root values. It can be noticed from the roots of the growth rate  $\omega$  that the interface becomes stable when the microradius  $r_0$  increases which means an increase in the inertia with  $r_0$ .

## 8. Conclusion

In this paper, we have examined the influence of the existence of the porous structure on the EHD instability of the free microcylindrical fluid surface with thermosolutal Marangoni convection. The surface tension depends linearly on the heat and mass transfer. The main results of our study can be epitomized in the following points.

- (1) The existence of the porous structure has a stabilizing effect for the free surface. Existence of the porous medium restricts the streaming velocity of the fluid. Similar behavior was obtained experimentally by [21] for the steam-liquid interface thorough a porous structure.



- (2) As it is known, the electric field has a stabilizing effect, and this result coincides with the previously published results in the literature [7, 20, 24, 25].
- (3) The heating of the axial microsolid cylinder reduces the surface tension and makes the free surface volatile easily and hence the surface becomes unstable and the inverse occurs for cooling the axial microsolid cylinder. The same results were obtained experimentally by [31].
- (4) The surface tension is proportional to the concentration variation. So, high concentration at the free surface inhibits the movement of the surface. This means stability of the free surface. The inverse behavior was obtained for a high concentration at the core region. Similar trend was obtained experimentally by [32].

Finally, our calculation of the free surface function was compared with the previous results of [3] in the absence of the porous medium and the electric field. Also, the present results were compared with the experimental results of [21, 31, 32]. There was compatibility between the results.

## Appendix

- (1) The functions  $g_1(k)$ ,  $g_2(k)$ ,  $G_1(k)$ , and  $G_2(k)$  are given as

$$\begin{aligned} g_1(k) &= K_0(kr_0) I'_0(kR_1) - I_0(kr_0) K'_0(kR_1), \\ g_2(k) &= K_0(kr_0) I'_0(kR_2) - I_0(kr_0) K'_0(kR_2), \\ G_1(k) &= I'_0(kr_0) K'_0(kR_1) - K'_0(kr_0) I'_0(kR_1), \\ G_2(k) &= I'_0(kr_0) K'_0(kR_2) - K'_0(kr_0) I'_0(kR_2). \end{aligned} \quad (\text{A.1})$$

- (2) The roots  $\omega_{\pm}$  are defined as

$$\omega_{\pm} = \frac{-a_0 \pm \sqrt{a_0^2 - 4b_0}}{2}, \quad (\text{A.2})$$

where

$$\begin{aligned} a_0 &= \frac{3\mu}{\rho} k^2 + \frac{\nu}{\rho}, \\ b_0 &= -\frac{\sigma_0 k^2}{2\rho r_0} + \frac{\sigma_0 r_0 k^4}{2\rho} \\ &\quad + \frac{E_0^2 k^3 r_0}{2\rho} \frac{(\varepsilon_2 - \varepsilon_1)^2 g_1(k) g_2(k)}{\varepsilon_2 G_2(k) g_1(k) - \varepsilon_1 G_1(k) g_2(k)}. \end{aligned} \quad (\text{A.3})$$

- (3) The functions  $a_1(k)$  and  $b_1(\omega, k)$  are defined as

$$\begin{aligned} a_1(k) &= \frac{3\mu}{\rho} k^2 + \frac{\nu}{\rho}, \\ b_1(\omega, k) &= -\frac{\sigma_0 k^2}{2\rho r_0} + \frac{\sigma_0 r_0 k^4}{2\rho} \\ &\quad + \frac{E_0^2 k^3 r_0}{2\rho} \frac{(\varepsilon_2 - \varepsilon_1)^2 g_1(k) g_2(k)}{\varepsilon_2 G_2(k) g_1(k) - \varepsilon_1 G_1(k) g_2(k)} \\ &\quad + \frac{\sigma_0 k^2}{2\rho r_0} [\gamma_T T_s(r_0) + \gamma_C C_s(r_0)]. \end{aligned} \quad (\text{A.4})$$

Also, the functions  $a(k)$  and  $b(\omega, k)$  are defined as

$$\begin{aligned} a(k) &= \frac{3\mu}{\rho} k^2 + \frac{\nu}{\rho}, \\ b(\omega, k) &= \frac{1}{2\rho} (-k^2 + k^4) \\ &\quad + \frac{E_0^2 k^3}{2\rho} \frac{(\varepsilon_2 - \varepsilon_1)^2 g_1(k) g_2(k)}{\varepsilon_2 G_2(k) g_1(k) - \varepsilon_1 G_1(k) g_2(k)} \\ &\quad + \frac{k^2}{2\rho} [\gamma_T T_s(r_0) + \gamma_C C_s(r_0)]. \end{aligned} \quad (\text{A.5})$$

## Nomenclature

$C$ :	Concentration
$C_0$ :	Concentration at the interface
$C_1$ :	Concentration at the microcylindrical solid axis
$E_0$ :	Intensity of the electric field
$F$ :	Interface function
$h$ :	Radius for the disturbed fluid surface
$H$ :	Curvature of the interface
$I_0, K_0$ :	Modified Bessel's function of the first and second kinds
$k$ :	Wave number
$\hat{n}$ :	Unit normal vector to the interface
$P$ :	Pressure
$P_0(z, t), P_2(z, t)$ :	Perturbed pressure functions
$(r, \theta, z)$ :	Cylindrical coordinates
$r_0$ :	Microradius of the fluid cylindrical surface
$R_1$ :	Microradius of the cylindrical solid axis
$R_2$ :	Radius of the surrounded vacuum
$t$ :	Time
$\hat{t}$ :	Unit tangential vector to the interface
$T$ :	Temperature
$T_0$ :	Temperature at the interface
$T_1$ :	Temperature at the surface of microcylindrical axis
$u(z, t)$ :	Axial streaming velocity function
$u_0$ :	Constant streaming velocity
$v$ :	Velocity vector



$v_r, v_z$ : Radial and axial velocity components  
 $v_0(z, t), v_2(z, t)$ : Perturbed velocity functions.

### Greek Symbols

$\alpha$ : Thermal diffusivity  
 $\beta$ : Mass diffusivity  
 $\sigma(z, t)$ : Surface tension  
 $\sigma_0$ : Unperturbed surface tension  
 $\sigma_1(z, t)$ : Perturbed surface tension  
 $\Delta\sigma$ : A constant variation of the surface tension  
 $\gamma_T = \pm(1/\sigma_0)(d\sigma/dT)$ : Temperature coefficient of the surface tension  
 $\gamma_C = \pm(1/\sigma_0)(d\sigma/dC)$ : Concentration coefficient of the surface tension  
 $\phi$ : Electric potential function  
 $\tau_{ij}$ : Stress tensor  
 $\omega$ : Growth rate of the surface wave  
 $\mu$ : Viscosity  
 $\mu_{\text{eff}}$ : Effective viscosity  
 $\nu$ : Darcy's coefficient  
 $\epsilon_1, \epsilon_2$ : Dielectric constants of the liquid and vacuum, respectively  
 $\delta(z, t)$ : Dimensionless radius of the disturbed fluid surface  
 $\eta = z - v_0 t$ : Transformation of the axial distance  
 $\rho$ : Density.

### References

- [1] S. Bhattacharyya and A. K. Singh, "Augmentation of heat transfer from a solid cylinder wrapped with a porous layer," *International Journal of Heat and Mass Transfer*, vol. 52, no. 7-8, pp. 1991-2001, 2009.
- [2] R. E. S. Moya, A. T. Prata, and J. A. B. C. Neto, "Experimental analysis of unsteady heat and moisture transfer around a heated cylinder buried into a porous medium," *International Journal of Heat and Mass Transfer*, vol. 42, no. 12, pp. 2187-2198, 1999.
- [3] E. P. Furlani, "Temporal instability of viscous liquid microjets with spatially varying surface tension," *Journal of Physics A*, vol. 38, no. 1, pp. 263-276, 2005.
- [4] E. P. Furlani and M. S. Hanchak, "Nonlinear analysis of the deformation and breakup of viscous microjets using the method of lines," *International Journal for Numerical Methods in Fluids*, vol. 65, no. 5, pp. 563-577, 2011.
- [5] Z. Gao, "Instability of non-Newtonian jets with a surface tension gradient," *Journal of Physics A*, vol. 42, no. 6, Article ID 065501, 2009.
- [6] Z. Gao and K. Ng, "Temporal analysis of power law liquid jets," *Computers & Fluids*, vol. 39, no. 5, pp. 820-828, 2010.
- [7] A. A. Mohamed and N. K. Nayyar, "Electrohydrodynamic stability of a liquid jet," *Journal of Physics A*, vol. 3, no. 3, pp. 296-303, 1970.
- [8] C. H. Chen, "Marangoni effects on forced convection of power-law liquids in a thin film over a stretching surface," *Physics Letters A*, vol. 370, no. 1, pp. 51-57, 2007.
- [9] L. G. Napolitano, "Microgravity fluid dynamics," in *Proceedings of the 2nd Levitch Conference*, Washington, DC, USA, 1978.
- [10] L. G. Napolitano, "Marangoni boundary layers," in *Proceedings of the 3rd European Symposium on Material Science in Space*, ESA SP-142, Grenoble, France, June 1979.
- [11] S. Hansen, G. W. M. Peters, and H. E. H. Meijer, "The effect of surfactant on the stability of a fluid filament embedded in a viscous fluid," *Journal of Fluid Mechanics*, vol. 382, pp. 331-349, 1999.
- [12] M. E. Timmermans and J. R. Lister, "The effect of surfactant on the stability of a liquid thread," *Journal of Fluid Mechanics*, vol. 459, pp. 289-306, 2002.
- [13] S. Kwak, M. M. Fyrillas, and C. Pozrikidis, "Effect of surfactants on the instability of a liquid thread. Part II: Extensional flow," *International Journal of Multiphase Flow*, vol. 27, no. 1, pp. 39-60, 2001.
- [14] R. V. Craster, O. K. Matar, and D. T. Papageorgiou, "Pinchoff and satellite formation in surfactant covered viscous threads," *Physics of Fluids*, vol. 14, no. 4, pp. 1364-1376, 2002.
- [15] B. Ambravaneswaran and O. A. Basaran, "Effects of insoluble surfactants on the nonlinear deformation and breakup of stretching liquid bridges," *Physics of Fluids*, vol. 11, no. 5, pp. 997-1015, 1999.
- [16] P. T. McGough and O. A. Basaran, "Repeated formation of fluid threads in breakup of a surfactant-covered jet," *Physical Review Letters*, vol. 96, no. 5, Article ID 054502, 4 pages, 2006.
- [17] D. M. Christopher and B. Wang, "Prandtl number effects for Marangoni convection over a flat surface," *International Journal of Thermal Sciences*, vol. 40, no. 6, pp. 564-570, 2001.
- [18] J. Straub, "The role of surface tension for two-phase heat and mass transfer in the absence of gravity," *Experimental Thermal and Fluid Science*, vol. 9, no. 3, pp. 253-273, 1994.
- [19] K. R. Rajagopal, "On a hierarchy of approximate models for flows of incompressible fluids through porous solids," *Mathematical Models and Methods in Applied Sciences*, vol. 17, no. 2, pp. 215-252, 2007.
- [20] A. E. K. Elcoot and G. M. Moatimid, "Nonlinear instability of finitely conducting cylindrical flows through porous media," *Physica A*, vol. 343, no. 1-4, pp. 15-35, 2004.
- [21] I. Catton and M. Chung, "An experimental study of steam injection into a uniform water flow through porous media," *Wärme—und Stoffübertragung*, vol. 27, no. 1, pp. 29-35, 1992.
- [22] D. A. Nield and A. Bejan, *Convection in Porous Media*, Springer, New York, NY, USA, 3rd edition, 2006.
- [23] S. Liu and J. H. Masliyah, "Dispersion in porous media," in *Handbook of Porous Media*, Taylor & Francis, Boca Raton, Fla, USA, 2nd edition, 2005.
- [24] J. R. Melcher, *Field Coupled Surface Waves*, MIT Press, Cambridge, Mass, USA, 1963.
- [25] J. R. Melcher, *Continuum Electrodynamics*, MIT Press, Cambridge, Mass, USA, 1981.
- [26] L. G. Leal, *Advanced Transport Phenomena*, Cambridge Series in Chemical Engineering, Cambridge University Press, Cambridge, UK, 2007.
- [27] G. M. Moatimid, "Nonlinear instability of two dielectric viscoelastic fluids," *Canadian Journal of Physics*, vol. 82, no. 12, pp. 1109-1133, 2004.
- [28] H. H. Woodson and J. R. Melcher, *Electromechanical Dynamics Part II: Fields, Forces, and Motion*, John Wiley & Sons, New York, NY, USA, 1986.
- [29] E. Magyari and A. J. Chamkha, "Exact analytical results for the thermosolutal MHD Marangoni boundary layers," *International Journal of Thermal Sciences*, vol. 47, no. 7, pp. 848-857, 2008.

- [30] S. Slavtchev, P. Kalitzova-Kurteva, and M. A. Mendes, "Marangoni instability of liquid-liquid systems with a surface-active solute," *Colloids and Surfaces A*, vol. 282-283, pp. 37-49, 2006.
- [31] A. D'Aubeterre, R. da Silva, and M. E. Aguilera, "Experimental study on Marangoni effect induced by heat and mass transfer," *International Communications in Heat and Mass Transfer*, vol. 32, no. 5, pp. 677-684, 2005.
- [32] D. Agble and M. A. Mendes-Tatsis, "Prediction of Marangoni convection in binary liquid-liquid systems with added surfactants," *International Journal of Heat and Mass Transfer*, vol. 44, no. 7, pp. 1439-1449, 2001.

## Research Article

# 3D Model-Based Simulation Analysis of Energy Consumption in Hot Air Drying of Corn Kernels

**Shiwei Zhang, Ninghua Kong, Yufang Zhu, Zhijun Zhang, and Chenghai Xu**

*School of Mechanical Engineering and Automation, Northeastern University, P.O. Box 319, Shenyang 110004, China*

Correspondence should be addressed to Shiwei Zhang; [shwzhang@mail.neu.edu.cn](mailto:shwzhang@mail.neu.edu.cn)

Received 11 March 2013; Accepted 9 May 2013

Academic Editor: Hua-Shu Dou

Copyright © 2013 Shiwei Zhang et al. This is an open access article distributed under the Creative Commons Attribution License, which permits unrestricted use, distribution, and reproduction in any medium, provided the original work is properly cited.

To determine the mechanism of energy consumption in hot air drying, we simulate the interior heat and mass transfer processes that occur during the hot air drying for a single corn grain. The simulations are based on a 3D solid model. The 3D real body model is obtained by scanning the corn kernels with a high-precision medical CT machine. The CT images are then edited by MIMICS and ANSYS software to reconstruct the three-dimensional real body model of a corn kernel. The Fourier heat conduction equation, the Fick diffusion equation, the heat transfer coefficient, and the mass diffusion coefficient are chosen as the governing equations of the theoretical dry model. The calculation software, COMSOL Multiphysics, is used to complete the simulation calculation. The influence of air temperature and velocity on the heat and mass transfer processes is discussed. Results show that mass transfer dominates during the hot air drying of corn grains. Air temperature and velocity are chosen primarily in consideration of mass transfer effects. A low velocity leads to less energy consumption.

## 1. Introduction

Hot air drying is a commonly used method for drying corn; it is often characterized by high energy consumption and low efficiency [1]. Many studies have been conducted on the drying characteristics and energy consumed when drying thin layers of vegetables, fruits, and food [2, 3]. These studies usually focus on the optimization of drying systems and drying methods. To date, no research has been devoted to the drying characteristics and energy consumed during the hot drying of a single corn kernel even though the drying process of each single grain is the theoretical basis of various drying techniques. In the current work, we investigate the drying characteristic of single corn kernels and provide theoretical support for reducing energy consumption in hot air drying.

Given that the kernel structures and shapes of grains are neither uniform nor regular, describing their drying processes on the basis of the original shape of a single grain kernel is difficult to accomplish. Most of the previously conducted simulations of material drying, especially for single-body corn kernels, are based on ideal models that are established by simplifying the shapes of dried materials. Shape

simplification enables easy simulation calculation but causes original shape-related errors in the simulations. Gustafson simplified a grain kernel into a 2D irregular shape on the basis of original grain size and then simulated the drying process by finite element method (FEM) [4]. Li and Cao simplified a single rough rice kernel as spherical to simulate moisture diffusion with a three-layer body model [5]. Zhang and Kong studied the heat and mass transfer of porous medium in the vacuum drying process by using a 1D model [6]. Jia and Cao simplified an irregular corn particle into a 2D irregular geometric model to analyze heat and mass transfer in corn drying by FEM [7]. Neményi and Czaba established a finite element model to investigate the heat and moisture distributions in a cross-sectional area of an individual maize kernel [8].

Grain kernel simulation based on a 3D real body model has recently become a trend in simulation studies because it generates more accurate results. The simulation of the heat and mass transfer in corn kernels with a 3D model has been carried out [9]. Ghosh et al. obtained a 3D geometric model of a wheat kernel by magnetic resonance imaging (MRI) and developed a mathematical model for moisture diffusion in

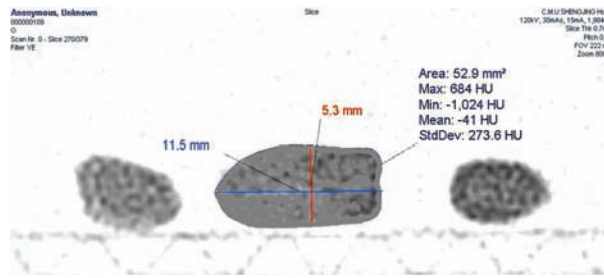


FIGURE 1: CT slice images of the corn grain.

a single wheat kernel during the drying process [10]. Perez et al. constructed a 3D model with tomographic images and simulated the mass transfer and hygroscopic cracks in rice grains [11]. The present work is carried out on the basis of the aforementioned studies.

## 2. Real Body Model

**2.1. Review of Real Body Model Reconstruction.** Grain kernels are usually simplified into spherical, cylindrical, ellipsoidal, and flat chip shapes because the shapes of grain particle shapes are irregular and variable. Given that a simplified model cannot reflect solid features, obtaining a more accurate model facilitates the understanding of the heat and mass transfer mechanism in grain kernels. MRI has recently been used to obtain 3D real body models. Song developed a 3D microscopic MRI with the 3D projection reconstruction (3DPR) technique to measure the moisture distribution in a single mature wheat grain [12]. Goñi obtained the slices of irregularly shaped food with nonuniform rational B-splines and MRI techniques and reconstructed a 3D geometric model [13]. Ghosh et al. constructed a 3D geometric model of wheat kernel by MRI [10], and Perez et al. built a 3D model with tomographic images [11]. Obtaining 3D geometric models by MRI presents high cost and complexity, driving the identification of a more convenient method. The CT scanning technique based on 3D medical image reconstruction is extensively used in the field of medicine. In this paper, the CT scanning technology is used to create a 3D real body model of a single corn kernel.

**2.2. Steps to Obtain the 3D Model.** The steps for creating the 3D real body model are as follows. (1) Several selected corn grains are scanned by high-precision medical CT to obtain serial transect image data. (2) The image data is treated by MIMICS software in turn. (3) The contour line image is transferred into ANSYS software and converted into a 3D real body model, which is nearly of the same shape as the original corn grain.

**2.2.1. Scanning with CT.** Scanning pertains to the use of computer technology for the tomographic reconstruction of a measured object into a 3D topographic image. Single axis X-rays are projected onto the object to be tested. On the basis of the difference in radiation absorption rate and transmissivity

among the tested objects, a computer collects data from the rays and reconstructs 3D images. This study uses the Philips Brilliance iCT 256 layer spiral quick CT at Shengjing Hospital, an affiliated hospital of the Chinese Medical University. Corn grains are scanned to obtain high-precision CT images, with a scanning thickness of 0.625 mm. The CT image files are stored in Digital Imaging and Communication in Medicine (Figure 1).

**2.2.2. Image Treatment in MIMICS.** MIMICS is a set of highly integrated software for generating, editing, and treating 3D images. It can accept various types of original scanning data (from CT or MRI), set up corresponding 3D models, and output these in general CAD format. In this study, MIMICS software is used to treat CT image data of corn kernels to generate a 3D geometric contour model of a corn grain, to modify parts of the contour model for surface smoothness, and to transmit the contour line image model to ANSYS software.

- (a) The CT images are input into MIMICS, and one corn kernel area is chosen, with adjustments on the threshold between  $-228$  and  $2872$  Hounsfield. The images are edited until a clear and intact contour is generated.
- (b) The “Crop Mash” function is used to divide contour regions, the “Calculate Polylines” function is used to generate the 3D geometric contour model of a corn grain, and the surface contour model is smoothed with the Magics 9.9.
- (c) The surface contour model is exported as a file in an “ANSYS area file” (.lis) format.

**2.2.3. Image Treatment in ANSYS.** The contour model is converted into a 3D real body model, which has nearly the same shape as the original corn grain. The 3D real body model of a corn grain is generated in ANSYS and exported as an “Initial Graphics Exchange Specification” (IGES) file for postprocessing in COMSOL software.

The 3D real body model obtained through the aforementioned method is more accurate than other simplified models [4–8]. This kind of reconstruction method is more convenient and practical.

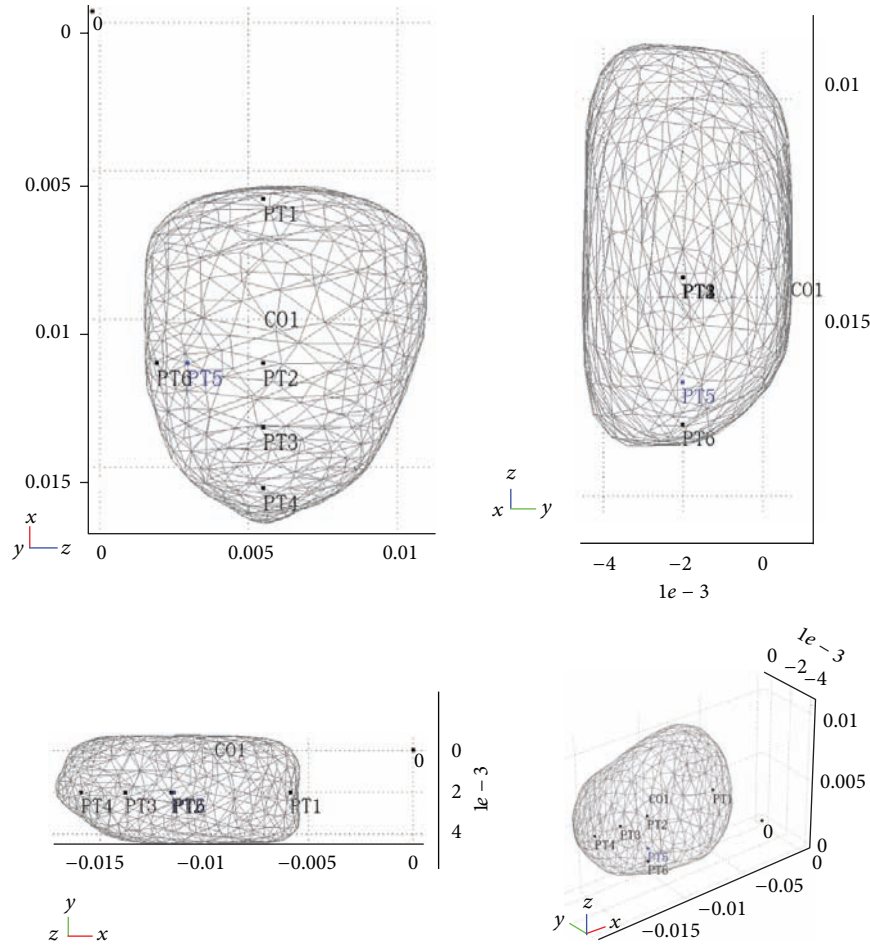


FIGURE 2: 3D real body model in COMSOL and locations of detection points.

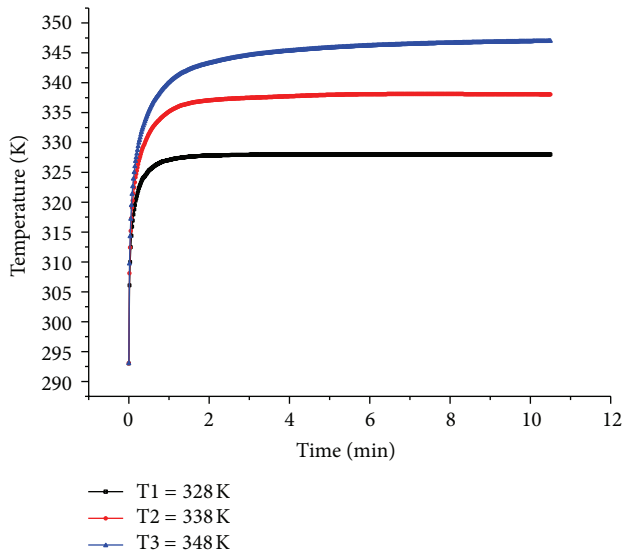


FIGURE 3: Average temperature curves of the corn kernel at different drying temperatures.

### 3. Mathematical Model

**3.1. Hypothesis.** For this study, we make the following assumptions. (1) The internal temperature and moisture of corn

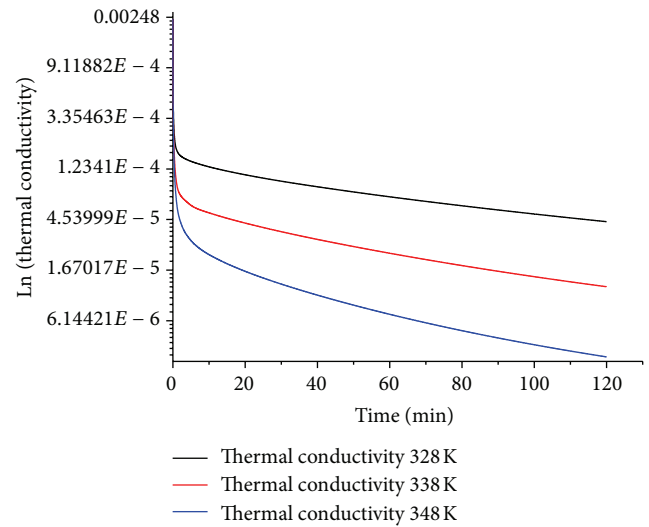


FIGURE 4: Thermal conductivity curves at different drying temperatures.

are evenly distributed at the beginning of drying process. (2) The changes in shrinkage and shape of the corn grain are disregarded during the drying process. (3) The various components of corn grain are isotropic and uniform. (4) Water



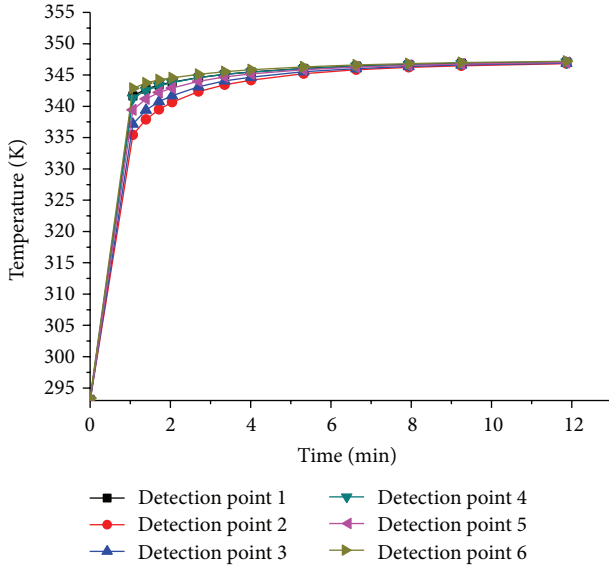


FIGURE 5: Temperature curves at detection points when  $T_3 = 348$  K.

is diffused to the external boundary, and water vaporization occurs on the grain surface.

**3.2. Heat Transfer Equation.** The heat transfer in the grain kernels is modeled following Fourier's law of heat conduction and the first law of thermodynamics [14]. Heat  $Q_i$  ( $i = x, y, z$ ) is generated by any microunit at a given position. Heat  $Q_t$  is generated by any microunit at a given time. Heat  $Q_H$  is conserved or released by changes in the temperature and material of a microunit:

$$\begin{aligned} Q_x &= \frac{\partial}{\partial x} \left( \lambda \frac{\partial T}{\partial x} \right) dx dy dz, \\ Q_y &= \frac{\partial}{\partial y} \left( \lambda \frac{\partial T}{\partial y} \right) dx dy dz, \\ Q_z &= \frac{\partial}{\partial z} \left( \lambda \frac{\partial T}{\partial z} \right) dx dy dz, \\ Q_t &= q_v dx dy dz, \\ Q_x + Q_y + Q_z + Q_t &= Q_H, \\ \frac{\partial}{\partial x} \left( \lambda \frac{\partial T}{\partial x} \right) + \frac{\partial}{\partial y} \left( \lambda \frac{\partial T}{\partial y} \right) + \frac{\partial}{\partial z} \left( \lambda \frac{\partial T}{\partial z} \right) + q_v &= \frac{\partial}{\partial t} (\rho H). \end{aligned} \quad (1)$$

If moisture vaporizes in the kernel,

$$\begin{aligned} H &= h_{fg} M + c_p T, \\ \frac{\partial H}{\partial t} &= h_{fg} \frac{\partial M}{\partial t} + c_p \frac{\partial T}{\partial t}. \end{aligned} \quad (2)$$

The 3D mathematical model of heat transfer is

$$\frac{\partial}{\partial x} \left( \lambda \frac{\partial T}{\partial x} \right) + \frac{\partial}{\partial y} \left( \lambda \frac{\partial T}{\partial y} \right) + \frac{\partial}{\partial z} \left( \lambda \frac{\partial T}{\partial z} \right) + q_v$$

$$= \rho c_p \frac{\partial T}{\partial t} + \rho h_{fg} \frac{\partial M}{\partial t}, \quad (3)$$

where  $x$ ,  $y$ , and  $z$  are the Cartesian coordinates that represent the corn kernel as a 3D body;  $q_v$  is the heat generating rate of the inner heat source ( $\text{J m}^{-3} \text{s}^{-1}$ );  $\rho$  is the density of corn ( $\text{kg m}^{-3}$ );  $c_p$  denotes the specific heat of corn ( $\text{J kg}^{-1} \text{K}^{-1}$ );  $\lambda$  represents the thermal conductivity of corn ( $\text{W m}^{-1} \text{K}^{-1}$ );  $M$  is the moisture content (dry base);  $T$  is the temperature of the corn kernel (K);  $h_{fg}$  is the latent heat of water vaporization ( $\text{J kg}^{-1}$ ).

The initial condition is

$$T|_{t=0} = T_0. \quad (4)$$

The boundary condition is

$$-\lambda \left( \frac{\partial T}{\partial x} + \frac{\partial T}{\partial y} + \frac{\partial T}{\partial z} \right) = h_t (T - T_a), \quad (5)$$

where  $h_t$  is the convective heat transfer coefficient ( $\text{W m}^{-2} \text{K}^{-1}$ ) and  $T_a$  is the temperature of the drying medium (K).

**3.3. Mass Transfer Equation.** The moisture diffusion differential equation is modeled following Fick's law [14]. The 3D mathematical model of mass diffusion is expressed as

$$\frac{\partial M}{\partial t} = D \frac{\partial^2 M}{\partial x^2} + D \frac{\partial^2 M}{\partial y^2} + D \frac{\partial^2 M}{\partial z^2}, \quad (6)$$

where  $D$  is the diffusion coefficient ( $\text{m}^2 \text{s}^{-1}$ ).

The initial condition is

$$M|_{t=0} = M_0. \quad (7)$$

The boundary condition is

$$-D \left( \frac{\partial M}{\partial x} + \frac{\partial M}{\partial y} + \frac{\partial M}{\partial z} \right) = h_m (M - M_e), \quad (8)$$

where  $h_m$  is the surface mass transfer coefficient ( $\text{m s}^{-1}$ ) and  $M_e$  is the equilibrium moisture content (d.b.).

**3.4. Energy Consumption Analysis.** The energy consumption in the hot air drying process is due primarily to the velocity and temperature of hot wind, as determined by dimensional analysis. The energy consumption dimension is  $\text{W J}/(\text{m}^2 \text{s})$ ; the dimension of hot wind velocity  $u$  is  $\text{m/s}$ ; the dimension of hot wind temperature  $T$  is K. The air mass flow is  $G = u \rho_a$  expressed in units of  $\text{kg}/(\text{m}^2 \text{s})$ . In accordance with the principle of dimensional homogeneity, density  $\rho$  ( $\text{kg/m}^3$ ) and specific heat  $C_p$  ( $\text{J}/(\text{kg K})$ ) are introduced to establish the equation. We can obtain the energy consumption per unit area; thus,

$$W = \phi \Delta T C_p G = \phi \rho_a \Delta T C_p u \text{ J}/(\text{m}^2 \text{s}), \quad (9)$$

where  $\phi$  is constant.



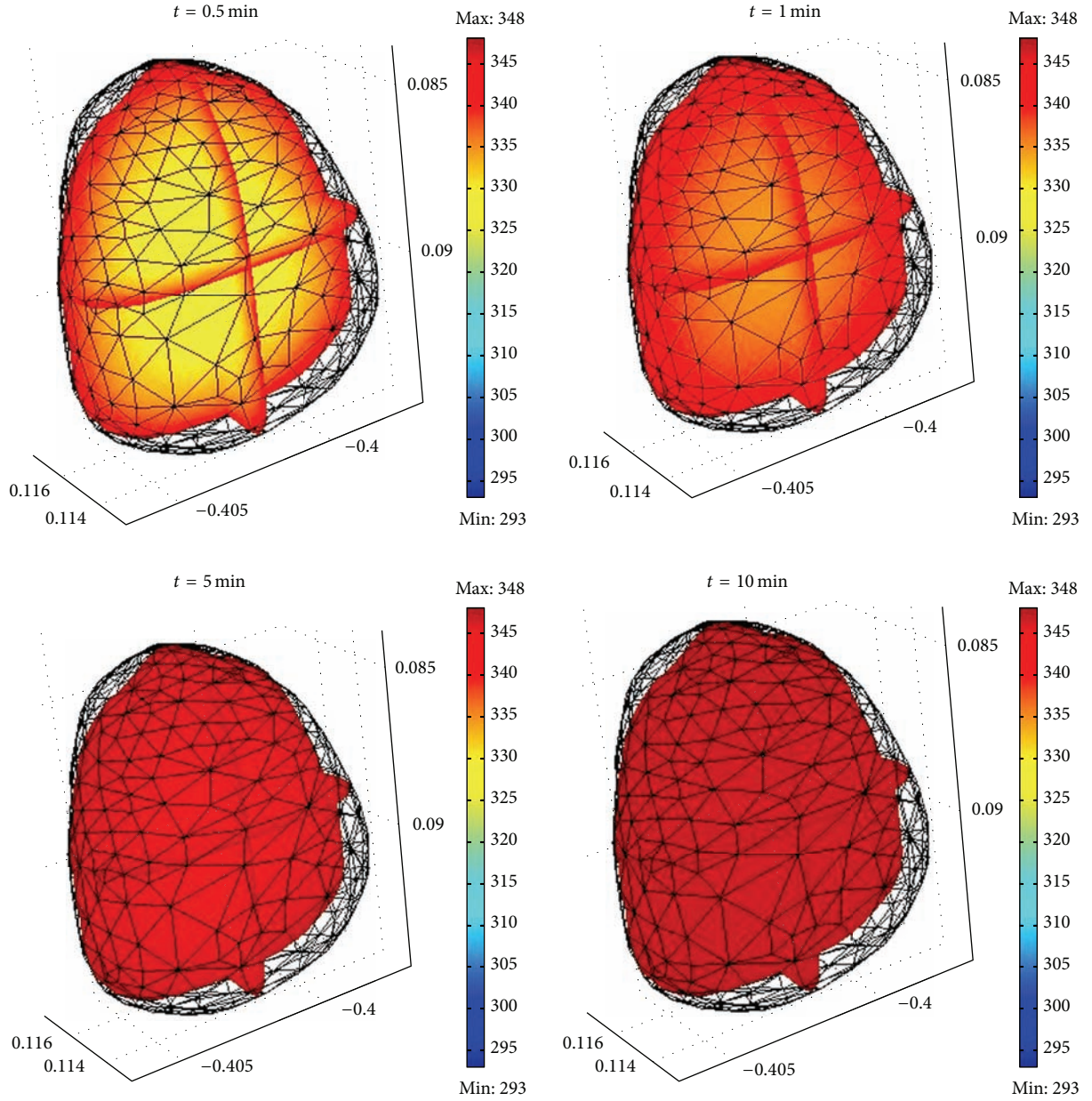


FIGURE 6: Slices of temperature distribution in the corn kernel at different periods.

**3.5. Physical and Material Properties.** The initial moisture is  $M = 0.23$  (d.b.); the initial temperature is  $T_0 = 293$  K; the drying temperatures are  $T_1 = 328$  K,  $T_2 = 338$  K, and  $T_3 = 348$  K; the hot air velocity is  $u_0 = 1.64$  m/s [7]. The density of the corn kernel [8] is uniform at  $\rho = 1150$  kg m<sup>-3</sup>; the density of air is  $\rho_a = 1.29$  kg m<sup>-3</sup>. The specific heat due to the moisture content of the germ and endosperm is expressed as

$$\begin{aligned} c_{p1} &= 3379M + 1433, \\ c_{p2} &= 2565M + 1272.7. \end{aligned} \quad (10)$$

The average specific heat [8] is  $c_{p2} = 2000$  J/(kg K); the latent heat of water vaporization [8] is  $h_{fg} = 2256267$  J kg<sup>-1</sup>; the surface mass transfer coefficient [15] is  $h_m = 0.05$  m s<sup>-1</sup>.

The surface heat transfer coefficient [14] is

$$h_t = 100G^{0.49} \text{ W}/(\text{m}^2 \text{ K}). \quad (11)$$

The thermal conductivity [7] is

$$\begin{aligned} \lambda = \exp \big( &-1.74 - 3.7M + 4.72 \times 10^{-3}T + 6.48M^2 \\ &- 1.5 \times 10^{-4}T^2 + 6.27 \times 10^{-2}MT \big). \end{aligned} \quad (12)$$

The diffusion coefficient [16] is

$$D = a_0 \exp(a_1 M) \exp\left(-\frac{a_2}{T}\right), \quad (13)$$

where  $a_0, a_1, a_2$  are constants;  $a_0 = 7.817 \times 10^{-5}$ ;  $a_1 = 5.5$ ;  $a_2 = 4850$ .

#### 4. Solution via COMSOL Multiphysics

The calculation process for the simulation is implemented with COMSOL Multiphysics 3.5a. The “diffusion module” and “heat transfer module” in COMSOL software are chosen to simulate the moisture migration and heat transfer process in the corn kernel during the hot air drying process. One of the models is shown in Figure 2. The point O is the origin point of the coordinate system in the model, the number of free grids is 14440, the volume is  $3.22701 \times 10^{-7} \text{ m}^3$ , and six detection points (1–6) are selected from different locations (Table 1). These points are the representative positions that show the calculation results. The points 1 and 6 are the detection points between the cortical layer and endosperm. The point 2 is the detection point at the inner endosperm. The points 3 and 5 are the detection points at the germ. The point 4 is the detection at the radicle.

After the material properties are defined, the governing equations and initial conditions for the inner component of the model and the boundary conditions on the surface of the model are established. The 3D real body model is now ready for simulation calculation. The mathematical calculation model, which includes the governing equation of heat and mass transfer and the defining equations of property parameters, is presented in the succeeding section. The simulation can be completed by loop computation.

#### 5. Results and Discussion

**5.1. Influence of Air Temperature on Heat Transfer.** In the simulation, the hot wind temperature changes from  $T_1$  to  $T_3$  ( $T_1 = 328 \text{ K}$ ,  $T_2 = 338 \text{ K}$ , and  $T_3 = 348 \text{ K}$ ). Figure 3 shows that the temperature of the corn kernel exhibits increasing curves during the drying process. The increasing trends of temperature are similar. They all reach equilibrium within 10 minutes. The higher the hot wind temperature is, the faster the temperature increases. However, it takes a little more time to reach a balanced drying temperature at a high hot wind temperature than at low hot wind temperature.

The comparison of the thermal conductivity logarithmic ( $\ln \lambda$ ) curves is shown in Figure 4. The figure shows the differences in heat transfer at different drying temperatures. As indicated in (12), thermal conductivity changes with temperature during the drying process. The higher the drying temperature, the lower the thermal conductivity.

The temperature at the detection points shows that the corn temperature increases to the equilibrium level in 8 minutes (Figures 5 and 6). The temperature increase at the points near the boundary proceeds at a faster rate than does the temperature increase at the internal points; the temperature distribution in the corn kernel also shows the short-term temperature changes (Figure 6). Figure 6 shows the temperature distribution in the corn kernel at  $t = 0.5 \text{ min}$ ,  $t = 1 \text{ min}$ ,  $t = 5 \text{ min}$ , and  $t = 10 \text{ min}$ . The heat transfer rapidly occurs in the hot air drying process. The resistance to

TABLE 1: Locations of detection points.

Point number	Location
1	(−0.006, −0.002, 0.0055)
2	(−0.0114, −0.002, 0.0055)
3	(−0.0135, −0.002, 0.0055)
4	(−0.0155, −0.002, 0.0055)
5	(−0.0114, −0.0025, 0.003)
6	(−0.0114, −0.002, 0.002)

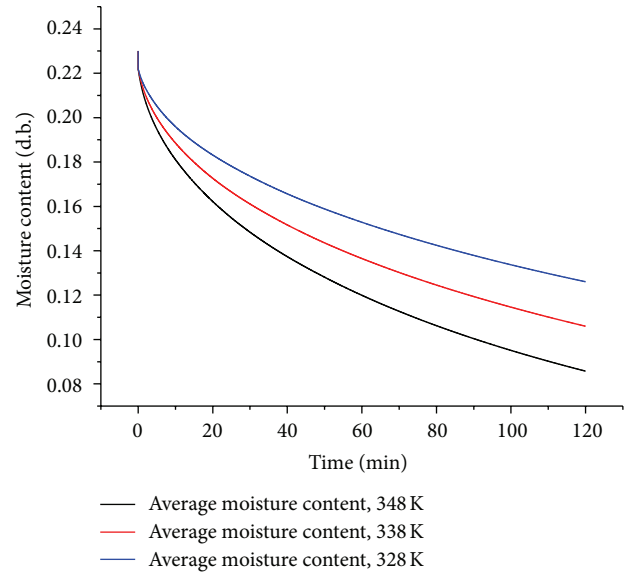


FIGURE 7: Drying curves (d.b.) at different temperatures.

heat transfer in the corn kernel is weak [9]. The influence of temperature change on heat transfer is limited, and the effects occur only at the beginning of the drying process.

**5.2. Influence of Air Temperature on Mass Transfer.** Figure 7 shows the moisture drying curves at different temperatures. At a drying temperature  $T_3 = 348 \text{ K}$ , moisture diffuses at the fastest rate. The higher the temperature is, the faster the moisture diffuses.

Representative model-derived images of the kernel slices are shown in Figures 8, 9, and 10. They show the moisture distribution in the corn kernel at  $t = 10 \text{ min}$ ,  $t = 30 \text{ min}$ ,  $t = 60 \text{ min}$ , and  $t = 120 \text{ min}$  at drying temperatures of  $T_1 = 328 \text{ K}$ ,  $T_2 = 338 \text{ K}$ , and  $T_3 = 348 \text{ K}$ . The different colors correspond to the special values of moisture content. The indication of moisture migration at different locations is visually represented with the 3D body model. The moisture content at  $t = 60 \text{ min}$  at a drying temperature of  $T_3 = 348 \text{ K}$  is nearly the same as that at  $t = 120 \text{ min}$  at a drying temperature of  $T_1 = 328 \text{ K}$ .

Diffusion coefficient  $D$  changes with temperature and moisture content, as indicated in (11). The average diffusion coefficient curves at different drying temperatures are shown in Figure 11. Diffusion coefficient  $D$  rapidly increases at the beginning of drying until it reaches the peak value. It then

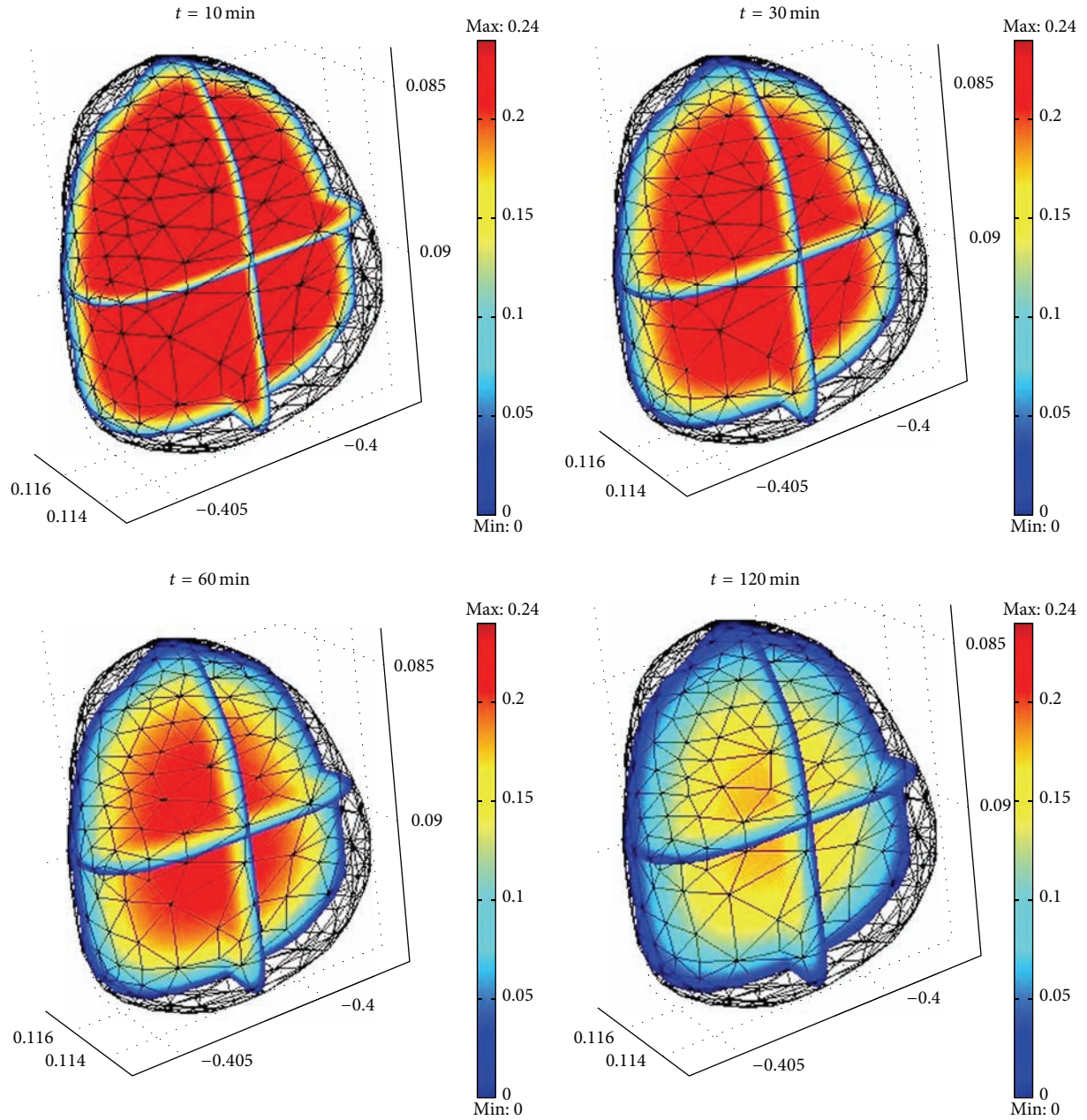


FIGURE 8: Slices of moisture distribution in the corn kernel at drying temperature  $T_1 = 348$  K.

approaches the equilibrium value. The value of the diffusion coefficient at  $T_3 = 348$  K is nearly two times higher than its value at  $T_1 = 328$  K. The equilibrium diffusion coefficient at drying temperature  $T_3 = 348$  K is higher than that at a drying temperature  $T_1 = 328$  K. The variation range at drying temperature  $T_3$  between the peak value and equilibrium value is larger than that at  $T_1 = 328$  K. The higher the drying temperature selected, the larger the diffusion coefficient.

The mass diffusion coefficient visibly changes with temperature before the temperature of the corn kernel reaches the equilibrium temperature (Figure 12). The temperature increase occurs within a short period at the beginning of drying (Figure 5). Temperature visibly influences mass

transfer at the beginning of the drying process. Selecting a reasonable drying temperature is necessary for improving drying efficiency and reducing energy consumption.

The moisture distribution in the corn kernel is nonuniform because of the unique organization of the corn kernel structure. Figure 13 shows the drying curves of different detection points (defined in Figure 2) in the corn kernel. The diffusion coefficient curves at different detection points in the drying process are shown in Figure 14. The closer the detection points are to the boundaries, the more easily moisture content is diffused.

The comparison of Figures 13 and 14 shows that the trend of the mass diffusion coefficient curves is similar to that of



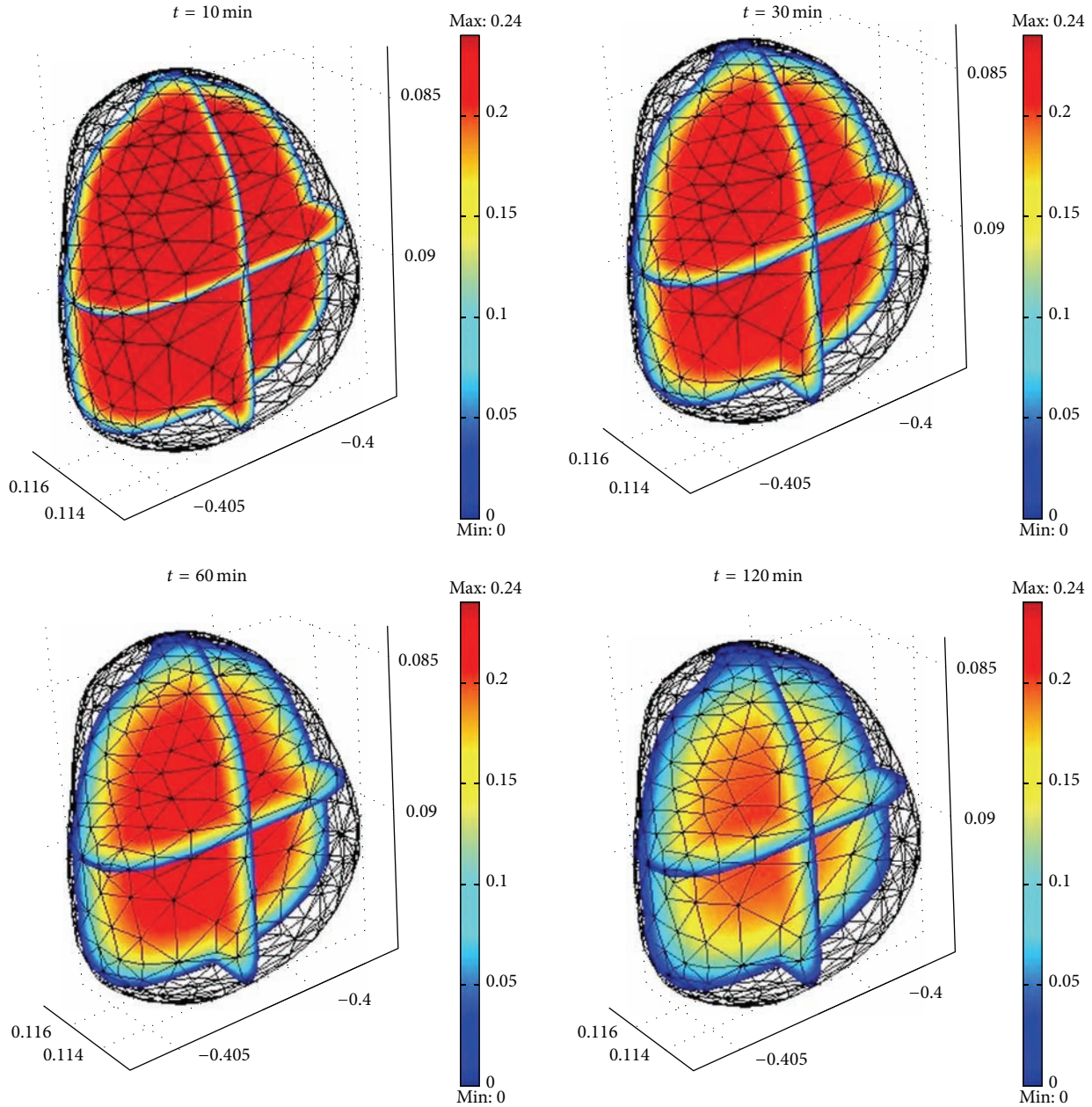


FIGURE 9: Slices of moisture distribution in the corn kernel at drying temperature  $T_2 = 338$  K.

the moisture content curves. We can deduce that the diffusion coefficient is influenced primarily by moisture content after temperature reaches the equilibrium drying temperature. Mass transfer resistance plays an important role in the drying process after the temperature reaches the equilibrium value.

**5.3. Influence of Air Velocity on Hot Air Drying.** Hot wind velocity influences energy consumption during hot air drying. In the simulation, the comparisons are processed at  $u_1 = u_0$ ,  $u_2 = u_0/2$ , and  $u_3 = u_0/10$ . The temperature and drying curves change with hot wind velocity at the same air temperature (Figures 15 and 16), indicating that effects on

heat and mass transfer could be disregarded. When hot wind velocity changes from  $u_1$  to  $u_2$ , almost no change occurs.

Figure 15 also shows the comparison between simulation drying curves and experiment drying curve (d.b.). In the experiment, the Ohaus MB45 Halogen Moisture Analyzer is used as a hot air dryer. The initial moisture content of corn kernel is 0.23 (d.b.). The condition of experiment is hot wind velocity  $u_1 = u_0$  and  $T = 348$  K. The experimental drying curve and the simulation curve change with the same trend.

Hot wind velocity directly influences the heat surface transfer coefficient, as shown in (11). The higher the hot wind velocity, the larger the surface transfer coefficient (Figure 17).

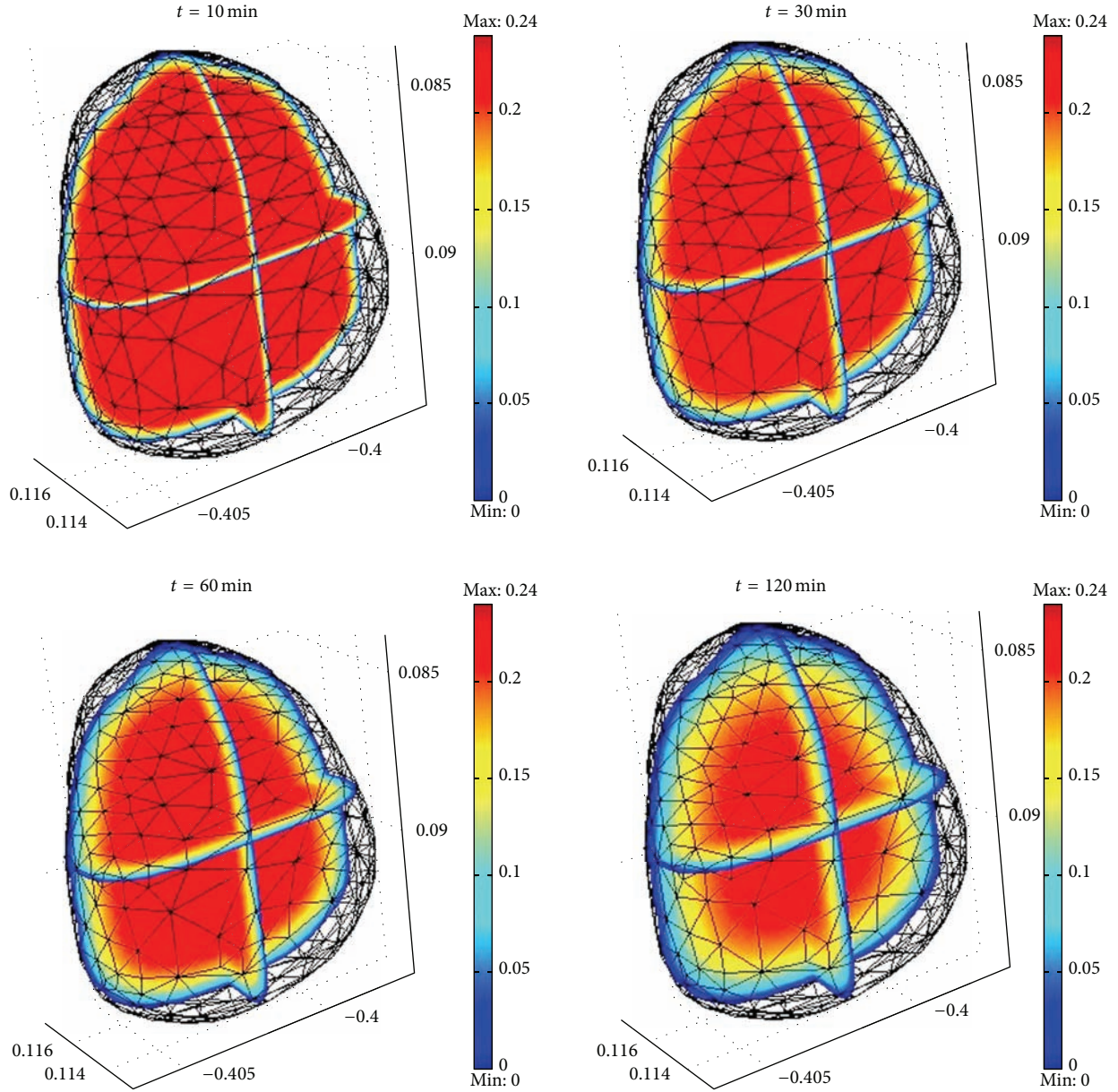


FIGURE 10: Slices of moisture distribution in the corn kernel at drying temperature  $T_1 = 328$  K.

In selecting hot wind velocity, we should ensure that mass transfer outside the corn kernel takes place.

**5.4. Energy Consumption Analysis.** The effects of temperature and velocity of hot wind on energy consumption are visibly seen in Figures 18 and 19. Temperature  $T_3 = 348$  K and hot wind velocity  $u_1 = u_0$  account for the largest energy consumption in the drying simulations. The temperature and hot wind velocity have a linear relationship with energy consumption. Figure 20 shows that energy consumption changes along with diffused moisture. Given that wind velocity setting is needed only in considering mass transfer effects, the equilibrium moisture content should be maintained at

a sufficiently low level. The air velocity can be appropriately reduced, thereby decreasing energy consumption. Heat transfer rapidly occurs and the drying of corn kernels is the process controlled by mass transfer. The choice of drying temperature depends primarily on the influence of mass transfer.

## 6. Conclusion

A 3D real body geometric model reconstruction of a single corn kernel is generated on the basis of CT with MIMICS and ANSYS. Based on the geometric model and a 3D drying mathematical model, the simulation calculation for the hot air drying of a corn kernel sample is

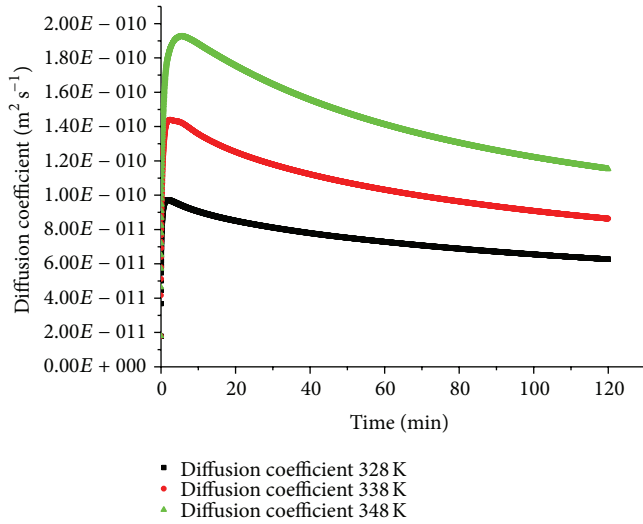


FIGURE 11: Average diffusion coefficient curves at different temperatures.

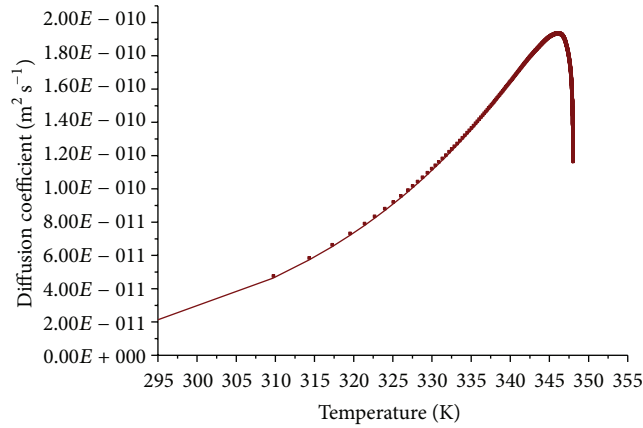


FIGURE 12: Diffusion coefficient via temperature at  $T_3 = 348$  K.

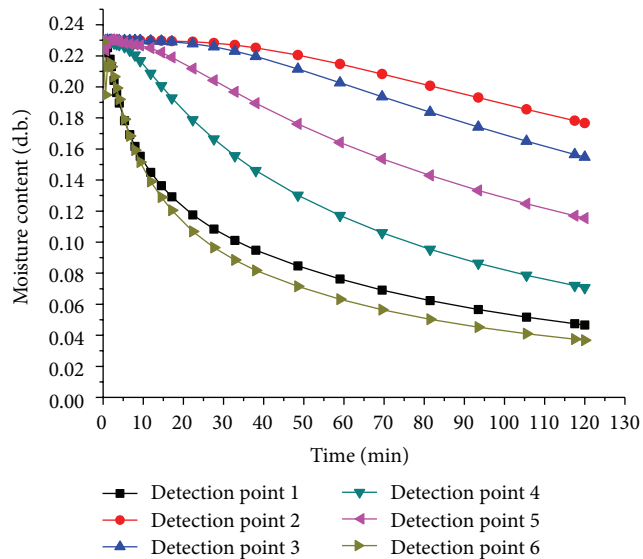


FIGURE 13: Moisture content curves at detection points when  $T_3 = 348$  K.

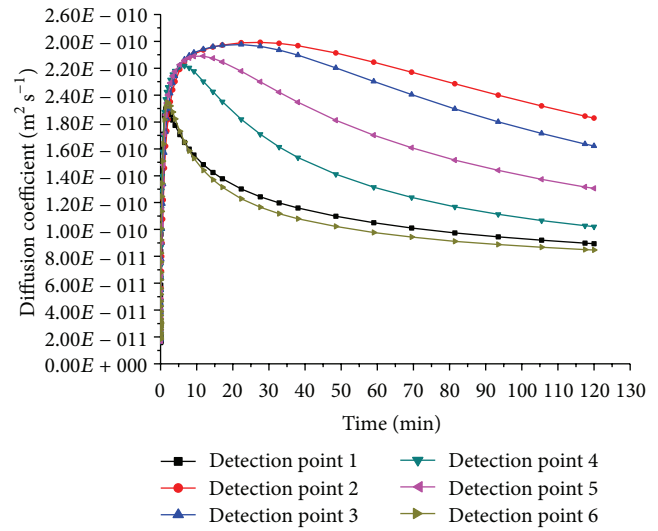


FIGURE 14: Diffusion coefficient curve of detection points at  $T_3 = 348$  K.

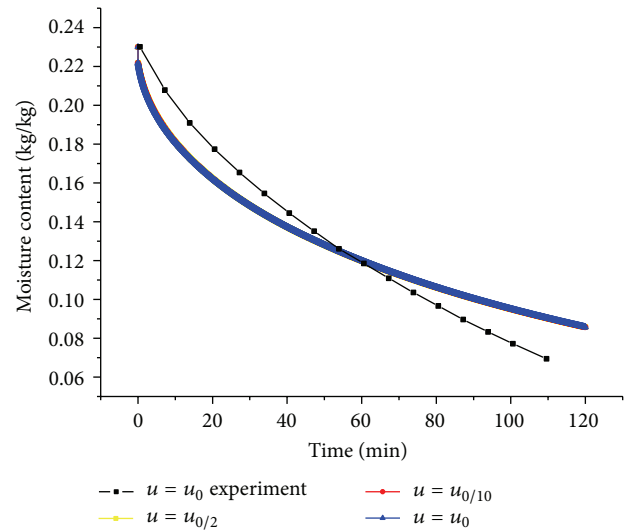


FIGURE 15: Drying curves at different hot wind velocities and the experiment drying curve at  $u = u_0$ .

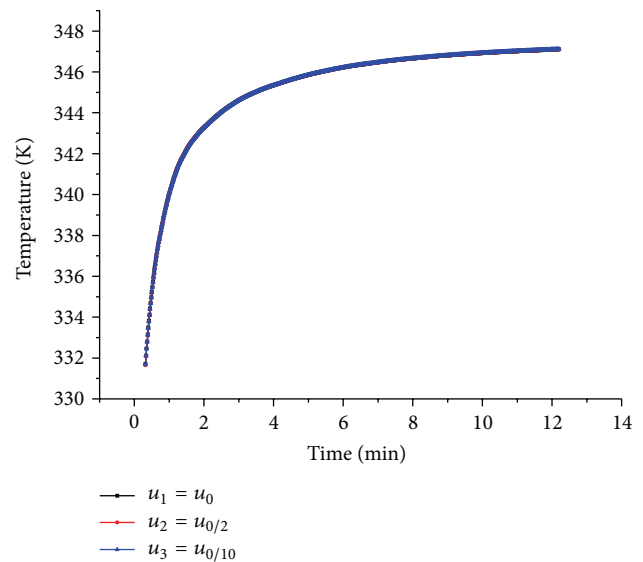


FIGURE 16: Temperature via different hot wind velocities.



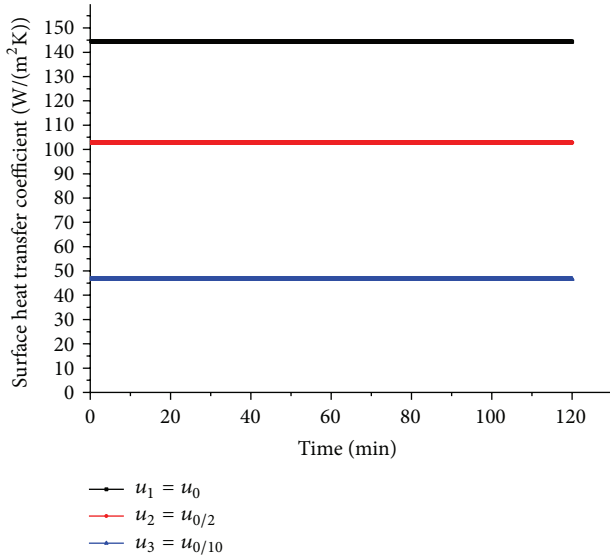


FIGURE 17: Comparison of surface heat transfer coefficients at different hot wind velocities.

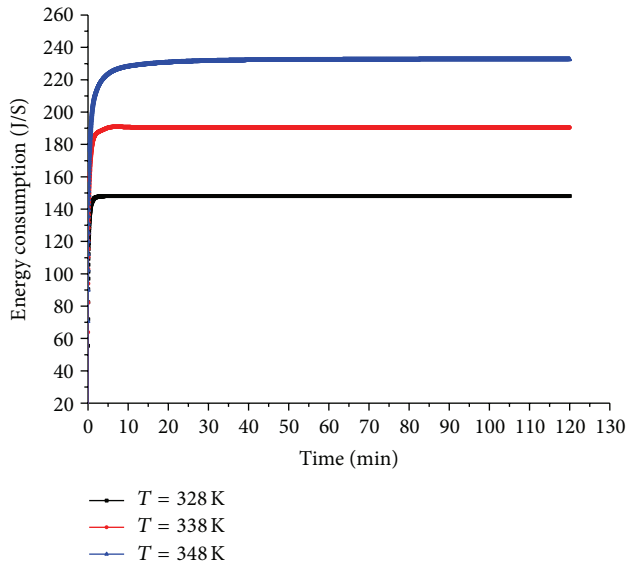


FIGURE 18: Different energy consumption curves at different drying temperatures.

carried out using COMSOL software. The results indicate that hot air drying is a process governed by interior mass transfer. Air velocity and temperature impose weak effects on heat transfer. Air temperature significantly affects the mass transfer process, whereas air velocity poses almost no effect. An essential requirement is that air velocity should ensure that external moisture diffuses from the corn surface to the ambient. The selection of air temperature and velocity depends primarily on mass transfer effects. A low velocity lessens energy consumption.

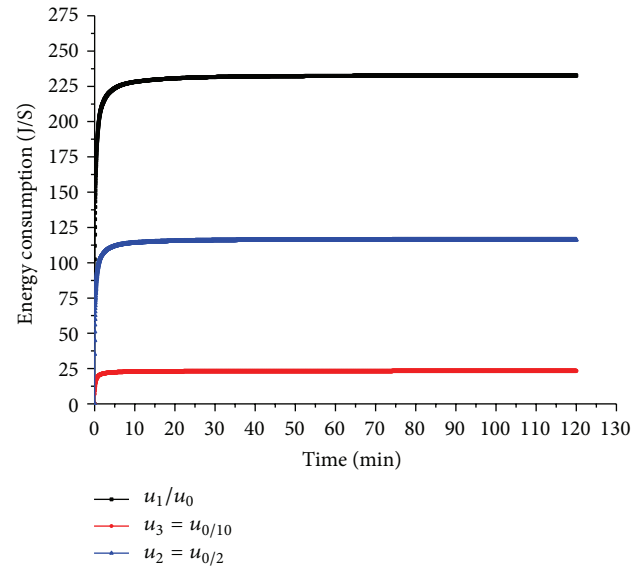


FIGURE 19: Different energy consumption curves at different hot wind velocities when  $T_3 = 348$  K.

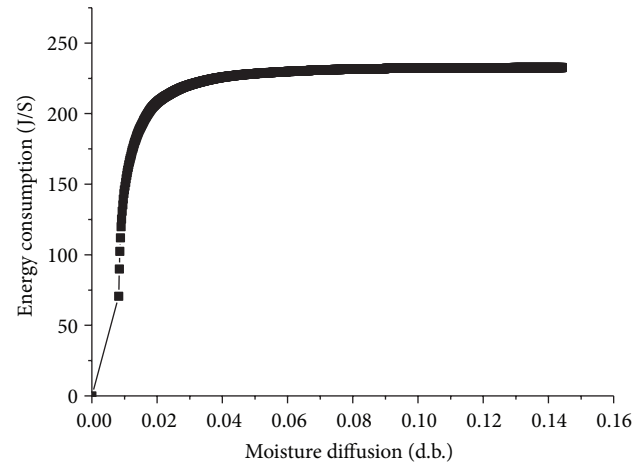


FIGURE 20: Energy consumption curves with diffused moisture at  $T_3 = 348$  K; initial moisture content is  $M_0 = 0.23$  (d.b.); wind speed  $u = u_0$ .

## Acknowledgment

This research was supported by the National Natural Science Foundation of China Grants no. 51176027 and no. 31000665.

## References

- [1] J. Yongsawatdigul and S. Gunasekaran, "Microwave-vacuum drying of cranberries. Part I: energy use and efficiency," *Journal of Food Processing and Preservation*, vol. 20, no. 2, pp. 121–143, 1996.
- [2] M. Aghbashlo, M. H. Kianmehr, and H. Samimi-Akhijahani, "Influence of drying conditions on the effective moisture diffusivity, energy of activation and energy consumption during the thin-layer drying of berberis fruit (Berberidaceae)," *Energy Conversion and Management*, vol. 49, no. 10, pp. 2865–2871, 2008.

- [3] D. R. Costa, A. F. de Lacerda Filho, J. de Sousa e Silva, D. Marçal de Queiroz, and J. P. Dadalto, "Energy consumption analysis of a system of drying of maize in mechanical dryer," *Revista Engenharia na Agricultura*, vol. 18, no. 2, pp. 151–164, 2010.
- [4] R. J. Gustafson, D. R. Thompson, and S. Sokhansanj, "Temperature and stress analysis of Corn kernel-finite element analysis," *Transactions of the American Society of Agricultural Engineers*, vol. 22, no. 4, pp. 955–960, 1979.
- [5] Y. Li and C. Cao, "Application of moisture diffusion model within an individual grain kernel," *Transactions of the CSAE*, vol. 9, no. 1, pp. 74–82, 1993.
- [6] Z. Zhang and N. Kong, "Nonequilibrium thermal dynamic modeling of porous medium vacuum drying process," *Mathematical Problems in Engineering*, vol. 2012, Article ID 347598, 22 pages, 2012.
- [7] C. Jia and C. Cao, "Process of tow-dimensional heat and mass transfer in corn kernel," *Journal of Beijing Agriculture Engineering University*, vol. 15, no. 1, pp. 45–51, 1995.
- [8] M. Neményi, I. Czaba, A. Kovács, and T. Jáni, "Investigation of simultaneous heat and mass transfer within the maize kernels during drying," *Computers and Electronics in Agriculture*, vol. 26, no. 2, pp. 123–135, 2000.
- [9] S. Zhang, J. Liu, N. H. Kong, and Z. J. Zhan, "Hot air drying simulation of corn grains based on 3D real body model," in *Proceedings of the 18th International Drying Symposium*, Xiamen, China, 2012.
- [10] P. K. Ghosh, D. S. Jayas, E. A. Smith, M. L. H. Gruwel, N. D. G. White, and P. A. Zhilkin, "Mathematical modelling of wheat kernel drying with input from moisture movement studies using magnetic resonance imaging (MRI), Part I: model development and comparison with MRI observations," *Biosystems Engineering*, vol. 100, no. 3, pp. 389–400, 2008.
- [11] J. H. Perez, F. Tanaka, and T. Uchino, "Modeling of mass transfer and initiation of hygroscopically induced cracks in rice grains in a thermally controlled soaking condition: with dependency of diffusion coefficient to moisture content and temperature—A 3D finite element approach," *Journal of Food Engineering*, vol. 111, no. 3, pp. 519–527, 2012.
- [12] H. P. Song, S. R. Delwiche, and M. J. Line, "Moisture distribution in a mature soft wheat grain by three-dimensional magnetic resonance imaging," *Journal of Cereal Science*, vol. 27, no. 2, pp. 191–197, 1998.
- [13] S. M. Goñi, E. Purlis, and V. O. Salvadori, "Three-dimensional reconstruction of irregular foodstuffs," *Journal of Food Engineering*, vol. 82, no. 4, pp. 536–547, 2007.
- [14] C. Cao and W. Zhu, *Computer Simulation of Drying Technology Process of Farm Products*, Chinese Agriculture Press, Beijing, China, 2001.
- [15] K. Haghighi and L. J. Segerlind, "Modeling simultaneous heat and mass transfer in anisotropic sphere-a finite element approach," *Transactions of the American Society of Agricultural Engineers*, vol. 31, no. 2, pp. 629–637, 1988.
- [16] M. Parti, "Evaluation of selected mathematical models for grain drying," in *Drying' 91*, 1991.

## Research Article

# Numerical Simulation of Air Inlet Conditions Influence on the Establishment of MILD Combustion in Stagnation Point Reverse Flow Combustor

**Xiao Liu and Hongtao Zheng**

*College of Power and Energy Engineering, Harbin Engineering University, Harbin, Heilongjiang 150001, China*

Correspondence should be addressed to Xiao Liu; liuxiao\_heu@163.com

Received 27 March 2013; Revised 24 April 2013; Accepted 24 April 2013

Academic Editor: Zhijun Zhang

Copyright © 2013 X. Liu and H. Zheng. This is an open access article distributed under the Creative Commons Attribution License, which permits unrestricted use, distribution, and reproduction in any medium, provided the original work is properly cited.

This paper presents a numerical study of the nonpremixed stagnation point reverse flow (SPRF) combustor, especially focusing on the influence of air inlet conditions. Modified eddy dissipation concept (EDC) with a reduced mechanism was used to calculate the characteristic of MILD combustion. The results show that the modified EDC with DRM19 mechanism is suitable for the present simulations. Seven additional runs are conducted to find out that it is not necessary to include the influence of low oxygen despite its conduciveness to the establishment of MILD combustion in SPRF combustor. In addition, for the same mass rate of air inlet, it is difficult to reach MILD combustion mode by changing the velocity of the air inlet. The influence of air inlet momentum is also investigated by keeping the air inlet velocity constant and increasing the mass. Although the degree of recirculation ( $R_{eg}$ ) is small, it can still achieve MILD combustion mode. Compared with the influence of air inlet velocity, it could be concluded that, rather than  $R_{eg}$ , the recirculation flow rate is the most important factor.

## 1. Introduction

With the world's increasing care for purifying and sustainability of environment, moderate or intense low-oxygen dilution combustion (MILD) [1] is becoming a credible candidate to simultaneously meet the mitigation of combustion-generated pollutants ( $\text{NO}_x$ ) and greenhouse gases ( $\text{CO}_2$ ) whilst meeting combustion efficiency needs. When the MILD combustion occurs, particularly firing gas and light oil, the entire furnace is bright and transparent and no flame is visible, so that it is often called "flameless combustion (FLOX) [2]" or "colorless combustion." This combustion is also named "high temperature air combustion" (HiTAC) [3] because the combustion air is usually preheated to beyond 1200 K for industrial regenerative combustor systems.

The German and Japanese researchers found at the beginnings of the 1990s that when preheating the air with regenerator to about 1600 K and injecting it approximately at 90 m/s, the visible flame disappeared and formed as the MILD combustion. Katsuki and Hasegawa [4] and J. Wüning and J. Wüning [2] reviewed advances in heat recirculating

combustion in industrial furnaces and found that the recirculation of burned gases and preheating air with low oxygen concentration for hot coflow combustion, were shown to be indispensable factors in realizing MILD combustion with low nitric oxide emissions. Dally et al. [5] reported a jet in hot coflow (JHC) burner which consists of an insulated and cooled central fuel jet and an annulus with a secondary burner. The secondary burner provides hot combustion products which are mixed with air and nitrogen using two side inlets upstream of the annulus exit, to control the oxygen level in the mixture. The cold mixture of air and nitrogen also assists in the cooling of the secondary burner. Oldenhof et al. [6] reported on the Delft jet-in-hot coflow (DJHC) burner which is based on that of Dally to study ignition kernels appearance. It is generally believed that the MILD combustion has to be achieved by preheating the air above the ignition point.

The air preheating requirements of the high temperature air combustion system limits the application of the MILD combustion technology. Because the reversed flow combustion configuration can avoid this procedure, more

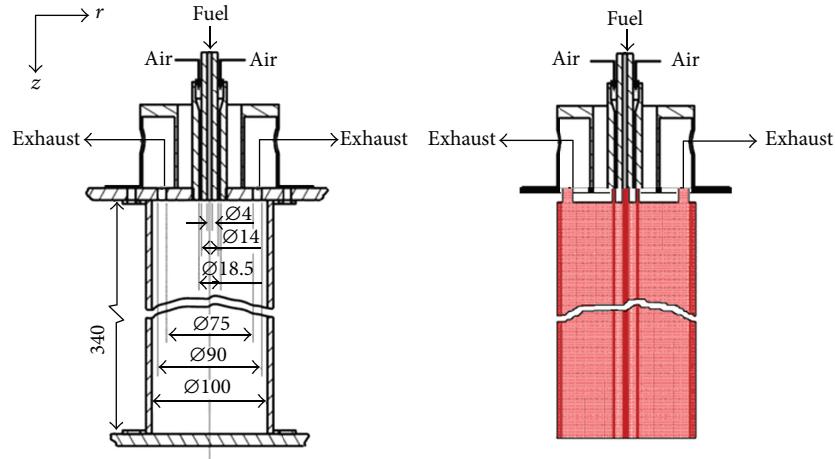


FIGURE 1: The schematic of the combustor and mesh of computational domain.

and more attention was focused here. Yang and Blasiak [7] showed that flameless oxidation can only be reached if the inlet velocities of the reactants are high enough to establish recirculation zones in the reversed flow combustion chamber. Unfortunately, high velocity of air inlet will lead to combustion instabilities, insufficient residence time, and high CO emission.

These issues may be overcome by a combustor design where both the burner and the exhaust port were mounted at the same end of the combustion chamber. Bobba et al. [8] developed a premixed Stagnation Point Reverse Flow (SPRF) combustor, and various optical diagnostic techniques were employed to elucidate the combustion processes in this novel combustor. The results showed that the SPRF combustor achieved internal exhaust gas recirculation and efficient mixing, which eliminated local peaks in temperature. Szegő et al. [9, 10] described the performance and stability characteristics of a parallel jet MILD combustion burner, the influence of equivalence ratio, combustion air temperature and heat extraction on performance were presented. Castela et al. [10] examined the combustion regimes occurring in a small-scale laboratory cylindrical combustor, in which the inlet and outlet were in the same side. The combustion regime developed from conventional lean combustion to flameless combustion by changing excess air coefficients ( $\lambda$ ) and detailed in-combustor measurements of temperature and  $O_2$ ,  $CO_2$ , CO, unburned hydrocarbons, and  $NO_x$  concentrations were reported.

On the other hand, many of these experimental studies have been complemented with Computational Fluid Dynamics (CFD) simulations. Kim et al. [11] investigated a global reaction mechanism for natural gas combustion to predict the observed nitrogen oxide and carbon monoxide levels in MILD combustion mode and concluded that the EDC turbulence-chemistry interaction model is suitable for the calculation of MILD combustion processes. Christo and Dally [12] found the EDC model with a detailed kinetic scheme, offering a practical and reasonably accurate tool for predicting the flow and flame characteristics of JHC configurations. Parente et al. [13] found a simple NO formation

mechanism based on the thermal and prompt routes which is found to provide NO emissions in relatively good agreement with experimental observations only when applied on temperature fields obtained with the EDC model and detailed chemistry. Galletti et al. [14] also found by CFD simulations that to save the computation time for engineering applications the 3D simulation of the MILD combustion should be simplified to the 2D case. They found quite small differences between the 2D and 3D calculations.

The present study is aimed at accurately capturing the characteristics of MILD combustion in this reversed flow small-scale combustor, using the modified Eddy Dissipation Concept (EDC) model with detailed mechanism. According to the test conditions of M. Castela [10], there are two variables from conventional lean combustion to flameless combustion: the total content of oxygen and the momentum (mass and velocity) of the air inlet; therefore, the main objective of the simulations is to investigate and explain the air inlet conditions impact on the establishment of MILD combustion.

## 2. Computation Details

**2.1. Furnace Configuration and Fuel.** Figure 1 shows the schematic of the combustor used in this study. The combustion chamber is a quartz-glass cylinder with an inner diameter of 100 mm and a length of 340 mm. During the tests, the quartz cylinder was insulated with a 30 mm thick ceramic fiber blanket. The burner and the exhaust port are mounted at the top end of the combustion chamber. The burner consists of a central orifice of 4 mm inner diameter, through which the fuel is supplied, surrounded by an annular orifice with 14 mm inner diameter and 18.5 mm outer diameter for the combustion air supply. The exhaust consists of an annular orifice, concentric with the burner, with 75 mm inner diameter and 90 mm outer diameter. A stainless steel plate is used to close the bottom end of the combustion chamber. This plate contains a moving hole with an inner diameter of 11 mm that allows for the introduction of probes. In this study, the natural gas ( $CH_4$ : 83.7%,  $C_2H_6$ : 7.6%,  $C_3H_8$ : 1.9%,  $N_2$ : 5.4%,

and other components with minor concentrations) was used as fuel.

**2.2. Computational Conditions and Models.** The governing equations are solved using CFD package ANSYS FLUENT 12.0. A two-dimensional mesh of the furnace was generated with the axial symmetry hypothesis to save the calculation cost; see also Figure 1. It is clear that the grids in the area of inlet and near the wall were refined; the optimal grid size was 22,563 cells after grid independent verification.

The SIMPLE method was used for velocity-pressure coupling. A second-order discretization scheme was used to solve all governing equations. Solution convergence was determined by two criteria. Standard wall functions were used for the velocity boundary conditions at the walls of the combustor. The wall temperature was set to 1300 K, based on experimental measurements, and the emissivity was set to 0.9. The first is ensuring that the residuals of the solved equations drop below specified thresholds set at  $10^{-3}$  for all variables, while a residual of  $10^{-6}$  was used for the energy equation. The second convergence criterion is ensuring that the value of a sensitive property (e.g., concentration of a radical species) at a critical spatial location has stabilized and is no longer changing with iterations.

**2.2.1. Turbulence Model.** Favre-averaged Navier-Stokes equations are solved by the standard  $k$ - $\varepsilon$  turbulence model. It is a semiempirical model based on model transport equations for the turbulence kinetic energy ( $k$ ) and its dissipation rate ( $\varepsilon$ ) which has become the workhorse of practical engineering flow calculations in the time since it was proposed by Launder and Spalding [15].

**2.2.2. Combustion Model.** The oxidation reaction has been taken into account using the Eddy Dissipation Concept (EDC) combustion model. The EDC is a compromise of accuracy and computational cost and was successfully applied to different regimes of combustion and steam cracking using detailed reaction mechanisms. It considers the interaction between the turbulence and the reaction and assumes that the molecular mixing and the reaction take place in small turbulent structures, called small scales. The length fraction of the small scales is modeled as [16]

$$\gamma = C_\gamma \left( \frac{v\varepsilon}{k^2} \right)^{1/4}, \quad \text{with } C_\gamma = 2.1377. \quad (1)$$

The volume fraction of the small scales is calculated as  $\gamma^3$ . Species are assumed to react in the fine structures over a time scale:

$$\tau = C_\tau \left( \frac{v}{\varepsilon} \right)^{1/2}, \quad \text{with } C_\tau = 0.4082. \quad (2)$$

The mean source term in the conservation equation for the species  $i$  is modeled as

$$R_i = \frac{\rho\gamma^2}{\tau(1-\gamma^3)} (Y_i^* - Y_i). \quad (3)$$

The species transport equation (conservation equation) is written as

$$\frac{\partial}{\partial t} (\rho Y_i) + \nabla \cdot (\rho \vec{v} Y_i) = -\nabla \cdot J_i + R_i. \quad (4)$$

The variable  $Y_i^*$  is the species mass fraction reached from the current value of  $Y_i$  by the action of the applied chemical reaction mechanism over a time scale  $\tau$ . So in the EDC model the mean chemical state evolves via a linear relaxation process, typical for mixing, towards a reacted state which would be reached by a nonlinear reaction process after a time scale  $\tau$ .

Both these constants have been set based on several experiments [17], and for most of combustion simulation, EDC model with default parameters can well capture the features of combustion field. However, for specific combustion conditions, which can only partly agree with the experimental data, for example, the effect of changing parameters on the prediction of high-pressure gasification process has been investigated by Rehm et al. [18]; early ignition of Delft-Jet-in-Hot-Coflow (DJHC) flame can be avoided with modified EDC by changing small structure volume and residence time constants; more detailed description of MEDC can be found in [19]. In this paper, the delay of ignition can be found comparing with experimental data, so the opposite change of  $C_\gamma$  and  $C_\tau$  is proposed to improve predictions.

The computation of the reaction rate source terms is accelerated with the In Situ Adaptive Tabulation (ISAT) algorithm [20] embodied in the solver. The default ISAT tolerance ( $10^{-3}$ ) was used until a moderately converged solution was obtained, and a smaller tolerance ( $10^{-4}$ ) was set thereafter.

**2.2.3. Reaction Mechanism.** The DRM19 chemical mechanism [21] was used in this work to describe the combustion of natural gas which is a subset of the GRI-Mech 1.2 full mechanism, with 19 species and 84 reactions, developed to obtain the smallest set of reactions needed to closely reproduce the main combustion characteristics predicted by the full mechanism. A two-step global chemical kinetic mechanism for  $\text{CH}_4$  was also used as comparison. In addition, one-step mechanism for  $\text{C}_2\text{H}_6$  and  $\text{C}_3\text{H}_8$  was applied.

**2.2.4. Radiation Model.** The discrete ordinate radiation model [22] was used in this work, as it is applicable across a wide range of optical thicknesses. Considering that the optical thickness in MILD flames is not well known, the DO model seems an appropriate choice. The model solves the radiative transfer equation (RTE) for a finite number of discrete solid angles across the computational domain. It also incorporates the weighted sum of gray gas model (WSGGM), in which spatial variation in the total emissivity is computed as a function of gas composition and temperature. The WSGGM is a reasonable compromise between the over-simplified gray gas model and a complete model, which takes into account particular absorption bands.

### 3. Results and Discussion

Table 1 presents the three experimental conditions in detail; excess air coefficient and air inlet momentum (velocity) are



TABLE 1: Three experiment conditions.

Run (experiment)	$\lambda$	$A_{\text{air}}$ (mm <sup>2</sup> )	$V_{\text{air}}$ (m/s)
1	1.5	114.8	66
2	2	114.8	88
3	2.4	114.8	108

For all conditions: atmospheric pressure; fuel thermal input = 8 kW, fuel inlet velocity = 17.7 m/s; air inlet temperature = 600 K; fuel inlet temperature = 300 K.

both increased from run 1 to run 3. Although the MILD combustion mode was achieved, the influence of air inlet conditions was not clear and definite. Unlike the traditional burner, MILD combustion can be achieved without preheating the air deeply in SPRF combustor.

This section presents the numerical results. At first, numerical predictions are validated against the measurements of MILD combustion mode (run 3); then the air inlet conditions influence on the establishment of MILD combustion is simulated and analysed.

### 3.1. Characteristic Parameters of Combustion

**3.1.1. Temperature Uniformity.** Temperature uniformity ratio  $R_{\text{tu}}$  is used to describe the gas temperature field uniformity inside the furnace. Many published works [7, 9, 23–25] in the literature stated that MILD technology gives much more uniform temperature field than traditional combustion. Furnace gas temperature uniformity ratio as defined below was used to describe the quality of temperature field in the furnace:

$$R_{\text{tu}} = \frac{T_{\text{max}} - \bar{T}}{\bar{T}}, \quad (5)$$

when  $R_{\text{tu}} = 0$  and there is no gas temperature gradient inside the furnace.

**3.1.2. Degree of Recirculation.** The flow pattern in the burner confirms the mechanism that promotes the exhaust gases recirculation. The degree of recirculation can be evaluated with the recirculation factor, defined as

$$R_{\text{eg}} = \frac{m_{\text{eg}}}{m_a + m_f} = \frac{m_{\text{down}} - m_{\text{out}}}{m_a + m_f}, \quad (6)$$

where  $m_{\text{eg}}$  is the mass flux of the recirculated exhaust gas and then entrained while  $m_a + m_f$  denotes the total mass flow rate of injecting reactants. For this reversed flow furnace,  $m_{\text{eg}}$  is equal to the downward mass flux  $m_{\text{down}}$  in cross section of recirculation center removing  $m_{\text{out}}$ . In addition,  $m_{\text{down}}$  is calculated by

$$m_{\text{down}} = \iint_A \rho v(x, y) dx dy. \quad (7)$$

**3.2. Assessment of the Numerical Model.** Prior to analysis, CFD simulations need to be validated against the experimental data of temperature and species mole fraction in MILD

TABLE 2: Characteristic parameters of combustion.

Run	Peak temperature	$R_{\text{tu}}$	$R_{\text{eg}}$
1	1870.6 K	8.03%	70.9%
2	1530.8 K	4.87%	82.7%
3	1426.9 K	3.65%	90.7%

combustion mode (run 3). The predicted and measured temperature and  $\text{CO}_2$  and  $\text{O}_2$  mole fraction are displayed in Figure 2 with different chemical mechanism, two-step global mechanism, and the DRM19 mechanism for  $\text{CH}_4$ ; in addition, a modified EDC with DRM19 mechanism is used.

Four sections along the axis are selected for comparison, namely, 70 mm, 150 mm, 204 mm, and 272 mm. It could be easily found that the results above have similar trend with two mechanisms. Significant discrepancies can be observed in the first three sections in terms of temperature and  $\text{CO}_2$  while mole fraction of  $\text{O}_2$  is in good agreement relatively. The experimental data of temperature and  $\text{CO}_2$  is higher than that of prediction near the centerline at 70 mm and 150 mm, which suggests that natural gas is in the slow oxidation state after 70 mm by DRM19 mechanism prediction; the outcome by global mechanism is even worse because combustion does not take place before 150 mm. For the same reason, mole fraction of  $\text{O}_2$  has the opposite trend. From the last section 272 mm, the distribution of DRM19 mechanism is more uniform than the global mechanism. Hence, taking the computing time and accuracy into account, the DRM19 mechanism is suitable for the present simulations.

The measured field almost has no obvious gradient all over the furnace; the tested combustion mode can well capture the features of MILD combustion except for the chemistry and temperature field in the fuel jet region, although the sophisticated chemical equilibrium model EDC with detailed chemical mechanism is used. The EDC model with default values of model constants appears to predict the occurrence of ignition too lately. A change of both of the two EDC model constants is found to lead to better agreement in the predictions of temperature profiles: the time scale constant is decreased from default value of  $C_\tau = 0.4082$  to  $C_\tau = 0.2$  and the volume fraction constant is increased from default value of  $C_\gamma = 2.1377$  to  $C_\gamma = 5$ . It is clear that using modified EDC parameters substantially improves the results.

Figure 3 shows the distributions of temperature in the furnace from run 1 to run 3. Two distinct conditions are observed when the air flow rate is changed; run 1 is a conventional lean combustion regime with local high-temperature region and run 3 corresponds to the MILD combustion regime with almost homogeneous distribution of temperature. The characteristic parameters of three combustion modes are listed in Table 2, which are used to determine whether the MILD combustion is established.

**3.3. Influence of Air Inlet Oxygen Content.** It is well known [14] that the most important factor for the establishment of MILD combustion is the assurance of local oxygen concentration to be less than 5%–10% in conventional MILD combustion system. As is mentioned in Table 3, the influence



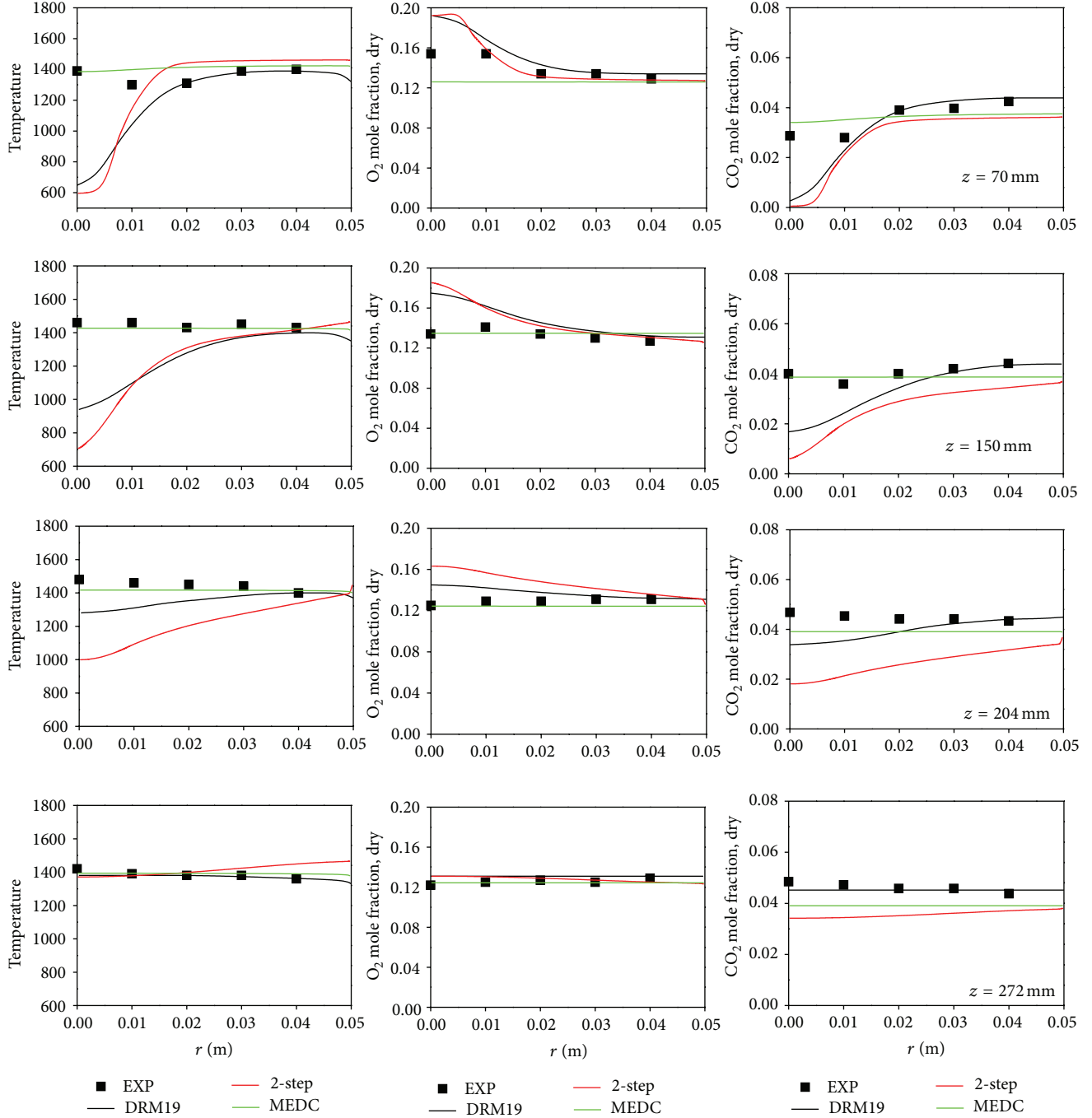
FIGURE 2: Comparison the predicted and measured temperature,  $CO_2$  and  $O_2$  mole fraction [10].

TABLE 3: CFD simulation conditions.

Run (CFD)	$\lambda$	$A_{air}$ (mm <sup>2</sup> )	$V_{air}$ (m/s)
1	1.5	114.8	66
4	1	114.8	66
5	0.6	114.8	66

of oxygen content is calculated in runs 4 and 5 based on the conditions of run 1. The mole fraction of oxygen is cut

down from 21% to 14% in run 4 and 8.7% (natural gas can completely react) in run 5 by diluting with nitrogen. The distribution of temperature in the furnace is shown in Figure 4. The ignition delay becomes longer, which means that the chemical reaction rate becomes slow, and it is the characteristic of MILD combustion. In addition, the peak temperature decreases and distributions of temperature become uniform with the drop of oxygen concentration, but the rate is very slight. Due to the dilution effect of high recirculated exhaust gas with fresh air, the content of  $O_2$

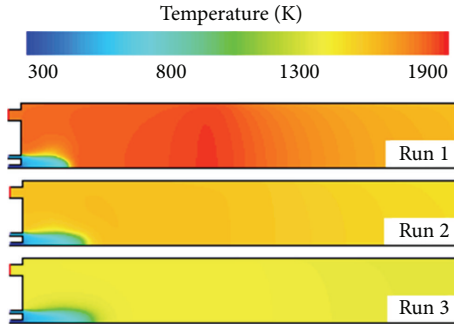


FIGURE 3: Distribution of temperature in the furnace from run 1 to run 3.

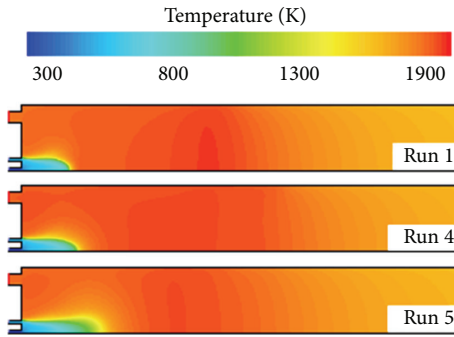


FIGURE 4: Distribution of temperature of runs 1, 4 and 5.

TABLE 4: CFD simulation conditions.

Run (CFD)	$\lambda$	$A_{\text{air}}$ (mm <sup>2</sup> )	$V_{\text{air}}$ (m/s)
1	1.5	114.8	66
6*	1.5	88.3	86
7	1.5	71.7	106
8	1.5	42.9	176
9	1.5	153.1	66
10	1.5	187.8	66

\* By keeping excess air coefficient constant with nitrogen dilution.

(almost less than 10%) meets the condition achieving MILD combustion.

Taking the complexity of the air dilution into account, the weak benefit of low oxygen content can be ignored. Therefore, there is no need to consider the influence of the oxygen, and standard air can be used in SPRF combustor.

**3.4. Influence of Air Inlet Momentum.** Consensus has been reached [26] that strong entrainment of high-temperature exhaust gases, which dilute fuel and air jets, is key technology of maintaining MILD combustion. However, from the velocity field of this combustor, the velocity is quite small near the bottom, where a quasi-stagnant region is present in SPRF combustor, so its mode of exhaust gas recirculation and dilution is different; thus the influence of air inlet momentum (mass and velocity) is simulated and the simulation conditions are listed in Table 4.

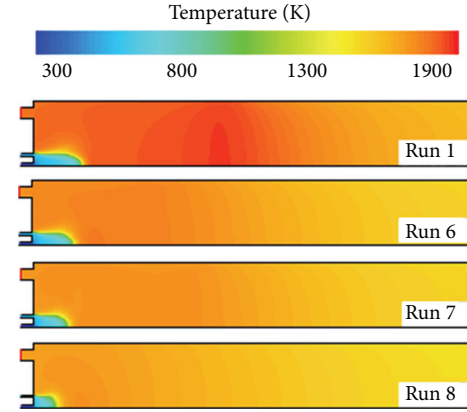


FIGURE 5: Distribution of temperature in the furnace of runs 1, 6, 7 and 8.

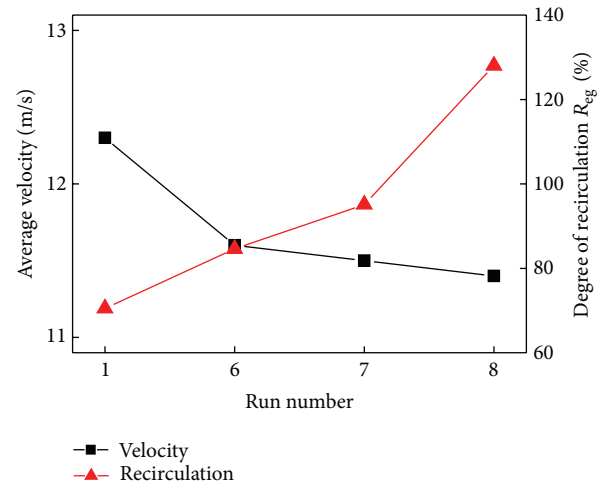


FIGURE 6: Trends of outlet average velocity and degree of recirculation.

**3.4.1. Influence of Air Inlet Velocity.** When the inlet mass flow rate of air remains constant, the area varies from 88.3 to 42.9 mm<sup>2</sup>, which leads the air inlet momentum to almost three times as that of run 1. For these runs, although the peak temperature decreases, the traditional combustion with visible flames (high-temperature zone) is expected to occur as shown in Figure 5; the ignition delay time becomes shorter because of high turbulent intensity of inlet air, which will accelerate the mixing and reaction of fuel and air. In general, for the same mass flux of circular air jet, as  $A_{\text{air}}$  decreases, the air jet injection momentum increases and consequently the air and fuel jet entrainment with the recirculation of exhaust gas is enhanced. It is obviously beneficial for the establishment of MILD combustion. Although the velocity of run 7 is almost three times of run 1, the variation of temperature uniformity is getting smaller and smaller.

Figure 6 presents the trends of outlet average velocity and  $R_{eg}$ . It is evident that the outlet velocity decreases by a large amount from run 1 to run 6 due to the more strongly momentum of inlet air, so the exhaust gas remains

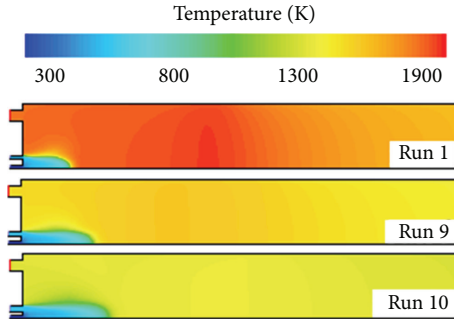


FIGURE 7: Distribution of temperature of runs 1, 9, and 10.

a longer time in the combustor; sufficient heat transfer with fresh air happened, which is beneficial for the establishment of MILD combustion, but the variation of outlet velocity decreases smaller and smaller from run 6 to run 8; the  $R_{eg}$  grows slowly from 85.1% to 128.8% and the rate of increase becomes more and more slowly. Many previous investigations were carried out to examine the influence of  $R_{eg}$  on MILD combustion [2, 27], and the results showed that in the MILD combustion zone, the internal recirculation rate ( $R_{eg}$ ) was greater than 2.5. The importance of  $R_{eg}$  in the establishment of MILD combustion may be overemphasized because the flow development differs in various configuration furnaces.

After a comprehensive analysis, it is difficult to achieve the MILD combustion mode for SPRF combustor by simply changing the velocity of the air inlet considering the critical flow rate and the system complexity of increasing the velocity.

**3.4.2. Influence of Air Inlet Mass.** Runs 9 and 10 are calculated to investigate the influence of air inlet mass based on run 1, where the air inlet velocity keeps constant and inlet area becomes large to increase the inlet momentum. Figure 7 presents the contour of temperature in run 1, run 9, and run 10. The distribution of temperature becomes homogeneous at a fast rate, the peak temperature decreases from 1870.6 K to 1583.2 K and finally 1406.7 K, and the reaction rate of  $\text{CH}_4$  decreases from  $0.0717 \text{ kg/m}^3 \cdot \text{s}$  to  $0.0617 \text{ kg/m}^3 \cdot \text{s}$  and finally  $0.0537 \text{ kg/m}^3 \cdot \text{s}$ , respectively. By comparison, the temperature uniformity is 3.68%, which is closer to that of the MILD combustion.

As presented in Figure 8, with the increase of the mass,  $R_{eg}$  first increases a little and then decreased. This is primarily because of the fact that the denominator in  $R_{eg}$  calculation formula  $m_a + m_f$  grows faster than the rate of recirculation flow. The  $R_{eg}$  is only 66.8% in run 10, and it does not match the previous conclusion [2, 27] where the internal recirculation rate ( $R_{eg}$ ) must be greater than 2.5. But the recirculation flow rate increases from 0.0032 to 0.005 kg/s, and the exhaust gas is sufficient to preheat and dilute the inlet air and it can still achieve to MILD combustion mode MILD combustion mode.

Figure 9 shows the fuel axial velocity in runs 1, 9, and 10. It can be seen that the fuel accelerates with the increase of air inlet mass, which means that the entrainment of the surrounding oxidant is enhanced due to the higher air inlet

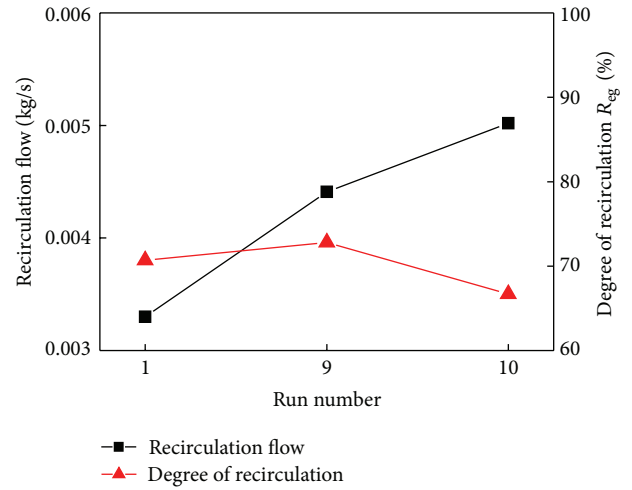


FIGURE 8: Trends of recirculation flow and degree of recirculation.

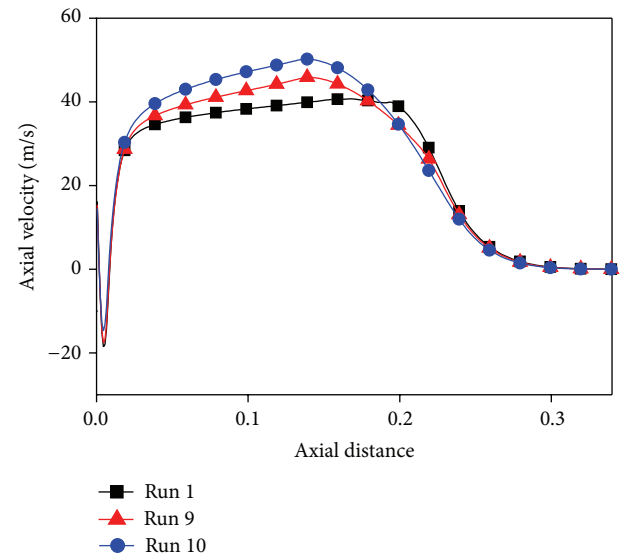


FIGURE 9: Fuel axial velocity along axis of runs 1, 9, and 10.

momentum. It provides some explanations as to why the MILD combustion can be established by increasing the mass of inlet air and without preheating the air for this configuration combustor according to the simulation. Compared with the influence of air inlet velocity, the recirculation flow is the most important factor, rather than  $R_{eg}$ . When reactants are preheated by exhaust gas, the mixture density decreases while their viscosity increases; it boosts the jet shear force and simultaneously increases the small-scale mixing and local scalar dissipation rate, thus hampering the formation of the flame front (local high temperature). Distributing the heat release to a larger volume leads to a nearly uniform temperature distribution with reduced peak temperatures. On the other hand, the high momentum gained by increasing air inlet mass strengthens exhaust recirculation and the influence of dilution on low oxygen concentration, which is also beneficial to the MILD combustion discussed previously.

## 4. Conclusions

A numerical study has been conducted to investigate the influence of air inlet conditions on the establishment of MILD combustion mode in an 8 kW nonpremixed Stagnation Point Reverse Flow (SPRF) combustor. The simulations are carried out by standard  $k$ - $\epsilon$  turbulence model and modified EDC combustion model with detailed mechanism DRM19; the combustion regime in the present combustor develops from conventional lean combustion to MILD combustion. The main conclusions are summarized as follows.

- (1) Compared with experimental data, the modified EDC combustion model with DRM19 mechanism can well capture the features of MILD combustion when computing time and accuracy are taken into account.
- (2) Based on the predicted data, reducing the oxygen content of air inlet is a little conducive to the establishment of MILD combustion, but the benefit of low oxygen content can be ignored due to the dilution effect of high recirculated exhaust gas with fresh air when the complexity of the air dilution is taken into account and standard air can be used in this SPRF combustor.
- (3) For the same mass rate of air inlet, it is difficult to reach MILD combustion mode by simply changing the velocity of the air inlet. For the same inlet velocity, although  $R_{eg}$  is small (its trend first went up and then dropped), it can still achieve MILD combustion mode. Compared with the influence of air inlet velocity, it could be concluded that, rather than  $R_{eg}$ , the recirculation flow is the most important factor in SPRF combustor.

## Nomenclature

$k$ :	Turbulent kinetic energy ( $\text{m}^2\cdot\text{s}^{-2}$ )
$Y_i^*$ :	Fine-scale species mass fraction
$Y_i$ :	Local mass fraction of each species
$S_i$ :	Source term for the rate of creation species $i$
$R_i$ :	Net rate of production of species $i$
$J_i$ :	Diffusion flux of species $i$
$C_\gamma$ :	Volume fraction constant equal to 2.1377
$C_\tau$ :	A time scale constant equal to 0.4082
$R_{tu}$ :	Temperature uniformity ratio
$R_{eg}$ :	Degree of recirculation
$m_f$ :	Mass flux of fuel inlet ( $\text{kg}\cdot\text{s}^{-1}$ )
$m_{out}$ :	Mass flux of flow out ( $\text{kg}\cdot\text{s}^{-1}$ )
$m_a$ :	Mass flux of air inlet ( $\text{kg}\cdot\text{s}^{-1}$ )
$m_{down}$ :	Downward mass flux ( $\text{kg}\cdot\text{s}^{-1}$ )
$m_{eg}$ :	Mass flux of the recirculated exhaust gas ( $\text{kg}\cdot\text{s}^{-1}$ )
$\bar{T}$ :	Average temperature (K)
$T_{max}$ :	Maximum temperature (K)
$V_{air}$ :	Velocity of air inlet ( $\text{m}\cdot\text{s}^{-1}$ )
$A_{air}$ :	Area of air inlet ( $\text{mm}^2$ ).

## Greek Symbols

$\rho$ :	Density of the mixture ( $\text{kg}\cdot\text{m}^{-3}$ )
$\lambda$ :	Excess air coefficients
$\epsilon$ :	Kinetic energy dissipation rate ( $\text{m}^2\cdot\text{s}^{-3}$ )
$\gamma_\lambda$ :	Mass fraction of fine structures
$\nu$ :	Kinematic viscosity ( $\text{m}^2\cdot\text{s}^{-1}$ )
$\tau^*$ :	Mean residence time in fine structures (s).

## References

- [1] A. Cavaliere and M. De Joannon, "Mild combustion," *Progress in Energy and Combustion Science*, vol. 30, no. 4, pp. 329–366, 2004.
- [2] J. Wüning and J. Wüning, "Flameless oxidation to reduce thermal NO-formation," *Progress in Energy and Combustion Science*, vol. 23, pp. 81–94, 1997.
- [3] H. Tsuji, A. Gupta, T. Hasegawa, M. Katsuki, K. Kishimoto, and M. Morita, *High Temperature Air Combustion: From Energy Conservation to Pollution Reduction*, CRC Press, 2003.
- [4] M. Katsuki and T. Hasegawa, "The science and technology of combustion in highly preheated air," *Proceedings of the Combustion Institute*, vol. 27, no. 2, pp. 3135–3146, 1998.
- [5] B. B. Dally, A. N. Karpetis, and R. S. Barlow, "Structure of turbulent non-premixed jet flames in a diluted hot coflow," *Proceedings of the Combustion Institute*, vol. 29, no. 1, pp. 1147–1154, 2002.
- [6] E. Oldenhof, M. J. Tummers, E. H. van Veen, and D. J. E. M. Roekaerts, "Ignition kernel formation and lift-off behaviour of jet-in-hot-coflow flames," *Combustion and Flame*, vol. 157, no. 6, pp. 1167–1178, 2010.
- [7] W. Yang and W. Blasiak, "Flame entrainments induced by a turbulent reacting jet using high-temperature and oxygen-deficient oxidizers," *Energy and Fuels*, vol. 19, no. 4, pp. 1473–1483, 2005.
- [8] M. K. Bobba, P. Gopalakrishnan, J. M. Seitzman, and B. T. Zinn, "Characteristics of combustion processes in a stagnation point reverse flow combustor," in *Proceedings of the ASME Turbo Expo 2006: Power for Land, Sea and Air*, GT2006-91217, pp. 867–875, Barcelona, Spain, May 2006.
- [9] G. G. Szegö, *Experimental and numerical investigation of a parallel jet MILD combustion burner system in a laboratory-scale furnace [Ph.D. thesis]*, The University of Adelaide, Adelaide, Australia, 2010.
- [10] M. Castela, A. S. Verissimo, A. M. A. Rocha, and M. Costa, "Experimental study of the combustion regimes occurring in a laboratory combustor," *Combustion Science and Technology*, vol. 184, pp. 243–258, 2012.
- [11] J. P. Kim, U. Schnell, and G. Scheffknecht, "Comparison of different global reaction mechanisms for MILD combustion of natural gas," *Combustion Science and Technology*, vol. 180, no. 4, pp. 565–592, 2008.
- [12] F. C. Christo and B. B. Dally, "Modeling turbulent reacting jets issuing into a hot and diluted coflow," *Combustion and Flame*, vol. 142, no. 1-2, pp. 117–129, 2005.
- [13] A. Parente, C. Galletti, and L. Tognotti, "Effect of the combustion model and kinetic mechanism on the MILD combustion in an industrial burner fed with hydrogen enriched fuels," *International Journal of Hydrogen Energy*, vol. 33, no. 24, pp. 7553–7564, 2008.

- [14] C. Galletti, A. Parente, and L. Tognotti, "Numerical and experimental investigation of a mild combustion burner," *Combustion and Flame*, vol. 151, no. 4, pp. 649–664, 2007.
- [15] B. E. Launder and D. B. Spalding, *Lectures in Mathematical Models of Turbulence*, Academic Press, London, UK, 1972.
- [16] I. R. Gran and B. F. Magnussen, "A numerical study of a bluff-body stabilized diffusion flame. Part 2: influence of combustion modeling and finite-rate chemistry," *Combustion Science and Technology*, vol. 119, no. 1–6, pp. 191–217, 1996.
- [17] I. S. Ertesvåg and B. F. Magnussen, "The Eddy dissipation turbulence energy cascade model," *Combustion Science and Technology*, vol. 159, no. 1–6, pp. 213–235, 2000.
- [18] M. Rehm, P. Seifert, and B. Meyer, "Theoretical and numerical investigation on the EDC-model for turbulence-chemistry interaction at gasification conditions," *Computers and Chemical Engineering*, vol. 33, no. 2, pp. 402–407, 2009.
- [19] A. De, E. Oldenhof, P. Sathiah, and D. Roekaerts, "Numerical simulation of Delft-Jet-in-Hot-Coflow (DJHC) flames using the eddy dissipation concept model for turbulence-chemistry interaction," *Flow, Turbulence and Combustion*, vol. 87, no. 4, pp. 537–567, 2011.
- [20] S. B. Pope, "Computationally efficient implementation of combustion chemistry using in situ adaptive tabulation," *Combustion Theory and Modelling*, vol. 1, no. 1, pp. 41–63, 1997.
- [21] A. Kazakov and M. Frenklach, <http://www.me.berkeley.edu/drm/>.
- [22] E. H. Chui and G. D. Raithby, "Computation of radiant heat transfer on a nonorthogonal mesh using the finite-volume method," *Numerical Heat Transfer*, vol. 23, no. 3, pp. 269–288, 1993.
- [23] B. Danon, E.-S. Cho, W. De Jong, and D. J. E. M. Roekaerts, "Numerical investigation of burner positioning effects in a multi-burner flameless combustion furnace," *Applied Thermal Engineering*, vol. 31, no. 17–18, pp. 3885–3896, 2011.
- [24] A. S. Verissimo, A. M. A. Rocha, and M. Costa, "Operational, combustion, and emission characteristics of a small-scale combustor," *Energy and Fuels*, vol. 25, no. 6, pp. 2469–2480, 2011.
- [25] A. S. Verissimo, A. M. A. Rocha, and M. Costa, "Importance of the inlet air velocity on the establishment of flameless combustion in a laboratory combustor," *Experimental Thermal and Fluid Science*, vol. 44, pp. 75–81, 2013.
- [26] E. Abtahizadeh, J. van Oijen, and P. De Goey, "Numerical study of mild combustion with entrainment of burned gas into oxidizer and/or fuel streams," *Combustion and Flame*, vol. 159, no. 6, pp. 2155–2165, 2012.
- [27] A. Effuggi, D. Gelosa, M. Derudi, and R. Rota, "Mild combustion of methane-derived fuel mixtures: natural gas and biogas," *Combustion Science and Technology*, vol. 180, no. 3, pp. 481–493, 2008.



## Research Article

# Research on Three-Dimensional Unsteady Turbulent Flow in Multistage Centrifugal Pump and Performance Prediction Based on CFD

Zhi-jian Wang,<sup>1</sup> Jian-she Zheng,<sup>1</sup> Lu-lu Li,<sup>2</sup> and Shuai Luo<sup>1</sup>

<sup>1</sup> School of Mechatronics Engineering, Shenyang Aerospace University, Shenyang, Liaoning 110136, China

<sup>2</sup> Haicheng Suprasuny Pump Co., Ltd., Haicheng, Liaoning 114216, China

Correspondence should be addressed to Zhi-jian Wang; wangzhijian1974@sina.com

Received 24 March 2013; Accepted 15 May 2013

Academic Editor: Zhijun Zhang

Copyright © 2013 Zhi-jian Wang et al. This is an open access article distributed under the Creative Commons Attribution License, which permits unrestricted use, distribution, and reproduction in any medium, provided the original work is properly cited.

The three-dimensional flow physical model of any stage of the 20BZ4 multistage centrifugal pump is built which includes inlet region, impeller flow region, guide-vane flow region and exit region. The three-dimensional unsteady turbulent flow numerical model is created based on Navier-Stoke solver and standard  $k-\epsilon$  turbulent equations. The method of multireference frame (MRF) and SIMPLE algorithm are used to simulate the flow in multistage centrifugal pump based on FLUENT software. The distributions of relative velocity, absolute velocity, static pressure, and total pressure in guide vanes and impellers under design condition are analyzed. The simulation results show that the flow in impeller is mostly uniform, without eddy, backflow, and separation flow, and jet-wake phenomenon appears only along individual blades. There is secondary flow at blade end and exit of guide vane. Due to the different blade numbers of guide vane and impeller, the total pressure distribution is asymmetric. This paper also simulates the flow under different working conditions to predict the hydraulic performances of centrifugal pump and external characteristics including flow-lift, flow-shaft power, and flow-efficiency are attained. The simulation results are compared with the experimental results, and because of the mechanical losses and volume loss ignored, there is a little difference between them.

## 1. Introduction

Pumps are widely used in many fields and the average electric power consumption is about 20.9% of the total consumption every year in China [1]. Because of the low level of manufacture and design of pumps, the efficiency of domestic pumps is about 10% lower than that of the developed countries. Among the pumps, the centrifugal ones are most widely applied, but there are many problems such as low efficiency, operated under off-design conditions, and low cavitations performance. Therefore, it will have very important practical significance to study the internal flow of centrifugal pumps in order to optimize the structure of main parts, improve the hydraulic performance, increase the efficiency and avoid being operated under off-design conditions, and thus reach the goal of increasing efficiency and saving energy.

Due to the complex shape of flow channel, high-speed-rotating viscous fluid and the interaction between moving

and stationary parts, the flow in centrifugal pumps is a three-dimensional, viscous, and unsteady complex flow. It becomes more and more popular to investigate the internal flow of the centrifugal pump based on computational fluid dynamic (CFD) owing to the short design time, low price, being observed directly, and making up the deficiency of traditional design methods. With the rapid development of the computer technology, CFD has been one of the main methods to study the flow in the centrifugal pump. Subsequently, it will be possible to design high-efficiency and energy-saving pumps and create huge social and economic benefits. Si and Dike [2] simulated the whole flow field of sectional multistage pump and the simulation was performed in a multiple reference frame and standard  $k-\epsilon$  turbulence model. Li et al. [3] combined sliding-mesh and moving-mesh methods to simulate internal flow during starting procedure of the single-stage pump. Liu and Wang [4] carried out computer-aided analysis



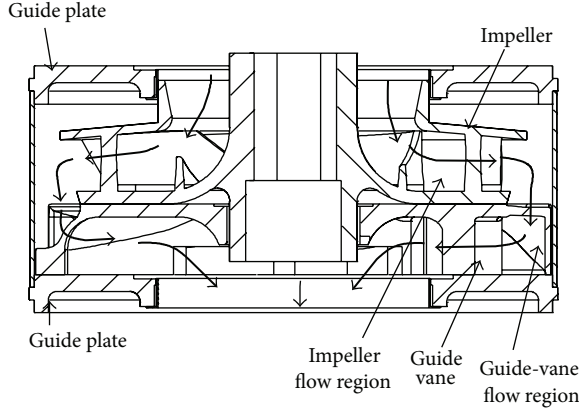


FIGURE 1: Sketch of centrifugal pump.

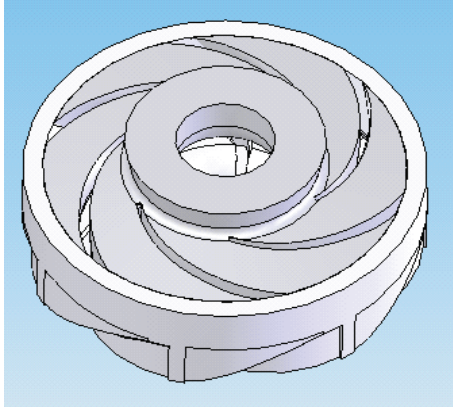


FIGURE 2: Flow region of impeller and guide vane.

on internal flow of stamping and welding centrifugal pump impeller based on CFD using ANSYS CFX and explored the flow mechanism in impeller. Barrio et al. [5] simulated internal flow of centrifugal pump through CFD such that they could predict radial force and torsion suffered by impeller. Jafarzadeh et al. [6] simulated fluid flow of low-specific-speed ratio centrifugal pump. Asuaje et al. [7] performed a 3D-CFD simulation of impeller and volute of a centrifugal pump using CFX code with a specific speed of 32 and found velocity and pressure fields for different flow rates and radial thrust on the pump shaft. Cui et al. [8] investigated the effect of number of splitting blades for long, mid, and short blades using a one-equation turbulent model. Their results show that the bulk flow in the impeller has an important influence on the pump performance. Anagnostopoulos [9] simulated 3D turbulent flow in a radial pump impeller for a constant rotational speed of 1500 rpm based on the solution of the RANS equations. Few of the previous works involved study of 3D modeling within a full domain considering interaction between rotor and stator of a high-speed multistage centrifugal pump using various turbulence models.

This paper uses commercial CFD software FLUENT, standard  $k-\varepsilon$  turbulent model and multiply reference frame to perform numerical modeling of the full three-dimensional

fluid field for any stage of 20BZ4 multistage centrifugal pump which includes the flow region of import channel, impellers, guide vanes, and exit channel. The pressure and velocity distributions in the pump under design condition are obtained and the numerical performance curves are compared with the experimental ones. It will provide theoretical basis for further optimizing the structures and improving the performances of centrifugal pump.

## 2. Numerical Simulation and Method

**2.1. Physical Model.** Figure 1 shows the sketch map and flow route in any stage unit of 20BZ4 multi-stage centrifugal pump, which includes guide plates, impellers, and guide vanes. The impeller is made up of front end plate, back end plate and blades. The blades are equipped between front and back end plates, and the number of blades is 5. The structure of guide vanes is radial and the number of blades is 7. It is made up of positive guide vane and negative guide vane. Positive vane can collect fluid and transform kinetic energy into pressure energy, while negative vane can change flow direction and transmit the fluid into next unit with the required speed and circulation. Guide plate can reduce reflux effectively and make uniform and stable flow velocity of the fluid into the impeller. Fluid flows downward through guide plate, then through the flow runner of impeller into guide vane and finally goes into the next pump unit from guide plate.

The impeller inlet and guide-vane outlet are extended, respectively, in order to ensure stable convergence of internal flow field. The physical model includes inlet region, impeller flow region, guide-vane flow region, and exit region. Figure 2 shows the flow region model of impeller and guide-vane. Structured grids are used in inlet region and exit region because of the cylindrical shape and the numbers of grids are 71607 and 69564, respectively. Unstructured grids are used to mesh impeller and guide-vane flow regions and the numbers of grids are 187561 and 133108, respectively. Figures 3 and 4 show the grids of impeller flow region and guide-vane flow region, respectively.

**2.2. Governing Equations and Turbulence Model.** The internal flow of centrifugal pump is a three-dimensional, viscous, and unsteady turbulent flow and flow law follows Navier-Stokes equation. Because the heat exchange is very little in centrifugal pump, energy conservation equation is not considered, and only mass conservation equation and momentum conservation equation need to be solved.

Mass conservation equation is as follows:

$$\frac{\partial \rho}{\partial t} + \frac{\partial}{\partial x_i} (\rho u_i) = 0. \quad (1)$$

Momentum conservation equation is as follows:

$$\frac{\partial}{\partial t} (\rho u_i) + \frac{\partial}{\partial x_j} (\rho u_i u_j) = -\frac{\partial p}{\partial x_i} + \frac{\partial}{\partial x_j} \left[ \mu \frac{\partial u_i}{\partial x_j} - \rho u_i' u_j' \right] + S_i, \quad (2)$$

where  $\rho$  is fluid density,  $u$  is velocity,  $p$  is pressure,  $t$  is time,  $\mu$  is

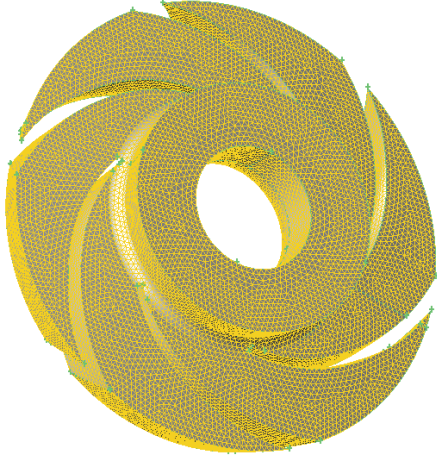


FIGURE 3: Grids of impeller flow region.

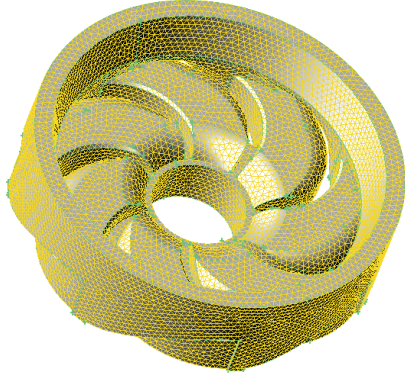


FIGURE 4: Grids of guide-vane flow region.

dynamic viscosity,  $S$  is source item, and  $\overline{\rho u_i' u_j'}$  is the Reynolds stress.  $x_i$  and  $x_j$  are the coordinates of  $x$ ,  $y$ , and  $z$ , and  $x_i \neq x_j$ .

Standard  $k$ - $\varepsilon$  turbulence model is used. Turbulence kinetic energy  $k$  equation is as follows:

$$\frac{\partial(\rho k)}{\partial t} + \frac{\partial(\rho k u_i)}{\partial x_i} = \frac{\partial}{\partial x_j} \left[ \left( \mu + \frac{\mu_t}{\sigma_k} \right) \frac{\partial k}{\partial x_j} \right] + G_k - \rho \varepsilon. \quad (3)$$

Dissipation rate  $\varepsilon$  equation is as follows:

$$\begin{aligned} \frac{\partial(\rho \varepsilon)}{\partial t} + \frac{\partial(\rho \varepsilon u_i)}{\partial x_i} = & \frac{\partial}{\partial x_j} \left[ \left( \mu + \frac{\mu_t}{\sigma_s} \right) \frac{\partial \varepsilon}{\partial x_j} \right] \\ & + \frac{C_{1\varepsilon} \varepsilon}{k} G_k - C_{2\varepsilon} \rho \frac{\varepsilon^2}{k}, \end{aligned} \quad (4)$$

where  $G_k$  is production term of turbulence energy  $k$  produced by average velocity gradient,  $c_{1\varepsilon}$ ,  $c_{2\varepsilon}$ , and  $c_{3\varepsilon}$  are empirical constants,  $\sigma_k$  and  $\sigma_s$  are Prandtl numbers of turbulence kinetic energy  $k$  and dissipation rate  $\varepsilon$ , and turbulence viscosity is defined as

$$\mu_t = \rho C_\mu \frac{k^2}{\varepsilon}, \quad (5)$$

where  $C_\mu$  is the empirical constant.

### 2.3. Boundary Conditions and Numerical Model

**2.3.1. Inlet Boundary Conditions.** Velocity inlet surface, where velocity and other scalars are defined, is chosen as the inlet boundary. Inlet velocity can be calculated by

$$u_{in} = \frac{Q}{\rho \pi (r_1^2 - r_2^2)}, \quad (6)$$

where  $Q$  is flow, and  $r_1$  and  $r_2$  are inlet cross section radii.

Inlet turbulence energy  $k$  is calculated as

$$k_{in} = 0.005 u_{in}^2. \quad (7)$$

Inlet dissipation rate  $\varepsilon$  is calculated as

$$\varepsilon_{in} = \frac{C_\mu k_{in}^{3/2}}{l_{in}}, \quad (8)$$

where  $l_{in}$  is inlet mixing length,  $D$  is inlet equivalent diameter, and  $l_{in} = 0.5 D$ .

**2.3.2. Outlet Boundary Conditions.** The exit is set as outflow boundary which is mainly used where the exit flow is under full-developed state. The outlet velocity  $u_{out}$ , turbulence kinetic energy  $k_{out}$ , and dissipation rate  $\varepsilon_{out}$  are described in the following equations:

$$\begin{aligned} \frac{\partial u_{i(out)}}{\partial n} &= 0 \quad (i = 1, 2, 3, \dots), \\ \frac{\partial k_{out}}{\partial n} &= 0, \\ \frac{\partial \varepsilon_{out}}{\partial n} &= 0, \end{aligned} \quad (9)$$

where  $n$  is the unit vector orthogonal to exit boundary.

**2.3.3. Wall Boundary Conditions.** No-slipping wall boundary conditions are assumed on the wall. The impeller boundary, front and back end plates are set as rotating wall, and other walls are stationary. Because the Reynolds number near the walls is small and standard  $k$ - $\varepsilon$  model is not appropriate to turbulent boundary layer region, logarithmic wall function is used.

**2.4. Numerical Method.** Multiple reference frame (MRF) is used in FLUENT and unsteady problem can be transferred into steady problem. Steady calculation is done in stator region, while centrifugal force and Coriolis force are calculated in rotor region in inertial frame and inner grids keep stationary during calculation. Flow parameters are switched between the interfaces of impellers and guide vanes in order to keep continuity of interfaces.

SIMPLE algorithm is used to couple pressure with velocity, and segregated solver and standard discrete scheme are chosen. First order upwind scheme is used to solve momentum conservation equation, turbulence energy equation, and dissipation rate equation. Underrelaxation factor controls the convergence speed and is properly updated based on actual convergence condition.

TABLE 1: Design condition and fluid physical properties.

Flow (m <sup>3</sup> /h)	Rotational speed (r/min)	Atmospheric pressure (Pa)	Medium density (kg/m <sup>3</sup> )	Dynamic viscosity (Pa·s)
20	2850	101325	998.2	$1.003 \times 10^{-3}$

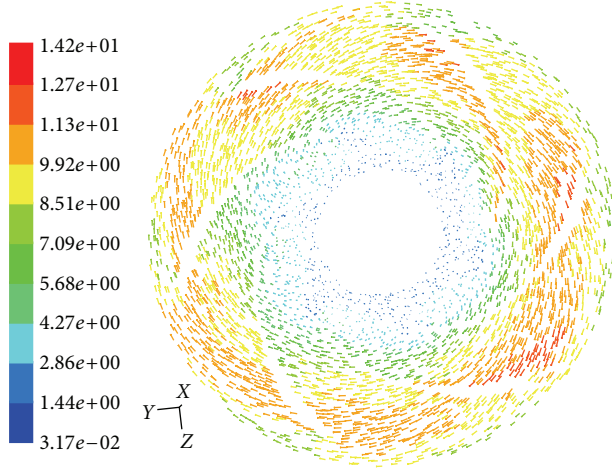


FIGURE 5: Relative velocity vector of impellers.

2.5. *Design Condition of Pump and Fluid Properties.* The design condition of pump and fluid physical properties are shown in Table 1.

### 3. Numerical Results

3.1. *Velocity Distribution.* Figure 5 shows the relative velocity vector of  $x = 0$  section in the middle of front end plate and back end plate of impellers under design condition. It can be seen from the figure that the flow is uniform in most fluid region of impellers without eddy, backflow, and separation flow. Jet-wake phenomenon happens only along individual blades. The flow velocity increases gradually from the inlet of impeller to exit, being slowest at the inlet and fastest at the exit. Because of diffusion function of guide blades, kinetic energy of high-speed fluid is transferred into pressure energy, and velocity becomes lower when fluid goes into the guide blade. Meanwhile a part of the energy is lost when the high-speed fluid flowing out of impellers collides into the pump case. The figure also shows that the relative velocity of suction surface is lower than that of pressure surface on the same radius surface. The pressure difference which is produced on the two sides of impellers due to the asymmetry creates the moment of resistance which is overcome by the prime mover to work on the spindle.

Figure 6 shows the absolute velocity of guide vanes under design condition. From the figure we can see that the velocity is fastest at the inlet of guide vane and slowest at the exit. The guide vanes transfer the kinetic energy of fluid into pressure energy. As a result, the velocity decreases gradually along the

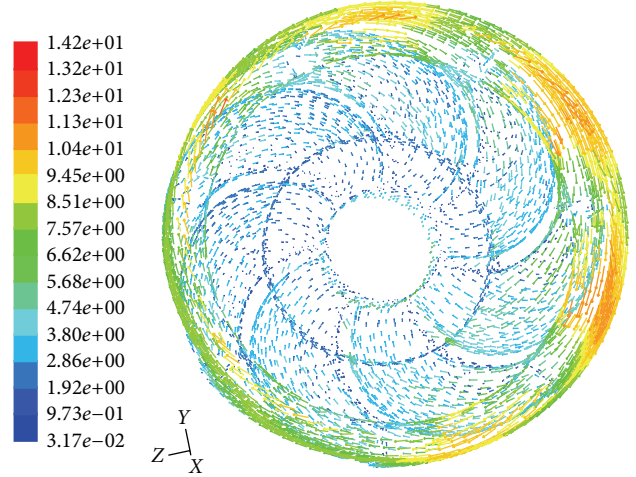


FIGURE 6: Absolute velocity vector of guide vanes.

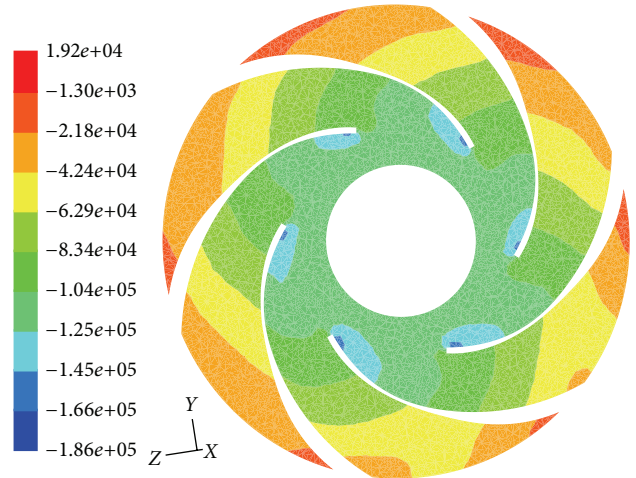


FIGURE 7: Static pressure distribution on impellers.

direction of the flow in the guide vane and secondary flow appears at blade end and exit.

3.2. *Static Pressure Distribution.* Figure 7 shows the static pressure distribution on the centrifugal pump impellers of  $x = 0$  section. It shows that the static pressure increases gradually and is ladder-like uniform distribution. The minimum pressure area appears at the suction surface of impeller inlet. The fluid can get the kinetic energy driven by impellers when it enters into the impeller flow channel vertically, but because the velocity direction changes quickly and some energy gets lost when the fluid collides into the impeller front end, cavitations could happen in these low-pressure areas. Figure 8 shows the static pressure distribution on suction surface and pressure surface of impellers, respectively. The pressure which shows ladder-like distribution gradually increases along the



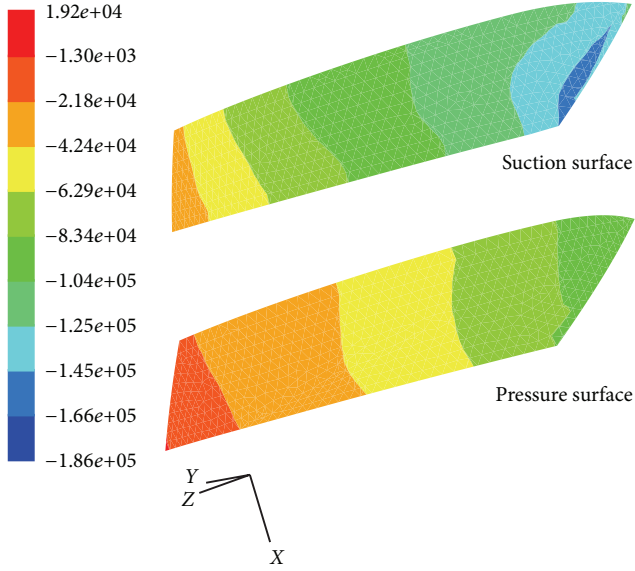


FIGURE 8: Static pressure distribution on suction surface and pressure surface of impellers.

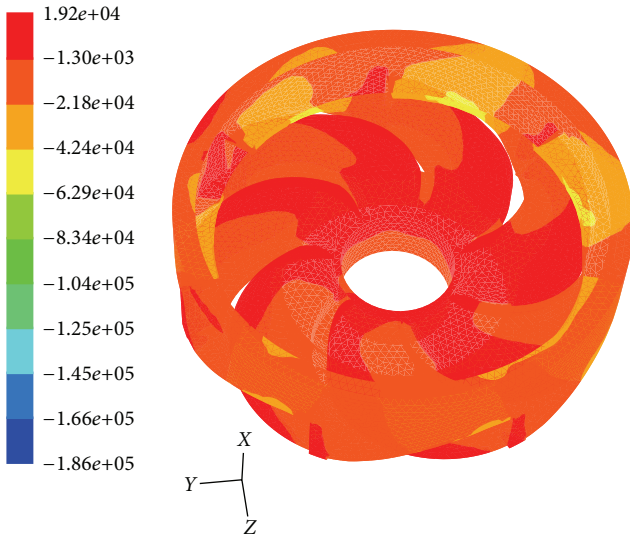


FIGURE 9: Static pressure distribution on guide vanes.

flow direction on both pressure and suction surfaces. The pressure on pressure surface is higher than that of suction surface and the pressure difference causes the moment of resistance on rotating axis. At the inlet of suction surface the pressure is lowest and cavitations may happen here.

Figure 9 shows the static pressure distribution on guide vanes of centrifugal pump under the design condition. It shows that the pressure increases gradually along the flow direction and reaches the maximum value at the exit of guide vanes. The function of guide vanes is to collect the high-speed fluid and then transfers kinetic energy of the fluid into pressure energy. Because of the crash between high-speed fluid from impellers and pump case, local low pressure appears in the interface of impellers and guide vanes,

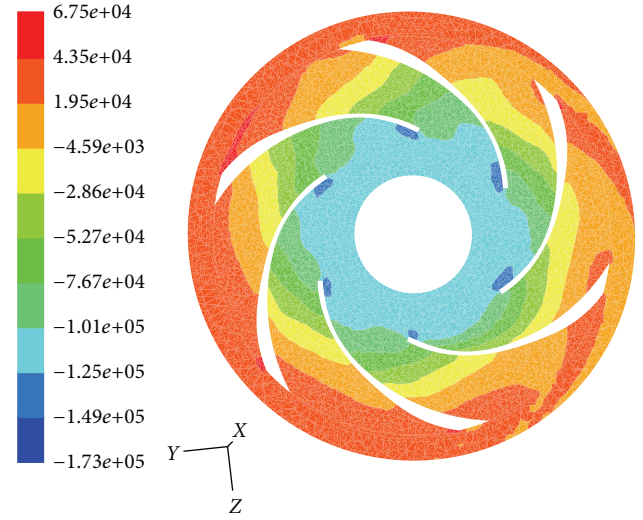


FIGURE 10: Total pressure distribution of centrifugal pump.

but it disappears when the fluid enters into the guide vanes. Figure 10 shows the total pressure distribution of the centrifugal pump on  $x = 0$  section. It shows that the total pressure increases gradually which is ladder-like uniform distribution when fluid flows from the impeller inlet exit, and then enters into the guide blade. It displays different pressure distribution at the impeller export and the entrance of guide vanes because the blade number of the guide vane is 7 and that of the impellers is 6. Due to the different blade number, the relative location of different flow channels displays asymmetric distribution when the impellers rotate.

#### 4. Performance Prediction Based on Numerical Simulation

In order to predict the hydraulic performances of centrifugal pump, the external characteristics including flow, shaft power, lift, and efficiency are calculated.

The flow of inlet surface  $Q$  in the centrifugal pump is defined as follows:

$$Q = \int_A (\rho \vec{v} \cdot \vec{n}) dA, \quad (10)$$

where  $A$  is the area of the inlet or exit of the centrifugal pump,  $\vec{v}$  is the velocity vector of the calculation element,  $\rho$  is fluid density, and  $\vec{n}$  is direction vector on the inlet surface or the exit surface.

The total pressure on the inlet and exit surfaces is respectively defined by the pattern of the mass average value as follows:

$$P_t = \frac{\int_A (\rho p_t |\vec{v} \cdot \vec{n}|) dA}{\int_A (\rho |\vec{v} \cdot \vec{n}|) dA}, \quad (11)$$

where  $p_t$  is the total pressure of the calculation element.

The lift of centrifugal pump is shown as follows:

$$H = \frac{p_{\text{out}} - p_{\text{in}}}{\rho g} + \frac{v_{\text{out}}^2 - v_{\text{in}}^2}{2g} + \Delta Z, \quad (12)$$

where  $P_{\text{in}}$  and  $P_{\text{out}}$  are, respectively, the total pressure of the inlet and exit.  $\Delta Z$  is the vertical distance between the inlet and exit.  $v_{\text{in}}$  and  $v_{\text{out}}$  are, respectively, the speed of the inlet and exit.  $g$  is gravity acceleration.

The shaft power is calculated as follows:

$$P = Mw, \quad (13)$$

$$w = \frac{2\pi n}{60},$$

where  $M$  is the total moment of pressure surface, suction surface, and front and back end plates around  $z$  axis,  $n$  is the rotated speed, and  $w$  is the angular velocity.

The centrifugal pump efficiency is shown as follows:

$$\eta = \frac{\rho g Q H}{M w}. \quad (14)$$

In addition to the design condition, the paper simulates different flow conditions of 0.5Q, 0.7Q, 0.8Q, 0.9Q, 1.1Q, 1.2Q, 1.3Q, and 1.5Q to attain the lift, shaft power, and efficiency, as shown in Table 2.

## 5. Experiment Verification

In order to verify the reliability of the results of numerical simulation, experiments are designed to test the flow, lift, shaft power, and efficiency of the 20BZ4 centrifugal pump. Figures 11, 12, and 13 show, respectively, the experimental characteristic curves of flow and lift, flow and shaft power, and flow and efficiency. The figures show that there are certain differences between the experimental results and numerical results. When the pump physical model is built, the gap region between front and back plates and case is ignored, so the rotation of pump is accompanied by a volume loss. Furthermore mechanical loss such as bearing friction loss and disc loss are also ignored.

Figure 11 shows the relation curve between the flow and lift. The simulation curve has no hump, and it demonstrates that the centrifugal pump has good performances. The trends of experimental curve and simulation curve are consistent. But in addition to the design condition, the experimental data and calculated data in the high flow and low flow have larger difference. MRF is a kind of assumed steady calculation flow model relative to the design condition, so the unsteady factors of flow field are fewer near the design condition and the calculated data and experimental data are consistent. However under off-design conditions, there are many unsteady factors such as the crash between the fluid and pump shell and blade boundary layer separation, which results in difference between calculated data and experimental data.

Figure 12 shows the relation curve between the flow and shaft power. Because the calculated moment is lower than

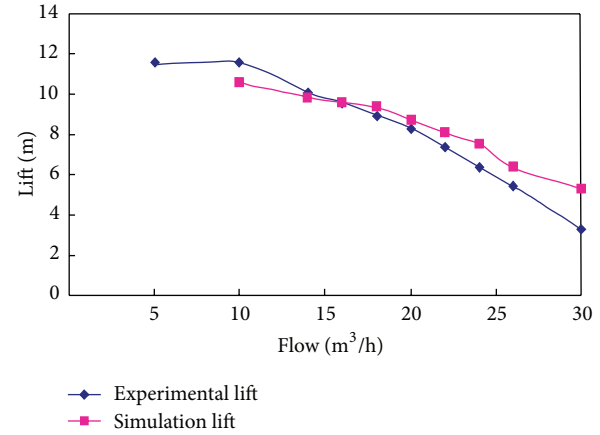


FIGURE 11: Performance curves of flow-lift.

the experimental moment, so the shaft power of numerical simulation is lower than that of experiment. However under high flow conditions, the shaft power of numerical simulation is higher than that of experiment, which is because the relative ideal numerical model is used and the distribution of the unsteady factors in the flow is not taken into account.

Figure 13 shows the relation curve between the flow and efficiency. It demonstrates that the curve first goes up and then down and it becomes relatively flat near the region of design condition. The flow region of high efficiency is wide which demonstrates that the performance is stable around the design condition. When the pump physical model is built, the gap region between front and back plates and case is ignored, so the rotation of pump is accompanied by a volume loss. Furthermore mechanical loss such as bearing friction loss and disc loss are also ignored. The actual losses cause the efficiency of numerical simulation to be higher than that of experiment, which can be seen from the figure.

## 6. Conclusions

(1) Complicated three-dimensional flow model is built including inlet region, impeller flow region, guide-vane flow region, and exit region to simulate flow in 20BZ4 multi-stage centrifugal pump. The method of multireference frame (MRF) is used to model rotating blades and stationary blades by FLUENT.

(2) The simulation results show that the flow in impellers is mostly uniform, no eddy, backflow, and separation flow. The Jet-wake along some blades influences the efficiency. There is secondary flow at blade end and exit of guide vanes. The pressure on pressure surface is higher than that of suction surface and the pressure difference causes the moment of resistance on rotating axis. At the inlet of suction surface the pressure is lowest and cavitations may happen there.

(3) Besides design condition, six off-design conditions are set to predict the external characteristics of hydraulic performances. The comparison between experimental data and simulation data shows that the experimental curve agrees well with the simulation curve under design condition, but

TABLE 2: Performance data under off-design conditions of simulation.

Flow (m <sup>3</sup> /h)	0.5Q	0.7Q	0.8Q	0.9Q	Q	1.1Q	1.2Q	1.3Q	1.5Q
Lift (m)	10.57	9.89	9.57	9.34	8.73	8.05	7.48	6.38	5.29
Shaft power (w)	546.3	617.9	634.7	666.5	686.4	711.7	763.3	760.7	856
Efficiency (%)	52.7	61.2	65.9	68.7	69.3	67.7	64	59.4	50.5

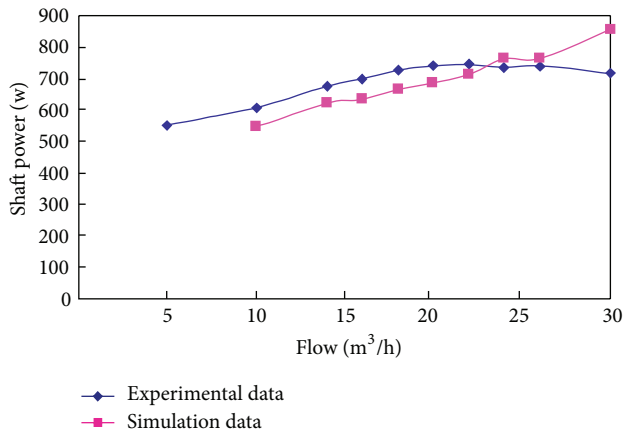


FIGURE 12: Performance curves of flow-shaft power.

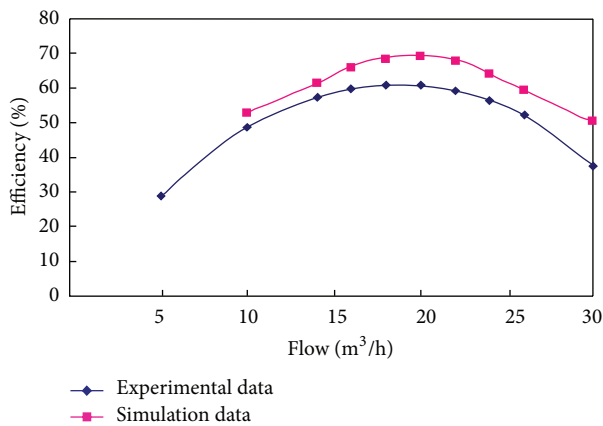


FIGURE 13: Performance curves of flow-efficiency.

under off-design conditions the unsteady factors of flow field influence the precision. The actual losses cause the efficiency of numerical simulation to be higher than that of experiment.

## References

- [1] J. Shi, "The energy conservation improvement and prospect of the centrifugal pump," *General Machinery*, vol. 9, pp. 24–28, 2012.
- [2] H. Si and S. Dike, "Numerical simulation of the three-dimensional flow field in a multistage centrifugal pump and its performance prediction," *Mechanical Science and Technology*, vol. 29, no. 6, pp. 706–708, 2010.
- [3] Z. Li, D. Wu, L. Wang, and B. Huang, "Numerical simulation on internal flow of centrifugal pump during transient operation," *Journal of Engineering Thermophysics*, vol. 30, no. 5, pp. 781–783, 2009.
- [4] Y. Liu and G. Wang, "Computer-aided analysis on inner flow in stamping and welding multistage centrifugal pump's impellers," *Chinese Journal of Mechanical Engineering*, vol. 43, no. 8, pp. 207–211, 2007.
- [5] R. Barrio, J. Fernandez, E. Blanco, and J. Parrondo, "Estimation of radial load in centrifugal pumps using computational fluid dynamics," *European Journal of Mechanics B*, vol. 30, no. 3, pp. 316–324, 2011.
- [6] B. Jafarzadeh, A. Hajari, M. M. Alishahi, and M. H. Akbari, "The flow simulation of a low-specific-speed high-speed centrifugal pump," *Applied Mathematical Modelling*, vol. 35, no. 1, pp. 242–249, 2011.
- [7] M. Asuaje, F. Bakir, S. Kouidri, F. Kenyery, and R. Rey, "Numerical modelization of the flow in centrifugal pump: volute influence in velocity and pressure fields," *International Journal of Rotating Machinery*, vol. 2005, no. 3, pp. 244–255, 2005.
- [8] B. Cui, Z. Zhu, J. Zhang, and Y. Chen, "The flow simulation and experimental study of low-specific-speed high-speed complex centrifugal impellers," *Chinese Journal of Chemical Engineering*, vol. 14, no. 4, pp. 435–441, 2006.
- [9] J. S. Anagnostopoulos, "Numerical calculation of the flow in a centrifugal pump impeller using Cartesian grid," in *Proceedings of the 2nd WSEAS International Conference on Applied and Theoretical Mechanics*, pp. 20–22, Venice, Italy, 2006.



## Research Article

# Heat and Mass Transfer with Free Convection MHD Flow Past a Vertical Plate Embedded in a Porous Medium

**Farhad Ali, Ilyas Khan, Sharidan Shafie, and Norzieha Musthapa**

*Department of Mathematics, Faculty of Science, Universiti Teknologi Malaysia (UTM), Skudai, 81310 Johor Bahru, Malaysia*

Correspondence should be addressed to Sharidan Shafie; [ridafie@yahoo.com](mailto:ridafie@yahoo.com)

Received 7 November 2012; Accepted 11 April 2013

Academic Editor: Zhijun Zhang

Copyright © 2013 Farhad Ali et al. This is an open access article distributed under the Creative Commons Attribution License, which permits unrestricted use, distribution, and reproduction in any medium, provided the original work is properly cited.

An analysis to investigate the combined effects of heat and mass transfer on free convection unsteady magnetohydrodynamic (MHD) flow of viscous fluid embedded in a porous medium is presented. The flow in the fluid is induced due to uniform motion of the plate. The dimensionless coupled linear partial differential equations are solved by using Laplace transform method. The solutions that have been obtained are expressed in simple forms in terms of elementary function  $\exp(\cdot)$  and complementary error function  $\text{erfc}(\cdot)$ . They satisfy the governing equations; all imposed initial and boundary conditions and can immediately be reduced to their limiting solutions. The influence of various embedded flow parameters such as the Hartmann number, permeability parameter, Grashof number, dimensionless time, Prandtl number, chemical reaction parameter, Schmidt number, and Soret number is analyzed graphically. Numerical solutions for skin friction, Nusselt number, and Sherwood number are also obtained in tabular forms.

## 1. Introduction

The process of heat transfer or heat and mass transfer together occurs simultaneously in a moving fluid and plays an important role in the design of chemical processing equipment, nuclear reactors, and formation and dispersion of fog. A detailed discussion on this topic can be found in Raptis [1], Kim and Fedorov [2], El-Arabawy [3], Takhar et al. [4], Alam et al. [5], Chaudhary and Arpita [6], Ferdows et al. [7], Rajesh et al. [8], Rajesh and Varma [9], Bakr [10], and the references therein. Dass et al. [11] considered the mass transfer effects on flow past an impulsively started infinite isothermal vertical plate with constant mass flux. Muthucumaraswamy et al. [12] presented an exact solution to the problem of flow past an impulsively started infinite vertical plate in the presence of uniform heat and mass flux at the plate using Laplace transform technique.

Recently, the free convection flow of magnetohydrodynamic fluid has attracted many researchers in view of its numerous applications in geophysics, astrophysics, meteorology, aerodynamics, magnetohydrodynamic power generators and pumps, boundary layer control energy generators, accelerators, aerodynamics heating, polymer technology, petroleum industry, purification of crude oil, and in material processing

such as extrusion, metal forming, continuous casting wire, and glass fibre drawing. Further, the convective flow through porous medium has applications in the field of chemical engineering for filtration and purification processes. In petroleum technology, it is used to study the movement of natural gas oil and water through oil channels or reservoirs, and in the field of agriculture engineering to study the underground water resources (see e.g., Hayat and Abbas [13], Rahman and Sattar [14], Kim [15], Kaviani [16], Vafai and Tien [17], Jha and Apere [18], Mandal et al. [19], Katagiri [20]). In view of such applications, Chaudhary and Jain [21] analyzed the magnetohydrodynamic free convection flow past an accelerated surface embedded in a porous medium and obtained the exact solutions for the velocity, temperature, and concentration fields using Laplace transform method. Seth et al. [22] investigated the unsteady MHD natural convection flow with radiative heat transfer past an impulsively moving plate with ramped wall temperature. Toki and Tokis [23] obtained the exact solutions for the unsteady free convection flows on a porous plate with time depending heating. Toki [24] developed the analytical solutions for free convection and mass transfer flow near a moving vertical porous plate. Das [25] developed the closed form solutions for the unsteady MHD free convection flow with thermal radiation and mass

transfer over a moving vertical plate. In this continuation, the effect of heat mass transfer on unsteady MHD free convection flow past a moving vertical plate in a porous medium was investigated by Das and Jana [26]. They considered the impulsive, uniform, and oscillating motions of the plate with constant heat and mass diffusion and developed the exact solutions using Laplace transform technique. Recently, Osman et al. [27] analyzed the thermal radiation and chemical reaction effects on unsteady MHD free convection flow through a porous plate embedded in a porous medium with heat source/sink and the closed form solutions are obtained. Khan et al. [28] and Sparrow and Cess [29] analyzed the effects of Hall current and mass transfer on the unsteady MHD free convection flow in a porous channel. The motion in fluid is induced to the external pressure gradient and the closed form solutions for the velocity, temperature, and concentration fields are obtained.

Motivated by the above investigations the present paper aims to study the combined heat and mass effects on the unsteady MHD free convection flow of an incompressible viscous fluid passing through a porous medium. The flow in the fluid is caused due to the uniform motion of the plate. Exact solutions are derived for the velocity distributions, temperature, and concentration fields by using Laplace transform technique and presented graphically for small as well as large times. To the best of authors' knowledge this problem has not been studied before and the reported results are new. The present study is of course of great practical and technological importance, for example, in astrophysical regimes, the presence of planetary debris, cosmic dust, and so forth and creates a suspended porous medium saturated with plasma fluids. Combined buoyancy-generated heat and mass transfer, due to temperature and concentration variations with unsteady MHD free convection flow in fluid-saturated porous media, has several important applications in a variety of engineering processes including heat exchanger devices, petroleum reservoirs, chemical catalytic reactors, solar energy porous water collector systems, and ceramic materials.

This paper is organized as follows. A brief description of the problem formulation is given in Section 2. The exact solutions for the uniformly uniform motion of the plate are derived in Section 3. The graphical results and discussion are provided in Section 4. The conclusions of the paper are given in Section 5 whereas some future recommendations are included in Section 6.

## 2. Description of the Problem Formulation

Let us consider the unsteady one dimensional flow of an incompressible and electrically conducting viscous fluid caused due to the uniform motion of the plate. The  $x^*$ -axis is taken along the plate in the vertical direction and  $y^*$ -axis is taken normal to the plate. The electrically conducting fluid occupies the porous half space  $y^* > 0$ . A uniform magnetic field  $\mathbf{B}_0$  is acting in the transverse direction to the flow. The magnetic Reynolds number is assumed to be small and therefore the induced magnetic field is negligible compared with the applied magnetic field. The applied magnetic field is also taken weak so that Hall and ion slip effects may be

neglected. Initially both the plate and fluid are at the same temperature  $T_\infty^*$  and concentration  $C_\infty^*$ . At time  $t = 0^+$ , the plate begins to slide in its own plane and accelerates against the gravitational field with uniform acceleration in  $x^*$ -direction. Then the temperature and concentration level are raised to  $T_w^*$  and  $C_w^*$  as shown in Figure 1.

The Soret and thermal buoyancy effects are also considered. In addition to the above assumptions, we assume that the internal dissipation is absent and the usual Boussinesq approximation is taken into consideration. Moreover, the pressure gradient in the flow direction is compensated by the gradient of the hydrostatic pressure gradient of the fluid. As a result the governing equations of momentum, energy, and concentration are derived as follows:

$$\frac{\partial u^*}{\partial t^*} = \nu \frac{\partial^2 u^*}{\partial y^{*2}} - \frac{\sigma B_0^2 u^*}{\rho} - \frac{\nu u^*}{K^*} + g\beta(T^* - T_\infty^*) + g\beta^*(C^* - C_\infty^*), \quad (1)$$

$$\rho c_p \frac{\partial T^*}{\partial t^*} = k \frac{\partial^2 T^*}{\partial y^{*2}} - \frac{\partial q_r^*}{\partial y^*}, \quad (2)$$

$$\frac{\partial C^*}{\partial t^*} = D \frac{\partial^2 C^*}{\partial y^{*2}} + \frac{DK_T}{T_m} \frac{\partial^2 T^*}{\partial y^{*2}} - K_r^*(C^* - C_\infty^*), \quad (3)$$

with the following initial and boundary conditions:

$$\begin{aligned} t^* \leq 0 : u^* &= 0, \quad T^* = T_\infty^*, \quad C^* = C_\infty^*, \\ &\forall y^* \geq 0, \\ t^* > 0 : u^* &= f(t^*), \quad T^* = T_w^*, \quad C^* = C_w^* \\ &\text{at } y^* = 0, \\ : u^* &\longrightarrow 0, \quad T^* \longrightarrow T_\infty^*, \quad C^* \longrightarrow C_\infty^* \\ &\text{as } y^* \longrightarrow \infty, \end{aligned} \quad (4)$$

where  $f(t^*)$  is the uniform acceleration of the plate,  $x^*$  and  $y^*$  (m) are the distances along and perpendicular to the plate,  $t^*$  (s) is the time,  $u^*$  ( $\text{ms}^{-1}$ ), denote the fluid velocity in the  $x^*$ -direction,  $T^*$  (K) temperature,  $T_\infty^*$  (K) temperature far from the plate,  $T_w^*$  (K) temperature at the wall,  $C^*$  ( $\text{mol m}^{-3}$ ) are the species concentration,  $C_w^*$  ( $\text{mol m}^{-3}$ ) surface concentration,  $C_\infty^*$  ( $\text{mol m}^{-3}$ ) species concentration far from the surface,  $\beta$  ( $1/\text{K}$ ) the volumetric coefficient of thermal expansion,  $\beta^*$  ( $\text{mol m}^{-3}$ ) $^{-1}$  or ( $\text{m}^3 \text{mol}^{-1}$ ) is the volumetric coefficient of expansion for concentration,  $\nu = \mu/\rho$  ( $\text{m}^2 \text{s}^{-1}$ ) the kinematic viscosity,  $\mu$  ( $\text{kgm}^{-1} \text{s}^{-1}$ ) viscosity,  $\rho$  ( $\text{kgm}^{-3}$ ) the fluid density,  $c_p$  ( $\text{kg}^{-1} \text{K}^{-1}$ ) is the specific heat capacity,  $q_r^*$  the radiative heat flux in  $x^*$ -direction,  $D$  ( $\text{m}^2 \text{s}^{-1}$ ) is mass diffusivity,  $k$  ( $\text{Wm}^{-1} \text{K}^{-1}$ ) is the thermal conductivity of the fluid,  $\sigma$  ( $\text{Sm}^{-1}$ ) the electrical conductivity of the fluid,  $K^* > 0$  ( $\text{m}^2$ ) is the permeability of the porous medium,  $T_m$  (K) is the mean fluid temperature,  $T_\infty^*$  is the free stream temperature,  $C_\infty^*$  is the free stream concentration of the species,  $K_T$  is the thermal-diffusion ratio, and  $K_r^*$  the chemical reaction constant. The radiative heat flux term for an optically

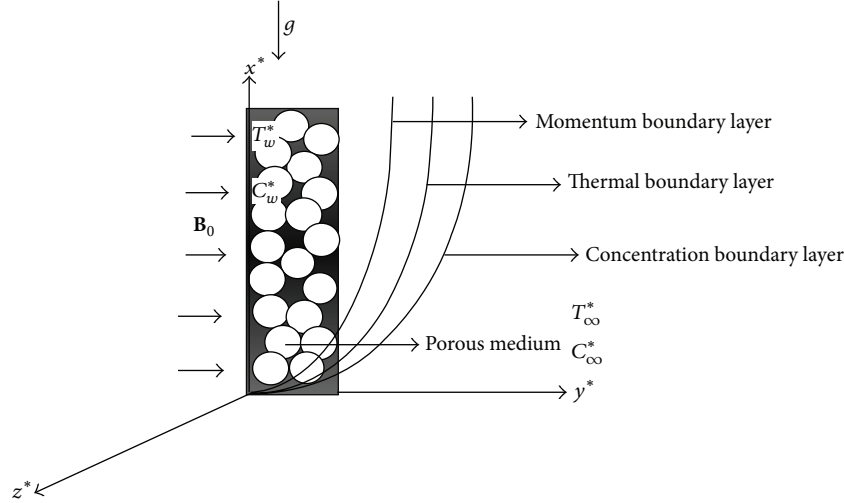


FIGURE 1: Flow geometry and physical coordinate system.

thin fluid is simplified by making use of the Rosseland approximation (Sparrow and Cess [29])

$$q_r^* = -\frac{4\sigma^*}{3k^*} \frac{\partial T^{*4}}{\partial y^*}, \quad (5)$$

where  $\sigma^*$  ( $\text{Wm}^{-2} \text{K}^{-4}$ ) is the Stefan-Boltzmann constant and  $k^*$  ( $\text{m}^{-1}$ ) is the mean absorption coefficient. It is assumed that the temperature differences within the flow are sufficiently small such that the term  $T^{*4}$  is expressed as the linear function of temperature. Thus expanding  $T^{*4}$  about  $T_\infty^*$  using Taylor series expansion and neglecting higher order terms we get

$$T^{*4} \cong 4T_\infty^{*3} T^* - 3T_\infty^{*4}. \quad (6)$$

From (5) and (6), (2) reduces to the following form:

$$\rho c_p \frac{\partial T^*}{\partial t^*} = k \frac{\partial^2 T^*}{\partial y^{*2}} + \frac{16\sigma^* T_\infty^{*3}}{3k^*} \frac{\partial^2 T^*}{\partial y^{*2}}. \quad (7)$$

### 3. Flow due to Uniform Motion of the Plate

For uniform motion of the plate, we take  $f(t^*) = At^*$  and define the following dimensionless variables:

$$u = \frac{u^*}{(\nu A)^{1/3}}, \quad y = y^* \left( \frac{A}{\nu^2} \right)^{1/3}, \quad t = t^* \left( \frac{A^2}{\nu} \right)^{1/3}, \quad (8)$$

$$\theta = \frac{T^* - T_\infty^*}{T_w^* - T_\infty^*}, \quad \phi = \frac{C^* - C_\infty^*}{C_w^* - C_\infty^*},$$

where  $A$  with dimension  $L/T^2$  denotes the uniform acceleration of the plate in  $x$ -direction,  $u$  is the dimensionless velocity,  $y$  dimensionless coordinate perpendicular to the plate,  $t$  is the dimensionless time,  $\theta$  is the dimensionless temperature and  $\phi$  is the dimensionless species concentration.

Hence the governing equations in dimensionless form are

$$\frac{\partial u}{\partial t} = \frac{\partial^2 u}{\partial y^2} - Hu + Gr\theta + Gm\phi, \quad (9)$$

$$u(0, t) = t, \quad u(\infty, t) = 0 \quad t > 0,$$

$$u(y, 0) = 0, \quad y \geq 0,$$

$$F^* \frac{\partial \theta}{\partial t} = \frac{\partial^2 \theta}{\partial y^2}, \quad (10)$$

$$\theta(0, t) = 1, \quad \theta(\infty, t) = 0, \quad t > 0,$$

$$\theta(y, 0) = 0, \quad y \geq 0,$$

$$\frac{\partial \phi}{\partial t} = \frac{1}{Sc} \frac{\partial^2 \phi}{\partial y^2} + Sr \frac{\partial^2 \theta}{\partial y^2} - \gamma \phi, \quad (11)$$

$$\phi(0, t) = 1, \quad \phi(\infty, t) = 0, \quad t > 0,$$

$$\phi(y, 0) = 0, \quad y \geq 0,$$

where

$$\frac{1}{K} = \frac{\nu^{4/3}}{K^* A^{2/3}}, \quad M^2 = \frac{\sigma B_0^2 \nu^{1/3}}{\rho A^{2/3}},$$

$$Sr = \frac{DK_T (T_w^* - T_\infty^*)}{T_m \nu (C_w^* - C_\infty^*)}, \quad Pr = \frac{\mu c_p}{k},$$

$$Gr = \frac{g\beta (T_w^* - T_\infty^*)}{A}, \quad Gm = \frac{g\beta^* (C_w^* - C_\infty^*)}{A}, \quad (12)$$

$$\gamma = \frac{K_r^* \nu^{1/3}}{A^{2/3}},$$

$$H = M^2 + \frac{1}{K}, \quad R = \frac{16\sigma^* T_\infty^{*3}}{3kk^*},$$

$$F^* = \frac{Pr}{1+R}, \quad Sc = \frac{\nu}{D}.$$

Here  $M$  is a magnetic parameter called Hartmann number,  $K$  is the dimensionless permeability,  $Sc$  is Schmidt number,  $R$  is Radiation parameter,  $Gr$  is Grashof number, and  $Sr$  is Soret number. The well-posed problems defined by (9)–(11) will be solved by using the Laplace transform technique. Hence the problem in the transformed plane is given as

$$\begin{aligned} \frac{d^2 \bar{u}}{dy^2} - (H + q) \bar{u} + Gr \bar{\theta} + Gm \bar{\phi} &= 0, \\ \bar{u}(0, q) &= \frac{1}{q^2}, \quad \bar{u}(\infty, q) = 0, \\ \frac{d^2 \bar{\theta}}{dy^2} - F^* q \bar{\theta} &= 0, \\ \bar{\theta}(0, q) &= \frac{1}{q}, \quad \bar{\theta}(\infty, q) = 0, \\ \frac{d^2 \bar{\phi}}{dy^2} - (\gamma + q) Sc \bar{\phi} + Sc Sr \frac{d^2 \bar{\theta}}{dy^2} &= 0, \\ \bar{\phi}(0, q) &= \frac{1}{q}, \quad \bar{\phi}(\infty, q) = 0, \end{aligned} \quad (13)$$

where  $q$  is the Laplace transformation parameter.

The solutions of (13) in the transformed  $q$ -plane are given by

$$\begin{aligned} \bar{u}(y, q) &= \frac{1}{q^2} \exp(-y\sqrt{q+H}) + \frac{a_8}{q} \exp(-y\sqrt{q+H}) \\ &\quad - \frac{a_9}{q+a_0} \exp(-y\sqrt{q+H}) \\ &\quad + \frac{a_{10}}{q-H_1^*} \exp(-y\sqrt{q+H}) \\ &\quad + \frac{a_{11}}{q-H^*} \exp(-y\sqrt{q+H}) \\ &\quad + \frac{a_5}{q-H_1^*} \exp(-y\sqrt{F^*q}) \\ &\quad - \frac{a_{11}}{q-H^*} \exp(-y\sqrt{F^*q}) + \frac{a_4}{q} \exp(-y\sqrt{F^*q}) \\ &\quad - \frac{a_6}{q} \exp(-y\sqrt{(q+\gamma)Sc}) \\ &\quad + \frac{a_9}{q+a_0} \exp(-y\sqrt{(q+\gamma)Sc}) \\ &\quad - \frac{a_7}{q-H_1^*} \exp(-y\sqrt{(q+\gamma)Sc}), \end{aligned} \quad (14)$$

$$\bar{\theta}(y, q) = \frac{1}{q} \exp(-y\sqrt{F^*q}), \quad (15)$$

$$\begin{aligned} \bar{\phi}(y, q) &= \frac{1}{q} \exp(-y\sqrt{(q+\gamma)Sc}) \\ &\quad + \frac{S^*}{q-H_1^*} \exp(-y\sqrt{(q+\gamma)Sc}) \\ &\quad - \frac{S^*}{q-H_1^*} \exp(-y\sqrt{F^*q}), \end{aligned} \quad (16)$$

where

$$\begin{aligned} Gr^* &= \frac{Gr}{F^*-1}, \quad H^* = \frac{H}{F^*-1}, \\ H_1^* &= \frac{\gamma Sc}{F^*-Sc}, \quad S^* = \frac{Sc Sr F^*}{F^*-Sc}, \\ a_0 &= \frac{\gamma Sc - H}{Sc - 1}, \quad a_1 = \frac{Gm S^*}{F^*-1}, \\ a_2 &= \frac{Gm}{Sc - 1}, \quad a_3 = \frac{Gm S^*}{Sc - 1}, \quad a_4 = \frac{Gr^*}{H^*}, \\ a_5 &= \frac{a_1}{H_1^* - H^*}, \quad a_6 = \frac{a_2}{a_0}, \\ a_7 &= \frac{a_3}{H_1^* + a_0}, \quad a_8 = a_6 - a_4, \quad a_9 = a_6 + a_7, \\ a_{10} &= a_7 - a_5, \quad a_{11} = a_4 + a_5. \end{aligned} \quad (17)$$

The inverse Laplace transform of (14)–(16) yields

$$u(y, t) = I_1 + a_8 I_2 - a_9 I_3 + a_{10} I_4 + a_{11} I_5 + a_5 I_6 - a_{11} I_7 + a_4 I_8 - a_6 I_9 + a_9 I_{10} - a_7 I_{11}, \quad (18)$$

$$\theta(y, t) = I_8, \quad (19)$$

$$\phi(y, t) = S^* (I_{11} - I_6) + I_9, \quad (20)$$

with

$$\begin{aligned} I_1 &= \frac{1}{2} \left[ \left( t - \frac{y}{2\sqrt{H}} \right) e^{-y\sqrt{H}} \operatorname{erfc} \left( \frac{y}{2\sqrt{t}} - \sqrt{Ht} \right) \right. \\ &\quad \left. + e^{y\sqrt{H}} \operatorname{erfc} \left( \frac{y}{2\sqrt{t}} + \sqrt{Ht} \right) \left( t + \frac{y}{2\sqrt{H}} \right) \right], \\ I_2 &= \frac{1}{2} \left[ e^{-y\sqrt{H}} \operatorname{erfc} \left( \frac{y}{2\sqrt{t}} - \sqrt{Ht} \right) \right. \\ &\quad \left. + e^{y\sqrt{H}} \operatorname{erfc} \left( \frac{y}{2\sqrt{t}} + \sqrt{Ht} \right) \right], \\ I_3 &= \frac{e^{-a_0 t}}{2} \left[ e^{-y\sqrt{H-a_0}} \operatorname{erfc} \left( \frac{y}{2\sqrt{t}} - \sqrt{(H-a_0)t} \right) \right. \\ &\quad \left. + e^{y\sqrt{H-a_0}} \operatorname{erfc} \left( \frac{y}{2\sqrt{t}} + \sqrt{(H-a_0)t} \right) \right], \\ I_4 &= \frac{e^{H_1^* t}}{2} \left[ e^{-y\sqrt{H_1^*+H}} \operatorname{erfc} \left( \frac{y}{2\sqrt{t}} - \sqrt{(H_1^*+H)t} \right) \right. \\ &\quad \left. + e^{y\sqrt{H_1^*+H}} \operatorname{erfc} \left( \frac{y}{2\sqrt{t}} + \sqrt{(H_1^*+H)t} \right) \right], \end{aligned}$$

$$\begin{aligned}
I_5 &= \frac{e^{H^*t}}{2} \left[ e^{-\gamma\sqrt{H^*+H}} \operatorname{erf} c \left( \frac{\gamma}{2\sqrt{t}} - \sqrt{(H+H^*)t} \right) \right. \\
&\quad \left. + e^{\gamma\sqrt{H^*+H}} \operatorname{erf} c \left( \frac{\gamma}{2\sqrt{t}} + \sqrt{(H+H^*)t} \right) \right], \\
I_6 &= \frac{e^{H_1^*t}}{2} \left[ e^{-\gamma\sqrt{F^*H_1^*}} \operatorname{erf} c \left( \frac{\gamma\sqrt{F^*}}{2\sqrt{t}} - \sqrt{H_1^*t} \right) \right. \\
&\quad \left. + e^{\gamma\sqrt{F^*H_1^*}} \operatorname{erf} c \left( \frac{\gamma\sqrt{F^*}}{2\sqrt{t}} + \sqrt{H_1^*t} \right) \right], \\
I_7 &= \frac{e^{H^*t}}{2} \left[ e^{-\gamma\sqrt{F^*H^*}} \operatorname{erf} c \left( \frac{\gamma\sqrt{F^*}}{2\sqrt{t}} - \sqrt{H^*t} \right) \right. \\
&\quad \left. + e^{\gamma\sqrt{F^*H^*}} \operatorname{erf} c \left( \frac{\gamma\sqrt{F^*}}{2\sqrt{t}} + \sqrt{H^*t} \right) \right], \\
I_8 &= \operatorname{erf} c \left( \frac{\gamma\sqrt{F^*}}{2\sqrt{t}} \right), \\
I_9 &= \frac{1}{2} \left[ e^{-\gamma\sqrt{\gamma\operatorname{Sc}}} \operatorname{erf} c \left( \frac{\gamma\sqrt{\operatorname{Sc}}}{2\sqrt{t}} - \sqrt{\gamma t} \right) \right. \\
&\quad \left. + e^{\gamma\sqrt{\gamma\operatorname{Sc}}} \operatorname{erf} c \left( \frac{\gamma\sqrt{\operatorname{Sc}}}{2\sqrt{t}} + \sqrt{\gamma t} \right) \right], \\
I_{10} &= \frac{e^{-a_0t}}{2} \left[ e^{-\gamma\sqrt{\operatorname{Sc}(\gamma-a_0)}} \operatorname{erf} c \left( \frac{\gamma\sqrt{\operatorname{Sc}}}{2\sqrt{t}} - \sqrt{(\gamma-a_0)t} \right) \right. \\
&\quad \left. + e^{\gamma\sqrt{\operatorname{Sc}(\gamma-a_0)}} \operatorname{erf} c \left( \frac{\gamma\sqrt{\operatorname{Sc}}}{2\sqrt{t}} + \sqrt{(\gamma-a_0)t} \right) \right], \\
I_{11} &= \frac{e^{H_1^*t}}{2} \left[ e^{-\gamma\sqrt{\operatorname{Sc}(H_1^*+\gamma)}} \operatorname{erf} c \left( \frac{\gamma\sqrt{\operatorname{Sc}}}{2\sqrt{t}} - \sqrt{(H_1^*+\gamma)t} \right) \right. \\
&\quad \left. + e^{\gamma\sqrt{\operatorname{Sc}(H_1^*+\gamma)}} \operatorname{erf} c \left( \frac{\gamma\sqrt{\operatorname{Sc}}}{2\sqrt{t}} + \sqrt{(H_1^*+\gamma)t} \right) \right], \tag{21}
\end{aligned}$$

where  $\operatorname{erf} c(x)$  is the complementary error function. It is important to note that the above solutions are valid for  $\operatorname{Pr} \neq 1$  and  $\operatorname{Sc} \neq 1$ . The solutions for  $\operatorname{Pr} = 1$  and  $\operatorname{Sc} = 1$ , can be easily obtained by substituting  $\operatorname{Pr} = \operatorname{Sc} = 1$  into (10) and (11) and repeating the same process as discussed above.

**3.1. Skin-Friction.** The expression for skin-friction is given by

$$\tau^* = -\mu \frac{\partial u^*}{\partial y^*} \Big|_{y^*=0}, \tag{22}$$

which in view of (8) reduces to

$$\tau = -\frac{\partial u}{\partial y}, \quad \tau = \frac{\tau^*}{\rho U_o^2}. \tag{23}$$

Hence from (18), we get

$$\begin{aligned}
\tau &= \frac{a_8 e^{-Ht}}{\sqrt{\pi t}} - \frac{a_{11} \sqrt{F^*}}{\sqrt{\pi t}} + \frac{a_4 \sqrt{F^*}}{\sqrt{\pi t}} + \frac{a_5 \sqrt{F^*}}{\sqrt{\pi t}} - \frac{a_6 e^{-\gamma t} \sqrt{\operatorname{Sc}}}{\sqrt{\pi t}} \\
&\quad + \frac{e^{-Ht} \sqrt{t}}{\sqrt{\pi}} + \frac{t \sqrt{H}}{2} (-1 + \operatorname{erf}(\sqrt{Ht})) + \frac{\operatorname{erf}(\sqrt{Ht})}{2\sqrt{H}} \\
&\quad + a_8 \sqrt{H} \operatorname{erf}(\sqrt{Ht}) + \frac{t \sqrt{H}}{2} (1 + \operatorname{erf}(\sqrt{Ht})) \\
&\quad - a_6 \sqrt{\operatorname{Sc} \gamma} \operatorname{erf}(\sqrt{\gamma t}) - a_{11} e^{H^*t} \sqrt{H^* F^*} \operatorname{erf}(\sqrt{H^* t}) \\
&\quad + a_5 e^{H_1^*t} \sqrt{F^* H_1^*} \operatorname{erf}(\sqrt{H_1^* t}) \\
&\quad - \frac{1}{2} a_{11} e^{H^*t} \left\{ -\frac{2e^{-Ht-H^*t}}{\sqrt{\pi t}} + \sqrt{H+H^*} \right. \\
&\quad \quad \times (-1 - \operatorname{erf}(\sqrt{(H+H^*)t}) + \sqrt{H+H^*}) \\
&\quad \quad \times (1 - \operatorname{erf}(\sqrt{(H+H^*)t})) \Big\} \\
&\quad - \frac{1}{2} a_{10} e^{H_1^*t} \left\{ -\frac{2e^{-(H+H_1^*)t}}{\sqrt{\pi t}} + \sqrt{H+H_1^*} \right. \\
&\quad \quad \times (-1 - \operatorname{erf}(\sqrt{(H+H_1^*)t})) \\
&\quad \quad \times \sqrt{H+H_1^*} (1 - \operatorname{erf}(\sqrt{(H+H_1^*)t})) \Big\} \\
&\quad - \frac{1}{2} a_9 e^{-a_0t} \left\{ \frac{2e^{a_0t-Ht}}{\sqrt{\pi t}} - \sqrt{H-a_0} \right. \\
&\quad \quad \times (-1 - \operatorname{erf}(\sqrt{-a_0t+Ht})) \\
&\quad \quad - \sqrt{H-a_0} (1 - \operatorname{erf}(\sqrt{-a_0t+Ht})) \Big\} \\
&\quad - \frac{1}{2} a_9 e^{-a_0t} \left\{ -\frac{2e^{a_0t-\gamma t} \sqrt{\operatorname{Sc}}}{\sqrt{\pi t}} + \sqrt{(-a_0+\gamma) \operatorname{Sc}} \right. \\
&\quad \quad \times (-1 - \operatorname{erf}(\sqrt{(-a_0+\gamma)t})) \\
&\quad \quad + \sqrt{(-a_0+\gamma) \operatorname{Sc}} \\
&\quad \quad \times (1 - \operatorname{erf}(\sqrt{(-a_0+\gamma)t})) \Big\} \\
&\quad - \frac{1}{2} a_7 e^{H_1^*t} \left\{ \frac{2e^{-(H_1^*+\gamma)t}}{\sqrt{\pi t}} - \sqrt{\operatorname{Sc} \sqrt{H_1^*+\gamma}} \right. \\
&\quad \quad \times (-1 - \operatorname{erf}(\sqrt{(H_1^*+\gamma)t}))
\end{aligned}$$

$$\begin{aligned}
& -\sqrt{Sc}\sqrt{H_1^* + \gamma} \\
& \times \left( 1 - \operatorname{erf} \left( \sqrt{(H_1^* + \gamma)t} \right) \right) \Big\}. \quad (24)
\end{aligned}$$

**3.2. Nusselt Number.** The rate of heat transfer for the present problem is given as

$$\begin{aligned}
Nu &= -k \frac{\partial T^*}{\partial y^*} \Big|_{y^*=0}, \\
Nu &= \frac{\partial \theta}{\partial y} \Big|_{y=0}, \quad (25) \\
Nu &= \sqrt{\frac{F^*}{\pi t}}.
\end{aligned}$$

**3.3. Sherwood Number.** The rate of mass transfer is given by

$$\begin{aligned}
Sh &= \frac{\partial C^*}{\partial y^*} \Big|_{y^*=0}, \\
Sh &= -\frac{1}{\sqrt{\pi t}} \left\{ e^{-\gamma t} \left( -e^{\gamma t} \sqrt{F^*} S^* + \sqrt{Sc} + S^* \sqrt{Sc} \right. \right. \\
& \quad \left. \left. - e^{H^* t + \gamma t} S^* \sqrt{\pi t H^* F^*} \operatorname{erf} \left( \sqrt{H^* t} \right) \right) \right. \quad (26) \\
& \quad \left. + e^{\gamma t} \sqrt{\gamma Sc \pi t} \operatorname{erf} \left( \sqrt{\gamma t} \right) + e^{H^* t + \gamma t} S^* \right. \\
& \quad \left. \times \sqrt{\pi t Sc} \sqrt{H^* + \gamma} \operatorname{erf} \left( \sqrt{(H^* + \gamma)t} \right) \right\}.
\end{aligned}$$

It is important to note that solutions (18)–(20) satisfy all the imposed boundary and initial conditions. Further, the solutions obtained here are more general and the existing solutions in the literature appeared as the limiting cases.

- (1) The present solutions given by (18)–(20) in the absence of radiation effect and by taking the thermal-diffusion ratio ( $K_T$ ) and the chemical reaction constant ( $K_r^*$ ) equal to zero reduce to the solutions of Das and Jana [26] (see (4.2), (3.8), and (3.9)).
- (2) The solutions (18)–(20) for the flow of optically thick fluid in a nonporous medium with  $K_r^* = K_T = 0$ , give the solutions of Das [25] (see (4.4), (3.1), and (3.2)).

## 4. Graphical Results and Discussion

An exact analysis is presented to investigate the combined effects of heat mass transfer on the transient MHD free convective flow of an incompressible viscous fluid past a vertical plate moving with uniform motion and embedded in a porous medium. The expressions for the velocity  $u$ , temperature  $\theta$ , and concentration  $\phi$  are obtained by using Laplace transform method. In order to understand the physical behavior of the dimensionless parameters such as Hartmann

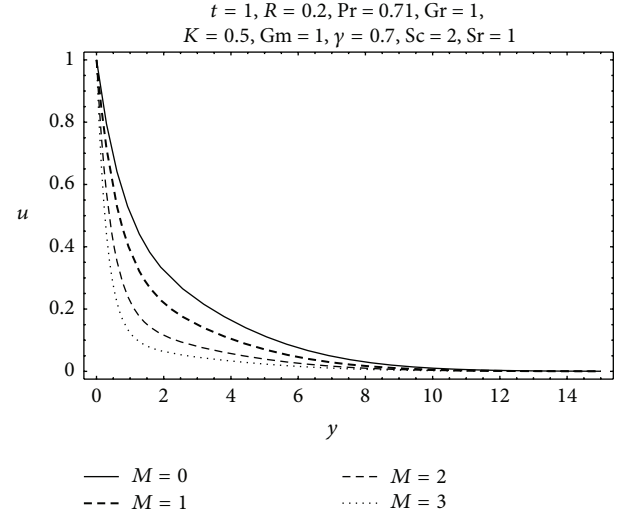


FIGURE 2: Velocity profiles for different values of  $M$ .

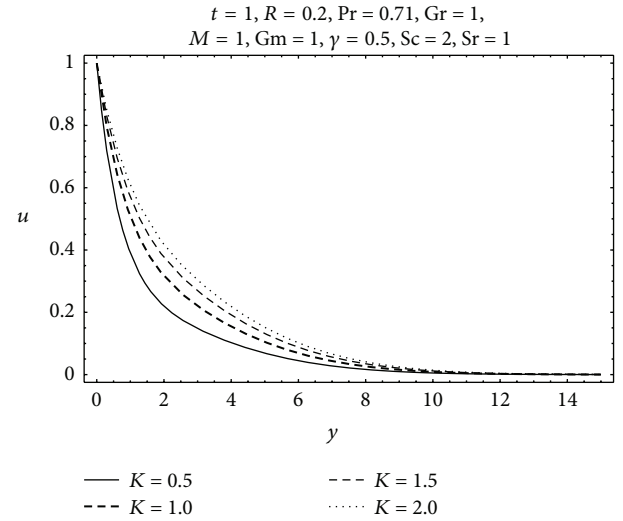
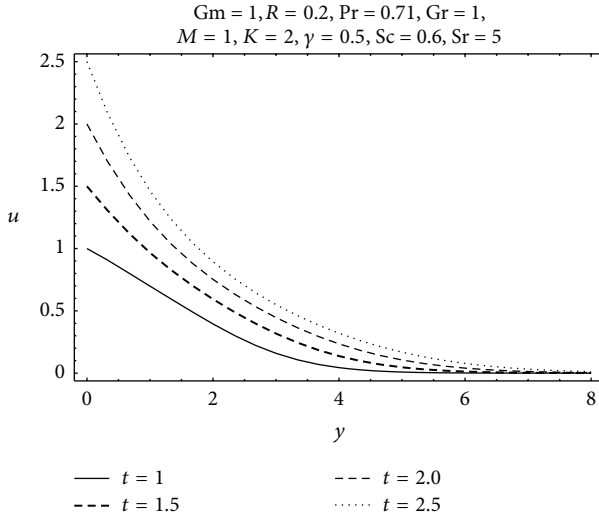
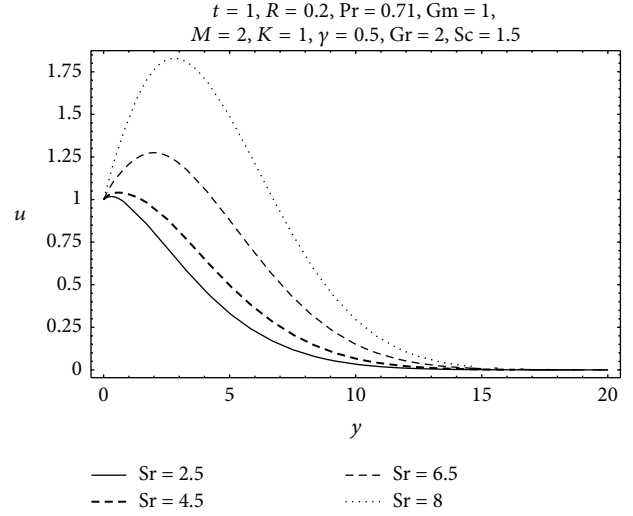
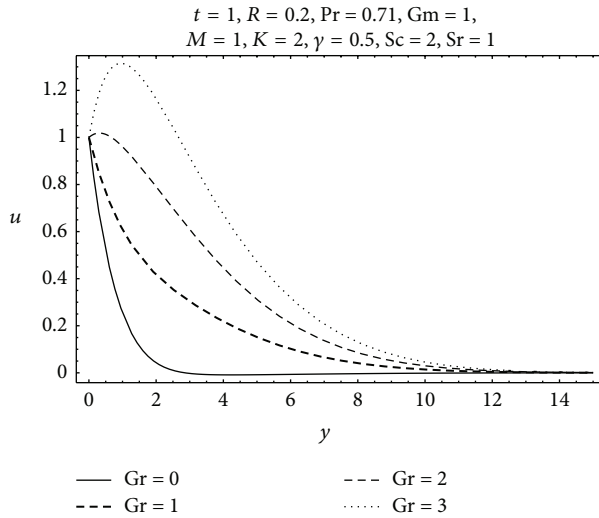
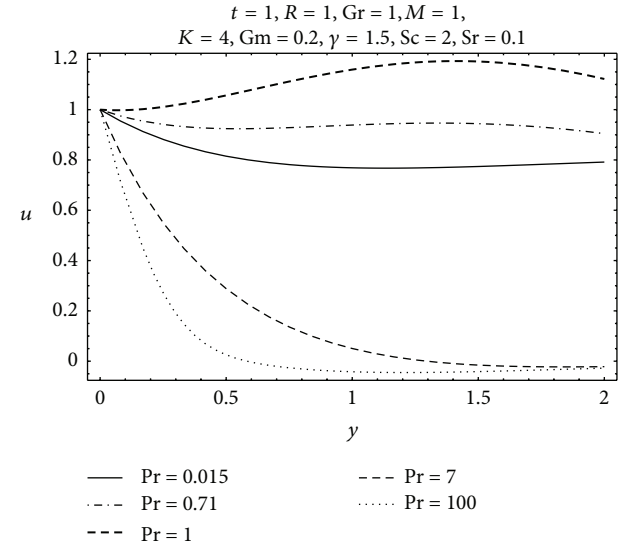
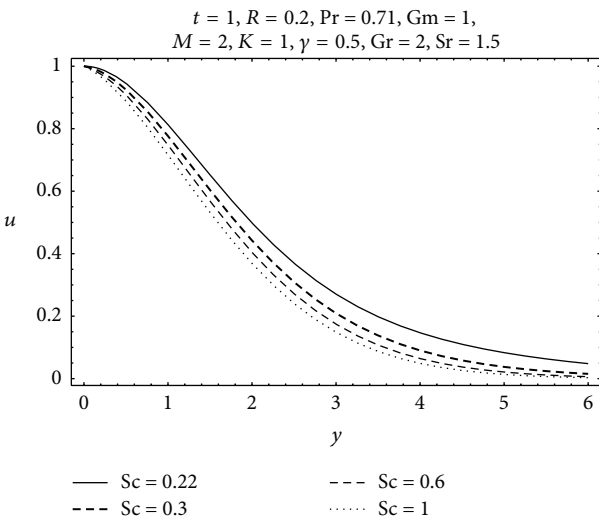


FIGURE 3: Velocity profiles for different values of  $K$ .

number  $M$  also called magnetic parameter, permeability parameter  $K$ , Grashof number  $Gr$ , dimensionless time  $t$ , Prandtl number  $Pr$ , radiation parameter  $R$ , chemical reaction parameter  $\gamma$ , Schmidt number  $Sc$ , and Soret number  $Sr$ , Figures 2–17 have been displayed for  $u$ ,  $\theta$ , and  $\phi$ .

Figure 2 presents the velocity profile for different values of  $M$ . It is observed that the velocity and boundary layer thickness decreases upon increasing the Hartmann number  $M$ . It is due to the fact that the application of transverse magnetic field results a resistive type force (called Lorentz force) similar to drag force and upon increasing the values of  $M$  increases the drag force which leads to the deceleration of the flow. Figure 3 is sketched in order to explore the variations of permeability parameter  $K$ . It is found that the velocity increases with increasing values of  $K$ . This is due to the fact that increasing values of  $K$  reduces the drag force which assists the fluid considerably to move fast. The variation of



FIGURE 4: Velocity profiles for different values of  $t$ .FIGURE 7: Velocity profiles for different values of  $Sr$ .FIGURE 5: Velocity profiles for different values of  $Gr$ .FIGURE 8: Velocity profiles for different values of  $Pr$ .FIGURE 6: Velocity profiles for different values of  $Sc$ .

velocity for different values of dimensionless time  $t$  is shown in Figure 4. It is noticed that velocity increases with increasing time. Further, this figure verifies the boundary conditions of velocity given in (9). Initially, velocity takes the values of time and later for large values of  $y$ , and the velocity tends to zero with increasing time. It is observed from Figure 5 that the fluid velocity increases with increasing  $Gr$ . Figure 6 reveals that velocity profiles decrease with the increase of Schmidt number  $Sc$ , while an opposite phenomenon is observed in case of Soret number  $Sr$  as shown in Figure 7.

Velocity, temperature, and concentration profiles for some realistic values of Prandtl number  $Pr = 0.015, 0.71, 1.0, 7.0, 100$ , which are important in the sense that they physically correspond to mercury, air, electrolytic solution, water, and engine oil, are shown in Figures 8–10, respectively. From Figure 8, it is found that the momentum boundary layer thickness increases for the fluids with  $Pr < 1$  and decreases for

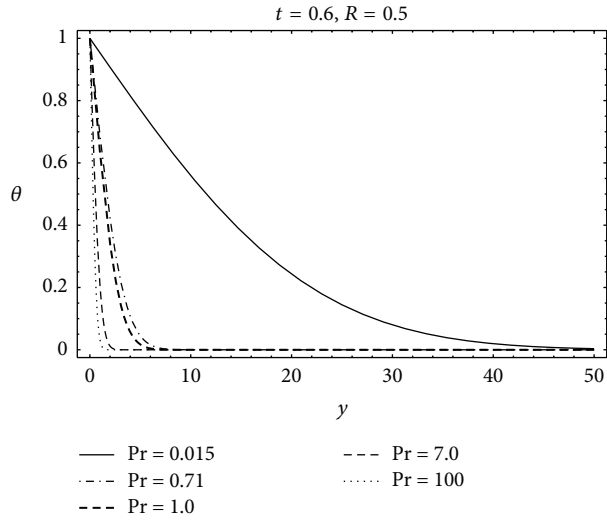


FIGURE 9: Temperature profiles for different values of Pr.

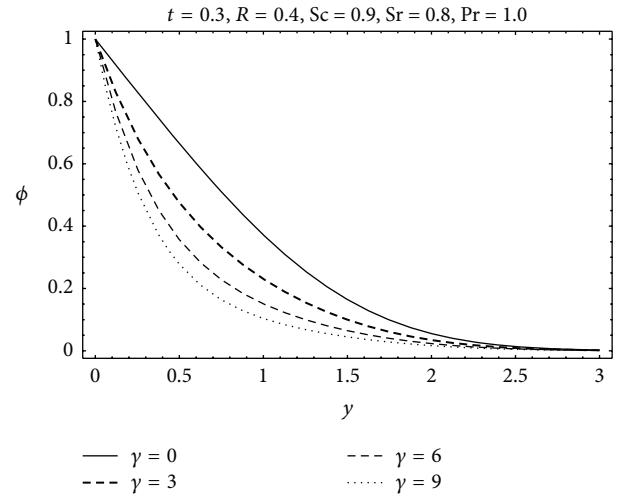
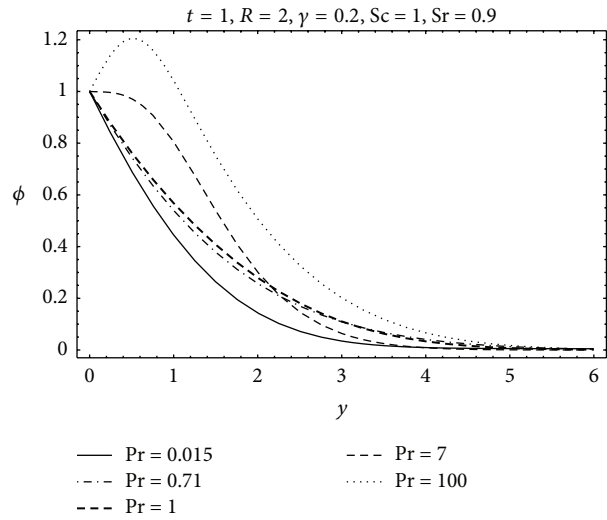
FIGURE 12: Concentration profiles for different values of  $\gamma$ .

FIGURE 10: Concentration profiles for different values of Pr.

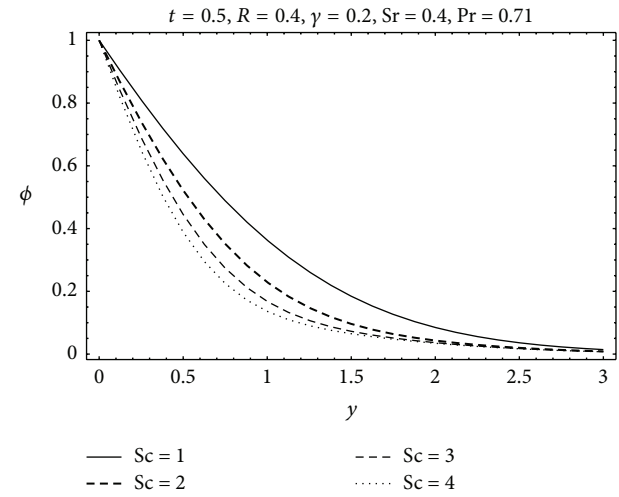


FIGURE 13: Concentration profiles for different values of Sc.

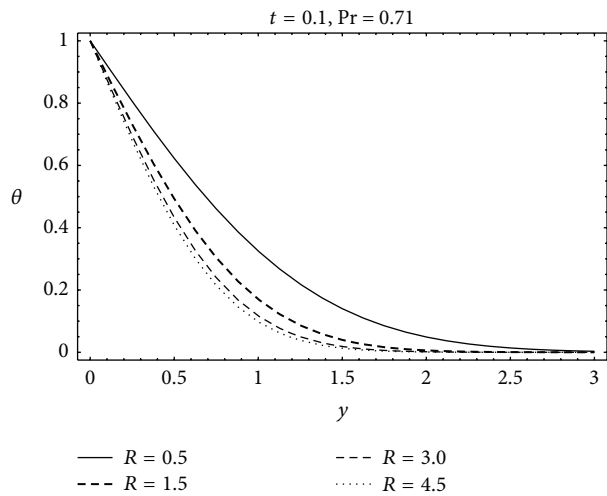


FIGURE 11: Temperature profiles for different values of R.

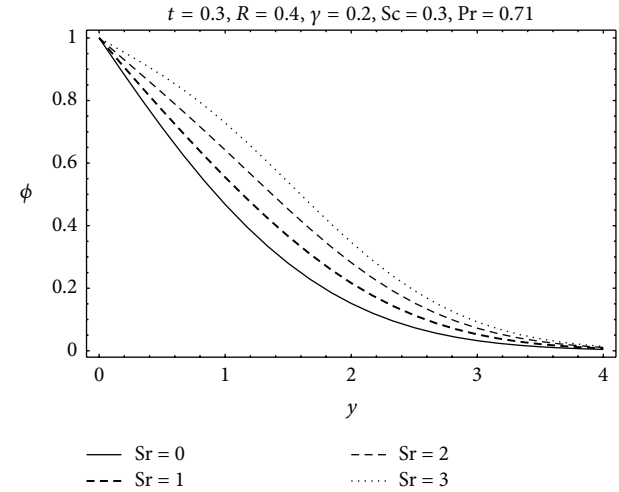
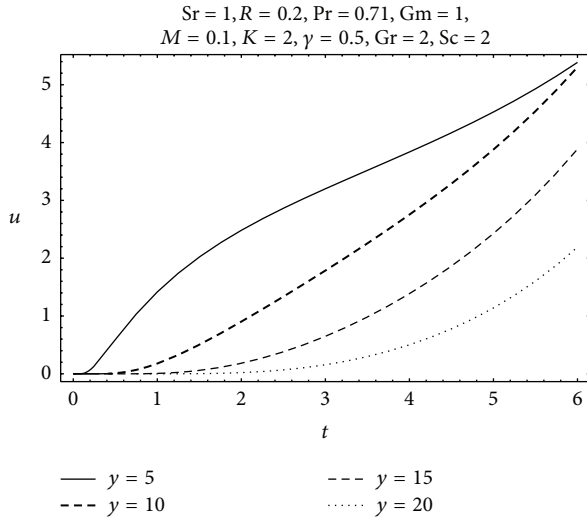
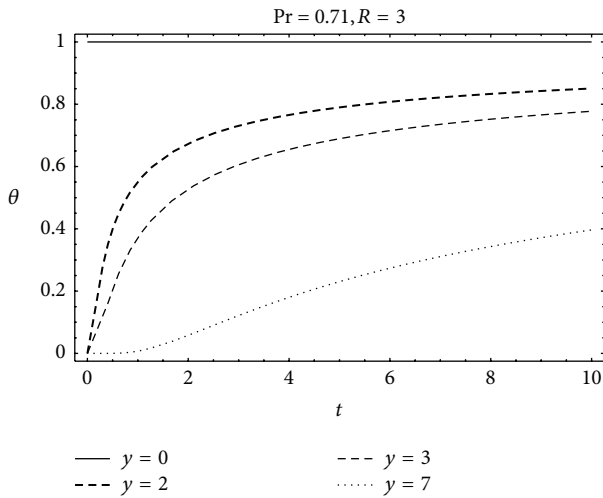
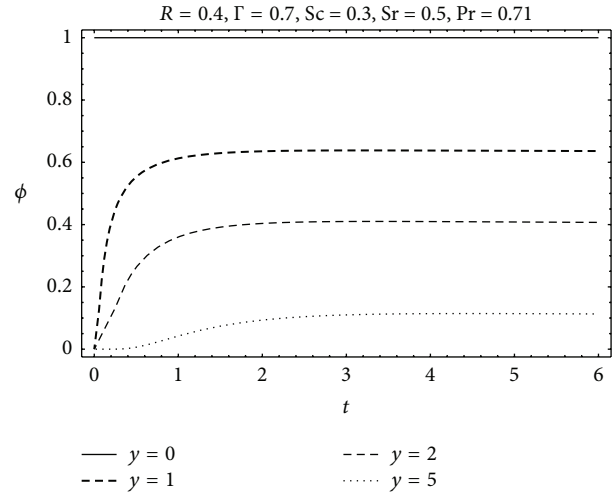


FIGURE 14: Concentration profiles for different values of Sr.

FIGURE 15: Velocity profiles for different values of  $\gamma$ .FIGURE 16: Temperature profiles for different values of  $\gamma$ .

$Pr > 1$ . The Prandtl number actually describes the relationship between momentum diffusivity and thermal diffusivity and hence controls the relative thickness of the momentum and thermal boundary layers. When  $Pr$  is small, that is,  $Pr = 0.015$ , it is noticed that the heat diffuses very quickly compared to the velocity (momentum). This means that for liquid metals the thickness of the thermal boundary layer is much bigger than the velocity boundary layer.

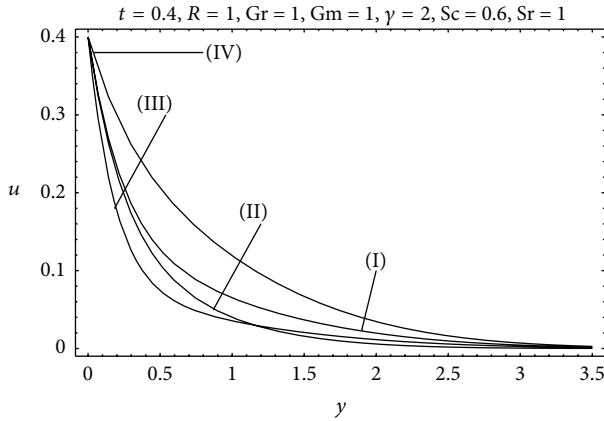
In Figure 9, we observe that the temperature decreases with increasing values of Prandtl number  $Pr$ . It is also observed that the thermal boundary layer thickness is maximum near the plate and decreases with increasing distances from the leading edge and finally approaches to zero. Furthermore, it is noticed that the thermal boundary layer for mercury which corresponds to  $Pr = 0.015$  is greater than those for air, electrolytic solution, water, and engine oil. It is justified due to the fact that thermal conductivity of fluid decreases with increasing Prandtl number  $Pr$  and hence

FIGURE 17: Concentration profiles for different values of  $\gamma$ .

decreases the thermal boundary layer thickness and the temperature profiles. We observed from Figure 10 that the concentration of the fluid increases for large values of Prandtl number  $Pr$ .

The effects of radiation parameter  $R$  on the temperature profiles are shown in Figure 11. It is found that the temperature profiles  $\theta$ , being as a decreasing function of  $R$ , decelerate the flow and reduce the fluid velocity. Such an effect may also be expected, as increasing radiation parameter  $R$  makes the fluid thick and ultimately causes the temperature and the thermal boundary layer thickness to decrease. The influence of  $\gamma$ ,  $Sc$ , and  $Sr$  on the concentration profiles  $\phi$  is shown in Figures 12–14. It is depicted from Figures 12 and 13 that the increasing values of  $\gamma$  and  $Sc$  lead to fall in the concentration profiles. Figure 14 depicts that the concentration profiles increase when Soret number  $Sr$  is increased. Furthermore, we observe that in the absence of Soret effects, the concentration profile tends to a steady state in terms of  $y$ ; this may be seen from (11). When Soret effects are present, then at large times, the solutal solution consists of this steady-state solution and an evolving “particular integral” due to the presence of the temperature term.

An important aspect of the unsteady problem is that it describes the flow situation for small times ( $t \ll 1$ ) as well as large times ( $t \rightarrow \infty$ ). Therefore, the present solutions for velocity distributions, temperature, and concentration profiles are displayed for both small and large times (see Figures 15–17). The velocity versus time graph for different values of independent variable  $y$  is plotted in Figure 15. It is found from Figure 15 that the velocity decreases as independent variable  $y$  increases. Further, it is interesting to note that initially, when  $t = 0$  the fluid velocity is zero which is also true from the initial condition given in (9). However, it is observed that as time increases, the velocity increases and after some time of initiation, this transition stops and the fluid motion becomes independent of time and hence the solutions are called steady-state solutions. This transition is smooth as we can see from the graph. On the other hand, from the velocity



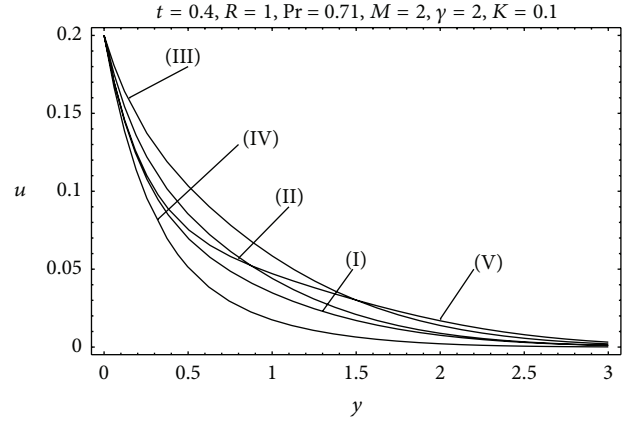
Curves	Pr	M	K
(I)	0.71	2	0.1
(II)	7	2	0.1
Curves	Pr	M	K
(III)	0.71	4	0.1
(IV)	0.71	2	0.4

FIGURE 18: Combined effect of various parameters on velocity profiles.

versus time graph for different values of the independent variable  $y$  (see Figure 15), it is found that the velocity at  $y = 0$ , is maximum and continuously decreases for large values of  $y$ . It is further noted from this figure that for large values of  $y$ , that is, when  $y \rightarrow \infty$ , the velocity profile approaches to zero. A similar behavior was also expected in view of the boundary conditions given in (9). Hence this figure shows the correctness for the obtained analytical result given by (18).

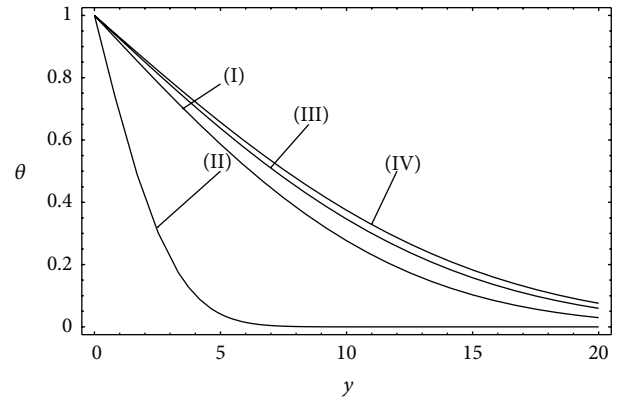
Similarly, the next two Figures 16 and 17 are plotted to describe the transient and steady-state solutions which include the effects of heating and mass diffusion. It is clear from Figure 16 that the dimensionless temperature  $\theta$  has its maximum value unity at  $y = 0$  and then decreasing for further large values of  $y$  and ultimately approaches to zero. A similar behavior was also expected due the fact that the temperature profile is 1 for  $y = 0$  and for large values of  $y$ , its value approaches to 0, which is mathematically true in view of the boundary conditions given in (10). From Figure 17, it is depicted that the variation of time on the concentration profile presents similar results as for the temperature profile in qualitative sense. However, these results are not the same quantitatively.

A very important phenomenon to see the combined effects of the embedded flow parameters on the velocity, temperature, and concentration profiles is analyzed in Figures 18–21. Figure 18 is plotted to observe the combined effects of  $Pr$ ,  $M$ , and  $K$  on velocity in case of cooling of the plate ( $Gr > 0$ ) as shown by Curves I–IV. Curves I & II are sketched to display the effects of  $Pr$  on velocity. The values of Prandtl number are chosen as  $Pr = 0.71$  (air) and  $Pr = 7$  (water), which are the most encountered fluids in nature and frequently used in engineering and industry. We can from the comparison of Curves I & II that velocity decreases upon increasing Prandtl number  $Pr$ . Curves I & III present the influence of Hartmann number  $M$  on velocity profiles. It is clear from



Curves	Gr	Gm	Sc	Sr
(I)	0.5	1	0.22	1
(II)	1	1	0.22	1
(III)	0.5	2	0.22	1
Curves	Gr	Gm	Sc	Sr
(IV)	0.5	1	0.6	1
(V)	0.5	1	0.22	2

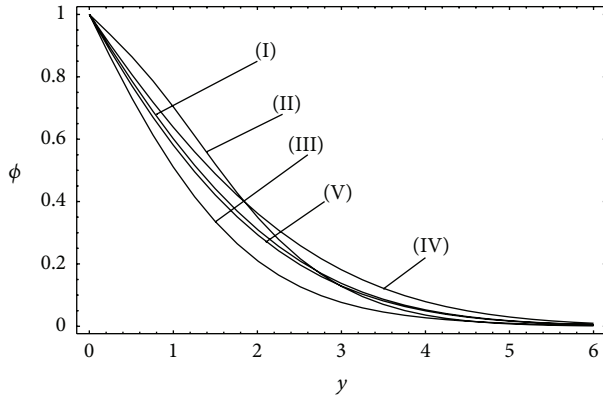
FIGURE 19: Combined effect of various parameters on velocity profiles.



Curves	Pr	R	t
(I)	0.71	0.5	2
(II)	1	0.5	2
Curves	Pr	R	t
(III)	0.71	1	2
(IV)	0.71	0.5	3

FIGURE 20: Combined effect of various parameters on temperature profiles.

these curves that velocity decreases when  $M$  is increased. The effect of permeability parameter  $K$  on the velocity is quite different to that of  $M$ . This fact is shown from the comparison of Curves I & IV. Figure 19 is plotted to show the effects of Grashof number  $Gr$ , modified Grashof number  $Gm$ , Schmidt number  $Sc$ , and Soret number  $Sr$  on velocity profiles. Curves I & II show that velocity increases when  $Gr$  is increased. It is observed that the effect of  $Gm$  on velocity is the same as  $Gr$ . This fact is shown from the comparison of Curves I & III. The effect of  $Sc$  on velocity is shown from the comparison of Curves I & IV. Here we choose the Schmidt number values as  $Sc = 0.22$  and  $Sc = 0.6$  which physically



Curves	Pr	Sc	Sr	$\gamma$	Curves	Pr	Sc	Sr	$\gamma$
(I)	0.71	0.6	0.5	0.1	(IV)	0.71	0.6	1	0.1
(II)	7	0.6	0.5	0.1	(V)	0.71	0.6	0.5	0.4
(III)	0.71	1	0.5	0.1					

FIGURE 21: Combined effect of various parameters on concentration profiles.

correspond to Helium and water vapours, respectively. From these curves it is clear that velocity decreases when  $Sc$  is increased. The effect of Soret number  $Sr$  on velocity is quite opposite to that of  $Sc$ .

Figure 20 is plotted to show the effects of Prandtl number  $Pr$ , radiation parameter  $R$ , and time  $t$  on the temperature profiles. The comparison of Curves I & II shows the effects of  $Pr$  on the temperature profiles. Two different values of Prandtl number  $Pr$ , namely,  $Pr = 0.71$  and  $Pr = 1$  corresponding to air and electrolyte are chosen. It is observed that temperature decreases with increasing  $Pr$ . Furthermore, the temperature profiles for increasing values of radiation parameter  $R$  indicate an increasing behavior as shown in Curves I & III. A behavior was expected because the radiation parameter  $R$  signifies the relative contribution of conduction heat transfer to thermal radiation transfer. The effect of time  $t$  on temperature is the same as observed for radiation. This fact is shown from the comparison of Curves I & IV. Graphical results of concentration profiles for different values of Prandtl number  $Pr$ , Schmidt number  $Sc$ , Soret number  $Sr$ , and chemical reaction parameter  $\gamma$  are shown in Figure 21. Comparison of Curves I & II shows that concentration profiles increase for the increasing values of  $Pr$ . The effect of  $Sc$  on the concentration is shown from the comparison of Curves I & III. Here we choose real values for Schmidt number as  $Sc = 0.6$  and  $Sc = 1$  which physically correspond to water vapours and methanol. It is observed that an increase in  $Sc$  decreases the concentration. The effect of Soret number  $Sr$  on the concentration is seen from the comparison of Curves I & IV. It is observed that concentration increases when  $Sr$  increases. The effect of chemical reaction parameter  $\gamma$  on the concentration is quite opposite to that of  $Sr$ . This fact is shown from the comparison of Curves I & V.

The numerical values of the skin friction ( $\tau$ ), Nusselt number ( $Nu$ ), and Sherwood number ( $Sh$ ) are computed in

TABLE 1: The effects of various parameters on skin friction ( $\tau$ ) when  $t = 1$ ,  $R = 0.2$ ,  $\gamma = 0.7$ .

Pr	$M$	$K$	Gr	Sc	Sr	Gm	$\tau$
0.71	1	0.5	1	2	1	1	1.27
<b>1</b>	1	0.5	1	2	1	1	1.30
0.71	<b>2</b>	0.5	1	2	1	1	2.05
0.71	1	<b>1</b>	1	2	1	1	0.94
0.71	1	0.5	<b>2</b>	2	1	1	0.85
0.71	1	0.5	1	<b>3</b>	1	1	1.31
0.71	1	0.5	1	2	<b>3</b>	1	1.25
0.71	1	0.5	1	2	1	<b>2</b>	0.96

TABLE 2: The effects of various parameters on Nusselt number ( $Nu$ ) when  $t = 1$ .

Pr	$R$	$Nu$
0.71	0.2	0.43
<b>1</b>	0.2	0.51
0.71	<b>0.4</b>	0.40

TABLE 3: The effects of various parameters on Sherwood number ( $Sh$ ) when  $t = 1$ ,  $R = 0.1$ ,  $Gr = 1$ ,  $M = K = 1$ ,  $Gm = 2$ .

Pr	$\gamma$	Sc	Sr	Sh
0.71	1	0.6	2	1.36
<b>1</b>	1	0.6	2	0.84
0.71	<b>2</b>	0.6	2	1.9
0.71	1	<b>1</b>	2	0.96
0.71	1	0.6	<b>3</b>	1.64

Tables 1–3. In all these tables, it is noted that the comparison of each parameter is made with first row in the corresponding table. It is found from Table 1 that the effect of each parameter on the skin friction shows quite opposite effect to that of the velocity of the fluid. For instance, when we increase the magnetic parameter  $M$ , the skin friction increases, as we observed previously velocity decreases. It is observed from Table 2 that Nusselt number increases with increasing values of Prandtl number  $Pr$ , whereas it decreases when the radiation parameter  $R$  is increased. From Table 3, we observed that Sherwood number goes on increasing with increasing  $\gamma$  and  $Sc$ , but the trend reverses for large values of  $Pr$  and  $Sr$ .

## 5. Conclusions

The exact solutions for the unsteady free convection MHD flow of an incompressible viscous fluid passing through a porous medium and heat and mass transfer are developed by using Laplace transform method for the uniform motion of the plate. The solutions that have been obtained are displayed for both small and large times which describe the motion of the fluid for some time after its initiation. After that time the transient part disappears and the motion of the fluid is described by the steady-state solutions which are independent of initial conditions. The effects of different parameters such as Grashof number  $Gr$ , Hartmann number  $M$ , porosity



parameter  $K$ , Prandtl number  $Pr$ , radiation parameter  $R$ , Schmidt number  $Sc$ , Soret number  $Sr$ , and chemical reaction parameter  $\gamma$  on the velocity distributions, temperature, and concentration profiles are discussed. The main conclusions of the problem are listed below.

- (i) The effects of Hartmann number and porosity parameter on velocity are opposite.
- (ii) The velocity increases with increasing values of  $K$ ,  $Gr$ , and  $t$ , whereas it decreases for larger values of  $M$  and  $Pr > 1$ .
- (iii) The temperature and thermal boundary layer decrease owing to the increase in the values of  $R$  and  $Pr$ .
- (iv) The fluid concentration decreases with increasing values of  $\gamma$  and  $Sc$ , whereas it increases when  $Sr$  and  $Pr$  are increased.

## 6. Future Recommendations

Convective heat transfer is a mechanism of heat transfer occurring because of bulk motion of fluids and it is one of the major modes of heat transfer and is also a major mode of mass transfer in fluids. Convective heat and mass transfer takes place through both diffusion—the random Brownian motion of individual particles in the fluid—and advection, in which matter or heat is transported by the larger-scale motion of currents in the fluid. Due to its role in heat transfer, natural convection plays a role in the structure of Earth's atmosphere, its oceans, and its mantle. Natural convection also plays a role in stellar physics. Motivated by the investigations especially those they considered the exact analysis of the heat and mass transfer phenomenon (see for example, Seth et al. [22], Toki [24], Das and Jana [26], Osman et al. [27], Khan et al. [28], and Sparrow and Cess [29]) and the extensive applications of non-Newtonian fluids in the industrial manufacturing sector, it is of great interest to extend the present work for non-Newtonian fluids. Of course, in non-Newtonian fluids, the fluids of second grade and Maxwell form the simplest fluid models where the present analysis can be extended. However, the present study can also be analyzed for Oldroyd-B and Burger fluids. There are also cylindrical and spherical coordinate systems where such type of investigations are scarce. Of course, we can extend this work for such type of geometrical configurations.

## Acknowledgment

The authors would like to acknowledge the Research Management Centre, UTM, for the financial support through vote numbers 4F109 and 02H80 for this research.

## References

- [1] A. Raptis, "Flow of a micropolar fluid past a continuously moving plate by the presence of radiation," *International Journal of Heat and Mass Transfer*, vol. 41, no. 18, pp. 2865–2866, 1998.
- [2] Y. J. Kim and A. G. Fedorov, "Transient mixed radiative convection flow of a micropolar fluid past a moving, semi-infinite vertical porous plate," *International Journal of Heat and Mass Transfer*, vol. 46, no. 10, pp. 1751–1758, 2003.
- [3] H. A. M. El-Arabawy, "Effect of suction/injection on the flow of a micropolar fluid past a continuously moving plate in the presence of radiation," *International Journal of Heat and Mass Transfer*, vol. 46, no. 8, pp. 1471–1477, 2003.
- [4] H. S. Takhar, S. Roy, and G. Nath, "Unsteady free convection flow over an infinite vertical porous plate due to the combined effects of thermal and mass diffusion, magnetic field and Hall currents," *Heat and Mass Transfer*, vol. 39, no. 10, pp. 825–834, 2003.
- [5] M. S. Alam, M. M. Rahman, and M. A. Samad, "Dufour and Soret effects on unsteady MHD free convection and mass transfer flow past a vertical porous plate in a porous medium," *Non-linear Analysis. Modelling and Control*, vol. 11, no. 3, pp. 217–226, 2006.
- [6] R. C. Chaudhary and J. Arpita, "Combined heat and mass transfer effect on MHD free convection flow past an oscillating plate embedded in porous medium," *Romanian Journal of Physics*, vol. 52, no. 5–7, pp. 505–524, 2007.
- [7] M. Ferdows, K. Kaino, and J. C. Crepeau, "MHD free convection and mass transfer flow in a porous media with simultaneous rotating fluid," *International Journal of Dynamics of Fluids*, vol. 4, no. 1, pp. 69–82, 2008.
- [8] V. Rajesh, S. Vijaya, and k. varma, "Heat Source effects on MHD flow past an exponentially accelerated vertical plate with variable temperature through a porous medium," *International Journal of Applied Mathematics and Mechanics*, vol. 6, no. 12, pp. 68–78, 2010.
- [9] V. Rajesh and S. V. K. Varma, "Radiation effects on MHD flow through a porous medium with variable temperature or variable mass diffusion," *Journal of Applied Mathematics and Mechanics*, vol. 6, no. 1, pp. 39–57, 2010.
- [10] A. A. Bakr, "Effects of chemical reaction on MHD free convection and mass transfer flow of a micropolar fluid with oscillatory plate velocity and constant heat source in a rotating frame of reference," *Communications in Nonlinear Science and Numerical Simulation*, vol. 16, no. 2, pp. 698–710, 2011.
- [11] U. N. Das, S. N. Ray, and V. M. Soundalgekar, "Mass transfer effects on flow past an impulsively started infinite vertical plate with constant mass flux—an exact solution," *Heat and Mass Transfer*, vol. 31, no. 3, pp. 163–167, 1996.
- [12] R. Muthucumaraswamy, P. Ganesan, and V. M. Soundalgekar, "Heat and mass transfer effects on flow past an impulsively started vertical plate," *Acta Mechanica*, vol. 146, no. 1-2, pp. 1–8, 2001.
- [13] T. Hayat and Z. Abbas, "Heat transfer analysis on the MHD flow of a second grade fluid in a channel with porous medium," *Chaos, Solitons and Fractals*, vol. 38, no. 2, pp. 556–567, 2008.
- [14] M. M. Rahman and M. A. Sattar, "Magnetohydrodynamic convective flow of a micropolar fluid past a continuously moving vertical porous plate in the presence of heat generation/absorption," *Journal of Heat Transfer*, vol. 128, no. 2, pp. 142–152, 2006.
- [15] Y. J. Kim, "Unsteady MHD convection flow of polar fluids past a vertical moving porous plate in a porous medium," *International Journal of Heat and Mass Transfer*, vol. 44, no. 15, pp. 2791–2799, 2001.
- [16] M. Kaviany, "Boundary-layer treatment of forced convection heat transfer from a semi-infinite flat plate embedded in porous

- media,” *Journal of Heat Transfer*, vol. 109, no. 2, pp. 345–349, 1987.
- [17] K. Vafai and C. L. Tien, “Boundary and inertia effects on flow and heat transfer in porous media,” *International Journal of Heat and Mass Transfer*, vol. 24, no. 2, pp. 195–203, 1981.
  - [18] B. K. Jha and C. A. Apere, “Combined effect of hall and ion-slip currents on unsteady MHD couette flows in a rotating system,” *Journal of the Physical Society of Japan*, vol. 79, Article ID 104401, 2010.
  - [19] G. Mandal, K. K. Mandal, and G. Choudhury, “On combined effects of coriolis force and hall current on steady MHD couette flow and hear transfer,” *Journal of the Physical Society of Japan*, vol. 51, no. 1982, 2010.
  - [20] M. Katagiri, “Flow formation in Couette motion in magnetohydro-dynamics,” *Journal of the Physical Society of Japan*, vol. 17, pp. 393–396, 1962.
  - [21] R. C. Chaudhary and J. Arpita, “An exact solution of magnetohydrodynamic convection flow past an accelerated surface embedded in a porous medium,” *International Journal of Heat and Mass Transfer*, vol. 53, no. 7-8, pp. 1609–1611, 2010.
  - [22] G. S. Seth, M. S. Ansari, and R. Nandkeolyar, “MHD natural convection flow with radiative heat transfer past an impulsively moving plate with ramped wall temperature,” *Heat Mass and Transfer*, vol. 47, pp. 551–561, 2011.
  - [23] C. J. Toki and J. N. Tokis, “Exact solutions for the unsteady free convection flows on a porous plate with time-dependent heating,” *Zeitschrift fur Angewandte Mathematik und Mechanik*, vol. 87, no. 1, pp. 4–13, 2007.
  - [24] C. J. Toki, “Free convection and mass transfer flow near a moving vertical porous plate: an analytical solution,” *Journal of Applied Mechanics, Transactions ASME*, vol. 75, no. 1, Article ID 0110141, 2008.
  - [25] K. Das, “Exact solution of MHD free convection flow and mass transfer near a moving vertical plate in presence of thermal radiation,” *African Journal of Mathematical Physics*, vol. 8, pp. 29–41, 2010.
  - [26] K. Das and S. Jana, “Heat and mass transfer effects on unsteady MHD free convection flow near a moving vertical plate in porous medium,” *Bulletin of Society of Mathematicians*, vol. 17, pp. 15–32, 2010.
  - [27] A. N. A. Osman, S. M. Abo-Dahab, and R. A. Mohamed, “Analytical solution of thermal radiation and chemical reaction effects on unsteady MHD convection through porous media with heat source/sink,” *Mathematical Problems in Engineering*, vol. 2011, Article ID 205181, 18 pages, 2011.
  - [28] I. Khan, F. Ali, S. Shafie, and N. Mustapha, “Effects of Hall current and mass transfer on the unsteady MHD flow in a porous channel,” *Journal of the Physical Society of Japan*, vol. 80, no. 6, Article ID 064401, pp. 1–6, 2011.
  - [29] E. M. Sparrow and R. D. Cess, *Radiation Heat Transfer*, Hemisphere, Washington, DC, USA, 1978.

## Research Article

# Analytical Solutions for Steady Heat Transfer in Longitudinal Fins with Temperature-Dependent Properties

**Partner L. Ndlovu and Raseelo J. Moitsheki**

*Center for Differential Equations, Continuum Mechanics and Applications, School of Computational and Applied Mathematics, University of the Witwatersrand, Private Bag 3, Johannesburg 2050, South Africa*

Correspondence should be addressed to Raseelo J. Moitsheki; [raseelo.moitsheki@wits.ac.za](mailto:raseelo.moitsheki@wits.ac.za)

Received 30 January 2013; Accepted 24 April 2013

Academic Editor: Ireneusz Zbicinski

Copyright © 2013 P. L. Ndlovu and R. J. Moitsheki. This is an open access article distributed under the Creative Commons Attribution License, which permits unrestricted use, distribution, and reproduction in any medium, provided the original work is properly cited.

Explicit analytical expressions for the temperature profile, fin efficiency, and heat flux in a longitudinal fin are derived. Here, thermal conductivity and heat transfer coefficient depend on the temperature. The differential transform method (DTM) is employed to construct the analytical (series) solutions. Thermal conductivity is considered to be given by the power law in one case and by the linear function of temperature in the other, whereas heat transfer coefficient is only given by the power law. The analytical solutions constructed by the DTM agree very well with the exact solutions even when both the thermal conductivity and the heat transfer coefficient are given by the power law. The analytical solutions are obtained for the problems which cannot be solved exactly. The effects of some physical parameters such as the thermogeometric fin parameter and thermal conductivity gradient on temperature distribution are illustrated and explained.

## 1. Introduction

Fins are surfaces that extend from a hot object (body) to increase the rate of heat transfer to the surrounding fluid. In particular, fins are used extensively in various industrial applications such as the cooling of computer processors, air conditioning, and oil carrying pipe lines. A well-documented review of heat transfer in extended surfaces is presented by Kraus et al. [1]. The problems on heat transfer particularly in fins continue to be of scientific interest. These problems are modeled by highly nonlinear differential equations which are difficult to solve exactly. However, Moitsheki et al. [2–4] have attempted to construct exact solutions for the steady state problems arising in heat flow through fins. A number of techniques, for example, Lie symmetry analysis [2], He's variational iteration method [5], Adomain decomposition methods [6], homotopy perturbation methods [7], homotopy analysis methods [8], methods of successive approximations [9], and other approximation methods [10] have been used to determine solutions of the nonlinear differential equations describing heat transfer in fins.

Recently, the solutions of the nonlinear ordinary differential equations (ODEs) arising in extended surface heat transfer have been constructed using the DTM [11–19]. The DTM is an analytical method based on the Taylor series expansion and was first introduced by Zhou [20] in 1986. The DTM approximates the exact solution by a polynomial, and previous studies have shown that it is an efficient means of solving nonlinear problems or systems with varying parameters [21]. Furthermore, DTM is a computational inexpensive tool for obtaining analytical solution, and it generalizes the Taylor method to problems involving procedures such as fractional derivative (see e.g., [22–24]). Also, this method converges rapidly (see e.g., [25]).

Models arising in heat transfer through fins may contain temperature-dependent properties such as thermal conductivity and heat transfer coefficient. The dependency of thermal conductivity and heat transfer coefficient on temperature renders such problems highly nonlinear and difficult to solve, particularly exactly. Thermal conductivity may be modeled for many engineering applications by the power law and by linear dependency on temperature. On the other hand, heat

transfer coefficient can be expressed as a power law for which values of the exponent represent different phenomena (see e.g., [26]).

In this paper, the DTM is employed to determine the analytical solutions to the nonlinear boundary value problem describing heat transfer in longitudinal fins of rectangular, exponential, and convex parabolic profiles. Both thermal conductivity and heat transfer coefficient are temperature dependent. We adopt the terminology exact solutions to refer to solutions given in terms of fundamental expressions such as logarithmic, trigonometric, and exponential. However, analytical solutions will be series solutions and in particular, those constructed using the DTM. The mathematical modelling of the problem under consideration is described in Section 2. A brief discussion on the fundamentals of the DTM is provided in Section 3. The comparison of the exact and analytical solutions constructed by DTM is given in Section 4. In Section 5, we provide analytical solutions for the heat transfer in longitudinal fins of various profiles. Here, heat transfer coefficient is given by the power law, and we consider two cases of the thermal conductivity, namely, the power law and the linear function of temperature. Furthermore, we describe the fin efficiency and the heat flux in Section 6. Some exciting results are discussed in Section 7. Lastly, the concluding remarks are provided in Section 8.

## 2. Mathematical Models

We consider a longitudinal one dimensional fin of cross-sectional area  $A_c$ . The perimeter of the fin is denoted by  $P$  and its length by  $L$ . The fin is attached to a fixed prime surface of temperature  $T_b$  and extends to an ambient fluid of temperature  $T_a$ . The fin thickness at the prime surface is given by  $\delta_b$  and its profile is given by  $F(X)$ . Based on the one dimensional heat conduction, the energy balance equation is then given by (see e.g., [1])

$$A_c \frac{d}{dX} \left( \frac{\delta_b}{2} F(X) K(T) \frac{dT}{dX} \right) = PH(T) (T - T_a) \quad (1)$$

$$0 \leq X \leq L,$$

where  $K$  and  $H$  are nonuniform temperature-dependent thermal conductivity and heat transfer coefficients, respectively,  $T$  is the temperature distribution,  $F(X)$  is the fin profile, and  $X$  is the space variable. The length of the fin is measured from the tip to the prime surface as shown in Figure 1. Assuming that the fin tip is adiabatic (insulated) and the base temperature is kept constant, then the boundary conditions are given by

$$T(L) = T_b, \quad \left. \frac{dT}{dX} \right|_{X=0} = 0. \quad (2)$$

Introducing the following dimensionless variables (see e.g., [1]):

$$\begin{aligned} x &= \frac{X}{L}, & \theta &= \frac{T - T_a}{T_b - T_a}, & h &= \frac{H}{h_b}, & k &= \frac{K}{k_a}, \\ M^2 &= \frac{Ph_b L^2}{A_c k_a}, & f(x) &= \frac{\delta_b}{2} F(X), \end{aligned} \quad (3)$$

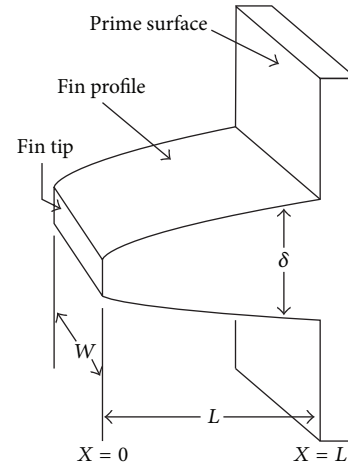


FIGURE 1: Schematic representation of a longitudinal fin of an unspecified profile.

with  $k_a$  being defined as the thermal conductivity at the ambient temperature and  $h_b$  as the heat transfer at the prime surface (fin base), reduces (1) to

$$\frac{d}{dx} \left[ f(x) k(\theta) \frac{d\theta}{dx} \right] - M^2 \theta h(\theta) = 0, \quad 0 \leq x \leq 1. \quad (4)$$

Here  $\theta$  is the dimensionless temperature,  $x$  is the dimensionless space variable,  $f(x)$  is the dimensionless fin profile,  $k$  is the dimensionless thermal conductivity,  $h$  is the dimensionless heat transfer coefficient, and  $M$  is the thermogeometric fin parameter. The dimensionless boundary conditions then become

$$\theta(1) = 1, \quad \text{at the prime surface} \quad (5)$$

$$\left. \frac{d\theta}{dx} \right|_{x=0} = 0, \quad \text{at the fin tip.} \quad (6)$$

We assume that the heat transfer coefficient is given by the power law

$$H(T) = h_b \left( \frac{T - T_a}{T_b - T_a} \right)^n, \quad (7)$$

where the exponent  $n$  is a real constant. In fact the values of  $n$  may vary as between  $-6.6$  and  $5$ . However, in most practical applications, it lies between  $-3$  and  $3$  [27]. In dimensionless variables, we have  $h(\theta) = \theta^n$ . We consider the two distinct cases of the thermal conductivity as follows:

(a) the power law

$$K(T) = k_a \left( \frac{T - T_a}{T_b - T_a} \right)^m, \quad (8)$$

with  $m$  being a constant and

(b) the linear function

$$K(T) = k_a [1 + \gamma(T - T_a)]. \quad (9)$$

The dimensionless thermal conductivity given by the power law and the linear function of temperature is  $k(\theta) = \theta^m$  and  $k(\theta) = 1 + \beta\theta$ , respectively. Here the thermal conductivity gradient is  $\beta = \gamma(T_b - T_a)$ . Furthermore, we consider a various fin profiles including the longitudinal rectangular  $f(x) = 1$ , the longitudinal convex parabolic  $f(x) = \sqrt{x}$ , and the exponential profile  $f(x) = e^{ax}$  with  $a$  being the constant (see also [16]).

### 3. Fundamentals of the Differential Transform Method

In this section, the basic idea underlying the DTM is briefly introduced. Let  $y(t)$  be an analytic function in a domain  $\mathcal{D}$ . The Taylor series expansion function of  $y(t)$  with the center located at  $t = t_j$  is given by [20]

$$y(t) = \sum_{\kappa=0}^{\infty} \frac{(t-t_j)^\kappa}{\kappa!} \left[ \frac{d^\kappa y(t)}{dt^\kappa} \right]_{t=t_j}, \quad \forall t \in \mathcal{D}. \quad (10)$$

The particular case of (10) when  $t_j = 0$  is referred to as the Maclaurin series expansion of  $y(t)$  and is expressed as

$$y(t) = \sum_{\kappa=0}^{\infty} \frac{t^\kappa}{\kappa!} \left[ \frac{d^\kappa y(t)}{dt^\kappa} \right]_{t=0}, \quad \forall t \in \mathcal{D}. \quad (11)$$

The differential transform of  $y(t)$  is defined as follows:

$$Y(t) = \sum_{\kappa=0}^{\infty} \frac{\mathcal{H}^\kappa}{\kappa!} \left[ \frac{d^\kappa y(t)}{dt^\kappa} \right]_{t=0}, \quad (12)$$

where  $y(t)$  is the original analytic function and  $Y(t)$  is the transformed function. The differential spectrum of  $Y(t)$  is confined within the interval  $t \in [0, \mathcal{H}]$ , where  $\mathcal{H}$  is a constant. From (11) and (12), the differential inverse transform of  $Y(t)$  is defined as follows:

$$y(t) = \sum_{\kappa=0}^{\infty} \left( \frac{t}{\mathcal{H}} \right)^\kappa Y(\kappa), \quad (13)$$

and if  $y(t)$  is expressed by a finite series, then

$$y(t) = \sum_{\kappa=0}^r \left( \frac{t}{\mathcal{H}} \right)^\kappa Y(\kappa). \quad (14)$$

Some of the useful mathematical operations performed by the differential transform method are listed in Table 1.

The delta function  $\delta(\kappa - s)$  is given by

$$\delta(\kappa - s) = \begin{cases} 1 & \text{if } \kappa = s, \\ 0 & \text{if } \kappa \neq s. \end{cases} \quad (15)$$

### 4. Comparison of Exact and Analytical Solutions

In this section, we consider a model describing temperature distribution in a longitudinal rectangular fin with both thermal conductivity and heat transfer coefficient being functions

TABLE 1: Fundamental operations of the differential transform method.

Original function	Transformed function
$y(t) = x(t) \pm z(t)$	$Y(t) = X(t) \pm Z(t)$
$y(t) = \alpha x(t)$	$Y(t) = \alpha X(t)$
$y(t) = \frac{dy(t)}{dt}$	$Y(t) = (\kappa + 1)Y(\kappa + 1)$
$y(t) = \frac{d^2 y(t)}{dt^2}$	$Y(t) = (\kappa + 1)(\kappa + 2)Y(\kappa + 2)$
$y(t) = \frac{d^s y(t)}{dt^s}$	$Y(t) = (\kappa + 1)(\kappa + 2) \cdots (\kappa + s)Y(\kappa + s)$
$y(t) = x(t)z(t)$	$Y(t) = \sum_{i=0}^{\kappa} X(i)Z(\kappa - i)$
$y(t) = 1$	$Y(t) = \delta(\kappa)$
$y(t) = t$	$Y(t) = \delta(\kappa - 1)$
$y(t) = t^s$	$Y(t) = \delta(\kappa - s)$
$y(t) = \exp(\lambda t)$	$Y(t) = \frac{\lambda^\kappa}{\kappa!}$
$y(t) = (1 + t)^s$	$Y(t) = \frac{s(s-1) \cdots (s - \kappa + 1)}{\kappa!}$
$y(t) = \sin(\omega t + \alpha)$	$Y(t) = \frac{\omega^\kappa}{\kappa!} \sin\left(\frac{\pi\kappa}{2!} + \alpha\right)$
$y(t) = \cos(\omega t + \alpha)$	$Y(t) = \frac{\omega^\kappa}{\kappa!} \cos\left(\frac{\pi\kappa}{2!} + \alpha\right)$

of temperature given by the power law (see e.g., [2]). The exact solution of (4) when both the power laws are given by the same exponent is given by [2]

$$\theta(x) = \left[ \frac{\cosh(M\sqrt{n+1}x)}{\cosh(M\sqrt{n+1})} \right]^{1/(n+1)}. \quad (16)$$

We use this exact solution as a benchmark or validation of the DTM. The effectiveness of the DTM is determined by comparing the exact and the analytical solutions. We compare the results for the cases  $n = 1$  and  $n = 2$  with fixed values of  $M$ .

**4.1. Case  $n=1$ .** Applying the DTM to (4) with the power law thermal conductivity,  $f(x) = 1$  (rectangular profile) and given  $\mathcal{H} = 1$ , one obtains the following recurrence relation:

$$\begin{aligned} & \sum_{i=0}^{\kappa} [\Theta(i)(\kappa - i + 1)(\kappa - i + 2)\Theta(\kappa - i + 2) \\ & + (i + 1)\Theta(i + 1)(\kappa - i + 1)\Theta(\kappa - i + 1) \\ & - M^2\Theta(i)\Theta(\kappa - i)] = 0. \end{aligned} \quad (17)$$

Exerting the transformation to the boundary condition (6) at a point  $x = 0$ ,

$$\Theta(1) = 0. \quad (18)$$

The other boundary conditions are considered as follows:

$$\Theta(0) = c, \quad (19)$$



where  $c$  is a constant. Equation (17) is an iterative formula of constructing the power series solution as follows:

$$\Theta(2) = \frac{M^2 c}{2} \quad (20)$$

$$\Theta(3) = 0 \quad (21)$$

$$\Theta(4) = -\frac{M^4 c}{24} \quad (22)$$

$$\Theta(5) = 0 \quad (23)$$

$$\Theta(6) = \frac{19M^6 c}{720} \quad (24)$$

$$\Theta(7) = 0 \quad (25)$$

$$\Theta(8) = -\frac{559M^8 c}{40320} \quad (26)$$

$$\Theta(9) = 0 \quad (27)$$

$$\Theta(10) = \frac{29161M^{10} c}{3628800} \quad (28)$$

$$\Theta(11) = 0 \quad (29)$$

$$\Theta(12) = -\frac{2368081M^{12} c}{479001600} \quad (30)$$

$$\Theta(13) = 0 \quad (31)$$

$$\Theta(14) = \frac{276580459M^{14} c}{87178291200} \quad (32)$$

$$\Theta(15) = 0 \quad (33)$$

$\vdots$

These terms may be taken as far as desired. Substituting (18) to (32) into (13), we obtain the following analytical solution:

$$\begin{aligned} \theta(x) = & c + \frac{M^2 c}{2} x^2 - \frac{M^4 c}{24} x^4 + \frac{19M^6 c}{720} x^6 \\ & - \frac{559M^8 c}{40320} x^8 + \frac{29161M^{10} c}{3628800} x^{10} - \frac{2368081M^{12} c}{479001600} x^{12} \\ & + \frac{276580459M^{14} c}{87178291200} x^{14} + \dots \end{aligned} \quad (34)$$

To obtain the value of  $c$ , we substitute the boundary condition (5) into (34) at the point  $x = 1$ . Thus, we have

$$\begin{aligned} \theta(1) = & c + \frac{M^2 c}{2} - \frac{M^4 c}{24} + \frac{19M^6 c}{720} - \frac{559M^8 c}{40320} \\ & + \frac{29161M^{10} c}{3628800} - \frac{2368081M^{12} c}{479001600} \\ & + \frac{276580459M^{14} c}{87178291200} + \dots = 1. \end{aligned} \quad (35)$$

TABLE 2: Results of the DTM and exact solutions for  $n = 1, M = 0.7$ .

$x$	DTM	Exact	Error
0	0.808093014	0.80809644	0.000003426
0.1	0.810072036	0.81007547	0.000003434
0.2	0.815999549	0.81600301	0.000003459
0.3	0.825847770	0.82585127	0.000003500
0.4	0.839573173	0.83957673	0.000003559
0.5	0.857120287	0.85712392	0.000003633
0.6	0.878426299	0.87843002	0.000003722
0.7	0.903426003	0.90342982	0.000003814
0.8	0.932056648	0.93206047	0.000003820
0.9	0.964262558	0.96426582	0.000003263
1.0	1.000000000	1.00000000	0.000000000

TABLE 3: Results of the DTM and Exact Solutions for  $n = 2, M = 0.5$ .

$x$	DTM	Exact	Error
0	0.894109126	0.894109793	0.000000665
0.1	0.895226066	0.895226732	0.000000666
0.2	0.898568581	0.898569249	0.000000668
0.3	0.904112232	0.904112905	0.000000672
0.4	0.911817796	0.911818474	0.000000678
0.5	0.921633352	0.921634038	0.000000685
0.6	0.933496900	0.933497594	0.000000694
0.7	0.947339244	0.947339946	0.000000702
0.8	0.963086933	0.963087627	0.000000694
0.9	0.980665073	0.980665659	0.000000586
1.0	1.000000000	1.000000000	0.000000000

We omit presenting the tedious process of finding  $c$ . However, one may obtain the expression for  $\theta(x)$  upon substituting the obtained value of  $c$  into (34).

4.2. Case  $n=2$ . Following a similar approach given in Section 4.1 and given  $n = 2$ , one obtains the analytical solution

$$\begin{aligned} \theta(x) = & c + \frac{M^2 c}{2} x^2 - \frac{M^4 c}{8} x^4 + \frac{23M^6 c}{240} x^6 \\ & - \frac{1069M^8 c}{13440} x^8 + \frac{9643M^{10} c}{134400} x^{10} - \frac{1211729M^{12} c}{17740800} x^{12} \\ & + \frac{217994167M^{14} c}{3228825600} x^{14} + \dots \end{aligned} \quad (36)$$

The constant  $c$  may be obtained using the boundary condition at the fin base. The comparison of the DTM and the exact solutions are reflected in Tables 2 and 3 for different values of  $n$ . Furthermore, the comparison of the exact and the analytical solutions is depicted in Figures 2(a) and 2(b).

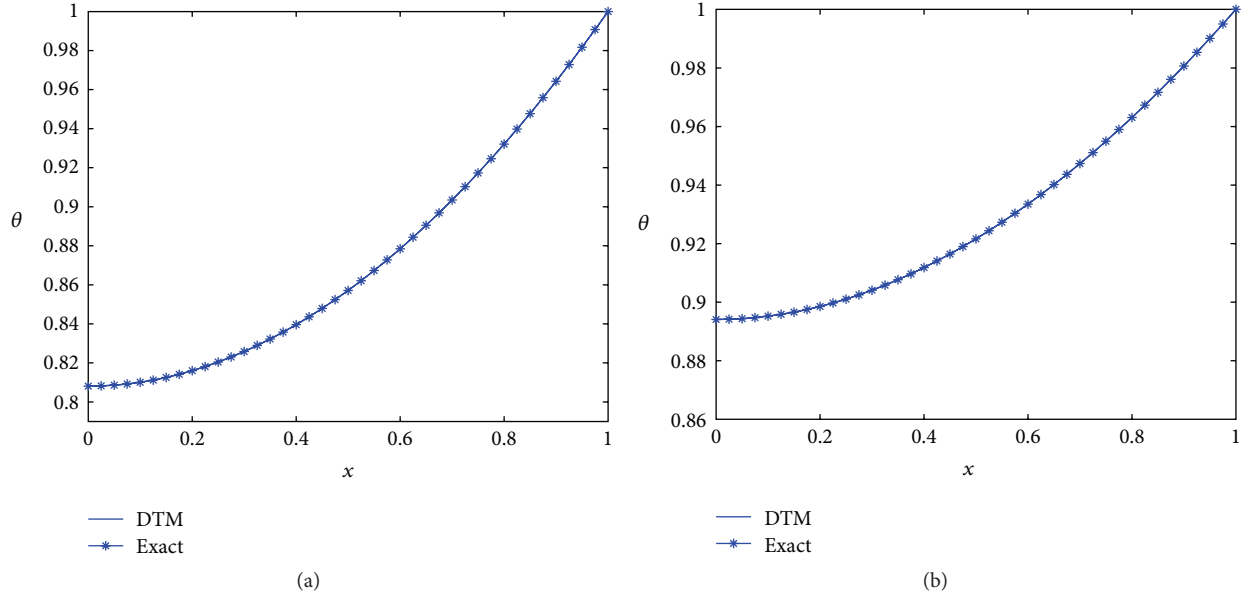


FIGURE 2: Comparison of analytical and exact solutions. In (a)  $n = 1$ ,  $M = 0.7$  and (b)  $n = 2$ ,  $M = 0.5$ .

## 5. Analytical Solutions

It is well known that exact solutions for ODEs such as (4) exist only when thermal conductivity and the term containing heat transfer coefficient are connected by differentiation (or simply if the ODE such as (4) is linearizable) [4]. In this section we determine the analytical solutions for the nonlinearizable (4), firstly when thermal conductivity is given by the power law and secondly as a linear function of temperature. In both cases and throughout this paper, the heat transfer coefficient is assumed to be a power law function of temperature. These assumptions of the thermal properties are physical realistic. We have noticed that DTM runs into difficulty when the exponent of the power law of the thermal conductivity is given by fractional values and also when the function  $f(x)$  is given in terms of fractional power law. One may follow Moradi and Ahmadikia [16] by introducing a new variable to deal with fractional powers of  $f(x)$ , and on the other hand, it is possible to remove the fractional exponent of the heat transfer coefficient by fundamental laws of exponent and binomial expansion.

**Proposition 1.** *A nonlinear ODE such as (4) may admit the DTM solution if  $f(x)$  is a constant or exponential function. However, if  $f(x)$  is a power law, then such an equation admits a DTM solution if the product,*

$$f(x) \cdot f'(x) = \alpha, \quad (37)$$

holds. Here  $\alpha$  is a real constant.

*Proof.* Introducing the new variable  $\xi = f(x)$ , it follows from chain rule that (4) becomes

$$\alpha \frac{d\xi}{dx} \frac{d}{d\xi} \left[ k(\theta) \frac{d\theta}{d\xi} \right] - M^2 \theta^{n+1} = 0. \quad (38)$$

The most general solution of condition (37) is

$$f(x) = (2\alpha x + \gamma)^{1/2}, \quad (39)$$

where  $\gamma$  is an integration constant.  $\square$

*Example 2.* (a) If  $f(x) = x^\sigma$ , then  $\xi = x^\sigma$  transforms (4) into

$$\frac{d}{d\xi} \left[ k(\theta) \frac{d\theta}{d\xi} \right] - 4M^2 \xi \theta^{n+1} = 0, \quad (40)$$

only if  $\sigma = 1/2$ .

This example implies that the DTM may only be applicable to problems describing heat transfer in fins with convex parabolic profile. In the next subsections, we present analytical solutions for (4) with various functions  $f(x)$  and  $k(\theta)$ .

**5.1. The Exponential Profile and Power Law Thermal Conductivity.** In this section, we present solutions for equation describing heat transfer in a fin with exponential profile and power law thermal conductivity and heat transfer coefficient. That is, given (4) with  $f(x) = e^{\sigma x}$ , and both heat transfer coefficient and thermal conductivity being power law functions of temperature, we construct analytical solutions. In our analysis, we consider  $n = 2$  and  $3$  indicating the fin subject to nucleate boiling and radiation into free space at zero absolute temperature, respectively. Firstly, given  $n = 3$  and  $m = 2$

and applying the DTM, one obtains the following recurrence revelation:

$$\sum_{i=0}^{\kappa} \sum_{l=0}^{\kappa-i} \sum_{p=0}^{\kappa-i-l} \left[ \frac{\sigma^p}{p!} \Theta(l) \Theta(i) (\kappa-i-l-p+1) \right. \\ \times (\kappa-i-l-p+2) \Theta(\kappa-i-l-p+2) \\ + 2 \frac{\sigma^p}{p!} \Theta(l) \Theta(i+1) \Theta(i+1) \\ \times (\kappa-i-l-p+1) \Theta(\kappa-i-l-p+1) \\ + 2\sigma \frac{\sigma^p}{p!} \Theta(l) \Theta(i) (\kappa-i-l-p+1) \\ \times \Theta(\kappa-i-l-p+1) \\ \left. - M^2 \Theta(p) \Theta(l) \Theta(i) \Theta(\kappa-i-l-p) \right] = 0. \quad (41)$$

One may recall the transformed prescribed boundary conditions (18) and (19). Equation (41) is an iterative formula of constructing the power series solution as follows:

$$\begin{aligned} \Theta(2) &= \frac{M^2 c^2}{2} \\ \Theta(3) &= -\frac{\sigma M^2 c^2}{3} \\ \Theta(4) &= \frac{M^2 c^2 (3\sigma^2 - 2M^2 c)}{24} \\ \Theta(5) &= -\frac{M^2 c^2 (\sigma^3 - 4\sigma M^2 c)}{30} \\ \Theta(6) &= \frac{M^2 c^2 (5\sigma^4 - 78\sigma^2 M^2 c + 58M^4 c^2)}{720} \\ &\vdots \end{aligned} \quad (42)$$

The pervious process is continuous and one may consider as many terms as desired (but bearing in mind that DTM converges quite fast). Substituting (18) to (19) and (42) into (13), we obtain the following closed form of the solution:

$$\begin{aligned} \theta(x) &= c + \frac{M^2 c^2}{2} x^2 - \frac{\sigma M^2 c^2}{3} x^3 \\ &+ \frac{M^2 c^2 (3\sigma^2 - 2M^2 c)}{24} x^4 \\ &- \frac{M^2 c^2 (\sigma^3 - 4\sigma M^2 c)}{30} x^5 \\ &+ \frac{M^2 c^2 (5\sigma^4 - 78\sigma^2 M^2 c + 58M^4 c^2)}{720} x^6 + \dots \end{aligned} \quad (43)$$

To obtain the value of  $c$ , we substitute the boundary condition (5) into (43) at the point  $x = 1$ . That is,

$$\begin{aligned} \theta(1) &= c + \frac{M^2 c^2}{2} - \frac{\sigma M^2 c^2}{3} + \frac{M^2 c^2 (3\sigma^2 - 2M^2 c)}{24} \\ &- \frac{M^2 c^2 (\sigma^3 - 4\sigma M^2 c)}{30} \\ &+ \frac{M^2 c^2 (5\sigma^4 - 78\sigma^2 M^2 c + 58M^4 c^2)}{720} + \dots = 1. \end{aligned} \quad (44)$$

Substituting this value of  $c$  into (43), one finds the expression for  $\theta(x)$ . On the other hand, given  $(n, m) = (2, 3)$ , one obtains the solution

$$\begin{aligned} \theta(x) &= c + \frac{M^2}{2} x^2 - \frac{\sigma M^2}{3} x^3 \\ &+ \frac{M^2 (\sigma^2 c - 2M^2)}{8c} x^4 - \frac{\sigma M^2 (2\sigma^2 c - 21M^2)}{60c} x^5 \\ &+ \frac{M^2 (180M^4 - 186\sigma^2 M^2 c + 5\sigma^4 c^2)}{720} x^6 + \dots \end{aligned} \quad (45)$$

Here, the constant  $c$  maybe obtained by evaluating the boundary condition  $\theta(1) = 1$ . The solutions (43) and (45) are depicted in Figures 3(b) and 3(a), respectively.

**5.2. The Rectangular Profile and Power Law Thermal Conductivity.** In this section, we provide a detailed construction of analytical solutions for the heat transfer in a longitudinal rectangular fin with a power law thermal conductivity; that is, we consider (4) with  $f(x) = 1$  and  $k(\theta) = \theta^m$ . The analytical solutions are given in the following expressions.

(a) Case  $(n, m) = (2, 3)$

$$\begin{aligned} \theta(x) &= c + \frac{M^2}{2} x^2 - \frac{M^4}{4c} x^4 + \frac{M^6}{4c^2} x^6 \\ &- \frac{33M^8}{122c^3} x^8 + \frac{127M^{10}}{336c^4} x^{10} + \dots \end{aligned} \quad (46)$$

(b) Case  $(n, m) = (3, 2)$

$$\begin{aligned} \theta(x) &= c + \frac{c^2 M^2}{2} x^2 - \frac{c^3 M^4}{12} x^4 + \frac{29c^4 M^6}{360} x^6 \\ &- \frac{307c^5 M^8}{5040} x^8 + \frac{23483c^6 M^{10}}{453600} x^{10} + \dots \end{aligned} \quad (47)$$

The constant  $c$  is obtained by solving the appropriate  $\theta(x)$  at the fin base boundary condition. The analytical solutions in (46) and (47) are depicted in Figures 4(a) and 4(b), respectively.

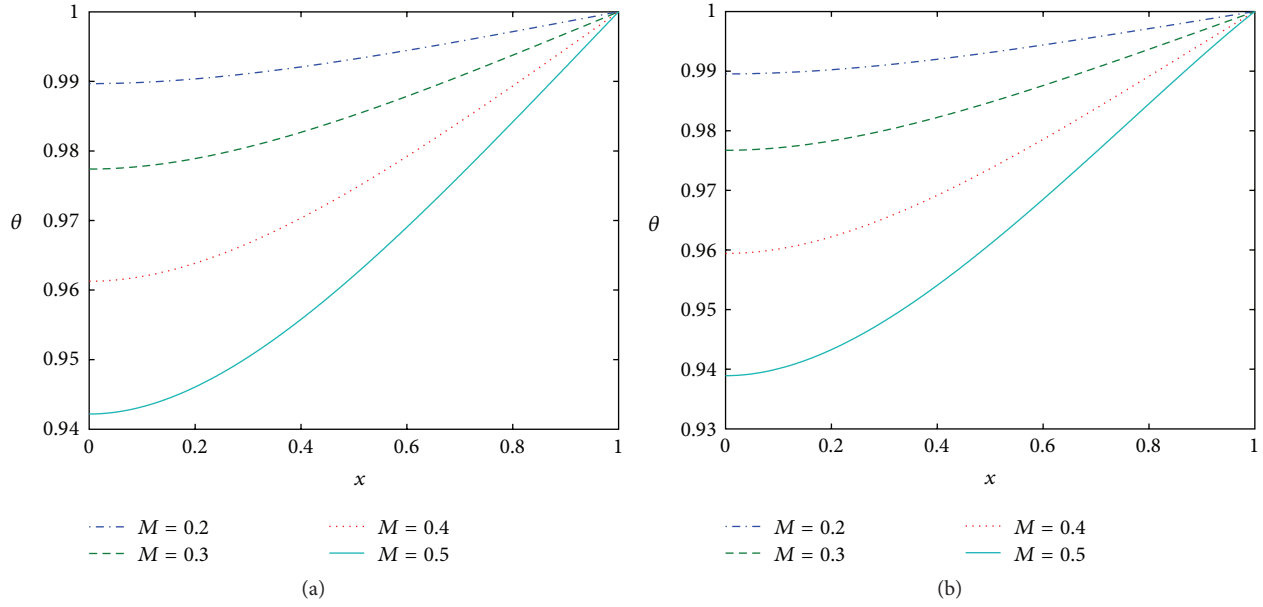


FIGURE 3: Temperature profile in a longitudinal fin with exponential profile and power law thermal conductivity. In (a) the exponents are  $(n, m) = (2, 3)$  and (b)  $(n, m) = (3, 2)$ .

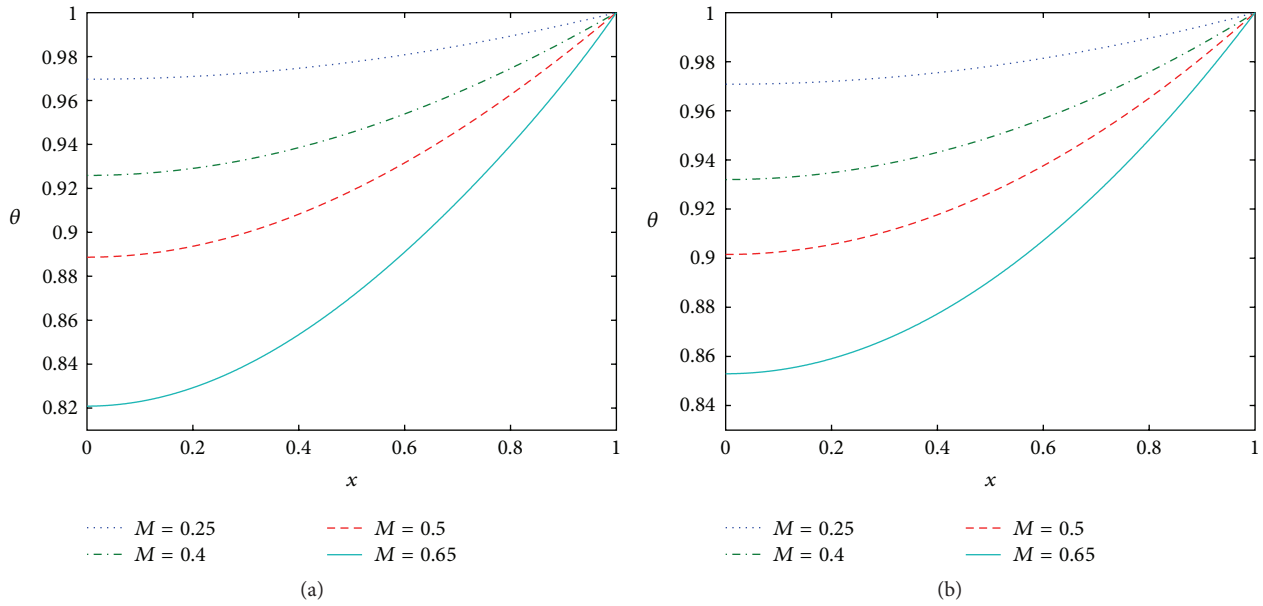


FIGURE 4: Temperature profile in a longitudinal fin with rectangular profile and power law thermal conductivity. In (a) the exponents are  $(n, m) = (2, 3)$  and (b)  $(n, m) = (3, 2)$ .

**5.3. The Convex Parabolic Profile and Power Law Thermal Conductivity.** In this section, we present solutions for the equation describing the heat transfer in a fin with convex parabolic profile and power law thermal conductivity. Equation (40) is considered. Here we consider the values  $\{(n, m) = (2, 3); (3, 2)\}$ . The final analytical solution is given by

(a) Case  $(n, m) = (2, 3)$

$$\theta(x) = c + \frac{2M^2}{3}x^{3/2} - \frac{2M^4}{5c}x^3 + \frac{23M^6}{45c^2}x^{9/2} - \frac{1909M^8}{2475c^3}x^6 + \frac{329222M^{10}}{259875c^4}x^{15/2} + \dots \quad (48)$$

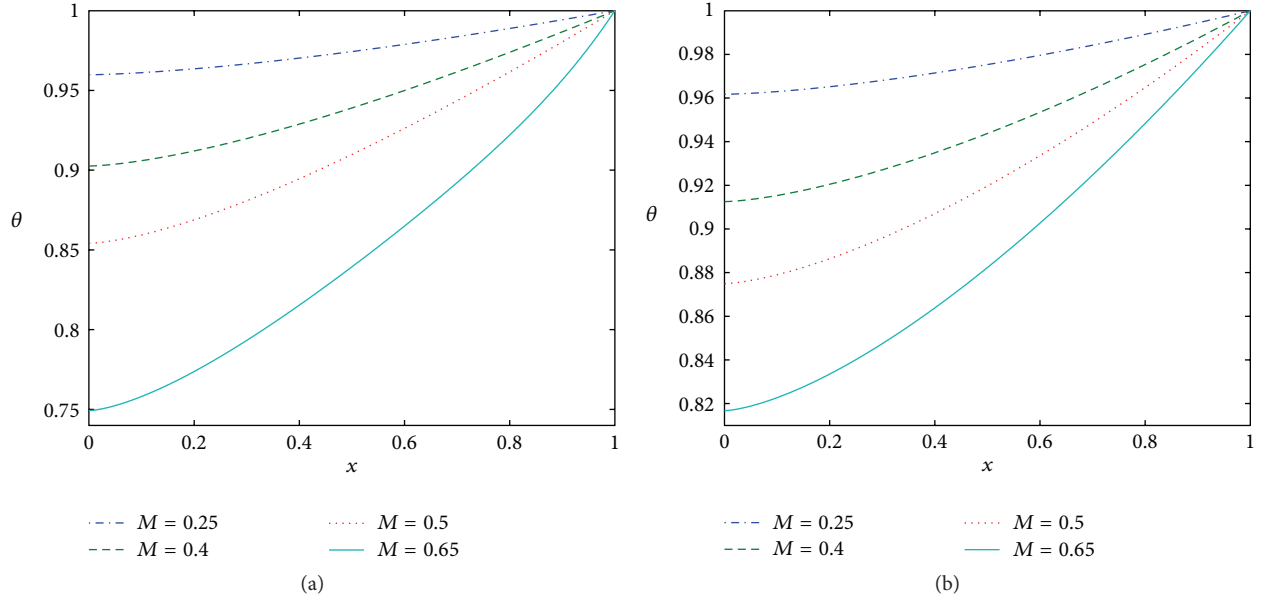


FIGURE 5: Temperature profile in a longitudinal fin with convex parabolic profile and power law thermal conductivity. In (a) the exponents are  $(n, m) = (2, 3)$  and (b)  $(n, m) = (3, 2)$ .

(b) Case  $(n, m) = (3, 2)$

$$\theta(x) = c + \frac{2c^2 M^2}{3} x^{3/2} - \frac{4c^3 M^4}{45} x^3 + \frac{4c^4 M^6}{27} x^{9/2} - \frac{992c^5 M^8}{7425} x^6 + \frac{30064c^6 M^{10}}{212625} x^{15/2} + \dots \quad (49)$$

The constant  $c$  is obtained by evaluating the appropriate  $\theta(x)$  at the fin base boundary condition. The solutions in (48) and (49) are depicted in Figures 5(a) and 5(b), respectively.

#### 5.4. The Rectangular Profile and Linear Thermal Conductivity.

In this section, we present solutions for the equation representing the heat transfer in a fin with rectangular profile and the thermal conductivity depending linearly on temperature. That is, we consider (4) with  $f(x) = 1$  and  $k(\theta) = 1 + \beta\theta$ . The analytical solutions for this problem for different values of  $n$  are given by

(a) Case  $n = 0$

$$\begin{aligned} \theta(x) &= c + \frac{M^2 c}{2(1 + \beta c)} x^2 - \frac{M^4 c(-1 + 2\beta c)}{24(1 + \beta c)^3} x^4 \\ &+ \frac{M^6 c(1 - 16\beta c + 28\beta^2 c^2)}{720(1 + \beta c)^5} x^6 \\ &- \frac{M^8 c(-1 + 78\beta c - 600\beta^2 c^2 + 896\beta^3 c^3)}{40320(1 + \beta c)^7} x^8 \\ &+ \frac{M^{10} c(1 - 332\beta c + 7812\beta^2 c^2 - 39896\beta^3 c^3 + 51184\beta^4 c^4)}{3628800(1 + \beta c)^9} x^{10} \\ &+ \dots \end{aligned} \quad (50)$$

(b) Case  $n = 1$

$$\begin{aligned} \theta(x) &= c + \frac{M^2 c^2}{2(1 + \beta c)} x^2 - \frac{M^4 c^3(-1 + 2\beta c)}{24(1 + \beta c)^3} x^4 \\ &+ \frac{M^6 c^4(10 - 16\beta c + 19\beta^2 c^2)}{720(1 + \beta c)^5} x^6 \\ &- \frac{M^8 c^5(-80 + 342\beta c - 594\beta^2 c^2 + 559\beta^3 c^3)}{40320(1 + \beta c)^7} x^8 \\ &+ \frac{M^{10} c^6(1000 - 7820\beta c + 24336\beta^2 c^2 - 36908\beta^3 c^3 + 29161\beta^4 c^4)}{3628800(1 + \beta c)^9} x^{10} \\ &+ \dots \end{aligned} \quad (51)$$

(c) Case  $n = 2$

$$\begin{aligned} \theta(x) &= c + \frac{M^2 c^3}{2(1 + \beta c)} x^2 + \frac{M^4 c^5}{8(1 + \beta c)^3} x^4 + \frac{M^6 c^7(3 + 2\beta^2 c^2)}{80(1 + \beta c)^5} x^6 \\ &+ \frac{M^8 c^9(49 - 20\beta c + 66\beta^2 c^2 - 40\beta^3 c^3)}{4480(1 + \beta c)^7} x^8 \\ &+ \frac{M^{10} c^{11}(427 - 440\beta c + 1116\beta^2 c^2 - 1020\beta^3 c^3 + 672\beta^4 c^4)}{134400(1 + \beta c)^9} x^{10} \\ &+ \dots \end{aligned} \quad (52)$$



(d) Case  $n = 3$ 

$$\begin{aligned}
\theta(x) &= c + \frac{M^2 c^4}{2(1+\beta c)} x^2 + \frac{M^4 c^7 (4+\beta c)}{24(1+\beta c)^3} x^4 \\
&+ \frac{M^6 c^{10} (52+32\beta c+25\beta^2 c^2)}{720(1+\beta c)^5} x^6 \\
&+ \frac{M^8 c^{13} (1288+1020\beta c+1212\beta^2 c^2-95\beta^3 c^3)}{40320(1+\beta c)^7} x^8 \\
&+ \frac{M^{10} c^{16} (52024+45688\beta c+77184\beta^2 c^2-680\beta^3 c^3+15025\beta^4 c^4)}{3628800(1+\beta c)^9} x^{10} \\
&+ \dots
\end{aligned} \quad (53)$$

The constant  $c$  may be obtained from the boundary condition on the appropriate solution. The solutions in (50), (51), (52), and (53) are depicted in Figure 6.

**5.5. The Convex Parabolic Profile and Linear Thermal Conductivity.** In this section, we present solutions for the equation describing the heat transfer in a fin with convex parabolic profile and the thermal conductivity depending linearly on temperature. That is, we consider (40) with  $k(\theta) = 1 + \beta\theta$ . The analytical solution for this problem for different values of  $n$  is given by

(a) Case  $n = 0$ 

$$\begin{aligned}
\theta(x) &= c + \frac{2M^2 c}{3(1+\beta c)} x^{3/2} - \frac{2M^4 c (-2+3\beta c)}{45(1+\beta c)^3} x^3 \\
&+ \frac{M^6 c (2-25\beta c+33\beta^2 c^2)}{405(1+\beta c)^5} x^{9/2} \\
&- \frac{M^8 c (-10+599\beta c-3582\beta^2 c^2+4059\beta^3 c^3)}{66825(1+\beta c)^7} x^6 \\
&+ \dots
\end{aligned} \quad (54)$$

(b) Case  $n = 1$ 

$$\begin{aligned}
\theta(x) &= c + \frac{2M^2 c^2}{3(1+\beta c)} x^{3/2} - \frac{2M^4 c^3 (-4+\beta c)}{45(1+\beta c)^3} x^3 \\
&+ \frac{2M^6 c^4 (9-11\beta c+10\beta^2 c^2)}{405(1+\beta c)^5} x^{9/2} \\
&- \frac{2M^8 c^5 (-330+1118\beta c-1584\beta^2 c^2+1093\beta^3 c^3)}{66825(1+\beta c)^7} x^6 \\
&+ \dots
\end{aligned} \quad (55)$$

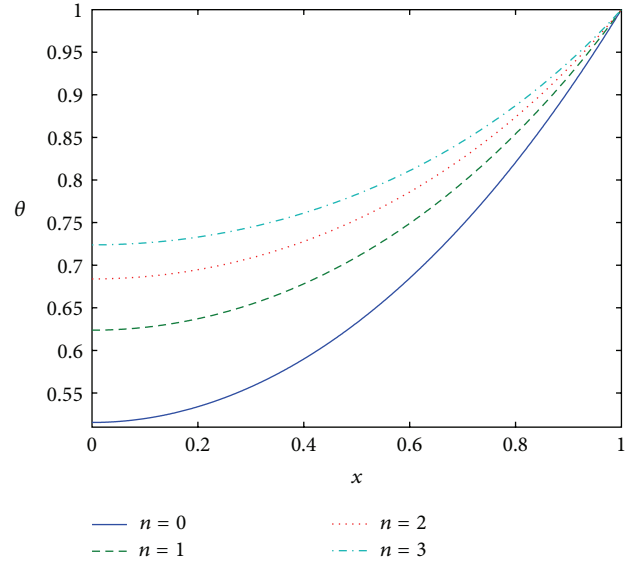


FIGURE 6: Temperature profile in a longitudinal rectangular fin with linear thermal conductivity and varying values of  $n$ . Here  $\beta = 0.5$  and  $M = 1.5$  are fixed.

(c) Case  $n = 2$ 

$$\begin{aligned}
\theta(x) &= c + \frac{2M^2 c^3}{3(1+\beta c)} x^{3/2} + \frac{2M^4 c^5 (6+\beta c)}{45(1+\beta c)^3} x^3 \\
&+ \frac{M^6 c^7 (16+3\beta c+7\beta^2 c^2)}{135(1+\beta c)^5} x^{9/2} \\
&+ \frac{M^8 c^9 (1160-107\beta c+1116\beta^2 c^2-367\beta^3 c^3)}{22275(1+\beta c)^7} x^6 \\
&+ \dots
\end{aligned} \quad (56)$$

(d) Case  $n = 3$ 

$$\begin{aligned}
\theta(x) &= c + \frac{2M^2 c^4}{3(1+\beta c)} x^{3/2} + \frac{2M^4 c^7 (8+3\beta c)}{45(1+\beta c)^3} x^3 \\
&+ \frac{4M^6 c^{10} (23+17\beta c+9\beta^2 c^2)}{405(1+\beta c)^5} x^{9/2} \\
&+ \frac{2M^8 c^{13} (5000+4868\beta c+4356\beta^2 c^2+363\beta^3 c^3)}{66825(1+\beta c)^7} x^6 \\
&+ \dots
\end{aligned} \quad (57)$$

The constant  $c$  may be obtained from the boundary condition on the appropriate  $\theta(x)$ . The solutions in (54), (55), (56) and (57) are depicted in Figure 7.

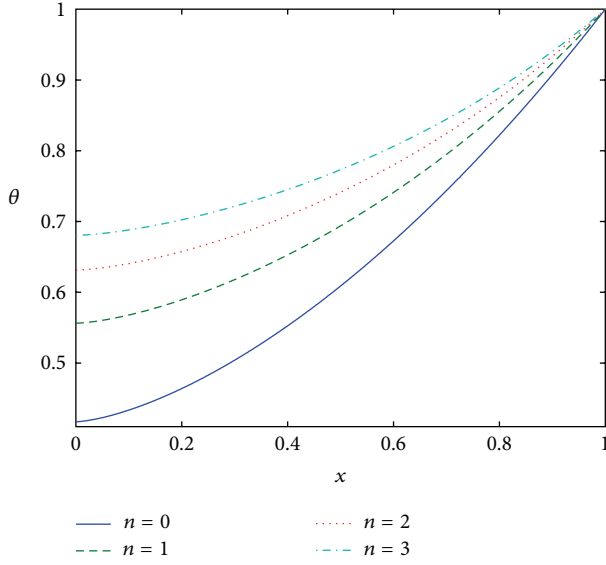


FIGURE 7: Temperature profile in a longitudinal convex parabolic fin with linear thermal conductivity and varying values of  $n$ . Here  $\beta = 0.5$  and  $M = 1.5$  are fixed.

**5.6. The Exponential Profile and Linear Thermal Conductivity.** In this section, we present solutions for equation heat transfer in a fin with convex parabolic profile and the thermal conductivity depending linearly on temperature. That is, we consider (4) with  $k(\theta) = 1 + \beta\theta$  and  $f(x) = e^{\sigma x}$ . Here  $\sigma$  is a constant. The analytical solutions for this problem for different values of  $n$  are given by

(a) Case  $n = 0$

$$\begin{aligned} \theta(x) &= c + \frac{M^2 c}{2(1+\beta c)} x^2 - \frac{\sigma M^2 c (2 + \beta c + \beta^2 c)}{6(1+\beta c)^2} x^3 \\ &+ \frac{M^2 c (M^2 (1 - 2\beta^2 c) + \sigma^2 (3 + 3\beta c + \beta^3 c^2 + \beta^4 c^2 + \beta^2 c (3 + c)))}{24(1+\beta c)^4} x^4 \\ &+ \dots \end{aligned} \quad (58)$$

(b) Case  $n = 1$

$$\begin{aligned} \theta(x) &= c + \frac{M^2 c^2}{2(1+\beta c)} x^2 - \frac{\sigma M^2 c^2 (2 + \beta c + \beta^2 c)}{6(1+\beta c)^2} x^3 \\ &+ \frac{M^2 c^2 (M^2 c (2 + \beta c - 2\beta^2 c) + \sigma^2 (3 + 3\beta c + \beta^3 c^2 + \beta^4 c^2 + \beta^2 c (3 + c)))}{24(1+\beta c)^3} x^4 \\ &+ \dots \end{aligned} \quad (59)$$

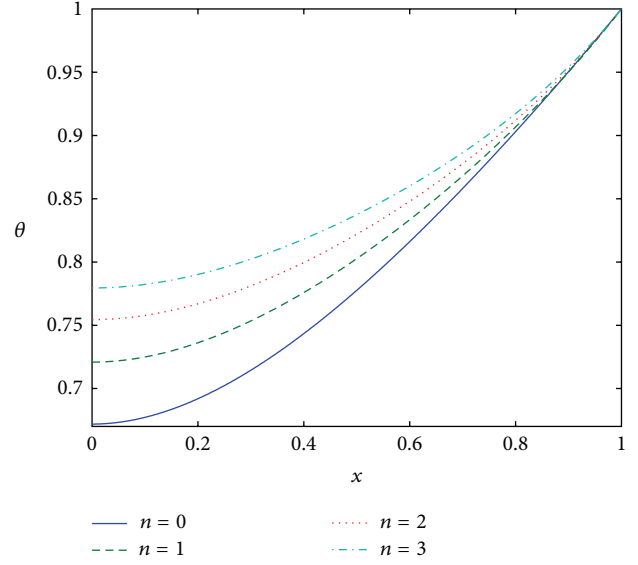


FIGURE 8: Temperature profile in a longitudinal fin of exponential profile with linear thermal conductivity and varying values of  $n$ . Here  $\beta = 0.5$  and  $M = 1.5$  are fixed.

(c) Case  $n = 2$

$$\begin{aligned} \theta(x) &= c + \frac{M^2 c^3}{2(1+\beta c)} x^2 - \frac{\sigma M^2 c^3 (2 + \beta c + \beta^2 c)}{6(1+\beta c)^2} x^3 \\ &+ \frac{M^2 c^3 (M^2 c^2 (3 + 2\beta c - 2\beta^2 c) + \sigma^2 (3 + 3\beta c + \beta^3 c^2 + \beta^4 c^2 + \beta^2 c (3 + c)))}{24(1+\beta c)^3} x^4 \\ &+ \dots \end{aligned} \quad (60)$$

(d) Case  $n = 3$

$$\begin{aligned} \theta(x) &= c + \frac{M^2 c^4}{2(1+\beta c)} x^2 - \frac{\sigma M^2 c^4 (2 + \beta c + \beta^2 c)}{6(1+\beta c)^2} x^3 \\ &+ \frac{M^2 c^4 (M^2 c^3 (4 + 3\beta c - 2\beta^2 c) + \sigma^2 (3 + 3\beta c + \beta^3 c^2 + \beta^4 c^2 + \beta^2 c (3 + c)))}{24(1+\beta c)^3} x^4 \\ &+ \dots \end{aligned} \quad (61)$$

The constant  $c$  may be obtained from the boundary condition on the appropriate  $\theta(x)$ . The solutions in (58), (59), (60), and (61) are depicted in Figure 8.

## 6. Fin Efficiency and Heat Flux

**6.1. Fin Efficiency.** The heat transfer rate from a fin is given by Newton's second law of cooling:

$$Q = \int_0^L PH(T)(T - T_a) dx. \quad (62)$$

Fin efficiency is defined as the ratio of the fin heat transfer rate to the rate that would be if the entire fin were at the base temperature and is given by (see e.g., [1])

$$\eta = \frac{Q}{Q_{\text{ideal}}} = \frac{\int_0^L PH(T)(T - T_a) dX}{Ph_b L (T_b - T_a)}. \quad (63)$$

In dimensionless variables, we have

$$\eta = \int_0^1 \theta^{n+1} dx. \quad (64)$$

We consider the solutions (50), (51), (52), and (53) and depict the fin efficiency (63) in Figure 9.

**6.2. Heat Flux.** The fin base heat flux is given by the Fourier's law

$$q_b = A_c K(T) \frac{dT}{dx}. \quad (65)$$

The total heat flux of the fin is given by [1]

$$q = \frac{q_b}{A_c H(T)(T_b - T_a)}. \quad (66)$$

Introducing the dimensionless variable as described in Section 2 implies

$$q = \frac{1}{Bi} \frac{k(\theta)}{h(\theta)} \frac{d\theta}{dx}, \quad (67)$$

where the dimensionless parameter  $Bi = h_b L / k_a$  is the Biot number. We consider a number of cases for the thermal conductivity and the heat transfer coefficient.

**6.2.1. Linear Thermal Conductivity and Power Law Heat Transfer Coefficient.** In this case (67) becomes

$$q = \frac{1}{Bi} (1 + \beta\theta) \theta^{-n} \frac{d\theta}{dx}. \quad (68)$$

The heat flux in (68) at the base of the fin is plotted in Figure 10.

**6.2.2. Power Law Thermal Conductivity and Heat Transfer Coefficient.** In this case (67) becomes

$$q = \frac{1}{Bi} \theta^{m-n} \frac{d\theta}{dx}. \quad (69)$$

Not surprisingly, heat flux in one-dimensional fins is higher given values  $Bi \ll 1$ . The heat flux in (69) is plotted in Figures 11(a), 11(b), and 11(c).

## 7. Some Discussions

The DTM has resulted in some interesting observations and study. We have observed in Figures 2(a) and 2(b) an excellent agreement between the analytical solutions generated by DTM and the exact solution obtained in [2]. In particular, we

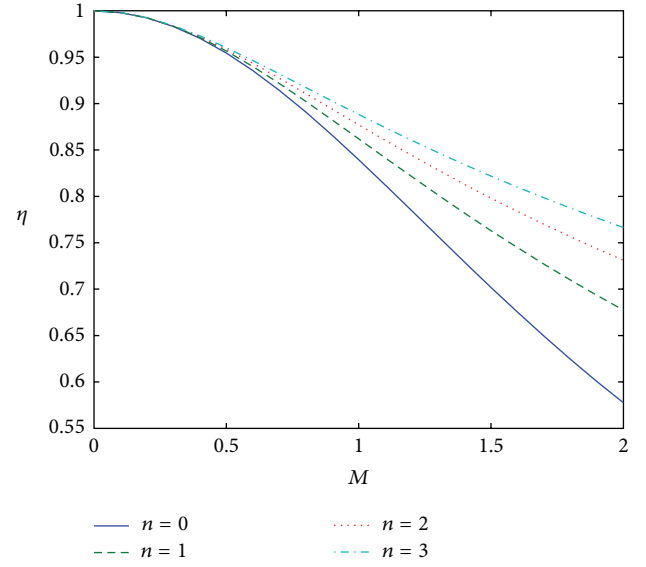


FIGURE 9: Fin efficiency of a longitudinal rectangular fin. Here  $\beta = 0.75$ .

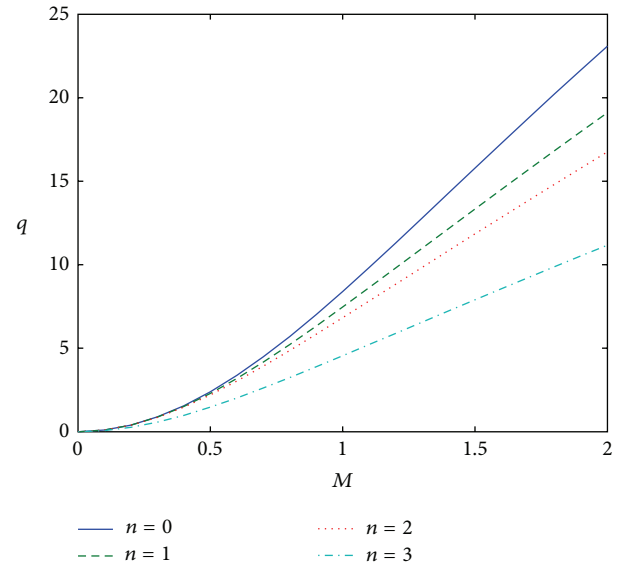


FIGURE 10: Base heat flux in a longitudinal rectangular fin with linear thermal conductivity. Here  $\beta = 0.1$ .

considered a fin problem in which both thermal conductivity and heat transfer coefficient are given by the same power law. Furthermore, we notice from Table 2 that an absolute error of approximately  $3.5e - 005$  is produced by DTM of order  $O(15)$ . In Table 3, an absolute error of approximately  $6.5e - 006$  is produced for the same order. This confirms that the DTM converges faster and can provide accurate results with a minimum computation. As such, a tremendous confidence in the DTM in terms of the accuracy and effectiveness was built, and thus we used this method to solve other problems for which exact solutions are harder to construct.

In Figures 3(a), 3(b), 4(a), 4(b), 5(a), and 5(b), we observe that the fin temperature increases with the decreasing

values of the thermogeometric fin parameter. Here, the values of the exponents are fixed. Also, we observe that fin temperature is higher when  $n - m > 0$ , that is, when heat transfer coefficient is higher than the thermal conductivity. We observe in Figures 6, 7, and 8 that the fin temperature increases with the increasing values of  $n$ . Furthermore, it appears that the fin with exponential profile performs the least in transferring the heat from the base, since the temperature in such a fin is much higher than that of the rectangular and the convex parabolic profiles. In other words, heat dissipation to the fluid surrounding the extended surface is much faster in longitudinal fins of rectangular and convex parabolic profiles. In Figure 9, fin efficiency decreases with increasing thermogeometric fin parameter. Also, fin efficiency increases with increasing values of  $n$ . It is easy to show that the thermogeometric fin parameter is directly proportional to the aspect ratio (extension factor) with square root of the Biot number being the proportionality constant. As such, shorter fins are more efficient than longer ones. Else, the increased Biot number results in less efficient fin whenever the space is confined, that is, where the length of the fin cannot be increased. Figure 10 depicts the heat flux at the fin base. The amount of heat energy dissipated from the fin base is of immense interest in engineering [28]. We observe in Figure 10 that the base heat flux increases with the thermogeometric fin parameter for considered values of the exponent  $n$  (see also [28]). Figures 11(a), 11(b), and 11(c) display the heat flux across the fin length. We note that the heat flux across the fin length increases with increasing values of the thermogeometric fin parameter.

## 8. Concluding Remarks

In this study, we have successfully applied the DTM to highly nonlinear problems arising in heat transfer through longitudinal fins of various profiles. Both thermal conductivity and heat transfer coefficient are given as functions of temperature. The DTM agreed well with exact solutions when the thermal conductivity and heat transfer coefficient are given by the same power law. A rapid convergence to the exact solution was observed. Following the confidence in DTM built by the results mentioned, we then solved various exciting problems. The exotic results have been shown in tables and figures listed in this paper.

The results obtained in this paper are significant improvements on the known results. In particular, both the heat transfer coefficient and the thermal conductivity are allowed to be given by the power law functions of temperature, and also we considered a number of fin profiles. We note that exact solutions are difficult if not impossible to construct when the exponents of these properties are distinct.

Perhaps the notable advantage of the DTM is the generalization of the Taylor method to problems involving unusual derivative procedures such as fractional, fuzzy, or  $q$ -derivative [22]. Some generalizations have been made by Odibat et al. [24], and they referred to their new method as the Generalized Differential Transform Method (GDTM). This showed great improvement compared to the Fractional Differential

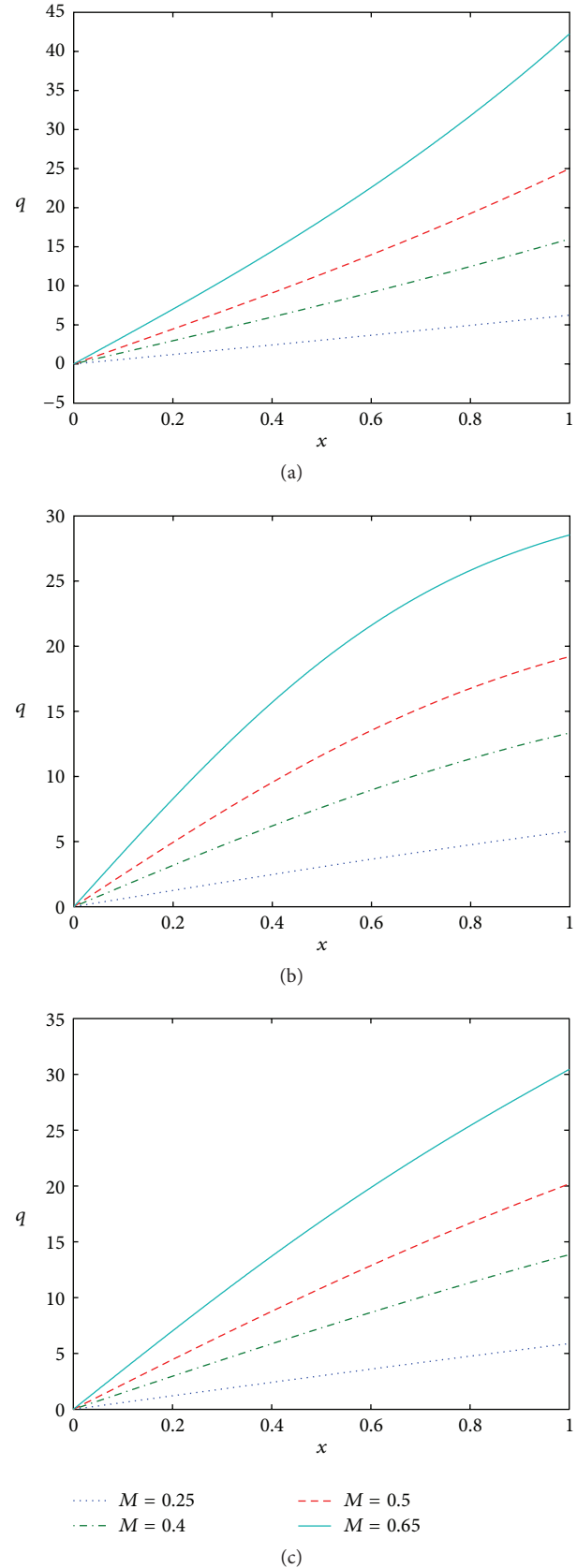


FIGURE 11: Heat flux across a longitudinal rectangular fin with linear thermal conductivity. (a)  $n - m < 0$ , (b)  $n - m > 0$ , and (c)  $n - m = 0$ . Here  $Bi = 0.01$ .

Transform Method (FDTM) introduced by Arikoglu and Ozkol [23].

We have shown with the help of an example that DTM may only be applied to fin problems involving heat transfer through fins with convex parabolic profile. Note that given an ODE such as (4) with a power law heat transfer coefficient of a fractional exponent, then one can easily remove the fraction by basic exponential rules and employment of the Binomial expansion. However, using the DTM, one runs into difficulty if the power law thermal conductivity in the same equation is given by the fractional exponent. We do not know whether these observations call for the “modified” DTM to solve problems arising in heat flow through fins with other profiles, such as longitudinal triangular and concave parabolic, and also with fractional power law thermal conductivity.

The main results obtained in this paper give insight into heat transfer in boiling liquids where the heat transfer coefficient is temperature dependent and may be given by a power law. The thermal conductivity of some materials such as gallium nitride (GaN) and Aluminium Nitride (AlN) may be modeled by power law temperature dependency [29, 30]. Thus, the solutions constructed here give a better comparison of heat transfer in terms of material used since in many engineering applications thermal conductivity is given as a linear function of temperature. Furthermore, a good study in terms of performance and efficiency of fin with different profiles is undertaken. These finding could help in the design of fins. It is claimed in [14] that DTM results are more accurate than those constructed by Variational Iteration Methods (VIM) and Homotopy Perturbation Methods (HPM). However, it would be risky to use the DTM approximate solutions as benchmarks for the numerical schemes. Nevertheless, we have also shown that DTM converges rapidly in just fifteen terms to the exact solution.

## Acknowledgments

The authors wish to thank the National Research Foundation of South Africa and the University of the Witwatersrand for the generous financial support. The authors are grateful to Professor D. P. Mason and the anonymous reviewers for their invaluable comments which improved this paper significantly.

## References

- [1] A. D. Kraus, A. Aziz, and J. Welty, *Extended Surface Heat Transfer*, Wiley, New York, NY, USA, 2001.
- [2] R. J. Moitsheki, T. Hayat, and M. Y. Malik, “Some exact solutions of the fin problem with a power law temperature-dependent thermal conductivity,” *Nonlinear Analysis. Real World Applications*, vol. 11, no. 5, pp. 3287–3294, 2010.
- [3] R. J. Moitsheki, “Steady one-dimensional heat flow in a longitudinal triangular and parabolic fin,” *Communications in Nonlinear Science and Numerical Simulation*, vol. 16, no. 10, pp. 3971–3980, 2011.
- [4] R. J. Moitsheki, “Steady heat transfer through a radial fin with rectangular and hyperbolic profiles,” *Nonlinear Analysis. Real World Applications*, vol. 12, no. 2, pp. 867–874, 2011.
- [5] Mo. Miansari, D. D. Ganji, and Me. Miansari, “Application of He’s variational iteration method to nonlinear heat transfer equations,” *Physics Letters A*, vol. 372, no. 6, pp. 779–785, 2008.
- [6] C. H. Chiu and C. K. Chen, “A decomposition method for solving the convective longitudinal fins with variable thermal conductivity,” *International Journal of Heat and Mass Transfer*, vol. 45, no. 10, pp. 2067–2075, 2002.
- [7] A. Rajabi, “Homotopy perturbation method for fin efficiency of convective straight fins with temperature-dependent thermal conductivity,” *Physics Letters A*, vol. 364, no. 1, pp. 33–37, 2007.
- [8] G. Domairry and M. Fazeli, “Homotopy analysis method to determine the fin efficiency of convective straight fins with temperature-dependent thermal conductivity,” *Communications in Nonlinear Science and Numerical Simulation*, vol. 14, no. 2, pp. 489–499, 2009.
- [9] A. Campo and R. J. Spaulding, “Coupling of the methods of successive approximations and undetermined coefficients for the prediction of the thermal behaviour of uniform circumferential fins,” *Heat and Mass Transfer*, vol. 34, no. 6, pp. 461–468, 1999.
- [10] A. Campo and F. Rodríguez, “Approximate analytic temperature solution for uniform annular fins by adapting the power series method,” *International Communications in Heat and Mass Transfer*, vol. 25, no. 6, pp. 809–818, 1998.
- [11] R. Chiba, “Application of differential transform method to thermoelastic problem for annular disks of variable thickness with temperature-dependent parameters,” *International Journal of Thermophysics*, vol. 33, pp. 363–380, 2012.
- [12] S. Sadri, M. R. Raveshi, and S. Amiri, “Efficiency analysis of straight fin with variable heat transfer coefficient and thermal conductivity,” *Journal of Mechanical Science and Technology*, vol. 26, no. 4, pp. 1283–1290, 2012.
- [13] M. Torabi, H. Yaghoori, and A. Aziz, “Analytical solution for convective-radiative continuously moving fin with temperature dependent thermal conductivity,” *International Journal of Thermophysics*, vol. 33, pp. 924–941, 2012.
- [14] M. Torabi and H. Yaghoobi, “Two dominant analytical methods for thermal analysis of convective step fin with variable thermal conductivity,” *Thermal Science*. In press.
- [15] A. Moradi, “Analytical solutions for fin with temperature dependent heat transfer coefficient,” *International Journal of Engineering and Applied Sciences*, vol. 3, no. 2, pp. 1–12, 2011.
- [16] A. Moradi and H. Ahmadikia, “Analytical solution for different profiles of fin with temperature-dependent thermal conductivity,” *Mathematical Problems in Engineering*, vol. 2010, Article ID 568263, 15 pages, 2010.
- [17] H. Yaghoobi and M. Torabi, “The application of differential transformation method to nonlinear equations arising in heat transfer,” *International Communications in Heat and Mass Transfer*, vol. 38, no. 6, pp. 815–820, 2011.
- [18] S. Ghafoori, M. Motevalli, M. G. Nejad, F. Shakeri, D. D. Ganji, and M. Jalaal, “Efficiency of differential transformation method for nonlinear oscillation: Comparison with HPM and VIM,” *Current Applied Physics*, vol. 11, no. 4, pp. 965–971, 2011.
- [19] A. A. Joneidi, D. D. Ganji, and M. Babaelahi, “Differential transformation method to determine fin efficiency of convective straight fins with temperature dependent thermal conductivity,” *International Communications in Heat and Mass Transfer*, vol. 36, no. 7, pp. 757–762, 2009.
- [20] J. K. Zhou, *Differential Transform Method and Its Applications for Electric circuits*, Huazhong University Press, Wuhan, China, 1986.



- [21] S. Mukherjee, "Reply to comment on 'solutions of the duffing-van der pol oscillator equation by the differential transform method,'" *Physica Scripta*, vol. 84, Article ID 037003, 2 pages, 2011.
- [22] C. Bervillier, "Status of the differential transformation method," *Applied Mathematics and Computation*, vol. 218, no. 20, pp. 10158–10170, 2012.
- [23] A. Arikoglu and I. Ozkol, "Solution of fractional differential equations by using differential transform method," *Chaos, Solitons and Fractals*, vol. 34, no. 5, pp. 1473–1481, 2007.
- [24] Z. Odibat, S. Momani, and V. S. Erturk, "Generalized differential transform method: application to differential equations of fractional order," *Applied Mathematics and Computation*, vol. 197, no. 2, pp. 467–477, 2008.
- [25] C. W. Bert, "Application of differential transform method to heat conduction in tapered fins," *Journal of Heat Transfer*, vol. 124, no. 1, pp. 208–209, 2002.
- [26] F. Khani and A. Aziz, "Thermal analysis of a longitudinal trapezoidal fin with temperature-dependent thermal conductivity and heat transfer coefficient," *Communications in Nonlinear Science and Numerical Simulation*, vol. 15, no. 3, pp. 590–601, 2010.
- [27] H. C. Ünal, "An analytical study of boiling heat transfer from a fin," *International Journal of Heat and Mass Transfer*, vol. 31, no. 7, pp. 1483–1496, 1988.
- [28] M. H. Chang, "A decomposition solution for fins with temperature dependent surface heat flux," *International Journal of Heat and Mass Transfer*, vol. 48, no. 9, pp. 1819–1824, 2005.
- [29] A. Jezowski, B. A. Danilchenko, M. Boćkowski et al., "Thermal conductivity of GaN crystals in 4.2–300 K range," *Solid State Communications*, vol. 128, no. 2-3, pp. 69–73, 2003.
- [30] S. Vitinov, V. Palankovski, S. Maroldt, and R. Quay, "High-temperature modeling of AlGaIn/GaN HEMTs," *Solid-State Electronics*, vol. 54, no. 10, pp. 1105–1112, 2010.

## Research Article

# Cortex Effect on Vacuum Drying Process of Porous Medium

Zhijun Zhang,<sup>1</sup> Shiwei Zhang,<sup>1</sup> Tianyi Su,<sup>1</sup> and Shuangshuang Zhao<sup>2</sup>

<sup>1</sup> School of Mechanical Engineering and Automation, Northeastern University, Shenyang 110004, China

<sup>2</sup> Shenyang Aircraft Design and Research Institute, Shenyang 110035, China

Correspondence should be addressed to Zhijun Zhang; zhjzhang@mail.neu.edu.cn

Received 25 February 2013; Accepted 5 April 2013

Academic Editor: Jun Liu

Copyright © 2013 Zhijun Zhang et al. This is an open access article distributed under the Creative Commons Attribution License, which permits unrestricted use, distribution, and reproduction in any medium, provided the original work is properly cited.

Corns, fruits, and vegetables are usually used as porous medium in drying process. But in fact, it must be considered as the cortex effect on mass transfer because the mass transfer of cortex is very difficult than inner medium. Based on the theory of heat and mass transfer, a coupled model for the porous medium vacuum drying process with cortex effect is constructed. The model is implemented and solved using COMSOL software. The water evaporation rate is determined using a nonequilibrium method with the rate constant parameter  $K_r$  that has been studied. The effects of different vapor pressures (1000, 5000, and 9000 Pa), initial moisture contents (0.3, 0.4, and 0.5 water saturation), drying temperatures (323, 333, and 343 K), and intrinsic permeability for cortex part ( $10^{-13}$ ,  $10^{-14}$ ,  $10^{-15}$  m<sup>2</sup>) on vacuum drying process were studied. The results facilitate a better understanding of the porous medium vacuum drying process that nearer to the reality.

## 1. Introduction

Scientists and engineers in China are currently studying vacuum drying equipment that could be used in corn drying [1–3]. However, the corn vacuum drying theory remains unclear. Hypothesized that corn is a porous medium, the vacuum drying of corn is a complicated heat and mass transfer process that has been the subject of intensive research [4–7]. All vacuum drying models have to address the water phase change during numerical solving. In one method, the vapor pressure is equal to its equilibrium value [8–11]. Another method is nonequilibrium method [12–16]. As the porous medium, the heat and mass transfer in vacuum drying process has been studied by nonequilibrium method [17]. The water evaporation rate is determined using a nonequilibrium method with the rate constant parameter  $K_r$ .  $K_r$  values of 1, 10, 1000, and 10000 are simulated. The effects of different vapor pressures (1000, 5000, and 9000 Pa), initial moisture contents (0.4, 0.5, and 0.6 water saturation), drying temperatures (323, 333, and 343 K), and intrinsic permeability ( $10^{-13}$ ,  $10^{-14}$ ,  $10^{-15}$  m<sup>2</sup>) are studied. It was observed that the temperature increased quickly at the start of drying and then lowered gradually. As the drying process continued, the temperature increased slowly. In the absence of free water, temperature

increased rapidly. As the drying process concluded, the temperature remained unchanged. The water evaporation rate could not be obtained during the porous medium vacuum drying process. The rate constant parameter is essential to the nonequilibrium method. When  $K_r \geq 1000$ , the simulation of the drying process was not evidently affected. Vapor pressure and heat transfer affected the transfer of mass. A similar effect was found in the initial moisture and the heat temperature. Intrinsic permeability had a greater effect on the drying process. In the study above, it is as the uniform porous medium. But in fact, it must be considered as the cortex effect on mass transfer because the mass transfer of cortex is more difficult than inner medium. The study of about cortex effect is very few.

In this paper, heat and mass transfer of porous medium with cortex in the vacuum drying process is implemented by using a nonequilibrium method. The effects of vapor pressure, initial moisture, heat temperature, and cortex intrinsic permeability on the drying process were then examined.

## 2. Physical Model

A physical one-dimensional (1D) model that explains the drying process is shown in Figure 1. The heat and mass

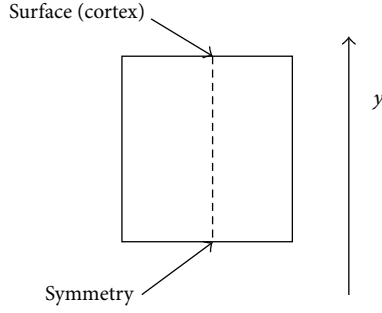


FIGURE 1: 1D model of porous medium with cortex.

transfer is considered only in the  $y$  direction. Because consider the cortex effect. The heat and mass transfer is through the surface of medium that is the cortex position. The total height of the porous medium is 1.05 cm, and the cortex height is 0.05 cm.

### 3. Mathematical Model

The porous medium consists of a continuous rigid solid phase, an incompressible liquid phase (free water), and a continuous gas phase that is assumed to be a perfect mixture of vapor and dry air, considered as ideal gases. For a mathematical description of the transport phenomenon in a porous medium, we adopt a continuum approach, wherein macroscopic partial differential equations are achieved through the volume averaging of the microscopic conservation laws. The value of any physical quantity at a point in space is given by its average value on the averaging volume centered at this point.

The moisture movement of the inner porous medium is liquid water and vapor movement; that is, the liquid water could become vapor, and the vapor and liquid water are moved by the pressure gradient. The heat and mass transfer theory could be found in everywhere [8].

The compressibility effects of the liquid phase are negligible, and the phase is homogeneous:

$$\bar{\rho}_l = \text{constant}. \quad (1)$$

The solid phase is rigid and homogeneous:

$$\bar{\rho}_s = \text{constant}. \quad (2)$$

The gaseous phase is considered an ideal gas. This phase ensures that

$$\begin{aligned} \bar{\rho}_a &= \frac{m_a P_a}{RT}, \\ \bar{\rho}_v &= \frac{m_v \bar{P}_v}{RT}, \\ \bar{P}_g &= \bar{P}_a + \bar{P}_v, \\ \bar{\rho}_g &= \bar{\rho}_a + \bar{\rho}_v. \end{aligned} \quad (3)$$

The assumption of the local thermal equilibrium between the solid, gas, and liquid phases involves

$$\bar{T}_s = \bar{T}_g = \bar{T}_l = \bar{T}. \quad (4)$$

Mass conservation equations are written for each component in each phase. Given that the solid phase is rigid, the following is given:

$$\frac{\partial \bar{\rho}_s}{\partial t} = 0. \quad (5)$$

The averaged mass conservation of the dry air yields

$$\frac{\partial (\varepsilon \cdot S_g \bar{\rho}_a)}{\partial t} + \nabla \cdot (\bar{\rho}_a \bar{V}_a) = 0. \quad (6)$$

For vapor,

$$\frac{\partial (\varepsilon \cdot S_g \bar{\rho}_v)}{\partial t} + \nabla \cdot (\bar{\rho}_v \bar{V}_v) = \dot{I}. \quad (7)$$

For free water,

$$\frac{\partial (\varepsilon \cdot S_w \bar{\rho}_l)}{\partial t} + \nabla \cdot (\bar{\rho}_l \bar{V}_l) = -\dot{I}. \quad (8)$$

For water, the general equation of mass conservation is obtained from the sum of the conservation equations of vapor ( $v$ ) and free water ( $l$ ). The general equation is written as follows:

$$\frac{\partial W}{\partial t} + \nabla \cdot \left\{ \frac{1}{\bar{\rho}_s} (\bar{\rho}_l \bar{V}_l + \bar{\rho}_v \bar{V}_v) \right\} = 0, \quad (9)$$

$$W = \frac{\varepsilon \cdot S_w \bar{\rho}_l + \varepsilon \cdot S_g \bar{\rho}_v}{(1 - \varepsilon) \bar{\rho}_s}. \quad (10)$$

For the Darcy flow of vapor,

$$\bar{\rho}_v \bar{V}_v = \bar{\rho}_v \bar{V}_g - \bar{\rho}_g D_{\text{eff}} \cdot \nabla \bar{\omega}. \quad (11)$$

For the Darcy flow of air,

$$\bar{\rho}_a \bar{V}_a = \bar{\rho}_a \bar{V}_g - \bar{\rho}_g D_{\text{eff}} \cdot \nabla \bar{\omega}, \quad (12)$$

where the gas and free water velocity is given by

$$\begin{aligned} \bar{V}_g &= \frac{k \cdot k_{rg}}{\mu_g} \cdot (\nabla \bar{P}_g - \rho_g \vec{g}), \\ \bar{V}_l &= \frac{k \cdot k_{rl}}{\mu_l} \cdot (\nabla \bar{P}_l - \rho_l \vec{g}). \end{aligned} \quad (13)$$

The effective diffusion coefficient [8] is given by

$$D_{\text{eff}} = D \underline{B}. \quad (14)$$

The vapor fraction in mixed gas is given by

$$\bar{\omega} = \frac{\bar{\rho}_v}{\bar{\rho}_g}. \quad (15)$$

TABLE 1: Parameters used in the simulation process.

Parameter	Symbol	Value	Unit
Rate constant parameter	$K_r$	1000	$s^{-1}$
Intrinsic permeability of inner medium	$k_{in}$	$10^{-13}$	$m^2$
Intrinsic permeability of cortex	$k_{cor}$	$10^{-13}, 10^{-14}, 10^{-15}$	$m^2$
Initial water saturation	$S_{l0}$	0.5, 0.4, 0.3	
Vapor pressure of vacuum drying chamber	$P_{vb}$	1000, 5000, 9000	Pa
Heat temperature	$T_h$	323, 333, 343	K
Porosity	$\varepsilon$	0.615	
Solid density	$\rho_s$	476	$kg\ m^{-3}$
Air pressure of vacuum drying chamber	$P_{ab}$	0.001	Pa

The pressure moving the free water is given by

$$\bar{P}_l = \bar{P}_g - \bar{P}_c. \quad (16)$$

For capillary pressure,

$$\bar{P}_c = 56.75 \times 10^3 (1 - S_l) \exp\left(\frac{1.062}{S_l}\right). \quad (17)$$

The saturation of free water and gas is

$$S_g + S_l = 1. \quad (18)$$

Free water relative permeability is given by

$$k_{rl} = \begin{cases} \left(\frac{S_l - S_{cr}}{1 - S_{cr}}\right)^3 & S_w > S_{cr} \\ 0 & S_w \leq S_{cr}. \end{cases} \quad (19)$$

Gas relative permeability is given by

$$k_{rg} = S_g. \quad (20)$$

The water phase change rate is expressed as

$$\dot{I} = K_r \frac{m_v (a_w P_{sat} - P_v) S_g \varepsilon}{RT}. \quad (21)$$

Water saturation vapor pressure is given by

$$P_{sat} = \frac{101325}{760} \times 10^{(8.07131 - (1730.63 / (233.426 + (T - 273))))}. \quad (22)$$

By considering the hypothesis of the local thermal equilibrium, the energy conservation is reduced to a unique equation:

$$\frac{\partial \bar{\rho} \bar{h}}{\partial t} + \nabla \cdot \{ (\bar{\rho}_a \bar{V}_a \bar{h}_a + \bar{\rho}_v \bar{V}_v \bar{h}_v + \bar{\rho}_l \bar{V}_l \bar{h}_l - \lambda_e \cdot \nabla \bar{T} - \Delta H \cdot \dot{I}) \} = 0, \quad (23)$$

$$\lambda_e = (1 - \varepsilon) \lambda_s + \varepsilon (S_l + S_g (\omega \lambda_v + (1 - \omega) \lambda_a)),$$

$$\bar{\rho} \bar{h} = \bar{\rho}_s \bar{h}_s + \varepsilon \cdot S_g \bar{\rho}_a \bar{h}_a + \varepsilon \cdot S_g \bar{\rho}_v \bar{h}_v + \varepsilon \cdot S_l \bar{\rho}_l \bar{h}_l.$$

#### 4. Boundary Condition and Parameters

The air pressure on the external surface of the porous medium is fixed, and the boundary condition for air is given by

$$P_a = P_{av}. \quad (24)$$

The boundary condition for vapor at the surface of the porous medium is given by

$$P_v = P_{vb}. \quad (25)$$

To simulate the vapor pressure of the vacuum drying chamber effect on the drying process, four different vapor pressure boundary values are used.

The boundary condition for free water at the top of the porous medium is

$$n \cdot (-D \nabla S_w) = 0. \quad (26)$$

The boundary condition at the surface of the porous medium is

$$T = T_h. \quad (27)$$

Three different  $T_h$  values are used in the simulation.

The initial moisture of the porous medium is represented by the liquid water saturation; different initial water saturation values are used. To compare the effects, drying base moisture content (d.b.) was also used, as shown in (9). The water phase change rate is used as 1000 that has been studied before [17]. Intrinsic permeability of inner medium is  $10^{-13} \text{ m}^2$ . Intrinsic permeability of cortex is  $10^{-14}, 10^{-15} \text{ m}^2$ . In order to compare the results, the intrinsic permeability of cortex  $10^{-13}$ , that is no cortex effect is simulated. In order to easily converge in, the parameter changer is used a smooth method. The modeling parameters are shown in Table 1.

#### 5. Numerical Solution

COMSOL Multiphysics 3.5a was used to solve the set of equations. COMSOL is an advanced software used for modeling and simulating any physical process described by partial derivative equations. The set of equations introduced above was solved using the relative initial and boundary conditions of each. COMSOL offers three possibilities for writing the

equations: (1) using a template (the Fick law and the Fourier law), (2) using the coefficient form (for mildly nonlinear problems), and (3) using the general form (for most nonlinear problems). Differential equations in the coefficient form were written using an unsymmetric-pattern multifrontal method. We used a direct solver for sparse matrices (UMFPACK), which involves significantly more complicated algorithms than solvers used for dense matrices. The main complication is the need to handle the fill-in in factors  $L$  and  $U$  efficiently.

A two-dimensional (2D) grid was used to solve the equations using COMSOL Multiphysics 3.5a. Given the symmetry condition setting at the left and the right sides, The 2D is applied to the 1D model shown in Figure 1. The mesh consists of  $2 \times 200$  elements (2D), and time stepping is 1 (from 0 s to 100 s of solution), 5 (from 100 s to 200 s of solution), 20 (from 200 s to 1000 s of solution), 30 (from 1000 s to 2000 s of solution), 40 (from 2000 s to 4000 s of solution), 50 (from 4000 s to 20000 s of solution), and 100 (from 20000 s to 50000 s of solution). Several grid sensitivity tests were conducted to determine the sufficiency of the mesh scheme and to ensure that the results are grid independent. The maximum element size was established as  $1e^{-4}$ . A backward differentiation formula was used to solve time-dependent variables. Relative tolerance was set to  $1e^{-3}$ , whereas absolute tolerance was set to  $1e^{-4}$ . The simulations were performed using a Tongfang PC with Intel Core 2 Duo processor with 3.0 GHz processing speed, and 4096 MB of RAM running Windows 7.

## 6. Results and Discussion

**6.1. Effect of Boundary Condition.** In the study before [17], the heat and mass transfer direction is the same. That is, the heat boundary is on the bottom of the medium. The heat transfer is from the bottom to top. The mass transfer boundary is on the top of bottom. The mass transfer is from the bottom to top by the pressure driving. But in this study, the cortex is considered. And the heat transfer and mass transfer are on the reversed direction as Figure 1. The heat and mass transfer with dryer is on the surface of the medium. The both condition was simulated to be compared as Figure 2. The simulation parameters are  $S_{i0} = 0.5$ ,  $K_r = 1000$ ,  $T_h = 323$  K,  $P_{vb} = 1000$  Pa,  $k_{in} = 10^{-13}$  m<sup>2</sup>, and no cortex. The moisture curve is just little different. The drying rate is little larger at the drying initial stage for same direction heat and mass transfer, and then it is little lower. The other condition is just reversed. The drying rate is little lower at the initial stage for reversed direction heat and mass transfer, and then it is little larger. The drying time for both is 6 hours.

**6.2. Effect of Cortex Resistance.** Intrinsic permeability of porous medium is an inherent property and cannot be changed, and measuring it is difficult. Intrinsic permeability has a greater effect because the transfer of free water and vapor is affected by (13). Usually, the cortex intrinsic permeability is less than inner medium. Figure 3 is the moisture curves of no cortex ( $k_{in}$  and  $k_{cor} = 10^{-13}$ ,  $10^{-14}$ , and  $10^{-15}$  m<sup>2</sup>, resp.), with cortex ( $k_{in} = 10^{-13}$  and  $k_{cor} = 10^{-14}$  and  $10^{-15}$  m<sup>2</sup> resp.). The other simulation parameters are  $S_{i0} = 0.5$ ,  $K_r =$

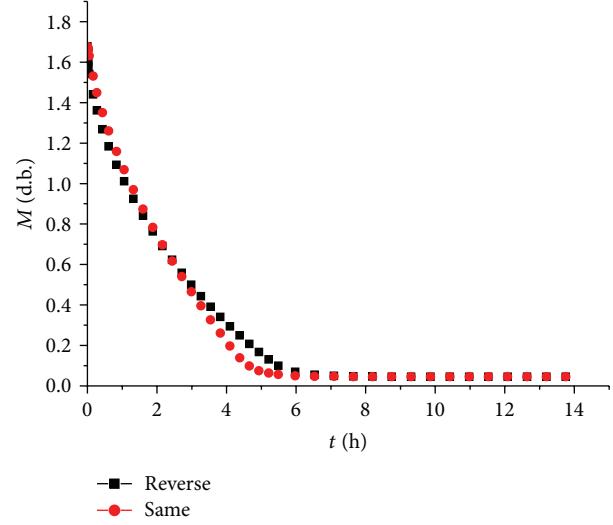


FIGURE 2: The effect of boundary condition, heat, and mass transfer is same and is reverse direction.

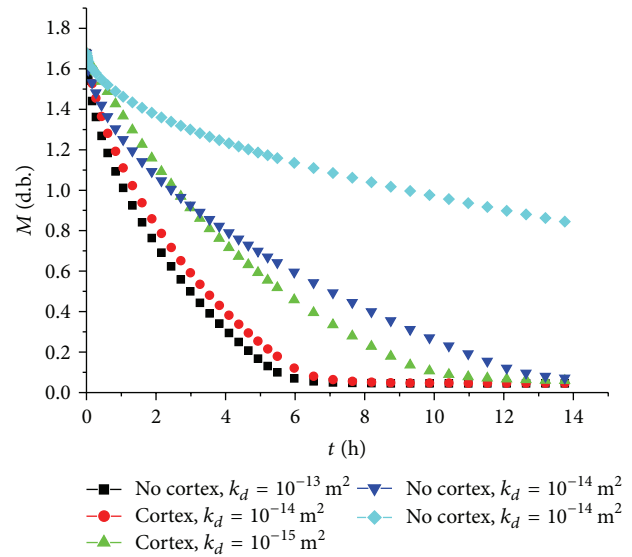


FIGURE 3: Moisture curves of no cortex ( $k_{in} = 10^{-13}$ ,  $k_{cor} = 10^{-13}$ ,  $10^{-14}$ , and  $10^{-15}$  m<sup>2</sup>), ( $k_{cor} = 10^{-14}$ ,  $10^{-15}$ ,  $k_{in} = 10^{-13}$  m<sup>2</sup>).

1000,  $T_h = 323$  K, and  $P_{vb} = 1000$  Pa. The drying time became evidently longer as the intrinsic permeability was reduced because the moisture movement velocity was lowered at the same pressure gradient. The different is not so obviously as the  $k_{cor} = 10^{-14}$  m<sup>2</sup>, that is lower 10-fold than inner medium. But when  $k_{cor} = 10^{-15}$  m<sup>2</sup>, the drying time is increased to 2-fold nearly. In order to compare, the no cortex,  $k_{cor} = 10^{-14}$  m<sup>2</sup>, and  $10^{-15}$  m<sup>2</sup> was shown. Because the numerical calculation is not convergence, the cortex  $k_{cor} = 10^{-16}$  m<sup>2</sup>,  $k_{in} = 10^{-13}$  m<sup>2</sup> result not gotten. The reason is that the material parameter changer is too big.

**6.3. Effect of Vapor Pressure in Vacuum Drying Chamber.** The pressure of a vacuum drying chamber, especially vapor



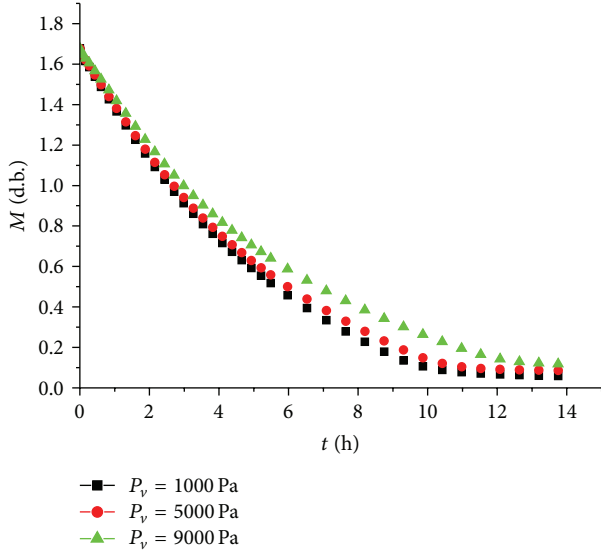


FIGURE 4: Moisture curves of different  $P_{vb} = 1000, 5000, 9000$  Pa,  $k_{cor} = 10^{-15} \text{ m}^2$ ,  $k_{in} = 10^{-13} \text{ m}^2$ .

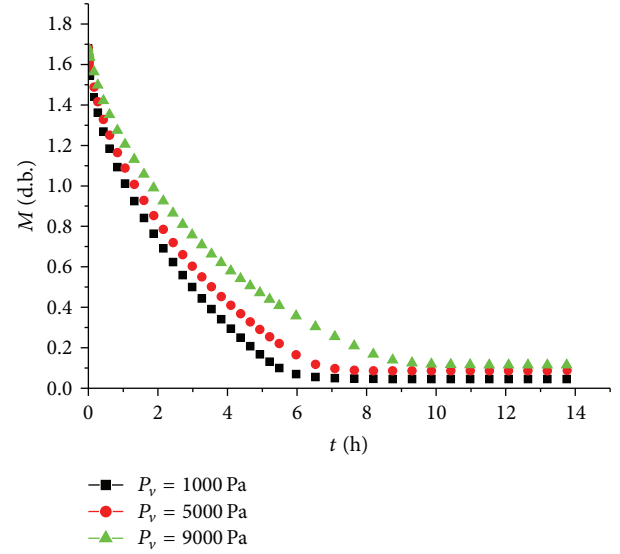


FIGURE 6: Moisture curves of different  $P_{vb} = 1000, 5000, 9000$  Pa, no cortex,  $k_{in} = 10^{-13} \text{ m}^2$ .

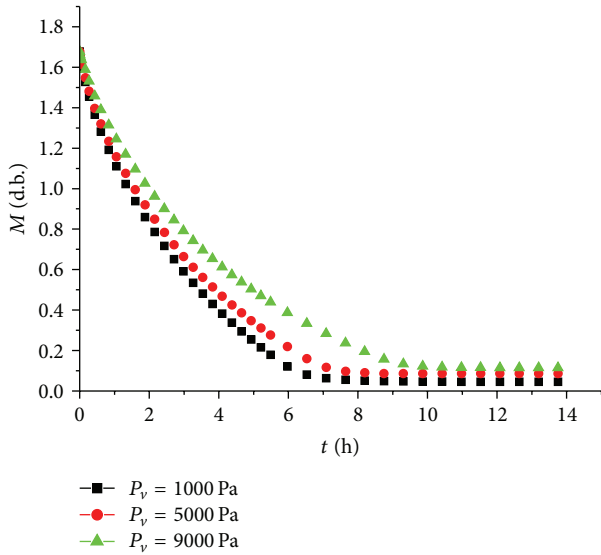


FIGURE 5: Moisture curves of different  $P_{vb} = 1000, 5000, 9000$  Pa,  $k_{cor} = 10^{-14} \text{ m}^2$ ,  $k_{in} = 10^{-13} \text{ m}^2$ .

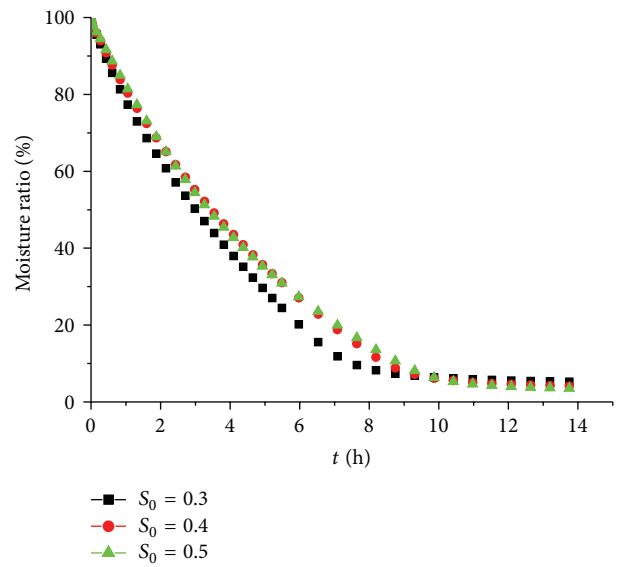


FIGURE 7: Moisture curves at different  $S_{i0} = 0.5, 0.4, 0.3$ ,  $k_{cor} = 10^{-15} \text{ m}^2$ ,  $k_{in} = 10^{-13} \text{ m}^2$ .

pressure, plays an important role in the vacuum drying process and is also linked to the drying cost. The moisture curves of  $P_{vb} = 1000, 5000$ , and  $9000$  Pa are shown in Figures 4, 5, and 6 with different cortex intrinsic permeability. The other simulation parameters are  $S_{i0} = 0.5$ ,  $K_r = 1000$ , and  $T_h = 323$  K. The vapor pressure has a greater effect on the drying process; a lower vapor pressure results in greater pressure degradation. The movements of free water and vapor as well as the free water evaporation rate are quicker, as given by (13) and (21), respectively. But the pressure effect is lower by the cortex intrinsic permeability reduced.

**6.4. Effect of Initial Moisture Content.** The effect of initial moisture content on the moisture curve is shown in Figures 7,

8, and 9 for  $S_{i0} = 0.5, 0.4, 0.3$  with different cortex intrinsic permeability. To compare the results, moisture is represented by the moisture ratio  $M/M_0$ . The other parameters are  $K_r = 1000$ ,  $P_{vb} = 1000$  Pa, and  $T_h = 323$  K. The drying time is about 10 hours, 6.5 hours, and 6 hours for  $S_{i0} = 0.5, 0.4, 0.3$ , respectively. In the same intrinsic permeability, the drying time is almost the same. The initial moisture has a less effect when initial moisture is 0.4 and 0.3, especially cortex intrinsic permeability  $k_{cor} = 10^{-15} \text{ m}^2$ . The drying rate is little larger for  $S_{i0} = 0.5$ , and the drying rate is almost the same for  $S_{i0} = 0.4, 0.3$ .

**6.5. Effect of Heat Temperature.** The effect of heat temperature on moisture is shown in Figures 10, 11, and 12 for the heat

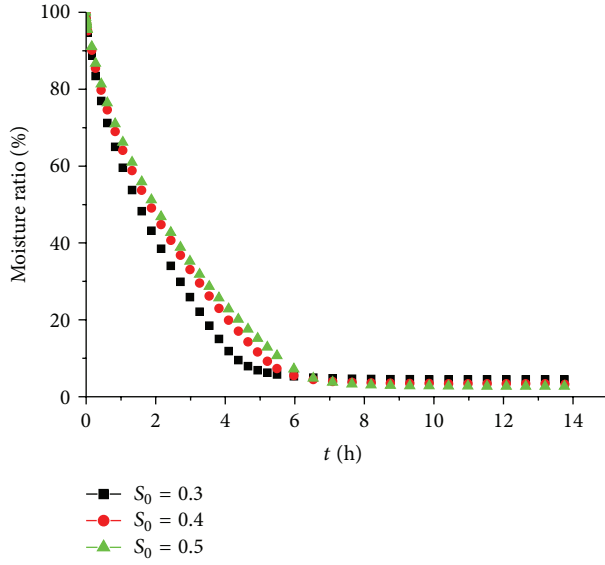


FIGURE 8: Moisture curves at different  $S_{i0} = 0.5, 0.4, 0.3$ ,  $k_{cor} = 10^{-14} \text{ m}^2$ ,  $k_{in} = 10^{-13} \text{ m}^2$ .

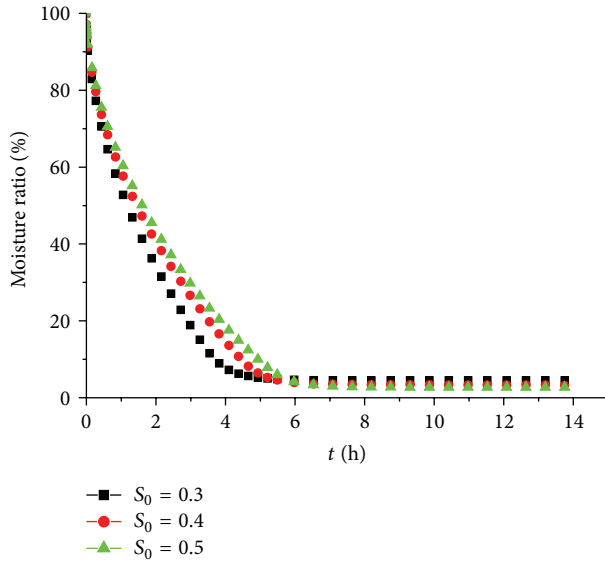


FIGURE 9: Moisture curves at different  $S_{i0} = 0.5, 0.4, 0.3$ , no cortex,  $k_{in} = 10^{-13} \text{ m}^2$ .

temperature  $T_h = 323, 333$ , and  $343 \text{ K}$ . The other parameters are  $S_{i0} = 0.5$ ,  $K_r = 1000$ , and  $P_v = 1000 \text{ Pa}$ . The effect of heat temperature is obviously in all simulation. The drying time is more than 14 hours for  $T_h = 323 \text{ K}$ ,  $k_{cor} = 10^{-15} \text{ m}^2$ , and  $k_{in} = 10^{-13} \text{ m}^2$ . And it is about 10 hours and 8 hours for  $T_h = 333, 343 \text{ K}$ ,  $k_{cor} = 10^{-15} \text{ m}^2$ , and  $k_{in} = 10^{-13} \text{ m}^2$ . The drying time is more than 9 hours for  $T_h = 333 \text{ K}$ ,  $k_{cor} = 10^{-15} \text{ m}^2$ , and  $k_{in} = 10^{-13} \text{ m}^2$ . It is about 7 hours and 6 hours for  $T_h = 333, 343 \text{ K}$ ,  $k_{cor} = 10^{-15} \text{ m}^2$ , and  $k_{in} = 10^{-13} \text{ m}^2$ . The drying time is more than 7 hours for  $T_h = 333 \text{ K}$ ,  $k_{cor} = 10^{-15} \text{ m}^2$ , and  $k_{in} = 10^{-13} \text{ m}^2$ . It is about 6 hours and 5 hours for  $T_h = 333, 343 \text{ K}$ ,  $k_{cor} = 10^{-15} \text{ m}^2$ , and  $k_{in} = 10^{-13} \text{ m}^2$ .

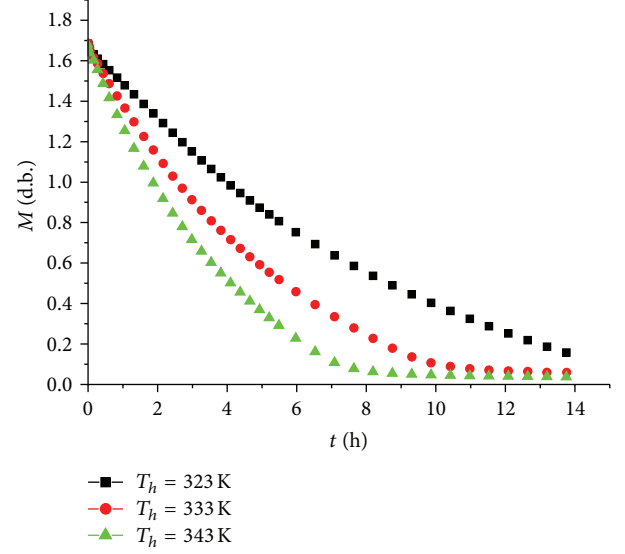


FIGURE 10: Moisture curves at different  $T_h = 323, 333, 343 \text{ K}$ ,  $k_{cor} = 10^{-15} \text{ m}^2$ ,  $k_{in} = 10^{-13} \text{ m}^2$ .

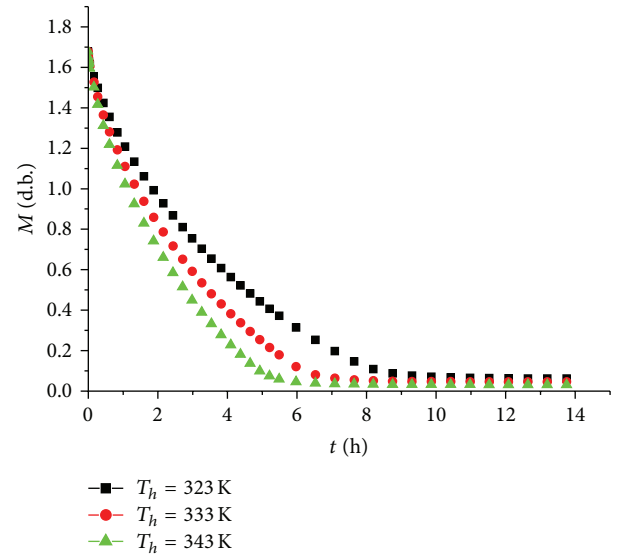


FIGURE 11: Moisture curves at different  $T_h = 323, 333, 343 \text{ K}$ ,  $k_{cor} = 10^{-14} \text{ m}^2$ ,  $k_{in} = 10^{-13} \text{ m}^2$ .

## 7. Conclusion

A coupled model of porous medium vacuum drying with cortex effect based on the theory of heat and mass transfer was implemented in this paper. The drying rate is little higher at the drying initial stage for the same direction of heat and mass transfer, and then it is little lower. The drying time became evidently longer as the intrinsic permeability was reduced because the moisture movement velocity was lowered at the same pressure gradient. The difference is not so obvious as the  $k_{cor} = 10^{-14} \text{ m}^2$ , that is lower 10-fold than inner medium. But when  $k_{cor} = 10^{-15} \text{ m}^2$ , the drying time is increased to 200% nearly. The vapor pressure has a greater effect on

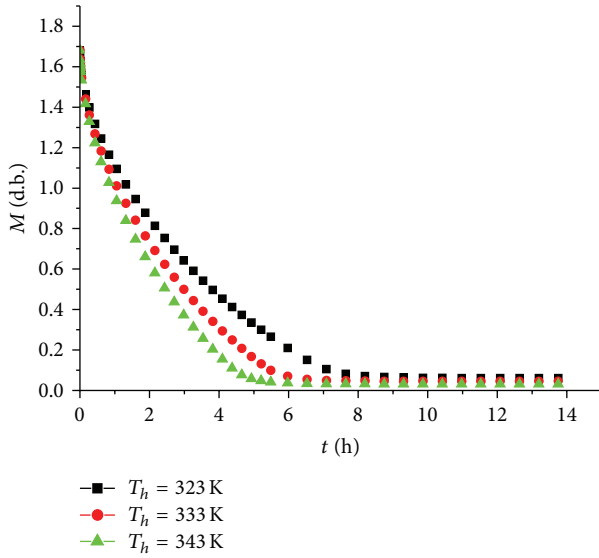


FIGURE 12: Moisture curves at different  $T_h = 323, 333, 343$  K, no cortex,  $k_{in} = 10^{-13} \text{ m}^2$ .

the drying process; a lower vapor pressure results in greater pressure degradation. But the pressure effect is lower by the reduction of the cortex intrinsic permeability. For initial moisture effect, in the same intrinsic permeability, the drying time is almost the same. The initial moisture is a less effect when initial moisture is 0.4 and 0.3, especially cortex intrinsic permeability  $k_{cor} = 10^{-15} \text{ m}^2$ . The drying rate is little larger for  $S_{i0} = 0.5$ , and the drying rate is almost the same for  $S_{i0} = 0.4, 0.3$ . The effect of heat temperature is obviously in all simulation.

## Nomenclature

$B$ :	Diagonal tensor
$D$ :	Diffusivity ( $\text{m}^2 \text{s}^{-1}$ )
$D_{\text{eff}}$ :	Diffusion tensor ( $\text{m}^2 \text{s}^{-1}$ )
$g$ :	Gravity vector ( $\text{m s}^{-2}$ )
$h$ :	Intrinsic averaged enthalpy ( $\text{J kg}^{-1}$ )
$I$ :	Water phase rate ( $\text{kg s}^{-1} \text{m}^{-3}$ )
$k$ :	Intrinsic permeability ( $\text{m}^2$ )
$k_r$ :	Relative permeability
$m$ :	Mass (kg)
$n$ :	Outer unit normal to the product
$P$ :	Pressure (Pa)
$P_c$ :	Capillary pressure (Pa)
$R$ :	Universal Gas constant ( $\text{J kmol}^{-1} \text{K}^{-1}$ )
$S$ :	Saturation
$t$ :	Time (s)
$T$ :	Temperature (K)
$W$ :	Moisture content (in dry basis).

## Greek Letters

$\Delta H$ :	Latent of phase change ( $\text{J kg}^{-1}$ )
$\lambda_{\text{ef}}$ :	Effective thermal conductivity tensor ( $\text{W m}^{-1} \text{K}^{-1}$ )

$\mu$ : Viscosity ( $\text{kg m}^{-1} \text{s}^{-1}$ )  
 $\rho$ : Density ( $\text{kg m}^{-3}$ )  
 $\omega$ : Vapor fraction.

## Subscripts

$a$ : Dry air  
 $g$ : Gas  
 $l$ : Liquid  
 $s$ : Solid  
 $v$ : Vapor  
 $\text{sat}$ : Vapor saturation  
 $\text{in}$ : Inner medium  
 $\text{cor}$ : Cortex.

## Mathematical Operators

$\Delta$ : Gradient operator  
 $\nabla \cdot$ : Divergence operator.

## Acknowledgment

This research was supported by the National Natural Science Foundation of China (Grant nos. 31000665 and nos. 51176027).

## References

- [1] C. H. Xu, Z. J. Zhang, S. W. Zhang, and X. He, "Probe into the structure of tower continuous vacuum dryer," in *Proceedings of the 5th Asia-Pacific Drying Conference (ADC '07)*, pp. 1261–1267, August 2007.
- [2] Z. J. Zhang, C. H. Xu, S. W. Zhang, and X. He, "The study of corn low temperature continuous tower type vacuum dryer," in *Proceedings of the 5th Asia-Pacific Drying Conference (ADC '07)*, pp. 330–337, August 2007.
- [3] Z. Zhang, C. Xu, S. Zhang, and L. Zhao, "Computer simulation of flow field in tower continuous vacuum dryer," in *Proceedings of the International Conference on Computer Science and Information Technology (ICCSIT '08)*, pp. 534–538, September 2008.
- [4] I. Yasuaki and A. P. S. Selvadurai, *Transport Phenomena in Porous Media, Aspects of Micro/Macro Behaviour*, Springer, 2012.
- [5] A. K. Haghi, "Transport phenomena in porous media: a review," *Theoretical Foundations of Chemical Engineering*, vol. 40, no. 1, pp. 14–26, 2006.
- [6] S. J. Kowalski, *Drying of Porous Materials*, Springer, 2007.
- [7] B. Jacob and Y. Bachmat, *Introduction to Modeling of Transport Phenomena in Porous Media*, Springer, 1990.
- [8] A. Erriguible, P. Bernada, F. Couture, and M. A. Roques, "Simulation of vacuum drying by coupling models," *Chemical Engineering and Processing*, vol. 46, no. 12, pp. 1274–1285, 2007.
- [9] A. Erriguible, P. Bernada, F. Couture, and M. A. Roques, "Modeling of heat and mass transfer at the boundary between a porous medium and its surroundings," *Drying Technology*, vol. 23, no. 3, pp. 455–472, 2005.
- [10] K. Murugesan, H. N. Suresh, K. N. Seetharamu, P. A. Aswatha Narayana, and T. Sundararajan, "A theoretical model of brick drying as a conjugate problem," *International Journal of Heat and Mass Transfer*, vol. 44, no. 21, pp. 4075–4086, 2001.

- [11] P. Perré and I. W. Turner, "A dual-scale model for describing drier and porous medium interactions," *AIChE Journal*, vol. 52, no. 9, pp. 3109–3117, 2006.
- [12] S. S. Torres, W. Jomaa, J.-R. Puiggali, and S. Avramidis, "Multiphysics modeling of vacuum drying of wood," *Applied Mathematical Modelling*, vol. 35, no. 10, pp. 5006–5016, 2011.
- [13] S. S. Torres, J. R. Ramírez, and L. Méndez-Lagunas, "Modeling plain vacuum drying by considering a dynamic capillary pressure," *Chemical and Biochemical Engineering Quarterly*, vol. 25, no. 3, pp. 327–334, 2011.
- [14] A. Warning, A. Dhall, D. Mitrea, and A. K. Datta, "Porous media based model for deep-fat vacuum frying potato chips," *Journal of Food Engineering*, vol. 110, no. 3, pp. 428–440, 2012.
- [15] A. Halder, A. Dhall, and A. K. Datta, "An improved, easily implementable, porous media based model for deep-fat frying. Part I: model development and input parameters," *Food and Bioprocess Processing*, vol. 85, no. 3 C, pp. 209–219, 2007.
- [16] A. Halder, A. Dhall, and A. K. Datta, "An improved, easily implementable, porous media based model for deep-fat frying. Part II: results, validation and sensitivity analysis," *Food and Bioprocess Processing*, vol. 85, no. 3, pp. 220–230, 2007.
- [17] Z. Zhang and N. Kong, "Nonequilibrium thermal dynamic modeling of porous medium vacuum drying process," *Mathematical Problems in Engineering*, vol. 2012, Article ID 347598, 22 pages, 2012.

## Research Article

# A Numerical Study on Premixed Bluff Body Flame of Different Bluff Apex Angle

Gelan Yang,<sup>1</sup> Huixia Jin,<sup>2</sup> and Na Bai<sup>3</sup>

<sup>1</sup> School of Information Science and Engineering, Hunan City University, Yiyang 413000, China

<sup>2</sup> School of Electronics and Communications Engineering, Hunan City University, Yiyang, China

<sup>3</sup> School of Electronics and Information Engineering, Anhui University, Hefei, China

Correspondence should be addressed to Gelan Yang; [glyang@mail.ustc.edu.cn](mailto:glyang@mail.ustc.edu.cn)

Received 21 October 2012; Revised 28 January 2013; Accepted 28 January 2013

Academic Editor: Zhijun Zhang

Copyright © 2013 Gelan Yang et al. This is an open access article distributed under the Creative Commons Attribution License, which permits unrestricted use, distribution, and reproduction in any medium, provided the original work is properly cited.

In order to investigate effects of apex angle ( $\alpha$ ) on chemically reacting turbulent flow and thermal fields in a channel with a bluff body V-gutter flame holder, a numerical study has been carried out in this paper. With a basic geometry used in a previous experimental study, the apex angle was varied from  $45^\circ$  to  $150^\circ$ . Eddy dissipation concept (EDC) combustion model was used for air and propane premixed flame. LES-Smagorinsky model was selected for turbulence. The grid-dependent learning and numerical model verification were done. Both nonreactive and reactive conditions were analyzed and compared. The results show that as  $\alpha$  increases, recirculation zone becomes bigger, and Strouhal number increases a little in nonreactive cases while decreases a little in reactive cases, and the increase of  $\alpha$  makes the flame shape wider, which will increase the chamber volume heat release ratio and enhance the flame stability.

## 1. Introduction

Flames can only be stabilized in high-velocity reactant streams over a certain range of conditions, while a variety of approaches are used to stabilize flames in a combustor, for example, bluff body flame holders such that V gutters are widely used in many modern combustion devices, such as augmenters or after burners in turbojet/turbofan engines and ramjet engines [1]. Combustors with bluff-body flame holders are characterized by a shear layer where vortices are shed due to Kelvin-Helmholtz instability [2], and this shear layer separates the region of high-speed fresh mixtures from the wake region of lower-speed hot products, and due to the boundary layer separation, a V-gutter bluff body creates a recirculation zone that acts as an ignition source for incoming fuel/air mixture by recycling hot products and radicals from the burned mixture.

Both experimental and numerical studies on bluff body flame have been done over years. Fujii et al. [3] and Yue et al. [4] carried out experiments to study nonreactive flow without reaction characteristics behind a flame stabilizer. Nakamura

[5] studied vortex-shedding frequency of bluff bodies with different after-body shape, his study showed that Strouhal number increases as the ratio of afterbody length to cross-flow dimension of the bluff body is increased. Sanquer et al. [6] investigated the chemically reacting flow characteristics behind V gutters. Cuppoletti et al. [6] measured the high-frequency combustion instabilities with a radial V gutter. Sjunnesson et al. [7, 8] used LDA and CARS measuring the velocities and turbulence in a bluff body stabilized flame and describe the rig in detail and report preliminary computations of the flow field using a two-step global mechanism solved online with Arrhenius expressions in conjunction with the Magnussen-Hjertager combustion model. Siewert [9] studied the methane/air premixed flames at high pressure using PIV and OH PILE. In numerical field, Eriksson [10] carried out numerical study of different RANS turbulence models efferent on rig VR-1 flame using CFD software CFX based on Zimont Turbulent Flame Closure (TFC) model, but they did not discuss LES model and vortex shedding. Engdar et al. [11] apply the Level-Set Flamelet Library approach in conjunction with varying 2-equation turbulence models,



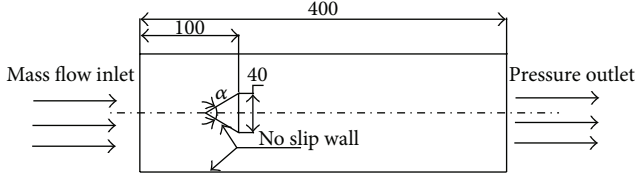


FIGURE 1: Geometry structure and boundary condition of bluff body.

flame speed models, and flame thickness models. 50 species and 402 elementary reactions were used to build the flamelet library. Giacomazzi et al. [12] used the fractal model as SGS model of LES for turbulence and EDC combustion model to compare experiment dates of VR-1 with LES-FM, RANS  $k-\epsilon$ , and LES-Smagorinsky model. Wang [13], Fureby [14], and Porumbel and Menon[15] had also performed LES computations on VR-1. Erickson and Soteriou [16] carried out numerical study on reactant temperature effect of a two-dimensional triangular bluff body flame. Park and Ko [17] introduced a G equation to Les subgrid scale combustion model for turbulent premixed flame stabilized by the bluff body.

Although direct numerical simulation (DNS) is able to resolve all turbulence scales, its computational resource requirements are prohibited for practical applications. In recent year, LES and hybrid RANS/LES approaches received great attentions among researchers as it can capture more transient turbulence structures than RANS for flame holder studies as discussed above. In order to investigate the bluff apex angle effects on flow field, 2D numerical study has been carried out using CFD software FLUENT 6.3.26 in this paper, EDC flame model which assumes that chemical reactions take place only at the dissipative scales of turbulence is used for premixed flame simulation. In turbulence, Smagorinsky subgrid LES model is applied.

## 2. Theoretical Fundamentals of the EDC Model

Most fuels are fast burning, and the overall rate of reaction is controlled by turbulent mixing. In premixed flames, the turbulence slowly convects/mixes cold reactants and hot products into the reaction zones, where reaction occurs rapidly. In such cases, the combustion is said to be mixing limited, and the complex chemical kinetic rates can be safely neglected. Both physical and chemical processes are important in simulating combustion systems. The formation of turbulent structures is a physical process, for which the concept of the eddy cascade model is the basis [19]. The largest turbulent structures have a size, which is of the magnitude of the system's dimensions. By interaction among themselves, eddies dissipate to smaller ones. The smallest eddies have an extension:

$$\eta \cdot \left( \frac{v^3}{\epsilon} \right), \quad (1)$$

where  $\eta$  is the Kolmogorov length scale. At these scales, dissipation of turbulent kinetic energy  $k$  takes place with a

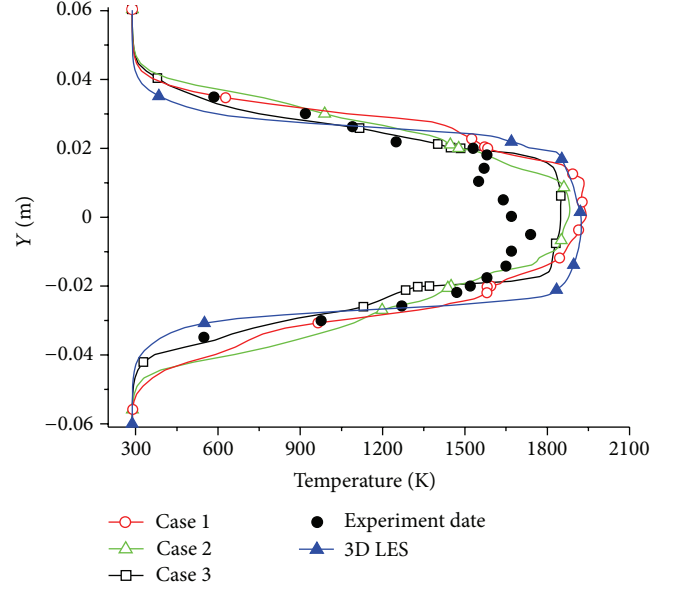


FIGURE 2: Temperature distribution at different grid sizes ( $X = 15$  cm) and reaction experiment date.

rate  $\epsilon$  where  $\nu$  is the kinematic viscosity. At a size smaller than  $\eta$  no turbulent structures exist, because in those regions molecular diffusion is faster than turbulent transport. From this thought the conception of the EDC was developed. There is a range in which the reactions can be regarded as ideally mixed. Thus, chemical reaction kinetics determines the speed of the process. while outside this range the reactants are not mixed and do not react, it assumes that reaction occurs in small turbulent structures, called the fine scales. The length fraction of the fine scales is modeled as

$$\gamma = C_\gamma \left( \frac{\nu \epsilon}{k^2} \right)^{1/4} \quad \text{with } C_\gamma = 2.1377. \quad (2)$$

The volume fraction of the fine scales is calculated as  $\gamma^3$ . Species are assumed to react in the fine structures over a time scale:

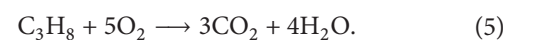
$$\tau = C_\tau \left( \frac{\nu}{\epsilon} \right)^{1/2} \quad (3)$$

with  $C_\tau = 0.4082$ .

The species transport equation (conservation equation) is written as

$$\begin{aligned} & \frac{\partial}{\partial t} (\rho Y_i) + \nabla \cdot (\rho \vec{v} Y_i) \\ & = -\nabla \cdot J_i + R_i \quad \text{with } R_i = \frac{\rho \gamma^2}{\tau (1 - \gamma^3)} (Y_i^* - Y_i). \end{aligned} \quad (4)$$

The computation of the reaction rate source terms is accelerated with the in-situ adaptive tabulation (ISAT) algorithm [19] embodied in the solver. For simplicity, the propane-air combustion was simulated using a one-step irreversible chemical reaction:



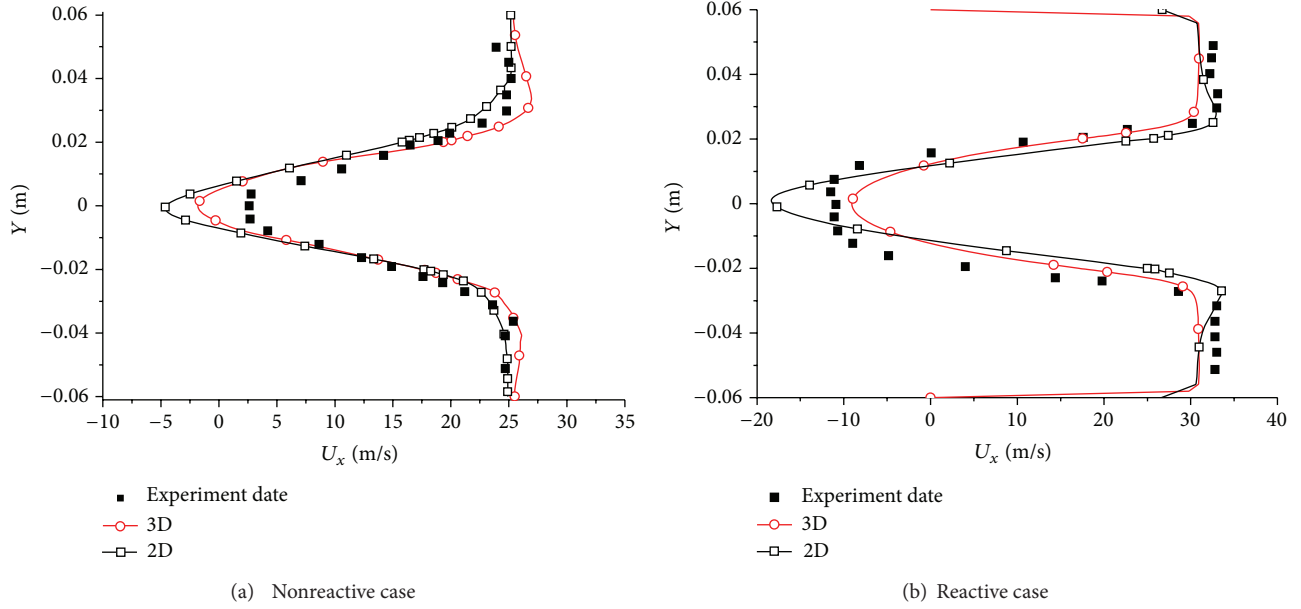
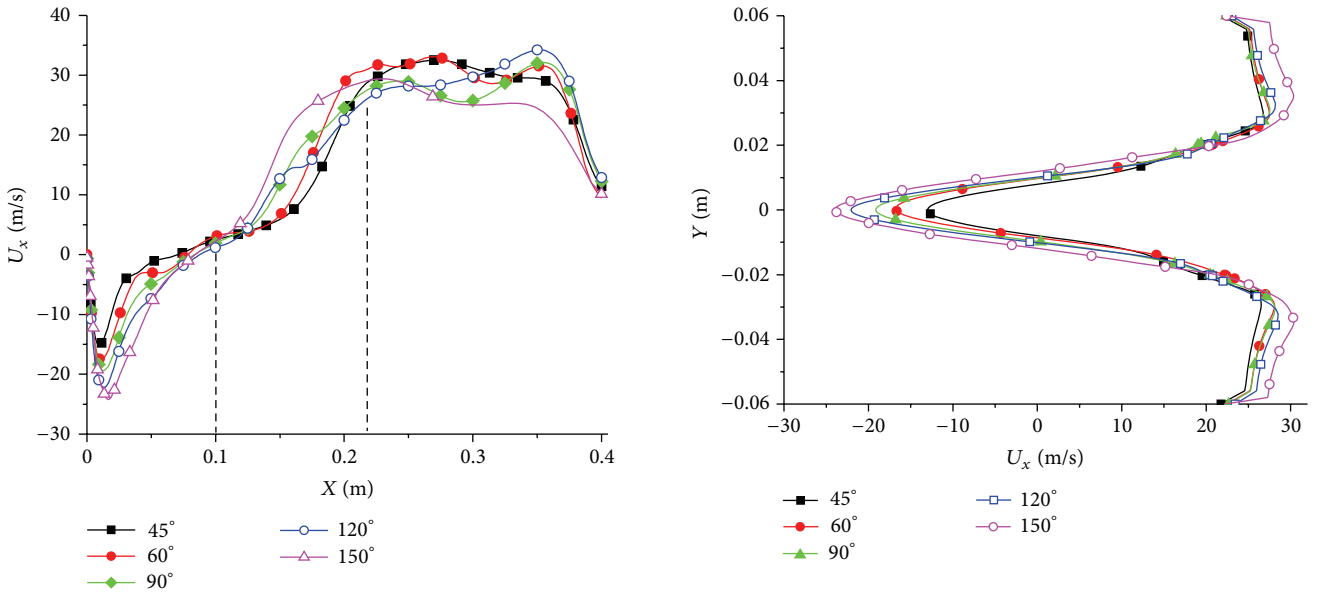
FIGURE 3: Comparison of streamwise velocity profiles with experimental data ( $X = 6.1$  cm).

FIGURE 4: Mean streamwise velocity distribution along the center line for nonreactive case.

### 3. Test Case Description and Computational Details

**3.1. Case Geometry and Boundary Conditions.** Volvo Aero Corporation (VAC) Triangular Bluff Body Stabilized Combustion rig VR-1 [8] has been extensively researched both in terms of experiments and theoretical treatment, and one case of VR-1 has been used in this paper. The flow field size is shown in Figure 1. The air and propane mixture is

introduced at an equivalence ratio  $\Phi = 0.65$ , the air mass flow rate is 0.6 kg/s, the inlet temperature is 288 K, and the mixture velocity at channel inlet is about 17.2 m/s. The nominal pressure is 1 atm. The Reynolds number based on the bluff-body dimension and the inlet velocity is nearly 50,000.

The governing equations are solved using CFD software ANSYS FLUENT 6.3.2.6. The mass flow inlet and pressure outlet boundary conditions are used. The mass flow rate, total temperature, and species mass fractions are assumed fixed while pressure was extrapolated at inlet. Outlet pressure

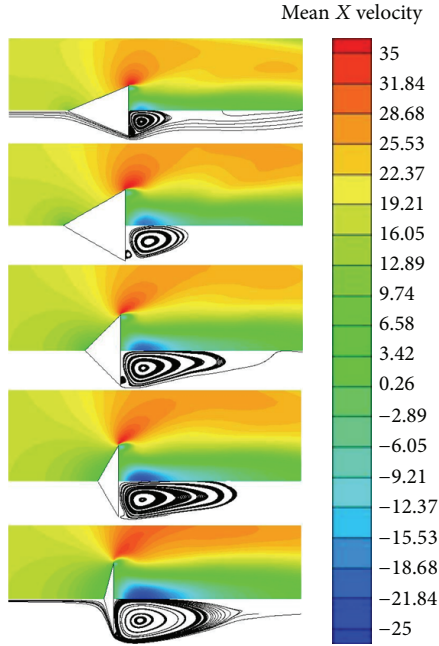


FIGURE 6: Time average streamline and streamwise velocity distribution at different  $\alpha$ .

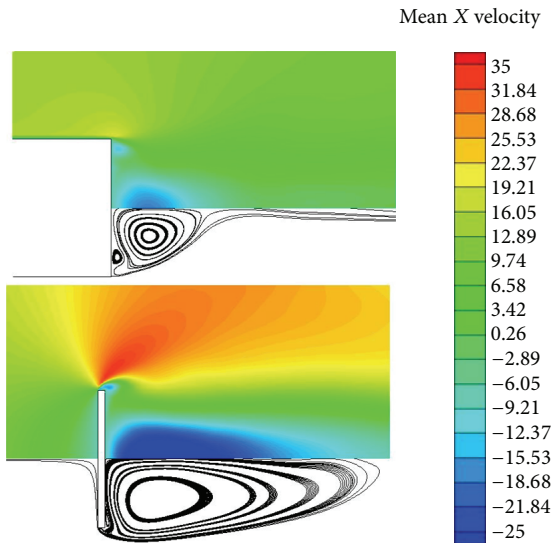


FIGURE 7: Time average streamline and streamwise velocity distribution at two limit conditions.

was 1 atm. No slip and zero normal velocity conditions are imposed at the side and bluff body wall. The flow field of different apex angle is solved in 2D and also been compared with 3D result at  $\alpha = 60^\circ$ . The finite-volume scheme is implicit, second order in time, and second order upwind in space. The integration time step of LES nonreactive field is

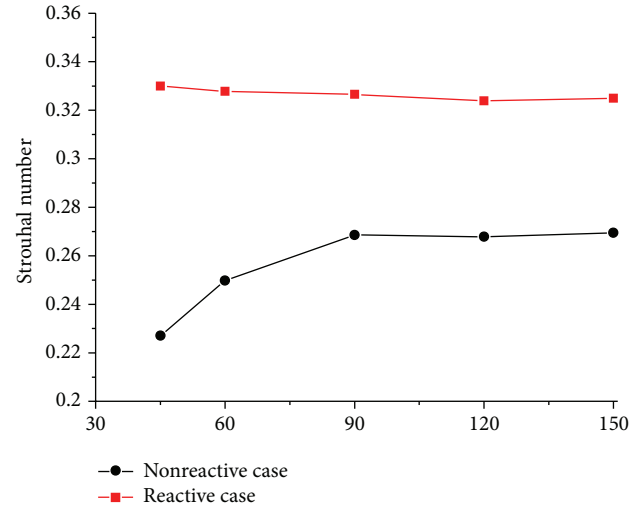


FIGURE 8: Strouhal number against apex angle for nonreactive and reactive case.

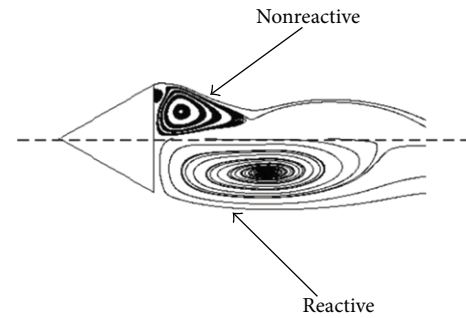


FIGURE 9: Comparison of the time average streamline distribution of  $= 60^\circ$ .

set to  $1e-04s$ , and  $8e-05s$  for reactive field. In this paper LES-Smagorinsky model has been used. Both nonreactive and reactive flow fields have been calculated and compared. When starting the reactive calculation, the nonreactive result is used as an initialization value. In LES simulation when the flow field becomes stable, 20 characteristic periods of the flow are sampled for plotting time-mean results.

**3.2. Grid-Dependent Learning and Verification.** It is important and necessary to carry out grid-dependent study for determining the optimal grid with a good balance of accuracy and speed; on the other hand, LES model needs more grid than RANS model, especially near the walls. The hexahedral grids ranged from approximately 30.950 cells to 71.267 cells are created by ICEM 11.0; the grids near bluff wall are refined which ensures the  $y^+$  values no larger than 2. Three grid size options are shown in Table 1, and the temperature distribution of different grid size cases at  $X = 15$  cm is shown in Figure 2. After examining the results with different grid sizes, it is found that the optimal grid size is approximately 71.267 cells.

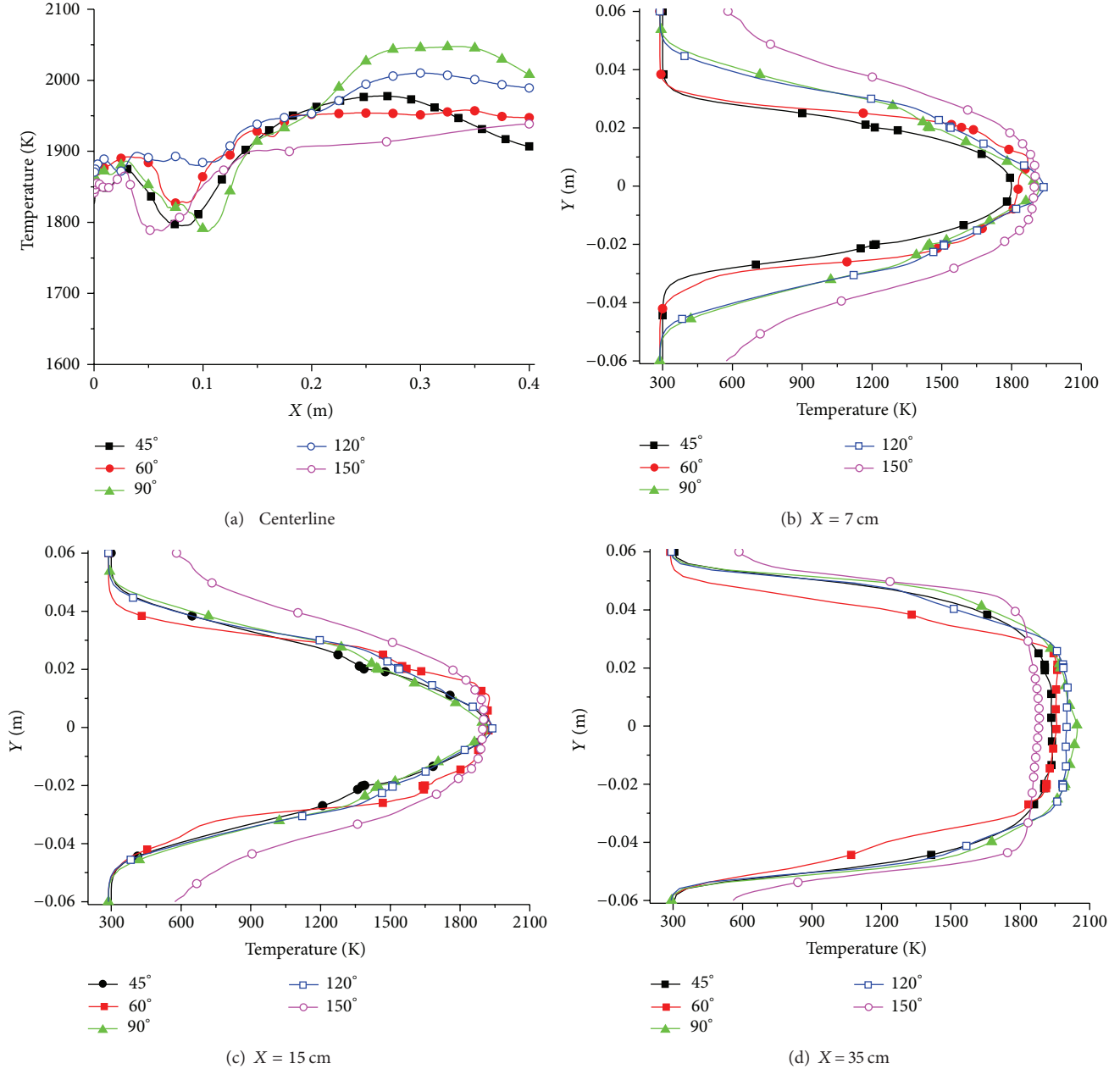


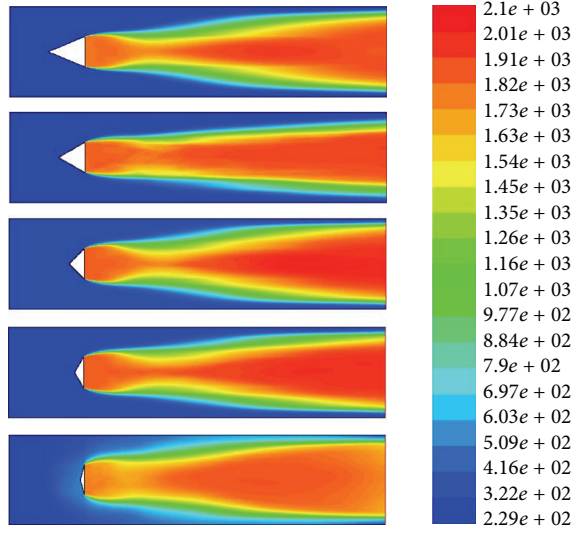
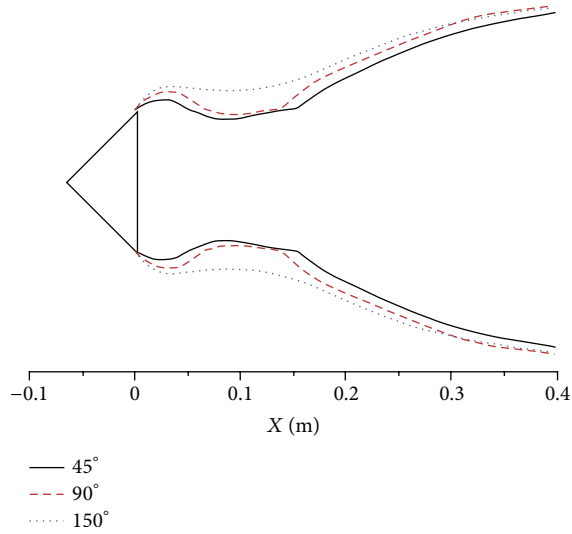
FIGURE 10: Time average temperature distribution at different location.

Although there are many studies on flow field using 2D LES problem such as flow past a cylinder or premixed bluff body flame, and 2D LES method could also provide important results as 3D model for basic research, it is important to find out dissimilarity between 2D and 3D models in order to understand difference between numerical simulation and actual result better. So the comparison between 2D and 3D (about 800,000 cells) model has been carried out in this section. From Figure 2 it can be seen that, at low temperature zone, the numerical result agrees well with experiment date, but both 2D and 3D maximum temperatures are little higher than experiment result; this is mainly because endothermic radicals reactions are missing when using one-step reaction and subgrid scale model for LES as discussed in [12]. Figure 3

shows  $U_x$  comparisons in recirculation region ( $X = 6.1$  cm); it can be seen that the  $U_x$  distributions agree well with experiment dates both in nonreactive and reactive case, but the reverse flow velocity is little higher using 2D model both nonreactive and reactive case. In reactive case, the curve shape is narrower than 3D model and experimental result.

## 4. Results and Analysis

**4.1. Nonreactive Case.** Figure 4 shows the mean streamwise velocity ( $U_x$ ) distribution along the center line. It is known that a recirculation region is formed because of vortex shedding; the mean recirculation zone is defined as the region

FIGURE 11: Contours of mean static temperature at different  $\alpha$ .FIGURE 12: Mean flame position ( $T = 1400$  K) at different  $\alpha$ .

where the mean streamwise velocity is negative ( $U_x < 0$ ). From Figure 4 it is found that as  $\alpha$  is increased, the mean length of recirculation zone increases, so does the backflow velocity magnitude. Figure 5 shows the  $U_x$  distribution at  $X = 1.5$  cm (this location is in recirculation region), and as  $\alpha$  is increased, the width of curve shape is increased within  $Y = -0.02$  m  $\sim$   $0.02$  m; this means that the width of recirculation zone is increased. So according to Figures 4 and 5, it can be concluded that when  $\alpha$  is increased, the recirculation zone area is increased and the backflow strength is enhanced.

From Figure 4, it can be seen that there are two critical points near  $X = 10$  mm and  $X = 22$  cm (marked by dash line), which divide  $U_x$  distribution into two parts: before  $X = 10$  mm it is recirculation zone, and as  $\alpha$  increases the backflow velocity is increased after  $X = 10$  mm and before  $X = 22$  cm,

TABLE 1: Grid dependence-learning cases.

Grid size	x nodes	Node bluff	Maximum mean temperature	% Difference
(1) 30,950	250	40	1902.5	—
(2) 47,627	300	50	1860.4	2.2129
(3) 71267	350	60	1850.8	0.51609

as  $\alpha$  increases; the  $U_x$  of  $150^\circ$  is bigger than other cases, but when  $X > 22$  cm,  $U_x$  is decreased as the flow develops, and  $150^\circ$  is lower than other cases, this is because the recirculation zone will make the transverse flow losses increase. The bigger recirculation zone, the more flow losses, and the flow losses will affect the streamwise velocity and make  $U_x$  of  $150^\circ$  that is the lowest case after  $X < 22$  cm.

Figure 6 shows the time-average streamlines after the bluff body, and it can be seen that when  $\alpha$  is increased, the recirculation area increases. The increases of  $\alpha$  (decrease of base angle) mean that the angle between flow direction and base edge of bluff is increased; two limit conditions can be assumed:  $\alpha$  tends to  $0^\circ$  and  $\alpha$  tends to  $180^\circ$ ; when  $\alpha$  tends to  $0^\circ$ , the flow mechanism near bluff base edge may correspond to the flow around a long square with angle of attack (AOA) close to  $0^\circ$ , and when  $\alpha$  tends to  $180^\circ$ , the flow mechanism near bluff base edge may correspond to the flow around a very thin plate with AOA close to  $0^\circ$ ; when the fluid flow past a thin plate, the rebound effects of wall are much stronger than long square, so the recirculation zone becomes bigger as Figure 7 shows.

In Figure 8 Strouhal number results in nonreactive and reactive are given. The Strouhal number is defined as

$$St = f \cdot \frac{h}{U_{in}}, \quad (6)$$

where  $h = 4$  cm,  $U_{in} = 17$  m/s, and  $f$  is the vortex shedding frequency, which is calculated through fast Fourier transform. For nonreactive case ( $\alpha = 60^\circ$ ), St-2D is 0.252 and 3D is 0.249 (experiment result is 0.25 [12]); for reactive case, St-2D is 0.37 and 3D is 0.364. It can be found that as  $\alpha$  increases, St increases in nonreactive cases but is almost unchanged in reactive cases. According to many scholars results about flow past body [20, 21] that St will be increased when Re is higher, higher Re means a bigger recirculation zone, so it can be learned that if Re is unchanged, a bluff body which has a bigger recirculation zone that will have a higher St. As Figure 6(a) shows when  $\alpha$  is increased from  $60^\circ$  to  $90^\circ$ , the recirculation zone length increases more than  $45^\circ$  to  $60^\circ$ , so the sudden increase of St of nonreactive case is easily explicable.

**4.2. Reactive Case.** The reacting simulations were carried out using the same numerical methodology and mesh utilized for the nonreacting simulation. Therefore, any changes in fluid dynamics can be attributed to the heat release from the combustion model described earlier. The dynamics of the reactive flow can be interpreted as due to coupling between vortex



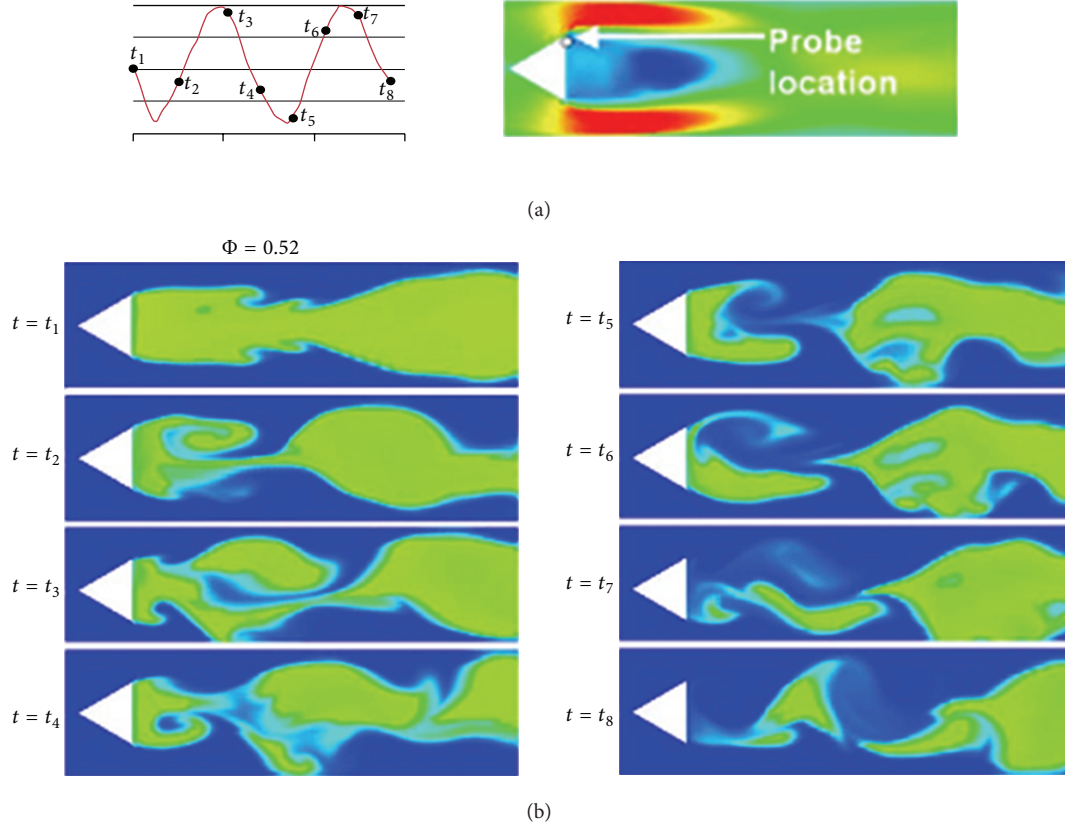


FIGURE 13: Time sequence of instantaneous temperature fields at the lean blow-out condition carried out by [18].

shedding and excitation of acoustic oscillations produced by heat release [18]. Comparing the nonreacting case and the reactive case, it is evident that combustion extended the recirculation region further downstream as Figure 9 shows. It was observed that in the instantaneous flow fields the asymmetric von shedding of coherent vortices no longer exists in the reacting case. Therefore, the reacting case does not possess any large-scale mixing mechanisms which typically reduce the recirculation zone length [18]. Mehta and Soteriou [22] attributed this absence of asymmetric von Karman shedding for reacting conditions to the dilatation effect of the heat release. They also found that baroclinic vorticity augments the impact of dilatation, but its effect is secondary. The recirculation zone is longer and broader in the reactive case, meaning a more gradual dissipation of momentum in the wake region with respect to the nonreactive case, and  $St$  is higher than nonreactive as Figure 8 shows.

Three typical locations are selected in order to discuss the temperature distribution against  $Y$  coordinate after the bluff; the three typical locations are  $X = 7$  cm (in the recirculation zone), 15 cm (after recirculation zone), and 35 cm (near the outlet). Figure 10(a) shows the temperature distribution along the centerline at different  $\alpha$ , it is found that case  $90^\circ$  has a large temperature fluctuation, the minimum mean temperature is about 1780 K, and the maximum temperature is close to 2050 K. Figures 10(b)–10(d) show the temperature distribution of three typical locations at different location.

It can be found from Figure 10(b) that as  $\alpha$  increases, the maximum temperature is almost unchanged, but the temperature distribution curve becomes wider and  $150^\circ$  is wider than other cases in recirculation zone; the wider curve means that the reaction area in  $Y$  directions is more bigger. This is because the recirculation zone becomes bigger as  $\alpha$  increases, the turbulence and flow pulsation are enhanced (see Section 4.1) which will make the combustion more efficiently. As the flow and reaction develop towards outlet,  $150^\circ$  is also the widest case (Figures 10(c) and 10(d)). When near the outlet the maximum temperature of  $150^\circ$  is little lower than other cases, this is because the streamwise velocity becomes lower which makes the turbulence fluctuation weak, and the flame temperature decreases near the outlet as  $\alpha$  is increased.

The curve shape difference means different flame shape. Figure 11 gives the mean static temperature contour at different  $\alpha$ , and Figure 12 summarizes the comparison between three typical conditions of flame shape ( $T = 1400$  K). There is a minimum width position of the flame shape, and it can be seen that  $\alpha$  has a strong effect on temperature distribution and flame shape: as  $\alpha$  is increased, the minimum width of flame shape increases and the heat release increases. This means that, at the same inlet condition, the bigger  $\alpha$ , the higher combustion chamber volume heat release rate (VHRR). VHRR is equal to the total release heat to burning chamber volume. A higher VHRR indicates that, to release the equal heat, smaller

combustion chamber is needed, which is very important for shortening the length of chamber in aircraft using a bluff body to stable the flame [23]. On the other hand, the effects of the turbulence are generally advantageous for the efficiency of the combustion since turbulence enhances the mixing of component chemical species and heat, but adverse effects upon combustion can also occur if the turbulence level is sufficiently high to create flame extinction. In turn, combustion may enhance the turbulence through dilatation and buoyancy effects caused by the heat release; the flame temperature is lower, the heat release is reduced which will make the flame unstable. According to Kim et al. [18]’s study, in a flame lean blow-out process the temperature distribution discontinuity first happens at the position where the flame is narrowest as Figure 13 shows, so it can be conjectured that the wider flame is more stable than narrow flame, so  $\alpha = 150^\circ$  is more stable than lower  $\alpha$  cases.

## 5. Conclusions

LES simulation based on Smagorinsky subgrid scale and EDC combustion model of a premixed bluff body flame is carried out in this paper; different apex angle effects on both nonreactive and reactive flow field have been discussed. The results obtained may be summarized as follows.

- (1) The recirculation zone area increases as apex angle is increased.
- (2) Combustion of the fluid could extend the recirculation region length. When apex angle is increased, St increases in nonreactive case, but decreases a little in reactive case. St of reactive case is higher than nonreactive case.
- (3) A bigger apex angle makes the flame shape wider, increases chamber volume heat release, and enhances the flame stability.

## Acknowledgments

This work was supported by Scientific Research Fund of Hunan Provincial Education Department under Grant no. 12B023. It is also supported by National Natural Science Foundation of China (nos. 61204039 and 61106029) and Scientific Research Foundation for Returned Scholars, Ministry of Human Resources, and Social Security of the People’s Republic of China.

## References

- [1] H. B. Ebrahimi, “Overview of gas turbine augmentor design, operation, and combustion oscillation,” in *Proceedings of the AIAA/ASME/SAE/ASEE 42nd Joint Propulsion Conference*, AIAA Paper no. 2006-4916, pp. 5658–5673, July 2006.
- [2] A. Prasad and C. H. K. Williamson, “The instability of the shear layer separating from a bluff body,” *Journal of Fluid Mechanics*, vol. 333, pp. 375–402, 1997.
- [3] S. Fujii, M. Gomi, and K. Eguchi, “Cold flow tests of a bluff-body flame stabilizer,” *Journal of Fluids Engineering ASME*, vol. 100, no. 3, pp. 323–332, 1978.
- [4] L. J. Yue, B. J. Liu, and M. L. Yang, “Study on the near-wake flow behind EBMC flameholder,” *Journal of Engineering Thermophysics*, vol. 22, no. 2, pp. 261–264, 2001.
- [5] Y. Nakamura, “Vortex shedding from bluff bodies and a universal strouhal number,” *Journal of Fluids and Structures*, vol. 10, no. 2, pp. 159–171, 1996.
- [6] D. R. Cuppoletti, J. Kastner, J. Reed, and E. J. Gutmark, “High frequency combustion instabilities with radial V-gutter flameholders,” in *Proceedings of the 47th AIAA Aerospace Sciences Meeting including the New Horizons Forum and Aerospace Exposition*, AIAA Paper no. 2009-1176, January 2009.
- [7] A. Sjunnesson, C. Nelsson, and E. Max, “LDA measurements of velocities and turbulence in a bluff body stabilized flame,” *Laser Anemometry*, vol. 3, pp. 83–93, 1991.
- [8] A. Sjunnesson, P. Henriksson, and C. Löfström, “CARS measurements and visualization of reacting flows in a bluff body stabilized flame,” in *Proceedings of the AIAA 28th Joint Propulsion Conference and Exhibit*, AIAA Paper no. 92-3650, Nashville, Tenn, USA, July 1992.
- [9] P. Siewert, *Flame front characteristics of turbulent lean premixed methane/air flames at high-pressure [Ph.D. thesis]*, Poznan University of Technology (PUT), Poznań, Poland, 2006.
- [10] P. Eriksson, “The Zimont TFC model applied to premixed bluff body stabilized combustion using four different RANS turbulence models,” in *Proceedings of the ASME Turbo Expo: Power for Land, Sea and Air (GT ’07)*, pp. 14–17, Montreal, Canada, May 2007.
- [11] U. Engdar, P. Nilsson, and J. Klingmann, “Investigation of turbulence models applied to premixed combustion using a level-set flamelet library approach,” *Journal of Engineering for Gas Turbines and Power*, vol. 126, no. 4, pp. 701–707, 2004.
- [12] E. Giacomazzi, V. Battaglia, and C. Bruno, “The coupling of turbulence and chemistry in a premixed bluff-body flame as studied by LES,” *Combustion and Flame*, vol. 138, no. 4, pp. 320–335, 2004.
- [13] P. Wang, *Large Eddy simulation of turbulent swirling flows and turbulent premixed combustion [Ph.D. thesis]*, Lund Institute of Technology, Lund, Sweden, 2005.
- [14] C. Fureby, “Large Eddy Simulation of combustion instabilities in a jet engine afterburner model,” *Combustion Science and Technology*, vol. 161, no. 1–6, pp. 213–243, 2000.
- [15] I. Porumbel and S. Menon, “Large Eddy simulation of bluff body stabilized premixed flame,” in *Proceedings of the 44th AIAA Aerospace Sciences Meeting*, AIAA Paper no. 2006-152, pp. 1808–1824, January 2006.
- [16] R. R. Erickson and M. C. Soteriou, “The influence of reactant temperature on the dynamics of bluff body stabilized premixed flames,” *Combustion and Flame*, vol. 158, no. 12, pp. 2441–2457, 2011.
- [17] N. S. Park and S. C. Ko, “Large Eddy simulation of turbulent premixed combustion flow around bluff body,” *Journal of Mechanical Science and Technology*, vol. 25, pp. 2227–2235, 2011.
- [18] W. W. Kim, J. J. Lienau, P. R. Van Slooten, M. B. Colket, R. E. Malecki, and S. Syed, “Towards modeling lean blow out in gas turbine flameholder applications,” *Journal of Engineering for Gas Turbines and Power*, vol. 128, no. 1, pp. 40–48, 2006.
- [19] B. F. Magnussen, “On the structure of turbulence and a generalized Eddy dissipation concept for chemical reaction in turbulent flow,” in *Proceedings of the AIAA 19th Aerospace Sciences Meeting*, St. Louis, Mo, USA, 1981.

- [20] A. Venugopal, A. Agrawal, and S. V. Prabhu, "Influence of blockage and upstream disturbances on the performance of a vortex flowmeter with a trapezoidal bluff body," *Measurement*, vol. 43, no. 4, pp. 603–616, 2010.
- [21] A. Venugopal, A. Agrawal, and S. V. Prabhu, "Influence of blockage and shape of a bluff body on the performance of vortex flowmeter with wall pressure measurement," *Measurement*, vol. 44, no. 5, pp. 954–964, 2011.
- [22] P. G. Mehta and M. C. Soteriou, "Combustion heat release effects on the dynamics of bluff body stabilized premixed reacting flows," in *Proceedings of the 41st AIAA Aerospace Sciences Meeting*, AIAA Paper no. 2003-0835, 2003.
- [23] S. J. Shanbhogue, S. Husain, and T. Lieuwen, "Lean blowoff of bluff body stabilized flames: scaling and dynamics," *Progress in Energy and Combustion Science*, vol. 35, no. 1, pp. 98–120, 2009.

## Research Article

# Mathematical Modeling of Double-Skin Facade in Northern Area of China

Zou Huifen,<sup>1</sup> Fei Yingchao,<sup>1</sup> Yang Fuhua,<sup>1</sup> Tang Hao,<sup>1</sup> Zhang Ying,<sup>1</sup> and Ye Sheng<sup>2</sup>

<sup>1</sup> School of Municipal and Environment Engineering, Shenyang Jianzhu University, Shenyang 110168, China

<sup>2</sup> Management School, Shenyang Jianzhu University, Shenyang 110168, China

Correspondence should be addressed to Fei Yingchao; ser478953481@126.com

Received 26 October 2012; Revised 9 January 2013; Accepted 9 January 2013

Academic Editor: Zhijun Zhang

Copyright © 2013 Zou Huifen et al. This is an open access article distributed under the Creative Commons Attribution License, which permits unrestricted use, distribution, and reproduction in any medium, provided the original work is properly cited.

This paper focuses on the operation principles of the double-skin facade (DSF) in winter of severe cold area. The paper discussed the main influence factors of building energy consumption, including the heat storage cavity spacing, the air circulation mode, the building envelope, and the building orientation. First, we studied the relationship among the thermal storage cavity spacing, the temperature distribution in the cavity of the DSF, and the indoor temperature. Then, we discussed the influence on the ambient temperature in the building exerted by the air circulation system of the double-skin facade. Finally, we analyzed the influence on the whole building energy consumption of the DSF buildings under the situation of different building envelopes and different building orientations. Based on the results of the numerical simulation, the paper put forward an operation strategy analysis of the DSF buildings in severe cold area, in order to achieve the purpose of building energy saving.

## 1. Introduction

Modern architecture is dominated by transparent buildings. The large glazed areas result in high building heating and cooling loads, leading to high levels of energy consumption and therefore significant financial and environmental burdens. The double-skin facade is one potential response to these problems. On the other hand, in both developed and developing countries, building energy consumption accounts a large part in the total world energy consumption. All the countries around the world put the building energy-saving as the focus of their work [1]. Architects have long been hoping to decrease the building energy consumption and make the shape of the building more beautiful and unique through the application of glass curtain wall in the meanwhile. Thus research on the thermophysical properties of the glass curtain wall has become a hot spot. The paper studied the energy-saving properties of the DSF in severe cold area based on the winter weather conditions of Shenyang, respectively, using the flow field simulation software FLUENT and the building energy simulation software DEST to analyze temperature characteristics and building energy consumption of the double-skin facade.

## 2. Thermal Properties of the Double Skin Facade

The structure of the DSF is shown in Figure 1. The main factors driving airflow within the cavity are buoyancy and wind pressure [2]. The pressure differences resulting from these forces can be determined with the equations below, respectively:

$$\Delta p_{\text{buoyancy}} = \rho_o g H \left( \frac{T_{\text{cav}}}{T_e} - 1 \right) (Pa), \quad (1)$$

where  $\rho_o$  is the outdoor air density ( $\text{kg/m}^3$ ),  $g$  is gravitational acceleration ( $9.8 \text{ m/s}^2$ ),  $H$  is the cavity height (m),  $T_{\text{cav}}$  is the average cavity temperature, and  $T_e$  is the outdoor air temperature;

$$\Delta P_{\text{wind}} = \frac{\rho_o U_{\text{met}}^2}{h_{\text{met}}} \left( \frac{\delta_{\text{met}}}{h_{\text{met}}} \right)^{2a_{\text{met}}} [h^{2a} - (h + H)^{2a}] (pa), \quad (2)$$

where  $U_{\text{met}}$  is the measured wind speed at height  $h_{\text{met}}$ ,  $\delta_{\text{met}}$  is the wind boundary layer thickness,  $a$  is the ASHRAE local terrain exponent,  $h$  is the height of the lower cavity opening,

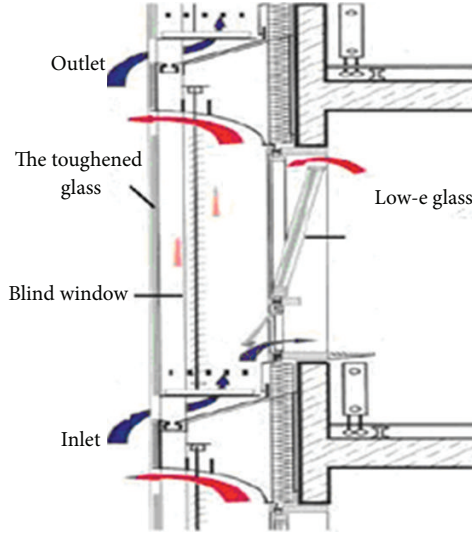


FIGURE 1: The structure of DSF.

and  $H$  is the distance between inlet and outlet openings. The airflow rate through the cavity can be determined by

$$V = a\Delta P^b \quad \text{m}^3/\text{hr}, \quad (3)$$

where  $a$  and  $b$  are pressure loss characteristics of the cavity and openings. In a summer condition, the DSF can exploit the chimney effect formed in the cavity—taking away the indoor heat through natural ventilation and reducing the indoor temperature. In winter condition, the DSF needs to exploit as much solar radiation as possible to form the greenhouse effect in the cavity which will improve the insulation effect of the cavity and reduce the heating energy consumption.

The DSF is a special 3-layer glass curtain wall system. Under the condition of no ventilation in winter, the forms of heat transfer in the air layer between heating storage of the glass curtain include convective heat transfer, radiation heat transfer and thermal conductivity [3]. The calculation formula for heat transfer coefficient  $K$  of common glass curtain wall is

$$K = \left( \frac{1}{h_e} + \frac{\delta}{\lambda} + \frac{1}{h_m} \right)^{-1}, \quad (4)$$

where  $K$  is the heat transfer coefficient  $K$  of common glass curtain wall;  $h_e$  and  $h_m$  the surface heat transfer coefficients of the outdoor side and the indoor side,  $\text{w}/(\text{m}^2 \cdot \text{K})$ ;  $\lambda$  the thermal conductivity of the glass,  $\text{w}/(\text{m}^2 \cdot \text{K})$ ;  $\delta$  the thickness of the glass.

The calculation formula for surface heat transfer coefficient of the outdoor side  $h_e$  is

$$h_e = 10.0 + 4.1v, \quad (5)$$

where  $v$  is the outdoor wind speed ( $\text{m/s}$ ).

In accordance with the standard above, when comparing the heat transfer of the glass, we set  $h_e$  as  $23 \text{ w}/(\text{m}^2 \cdot \text{K})$  when

the outdoor wind speed is  $3 \text{ m/s}$ . And the calculation formula for surface heat transfer coefficient of the indoor side  $h_{in}$  is

$$h_{in} = 3.6 + \frac{4.4\varepsilon}{0.83}, \quad (6)$$

where  $\varepsilon$  is the Emission rate of the indoor side and the indoor side of the DSF is ordinary transparent glass, which will be taken as  $0.83$ ,  $h_{in} = 8.0$ . Thermal conductivity of the ordinary toughened glass is  $0.76 \text{ w}/(\text{m}^2 \cdot \text{K})$ , when the thickness of the glass is  $6 \text{ mm}$ , and the glass thermal resistance is  $0.008 \text{ w}/(\text{m}^2 \cdot \text{K})$ . According to the calculation formula above, we can get heat transfer coefficient of  $6 \text{ mm}$  thick ordinary toughened glass is  $6.16 \text{ w}/(\text{m}^2 \cdot \text{K})$ . Similarly we can compute out that heat transfer coefficient of the  $24 \text{ mm}$  thick Low-e insulating glass is  $1.76 \text{ w}/(\text{m}^2 \cdot \text{K})$ . In the setting of FLUENT material properties, all the glasses are set to translucent transmission medium [4].

### 3. CFD Numerical Simulations

Building indoor thermal environment in severe cold area is mainly influenced by the combined effect of thermal environment, wet environment, the air environment of the microclimate, and the atmospheric environment. These effects either directly or indirectly cause a certain degree of influence on the building indoor environment [5]. In severe cold area, the design of the building envelope, especially the thermal design for adaptive glass curtain wall, has its own characteristics [6], which is different from the other thermal design areas in China. The severe cold area mainly controls the indicator of envelope insulation and generally does not take summer heat insulation into consideration. We will use the software FLUENT to explore the relationship among different spacing values of the heat storage cavity, different gas circulation systems, the temperature in the cavity of the double-skin facade, and the indoor temperature.

#### 3.1. Simulation about Influence of the Heat Storage Cavity

##### Spacing on Thermal Performance of the DSF

**3.1.1. Selection of the CFD Model.** The model of the double-skin facade uses the single outer layer of  $6 \text{ mm}$  thick toughened glass and the inner layer of  $6 \text{ mm} + 12 \text{ mm} + 6 \text{ mm}$  Low-e hollow glass. This model consists of DSF and indoor room. The structure size (length  $\times$  height) of the DSF is  $3 \text{ m} \times 4 \text{ m}$ , and indoor room (length  $\times$  width  $\times$  height) is  $2.4 \text{ m} \times 3 \text{ m} \times 4 \text{ m}$ . The model, respectively, takes  $0.2 \text{ m}$ ,  $0.4 \text{ m}$ , and  $0.6 \text{ m}$ , as the cavity spacing value. Figure 2 shows the geometric model established by GAMBIT when the cavity spacing is  $0.4 \text{ m}$ .

This subject is mainly to simulate the flow state of the airflow inside the DSF and the influence on airflow in the room which is exerted by curtain wall. The airflow inside the channel of DSF is a heat and mass transfer problem, so we adopt RNG  $k - \varepsilon$  turbulent model and DO radiation model in the research. Hypothesis Boussinesq is used to make the processing of the buoyancy lift items produced by temperature differ easier [7]. Select the climate characteristic of Shenyang prefecture as the research object, Shenyang:



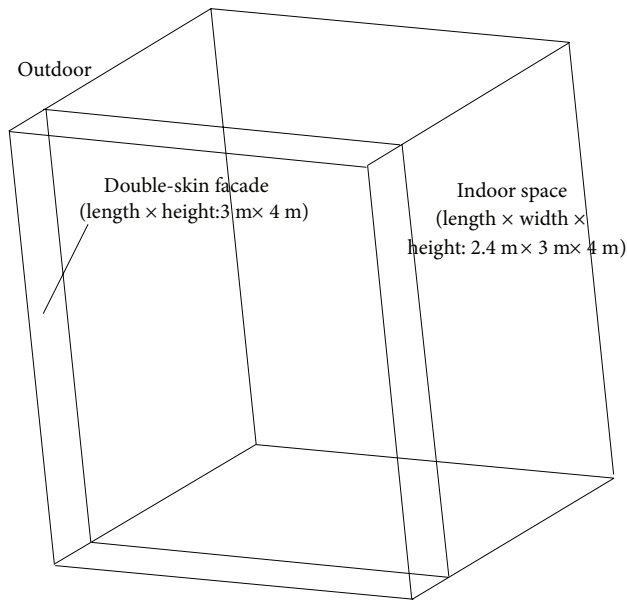


FIGURE 2: The geometric model.

northern latitude  $41.8^\circ$  and east longitude  $123.38^\circ$ , in the east eighth zone. According to the Heating and Ventilation Design Specification. The designed indoor comfort conditions are as follows: temperature:  $18 \sim 22^\circ\text{C}$ ; relative humidity:  $40\% \sim 60\%$ ; wind speed should not be more than  $0.2\text{ m/s}$ ; the solar radiation of winter solstice in Shenyang was shown in Table 1.

**3.1.2. Simulation Results Analysis.** In winter condition, the DSF generally uses a closed and no-cyclic form, in order to form greenhouse effect and to improve the indoor temperature [8]. The subject selects the main time on the winter solstice to have the simulation, for on the day, we can accept solar radiation of shortest duration during the daytime. Under this condition and when thermal channel spacing, respectively, choose  $200\text{ mm}$ ,  $400\text{ mm}$ ,  $600\text{ mm}$ , simulate the temperature in the thermal channels and the changes of indoor temperature. We use FLUENT to simulate these 27 examples, respectively, and the simulation results are shown in Figures 4 and 5. With reference to the change curve of solar radiation in the winter solstice day (Figure 3), solar radiation is an important parameter which affects the temperature of the cavity and the indoor temperature, and the changes of cavity temperature and indoor temperature are in proportion to changes of the solar radiation.

Figure 4 shows that during the daytime in the winter the temperature of DSF with three different spacing value in the cavity is obviously higher than that of the outdoor temperature; exactly the maximum temperature difference between temperature in the cavity and the outdoor temperature can be up to  $26^\circ\text{C}$ . Visibly the effect of the greenhouse is very significant, which can play a role in improving the cavity temperature. Meanwhile during the daytime in the winter the larger cavity spacing will be conducive to gain more solar

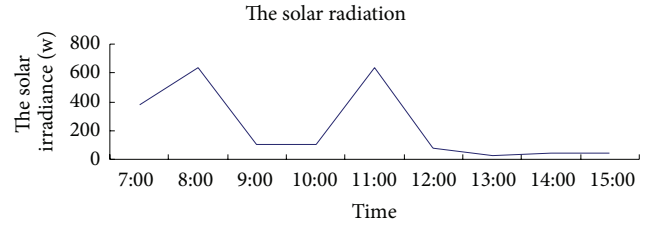


FIGURE 3: The solar radiation of the winter solstice.

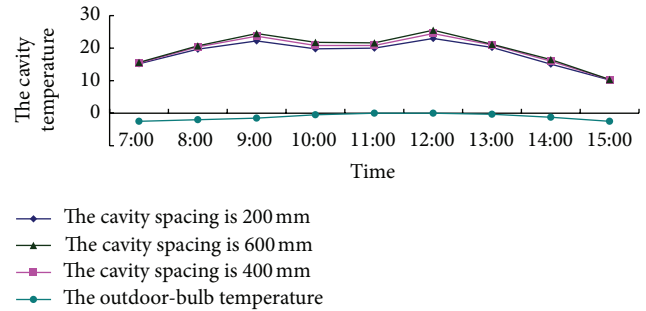


FIGURE 4: The interior temperature distributions when the cavity spacing of DSF is different.

radiation heat, which will come out with a positive effect on improving the cavity temperature.

As shown in Figure 5, similar to the change rules of cavity temperature, the changes of indoor temperature are consistent with changes of solar radiation. When the solar radiation arrives at maximum value, the indoor temperature gets to the maximum; when the solar radiation gradually decreases, the cavity temperature reduces gradually. But double-skin facade of short cavity spacing is conducive to extend the exothermic time from the interior and cavity to the outside. So in a short period of time, solar radiation can play the role of thermal insulation.

#### 4. Simulation about the Influence of Gas Circulation Mode on the Thermal Performance of the Double-Skin Facade

In severe cold area, it is usual to adopt the double-skin facade of external cycle in the summer [9]. To make full use of solar radiation to reach the greenhouse effect in winter, we generally close the air inlet and outlet on the inner side of the south DSF. Under the action of direct sunlight, there will be a closed greenhouse in the cavity with a high temperature so that the heat dissipation from interior to outer environment will be reduced. But generally the north double-skin facade cannot get enough direct sunlight. In order to increase the thermal resistance of heat storage cavity effectively and reduce the indoor heat loss, the general approach is sending the indoor exhaust through the delivery outlet which is on the indoor side to the cavity, and then discharging the exhaust from the air outlet on the upper side of the cavity

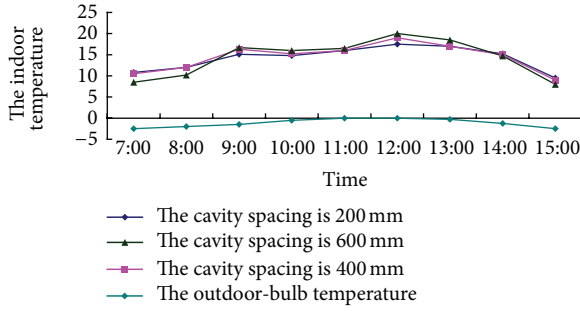


FIGURE 5: The room temperature distributions when the cavity spacing of DSF is different.

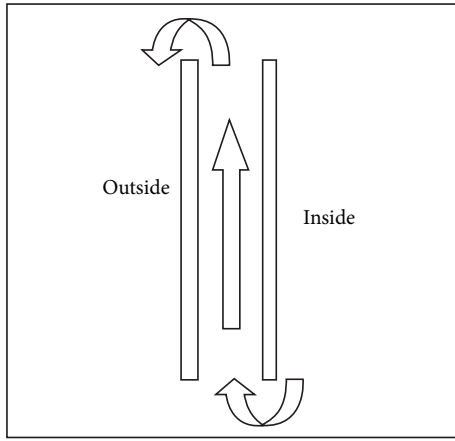


FIGURE 6: The schematic diagram of exhaust air in the north of DSF.

to outdoor environment (as shown in Figure 6). The exhaust whose temperature is close to the indoor temperature has a preheating effect on the ventilated cavity, and so to some degree, the effect reduces the heat loss through DSF to the outside and decreases the indoor air conditioning load which causes the decrease of air conditioning energy consumption through DSF [10].

**4.1. Scheme Design of Gas Circulation Way Simulation.** From the analysis above, it is known that orientation and air distribution mode have an important influence on the thermal performance of the DSF. In the case of different orientations, the operational mode of the DSF will be different because of the solar radiation; while in the case of the same orientation, it is apparent that there are large distinctions between the thermal performances of the DSF with no air circulation and that with air circulation. Meanwhile the amount of air circulation to some degree influences the thermal performance of the DSF. The scheme design of the simulation is shown in Table 2.

**4.2. The Numerical Simulation and Comparative Analysis about the DSF Air circulation in Winter.** This section is the first experimental comparison of the gas cycle simulation program. Choose the climatic characteristics of Shenyang as a simulated external conditions at the moment of the winter

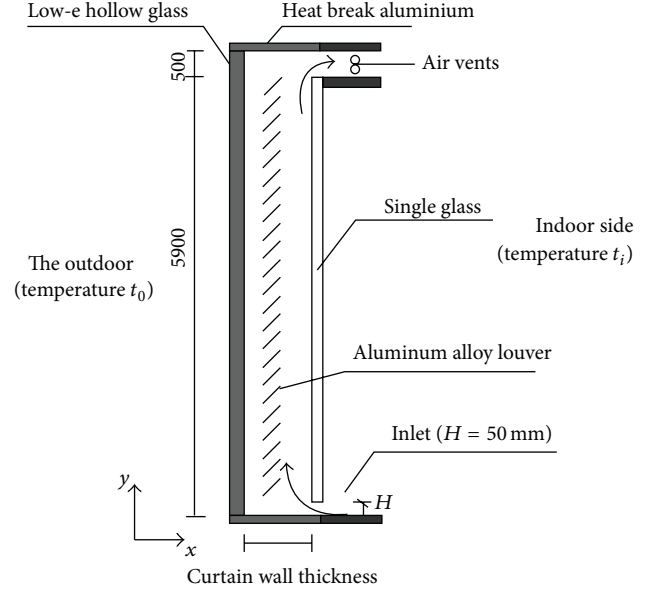


FIGURE 7: The inner loop of DSF.

solstice: we simulate south-facing DSF hourly from 7:00 am to 15:00 am. We calculate the cavity of DSF and the indoor temperature in order to increase the air circulation inside the south-facing DSF in winter.

(1) *Geometric Model.* This group of simulations is whether there is a simulation for air circulation. So when the simulation is going on, we need to build two sets of physical models. One group is no air circulation double-skin facade model, also known as a closed the DSF. It has already been built under the influence of regenerative cavity spacing on the thermal performance of the DSF construction, as shown in Figure 2. Another group is a model of the DSF with a group of air circulation, also known as the inner loop the DSF, as shown in Figure 7.

The simulation of two models using regenerative cavity spacing of 0.4 m glass curtain wall makes use of the geometry model cycle with a set of the DSF which is created by GAMBIT, as shown in Figure 8. The model and boundary conditions are selected as previously mentioned.

(2) *The Analysis of Simulation Results.* We still choose hourly simulation of major moment of the winter solstice, select the comparison of the hot channel spacing 0.4 m inner loop and airless cycle of the double skin-facade temperature and totally simulate 18 examples.

The simulation results are shown in Figures 9 and 10. By comparing, we can see that the DSF with the inner loop is more conducive to improving the indoor air temperature in the winter during the day, but during smaller solar radiation time or at night, the room temperature will lost quickly from the inside out. However, in the winter night, no air circulation double-skin glass curtain wall is more conducive to the holding of the indoor temperature. Double-skin glass curtain wall with an inner loop is virtually equivalent to an increase of the spacing of the heat storage cavity, which is

TABLE 1: The South solar radiation of winter solstice in Shenyang.

Time	Dry-bulb temperature (°C)	Wet bulb temperature (°C)	Horizontal radiation intensity (w/m <sup>2</sup> )	South radiation intensity (w/m <sup>2</sup> )
7 am	-2.6	-5.4	132.99	370.73
8 am	-2.1	-5.2	280.12	524.48
9 am	-1.4	-4.7	403.44	643.98
10 am	-0.6	-4.3	219.05	109.53
11 am	0.0	-4.0	220.19	110.10
12 am	0.2	-4.0	410.32	650.53
1 pm	-0.2	-4.4	133.74	66.87
2 pm	-1.4	-5.2	66.12	33.06
3 pm	-3.0	-6.4	3.48	36.83

TABLE 2: The simulation program of airflow movement.

The first group: contrast simulation with and without air circulation	DSF without air circulation
	Group 1 of double-skin façade with air circulation
The second group: contrast simulation with and without air circulation	Group 1 of double-skin façade with air circulation
	Group 2 of double-skin façade with air circulation

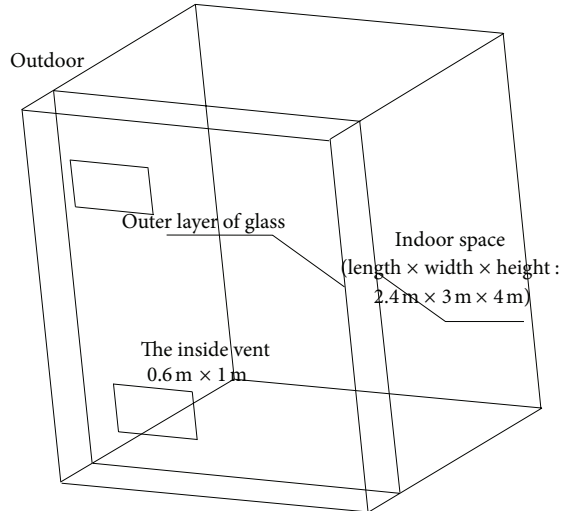


FIGURE 8: The structure of DSF which has one pair of inner loops.

not conducive to indoor delay insulation, which corroborated analog conclusions of the previous section from the side again. At night or solar radiation small moment, the small regenerative cavity spacing of the DSF is more conducive to hold the indoor temperature [11].

*4.3. The Numerical Simulation and Comparative Analysis of the Amount of the DSF Air Circulation in Winter.* The simulation of this section needs to build a geometric model of

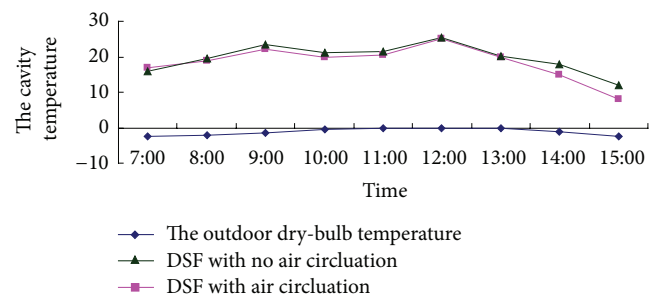


FIGURE 9: The contrast of interior temperature of DSF when the inner loop is set or not.

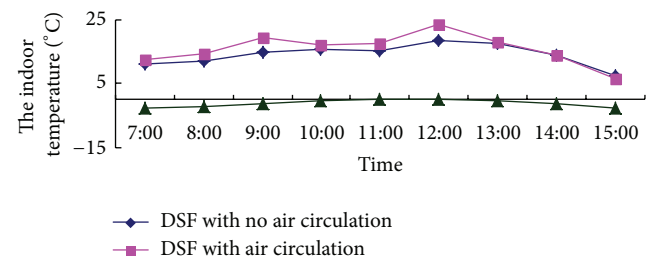


FIGURE 10: The contrast of indoor temperature when the inner loop is set or not.

two groups, one for a group of the air circulation mode of the DSF; this model has been constructed in a simulate analysis in the last section. For two sets of the air circulation mode a DSF geometry model is shown in Figure 11.

The choice of a model and the boundary conditions set as previously indicated, based on the simulation results shown in Figures 12 and 13, the analysis shows that the larger period of radiation in the winter sun, the set of air circulation is conducive to raise the average temperature in the room, with the increase in the amount of air circulation, the indoor temperature will be more improved. However, in a small period of solar radiation or at night, the air circulation does not have good insulation effect. It will speed up the heat transmission from the indoor to the outdoor, resulting in the decrease of room temperature rapidly. The greater the amount

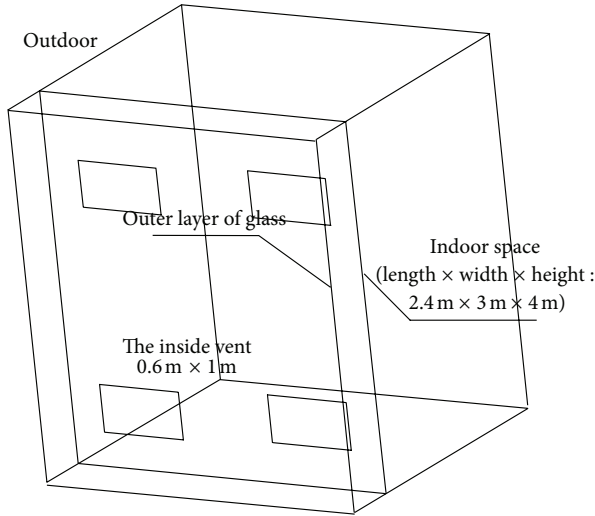


FIGURE 11: The structure of DSF which has two pairs of inner loop.

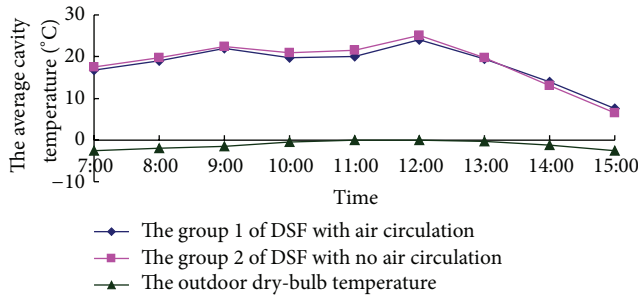


FIGURE 12: The contrast of interior temperature of DSF when the amount of airflow is changed.

TABLE 3: The heat transfer coefficient of DSF.

Cavity spacing (mm)	200	400	600
Heat transfer coefficient $w/m^2 \cdot k$	1.13	1.14	1.12

of air circulation, the faster heat loss will be. So when solar radiation is small or at night, it is better to use the closed no-loop DSF [12], in order to facilitate the preservation room temperature and reduce indoor heat loss.

## 5. DEST Numerical Simulations

This section mainly uses the DEST energy analysis tool to simulate the energy consumption of the DSF in the case of different external structures and different building orientations [13]. Using front FLUENT simulation results, we can see that the major moment of the winter solstice, the temperature of the glass surface of the inner and outer layers of the DSF. Here first calculate the cavity width of 200 mm, 400 mm, 600 mm South to the DSF [14], Substituting into the previously described heat transfer coefficient calculation formula. When the outdoor temperature is  $2.1^\circ\text{C}$ , the solar radiation is  $650 w/m^2$ ; the calculated results are shown in Table 3.

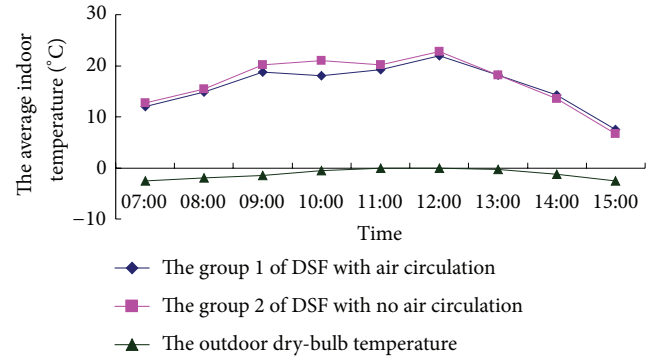


FIGURE 13: The contrast of indoor temperature when the amount of airflow is changed.

TABLE 4: The performance of wall.

External structure coefficient type	Heat transfer ( $w/m^2 \cdot k$ )	Remark
Concrete walls-Jane-85	0.486	20 mm cement mortar + 200 mm reinforced concrete + 85 mm expanded perlite + 20 mm no cement fiberboard
Plating Low-e film insulating glass curtain wall	2.1	6 (Low-e) + 9 mm hollow + 6, the solar transmittance of 33%, and the reflectance 26%
Double-skin glass curtain wall	1.14	Outer layer of 8 mm tempered + 400 mm cavity + inner plated Low-e membrane 24 mm hollow glass

We can see from the table above that the cavity spacing has 200 mm~600 mm range, the heat transfer coefficient of the DSF does not cause too much influence, and the cavity changes to only 0.8%. Therefore, the effect of cavity spacing can be roughly ignored in the energy simulation.

**5.1. Establishing the Model.** By using the DEST energy analysis tool, we can make it more accurately on the office building energy simulation. The typical office building is a five-story office building; main room types are ordinary office, reception room, office, leading the rest room, the bathroom, and the exhibition rooms. The established model shown in Figure 14 is three-dimensional model of the building generated by the DEST.

In order to investigate the power saving features of the DSF in cold regions, the DSF model is set as a typical office building with plated Low-e membrane hollow glass curtain wall, concrete wall-Jane-85 for energy simulation. The characteristics of these a three-envelope structure are shown in Table 4, respectively.

The DSF in winter with no shade measures the hot channel is closed, no external circulation ventilation mode; to the external structure plated of Low-e membrane hollow glass

TABLE 5: Building energy consumption when the external wall is changed.

External structure type	Concrete-perlites-85	Low-e hollow glass curtain wall	The DSF
Total annual heat load (kw · h)	411844.3	514763	439217.6
Total annual cooling (kw · h)	183457.6	409413.4	369627.6
Total annual load statistics (kw · h)	595301.9	924176.4	808845.2
Heating season heat load indicators ( $w/m^2$ )	27.5	34.3	29.3
Air conditioning season's cold load indicators ( $w/m^2$ )	17.65	31.4	24.6

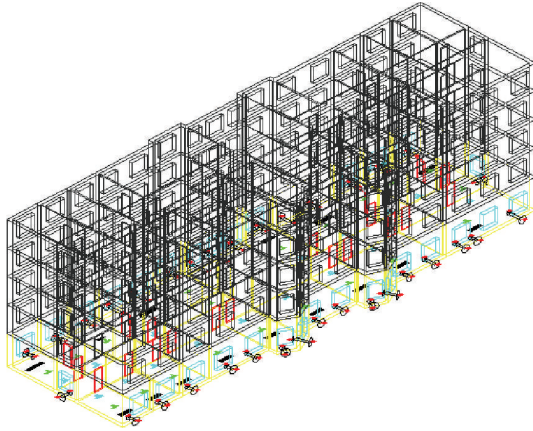


FIGURE 14: The building model generated by DEST.

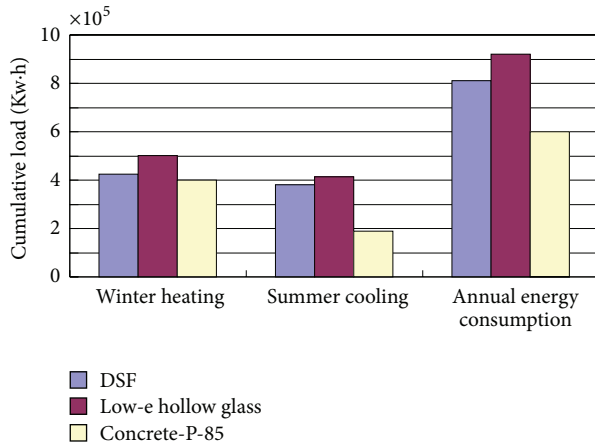


FIGURE 15: The contrast of energy consumption of the three kinds of external wall.

curtain wall and concrete wall plus steel outsider window, winter also using the no shading form [15].

**5.2. External Structure of the Different Types of the DSF to the Influence of Building Energy Consumption.** Doing DEST simulation for these three different external structure building models generates a load summary table about the building energy consumption as shown in Table 5.

Table 5 shows that the DSF has a better energy-saving effect than Low-e hollow glass curtain wall, about 17.2% energy saving higher than Low-e hollow glass curtain wall, and 6.2% higher than concrete-perlites-85 energy consumption; the heating indicator is  $29.3 w/m^2$  [16–18]. In summer cooling load, the DSF has 26.4% more energy consumption than the commonly used concrete-Perlites-85 exterior wall more and 12.5% energy saving than plated Low-e hollow glass curtain wall [19].

Thus, the DSF will not play an outstanding energy-saving role in the summer. The summer air conditioning cold indicators also showed a similar rule with the cooling load. This reflected that the energy-saving effect of the DSF is more suitable for the cold climate region; cold region has a short-term summer with little requirements for air conditioning and a cold long winter with higher heating requirements [20, 21]. Figure 15 obviously reflected the energy consumption of the DSF compared to other building envelopes in each season.

**5.3. Low-e Hollow Glass Curtain Wall of Different Building toward to the Influence of Building Energy Consumption.** Different building orientation has a great impact on the thermal performance of the DSF. In this paper, a typical five-story office building in cold regions is using for the construction of instance, simulate three external structure column in Table 5 respectively by the use of DEST, each toward of the DSF adopts closed without internal circulation of the DSF, a total of nine examples. Due to the area of the DSF and indoor space of the architecture model in the southward, northward, eastward and westward are all different, directly compare of annual cumulative load have no practical significance, therefore choose the plated Low-e hollow glass curtain wall and concrete-perlites-85 as [22–24] the reference, compare the cumulative load. The specific simulation results are shown in Table 6.

Basis on the DSF, with reference to cooling and heating loads and annual cumulative load of the low-e hollow glass curtain wall and concrete-perlites-85 exterior wall, each toward lower energy efficiency ratio were calculated, the energy saving ratio tables are shown in Table 7.

Figures 16 and 17 were in the case of a different building toward the DSF total annual heating load being compared and the annual heating energy saving rate comparison. Normative provisions of the cold regions must consider the



TABLE 6: The heat and cold load of the building when the building orientation is changed.

Building orientation	External structure (total annual kw · h)	The DSF	Low-e hollow glass curtain wall	Concrete-perlites-85
Northward	Heat load	448910	484823	411844
	Cooling load	332721	422651	183458
	Load statistics	781632	907474	595302
Westward	Heat load	441909	483890	411844
	Cooling load	290313	404294	183458
	Load statistics	732222	888185	595302
Southward	Heat load	453853	482445	411844
	Cooling load	325993	442176	183458
	Load statistics	779846	904621	595302
Eastward	Heat load	437379	481554	411844
	Cooling load	315083	413133	183458
	Load statistics	752462	894677	595302

TABLE 7: The contrast of the ratio of energy conversion when the building orientation is changed.

Building orientation	The energy saving ratio of the DSF (%)	Reference to Low-e hollow glass curtain wall	Reference to concrete-perlites-85
Northward	Heat energy saving rate	8.0	−9.0
	Air conditioning energy saving rate	21.3	−44.9
	Annual energy saving rate	16.1	−31.3
Westward	Heat energy saving rate	9.5	−7.3
	Air conditioning energy saving rate	28.2	−36.8
	Annual energy saving rate	21.3	−23.0
Southward	Heat energy saving rate	6.3	−10.2
	Air conditioning energy saving rate	26.3	−43.7
	Annual energy saving rate	16.0	−31.0
Eastward	Heat energy saving rate	10.1	−6.2
	Air conditioning energy saving rate	23.7	−41.8
	Annual energy saving rate	18.9	−26.4

heating; air conditioning requirements generally may not be considered [25], and in this topic do comparative analysis mainly for winter heating energy consumption. Shown in Figure 16, the concrete-perlites-85 facades shows the energy-saving sexual insulation exterior good performance; its energy consumption of winter heating is significantly lower than the DSF and Low-e hollow glass curtain wall regardless of the facing choice.

The DSF is lower than the low-e hollow glass curtain wall in the construction winter heating energy consumption in each toward, in the case of similar material; the DSF reveals strong advantage regarding the structure and function [26, 27]. Referring to Figure 17 histogram, the energy saving rate descends from eastward, westward, and northward to southward.

## 6. Conclusion

This subject starting from climatic characteristic of the cold regions, combined the operation principle in the winter, getting the conclusion of the energy-saving design of the DSF adapting to cold regions.

- (1) We simulate the different cavity spacing of the DSF by using the CFD software, found that during the solar radiation during the hot cavity spacing a large DSF with higher indoor temperature as well as empty cavity temperature in the winter daytime, solar radiation is small or at night time, the smaller cavity spacing of DSF has the better thermal insulation properties.

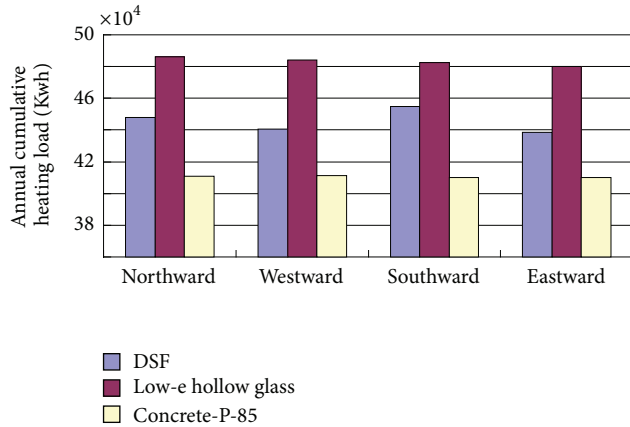


FIGURE 16: The contrast of heating load in one year when the building orientation is changed.

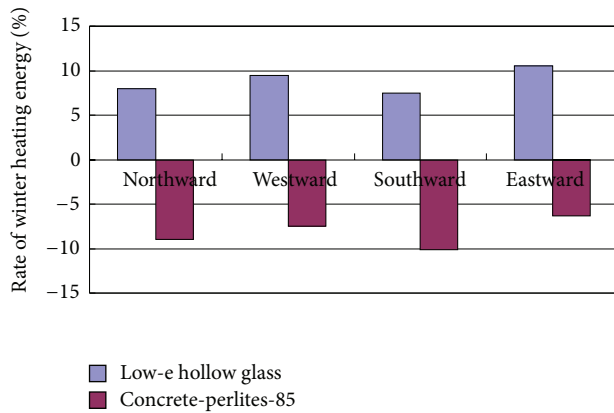


FIGURE 17: The contrast of the ratio of heating in winter when the building orientation is changed.

- (2) In general winter conditions use the circulation of the DSF, but the simulation found that winter daytime with air circulation of the DSF will get more favorable indoor environment. With the increase in the amount of air circulation, this phenomenon became more apparent. Closing the DSF could maintain indoor temperatures favor at night.
- (3) Building energy simulation analysis, respectively, for the DSF, Low-e hollow glass curtain wall, and concrete-perlites-85, the simulation found that the double-skin glass curtain wall with a good energy saving effect in winter has a good energy saving effect in winter but in summer it cannot show outstanding energy-saving features; such energy-saving effect decides that it is suitable for the climate characteristics in cold regions with long cold winter and short summer.
- (4) Total annual heating load calculation through four different buildings orientations shows that the energy saving rate of the DSF ranging from high to low is eastward, westward, northward, and southward.

## References

- [1] H. Zou, G. Wang, L. Guo, X. Wang, and H. Li, "The impact analysis on the building energy consumption of the windows in the sub-zero area," *Journal of Shenyang Jianzhu University*, vol. 25, no. 5, pp. 982–986, 2009.
- [2] J. Von Grabe, "A prediction tool for the temperature field of double facades," *Energy and Buildings*, vol. 34, no. 9, pp. 891–899, 2002.
- [3] H. Manz and T. Frank, "Thermal simulation of buildings with double-skin façades," *Energy and Buildings*, vol. 37, no. 11, pp. 1114–1121, 2005.
- [4] N. Ren and N. Yang, "The analysis of the double glass facades at north area," *Journal of Shenyang Jianzhu University*, no. 6, pp. 138–140, 2008.
- [5] J. J. Liu, *Study on energy efficient design of double-skin facades [M.S. thesis]*, Tsinghua University, Beijing, China, 2006.
- [6] X. Cen, J. Zhan, and S. Yang, "CFD simulation and optimization design of double skin façade," *Acta Scientiarum Naturalium Universitatis Sunyatseni*, no. 11, pp. 18–21, 2008.
- [7] D. Saelens, J. Carmeliet, and H. Hens, "Energy performance assessment of multiple-skin facades," *HVAC and R Research*, vol. 9, no. 2, pp. 167–185, 2003.
- [8] M. Liu and W. Long, "Exhaust air strategies of northward internal circulating DSF under winter working conditions in cold area," *Building Science*, vol. 25, no. 12, pp. 71–74, 2009.
- [9] L. Peng, C. Liyong, and L. Wenjuan, "Research on ventilation performance of high-rise office building with double-skin facade by wind tunnel tests," *Heating Ventilating and Air Conditioning*, vol. 34, no. 11, pp. 15–18, 2004.
- [10] H. Poirazis and J. L. J. Rosenfeld, "Modeling of double skin facades-results obtained using WIS," *Technical University of Denmark (DTU) Sags Rapport*, vol. 23, no. 8, pp. 13–17, 2003.
- [11] N. Du, *The impact of different structure of double-skin glass facades to room heat environment [M.S. thesis]*, Chang'an University, Xi'an, China, 2007.
- [12] M. Du, *Study on thermal performance of double-skin facade of cold region [M.S. thesis]*, Tianjin University, Tianjin, China, 2007.
- [13] J. Li, "Analysis and prospects of hot channel glass curtain wall," *Shanxi Architecture*, vol. 16, no. 4, pp. 10–13, 2002.
- [14] Q. Wei, *Dynamic analysis on double-skin facade using solar radiation [M.S. thesis]*, Chang'an University, Xi'an, China.
- [15] Y. He, *Experimental research and energy analysis of double glass curtain wall [M.S. thesis]*, Nanjing University of Science and Technology, Nanjing, China, 2010.
- [16] B. Li, *The research on climatic-active design strategy of building skin in hot-summer and cold-winter zone [M.S. thesis]*, Tsinghua University, Beijing, China, 2004.
- [17] Y. Gao and L. Zhao, "Simulation and analysis of thermal performance of external respiration double skin facade," *Heating Ventilating and Air Conditioning*, vol. 37, no. 1, pp. 20–22, 2007.
- [18] E. Djunaedy, J. Hensen, and M. Loomans, "Strategy for air flow simulation in building design center for building and systems," *Technische Universiteit Eindhoven*, vol. 31, no. 5, pp. 43–49, 2002.
- [19] H. Jan and M. Wigginton, "Modeling and simulation of a double-skin facade system," *Solar Energy*, vol. 12, no. 6, pp. 115–132, 2000.
- [20] J. Von Grabe, "A prediction tool for the temperature field of double facades," *Energy and Buildings*, vol. 34, no. 9, pp. 891–899, 2002.

- [21] E. Gratia and A. De Herde, "Natural ventilation in a double-skin facade," *Energy and Buildings*, vol. 36, no. 2, pp. 137–146, 2004.
- [22] T. Pasquay, "Natural ventilation in high-rise buildings with double facades, saving or waste of energy," *Energy and Buildings*, vol. 36, no. 4, pp. 381–389, 2004.
- [23] Z. Tian, S. K. Chou, and T. Y. Bong, "Building simulation: an overview of developments and information sources," *Building and Environment*, vol. 35, no. 4, pp. 347–361, 2000.
- [24] D. Prasad and M. Snow, *Designing With Solar Power*, Images Publishing Group PTV, Australia, 2002.
- [25] G. Augenbroe, "Trends in building simulation," *Building and Environment*, vol. 37, no. 8-9, pp. 891–902, 2002.
- [26] A. J. B. Tadeu and D. M. R. Mateus, "Sound transmission through single, double and triple glazing. Experimental evaluation," *Applied Acoustics*, vol. 62, no. 3, pp. 307–325, 2001.
- [27] A. Tzempelikos and A. K. Athienitis, "The impact of shading design and control on building cooling and lighting demand," *Solar Energy*, vol. 81, no. 3, pp. 369–382, 2007.

## Research Article

# Numerical Simulation and Stability Study of Natural Convection in an Inclined Rectangular Cavity

Hua-Shu Dou,<sup>1</sup> Gang Jiang,<sup>1</sup> and Chengwang Lei<sup>2</sup>

<sup>1</sup> Faculty of Mechanical Engineering and Automation, Zhejiang Sci-Tech University, Hangzhou 310018, China

<sup>2</sup> School of Civil Engineering, The University of Sydney, NSW 2006, Australia

Correspondence should be addressed to Hua-Shu Dou; huashudou@yahoo.com

Received 18 December 2012; Accepted 22 January 2013

Academic Editor: Zhijun Zhang

Copyright © 2013 Hua-Shu Dou et al. This is an open access article distributed under the Creative Commons Attribution License, which permits unrestricted use, distribution, and reproduction in any medium, provided the original work is properly cited.

This paper examines the process of instability of natural convection in an inclined cavity based on numerical simulations. The energy gradient method is employed to analyze the physics of the flow instability in natural convection. It is found that the maximum value of the energy gradient function in the flow field correlates well with the location where flow instability occurs. Meanwhile, the effects of the flow time, the plate length, and the inclination angle on the instability have also been discussed. It is observed that the locations of instabilities migrate right as the flow time increased. With the increase of plate length, the onset time of the instability on the top wall of the cavity decreases gradually and the locations of instabilities move to the right side. Furthermore, the locations of instability move left with the increase of the inclination angle in a certain range. However, these positions move right as the accumulation of the heat flux is restrained in the lower left corner of the cavity once the inclination angle exceeds a certain range.

## 1. Introduction

Transient natural convection flows in a cavity are common in industrial applications such as in heat exchangers, solar collectors, and nuclear reactors and in our daily life such as in light emitting diode (LED) street lights, computers, and mobile phones. Actually, some engineering problems are related to the cases with an inclined cavity. Yet, natural convection adjacent to an inclined plate has received less attention than the classic cases of vertical and horizontal plates. Natural convection heat transfer is regarded as one of the three basic forms of heat transfer, and there exists some difference of heat transfer efficiency between different manners of natural convection. The achieved results suggested that turbulent flow has a more powerful ability to transfer heat in natural convection compared to laminar flow.

Patterson and Imberger [1] carried out extensive investigations on the transient behavior of natural convection of a two-dimensional rectangular cavity in which the two opposing vertical sidewalls are simultaneously heated and cooled by an equal amount. The authors present several flow regimes

of the flow development of the boundary layer which were named as “conduction regime,” “stable convection regime,” and “unstable convection regime,” respectively. These studies are based on the relative values of the Rayleigh number  $Ra$ , the Prandtl number  $Pr$ , and the aspect ratio of the cavity. It was found that the flow of natural convection in an inclined cavity loses its stability by forming longitudinal vortices. Sparrow and Husar [2] made experiments on inclined plates to reveal the presence of cellular secondary flows superposed upon the natural convection main flow and believed that these longitudinal vortices were the first stage of the laminar-turbulent transition process. Haaland and Sparrow [3] tried to use linear stability theory to predict a critical angle (or range of angles) at which the disturbances change their character from travelling waves to longitudinal vortices. They finally found that it is difficult to predict the critical angle theoretically by treating each type of disturbance separately.

Lloyd and Sparrow [4] made some investigations with the aim of establishing the relationship between the inclination angle and the nature of the instability. They tried to determine accurate quantitative information on the angular dependence

of the Rayleigh number for instability. They found that waves were the mode of instability for inclination angles of less than 14 deg (relative to the vertical). Further, when the inclination angle is beyond 17 deg, the instability was characterized by longitudinal vortices. The range between 14 deg and 17 deg was a zone of continuous transition, with the two modes of instability coexisting.

Ganesan and Palani [5] proposed to study the natural convection effects on impulsively started inclined plate with heat and mass transfer by an implicit finite difference scheme of the Crank-Nicolson type. In order to access the accuracy of the numerical results, they compared their study with available exact solution of Moutsoglou and Chen [6] and achieved a good agreement. In addition, they observed that local wall shear stress decreases as the angle of inclination decreases.

Xu et al. [7] researched transient natural convection flows around a thin fin on the sidewall of differentially heated cavity, which illustrated that the fluid boundary layer adjacent to a vertical thermal wall included three sublayers, and these sublayers were determined by different dynamic and energy balances. When the initial time  $t_1$  is sufficiently small, the balance was determined by viscous term and buoyancy term which yields the inner viscous layer. Subsequently, as the flow time increases to  $t_2$ , the balance is still determined by viscous term and buoyancy term, which yields a viscous layer within the thermal boundary layer but outside the inner viscous layer. At the same time, with the formation of inner viscous layer and viscous layer, there is a balance between the conduction term and the unsteady term which yields the thermal boundary layer. Saha et al. [8] studied natural convection of an inclined flat plate under a sudden cooling condition, and they found that the cold boundary layer adjacent to the plate is potentially unstable, if the Rayleigh number  $Ra$  exceeded a critical value. In other words, the boundary layer would be always stable if  $Ra$  was below a threshold.

Said et al. [9] made some numerical investigations on turbulent natural convection in a parallel-walled channel which is inclined with respect to gravity. They found that the channel overall average Nusselt number was reduced as the inclination angle was increased. The rate of reduction in the overall Nusselt number decreases as the Rayleigh number increases. Additionally, they observed that the local Nusselt number was much higher along the lower wall of the horizontal channel where cold air entered in comparison to the upper wall where hot air existed at both channel openings.

Lin [10] presented a numerical experiment for the onset and its linear development of longitudinal vortices in natural convection over inclined plates. It was observed that the critical Grashof number increases with the increase of the inclination angle while the effect of inclination angle on the Nusselt number is less pronounced when the value of the inclined angle increases.

Iyer and Kelly [11] did not agree with the conclusions made by Haaland and Sparrow [3]. They found that these experiments in [3] were not sensitive enough to detect the first instabilities predicted by theoretical analysis. Iyer and Kelly used a spatial linear stability analysis with the

parallel flow assumption to examine the formation and growth of both wave instabilities and longitudinal vortices and attempted to find a correlation between experimental and theoretical results by finding the total amplification between the earliest disturbances and the observed disturbances.

Thus, there are many factors to affect the natural convection heat transfer efficiency, in particular, the difference of laminar flow and turbulence. In order to achieve a flow field where the flow is in turbulent state, it is helpful to ascertain the locations where instabilities could occur and where instability would occur firstly.

After almost 20 years of work, Dou and co-authors [12–18] suggested a new approach to analyze flow instability and turbulence transition based on “energy gradient method.” This approach is different from the linear stability theory, the weak nonlinear stability theory, the secondary instability theory, and the energy method. This approach explains the mechanism of flow instability from physics and derives the criteria of turbulence transition. The theoretical results are in agreement with the experimental data of the pipe Poiseuille flow, plane Poiseuille flow, plane Couette flow, Taylor-Couette flow, boundary layer flow, and so on.

In this study, numerical simulation is used to obtain the flow field at various geometrical and flow parameters. Then, the energy gradient method is used to investigate the physical mechanism of flow instability in natural convection. The paper is divided into two sections. In the first section, the same computational geometries and numerical scheme of Saha et al. [8] are used to validate the numerical method used in this study. In the second section, energy gradient method is briefly introduced to calculate the value of  $K$  in the whole flow field and make some further investigations on the effects of the flow time, plate length, and the inclination angle on flow instability of natural convection. This is the first time for the energy gradient method to be used in natural convection.

## 2. Computational Geometry and Numerical Procedures

**2.1. Computational Geometry.** The computational geometry is shown in Figure 1. We consider the top wall as a cooled inclined flat plate where the temperature is fixed at  $T_c$ . Initially, the fluid temperature in the domain is  $T_0$  which is higher than  $T_c$ . The four side walls of the domain are rigid and nonslip. Except for the top plate, all the three other walls of the rectangle cavity are assumed to be insulated. The length and the width of the cavity are defined as  $L$  and  $W$ , respectively. The inclination angle of the cavity is expressed with  $\theta$ .

### 2.2. Numerical Procedures

**2.2.1. Governing Equations.** The development of natural convection adjacent to an inclined cavity is governed by the following two-dimensional Navier-Stokes and energy



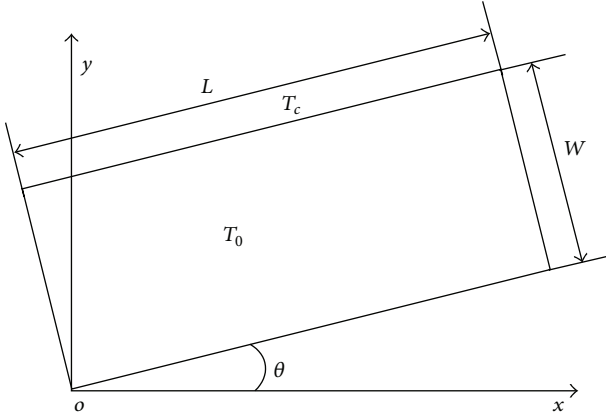


FIGURE 1: Schematic of the inclined cavity.

equations, and these equations are based on the Boussinesq approximation:

$$\begin{aligned}
 \frac{\partial u}{\partial x} + \frac{\partial v}{\partial y} &= 0, \\
 \frac{\partial u}{\partial t} + u \frac{\partial u}{\partial x} + v \frac{\partial u}{\partial y} &= -\frac{1}{\rho} \frac{\partial p}{\partial x} + \nu \left( \frac{\partial^2 u}{\partial x^2} + \frac{\partial^2 u}{\partial y^2} \right) + g\beta \sin \theta (T - T_0), \\
 \frac{\partial v}{\partial t} + u \frac{\partial v}{\partial x} + v \frac{\partial v}{\partial y} &= -\frac{1}{\rho} \frac{\partial p}{\partial y} + \nu \left( \frac{\partial^2 v}{\partial x^2} + \frac{\partial^2 v}{\partial y^2} \right) + g\beta \cos \theta (T - T_0), \\
 \frac{\partial T}{\partial t} + u \frac{\partial T}{\partial x} + v \frac{\partial T}{\partial y} &= k \left( \frac{\partial^2 T}{\partial x^2} + \frac{\partial^2 T}{\partial y^2} \right),
 \end{aligned} \tag{1}$$

where  $x$  and  $y$  are the horizontal and vertical coordinates with origin at the lower left corner of the cavity,  $t$  is the time,  $T$  is the temperature,  $p$  is the pressure,  $u$  and  $v$  are the velocity components in the  $x$  and  $y$  directions,  $g$  is the acceleration due to gravity,  $\beta$  is the coefficient of thermal expansion,  $\rho$  is the fluid density,  $k$  is the thermal diffusivity, and  $\nu$  is the kinematic viscosity.

**2.2.2. Numerical Scheme.** The governing equations (1) are implicitly solved using a finite-volume SIMPLE scheme, with the QUICK scheme approximating the advection term. The diffusion terms are discretized using central differencing with second-order accurate. A second-order implicit time-marching scheme will be used for the unsteady term. The discretized equations are iterated with specified underrelaxation factors. The boundary condition of the left wall and the right wall is  $\partial T / \partial x = 0$ ,  $u = v = 0$ ; the boundary condition of the bottom is:  $\partial T / \partial y = 0$ ,  $u = v = 0$ . In addition, we should note that the flow is unsteady, and all the plots depend on the time.

### 3. Criteria of Instability Based on the Rayleigh Number

The natural convection boundary layer adjacent to an inclined cavity is subjected to sudden cooling boundary condition which yields a thermal boundary layer along the wall. At the same time with the formation of the thermal boundary layer, the viscous boundary layer is formed which is determined by the balance between viscous term and inertial term. Meanwhile, the velocity inside the boundary layer develops, governed by the balance of viscous and inertial terms with the buoyancy term. It is known from [7, 19] that the thickness of thermal boundary layer, the velocity inside the thermal boundary layer, and the thickness of the viscous boundary layer are related to the balance between conduction and advection terms.

We can find in [8] that, when the balance between conduction and advection terms plays a leading role in exchange of momentum and energy, the steady-state scales of the boundary layer ( $t_s$ ) can be achieved:

$$t_s \sim \frac{(1 + \text{Pr})^{1/2} (1 + \tan^2 \theta)^{1/2}}{\tan \theta \cdot \text{Ra}^{1/2} \text{Pr}^{1/2}} \left( \frac{L^2 \sin^2 \theta}{k} \right), \tag{2}$$

where  $\text{Ra}$  is the Rayleigh number,  $\text{Ra} = g\beta\Delta T(L \sin \theta)^3 / \nu k$  and  $\text{Pr}$  is the Prandtl number,  $\text{Pr} = \nu / k$ . In the present case, the thermal boundary layer is bounded by a rigid surface of the plate and a cold air layer, which is equivalent to the free-rigid boundary configuration [20–24], in which there is a critical Rayleigh number  $\text{Ra}_c = 1106.5$ . Also, there exists a critical time scale  $t_B$  for the onset of thermal layer instability at a given  $\text{Ra}$ . If  $t > t_B$ , the instability will set in before the growth of the thermal boundary layer completes. On the other hand, if  $t < t_B$ , the instability will never occur no matter how much time it iterates. The critical time scale  $t_B$  is described as follows [8]:

$$t_B = \left( \frac{\text{Ra}_c}{\text{Ra}} \right)^{2/3} \frac{L^2 \sin^2 \theta}{k}. \tag{3}$$

The ratio between the growth time of thermal boundary layer  $t_s$  and the critical time scale  $t_B$  described as follows [8],

$$\frac{t_s}{t_B} = \left[ \frac{(1 + \text{Pr})^3 (1 + \tan^2 \theta)^3 \text{Ra}}{\text{Pr}^3 \tan^6 \theta \cdot \text{Ra}_c^4} \right]^{1/6}. \tag{4}$$

Absolutely, if  $\text{Ra} > \text{Pr}^3 \tan^6 \theta \cdot \text{Ra}_c^4 / (1 + \text{Pr})^3 (1 + \tan^2 \theta)^3$ , that is,  $t_s > t_B$ , the instability will set in before the growth of the thermal boundary layer completes, or else, if  $\text{Ra} < \text{Pr}^3 \tan^6 \theta \cdot \text{Ra}_c^4 / (1 + \text{Pr})^3 (1 + \tan^2 \theta)^3$ , that is,  $t_s < t_B$ , the instability will never occur.

### 4. Validation of Numerical Methods

**4.1. Numerical Scheme Test.** In order to verify the accuracy of the numerical scheme used in this study, the computational geometry of Saha et al. [8] is considered. In the following numerical simulations, the condition  $\text{Pr} < 1$  should be

TABLE 1: Values of configuration dimensions,  $Ra$ ,  $t_s$ , and  $t_B$  shown in Figure 6.

Runs	Configuration dimension	$Ra$	$t_s$	$t_B$
(a1)	$W (0.5 \text{ m}) \times L (5 \text{ m})$	$5.33 \times 10^4$	815.6 s	915.5 s
(b1)	$W (0.5 \text{ m}) \times L (5 \text{ m})$	$5.33 \times 10^5$	257.9 s	197.2 s
(c1)	$W (0.5 \text{ m}) \times L (2 \text{ m})$	$6.83 \times 10^3$	364.7 s	576.8 s
(d1)	$W (0.5 \text{ m}) \times L (15 \text{ m})$	$2.88 \times 10^6$	998.9 s	576.8 s

satisfied. If  $Pr > 1$ ,  $Pr^3 \tan^6 \theta \cdot Ra_c^4 / (1 + Pr)^3 (1 + \tan^2 \theta)^3$  is very large. Thus, it is difficult to observe instability if the value of  $Ra$  is low.

Figure 2 shows the simulated temperature contours with three different cavity dimensions at 1000 s, which is taken from Saha et al. [8]. The lengths are 5.4 m, 10.8 m, and 16.2 m, respectively, and the width is 0.6 m.

Figure 3 presents the current results of numerical simulations at 1000 s for the cavity sizes in Figure 2. Comparing Figure 3 with Figure 2, it can be found that the present simulations are in agreement with those in [8], which demonstrates that the numerical scheme is reliable and accurate.

**4.2. Grid Independence Test.** Grid independence will be examined with three different mesh sizes for the same domain. The three mesh sizes are as follows (Figure 4): (a)  $100 \times 300$  with 30000 cells, 60400 faces, and 30401 nodes; (b)  $150 \times 450$  with 67500 cells, 135600 faces, and 60801 nodes; (c)  $200 \times 600$  with 120000 cells, 240800 faces, and 120801 nodes.

The simulation results of temperature contours at 300 s with these three meshes are shown in Figure 4. The temperature versus time with three different mesh sizes is shown in Figure 5, which is recorded at the same monitor point (2, 1). It can be seen from Figures 4 and 5 that mesh convergence has been achieved with these meshes.

**4.3. Test of Simulation Results.** Four different configurations are listed in Table 1, and substituting these corresponding data into (2) and (3), we will get  $t_s$  and  $t_B$ , respectively. All the numerical models in Figure 5 satisfy the following conditions:  $Pr = 0.72$ ,  $\theta = 5.71^\circ$ , and  $k = 2.04 \times 10^{-5}$ . Figures 6(a2), 6(b2), 6(c2), and 6(d2) are partial enlarged drawings of the middle portion of the plate in Figures 6(a1), 6(b1), 6(c1), and 6(d1), respectively.

By comparing these four groups of pictures in Figure 6, some conclusions may be written as follows.

- (1) It is observed that there is an “end effect” at the top right corner of the enclosure in each case, and this phenomenon is affected by the configuration and inclination angle of the cavity.
- (2) The iterative time reaches  $t = t_s$  both in Figures 6(a1) and 6(c1), and it is very clear that the flow is still stable which can be seen from the partial enlarger of the middle portion of the plate.
- (3) The oscillation of the curves from the isotherms in Figures 6(b1) and 6(d1) indicates the onset of instability. It is clearly seen that the thermal boundary

layer travels in waveform rather than in a smooth manner.

- (4) It can be found that  $t_s < t_B$  is satisfied for the simulated results shown in Figures 6(a1) and 6(c1), and it is observed that the thermal boundary layer is stable at these cases. While, in Figures 6(b1) and 6(d1),  $t_s > t_B$ , the stability criterion is violated. Thus, the flow instability occurs at a proper time. These results are in good agreement with the predictions of criteria of instability based on  $Ra$ .

Nevertheless, we observe some unique phenomena from these previous instability cases. Firstly, instabilities do not occur in the whole flow field. Secondly, there exists a distinctive time difference of instabilities at different locations. In other words, it is expected to employ a theory to predict the locations where instabilities could occur and positions where instability would take place firstly. In the following study, we will briefly introduce the energy gradient method to analyze the above phenomena observed.

## 5. Application of Energy Gradient Method

**5.1. Energy Gradient Method.** From the classical theory of the Brownian motion, the fluid particles exchange energy and momentum all the time via collisions. The fluid particle will collide with other particles in transverse directions as it flows along its streamline, and this particle would obtain energy expressed as  $\Delta E$  after many cycles; at the same time, the particle would drop energy due to viscosity along the streamline; with the same periods, the energy loss expressed as  $\Delta H$  would be considerable. Consequently, there exists a critical value of the ratio of  $\Delta E$  and  $\Delta H$ , above which the particle would leave its equilibrium by moving to a new streamline with higher energy or lower energy and below which the particle would not leave its streamline for its oscillation would be balanced by the viscosity along the streamline. Making reference to [13–18], we can express the criteria of instability as follows:

$$F = \frac{\Delta E}{\Delta H} = \frac{((\partial E / \partial n) (2\bar{A} / \pi))}{((\partial H / \partial s) (\pi / \omega_d) u)} \quad (5)$$

$$= \frac{2}{\pi^2} K \frac{\bar{A} \omega_d}{u} = \frac{2}{\pi^2} K \frac{v'_m}{u} < \text{Const},$$

where

$$K = \frac{\partial E / \partial n}{\partial H / \partial s}. \quad (6)$$

Here,  $F$  is a function of coordinates which expresses the ratio of the energy gained in a half period by the particle and the energy loss due to viscosity in the half period.  $K$  is a dimensionless field variable (function) and expresses the ratio of transversal energy gradient and the rate of the energy loss along the streamline.  $E = p + 1/2 \rho V^2$  is the kinetic energy per unit volumetric fluid,  $s$  is along the streamwise direction, and  $n$  is along the transverse direction.  $H$  is the loss of the

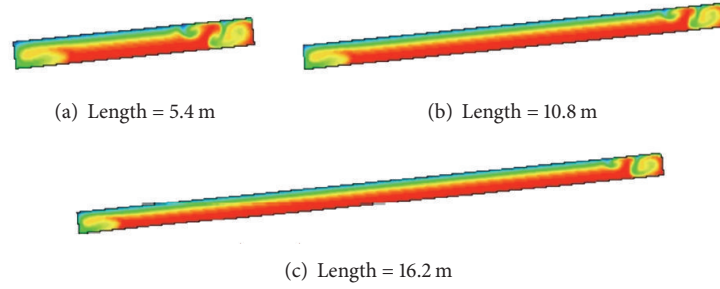


FIGURE 2: Temperature contours of three different geometries in [8].

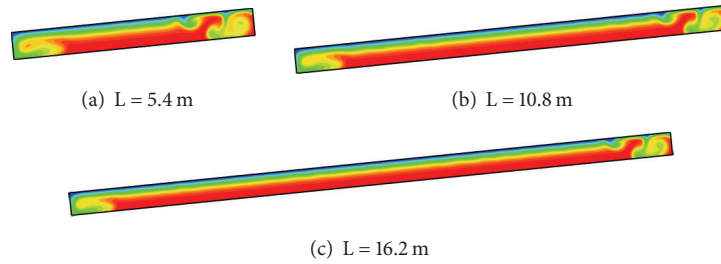


FIGURE 3: Temperature contours of three different geometries (present calculation).

total mechanical energy per unit volumetric fluid along the streamline for finite length, which can be calculated from the Navier-Stokes equations. Further,  $\rho$  is the fluid density,  $u$  is the streamwise velocity of main flow,  $A$  is the amplitude of the disturbance distance,  $\omega_d$  is the frequency of the disturbance, and  $v'_m = A\omega_d$  is the amplitude of the disturbance of velocity.

Equation (5) represents the criteria of instability; that is, if  $F$  exceeds its threshold, the fluid particle would lose its stability or the instability would never set in. Equation (6) represents characteristic of instability; that is, it shows the most dangerous positions in a flow field, and it indicates that instability would occur firstly at the position with the maximum value of  $K$  once instability sets in.

**5.2. Criterion of Instability Based on Energy Gradient in Natural Convection.** Dou and Phan-Thien [25] proposed an energy gradient theory which describes the rules of fluid material stability from the viewpoint of energy field and can be considered as a supplement to the Newtonian mechanics. They claimed that the instability of natural convection could not be resolved by Newton's three laws, for the reason that a material system moving in some cases is not simply due to the role of forces. This method does not attribute the Rayleigh-Benard problem to forces, but to energy gradient. It postulates that when the fluid is placed on a horizontal plate and it is heated from below, the fluid density in the bottom becomes low which leads to energy gradient  $\partial E/\partial y > 0$  along  $y$ -coordinate. Only when  $\partial E/\partial y$  is larger than a critical value, will the flow become unstable, and then fluid cells of vorticities will be formed. This conclusion is in accordance with the former criteria of instability.

When the fluid is placed on an inclined plate or a box, the criterion of natural convection can be written as (Figure 7)

$$K = \sqrt{\left(\frac{\partial E}{\partial x}\right)^2 + \left(\frac{\partial E}{\partial y}\right)^2}. \quad (7)$$

In present study, neglecting the influence of the gravity, we get  $E \sim p_0$ .

Besides the ability to predict whether instability could occur in natural convection [25], energy gradient method has another two functions in natural convection when instabilities had occurred. It can predict the locations where instabilities could occur and the position where instability would take place firstly via the value of  $K$ . In the proposed method, the flow is expected to be more unstable in the area with high value of  $K$  than that in the area with low value of  $K$ . This is the distinctive difference between energy gradient theory and the criteria of instability based on the Rayleigh number and is also the focus of investigation in this paper.

We should clarify that the value of  $K$  derived from energy gradient method can only be applied in situations where instabilities could occur. Thus, all the subsequent numerical simulations should satisfy the condition that  $Ra$  is larger than  $Pr^3 \tan^6 \theta \cdot Ra_c^4 / (1 + Pr)^3 (1 + \tan^2 \theta)^3$ , in order to study the cases of instability occurrence.

## 6. Results and Discussions

**6.1. Results with New Geometries.** We will use the same numerical scheme as that described previously to simulate the natural convection in a cavity. The numerical results and analysis are discussed as follows. In order to avoid the influence of "end effect" on numerical results, we choose

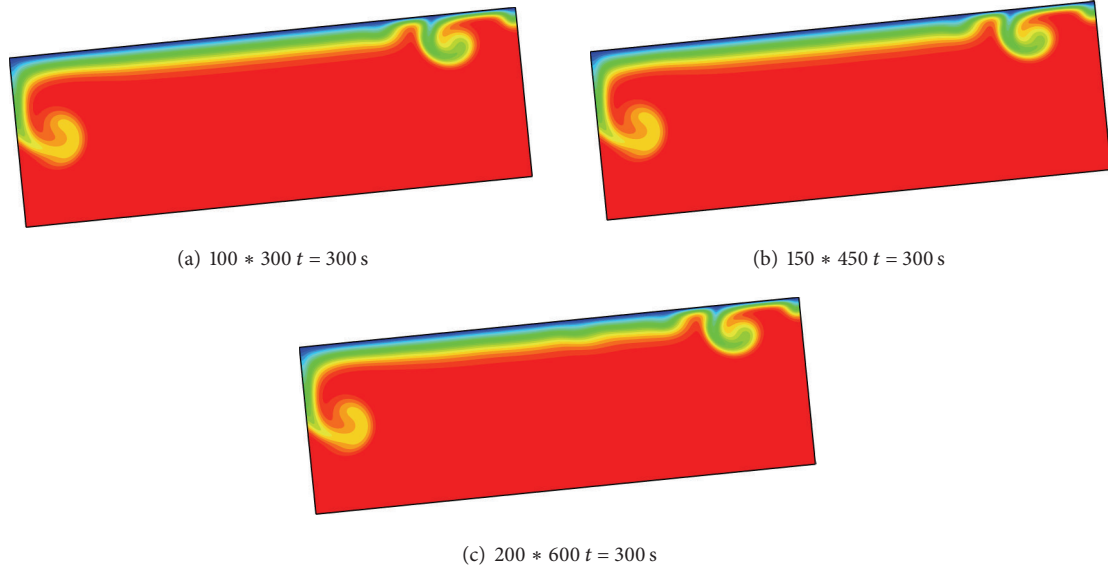


FIGURE 4: Comparison of the calculated results with three different mesh sizes: (a)  $\Delta x = 0.054$ , (b)  $\Delta x = 0.036$ , and (c)  $\Delta x = 0.027$ .

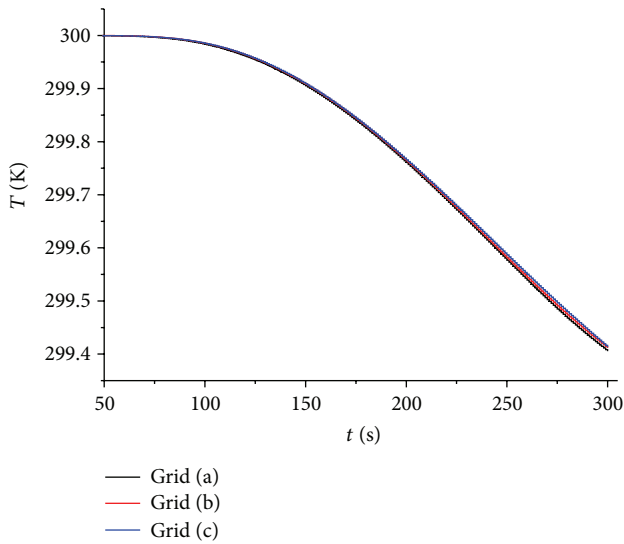


FIGURE 5: Temperature profile calculated with three different grid sizes.

another computational domain as shown in Figure 8. The aspect ratio of the domain is as  $L$  (16.2 m)  $\times$   $W$  (2 m). The calculated results at  $Ra = 2.1 \times 10^8$  are shown in Figure 8. According to the criterion based on the Rayleigh number, the flow is unstable. Figure 8(a) shows the total pressure contours. It is found from this picture that there are two areas of unstable region in the domain. This phenomenon is explained as follows. As the boundary conditions are defined, the temperature on the top wall is lower than the temperature of the fluid, which leads the fluid with higher temperature in the cavity to move upwards and gather together. Consequently, pressure difference develops gradually due to the movement of the fluid in the cavity, and the irregular phenomena of the

total pressure contours indicate that the flow of the fluid is unstable.

Figure 8(b) shows the velocity contours along  $x$ -coordinate, the straight line m-m splits the cavity into a left region and a right region, and the minus symbol of velocity means particles move along negative direction of  $x$ -coordinate. It is noticeable that the velocity is distinctive in the left area, while the velocity in the right area tends to be 0. However, we attribute this phenomenon to inclination of the cavity. For a horizontal plate, the velocity profile is symmetrical in the whole domain. Furthermore, we observe that the negative speed appears mainly close to the top wall. When the heated fluid expands and moves upwards to the top wall, it can be seen from Figure 8(a) that the pressure close to the top wall is much higher than any other area, and this higher pressure would drive the fluid near the top wall to travel to the left side; therefore, the negative velocity is formed. At the same time, we notice that there exists a continuous area above the top wall where the value of  $x$ -velocity ( $u$ ) is large. In [26], we obtain that the thermal boundary layer, containing lots of heat flux, travels along the bottom wall in the process of natural convection; hence, the flow, we observed, is actually the heat flux; furthermore, the movement direction of the heat flux accords well with the value of  $x$ -velocity ( $u$ ).

Figure 8(c) shows the velocity contours along  $y$ -coordinate; the straight line m-m splits the cavity into a left region and a right region. Similar to Figure 8(b), speed is fierce in the left district and is faint in the right district. Here, we get some new discoveries. Firstly, in comparison to Figure 8(b), we can find that the district with high value of  $y$ -velocity ( $v$ ) is in good accordance with the district with high value of  $x$ -velocity ( $u$ ); however, the areas with high value of  $v$  are obviously much larger than the areas with the high value of  $u$ ; this phenomenon confirms that lots of fluid particles move upwards in this cavity, while, at the same time

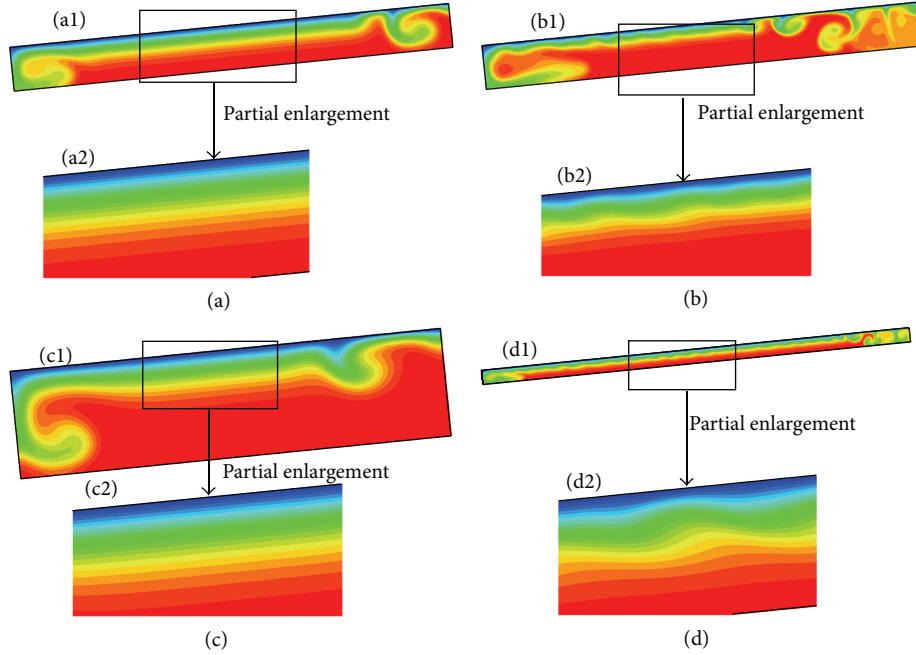


FIGURE 6: Four groups of geometries with different Ra: (a1)  $Ra = 5.335e4$ , (b1)  $Ra = 5.335e5$ , (c1)  $Ra = 6.83e3$ , and (d1)  $Ra = 2.88e6$ .

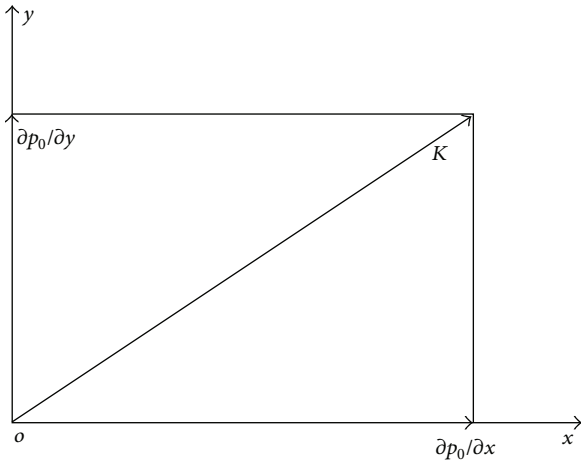


FIGURE 7: Calculation of the value of  $K$ .

with the fluid moving upwards, the fluid also travels along the horizontal direction. Secondly, we find that the minus velocity along the negative vertical direction still exists in this cavity. For the temperature on the top wall is lower than that in the cavity, which leads to a large density of fluid near the top wall, then the fluid with large density moves downwards due to the buoyancy. Meanwhile, it is known from Figure 8(a) that the pressure near the top wall is much larger than that of the bottom, and the pressure difference would drive the fluid to move downwards. Consequently, the negative speed is produced under the action both of the buoyancy and the pressure difference.

Figure 8(d) shows the temperature contours in this cavity; the straight line m-m splits the cavity into a left region and a right region. Firstly, it is surveyed that the locations of instabilities concentrate mainly in the left region close to the top wall, while instabilities seldom occur in the right region of this cavity, and this is due to the inclination of the cavity resulting in lots of heat flux concentrated on the top wall in the left region. In addition, we find a unique location of instability above the bottom. It is known from [26] that the movement of thermal boundary layer leads to the accumulation of heat flux above the bottom; with reference to Figure 8(a), we know that there exists an obvious pressure difference at the location where heat flux is accumulated which leads to the fact that the fluid loses its stability and moves upwards. At last, we observe that the locations of instabilities accord well with the locations with high value of velocity. This illustrates that the instabilities result in the dramatic change of velocity.

Figure 8(e) shows the contours of the value of  $K$ ; the straight line m-m splits the cavity into a left region and a right region. It is easy to get some similar and new discoveries by comparing Figure 8(d) to Figure 8(e). First, the area with high value of  $K$  is mainly concentrated in the left side of this cavity, and this is similar to the previous discoveries. Second, the area with high value of  $K$  is in excellent agreement with the locations of instabilities. This result can verify the accurate prediction of energy gradient method. Third, the manifestation of instability is the formation of vorticity, and positions with the formation of vorticities accord well with the locations with high value of  $K$ ; however, there exists a region with low value of  $K$  inside the vorticity, as the blue area shows in the contours of the value of  $K$  in Figure 8(e). Fourth, there exists an area with high value of  $K$  on the



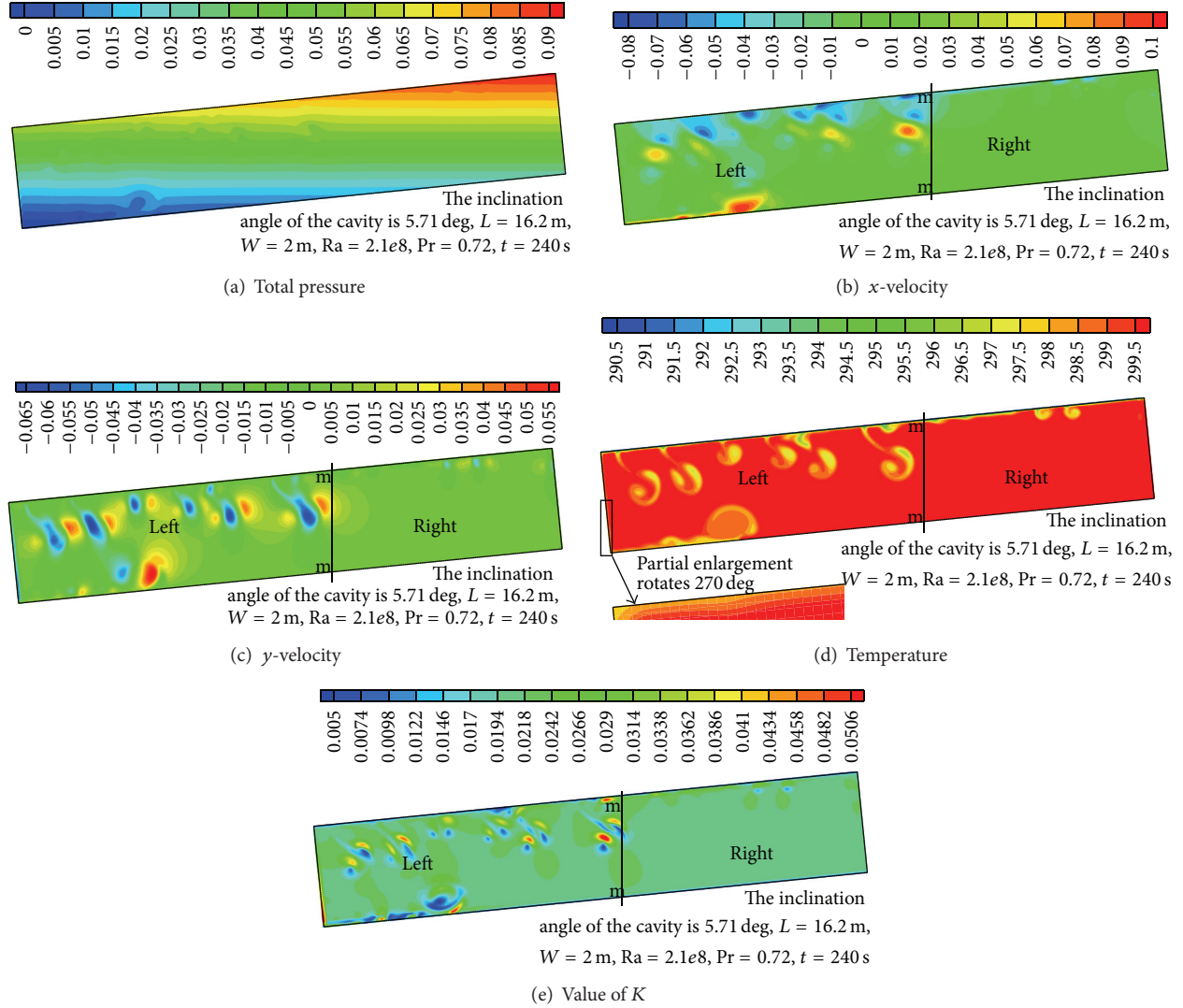
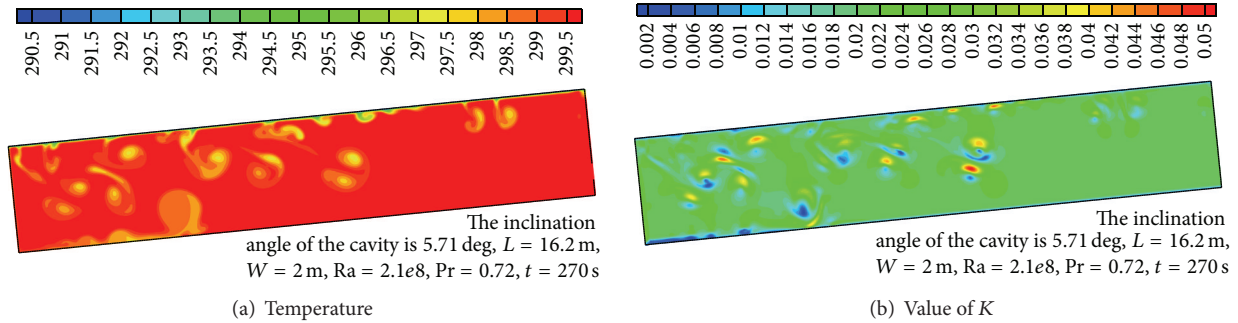
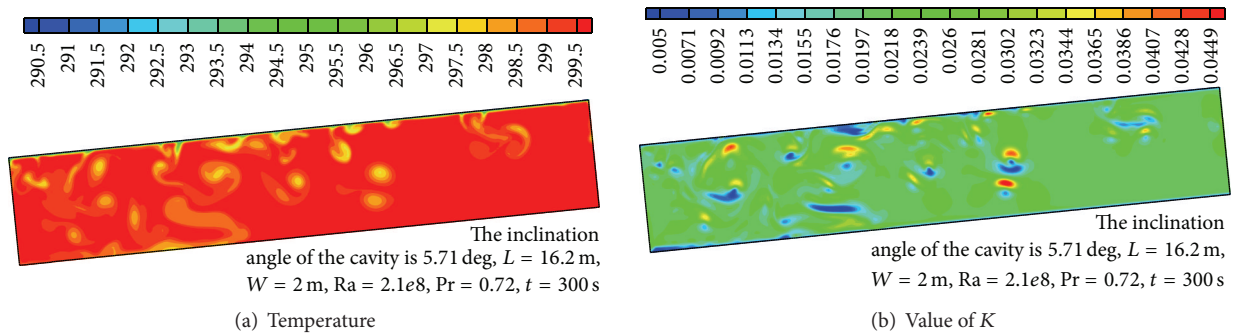


FIGURE 8: Calculated results of various parameters: (a) total pressure contours, (b)  $x$ -velocity contours, (c)  $y$ -velocity contours, (d) temperature contours, and (e)  $K$  contours.

left wall, yet no vorticity is formed. We can observe from the partial enlargement of isotherms in Figure 8(d) that the thermal boundary layer has lost its stability for it travels in a waveform. The reason why it does not form a vorticity is that the thermal boundary travels along the wall, and the heat flux is accumulated above the bottom which leads to the onset of instability. Except for the above discoveries, there exit two problems to be solved: the first one is that we cannot determine the critical value of  $K$  which can predict whether instability could occur in natural convection. The other is that we do not comprehend so far why the area with high value of  $K$  and the area with the low value of  $K$  coexist at the locations of instabilities.

**6.2. Effect of Flow Time and Discussions.** In order to investigate the effect of the flow time, we choose the same geometry

and numerical scheme to achieve some numerical simulations. Figures 9 and 10 show the contours of temperature and the value of  $K$  at 270 s and 300 s, respectively. The basic parameters are showed in the corresponding figures. Comparing Figures 9 and 10 with Figures 8(d) and 8(e), we can observe the following characteristics. First, the regions with high value of  $K$  coincide with the locations of instabilities. Second, with the flow time accumulated, the positions and areas of instabilities are increasing. Third, the area with high value of  $K$  and the area with the low value of  $K$  coexist at the locations of instabilities, and the reason is still unknown till now. Fourth, the locations of instabilities spread right along the top wall with the increase of the flow time. This is because the accumulation of heat flux above the bottom wall is restricted; in other words, the movement of the thermal boundary layer on the top wall is restrained. Thus, lots of heat flux is accumulated on the top wall near the right side which leads to the occurrence of instabilities. Fifth, the

FIGURE 9: Calculated results at 270 s: (a) temperature contours and (b)  $K$  contours.FIGURE 10: Calculated results at 300 s: (a) temperature contours and (b)  $K$  contours.

fluid in the cavity tends to flow in a turbulent manner. It is suggested in energy gradient method that the amplification of local turbulence phenomenon would lead to that the whole domain loses its stability. In the current case, the natural convection cannot be restricted so that the fluid tends to be turbulence, and this phenomenon is in good agreement with energy gradient method.

In summary, the flow time affects numerical results to a considerable degree. Two features are distinctive particularly: the locations of instabilities migrate right on the top wall and the fluid in the whole domain tends to flow in a turbulent manner as the flow time increases.

**6.3. Effect of Plate Length and Discussions.** Figure 11 shows the contours of temperature and the value of  $K$ , respectively, with a plate length of 24.3 m. The basic parameters are showed in the corresponding figures. Comparing Figures 8(d) and 8(e) with Figures 11(a) and 11(b), we can also make some conclusions. First, the regions with high value of  $K$  coincide with the locations of instabilities. Second, the area with high value of  $K$  and the area with the low value of  $K$  coexist at the locations of instabilities. The above two viewpoints are similar to the former conclusions. Third, the onset time of instability is inversely proportional to the length of the plate; that is, the onset time of instability decreases with the increase of  $L$ . Corcione [27] stated that the heat transfer rate from any heated or cooled boundary surface of the enclosure increases as the Rayleigh number increases. This phenomenon is in good accordance with the results in [27]. In all the related

cases,  $Ra$  is actually proportional to the length of the cavity  $L$ . Consequently, when we substitute the larger parameter of  $L$  into (2), it is easy to get a shorter time of  $t_s$ , which means that the flow is easier to lose its stability. Fourth, the locations of instabilities migrate right as the plate length increases. Because the migration length of the thermal boundary on the top wall is prolonged, the heat flux transfer would be limited as long as the instabilities set in, which in turn leads to the accumulation of heat flux on the top wall near the right side, and the heat flux loses its stability.

In summary, the length of the cavity has an obvious effect on numerical simulation. Two features are distinctive particularly: the onset time of instabilities will get shorter and the locations of instabilities on the top wall will migrate right with the increase of the plate length.

**6.4. Effect of Inclination Angle and Discussions.** Figures 12 and 13 show the contours of temperature and the value of  $K$  with inclination angle  $\theta = 10^\circ$  and  $\theta = 15^\circ$ , respectively. The basic parameters are showed in the corresponding figures. Kurian et al. [28] studied laminar natural convection inside inclined cylinders of unity aspect ratio and demonstrated that there exists a threshold of inclination angle. As the inclination angle increased from 0 deg to its threshold, convection increased to a maximum. However, when the inclination angle was greater than its critical value, the convection effects and the dimensionless axial temperature gradient decreased relatively small with the increase of inclination angle. Comparing these figures with Figures 8(d) and 8(e), we can obtain some

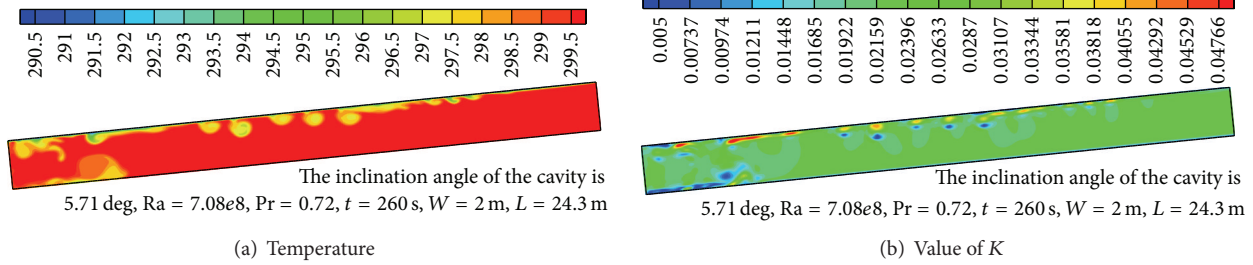


FIGURE 11: Calculated results with length of 24.3 m: (a) temperature contours and (b)  $K$  contours.

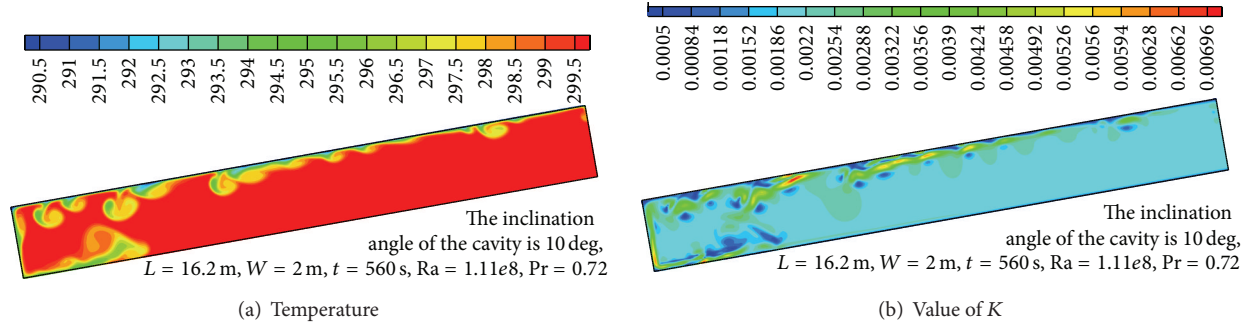


FIGURE 12: Calculated results with 10 degrees of angle: (a) temperature contours and (b)  $K$  contours.

similar and different observations. First, the regions with high value of  $K$  still coincide with the locations of instabilities. Second, the area with high value of  $K$  and the area with the low value of  $K$  coexist at the locations of instabilities. The above two observations are similar to the former conclusions, while the following three conclusions are different. Third, the intensity of flow instability in the left region is much stronger than that in the right region as the inclination angle increases. Upton and Watt [29] made experimental study in an inclined rectangular enclosure, and the results showed that the angle of inclination has a significant effect on the flow and heat transfer in natural convection in an enclosure. Buoyancy in the intrusion layer was found to be the main factor determining the character of these flows. When the angle of the inclined plate increases, more components of buoyancy will be imposed on the top wall which leads to that more heat flux will be accumulated in the left region. Hence, it is easy to observe that the intensity of flow instability is much stronger in the left region. This result is in good accordance with the conclusion stated by Upton and Watt [29]. Fourth, the locations of instabilities would spread left along the top wall with the increase of inclination angle in a certain range. Due to the same reason as stated previously, more heat flux will be accumulated in the left region; thus, it is easy to observe that more instabilities would occur in the left region as the inclination angle increases in a certain range which in turn hinders the movement of the heat flux. Fifth, the locations of instabilities would migrate right once the inclination angle exceeds a certain range. Although the increased component of buoyancy along the top wall can accelerate the movement of heat flux to the left side, the width of the cavity and the higher pressure difference will restrict

the accumulation of heat transfer severely in the lower left corner. As a result, more heat flux will be accumulated on the top wall near the right side, and it is easy to observe lots of instabilities on the right side of the top wall. At the same time, we are surprised to find that the fourth and fifth viewpoints accord well with the results of Kurian et al. [28] to some extent.

In summary, the inclination angle of the cavity has a distinctive affection on numerical simulations. Three features are distinctive particularly. First, the intensity of flow instability in the left region is much stronger than that in the right region with the increase of inclination angle. In addition, the locations of instabilities will migrate left with the increase of inclination angle in a certain range. At last, the locations of instabilities will migrate right once the inclination angle exceeds a certain range.

## 7. Conclusions

Numerical simulations on natural convection in an inclined cavity have been carried out using the unsteady Navier-Stokes equations for various parameters such as the domain length and the inclined angle. The main conclusions are as follows.

- (1) The energy gradient method is successfully employed to study the instability of the thermal boundary layer. It is found that instability occurs firstly at the position where the energy gradient function gets its maximum  $K_{\max}$ . The regions with high value of  $K$  coincide with the locations of instabilities. These observations accord well with the energy gradient theory.

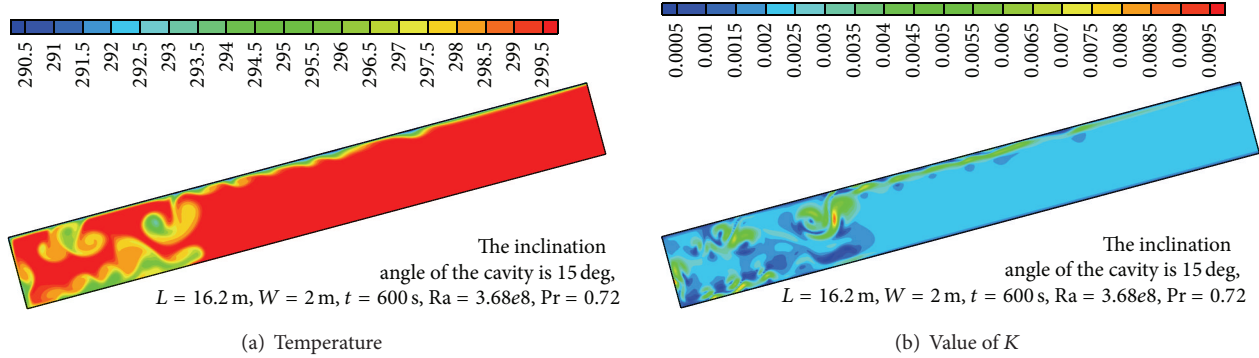


FIGURE 13: Calculated results with 15 degrees of angle: (a) temperature contours and (b)  $K$  contours.

- (2) The fluid within the whole domain tends to flow in a turbulent state with the increase of flow time if  $Ra$  is larger than its critical value.
- (3) With the increase of plate length, the onset time of instability decreases and the locations of instabilities migrate right along the top wall.
- (4) The intensity of instabilities in the left region of the studied inclined cavity is much stronger than that in the right region. When the inclined angle increases in a certain range, the locations of instabilities along the top wall migrate left.
- (5) Once the inclined angle exceeds a certain range, the positions of instabilities would move right since the accumulation of the heat flux in the lower left corner of the cavity is restrained.

## Nomenclature

$Ra$ : Rayleigh number  
 $Pr$ : Prandtl number  
 $t$ : Time  
 $t_s$ : Steady-state time scale  
 $t_B$ : Critical time scale  
 $T$ : Temperature  
 $T_c$ : Temperature of the top wall  
 $T_0$ : Temperature of the fluid  
 $L$ : Length of the cavity  
 $W$ : Width of the cavity  
 $x, y$ : Coordinates cavity  
 $p$ : Pressure  
 $p_0$ : Total pressure  
 $u, v$ : Velocity components in  $x, y$  directions, respectively  
 $g$ : Gravity acceleration  
 $k$ : Thermal diffusivity  
 $Ra_c$ : Critical Rayleigh number  
 $n$ : Transverse direction  
 $s$ : Streamwise direction  
 $K$ : Dimensionless function expresses the ratio of transversal energy gradient and streamwise energy gradient

$\bar{A}$ : Amplitude of the disturbance distance  
 $\omega_d$ : Frequency of the disturbance  
 $v'_m$ : Amplitude of the disturbance of velocity.

## Greek Symbols

$\theta$ : Inclination angle  
 $\beta$ : Coefficient of thermal expansion  
 $\rho$ : Fluid density  
 $\nu$ : Kinematic viscosity  
 $\Delta E$ : Energy difference along transverse direction  
 $\Delta H$ : Energy difference along streamwise direction  
 $\Delta T$ : Temperature difference.

## Acknowledgment

This work is supported by the Science Foundation of Zhejiang Sci-Tech University (ZSTU) under Grant no. 11130032241201.

## References

- [1] J. C. Patterson and J. Imberger, "Unsteady natural convection in a rectangular cavity," *Journal of Fluid Mechanics*, vol. 100, no. 1, pp. 65–86, 1980.
- [2] E. M. Sparrow and R. B. Husar, "Longitudinal vortices in natural convection flow on inclined plates," *Journal of Fluid Mechanics*, vol. 37, no. 2, pp. 251–255, 1969.
- [3] S. E. Haaland and E. M. Sparrow, "Vortex instability of natural convection flow on inclined surfaces," *International Journal of Heat and Mass Transfer*, vol. 16, no. 12, pp. 2355–2367, 1973.
- [4] J. R. Lloyd and E. M. Sparrow, "On the instability of natural convection flow on inclined plates," *Journal of Fluid Mechanics*, vol. 42, no. 3, pp. 465–470, 1970.
- [5] P. Ganesan and G. Palani, "Natural convection effects on impulsively started inclined plate with heat and mass transfer," *Heat and Mass Transfer*, vol. 39, no. 4, pp. 277–283, 2003.
- [6] A. Moutsoglou and T. S. Chen, "Buoyancy effects in boundary layers on inclined, continuous, moving sheets," *ASME Journal of Heat Transfer*, vol. 102, no. 2, pp. 371–373, 1980.
- [7] F. Xu, J. C. Patterson, and C. Lei, "Transient natural convection flows around a thin fin on the sidewall of a differentially heated cavity," *Journal of Fluid Mechanics*, vol. 639, pp. 261–290, 2009.
- [8] S. C. Saha, J. C. Patterson, and C. Lei, "Scaling of natural convection of an inclined flat plate: Sudden cooling condition,"

- ASME *Journal of Heat Transfer*, vol. 133, no. 4, Article ID 041503, pp. 1–9, 2011.
- [9] S. A. M. Said, M. A. Habib, H. M. Badr, and S. Anwar, "Turbulent natural convection between inclined isothermal plates," *Computers and Fluids*, vol. 34, no. 9, pp. 1025–1039, 2005.
  - [10] M. H. Lin, "Numerical study of formation of longitudinal vortices in natural convection flow over horizontal and inclined surfaces," *International Journal of Heat and Mass Transfer*, vol. 44, no. 9, pp. 1759–1766, 2001.
  - [11] P. A. Iyer and R. E. Kelly, "The stability of the laminar free convection flow induced by a heated inclined plate," *International Journal of Heat and Mass Transfer*, vol. 17, no. 4, pp. 517–525, 1974.
  - [12] H.-S. Dou, "Viscous instability of inflectional velocity profile," in *Proceedings of the 4th International Conference on Fluid Mechanics*, F. Zhuang and J. Li, Eds., pp. 76–79, Tsinghua University Press, 2004.
  - [13] H.-S. Dou, "Mechanism of flow instability and transition to turbulence," *International Journal of Non-Linear Mechanics*, vol. 41, no. 4, pp. 512–517, 2006.
  - [14] H.-S. Dou, "Physics of flow instability and turbulent transition in shear flows," *International Journal of Physical Sciences*, vol. 6, no. 6, pp. 1411–1425, 2011.
  - [15] H.-S. Dou, B. C. Khoo, and K. S. Yeo, "Instability of Taylor-Couette flow between concentric rotating cylinders," *International Journal of Thermal Sciences*, vol. 47, no. 11, pp. 1422–1435, 2008.
  - [16] H.-S. Dou and B. C. Khoo, "Mechanism of wall turbulence in boundary layer flow," *Modern Physics Letters B*, vol. 23, no. 3, pp. 457–460, 2009.
  - [17] H.-S. Dou and B. C. Khoo, "Criteria of turbulent transition in parallel flows," *Modern Physics Letters B*, vol. 24, no. 13, pp. 1437–1440, 2010.
  - [18] H.-S. Dou and B. C. Khoo, "Investigation of turbulent transition in plane Couette flows using energy gradient method," *Advances in Applied Mathematics and Mechanics*, vol. 3, no. 2, pp. 165–180, 2011.
  - [19] S. C. Saha, *Natural convection adjacent to an inclined flat plate and in an attic space under various thermal forcing conditions [Ph.D. thesis]*, James Cook University, Queensland, Australia, 2008.
  - [20] U. H. Kurzweg, "Stability of Natural Convection Within an Inclined Channel," *ASME Journal of Heat Transfer C*, vol. 92, pp. 190–191, 1970.
  - [21] Y. M. Chen and A. J. Pearlstein, "Stability of free-convection flows of variable-viscosity fluids in vertical and inclined slots," *Journal of Fluid Mechanics*, vol. 198, pp. 513–541, 1989.
  - [22] C. Lei and J. C. Patterson, "Unsteady natural convection in a triangular enclosure induced by absorption of radiation," *Journal of Fluid Mechanics*, vol. 460, pp. 181–209, 2002.
  - [23] S. Chandrasekhar, *Hydrodynamic and Hydromagnetic Stability*, Dover, New York, NY, USA, 1961.
  - [24] P. G. Drazin and W. H. Reid, *Hydrodynamic Stability*, Cambridge University Press, Cambridge, UK, 1981.
  - [25] H.-S. Dou and N. Phan-Thien, "Instability of fluid material systems," in *Proceedings of the 15th Australasian Fluid Mechanics Conference*, pp. 13–17, The University of Sydney, Sydney, Australia, December 2004.
  - [26] F. Xu, J. C. Patterson, and C. Lei, "Transient natural convection flows around a thin fin on the sidewall of a differentially heated cavity," *Journal of Fluid Mechanics*, vol. 639, pp. 261–290, 2009.
  - [27] M. Corcione, "Effects of the thermal boundary conditions at the sidewalls upon natural convection in rectangular enclosures heated from below and cooled from above," *International Journal of Thermal Sciences*, vol. 42, no. 2, pp. 199–208, 2003.
  - [28] V. Kurian, M. N. Varma, and A. Kannan, "Numerical studies on laminar natural convection inside inclined cylinders of unity aspect ratio," *International Journal of Heat and Mass Transfer*, vol. 52, no. 3–4, pp. 822–838, 2009.
  - [29] T. D. Upton and D. W. Watt, "Experimental study of transient natural convection in an inclined rectangular enclosure," *International Journal of Heat and Mass Transfer*, vol. 40, no. 11, pp. 2679–2690, 1997.



## Research Article

# A Numerical Study on the Supersonic Steam Ejector Use in Steam Turbine System

**Lin Cai and Miao He**

*China Ship Development and Design Center, Wuhan, Hubei 433064, China*

Correspondence should be addressed to Lin Cai; [cailin03313@163.com](mailto:cailin03313@163.com)

Received 11 October 2012; Revised 22 November 2012; Accepted 6 December 2012

Academic Editor: Zhijun Zhang

Copyright © 2013 L. Cai and M. He. This is an open access article distributed under the Creative Commons Attribution License, which permits unrestricted use, distribution, and reproduction in any medium, provided the original work is properly cited.

Supersonic steam ejector is widely used in steam energy systems such as refrigeration, wood drying equipment, papermaking machine, and steam turbine. In this paper the Computational Fluids Dynamics (CFD) method was employed to simulate a supersonic steam ejector, SST k- $\omega$  turbulence model was adopted, and both real gas model and ideal gas model for fluid property were considered and compared. The mixing chamber angle, throat length, and nozzle exit position (NXP) primary pressure and temperature effects on entrainment ratio were investigated. The results show that performance of the ejector is underestimated using ideal gas model, and the entrainment ratio is 20%–40% lower than that when using real gas model. There is an optimum mixing chamber angle and NXP makes the entrainment ratio achieve its maximum; as throat length is decreased within a range, the entrainment ratio remains unchanged. Primary fluid pressure has a critical value, and the entrainment ratio reaches its peak at working critical pressure; when working steam superheat degree increases, the entrainment ratio is increased.

## 1. Introduction

The supersonic steam ejector (SSE) is widely used in many industry fields which are steam powered such as oil, thermoelectric, and refrigeration [1–3]. A steam jet refrigeration can be considered as one of the most suitable refrigeration systems for the present energy and environment situations, because of simple mode of function, lack of moving parts, and capability of driving a refrigeration device primarily through the use of waste heat or solar energy making them particularly attractive in this energy-conscious era. In addition, using waste heat or solar energy to power a refrigeration system will reduce the electrical energy consumption used to power vapour-compression refrigeration systems, potentially reducing the emissions of greenhouse gases that are associated with the production of electricity from fossil fuel burning power plants. In view of the numerous publications available on this subject, it is perhaps one of the most important application areas for ejectors. A good overview of the different applications in this field may be found in the review article by Sun and Eames (1995) [4]. So a lot of studies of SSE performance with various types of working fluid in refrigeration

field could be found; for example, Eames et al. [5] provided the results of 1D model theoretical and experimental study of a steam jet refrigerator. Huang [6] carried out a 1D model on ejector performance at critical-mode operation; Ouzzane and Aidoun (2003) [7] proposed a 1D model allowing to track flow conditions along the ejector. In their study, fluid properties were evaluated by using NIST (1980) subroutines for equations of state of refrigerants. CFD tools have been proved to be valuable tools for understanding and solving complex fluid flow problems, such as the entrainment and mixing processes in ejectors. Bartosiewicz et al. [8] compared the pressure distribution by using different turbulence models for the simulation of an ejector with experimental data. It was concluded that, for certain conditions, simulated results were in excellent agreement with measured data. However, the choice of air as a working fluid and other test conditions was not very fortunate, especially when a cooling cycle is concerned. Later they extended their work using R142b as the working fluid. Rusly et al. [9] presented CFD results compared to published experimental data and 1D model predictions, using R141b. The effect of ejector geometry on the flow field was investigated. It was pointed out that according

TABLE 1: Summary of ejector research using CFD software compared with experimental results.

Auto	Working fluids	State equation	Numerical method	Inlet pressure (range)	Error range
Eames et al. [5]	Water steam	Ideal gas model	1D model	0.3615 MPa	22.6~32.25%
Huang et al. [6]	R141b	Ideal gas model	1D model	0.4–0.6 MPa	0.56~22.9%
Rusly et al. [9]	R141b	Ideal gas model	FLUENT	0.4–0.6 MPa	–5.82~5.11%
Pietrowicz and Kasperski [10]	Water steam	IAPWS-IF97	CFX	0.474 KPa	1.3~8.2%
Sriveerakul et al. [11]	Water steam	Ideal gas model	FLUENT	0.27 Mpa	–1.89~12.9%
Pianthong et al. [12]	Water steam	Ideal gas model	FLUENT	0.3615 MPa	1% ~13.4%
Scott et al. [13]	R245fa	NIST	PHOENICS	0.4–0.6 MPa	–4.9~10.6%

to CFD model results, 1D model assumptions were not met under test conditions. In this work, evaporator temperatures were very high for a simple ejector cooling cycle. T. Pietrowicz and Kasperski [10] used a commercial CFD package to predict performance of a steam ejector, and the maximum errors of many different working conditions such as effect of primary nozzle, throat diameter, and throat length are 12.9%. A pithy review is listed in Table 1.

In this paper, the SSE used in steam turbine system has been calculated using CFD package CFX 11.0; applying the SSE to steam turbine system could hold the vacuum; it could also pump the noncondensable gas and enhance the efficiency of Rankine cycle indirectly [3]. According to the review of ejector studies above, it could be found that the ejector working pressure is less than 1 MPa; water vapour, used as the working fluid of the model, was treated as the assumption of an ideal gas, for the ejector application where the operating pressure is relatively low; it was proved by some researchers [10] that it provided similar results to a real gas model, but the SSE investigated in this paper is working at 1.6 MPa or even higher, so the ideal gas model does not apply at all to water vapour; on the other hand, it can be found from Table 1 that, in the literature review, the CFD and experiment works of SSE primary pressure are almost lower than 1 MPa, so the SSE working at a higher primary pressure should be investigated in order to learn the performance of the SSE used in steam turbine system and provide some theoretical foundations for designing the SSE with high primary pressure. The previous part of this paper, both Laval nozzle and ejector results of different equations of state have been compared; then the geometry and operation condition effects on SSE entrainment ratio ( $EM = \text{mass flow rate of secondary inlet} / \text{mass flow rate of primary inlet}$ ) are discussed. This paper could provide the theory basis for the high primary SSE design.

## 2. Ejector Geometry

The ejector simulated in this paper is shown in Figure 1 and the original geometry detail is shown in Table 2. The mixing chamber angle  $\alpha$ , throat length  $L$ , and nozzle exit position (NXP) effects on ejector entrainment ratio have been considered,  $\alpha$  is changed from  $4.5^\circ$  to  $13.25^\circ$ , which means that the mixing chamber length is changed from 75 mm to

225 mm, and the throat length is changed from 2D to 6D. When considering one parameter effect, the other remains unchanged at original or optimal value.

## 3. CFD Model

The calculation area is meshed with structural mesh hexahedral-type elements using ICEM 11.0 (Figure 2); 1/4 model is considered for saving calculation time; if the apex angle between two symmetry faces is small, the mesh quality becomes very poor, so a 1/4 geometry model with apex angle  $90^\circ$  was used. CFD software CFX 11.0 is used to solve the governing equations. The pressure inlet type is taken into primary and secondary inlet, for primary inlets; the total pressure 1.6 MPa and total temperature 556.85 K are given; for secondary inlet, the total pressure 0.01 MPa and total temperature 315 K are given. The pressure outlet boundary with a known mean value of absolute pressure at 33170 Pa is adopted for ejector outlet. No-slip and adiabatic wall type have been used on the ejector wall. Automatic near-wall treatment has been applied. The SST k- $\omega$  model is utilized for simulating turbulence flow.

The grid-dependent learning is done using  $d = 40$  mm geometry as shown in Table 1, and four options are considered as shown in Table 3; it can be seen that the entrainment ratio is changed within 3.88%; the scheme 3 is used in this paper.

The fluid property is important for simulation steam flow problem, especially when the steam is far away from critical region, so the IAPWS IF97 model is used as equation of state. The IAPWS-IF97 database represents an accurate equation of state for water and steam properties. The IAPWS-IF97 [15] database uses formulations for five distinct thermodynamic regions (Figure 3) for water and steam, namely, (1) subcooled water, (2) supercritical water/steam, (3) superheated steam, (4) saturation data, and (5) high temperature steam. When developing the IAPWS database for ANSYS CFX, therefore, properties must be evaluated as functions of pressure and temperature. For the most part, this involves a straightforward implementation of the equations described in the IAPWS theory. Region 4 involves saturation data that uses only pressure or temperature information. However, when evaluating the properties around Region 3 (near the critical point), where the EOS is defined explicitly in terms of density and temperature. In this region, the density must be

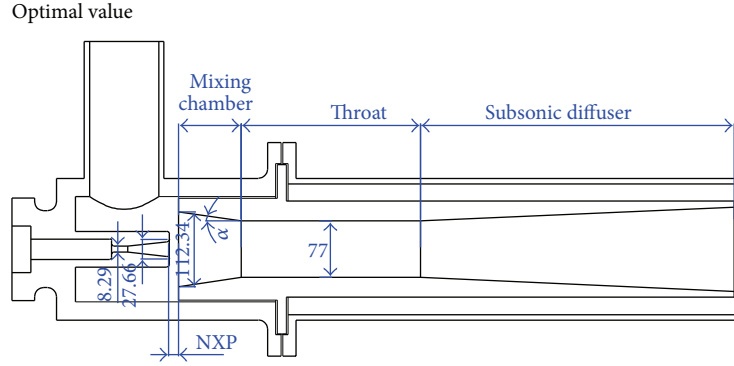


FIGURE 1: Schematic diagram of steam ejector (not in scale).

TABLE 2: The original geometry details of the ejector.

Mixing chamber angle	$\alpha$ (°)	9.55
Throat length	$L$ (mm)	485
Diffuser length	$L_d$ (mm)	305
Diameter of throat	$D_t$ (mm)	77
Diameter of diffuser outlet	$D_d$ (mm)	141.5
Distance between primary nozzle and mixing chamber	$d$ (mm)	10

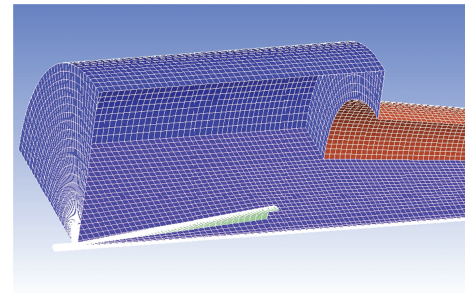


FIGURE 2: Mesh of flow region.

TABLE 3: Grid-dependent results.

Scheme	Total elements	$L$	$L_d$	$E_m$
1	124136	63	51	0.670
2	332668	90	72	0.691
3	519486	104	84	0.693
4	608685	155	94	0.697

evaluated using Newton-Raphson iteration. This algorithm is further complicated in that the EOS is applicable on both the subcooled liquid and superheated vapor side leading up to critical conditions. Therefore, depending on the pressure-temperature state, one may be evaluating a subcooled liquid or a superheated vapor with the same EOS. To apply the Newton-Raphson scheme in a reliable way, one must detect on which side of the saturation dome the pressure-temperature state applies, and apply an appropriate initial guess. Such an iteration scheme, including logic for an initial guess, has been implemented in ANSYS CFX so that table generation around the critical region is possible.

## 4. Numerical Results

**4.1. Numerical Validation.** In order to verify the reliability of the theoretical model, a converging-diverging nozzle flow field has been calculated. The geometry and inlet conditions of the nozzle were taken to be the same as the Nozzle B used in the experiment of Moore and Walters (1973) [14], which was

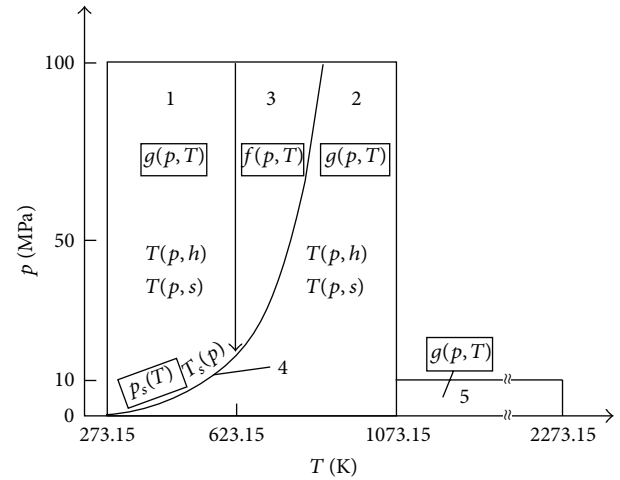


FIGURE 3: Regions of IAPWS-IF97.

very classic and had been quoted by other scholars [16, 17]; also a quarter of the geometry with symmetry boundary conditions was used. At the nozzle inflow, subsonic flow was specified using total pressure (25 KPa), total temperature (354.6 K), and the outflow is supersonic. With comparison to the IAWPS-IF97 model and the experiment value as Figure 4 shows, it can be seen that IF97 model has a good agreement with the experimental values and is better than ideal gas model.

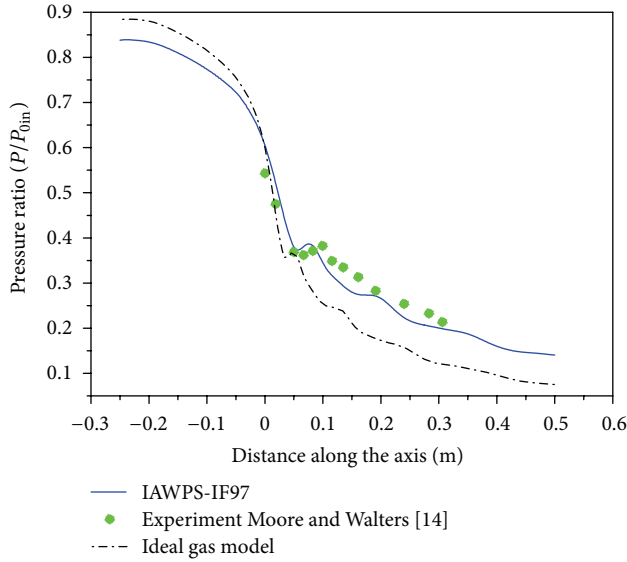


FIGURE 4: Pressure distribution of different EOS compared with the Experiments of Moore and Walters [14].

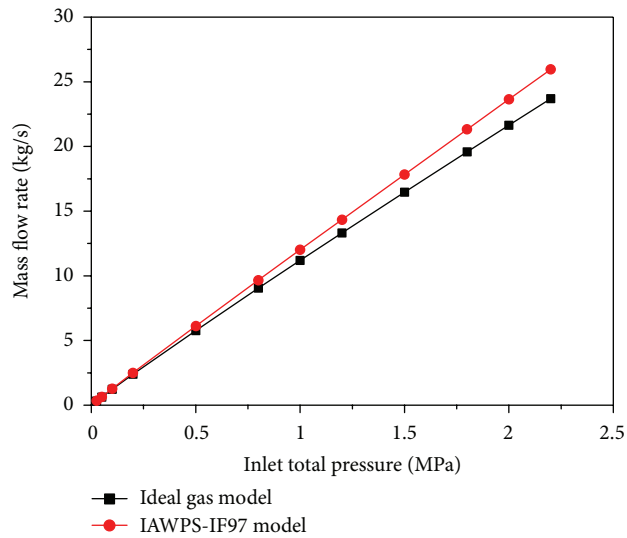


FIGURE 5: Mass flow rate of nozzle B at different inlet pressure.

**4.2. Comparison Results of Different Equations of State.** The mass flow rate results of nozzle B at different inlet pressures have been obtained, in order to see how much difference there is between ideal gas model and real gas model. From Figures 5 and 6 it can be seen clearly that when the inlet pressure is lower, for example 0.025 MPa, the mass flow rate of real gas model is about 4% higher than that of ideal gas model, but as the inlet pressure is increased, the difference becomes higher; for example, when inlet pressure is 1.6 MPa, the difference is increased to 8.9%, which cannot be ignored.

Figures 7–12 show comparison results of SSE using different EOS. Entrainment ratio is highly underestimated while using ideal gas model, as shown in Figure 7; the entrainment ratio is 40% lower than real gas model at

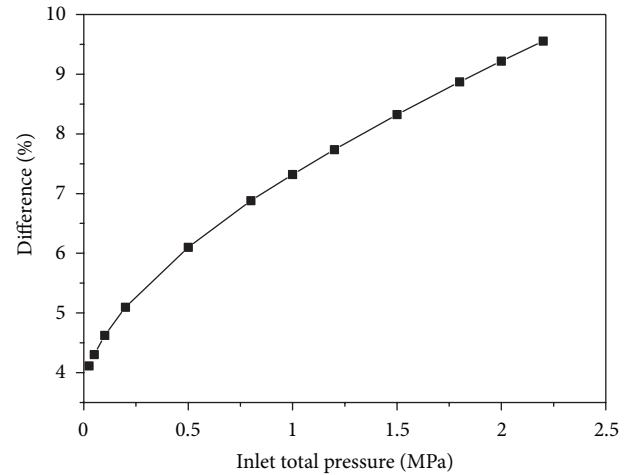


FIGURE 6: Percent difference of mass flow rate using different EOS.

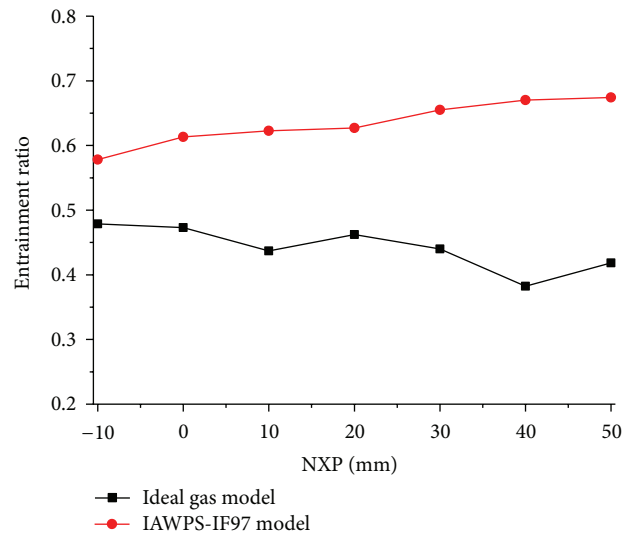


FIGURE 7: Entrainment ratio of the steam ejector at different NXP.

$d = 40$  mm; this means that when calculating steam ejector flow field, the performance of ejector (entrainment ratio) will be underestimated if using ideal gas model. As Figure 8 shows, the static pressure in mixing chamber is different; when using ideal gas model, static pressure is higher than real gas model.

The working mechanism of the steam ejector could be understood at two aspects: one is viscous drag effect between working and secondary fluid; the other is that with the supersonic expansion of primary fluid, the static pressure in mixing chamber decreases lower than secondary fluid pressure, so the secondary steam will flow into the mixing chamber and will mix with primary fluid (working steam), complete exchange of momentum and energy, so if mixing chamber pressure is higher, the entrainment ratio will be lower; on the other hand, the mass flow rate of ideal gas model is lower than real gas model in a converging-diverging nozzle (Figures 5 and 6); this means that the working fluid

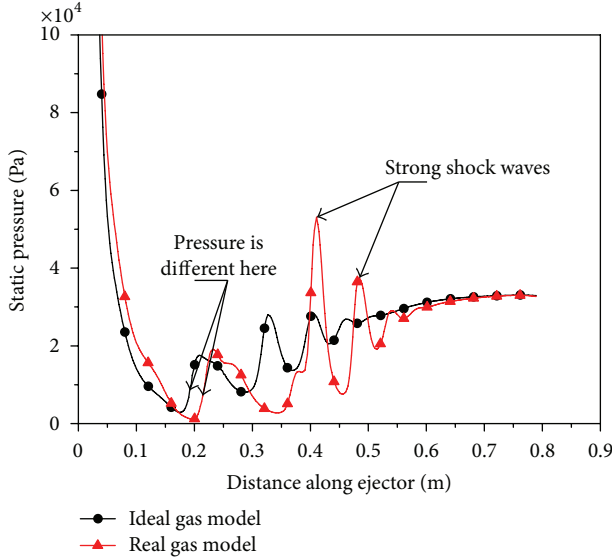


FIGURE 8: Static pressure distribution along the centerline using different EOS.

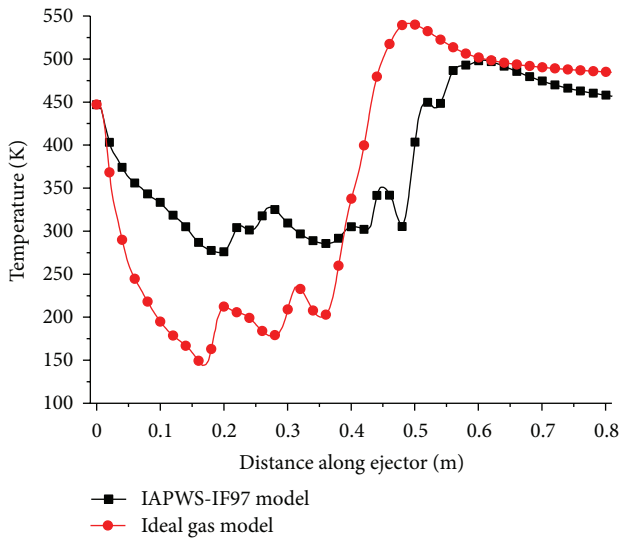


FIGURE 9: Static temperature distribution along the centerline using different EOS.

momentum of ideal gas model is lower, so its dragging ability is poor.

Figure 9 gives the temperature field distribution at middle line; the temperature drops sharply because of the supersonic expansion, and it rises in diffuser. When using ideal gas model the temperature is lower than real gas model; this is because the phase transition phenomenon occurs in the ejector when using the real gas model, the maximum mass fraction of saturated water is larger than 20% (Figure 10). There are two reasons for phase transition: one is that temperature drops caused by supersonic expansion and shock waves; the other is the secondary fluid's temperature is lower than the primary fluid, latent heat is released when the phase transition phenomenon occur, and the temperature will go

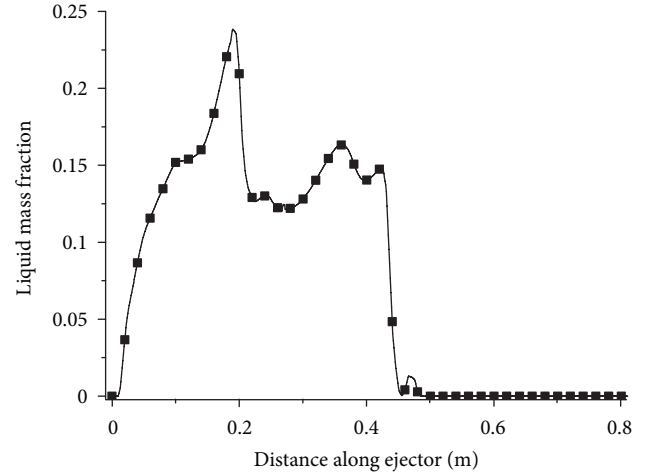


FIGURE 10: Liquid mass fraction distribution along the centerline using IF97.

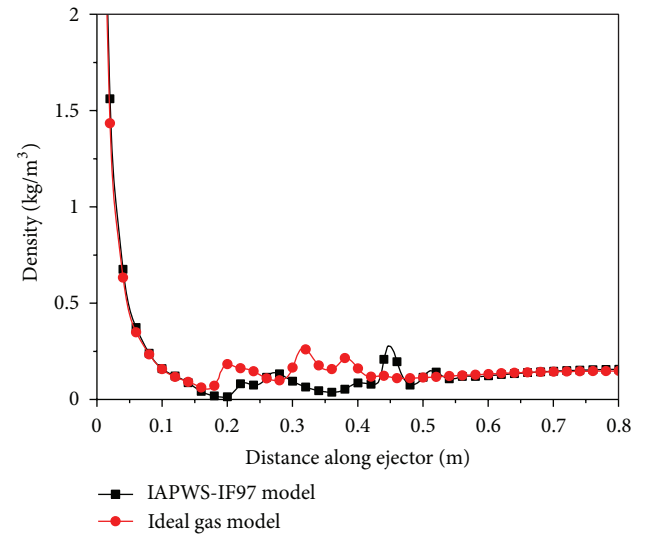


FIGURE 11: Density distribution along the centerline using different EOS.

up. The so-called condensation shock makes the shock waves of real gas model stronger than ideal gas. As the temperature field is underestimated using ideal gas, the mach number and fluid density is also different from IF97 model as Figures 11 and 12 show.

**4.3. Geometry Effects on Ejector Entrainment Ratio.** As Figure 13 shows, there is an optimum value of  $\alpha$  which makes the entrainment ratio be maximum; Figure 14 gives the mach number distribution along the axis; if  $\alpha$  is smaller than the optimum value, the mixing chamber cannot mix the fluid very well, the choking flow is formed, and a strong shock wave appears in mixing chamber. When  $\alpha$  is bigger than optimum value, shock wave attenuation is stronger, and the moment loss in mixing chamber becomes bigger.



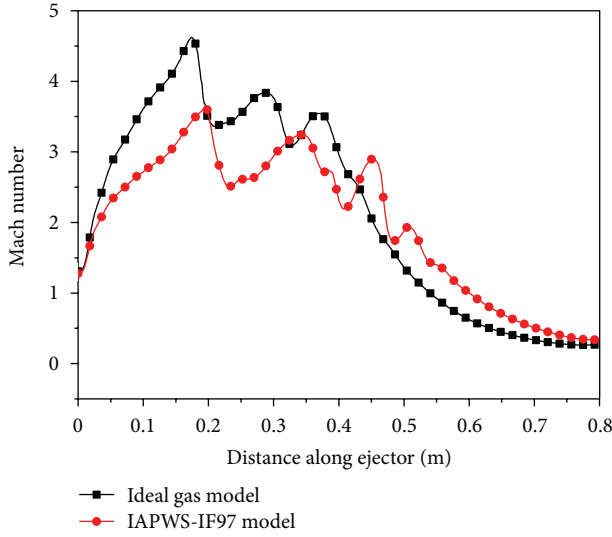


FIGURE 12: Mach number distribution along the centerline using different EOS.

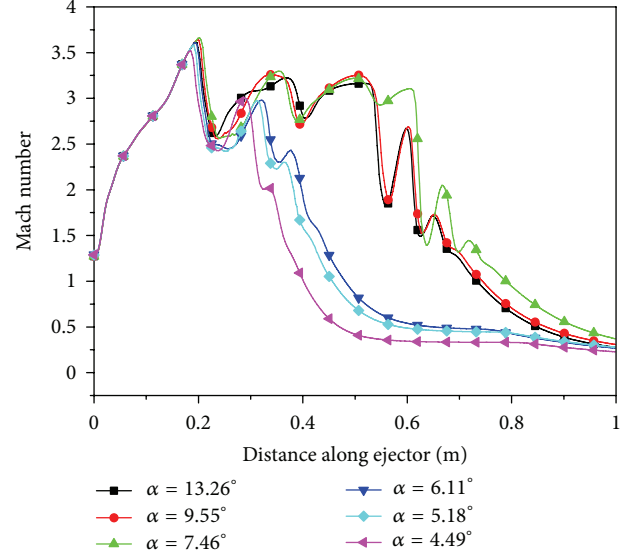


FIGURE 14: Mach distribution along the centerline at different  $\alpha$ .

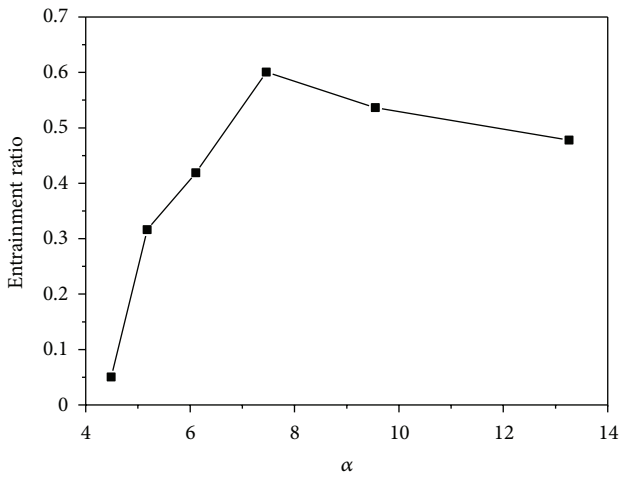


FIGURE 13: Entrainment ratio of the steam ejector at different  $\alpha$ .

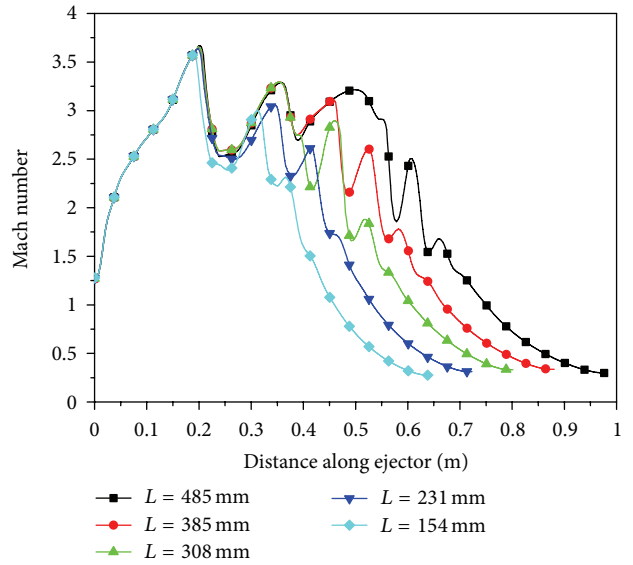


FIGURE 15: Mach distribution along the centerline at different  $L$ .

The throat length effects on ejector could be understood as shock waves move toward to mixing chamber when  $L$  is decreases. As shown in Figure 15 there are three obvious shock waves when  $L = 485$  mm. The third shock wave has a slight attenuation when  $L = 385$  mm; this is because as  $L$  decreases, the high-pressure position in throat exit will move towards mixing chamber; the position of shock wave moves towards mixing chamber; if the choking flow happens in mixing chamber, the entrainment ratio will decrease sharply. For example, the third shock wave in throat disappears when  $L = 308$  mm, and the second shock wave has an apparent attenuation when  $L = 231$ ; there is only one shock wave when  $L = 154$  mm. The performance of the ejector is almost unchanged as  $L = 485$  mm, 385 mm, and 308 mm, but as  $L$  decreases to 231 mm, 154 mm, the entrainment ratio decreases as shown in Figure 16; the shock waves will move

towards mixing chamber, leading to static pressure in mixing chamber increased, and make the entrainment decrease.

The primary fluid will be compressed when it is mixed with the second fluid. The distance between primary nozzle and mixing chamber ( $d$ ) will influence the performance of ejector, but the effects of  $d$  on the different ejectors are different. As Figure 4 shows, the optimum value of this ejector is 40 mm, when  $d$  is smaller than 40 mm; the max pressure in mixing chamber and throat becomes higher, which makes the flow developly inadequate; when  $d$  is larger than 40 mm, the speed of fluid reaching mixing chamber droops, and the entrainment ratio decreases a little. It can be seen from Figures 17 and 18 that  $d$  does not affect the shock waves distribution in throat and diffuser very much.

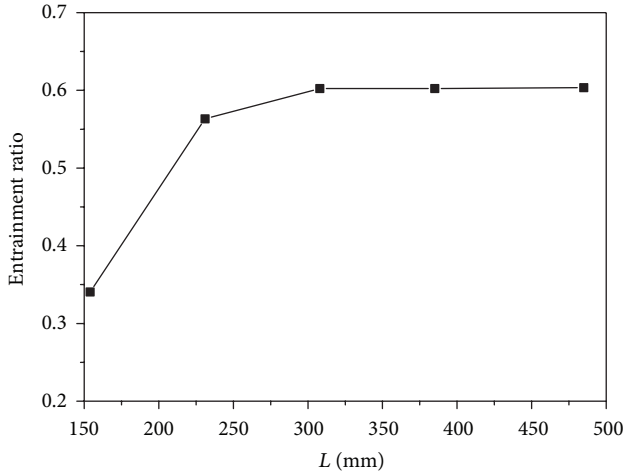
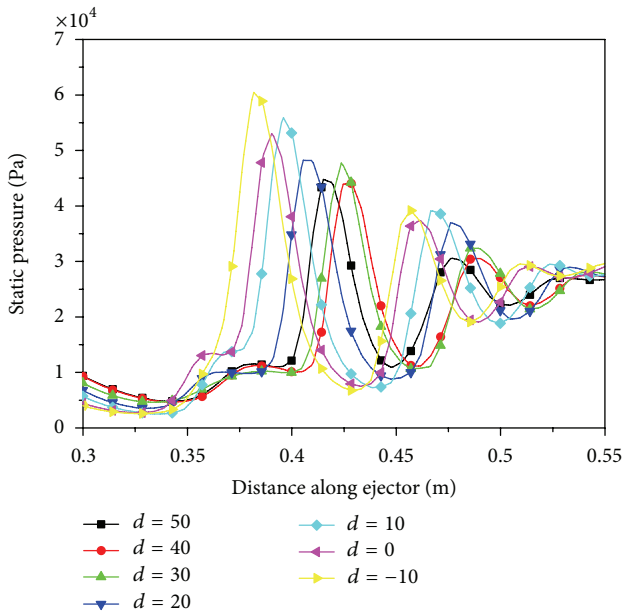
FIGURE 16: Entrainment ratio of the steam ejector at different  $L$ .

FIGURE 17: Static pressure distribution along the centerline at different NXP.

**4.4. Working Fluid Condition Effects on Ejector Entrainment Ratio.** In practice, we always want to eject the secondary fluid using lower primary pressure, which makes better energy saving effect and the entrainment be ratio maximum. It can be found in Figure 19 that when the primary pressure is equal to 1.56 MPa, the entrainment ratio reaches its maximum value. When  $P_p$  is higher than 1.56 MPa, the choking flow is formed in the mixing chamber area; the block wave will move towards to diffuser when the primary pressure rises as Figure 20 shows. It can be found that when the primary pressure is higher than its critical value, the entrainment is almost unchanged, and the ejector will waste primary steam energy.

The primary fluid often works at saturation state, but this ejector working fluid is superheated; when working

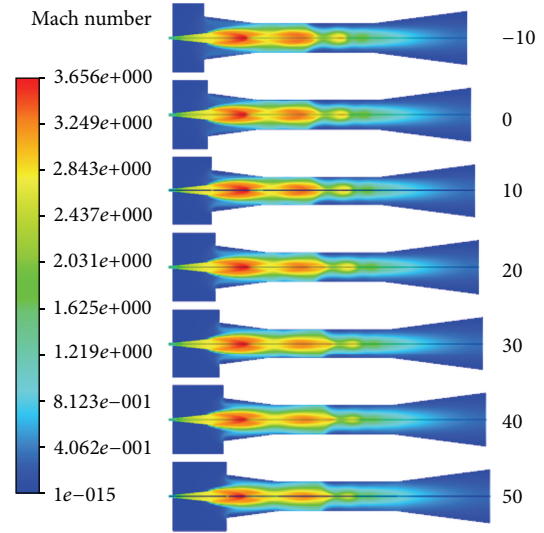
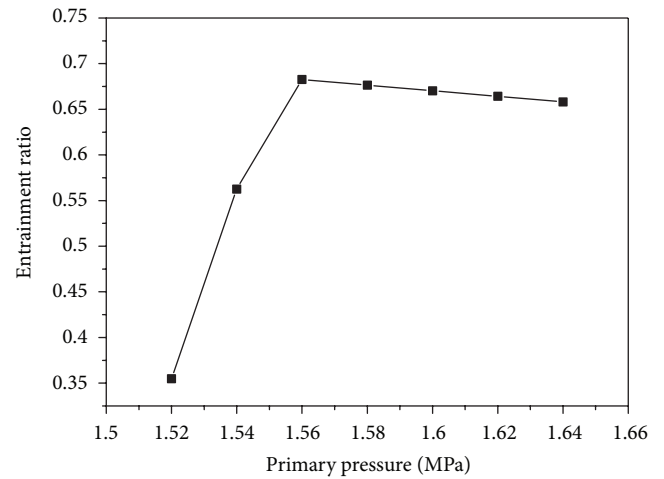


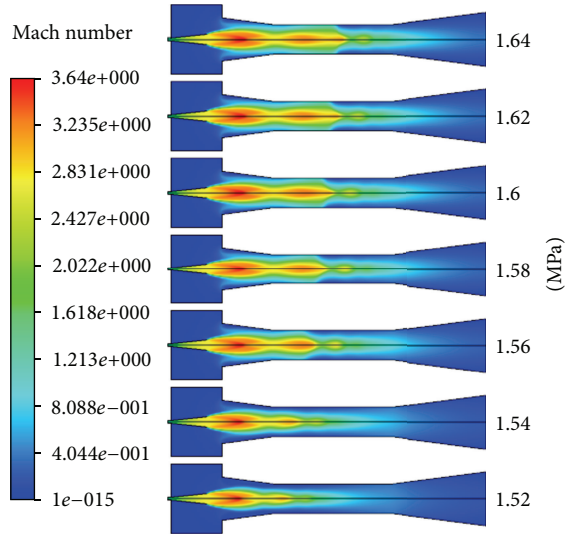
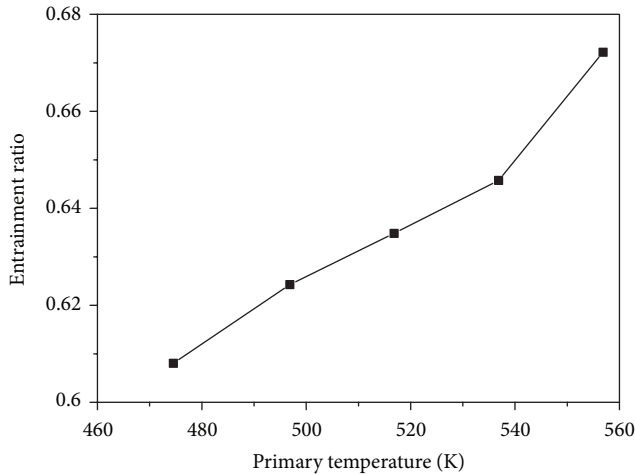
FIGURE 18: Filled contours of mach number at different NXP.

FIGURE 19: Entrainment ratio of the steam ejector at different  $P_p$ .

steam superheat degree increases, the entrainment ratio is increased; a higher temperature means higher energy and will enhance the ejector performance as Figure 21 shows. The static temperature distribution in mixing chamber and throat is almost the same, but in diffuser it is obvious that a higher primary temperature makes a higher static temperature (Figure 22).

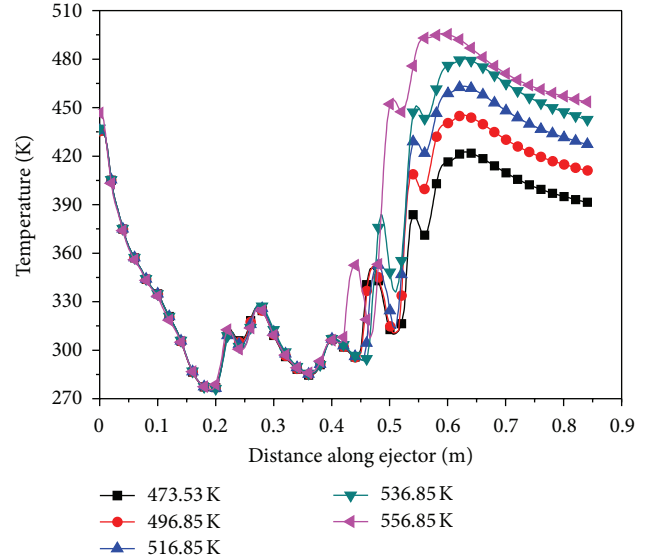
## 5. Conclusion

This paper calculates the flow field of supersonic steam ejector using steam turbine system. The real gas model has been used and compared with ideal gas model first, the water liquid mass fraction in steam ejector has been simulated successfully using IAPWS IF97 real gas model, and the maximum mass fraction of saturated water is higher than 20%. Mixing chamber angel, throat length, and nozzle exist

FIGURE 20: Filled contours of mach number at different  $P_p$ .FIGURE 21: Entrainment ratio of the steam ejector at different  $P_p$ .

position effects on ejector performance have been discussed. The other conclusions are summarized as follows.

- (1) The verification calculation result of converging-diverging nozzle shows that if the inlet pressure is higher, the ideal gas model is no longer fit for steam flow problems.
- (2) The mass flow rate and static pressure are the main causes of difference between two equations of state; for the ejector in this paper, the performance of the ejector will be underestimated and the temperature field is distorted using ideal gas model; the entrainment ratio of ideal gas is maximum 40% lower than IF97 model.
- (3) There are an optimum mixing chamber angle and NXP makes the entrainment ratio achieves its maximum. As throat length decreased within a range (3D length in this paper), the entrainment ratio remains

FIGURE 22: Filled contours of mach number at different  $P_p$ .

unchanged. The influence mechanism to entrainment ratio could be understood as choking flow exists in mixing chamber, and if choking flow happens in mixing chamber, the performance of ejector will be reduced.

- (4) The primary pressure has a critical value at a certain primary temperature; when it is higher than critical value, the entrainment ratio decreases a little. The entrainment ratio increases as the superheat degree of primary steam increases.

## References

- [1] S. Akterian, "Improving the energy efficiency of traditional multi-stage steam-jet-ejector vacuum systems for deodorizing edible oils," *Procedia Food Science*, vol. 1, pp. 1785–11791, 2011.
- [2] M. L. Ferrari, D. Bernardi, and A. F. Massardo, "Design and testing of ejectors for high temperature fuel cell hybrid systems," *Journal of Fuel Cell Science and Technology*, vol. 3, no. 3, pp. 284–291, 2006.
- [3] K. Zhang and F. Xue, "Experiment study and guidelines of high-pressure gas ejector," *Journal of Thermal Science and Technology*, vol. 3, pp. 133–138, 2004.
- [4] D. W. Sun and I. W. Eames, "Recent developments in the design theories and applications of ejectors—a review," *Journal of the Institute of Energy*, vol. 68, no. 475, pp. 65–79, 1995.
- [5] I. W. Eames, S. Aphornratana, and H. Haider, "A theoretical and experimental study of a small-scale steam jet refrigerator," *International Journal of Refrigeration*, vol. 18, no. 6, pp. 378–386, 1995.
- [6] B. J. Huang, J. M. Chang, C. P. Wang, and V. A. Petrenko, "A 1-D analysis of ejector performance," *International Journal of Refrigeration*, vol. 22, no. 5, pp. 354–364, 1999.
- [7] M. Ouzzane and Z. Aidoun, "Model development and numerical procedure for detailed ejector analysis and design," *Applied Thermal Engineering*, vol. 23, no. 18, pp. 2337–2351, 2003.

- [8] Y. Bartosiewicz, Z. Aidoun, P. Desevaux, and Y. Mercadier, "Numerical and experimental investigations on supersonic ejectors," *International Journal of Heat and Fluid Flow*, vol. 26, no. 1, pp. 56–70, 2005.
- [9] E. Rusly, L. Aye, W. W. S. Charters, and A. Ooi, "CFD analysis of ejector in a combined ejector cooling system," *International Journal of Refrigeration*, vol. 28, no. 7, pp. 1092–1101, 2005.
- [10] S. Pietrowicz and J. Kasperski, "The Thermo-flow processes proceeding during the two-phase flow in supersonic ejector applied in low power solar air conditioning Systems," in *Proceedings of the International Congress of Refrigeration*, Beijing, China, 2007, ICR07-E1-1073.
- [11] T. Sriveerakul, S. Aphornratana, and K. Chunnanond, "Performance prediction of steam ejector using computational fluid dynamics: part 1. Validation of the CFD results," *International Journal of Thermal Sciences*, vol. 46, no. 8, pp. 812–822, 2007.
- [12] K. Pianthong, W. Seehanam, M. Behnia, T. Sriveerakul, and S. Aphornratana, "Investigation and improvement of ejector refrigeration system using computational fluid dynamics technique," *Energy Conversion and Management*, vol. 48, no. 9, pp. 2556–2564, 2007.
- [13] D. Scott, Z. Aidoun, O. Bellache, and M. Ouzzane, "CFD simulations of a supersonic ejector for use in refrigeration applications," in *Proceedings of the International Refrigeration and Air Conditioning Conference at Purdue*, July 2008, paper 927.
- [14] M. J. Moore and P. T. Walters, "Predicting the fog drop size in wet steam turbines," in *Proceedings of the Wet Steam 4 Conference*, Institute of Mechanical Engineers (UK), University of Warwick, 1973, paper C37/73.
- [15] W. Wagner, J. R. Cooper, A. Dittmann et al., "The IAPWS industrial formulation 1997 for the thermodynamic properties of water and steam," *Journal of Engineering for Gas Turbines and Power*, vol. 122, no. 1, pp. 150–180, 2000.
- [16] Y. Yang and S. Shen, "Numerical simulation on non-equilibrium spontaneous condensation in supersonic steam flow," *International Communications in Heat and Mass Transfer*, vol. 36, no. 9, pp. 902–907, 2009.
- [17] M. J. Kermani and A. G. Gerber, "A general formula for the evaluation of thermodynamic and aerodynamic losses in nucleating steam flow," *International Journal of Heat and Mass Transfer*, vol. 46, no. 17, pp. 3265–3278, 2003.

## Research Article

# Research on Performance of H<sub>2</sub> Rich Blowout Limit in Bluff-Body Burner

Hongtao Zheng,<sup>1</sup> Yajun Li,<sup>1</sup> and Lin Cai<sup>2</sup>

<sup>1</sup> College of Power and Energy Engineering, Harbin Engineering University, Harbin 150001, China

<sup>2</sup> Department of Power and Energy, China Ship Development and Design Center, Wuhan 430064, China

Correspondence should be addressed to Yajun Li, fage9000@163.com

Received 19 September 2012; Revised 24 October 2012; Accepted 24 October 2012

Academic Editor: Zhijun Zhang

Copyright © 2012 Hongtao Zheng et al. This is an open access article distributed under the Creative Commons Attribution License, which permits unrestricted use, distribution, and reproduction in any medium, provided the original work is properly cited.

In order to investigate H<sub>2</sub> rich blowout limit at different blockage ratios and flow velocities, a CFD software FLUENT was used to simulate H<sub>2</sub> burning flow field in bluff-body burner, and the software CHEMKIN was adopted to analyze the sensitivity of each elementary reaction. Composition Probability Density Function (C-PDF) model was adopted to simulate H<sub>2</sub> combustion field in turbulence flame. The numerical results show that reactions R2 and R9 possess the largest positive and negative temperature sensitivity. Temperature has a very important influence on these two reactions. When equivalence ratio is 1, the mixture is most ignitable, and the critical ignition temperature is 1550 K. There should be an optimal blockage ratio which can stabilize the flame best. When the blockage ratio remains unchanged, the relationship between H<sub>2</sub> RBL and flow velocity is a logarithmic function. When the flow velocity remains unchanged, the relationship between H<sub>2</sub> RBL and blockage ratio is a parabolic function. A complete extinction requires three phases: the temperature sudden decline in the main stream, the energy dissipation from the recirculation zone to the main stream, and the complete extinction of the flame.

## 1. Introduction

Bluff-body stabilized combustion with triangular or cone stabilizers is common in after-burners of military aircraft. A central recirculation zone (CRZ) will form in the wake of the bluff-body burner [1]. The heat will diffuse to the main stream from the flame frontier. The entrainment of hot gases will improve the combustion stabilization. If the fuel concentration is ultralean or ultrarich, the heat released from the flame frontier cannot compensate that of dissipation to the main stream, and then the temperature will decrease gradually, finally inducing extinction.

Lots of researches on flame stabilized mechanism in a bluff-body burner have been carried out both in terms of experiment and theoretical treatment. Experimental researches



on this problem are extremely important, but a large-scale systematic mechanism analysis via experiments is both expensive and time consuming. The Volvo Aero Corp. [2] carried out a lot of experiments on triangular bluff-body stabilized combustion rig. Shanbhogue et al. [1] found that the flame instability is dominated by the lower intensity and the convective instability of the shear layer. He put forward that blow off will occur in multiple steps: local extinction along the flame sheer, large-scale wake disruption, and a final blow off. Frolov et al. [3] formulated a flame stabilization criterion called Michelson Criterion, according to this criterion, a flame will be blown off from the flameholder when Michelson number is  $<1$ ; his result shows that there will be an optimal flame-holder size at which the best stabilization parameters were achieved. Wright [4] performed lots of experiments to define the influence of blockage on flame stabilization by bluff-bodies in ducted flow. His experiments indicated that the length of the recirculation zone varies inversely as the square root of the blockage and the flow speed past the wake increases almost linearly with blockage. He found that while the combustion was taking place, the flow speeds and flame geometry depended on the blockage ratio. However, at the flame blow off, the characteristic mechanical time is independent of that. The most important conclusion gained by Wright is that the maximum blow off speed occurs at a relatively low blockage ratio. Dawson et al. [5] found that blow off is approached by increasing the bulk velocity or decreasing the equivalence ratio. Griebel et al. [6] and Schefer [7] found that the maximum blowout velocity occurred at stoichiometric conditions. Barlow et al. [8] made use of an experimental method to study the importance of molecule diffusion and turbulence transport on flame structure. His study showed that there will be an evolution in those flames from a scalar structure dominated by molecular diffusion to one dominated by turbulent transport with  $Re$  increasing.

On the other hand, computational fluid dynamics (CFD) has been widely used to study the turbulent reacting flows, fluid machinery, and combustion systems to predict device performance and optimize their structures. Many experiment studies are used to validate the simulation accuracy and to explain the flame extinction mechanism. For example, Giacomazzi et al. [9] tested the applicability of a sub grid scale Fractal Model for LES (FM-LES) simulation of turbulent combustion by simulating a bluff-body premixed flame anchored in a straight channel. Eugenio found that 3D vortex structures periodically shortening the recirculation zone downstream of the bluff-body and entraining fresh mixture into the hot zone, this physical mechanism is involved in flame anchoring. Eriksson [2] investigated Zimont Turbulent Flame Closure Model (TFC) in conjunction with different turbulent models in simulating premixed bluff-body stabilized flame. And he found that the TFC model combined with  $k-\omega$  model accurately captures the recirculation zone length and overall turbulent flame speed, the combined effect is not captured well in steady state RANS. Lin and Holder [10] studied the effects of inlet turbulent intensity and angle of attack on the chemically reacting turbulent flow and thermal fields in a channel with an inclined bluff-body flame holder. Sjunnesson [2] reported the computation of the triangular bluff-body stabilized combustion using a two-step reaction solved with Arrhenius Expression in conjunction with the Magnussen-Hjerthager combustion model and  $k$ -epsilon turbulent model. Kim et al. [11] found that LES modeling approach can reproduce the variation of recirculation zone length while the equivalence ratio changed. This approach was successfully used to assess the lean blowout condition and evaluate its behavior and physics of combustion instability. Jones and Prasad [12] adopted C-PDF/LES model to exhibit the local extinction and re-ignition in turbulent combustions and to describe the interaction between turbulence and combustion. His numerical result was in good agreement with American Sandia Flame experiment data.

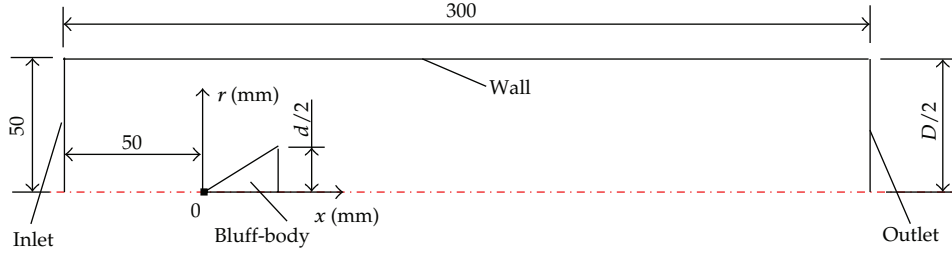


Figure 1: Geometry structure of bluff-body burner.

Even though there is a recirculation region in a bluff-body burner, the extinction will still occur if the stabilized ignition point was blown to the outside of CRZ. CRZ takes a very important effect on flammability. So the aim of the present work is to study the influence of flow velocity and blockage ratio on  $H_2$  Rich Blowout Limit (RBL) and finally summarize a formula for  $H_2$  RBL.

## 2. Geometry and Mathematical Model

Figure 1 shows the geometry of the burner with cone bluff-body and straight channel. To save the calculation expend, 2-dimension axis-symmetry model was used. Figure 2 shows the mesh adopted for the calculation domain, and the total grid number is  $6.0e + 04$ .

Boundary conditions: mixture inlet temperature is 293 K, inlet pressure is 1 atm and inlet velocities are shown in Table 1. The mixture is made up of  $H_2$  and air, and the concentration of  $H_2$  is shown in Table 5.

Outlet: pressure outlet.

Wall: adiabatic boundary.

The computations are repeated for different combinations of gas velocity and blockage ratio. The definition of Reynolds number based on the channel width has been given out as follows:

$$Re_D = \frac{\rho u D}{\mu}, \quad (2.1)$$

where  $\rho$  is mixture density,  $u$  is mixture velocity,  $D$  is Channel width,  $\mu$ -mixture viscosity.

The blockage ratio  $B$  is defined as

$$B = \frac{d}{D}. \quad (2.2)$$

In combustion flows, conservation equations for mass, momentum, energy, and species are solved. The standard  $k-\varepsilon$  and LES models were adopted, respectively, to simulate the turbulence flow in conjunction with C-PDF and Eddy-Dissipation-Concept (EDC) combustion mode.

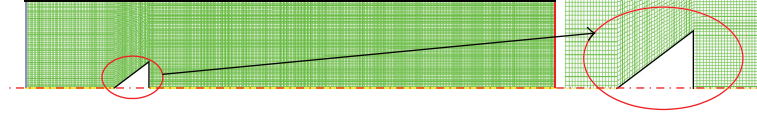


**Figure 2:** The calculation mesh.

**Table 1:** Blockage ratio and gas flow velocities (1 atm, 293 K).

Bluff-body diameter $d$ /mm	20	30	40	50	60	70
Blockage ratio $B$	0.2	0.3	0.4	0.5	0.6	0.7
Gas velocity $V$ /(m/s)	1	2	5	10	20	50
$Re_D$	$4.0e+3$	$8.3e+3$	$2.2e+4$	$4.4e+4$	$9.1e+4$	$2.4e+5$

Composition PDF Transport Equation (C-PDF) is as follows:

$$\frac{\partial}{\partial t}(\rho P) + \frac{\partial}{\partial x_i}(\rho u_i P) + \frac{\partial}{\partial \psi_k}(\rho \omega_k P) = -\frac{\partial}{\partial x_i}[\rho \langle u_i'' | \psi \rangle P] + \frac{\partial}{\partial \psi_k} \left[ \rho \left\langle \frac{1}{\rho} \frac{\partial J_{i,k}}{\partial x_i} | \psi \right\rangle P \right]. \quad (2.3)$$

The two terms on the right-hand side represent the PDF change due to scalar convection by turbulent scalar flux and molecular mixing/diffusion, respectively.

The flow field researched in this paper is turbulence refer is to  $Re_D$  as shown in Table 1. Because the reaction rate highly nonlinear, modeling the mean reaction rate in a turbulent flow is extremely difficult. C-PDF is an alternative effective method to solve the premixed combustion in a turbulent flow. The principal strength of C-PDF transport approach is that the highly nonlinear reaction term is completely closed and requires no modeling. The turbulent scalar flux term is modeled by gradient-diffusion assumption. The molecular mixing/diffusion is modeled by MC, IEM, or EMST models [13]. C-PDF transport model adopts a detailed chemical mechanism for modeling the reaction rate in a turbulent flame. With an appropriate chemical mechanism, kinetically controlled species such as CO and NO<sub>x</sub>, as well as flame ignition and extinction, can be predicted by C-PDF model. Bisetti and Chen [14] adopted Join-PDF/LES approach to research Sandia Flame D, and their result showed that the prediction by EMST is quite accurate near stoichiometric, but overall trend remains unpredicted at other conditions. While Lindstedt et al. [15] found that the numerical result is in good agreement with the experiment data by MC molecular mixing model, if it turns to IEM model, it cannot capture extinction and reignition. Finally, MC molecular mixing model was used in this paper.

C-PDF transport equation cannot be solved by finite volume method; a Lagrangian Monte Carlo [13] method has been used to solve it. Because time scales of some reactions are very fast, while others are very slow, disparity of time scales results in numerical stiffness problem. It means that extensive computational load is required to integrate the chemical source term. To solve the numerical stiffness problem, in-situ adaptive tabulation (ISAT) has been employed to dynamically accelerate the chemistry calculations. Correa and Pope [16] made use of this method to calculate the burning process for one bluff-body burner, and the numerical result was in coincidence with the experiment data.

Table 2 gives out the detailed chemical mechanism of hydrogen adopted in this paper.

**Table 2:** Hydrogen chemistry reaction.

No.	Reaction	$A_i$	$\beta_i$	$E_i$
1	$O_2 + H \Rightarrow OH + O$	$2.000E + 14$	0.00	70.30
2	$OH + O \Rightarrow O_2 + H$	$1.568E + 13$	0.00	3.52
3	$H_2 + O \Rightarrow OH + H$	$5.060E + 04$	2.67	26.30
4	$OH + H \Rightarrow H_2 + O$	$2.222E + 04$	2.67	18.29
5	$H_2 + OH \Rightarrow H_2O + H$	$1.000E + 08$	1.60	13.80
6	$H_2O + H \Rightarrow H_2 + OH$	$4.312E + 08$	1.60	76.46
7	$OH + OH \Rightarrow H_2O + O$	$1.500E + 09$	1.14	0.42
8	$H_2O + O \Rightarrow OH + OH$	$1.473E + 10$	1.14	71.09
9	$O_2 + H + M \Rightarrow HO_2 + M$	$2.300E + 18$	-0.80	0.00
10	$HO_2 + M \Rightarrow O_2 + H + M$	$3.190E + 18$	-0.80	95.39
11	$HO_2 + H \Rightarrow OH + OH$	$1.500E + 14$	0.00	4.20
12	$HO_2 + H \Rightarrow H_2 + O_2$	$2.500E + 13$	0.00	2.90
13	$HO_2 + OH \Rightarrow H_2O + O_2$	$6.000E + 13$	0.00	0.00
14	$HO_2 + H \Rightarrow H_2O + O$	$3.000E + 13$	0.00	7.20
15	$HO_2 + O \Rightarrow OH + O_2$	$1.800E + 13$	0.00	-1.70
16	$H + H + M \Rightarrow H_2 + M$	$1.800E + 18$	-1.00	0.00
17	$OH + H + M \Rightarrow H_2O + M$	$2.200E + 22$	-2.00	0.00
18	$O + O + M \Rightarrow O_2 + M$	$2.900E + 17$	-1.00	0.00
M	$H_2O/6.5 O_2/0.4 N_2/0.4/$	Third body efficiency		
Unit	$A_i$ -cm · mole · s · K, $\beta_i - 1$ , $E_i$ -kJ/mole.			

### 3. Validations of Mathematical Model

#### 3.1. Validations of Independence of Grid Size and Time Step

The studies on grid size and time step independence have been performed to determine the optimal grid and time step with a good accuracy for the simulation. Also, the k-epsilon-C-PDF model was used.

Table 3 gives out the grid size range which changes from 0.5 mm to 2.0 mm (the grid number varies from  $1.0e + 05$  to  $1.6e + 04$ ). The time step is, respectively, 0.05 ms, 0.10 ms, 0.20 ms, and 0.50 ms, as shown in Table 4. The average temperatures on section  $x = 150$  mm and  $x = 350$  mm were adopted to verify the accuracy of grid size and time step. Table 3 shows that on section  $x = 150$  mm, the average temperature at grid size  $\Delta = 1.0$  mm is only 1°C higher than that at grid size  $\Delta = 0.5$  mm. On section  $x = 350$  mm, the average temperature at grid size  $\Delta = 1.0$  mm is 13°C higher than that at grid size  $\Delta = 0.5$  mm. So, the numerical simulation is independent when grid size is  $\Delta = 1.0$  mm (the grid number is  $6.0e + 04$ ). Table 4 shows that on section  $x = 350$  mm, the maximum temperature error is only 20°C between time step 0.1 ms and 0.05 ms. So, when the time step is 0.1 ms, the numerical result does not rely on it.

Figure 3 shows the temperature curves at different grid size and time step. It indicates that when the grid size is 1.0 mm and the time step is 0.1 ms, the temperature error between the numerical result and the experiment data is extremely small. So, it can be included from the results that the optimal grid size is  $\Delta = 1.0$  mm and the optimal time step is  $\Delta t = 0.1$  ms.

**Table 3:** Grid size independence validation with time step 0.1 ms.

Grid size/mm	$\overline{T}_{x=150}/K$	$\Delta T/K$	$\overline{T}_{x=350}/K$	$\Delta T/K$	Grid amount
0.5	419	—	768	—	$1.0e+05$
0.8	420	1	760	8	$9.2e+04$
1.0	420	1	755	13	$6.0e+04$
1.5	415	4	707	61	$2.8e+04$
2.0	414	5	666	102	$1.6e+04$

**Table 4:** Time step independence validation with grid size 1.0 mm.

Time step/ms	$\overline{T}_{x=150}/K$	$\Delta T/K$	$\overline{T}_{x=350}/K$	$\Delta T/K$	Remark
0.05	424	—	775	—	—
0.10	419	5	755	20	Independent
0.20	405	14	707	68	Worse
0.50	402	22	604	171	Worse

### 3.2. Experiment Validation for Model Accuracy

Figure 4 shows the combustion device of Volvo Aero Corp. triangular bluff-body which has been widely used to research the flame stabilization mechanism both in terms of experiments and theoretical data. Over the years, many CFD researches relied on the experiment data of this device have been carried out to investigate its stabilized mechanism [2]. In order to validate the accuracy of the mathematical model, this combustion rig was used with Smagorinsky-Lily-LES-EDC (SL-LES-EDC) model, k-epsilon-EDC model, and k-epsilon-C-PDF model.

Geometry model and boundary conditions are as follows:

Length  $\times$  width  $\times$  height = 660  $\times$  240  $\times$  120 mm;

Side length of bluff-body with the equilateral triangular cross-section: 40 mm;

Inlet condition of mixture of air and propane:  $T = 288\text{ K}$ ,  $V = 17\text{ m/s}$ ,  $p = 1\text{ atm}$ , mass flow rate is 0.6 kg/s, equivalence ratio is  $\phi = 0.65$ ;

Outlet: pressure outlet;

Wall: adiabatic boundary;

Fuel oxidation was modeled by one-step global reaction:



The reaction rate is that proposed by Fluent Database according to Arrhenius Law [9].

$$\dot{\omega} = \frac{d[\text{C}_3\text{H}_8]}{dt} = -4.836 \times 10^{-9} e^{-15100/T} \times [\text{C}_3\text{H}_8]^{0.1} [\text{O}_2]^{1.65}. \quad (3.2)$$

The Reynolds number based on the bluff-body burner device and on the velocity at the bluff-body location is about  $10^5$ . The flow field is simulated using compressible N-S equations.



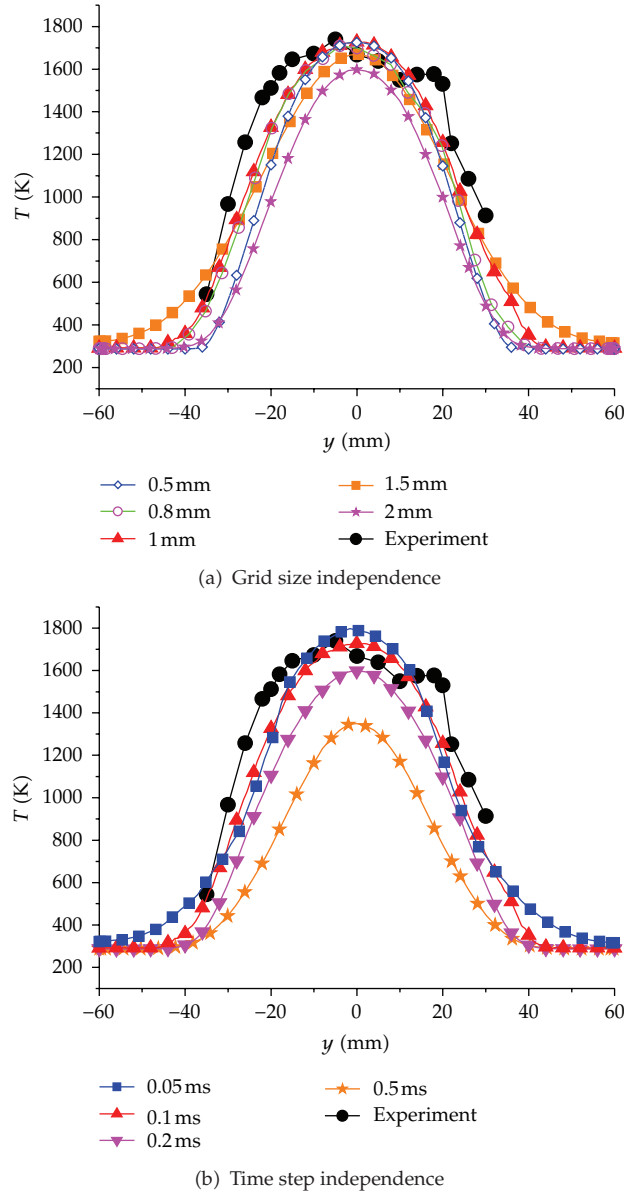


**Figure 3:** Profiles of temperature on section  $x = 150$  mm at different grid size and time step.

Figures 5, 6, and 7 show the comparison between numerical results and the experiment data. The results indicate that SL-LES-EDC model will overpredict the recirculation length and underestimate its width. Giacomazzi et al. [9] found that FM-LES-EDC model can accurately predict the recirculation zone position, but in combustion flow field, it will underestimate the velocity nearby the channel wall, and it may be because of the disadvantage of the FM-LES-EDC in dealing with the turbulent viscosity nearby the channel wall. Relatively, the k-epsilon-C-PDF, k-epsilon-EDC, and SL-LES-EDC models can predict the velocity better than FM-LES nearby the channel wall.

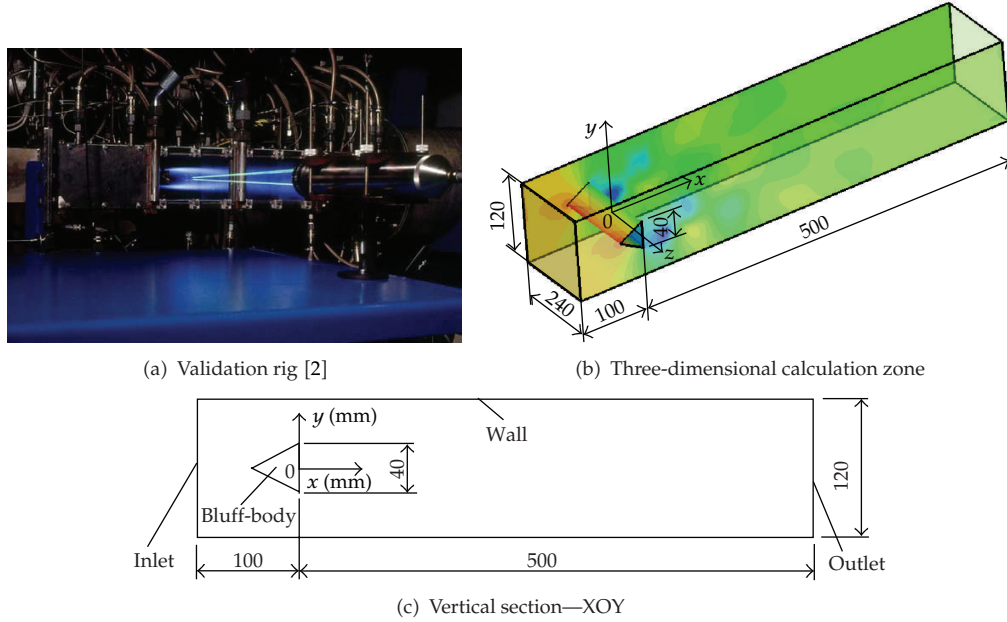


**Figure 4:** Validation rig and calculation zone geometry.

Figures 7 and 8(b) show that in reacting case, SL-LES-EDC model will overestimate the flame width and the temperature in the flame zone. The maximal temperature of the flame from SL-LES-EDC is 400 K higher than that of the experiment data. The k-epsilon-EDC model will also overestimate the temperature in the flame center, but it will underestimate the flame temperature at the outside of the flame zone (see Figures 7 and 8(c)). Figure 7 shows that FM-LES-EDC can relatively accurately predict the flame temperature, except for the maximal temperature, and it will overestimate its value about 100 K. In spite of this situation, it can reproduce the flame vortex structures and the flame periodic fluctuation. Compared with FM-LES-EDC model, k-epsilon-C-PDF can predict the flame temperature more accurately but it cannot capture the flame vortex shell accurately.

In a word, the agreement observed between k-epsilon-C-PDF model result and published classics experiment data is acceptable. The k-epsilon-C-PDF combustion model can accurately predict the flame temperature, while SL-LES-EDC model can accurately predict the vortex structures and explain the extinction mechanism.

Figure 9 shows the comparison of recirculation zone between cold field and combustion field based on k-epsilon-C-PDF model. The figures indicate that the performance of recirculation zone of combustion field is apparently different from that of the cold flow. The recirculation length of combustion field is about two times more than that of the cold flow. This should be attributed to the flame fluctuation and the dramatic heat releasing from chemistry reaction. The flame propagation extends the axis momentum of the velocity and lengthens the recirculation zone further downstream from the bluff-body.

Figure 10 shows the streamlines of cold field and combustion field from SL-LES-EDC model and k-epsilon-CPDF model. The results show that, in the cold field, SL-LES-EDC model can capture the asymmetric von Karman vortex street at the wake zone of the bluff-body. The period of the vortex shedding is 110 Hz, in agreement with the measurements

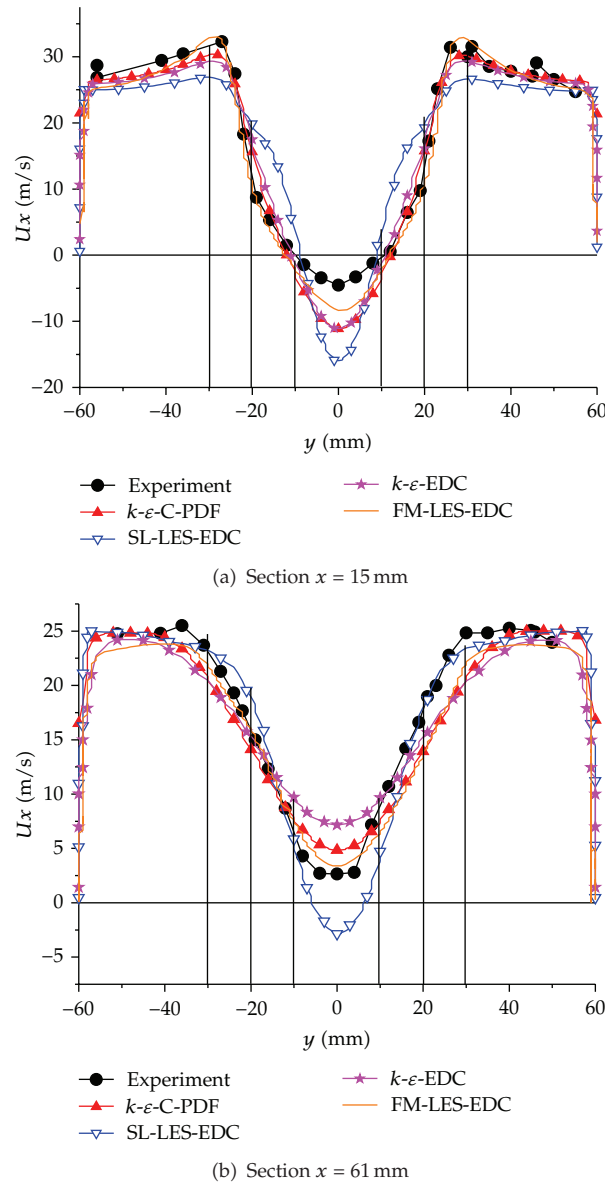


**Figure 5:** Profile of  $U_x$  of cold field at sections (a)  $x = 15$  mm, (b)  $x = 61$  mm.

(105 Hz) [9]. The asymmetric von Karman shedding of coherent vortices no longer exists in the reacting case. Shanbhogue et al. [1] attributed this absence of Karman vortex street for reacting case to the dilatation effect of the heat release. However, what can be concluded from the numerical simulation is that the asymmetric Karman Vortex Street does not disappear in the reacting case, it just converges with the downstream nearby the bluff-body, and the direction of the vortex at the wake zone is still also changed periodically.

Figure 10 shows that k-epsilon turbulent model cannot capture the asymmetric von Karman vortex street shedding, while the model can just capture the central recirculation zone after the flameholder. Also, in the cold field, k-epsilon model can predict the velocity

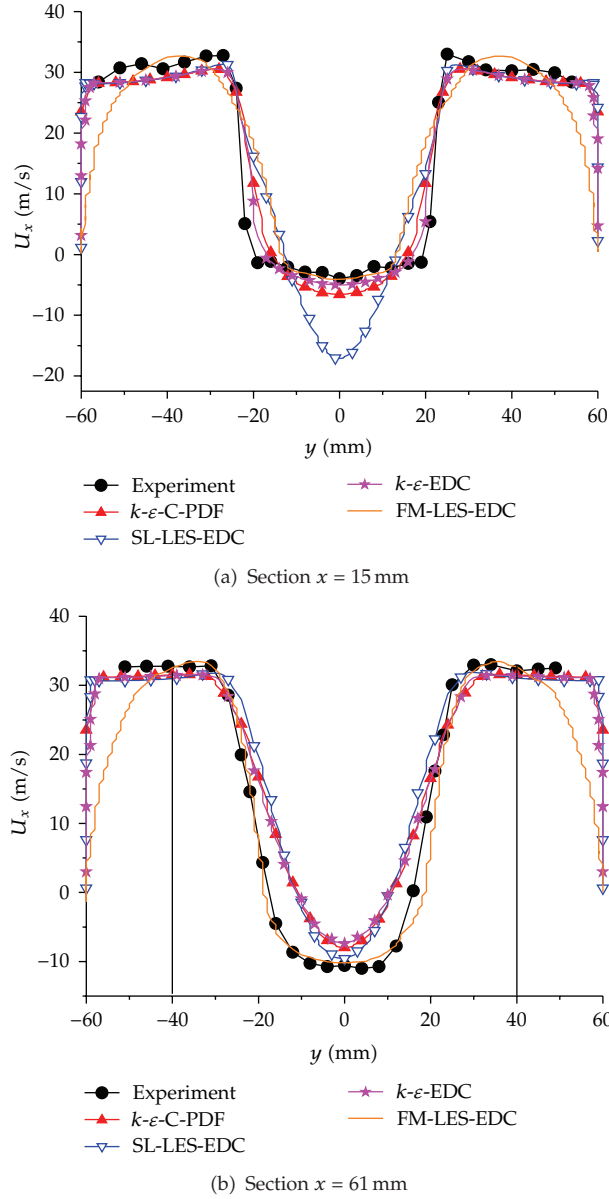


**Figure 6:** Profile of  $U_x$  of combustion field at sections (a)  $x = 15$  mm, (b)  $x = 61$  mm.

fluctuation like “a polliwog tail” alternation periodically. That is because the dilatation effect of the heat releases possessing the dominant influence than the fluctuation of Karman Vortex Street. Figure 11 gives out an image of a combustion experiment based on a triangular bluff-body [1].

Figure 12 shows the extinction process of the triangular bluff-body combustion field. What can be included from the numerical is that the entire extinction process experiences three phases: (1) the appearance of discontinuous flame; (2) the flame local extinction and reignition in the recirculation zone; (3) global extinction.

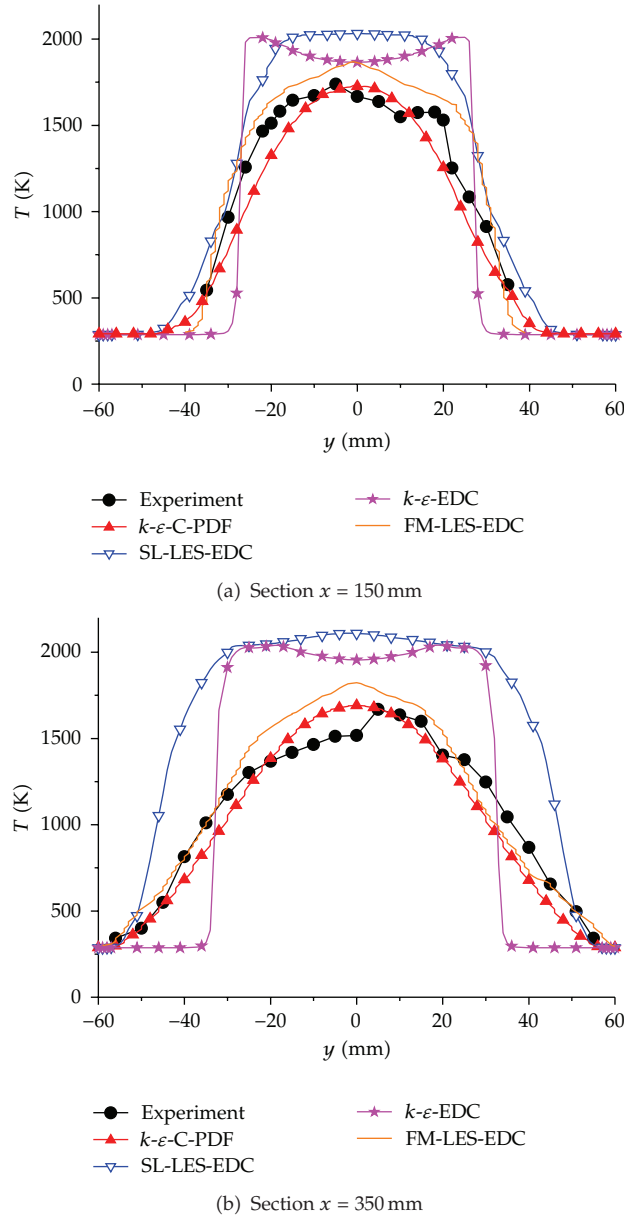
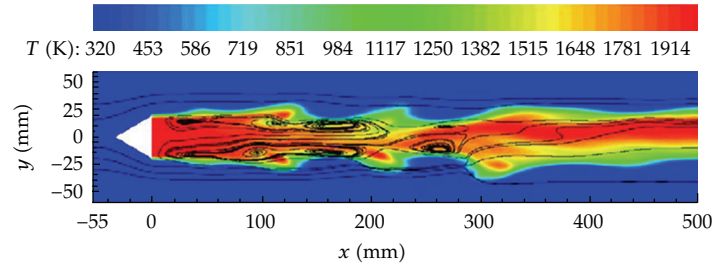


**Figure 7:** Profiles of temperature at sections (a)  $x = 150$  mm, (b)  $x = 350$  mm.

- (1) Discontinuous flame: when the equivalence ratio is close to blow off, the flame temperature would decline rapidly, chemistry reaction would be slower, and the heat transfer and dissipation to the flame sheet can ignite the fresh mixture and, finally, induce the discontinuous flame. The first discontinuous position presents at the recirculation zone stagnant point.
- (2) Local extinction and reignition: if the cold mixture is heated up and reignited by flame kernel exactly, the flame is at critical blowout limit state of being acute and





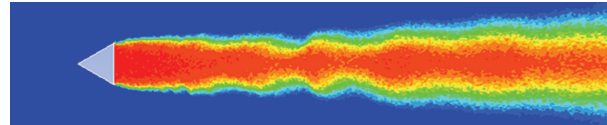
(a) Temperature field from Eugenio by FM-LES-EDC [9]



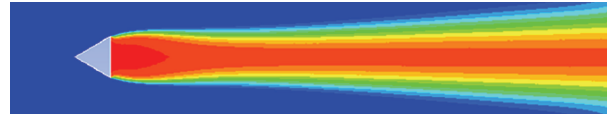
(b) Instantaneous temperature by SL-LES-EDC model



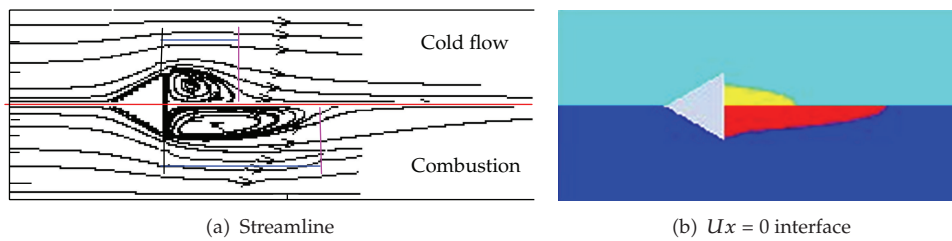
(c) Instantaneous temperature by k-epsilon-EDC model



(d) Instantaneous temperature by k-epsilon-C-PDF model



(e) Mean temperature by k-epsilon-C-PDF model of 10 periodic

**Figure 8:** Comparison of temperature field by different mathematical model.**Figure 9:** Comparison of recirculation zone between cold flow and combustion field.

unstable. The local extinction and reignition will alternately appear in the recirculation zone. During the blow off, significant fragmentation of the flame occurred, with branches of flame remaining anchored in the bluff-body wake zone.

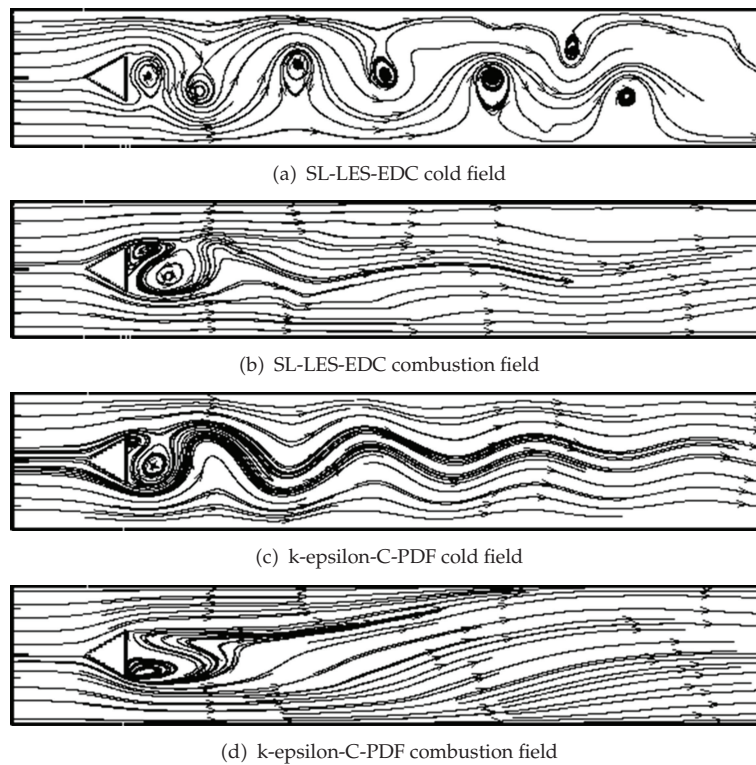


**Figure 10:** Streamline of cold flow field and combustion field.

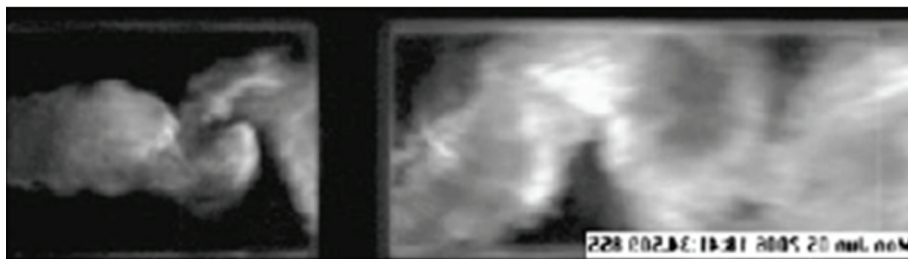


**Figure 11:** Image of combustion experiment [1].

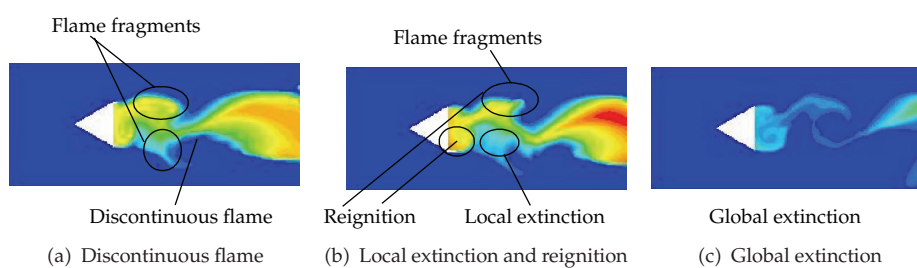


**Figure 12:** Extinction process.

- (3) Global extinction: the fame pockets moved to the downstream of the recirculation and finally induced the global extinction. Overall blow off occurred with the gradual elimination of these flame fragments and local extinction [1].

## 4. Result and Analysis

### 4.1. Hydrogen Rich Blowout Limit

H<sub>2</sub> RBL is defined as the mole fraction of H<sub>2</sub> in the mixture. It is the H<sub>2</sub> mole concentration limit beyond which the extinction will occur. So, it is dimensionless (%) consider

$$\text{RBL} = \frac{n_{\text{H}_2}}{n_{\text{mixture}}}, \quad (4.1)$$

where,  $n_{\text{H}_2}$ -mole flow rate of H<sub>2</sub> in mixture,  $n_{\text{mixture}}$ -mole flow rate of mixture. Because the higher H<sub>2</sub> RBL means the wider operation range and the mixture species can change in a wider range. And it is beneficial for the bluff-body burner, so it is interesting to find a way to improve H<sub>2</sub> RBL.

Table 5 and Figure 13 show the numerical results of H<sub>2</sub> RBL at different blockage ratio and gas velocities. It can be found that when blockage ratio remains unchanged, H<sub>2</sub> RBL decreases as gas flow velocity is increased. The increasing of the gas velocity will enhance the flow fluctuation and the turbulence intensity, at the same time, the convection and conduction between reactant and product will be improved, and the burning will be enhanced. But when the gas velocity is too large, the flame is close to blowout limit, the turbulence fluctuation will affect the flame's propagation greatly near blowout flames. There will be more and more burning mass which will penetrate into the cooling mixture, at the same time, fresh reactants will penetrate through the CRZ from the flame forward region and abundant of flame fragments will occur, then the separate flame fragments will move randomly inside the CRZ or cooling mixture. When the heat released from chemical reaction is not sufficient to maintain its burning, the flame local extinction will occur. In a word, the main reason of flame blow-out is the generation and elimination of the flame fragments caused by gas velocity increase. So the flame blow out will be approached by increasing the gas velocity, and increasing the mainstream velocity has an adverse effect on flame flammability. This conclusion is accordance with that of EL-feky and Penninger [17] and Dawson's [5] experiment result. Shanbhogue [1] also found that temporally localized extinction occurred sporadically on near blow off flames. Under certain conditions the flame cannot persist indefinitely when Re is too large. The number of local extinction per unit time increase as blow off is approached, and the ultimate blow off event results from more and more local extinction. His conclusion does also support the conclusion summarized in this paper, and the numerical results from the present work are in accordance with his conclusion.

Table 5 and Figure 13 also show that when the gas velocity remains unchanged, the H<sub>2</sub> RBL will rise first and decline later as the blockage ratio is increased. It means that there will be an optimal blockage ratio (in the present work, the optimal blockage ratio is  $B = 0.5$ , as shown in Figure 13(b)) which can stabilize the flame best. Also at the optimal blockage ratio, the H<sub>2</sub> RBL will reach the largest value. Blockage ratio has a very important effect on the flame geometry, flow speeds, and CRZ length which will influence the flame stability greatly. When the blockage ratio is increased, both the length of CRZ and the gas velocity at the bluff-body channel will increase rapidly. However, they have an opposite effect on H<sub>2</sub> RBL; for

**Table 5:** H<sub>2</sub> RBL (volume concentration).

$V$	$B$					
	0.2	0.3	0.4	0.5	0.6	0.7
1	0.775	0.782	0.783	0.786	0.779	0.777
2	0.765	0.775	0.774	0.776	0.770	0.767
5	0.753	0.763	0.763	0.765	0.757	0.754
10	0.745	0.755	0.753	0.754	0.749	0.746
20	0.735	0.743	0.743	0.745	0.740	0.737
50	0.723	0.728	0.728	0.731	0.725	0.724

example, the H<sub>2</sub> RBL will rise as the length of CRZ is increased, while it will decrease as the gas velocity is increasing. As a result, there would be an optimal blockage ratio. So, the curves in Figure 13(b) are concave. Frolov et al. [3] have carried out the same conclusion about the optimal bluff body diameter by numerical simulation and experiment. Wright [4] found that the maximum blow off speed will occur at  $B = 0.35$  for flat-plate flame-holders. He found that the blockage ratio has a very important effect on the flame geometry, flow speeds, and CRZ length which will influence the flame stability greatly.

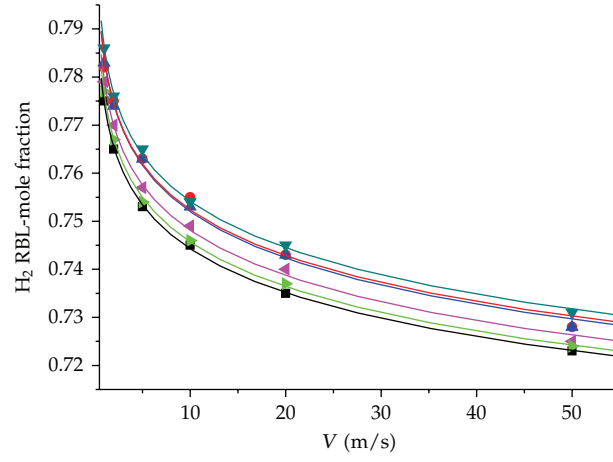
In a word, the H<sub>2</sub> RBL will be improved by decreasing the gas velocity, or by increasing the blockage ratio before the optimal value. But if the blockage ratio increases when it has exceeded the optimal value, the H<sub>2</sub> RBL will decline. So, when the surroundings remain unchanged in bluff-body burner, the H<sub>2</sub> RBL is a function of gas flow velocity and blockage ratio. To investigate the relationship between gas flow velocity, blockage ratio, and H<sub>2</sub> RBL, the gas velocity has been denoted by logarithmic coordinates (named, logarithmic velocity- $\lg V$ ) as shown in Figure 14(a). It can be seen that the function relationship between H<sub>2</sub> RBL and  $\lg V$  is nearly linear. The H<sub>2</sub> RBL will linearly decline with the increase of  $\lg V$ , so the H<sub>2</sub> RBL fitting formula could be assumed as follows:

$$Y = a \lg V + b \quad (a, b \text{-undetermined coefficient}). \quad (4.2)$$

Linear fitting of the numerical data results by Least Square Method, and the value of  $a$ ,  $b$  can be gained as shown in Table 6. Figure 14(b) shows the numerical results and the fitting curve originated from fitting formula when  $B = 0.3$ . It can be concluded that the errors between the numerical results and fitting curve are very small, which means that the assumption of H<sub>2</sub> RBL is acceptable.

Figure 15 shows the relationship between  $a$  or  $b$  and  $B$ . Table 6 and Figure 15 show that as the blockage ratio increases, the slope  $a$  will increase first and decrease later, while the intercept  $b$  will decrease first and increase later. The relationship between  $a$  or  $b$  and  $B$  is approximately a quadratic function, so the formula for  $a$ ,  $b$  and  $B$  can be assumed as follows:

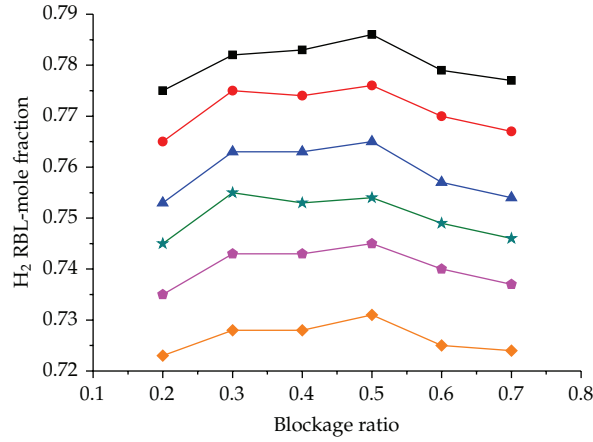
$$\begin{aligned} a &= m_0 + m_1 B + m_2 B^2, \\ b &= n_0 + n_1 B + n_2 B^2. \end{aligned} \quad (4.3)$$



Blockage ratio



(a) Linear coordinate



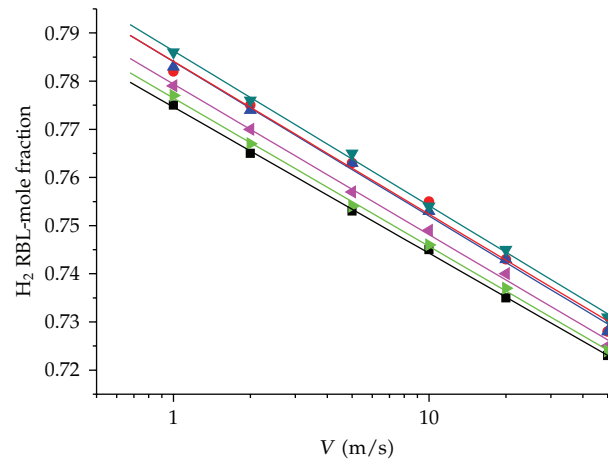
(b) Curves of H<sub>2</sub> RBL versus blockage ratio

**Figure 13:** H<sub>2</sub> RBL versus gas flow velocity and blockage ratio.

Fitting the curve with a quadratic function by Least Square Method, then a formula for  $a$ ,  $b$  and  $B$  can be summarized as follows ( $V \leq 50$  m/s):

$$\begin{aligned} a &= -0.02646 - 0.025088B + 0.027977B^2, \\ b &= 0.75327 + 0.145B - 0.1625B^2. \end{aligned} \quad (4.4)$$





Blockage ratio

■ 0.2

● 0.3

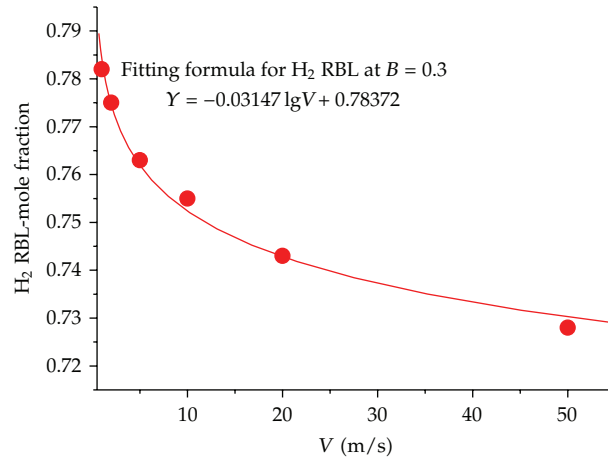
▲ 0.4

▼ 0.5

▼ 0.6

▼ 0.7

(a) Logarithmic coordinate



● Numerical result

— Fitting curve

(b) Linear coordinate

**Figure 14:** Curves of  $H_2$  RBL versus gas flow velocity and fitting curve (the symbols are numerical results and the lines originate from the fitting formula).

Figure 16 shows that the distance from the bluff-body to the recirculation center will increase as the blockage ratio increases, and so does the recirculation length. But while the blockage ratio remains unchanged, the position and length of the recirculation region is unchanged, no matter how large the flow velocity is. It means that blockage ratio significantly influences the recirculation region length. Wright [4] found that when the situation is approaching to blow off, the residual flame occupies just the recirculation zone region, and the recirculation-zone length remains unchanged. Only the blockage has a strong influence

**Table 6:** Fitting formulas about H<sub>2</sub> RBL and gas flow velocity.

$B$	RBL fitting formula/100%
0.2	$Y = -0.03035 \lg V + 0.77462$
0.3	$Y = -0.03147 \lg V + 0.78372$
0.4	$Y = -0.03205 \lg V + 0.78404$
0.5	$Y = -0.03212 \lg V + 0.78627$
0.6	$Y = -0.03125 \lg V + 0.77937$
0.7	$Y = -0.03080 \lg V + 0.77650$

on recirculation-zone length. For a given blockage ration, the wake with after the bluff-body is virtually constant, independent of mixture ratio and flow speed. So, people cannot judge the blowout limit just by recirculation length.

#### 4.2. Ignition Process Analysis

The simulation of ignition process is done in the condition of  $d = 30$  mm,  $V = 2$  m/s, and equivalence ratio  $\phi = 0.5$ . A small zone is patched with high temperature, so the burning will begin. With the development of ignition process, the flame flied becomes stable after  $t = 200$  ms, and the calculation of ignition process continues to  $t = 500$  ms for ensuring the stability of the flow field. When  $t = 500$  ms, reduce the H<sub>2</sub> volume concentration to 0.095 ( $\phi = 0.25$ , below the H<sub>2</sub> RBL) to simulate the extinction process.

Start ignition:  $t = 0$  ms (equivalence ratio is  $\phi = 0.5$ );

Ignition process:  $t = 0$ –500 ms;

Extinction process:  $t = 500$ –1400 ms (equivalence ratio is  $\phi = 0.25$ ).

First half parts of Figure 17 (before the vertical dash line) and Figure 18(a) show the species mass fraction and temperature distribution of section  $x = 40$  mm in ignition process. When  $t = 100$  ms, the average temperature of section  $x = 40$  will increase sharply, so does the mass fraction of H<sub>2</sub>O, OH, O, H, while the mass fraction of hydrogen and oxygen will decrease greatly, these phenomena mean that the flame has been ignited at this time. In the period of 100 ms to 200 ms, the average temperature of section  $x = 40$  mm will decrease suddenly, and meanwhile, the mass fraction of H<sub>2</sub>O, OH, O, and H will also decrease, and then remain unchanged. The concentration of H<sub>2</sub> and O<sub>2</sub> would rebound after  $t = 100$  ms, and this means that the flame is not stable until  $t = 200$  ms, so it can be seen that the ignition sequence is not successful until  $t = 200$  ms.

Figure 18(a) shows the temperature field of whole ignition process. There is a fluctuation of the flame during ignition process as shown in Figures 17 and 18(a) This is mainly because when the burning has just taken place first in CRZ, a large amount of combustion and intermediate products generated with heat releasing from chemical reaction, but the heat and the intermediate products cannot spread to the main stream immediately, and they would accumulate rapidly at this time. While  $t = 100$  ms, the remainder reactants and the accumulated intermediate products have almost been consumed completely. In order to maintain burning, fresh reactants are required, and at this moment, the heat which spread to the main stream from recirculation zone is more than the heat released from burning, so the temperature and the chemical reaction in the recirculation zone will decline. When  $t = 200$  ms, the heat released from fresh burning in the recirculation zone is adequate to compensate for the heat taken away by the main stream, and up to now, the combustion is steady.

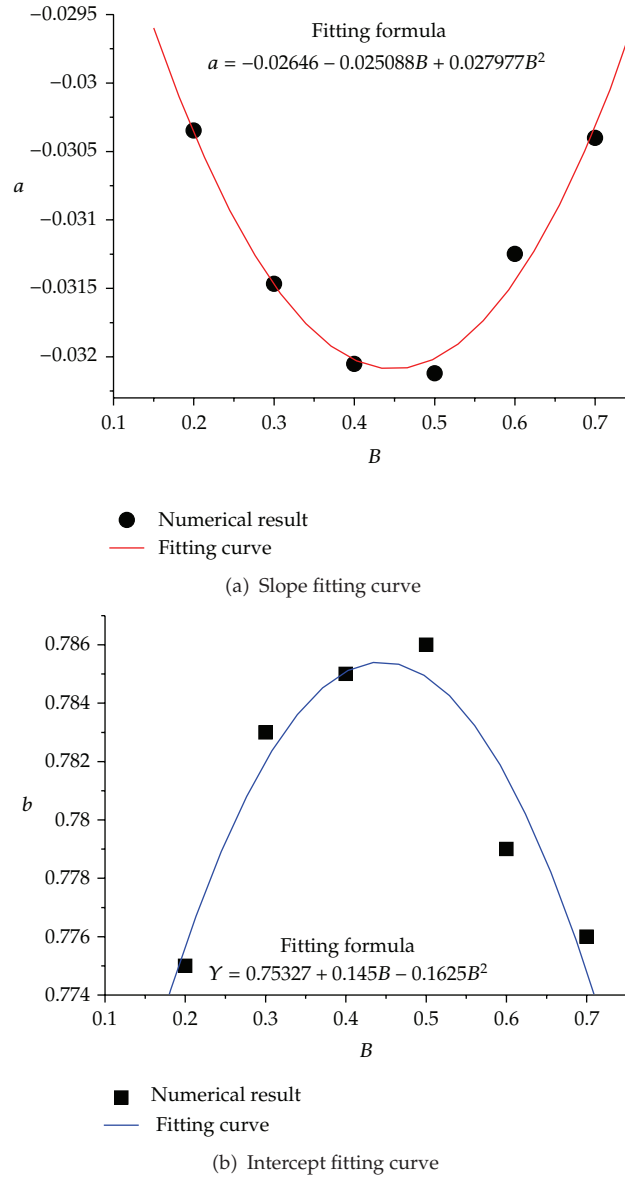


**Figure 15:** Slope and intercept of fitting function of  $H_2$  RBL versus blockage ratio  $B$ .

It can be concluded that a successful ignition sequence in a bluff-body burner requires three phases: (1) the startup of ignition in the recirculation zone; (2) the energy accumulation in the recirculation zone; (3) the flame propagation from the recirculation zone to the main stream.

### 4.3. Extinction Process Analysis

When  $t = 500$  ms, in order to investigate the flame extinction process, hydrogen concentration was reduced to 0.095 (lower than the flammable limit), and the extinction will happen.

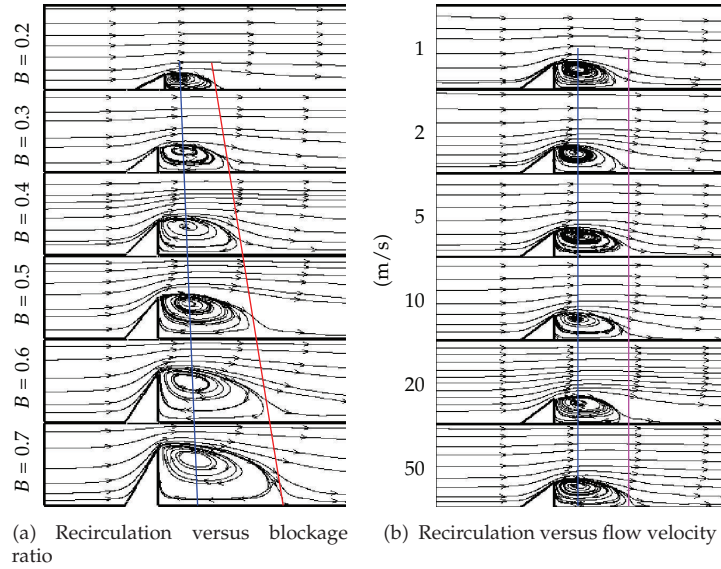


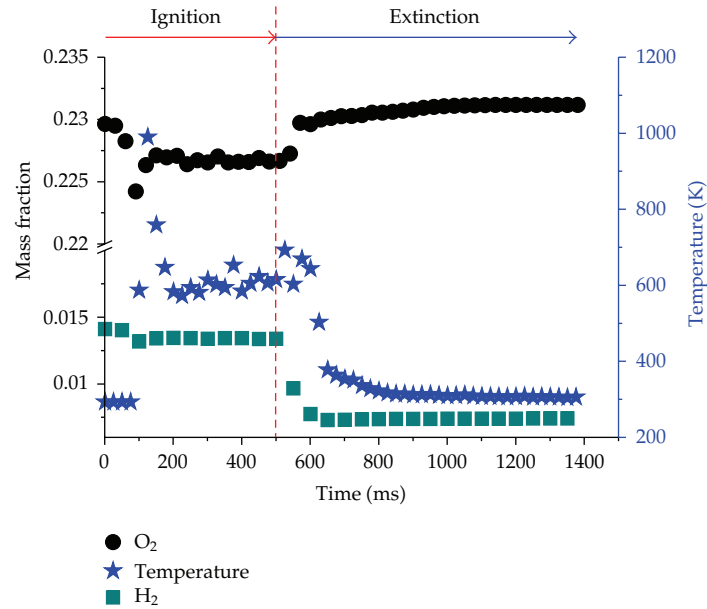
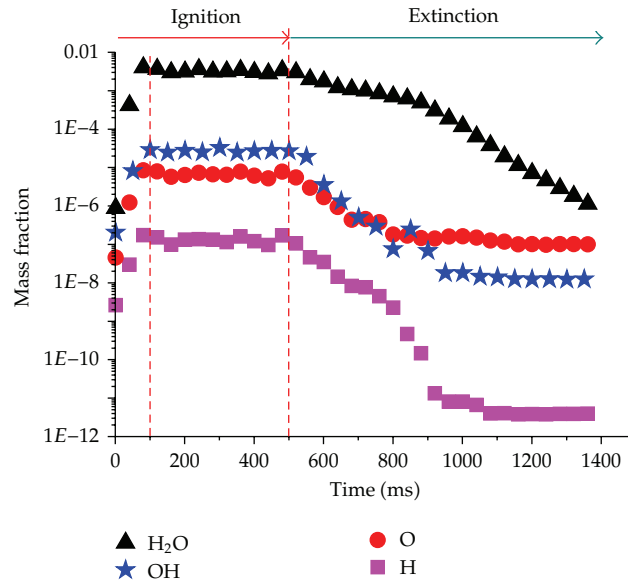
**Figure 16:** Streamlines of recirculation zone.

Latter half parts of Figure 17 (after the vertical dash line) show that it takes about 100 ms for the whole combustion field to reduce  $H_2$  mass fraction to the new value 0.095. It can be seen from Figure 17 that the whole extinction process takes about 600 ms, which is longer than ignition. When  $t = 600$  ms, the fresh mixture has reached the CRZ completely, and the gas concentration in the recirculation is below the flammable limit, but the flame does not extinguish immediately, this is because the energy dissipation from the recirculation zone to the main stream is slow, so the temperature in the recirculation zone is still high enough to maintain the burning for a while, and the flame will not extinguish until the energy in the recirculation totally diffuse to the main flow after the temperature in the recirculation zone reduces to the extinguish level, and the flame goes out totally as Figure 18(b) shows.

During  $t = 600\text{--}800$  ms, the temperature attenuation rate would reach a new value, meaning that the burning is still going on below  $H_2$  RBL, and the flame length would reduce gradually. When  $t = 800\text{--}1400$  ms, the average temperature will slowly decrease to the cold field level, this process is the burning of remaining gas in the recirculation. So far, the flame has extinguished completely. Figure 18(b) shows that the flame will take an “M” shape with reaction fronts inside the CRZ near the blow off condition. This flame shape is in well agreement with that gained by Dawson et al. [5] in their experiment measurement.

In a word, C-PDF model is accurate enough to capture the flame extinction. In terms of control of marine power, it can be concluded that the flame will extinguish as soon as the average temperature is lower than that at 800 ms. Feedback should be provided to fuel and air control system promptly to regulate fuel supply in order to avoid extinction.

So, a complete flame extinction process requires three phases: (1) the sudden decline of temperature in the burner because of the decline of fuel concentration; (2) the energy dissipation from the recirculation zone to the main stream; (3) the flame complete extinction.

(a)  $O_2$ ,  $H_2$ , Temperature(b)  $H_2O$ ,  $OH$ ,  $H$ 

**Figure 17:** Profiles of species average mass fraction and average temperature on section  $x = 40$  mm versus time from ignition (0–500 ms) to extinction (500–1400 ms).

#### 4.4. Sensitivity Analysis for Chemistry Reaction

The sensitivity analysis is a powerful tool in interpreting the results of computational simulations, and it can be used to research the influence of temperature, species concentration, and equivalence ratio on each elementary reaction [18, 19]. Rate-of-production analysis provides



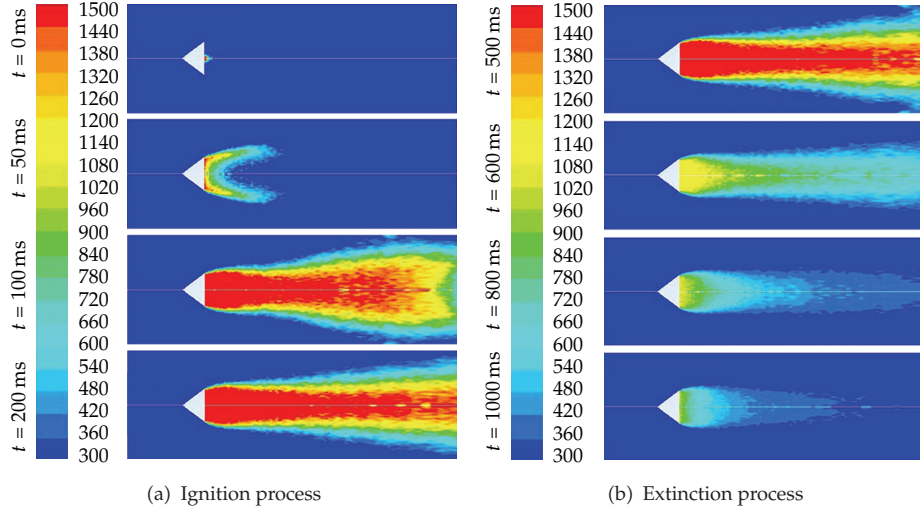


**Figure 18:** Temperature distribution from ignition process to extinction process.

complementary information on the direct contributions of individual reactions to species net production rates.

To investigate the contribution of each elementary reaction to  $H_2$  burning, the software CHEMKIN [18] was used to analyze the first-order sensitivity coefficient of temperature and species according to the  $H_2$  18 steps reaction mentioned earlier in the paper. Finally, make use of sensitivity coefficient to investigate the ignition and extinction process. CHEMKIN assumes a variable  $Z$  as

$$\frac{dZ}{dt} = F(Z, t, \vec{a}), \quad (4.5)$$

where  $Z = (Y_1, Y_2, \dots, Y_k)^T$  are standards for mass fraction of each species,  $\vec{a} = (A_1, A_2, \dots, A_N)$ -preexponential factor of each species, and the first-order sensitivity coefficient is defined as

$$w_{l,i} = \frac{\partial Z}{\partial a_i}, \quad (4.6)$$

$$\frac{dw_{l,i}}{dt} = \frac{\partial F_l}{\partial Z} \cdot w_{l,i} + \frac{\partial F_l}{\partial a_i}.$$

For heat-of-formation sensitivity,  $\vec{a}$  represents the vector of heats of formation for all the species in the system. The change of  $\vec{a}$  will bring in the species concentration variety. The bigger sensitivity coefficient means the more significant influence caused by  $\vec{a}$ .

The equivalence ratio for calculation case in Figure 19 to Figure 23 was 1. Figure 19 shows that reaction R2 possesses the largest positive temperature sensitivity coefficient other than all the other elementary reactions. The sensitivity coefficient reaches the peak value at 1550 K. It indicates that at  $T = 1550$  K, a little temperature variation will induce a large chemistry reaction rate change for R2 and R9. So, temperature has a very important influence

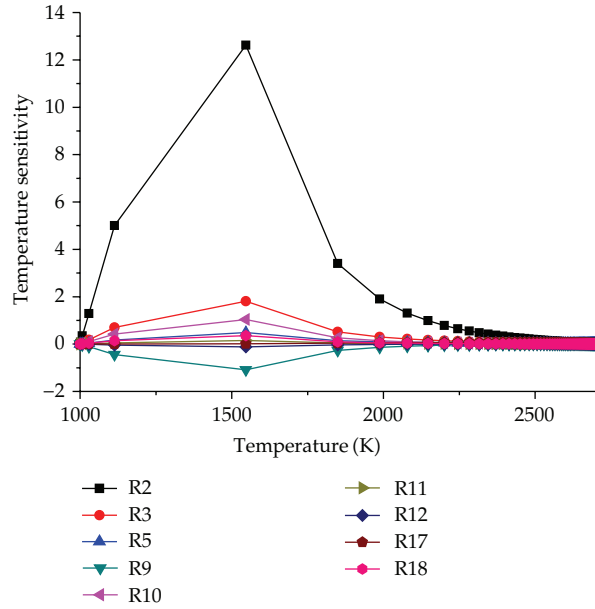


Figure 19: Temperature sensitivity for each reaction.

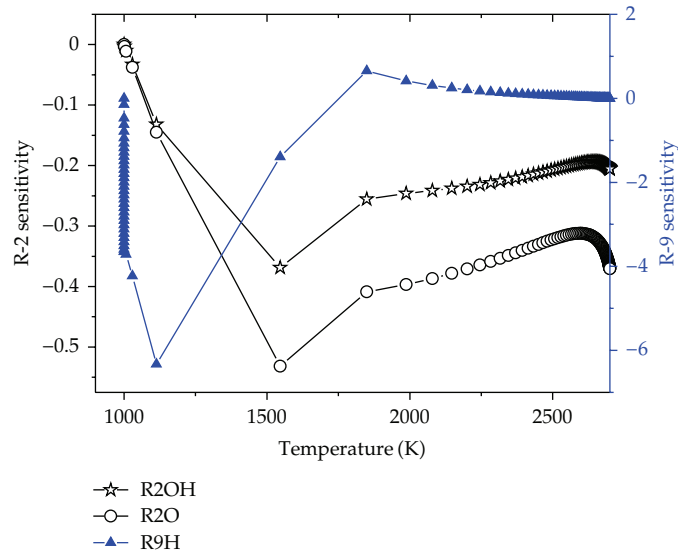


Figure 20: Temperature sensitivity for intermediate species of R2 and R9.

on reactions R2 and R9. According to formula (4.8), R2 is an exothermic reaction, so in ignition process, if we can improve the mixture temperature to 1550 K by a spark in a short time, the exothermic reaction R2 will occur immediately, and the heat will be released from R2 rapidly. So R2 is very important to ignition process. In contrast, reaction R9 possesses the largest negative temperature sensitivity coefficient in all the elementary reactions. It means that increasing its rate will lead to a lower temperature. So, reactions R2 and R9 dominate

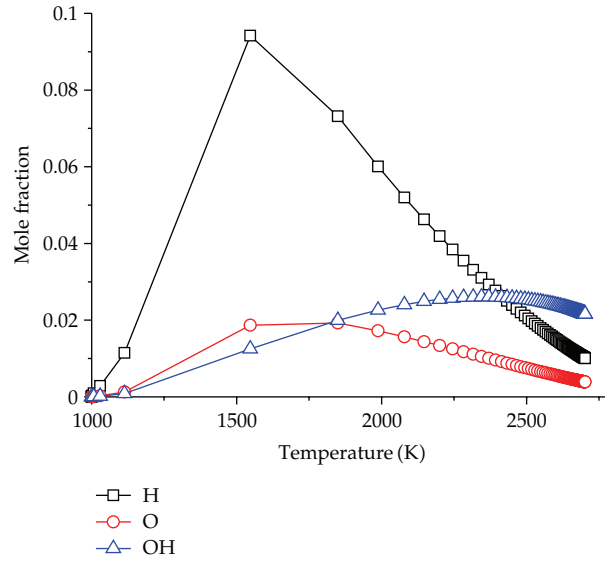


Figure 21: Profiles of intermediate species versus temperature.

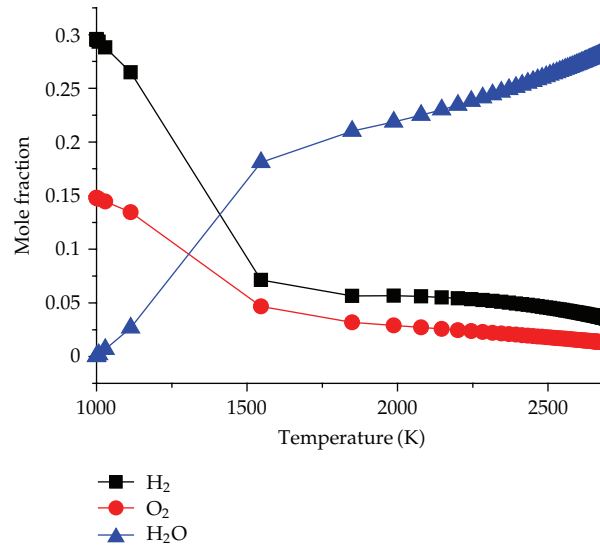
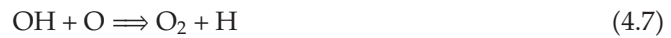


Figure 22: Profiles of reactants and production versus temperature.

the ignition and extinction processes. R9 ought to be the first reaction taking place in ignition process, and R2 ought to be the last one consider



$$\Delta h = [h(\text{O}_2) + h(\text{H})] - [h(\text{O}) + h(\text{OH})] = -70(\text{kJ}/\text{mole}) \quad (4.8)$$

To investigate the influence of species concentration on chemistry reaction, the species sensitivity of intermediate species (H, O, and OH), reactants, and production were carried

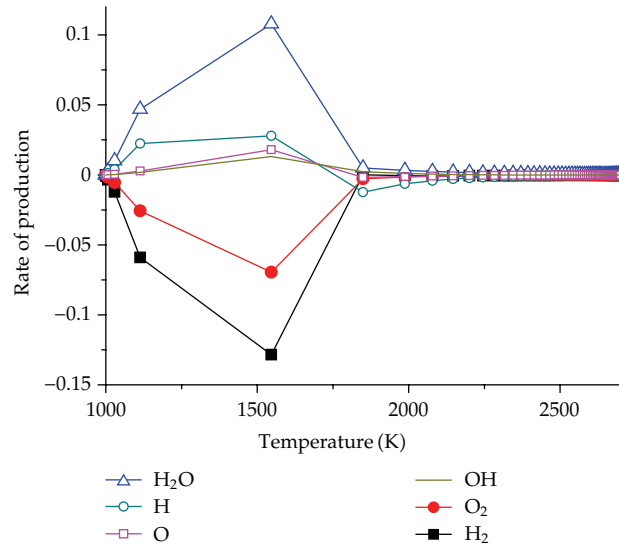


Figure 23: Rate of production versus temperature.

out. Figure 20 shows that to R2, the species sensitivity (O, OH) would decrease first and rise up later as temperature increases. When the temperature reaches 1550 K, the species sensitivity reaches the lowest value. It means that the species change rate reaches the maximum value. The H sensitivity of R9 reaches to the lowest value at 1120 K which is earlier than species O and OH, which indicates that reaction R9 ought to be taking place earlier than R2. Because in ignition process the fresh mixture must obtain heat from igniter source, the ignition will not be successful until the flame core accumulates enough heat. Figures 21 and 22 show that before 1550 K, the reactant (H<sub>2</sub>, O<sub>2</sub>) mole fraction will decline rapidly and the intermediate species and production concentration will rise greatly. It means that the endothermic reactions R1, R3, R5, and R9 take place immediately when the temperature rises from 1000 K to 1550 K. When the temperature exceeds 1550 K, the decreasing rate of species H<sub>2</sub> and O<sub>2</sub> is lower than that before 1550 K, which indicates that the flame was not ignited until  $T = 1550$  K.

Figure 23 shows that the consumed rate of the reactant (O<sub>2</sub>, H<sub>2</sub>) increases rapidly before 1550 K and changes a little when the temperature reaches to 1850 K then remains unchanged. The same is done to intermediate species (O, OH, H) and production. It indicates that the ignition is successful after  $T = 1550$  K, and the flame comes into being homeostasis after 1850 K.

Figure 24 shows the relationship between temperature sensitivity and equivalence ratio ( $\Phi = 0.1 \sim 10.0$ ). It can be seen that the temperature sensitivity of reaction R2 will rise first and decrease later as equivalence ratio increases. The temperature sensitivity reaches to the peak value when equivalence ratio rises to 2. When equivalence ratio is lower than 0.1 or higher than 10, the chemistry reaction will not take place because it has exceeded the combustibility limit. Figure 25 shows that the temperature sensitivity of R9 will decrease first and increase later with the increasing equivalence ratio, and it will reach the lowest value when equivalence ratio reaches 1. It means that when equivalence ratio is 1, the mixture is most ignitable. In a word, people can control the chemistry reaction process, flame temperature, or ignition process by adjusting the mixture equivalence ratio.

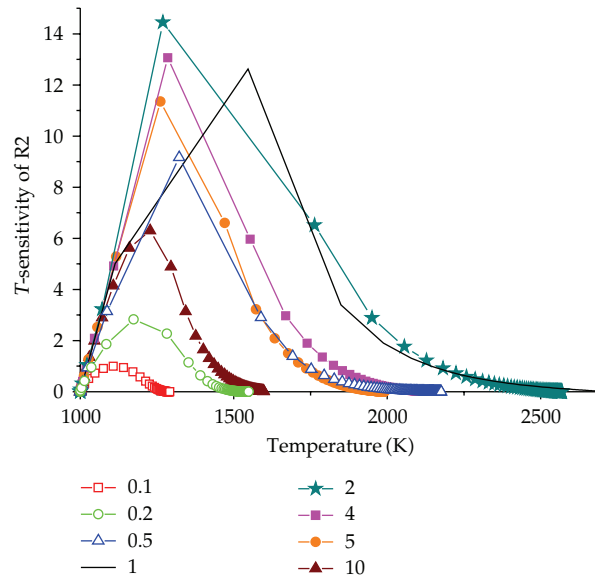


Figure 24: Temperature sensitivity coefficient of R2 versus equivalence ratio.

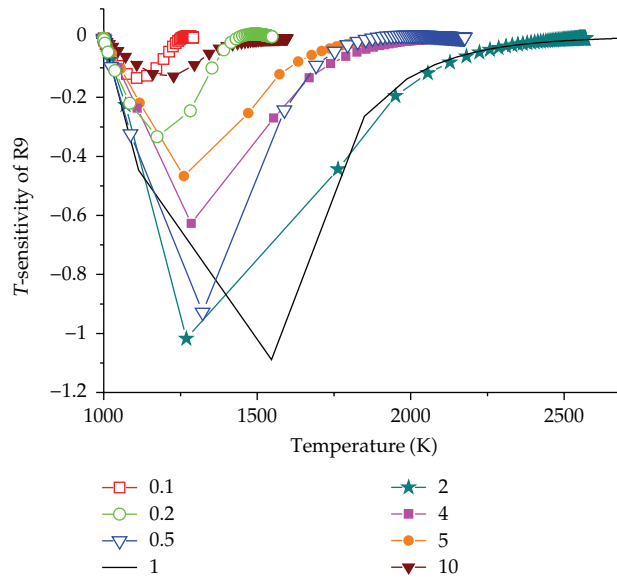


Figure 25: Temperature sensitivity coefficient of R9 versus equivalence ratio.

## 5. Conclusion

The numerical simulation on  $H_2$  premixed flame in a bluff-body burner has been carried out. The  $H_2$  flame ignition and extinction process is analyzed, and a function formula is summarized for  $H_2$  RBL. The results showed that k-epsilon-C-PDF model is a reasonable method to capture  $H_2$  RBL. There should be an optimal blockage ratio, which can stabilize the flame best. The flame will take an “M” shape with reaction fronts inside the CRZ



near the blow off condition. This research can provide theoretical instruction for bluff-body burner design, gas flow velocity control, fuel concentration matching, and the flame stability research. To systematically analyze the role of each elementary chemistry reaction taking place in the global combustion, CHEMKIN software was adopted to investigate the sensitivity of each elementary reaction. Other conclusions are as follows.

- (1) When the blockage ratio remains unchanged,  $H_2$  rich blowout limit is gas flow velocity's logarithmic function.
- (2) When the gas flow velocity remains unchanged,  $H_2$  rich blowout limit is blockage ratio's quadratic function.
- (3) The fitting formula of  $H_2$  rich blowout limit is  $Y = a \lg V + b$  ( $V \leq 50$  m/s), where,  $B$  is blockage ratio,  $a = -0.02646 - 0.025088B + 0.027977B^2$ , and  $b = 0.75327 + 0.145B - 0.1625B^2$ .
- (4) A complete extinction process in a bluff-body burner requires three phases, the suddenly decline of the temperature in the main stream, the energy dissipation from the recirculation zone to the main stream, and the flame complete extinction.
- (5) Reactions R2 and R9 possess the largest positive and negative temperature sensitivity. Increasing the rate of R2 will lead to a higher temperature, and increasing the rate of R9 will lead to a lower temperature. When equivalence ratio is 1, the mixture is most ignitable. The critical ignition temperature is 1550 K. Temperature has a very important influence on reactions R2 and R9.

## References

- [1] S. J. Shanbhogue, S. Husain, and T. Lieuwen, "Lean blowoff of bluff body stabilized flames: scaling and dynamics," *Progress in Energy and Combustion Science*, vol. 35, no. 1, pp. 98–120, 2009.
- [2] P. Eriksson, "The Zimont TFC model applied to premixed bluff body stabilized combustion using four different rans turbulence models," in *Proceedings of the Turbo Expo: Power for Land, Sea, and Air Conference*, pp. 353–361, Montreal, Canada, May 2007.
- [3] S. M. Frolov, V. Y. Basevich, and A. A. Belyaev, "Mechanism of turbulent flame stabilization on a bluff body," *Chemical Physics Reports*, vol. 18, no. 8, pp. 1495–1516, 2000.
- [4] F. H. Wright, "Bluff-body flame stabilization: blockage effects," *Combustion and Flame*, vol. 3, pp. 319–337, 1959.
- [5] J. R. Dawson, R. L. Gordon, J. Kariuki, E. Mastorakos, A. R. Masri, and M. Juddoo, "Visualization of blow-off events in bluff-body stabilized turbulent premixed flames," *Proceedings of the Combustion Institute*, vol. 33, no. 1, pp. 1559–1566, 2011.
- [6] P. Griebel, E. Boschek, and P. Jansohn, "Lean blowout limits and NOx emissions of turbulent, lean premixed, hydrogen-enriched methane/air flames at high pressure," *Journal of Engineering for Gas Turbines and Power*, vol. 129, no. 2, pp. 404–410, 2007.
- [7] R. W. Schefer, "Hydrogen enrichment for improved lean flame stability," *International Journal of Hydrogen Energy*, vol. 28, no. 10, pp. 1131–1141, 2003.
- [8] R. S. Barlow, J. H. Frank, A. N. Karpetis, and J. Y. Chen, "Piloted methane/air jet flames: transport effects and aspects of scalar structure," *Combustion and Flame*, vol. 143, no. 4, pp. 433–449, 2005.
- [9] E. Giacomazzi, V. Battaglia, and C. Bruno, "The coupling of turbulence and chemistry in a premixed bluff-body flame as studied by LES," *Combustion and Flame*, vol. 138, no. 4, pp. 320–335, 2004.
- [10] C. X. Lin and R. J. Holder, "Reacting turbulent flow and thermal field in a channel with inclined bluff body flame holders," *Journal of Heat Transfer*, vol. 132, no. 9, pp. 1–11, 2010.
- [11] W. W. Kim, J. J. Lienau, P. R. Van Slooten, M. B. Colket, R. E. Malecki, and S. Syed, "Towards modeling lean blow out in gas turbine flameholder applications," *Journal of Engineering for Gas Turbines and Power*, vol. 128, no. 1, pp. 40–48, 2006.
- [12] W. P. Jones and V. N. Prasad, "Large eddy simulation of the sandia flame series (D-F) using the Eulerian stochastic field method," *Combustion and Flame*, vol. 157, no. 9, pp. 1621–1636, 2010.

- [13] Ansys Fluent 12.0 Documentation.
- [14] F. Bisetti and J. Y. Chen, *LES of Sandia Flame D with Eulerian PDF and Finite-Rate Chemistry*, Combustion Modeling, Combustion Processes Laboratories, Berkeley, Calif, USA, 2005.
- [15] R. P. Lindstedt, S. A. Louloudi, and E. M. Váos, "Joint scalar probability density function modeling of pollutant formation in piloted turbulent jet diffusion flames with comprehensive chemistry," *Proceedings of the Combustion Institute*, vol. 28, no. 1, pp. 149–156, 2000.
- [16] S. M. Correa and S. B. Pope, "Comparison of a monte carlo PDF/finite-volume mean flow model with bluff-body raman dsata," in *Proceedings of the 24th Symposium International on Combustion*, pp. 279–285, The Combustion Institute, 1992.
- [17] S. M. S. El-feky and A. Penninger, "Study of flammability lean limit for a bluff body stabilized flame," *Periodica Polytechnica, Mechanical Engineering*, vol. 38, no. 1, pp. 33–45, 1994.
- [18] Reaction Design, "Theory manual," CHEMKIN Release 4. 1. 1.
- [19] Y. T. Liang and W. Zeng, "Kinetic simulation of gas explosion in constant volume bomb," *Journal of Combustion Science and Technology*, vol. 16, no. 4, pp. 375–381, 2010.